National Technical
University of Athens

SCHOOL OF NAVAL ARCHITECTURE AND MARINE ENGINEERING

Study of Environmentally Friendly Antifouling Coatings to Optimize the Energy Efficiency of Ships

Evangelia Kiosidou

Naval Architect and Marine Engineer, NTUA

Supervisor: D.I. Pantelis, Professor NTUA

A thesis submitted for the degree of

Doctor of Philosophy

Athens, March 2018

National Technical
University of Athens

SCHOOL OF NAVAL ARCHITECTURE AND MARINE ENGINEERING

Study of Environmentally Friendly Antifouling Coatings to Optimize the Energy Efficiency of Ships

Evangelia Kiosidou

Naval Architect and Marine Engineer, NTUA

Supervisor: D.I. Pantelis, Professor NTUA

A thesis submitted for the degree of

Doctor of Philosophy

Athens, March 2018

National Technical
University of Athens

SCHOOL OF NAVAL ARCHITECTURE AND MARINE ENGINEERING

Study of Environmentally Friendly Antifouling Coatings to Optimize the Energy Efficiency of Ships

Evangelia Kiosidou

Naval Architect and Marine Engineer, NTUA

PhD Advisory Committee	PhD Examination Committee
D.I. Pantelis, Prof. NTUA (Supervisor)	D.I. Pantelis, Prof. NTUA (Supervisor)
A. Karantonis, Asst. Prof. NTUA	A. Karantonis, Asst. Prof. NTUA
G. Tzabiras, Prof. NTUA	G. Tzabiras, Prof. NTUA
	E. Pavlatou, Prof. NTUA
	N. Tsouvalis, Prof. NTUA
	G. Triantafyllou, Prof. NTUA
	D. Manolakos, Prof. NTUA

A thesis submitted for the degree of

Doctor of Philosophy

Athens, March 2018

This thesis is dedicated to my family and especially to my newborn niece.

Acknowledgements

With the completion of the present Thesis, there are many people who I am deeply thankful to, because their contribution was more than significant, in order to conduct all the different types of experimets that were performed throughout this thesis. First of all I would like to express my gratitude to my PhD Advisory Committee:

I would like to deeply thank my PhD supervisor Prof. D.I. Pantelis for entrusting me this thesis, which was something totally new and challenging for me. Prof. D.I. Pantelis offered me also the opportunity to participate in a large-scale European Collaborative project, in the smaller-scale SFERA project twice, while he also gave me the opportunity to participate in a case study. All these tasks and projects enriched my scientific background, while they also helped me gain analytical thinking, self-descipline and, through his valuable guidance, a more mature professional attitude. Above all, though, I would like to thank him for giving me the freedom and support to undertake research on, until recently, unknown for me scientific fields. Prof. Pantelis always showed trust in my research instict and encouraged my research leaps, essentially contributing to the development of my character, helping me become responsible, decisive and initiative.

I am thoroughly grateful to Asst. Prof. Antonis Karantonis, whose support has been instrumental in getting this thesis to completion. I would like to thank him for his genuine interest in my research, his priceless scientific, technical and ethical support and suggestions and his constant encourangememnt throughout the PhD period. His natural enthusiasm and his attitude for helping and providing his knowledge to his students seamlessly, served as great motivation towards completion of this thesis. His immense knowldege in diversified disciplines played a catalytic role in finding solutions for very difficult scientific problems. Last but not least, Prof. Karantonis implanted me with the tenets of morality, kindness, modesty, generosity and dedication to research, which will always constitute life-values for me.

I am deeply grateful to Prof. George Tzabiras for his kindness and valuable guidance and advice towards the successful performance and interpretation of the hydrodynamic resistance tests. Professor Tzabiras showed me trust and encouraged me throughout the hydrodynamic investigation, providing solutions to scientific problems and helping me gain confidence on this scientific field. Along with Prof. Tzabiras I would like to thank all the people that I collaborated with, at the Laboratory of Ship and Marine Hydrodynamics, throughout these experiments. Hence,

I would like to thank Anastasios Venetis for the successful and effective collaboration during these experiments. Moreover, I would like to thank Spyros Ermidis for the short-term collaboration we had, during the design and 3D printing of the fouling units. However, successful completion of the experiments would not be feasible without the genuine interest, wide experience and extensive scientific and technical background of Dimitrios Liarokapis, George Mylonas, Ioannis Trachanas, Fotios Chasapis and Spyros Balis, who represent a model-team, that always finds or creates solutions even for the hardest problems. I am grateful because with them, successful completion of the experiments is always guaranteed, while they create a very nice and warm working environment. During these experiments, I collected very nice memories which I will always happily recall.

Moreover, starting with a chronological order, I would like to thank:

- Asst. Prof. Antonis Karantonis, of School of Chemical Engineering NTUA, for giving me thorough access to the facilities of the Laboratory of Physical Chemistry and Applied Electrochemistry, where all the electrochemical measurements of the present thesis were conducted (during the whole duration of the PhD), along with the measurements related to water quality (titration, pH, conductivity) and some supplementary measurements during determination of mechanical and physical properties of organic coatings. I am deeply thankful to Prof. Antonis Karantonis for making all these measurements feasible, and especially for the electrochemical measurements, which constitute a wide and essential part of the present Thesis.
- PhD Candidate George Sakalis, School of Naval Architecture and Marine Engineering, for his valuable contribution in the regression procedure of the experimental curves which were obtained through electrochemical impedance spectroscopy and are presented in Chapter 3 and in Appendices A and B. His effort and collaboration were priceless and much appreciated.
- CHROTEX company, starting with the owners, Mr. B. Nikologiannis and G. Tsimpoukis, who are always open to collaborations with the Academia and their company culture enhances and promotes scientific knowledge. I would like to thank the company for the sponsorship of the three types of painting systems (alkyd, polyurethane and aspartic polyurethane), which I examined in the beginning of my PhD. The technical staff of the company undertook professional application of the painting systems as well. More specifically, I would like to show my gratitude to Ms. A. Karana, M. Moschakou, A. Mavroudis, T. Tsoukatos and A. Gournia who offered their know-how generously and for offering me the opportunity to perform essential experiments in their facilities, such as König pendulum hardness, pull-off and gloss measurements, during the period that I was becoming familiar with the field of paints. The CHROTEX

staff were always friendly and amenable providing me with essential scientific and technical knowledge and helping me build a strong foundation in the field of organic coatings.

- WILCKENS company, for offering an alkyd and an antifouling system, during the same period as previously reported. I am thankful to Mr. E. Tsaousoglou who responded to our request and offered the paints.
- Prof. A. Moropoulou and especially Ms. E. Delegou, of School of Chemical Engineering NTUA, for offering access to the climatic chamber in School of Chemical Engineering, NTUA, in order to perform the accelerated aging tests.
- HALYVOURGIKI S.A. for offering us access to their facilities in Elefsis Gulf, thus, giving us the opportunity to perform the field tests. The static immersion tests included immersion of painted steel samples in 2.5 m depth in the territory of HALYVOURGIKI facilities, in a water channel which was in contact with the open sea. More specifically, I would like to thank Mr. I. Nikolaou, who responded to our request in 2013 offering access to the facilities. However, I am deeply thankful to Mr. I. Panagiotoulias, with whom I cooperated for the rest of the examination period of the specimens, i.e. during years 2013-2015. Mr. Panagiotoulias ensured easy access to the facilities, allowed collection of water samples from the immersion site and he was always kind and helpful. Many times he offered me advice and valuable information concerning geological or environmental issues concerning the Elefsis Gulf. I am deeply grateful to him, because with his help I managed to complete a very crucial experiment, with regard to the evaluation of antifouling marine paints.
- Prof. M. Ochsenkuehn-Petropoulou, of School of Chemical Engineering NTUA, for allowing us access to the FTIR equipment. More specifically, I would like to thank Dr. O. Serifi and Ms. B. Tsakanika for their willingness and valuable assistance in performing these measurements.
- Asst. Prof. C. Papadopoulos, of School of Naval Architecture and Marine Engineering NTUA, for giving us prompt access for use of the home-made hydrophobicity equipment.
- Ms. Kerasia Bikli and Mr. E. Prionas, with whom I cooperated during the period 2012-2013 and 2014-2015, respectively, during their graduation theses. Their eagerness and self-discipline, as well as their genuine ideas, were essential for the successful performance of the wide range of experiments, which were conducted during both diploma theses and helped in the progress of my PhD.
- The Professors of the Laboratory of Manufacturing Technology of School of Mechanical Engineering NTUA, G.-C. Vosniakos and D. Manolakos, for giving me access to the laboratory, in order to perform manufacturing processes related to the experimental setup for the flat plate experiments at Laboratory

of Ship and Marine Hydrodynamics. I would like to thank Mr. N. Melissas for his genuine interest and valuable contribution, with regard to the performance of these manufacturing tasks.

- Prof. E. Pavlatou, of School of Chemical Engineering NTUA, who facilitated prompt use of XRD and micro-Raman equipment. Also, I am grateful to PhD Candidate Ms. E. Rosolymou and Dr. E. Siranidi, for their valuable aid in performing the measurements on each equipment, respectively.
- The staff of the Shipbuilding Technology Laboratory, of School of Naval Architecture and Marine Engineering, C. Xanthis, A. Markoulis, Dr. C. Sarafoglou and T. Tsiourva for the nice cooperation and working atmosphere and their valuable assistance.

  My colleagues and friends from the Shipbuilding Technology Laboratory, Dr. N. Daniolos, Dr. K. Triantou, PhD Candidate P. Karakizis and PhD Candidate M. Kazasidis. I would like to deeply thank V. Bougiouri for her positive attitude, kindness, continuous support and valuable advice during my PhD. Vera is a trustworthy colleague and friend and I am really happy that we collaborated at the STL laboratory.

All my close friends who continuously encouraged and supported me.

Last but not least, I am deeply grateful to my family for their continuous patience and support throughout my PhD. Their support was pivotal for the completion of this thesis.

Abstract

In the present thesis, commercial and experimental antifouling painting systems were examined, in terms of antifouling, anticorrosion and hydrodynamic efficiency and with regard to their mechanical and physical properties. The examined paints were of silicone, polyurethane (PU) and acrylic formulations. Five antifouling (AF) systems were tested, while also an anti-corrosive system, without antifouling effect, was examined for comparative purposes. The experimental formulations were developed in the framework of the FP7 European Collaborative Project Foul-X-Spel (Grant Agreement 285552).The novelty of the experimental formulations arises from the immobilization of the biocide which minimizes leaching and was accomplished via a newly developed functionalization method, based on reaction of the biocide with highly reactive isocyanate functionality. All the examined painting systems are presented in Table 1.

Table 1: Painting systems examined

Painting system	Abbreviated name	Characteristics/ Type of action	Biocides
Silicone-based	Ref. Si	Commercial/ Foul-release	No biocides
Acrylic-based	Acrylic	Commercial/ Self polishing Copolymer(SPC)	10%≤Cu_2O≤25% 5%≤Zineb≤10%
Silicone-based	Exp. Si	Experimental	0.56% immobilized Econea
PU-based	Exp. PU (or Exp. PU1)	Experimental	2% immobilized Econea
PU-based	Exp. PU2	Experimental	Mixture of biocides
PU-based	PU	Newly developed anti-corrosive	No biocides

Anticorrosion assessment was performed through accelerated aging tests, namely salt spray tests (ISO 14993:2001), UV tests (ASTM G 154-06) and immersion in 3.5% NaCl at room temperature. The aim of these tests is to impose larger thermal stresses than those encountered in the field, in order to cause an accelerated degradation effect. The paints examined during these tests were in intact state, meaning that no flaw, such as scratches, existed. The objective of these experiments was to determine the barrier properties of each painting system. The first two experiments lasted 9 weeks, while continuous immersion was performed for 12 months. Examination of specimens was performed regularly and involved electrochemical impedance spectroscopy (EIS), König pendulum hardness (ISO 152:2006),

gloss and color measurements. Painted specimens of Grade A steel substrate and of dimensions 100 mm × 100 mm × 6 mm were used, unless otherwise specified.

Experiments on painted samples with scribes and of the same dimensions as above were performed for 12 weeks in salt spray exposure. The aim of this test was to examine the barrier properties that the unscratched part of the paint provides. The observed rust morphology in the area of the scribes was correlated with the paint efficiency and a ranking between the examined painting systems was performed. Rust morphology characterization was performed through XRD, Raman spectroscopy and SEM observation. The next step of this study included electrochemical examination of the rusted, scribed specimens at 6, 8 and 12-week intervals and included EIS and linear polarization resistance (LPR) methods. Fitting of the experimental impedance curves was performed using a Particle Swarm Optimization algorithm for a selected number of representative corrosion models, which could potentially describe the mode of corrosion during the course of the salt spray experiment.

Antifouling assessment included static immersion tests in Elefsis Gulf for one year. Six (6) specimens per painting system, of the same dimensions and substrate as previously stated were immersed at 2.5 mm depth. Every two months a specimen was removed from site and examined in the laboratory, in terms of fouling density, types of foulers and physical damage of the paint, according to ASTM D 3623 and ASTM D 6990 standards. Periodic examination included also EIS measurement of barrier properties, gloss, color and König pendulum hardness.

Hydrodynamic tests included flat plate resistance tests in three conditions: smooth, painted with AF coating systems and covered with sandpapers of 40 and 80-grit size. The experiments were performed in the experimental towing tank of the Laboratory of Ship and Marine Hydrodynamics (LSMH) at various speeds (or Reynolds numbers) and drag measurements for each case were performed, in order to compare the drag effect caused by each condition.

Examination of the painting systems in terms of mechanical and physical properties included water-liquid transmission rate, cupping, chalking and dirt pick up tests. Cupping test (ISO 1520) measures the resistance to deep drawing, which is a form of adhesion. Chalking test (ASTM D 4214) measures the chalking character of the paint (loss of pigments). Dirt pick up test (ASTM D 3719-00) is a tool for quantifying the dirt collection of paints during outdoor exposure for 61 days. Water-liquid transmission rate test is used to determine the permeability of the paint to water liquid, according to the BS EN 1062-3 standard. For these tests, specimens of specific dimensions and/or substrate were used and are described in the corresponding section.

The investigation performed during the present thesis intended to offer a thorough analysis for a comprehensive assessment of the efficiency of commercial and experimental antifouling (or organic, in general) paints.

Περίληψη

Στην παρούσα διδακτορική διατριβή εξετάστηκαν εμπορικά και πειραματικά αντιρρυπαντικά υφαλοχρώματα ως προς την αντιρρυπαντική, αντιδιαβρωτική και υδροδυναμική τους αποδοτικότητα, καθώς και σε σχέση με τις μηχανικές και φυσικές τους ιδιότητες. Τα συστήματα βαφής που εξετάστηκαν ήταν σιλικονούχας, πολυουρεθανικής και ακρυλικής πολυμερικής μήτρας. Συνολικά πέντε αντιρρυπαντικά υφαλοχρώματα εξετάστηκαν, καθώς και ένα χρώμα πολυουρεθάνης αντιδιαβρωτικό, το οποίο χρησιμοποιήθηκε ως μέτρο σύγκρισης για τις αντίστοιχες πειραματικές βαφές πολυουρεθάνης. Οι πειραματικές συνθέσεις αναπτύχθηκαν στο πλαίσιο του Ευρωπαϊκού Προγράμματος Foul-X-Spel (Grant Agreement 285552). Η καινοτομία των πειραματικών υφαλοχρωμάτων έγκειται στην ακινητοποίηση του βιοκτόνου (ή μείγματος αυτών) μέσα στην πολυμερική μήτρα, μία διαδικασία γνωστή ως «biocide immobilization». Με τον τρόπο αυτό το υφαλόχρωμα δρα εξ' επαφής (τοπικά) κι έτσι αποφεύγεται η απελευθέρωση του βιοκτόνου στη θάλασσα («leaching»), μία διαδικασία με πολύ σημαντικό, αρνητικό, περιβαλλοντικό αντίκτυπο. Τα συστήματα που μελετήθηκαν κατά τη διάρκεια της διατριβής, καθώς και η σύστασή τους σε βιοκτόνα, εφόσον διαθέτουν, έχουν παρουσιαστεί στον Πίνακα 1 της αγγλικής περίληψης.

1. Μελέτη αντιδιαβρωτικής προστασίας χρωμάτων

Η αντιδιαβρωτική προστασία των χρωμάτων μελετήθηκε τόσο σε άθικτα δοκίμια όσο και σε δοκίμια με σχισμές. Στην πρώτη περίπτωση μελετώνται οι ιδιότητες φραγμού του άθικτου συστήματος βαφής, δηλαδή η αντίσταση της βαφής σε εισχώρηση του ηλεκτρολύτη (συνήθως 3.5% NaCl). Στη δεύτερη περίπτωση μελετώνται οι ιδιότητες φραγμού παρουσία σφάλματος, δηλαδή κατά πόσο το ανεπηρέαστο κομμάτι της βαφής μπορεί να αποτελέσει φραγμό σε εισχώρηση ηλεκτρολύτη ή/και σε εξάπλωση προϊόντων διάβρωσης κάτω από το στρώμα βαφής.

1.1. Μελέτη αντιδιαβρωτικής προστασίας σε βαμμένα δοκίμια χάλυβα με σχισμές έπειτα από έκθεση σε περιβάλλον αλατονέφωσης

Η αντιδιαβρωτική προστασία παρουσία σχισμών μελετήθηκε με έκθεση βαμμένων δοκιμίων χάλυβα, διαστάσεων 100 mm × 100mm × 6mm, που έφεραν δύο διαγώνιες σχισμές μήκους 9cm και πλάτους περίπου 1mm, σε περιβάλλον αλατονέφωσης. Δύο δοκίμια ανά σύστημα βαφής (Ref. Si, Exp. Si, Exp. PU1, Acrylic) μελετήθηκαν σε αλατονέφωση για συνολικό διάστημα 12 εβδομάδων. Οι συνθήκες του πειράματος είναι εκείνες που υπαγορεύονται από την οδηγία ISO 14993:2001 και περιλαμβάνουν 2h αλατονέφωσης στους 35^{o}C με διάλυμα NaCl 5%, ακολουθούμενο από 4h ξηρής ατμόσφαιρας στους 60^{o}C και έπειτα από 2h υγρασίας στους 50^{o}C με σχετική υγρασία 95%. Αυτός ο κύκλος 8h επαναλαμβάνεται συνεχώς και διακόπτεται μόνο κατά την περιοδική αξιολόγηση των δοκιμίων. Στη συγκεκριμένη έρευνα έγινε συσχέτιση του είδους των προϊόντων διάβρωσης στην περιοχή των σχισμών με την αποδοτικότητα του εκάστοτε συστήματος βαφής. Ο χαρακτηρισμός των φάσεων στη σκωρία έγινε μέσω XRD και φασματοσκοπία Raman, καθώς και μέσω παρατήρησης σε μικροσκόπιο SEM. Η μακροσκοπική παρατήρηση των σχισμών και της συμπεριφοράς της βαφής κατά την έκθεση, έγινε μέσω οπτικού στερεοσκοπίου.

Η συγκεκριμένη έρευνα είναι χωρισμένη σε δύο μέρη. Στο πρώτο μέρος έγινε σύγκριση της αντιδιαβρωτικής ικανότητας της πειραματικής σιλικονούχας βαφής, η οποία περιέχει 0.56% ακινητοποιημένης Econea (Exp. Si), με την εμπορική εκδοχή της, η οποία δεν περιλαμβάνει βιοκτόνα (Ref. Si). Στο δεύτερο μέρος έγινε μελέτη της συμπεριφοράς της πειραματικής πολυουρεθάνης με 2% Econea (Exp. PU1), ενώ παράλληλα μελετήθηκε και η ακρυλική αυτολειαινόμενη (self-polishing copolymer) εμπορική βαφή (Acrylic) για λόγους πληρότητας. Στο τέλος πραγματοποιήθηκε μία σύγκριση ανάμεσα σε όλα τα εξεταζόμενα συστήματα.

Αναφορικά με το σύστημα Exp. Si, η περιοχή των σχισμών παρουσίασε περιορισμένη απώλεια υλικού, η οποία έγινε αντιληπτή ως κοιλάδες στο μεταλλικό υπόστρωμα, ενώ το στρώμα των προϊόντων διάβρωσης ήταν σχετικά συμπαγές. Αντίθετα, η εμπορική εκδοχή του εν λόγω συστήματος (Ref. Si) παρουσίασε εκτενή απώλεια υλικού και μία αρκετά ανομοιόμορφη δομή στρώματος διάβρωσης με κενά, υποδηλώνοντας πιο έντονη διάβρωση. Παράλληλα, τα προϊόντα διάβρωσης που παρατηρήθηκαν και στα δύο συστήματα ήταν κυρίως οξυ-υδροξείδια, γεγονός που υποδηλώνει περιορισμένη αντιδιαβρωτική προστασία στην περιοχή των σχισμών, ενώ η μορφολογία αυτή συνδέθηκε με την «ανασήκωση» της βαφής κατά τη διάρκεια του πειράματος (paint swelling), η οποία οδήγησε στο σχηματισμό μεγάλων, συμπαγών συσσωματωμάτων σκωρίας χωρίς πρόσφυση με το μεταλλικό υπόστρωμα. Η συχνή αποκόλληση αυτών των συσσωματωμάτων θα οδηγούσε στην επανεκκίνηση της διάβρωσης, συνεπώς στη δημιουργία νέου στρώματος σκωρίας, αποτελούμενο κυρίως από τα πρώιμα σχηματιζόμενα οξυ-υδροξείδια, όπως παρατηρήθηκε και στην εν λόγω έρευνα.

Η μορφολογία της σκωρίας στην περιοχή των σχισμών του συστήματος Exp. Si περιελάμβανε κυρίως μείγμα ακαγανίτη (β-FeOOH-akaganeite)/ γκετίτη (α-FeOOH-goethite) στις άσπρες, κίτρινες και πορτοκαλί περιοχές, ενώ ο μαγνητίτης (Fe_3O_4-magnetite) ήταν η κύρια φάση στις μαύρες περιοχές. Αντίστοιχες φάσεις παρατηρήθηκαν και για το σύστημα Ref. Si, στο οποίο παρατηρήθηκε επιπλέον λεπιδοκροκίτης (γ-FeOOH-lepidocrocite) στην άσπρη περιοχή και σε μέρος της κίτρινης. Η σύγκριση των μορφολογιών σκωρίας ανάμεσα στα δύο συστήματα για τις κίτρινες και πορτοκαλί περιοχές, όπου οι φάσεις ήταν παρεμφερείς, ανέδειξε την καλύτερη αντιδιαβρωτική προστασία της πειραματικής σιλικόνης σε σχέση με την εμπορική, λόγω του σχετικά υψηλότερου ποσοστού σταθερού γκετίτη στο μείγμα ακαγανίτη/γκετίτη.

Η μελέτη του συστήματος Exp. PU1 έδειξε ότι η εν λόγω βαφή δεν υπέστη επιφανειακή αλλοίωση ή παραμόρφωση κατά τη γήρανση, παρουσίασε μόνο μία ελαφρά «ανασήκωση» (swelling) στην περιοχή των σχισμών, η οποία προήλθε από συσσώρευση προϊόντων διάβρωσης στην περιοχή και όχι λόγω ίδιας παραμόρφωσης της βαφής. Αξίζει να σημειωθεί ότι τα προϊόντα διάβρωσης δεν είχαν εξαπλωθεί πέραν της περιοχής των σχισμών. Αντίθετα, τα δοκίμια που ήταν βαμμένα με το ακρυλικό υφαλόχρωμα (Acrylic) παρουσίασαν εκτενή απώλεια υλικού του υποστρώματος, φλύκταινες (blistering), ρωγμάτωση του τελικού επιχρίσματος (topcoat checking) και εκτεταμένη εξάπλωση σκωρίας σε όλο το δοκίμιο, η οποία κάλυψε το μεταλλικό υπόστρωμα κάτω από το πολυστρωματικό σύστημα βαφής. Ως εκ τούτου, οι ιδιότητες φραγμού της ακρυλικής βαφής παρουσία σφαλμάτων ήταν ανεπαρκείς.

Η σκωρία που παρατηρήθηκε στην περιοχή των σχισμών για την πειραματική πολυουρεθάνη αποτελούνταν από μείγμα οξειδίων, που θεωρούνται πιο προστατευτικά από άποψη διάβρωσης, και των λιγότερο επιβλαβών από τα οξυ-υδροξείδια. Αυτή η μορφολογία επιβεβαίωσε την καλύτερη αντιδιαβρωτική συμπεριφορά του Exp. PU1 συστήματος και συνδέθηκε με την απουσία παραμόρφωσης του συστήματος βαφής κατά τη διάρκεια του πειράματος, γεγονός που επέτρεψε το σχηματισμό συμπαγούς στρώματος διάβρωσης, το οποίο παρείχε επαρκή μόνωση του μεταλλικού υποστρώματος. Αυτό με τη σειρά του παρείχε αρκετό χρόνο για να συντελεστούν μετασχηματισμοί των θερμοδυναμικά μετασταθών οξυ-υδροξειδίων σε πιο προστατευτικές δομές, όπως παρατηρήθηκαν στην παρούσα μελέτη, εμποδίζοντας περαιτέρω εξέλιξη της διάβρωσης.

Η μορφολογία της σκωρίας για τα χαλύβδινα δοκίμια με σχισμές που είχαν βαφτεί με το σύστημα Exp. PU1 περιελάμβανε αιματίτη (α-Fe_2O_3-hematite), ως κυρίαρχη φάση στην άσπρη περιοχή και μαγκεμίτη (γ-Fe_2O_3-maghemite) στις πορτοκαλί και μαύρες περιοχές. Η κίτρινη περιοχή είχε σαν κυρίαρχη φάση λεπιδοκροκίτη (γ-FeOOH-lepidocrocite). Το ακρυλικό σύστημα παρουσίασε αιματίτη ως κυρίαρχη φάση στην άσπρη περιοχή, μείγμα ακαγανίτη/γκετίτη στην κίτρινη περιοχή, μαγκεμίτη στην πορτοκαλί περιοχή και γκετίτη στην μαύρη περιοχή, εκδηλώνοντας υποδεέστερες αντιδιαβρωτικές ιδιότητες σε σχέση με την πειραματική πολυουρεθάνη. Συνεπώς, η πειραματική πολυουρεθάνη παρουσίασε συνολικά καλύτερη συμπεριφορά σε διάβρωση σε σχέση με το ακρυλικό σύστημα.

Συγκριτικά με την αντιδιαβρωτική συμπεριφορά των σιλικονούχων συστημάτων βαφής, η πειραματική πολυουρεθάνη κατατάσσεται στην πρώτη θέση, ακολουθούμενη από την πειραματική σιλικόνη, έπειτα από την εμπορική σιλικόνη και τελικά από το ακρυλικό SPC σύστημα. Συνεπώς, τα νέα πειραματικά συστήματα βαφής παρουσίασαν συνολικά καλύτερη συμπεριφορά από τα εμπορικά χρώματα αλλά μεταξύ των δύο πειραματικών συνθέσεων, η πολυουρεθάνη αποδείχτηκε πιο αποδοτική.

1.2. Φασματοσκοπία ηλεκτροχημικής εμπέδησης σε βαμμένα δοκίμια χάλυβα με σχισμές έπειτα από έκθεση σε περιβάλλον αλατονέφωσης

Τα δοκίμια με σχισμές που εξετάστηκαν στην προηγούμενη παράγραφο μελετήθηκαν έπειτα από 6, 8 και 12 εβδομάδες ηλεκτροχημικά, μέσω φασματοσκοπίας ηλεκτροχημικής εμπέδησης (Electrochemical Impedance Spectroscopy-EIS) και με τη μέθοδο της γραμμικής πόλωσης (Linear Polarization Resistance Method-LPR). Ο σκοπός των μετρήσεων αυτών έγκειται στην αξιολόγηση της διαβρωτικής συμπεριφοράς των δοκιμίων με την πάροδο του χρόνου. Τα σήματα που προέκυψαν κατά την αξιολόγηση των δοκιμίων αυτών ήταν αρκετά πολύπλοκα, παρόλα αυτά υπήρχαν ομοιότητες μεταξύ των σημάτων διαφορετικών δοκιμίων. Για το λόγο αυτό, στην παρούσα μελέτη έγινε ανάλυση των σημάτων EIS για ένα βαμμένο δοκίμιο με σχισμές έπειτα από 6, 8 και 12 εβδομάδες σε αλατονέφωση, θεωρώντας τα σήματά του αντιπροσωπευτικά του συνόλου. Το δοκίμιο που επιλέχθηκε ήταν ένα από τα δύο βαμμένα δοκίμια με το σύστημα Exp. PU1.

Τα πειραματικά σήματα αναλύθηκαν, προκειμένου να διασαφηνιστεί ο μηχανισμός διάχυσης διαλυμένου οξυγόνου μέσα στο ηλεκτρολυτικό διάλυμα, θεωρώντας ότι η διάχυση του οξυγόνου καθορίζει το συνολικό ρυθμό διάβρωσης. Για το σκοπό αυτό, μελετήθηκαν διάφορα μοντέλα που περιγράφουν εμπέδηση διάχυσης και αξιολογήθηκαν ως προς την ικανότητά τους να περιγράψουν τις πειραματικές καμπύλες. Οι παράμετροι των μαθηματικών εκφράσεων αυτών των μοντέλων υπολογίστηκαν με ανάλυση παλινδρόμησης (regression analysis), μέσω αλγορίθμου βελτιστοποίησης που σχεδιάστηκε ειδικά για αυτόν τον σκοπό. Τα σήματα EIS που προέκυψαν από τα μοντέλα μέσω της βελτιστοποίησης αξιολογήθηκαν με βάση τις τιμές των φυσικοχημικών παραμέτρων, θεωρώντας το κατάλληλο ισοδύναμο ηλεκτρικό ανάλογο (equivalent circuit). Ο σκοπός της μελέτης αυτής είναι να προτείνει μία μεθοδολογία για την ερμηνεία φασμάτων EIS πολύπλοκων συστημάτων και το συγκεκριμένο παράδειγμα της διάβρωσης του βαμμένου χάλυβα με σχισμές χρησιμοποιήθηκε για να γίνει επίδειξη της εν λόγω διαδικασίας.

Τα μοντέλα που περιέγραψαν ικανοποιητικά την διαδικασία διάχυσης διαλυμένου οξυγόνου κατά τη διάρκεια της αλατονέφωσης βασίζονται στον μηχανισμό πεπερασμένης διάχυσης, υποδεικνύοντας ότι η διάχυση συντελείται εντός του πορώδους στρώματος προϊόντων διάβρωσης. Δηλαδή η διαβάθμιση της συγκέντρωσης του οξειδωτικού (εδώ του οξυγόνου) που εκκινεί τη διάχυση αναπτύσσεται μέσα στους πόρους του στρώματος οξειδίων. Έτσι, το μήκος του στρώματος διάχυσης (L_D), όπως αυτό προκύπτει για την ενδεικτική τιμή του συντελεστή διάχυσης 1.9 10^{-5} cm^2/s, εκφράζει το πάχος του στρώματος προϊόντων διάβρωσης στο εκάστοτε διάστημα αξιολόγησης (6, 8 ή 12 εβδομάδες). Το στρώμα των οξειδίων αυξήθηκε βαθμιαία από 0.38 mm έπειτα από 6 εβδομάδες, σε 0.72 mm έπειτα από 8 εβδομάδες και τελικά σε 0.88 mm μετά το πέρας των 12 εβδομάδων. Αυτή η αύξηση του πάχους συνοδεύτηκε από μία αύξηση στην αντίσταση διάχυσης, R_D, έπειτα από 8 εβδομάδες, η οποία όμως δεν ήταν στατιστικώς σημαντική, όπως αποδείχθηκε με χρήση της διαδικασίας CNLLS (complex non-linear least squares). Ωστόσο, έπειτα από 12 εβδομάδες η τιμή της R_D έπεσε σε περίπου 47 Ω cm^2, υποδεικνύοντας ευκολότερη διάχυση. Η παρατήρηση αυτή επιβεβαιώθηκε για το σύνολο των εξεταζόμενων δοκιμίων. Συνεπώς, έπειτα από 12 εβδομάδες, το στρώμα διάβρωσης δεν προσέφερε κάποιου είδους δυσκολία στην διάχυση του οξυγόνου, οδηγώντας σε μείωση της αντίστασης πόλωσης και σε αύξηση του ρυθμού διάβρωσης.

Τα σήματα EIS της εν λόγω έρευνας θα μπορούσαν να αντιστοιχιστούν με την ηλεκτροχημική απόκριση της δομής μεταλλικού υποστρώματος/μαγνητίτη, η οποία πιθανόν να αποτελεί και την επιφάνεια πάνω στην οποία συντελείται η αναγωγή του οξυγόνου. Πάνω από το στρώμα αυτό υπάρχει το κόκκινο στρώμα σκωρίας, αποτελούμενο κατά βάση από αιματίτη (το οποίο δεν επηρεάζει την κινητική), πιθανόν

συμπεριλαμβανομένων των φάσεων μαγκεμίτη και δ-FeOOH (feroxyhyte), ενώ το ανώτερο στρώμα σκωρίας πιθανόν να περιλαμβάνει λεπιδοκροκίτη. Από μία άλλη οπτική, το στρώμα σκωρίας μπορεί να θεωρηθεί οτί αποτελείται από δύο επιμέρους στρώματα: το στρώμα του αγώγιμου μαγνητίτη πάνω από το ηλεκτρόδιο και το στρώμα όλων των υπόλοιπων προϊόντων διάβρωσης (οξειδίων και οξυ-υδροξειδίων) διαμέσου των οποίων συντελείται η διάχυση του οξυγόνου.

1.3. Μελέτη αντιδιαβρωτικής προστασίας σε άθικτα βαμμένα δοκίμια χάλυβα έπειτα από δοκιμές επιταχυνόμενης γήρανσης

Πειράματα επιταχυνόμενης γήρανσης πραγματοποιήθηκαν στα συστήματα βαφής που μελετήθηκαν ανωτέρω, καθώς και στην αντιδιαβρωτική πολυουρεθάνη (PU). Τα πειράματα αυτά προκαλούν μεγαλύτερες τάσεις στο εξεταζόμενο σύστημα, από αυτές που θα αντιμετώπιζε υπό πραγματικές συνθήκες λειτουργίας και για τη συγκεκριμένη μελέτη περιελάμβαναν έκθεση σε περιβάλλον αλατονέφωσης, σε υπεριώδη ακτινοβολία και σε εμβάπτιση σε τεχνητό θαλασσινό νερό σε συνθήκες περιβάλλοντος. Στην παρούσα μελέτη οι συνθήκες αλατονέφωσης ήταν ίδιες με αυτές που παρουσιάστηκαν στην προηγούμενη παράγραφο. Δύο δοκίμια ανά σύστημα βαφής μελετήθηκαν για συνολικά 9 εβδομάδες. Αναφορικά με τα πειράματα υπό υπεριώδη ακτινοβολία, ακολουθήθηκε η οδηγία ASTM G 154-06, σύμφωνα με την οποία τα δοκίμια εκτίθενται για 4h σε συνθήκες μέρας (UV on) στους 60^{o}C ακολουθούμενες από άλλες 4h σε συνθήκες νύχτας (UV off) στους 50^{o}C και με RH 98%. Η πηγή ακτινοβολίας που χρησιμοποιήθηκε στα πειράματα εξέπεμπε στο εύρος UVB+UVC. Το πείραμα αυτό διήρκησε επίσης 9 εβδομάδες και μελετήθηκαν 2 δοκίμια ανά σύστημα βαφής. Τα πειράματα εμβάπτισης σε τεχνητό θαλασσινό νερό (3.5% NaCl) διήρκησαν 12 μήνες. Δύο δοκίμια ανά σύστημα βαφής εξετάστηκαν και σε αυτήν την περίπτωση. Η αντιδιαβρωτική πολυουρεθάνη δεν μελετήθηκε σε αυτό το πείραμα. Κάθε ζεύγος δοκιμίων ανά σύστημα βαφής ήταν εμβαπτισμένο στο ίδιο δοχείο που περιείχε 0.5L διαλύματος 3.5% NaCl. Η περιοδική αξιολόγηση των δοκιμίων στα πρώτα δύο πειράματα πραγματοποιήθηκε έπειτα από 4, 6 και 9 εβδομάδες, εκτός από τα δοκίμια που ήταν βαμμένα με τα συστήματα Ref. Si και Acrylic και που εκτέθηκαν σε ακτινοβολία UV, τα οποία μελετήθηκαν έπειτα από 6 και 9 εβδομάδες. Τα δοκίμια που εξετάστηκαν σε συνεχή εμβάπτιση στο ηλεκτρολυτικό διάλυμα αξιολογούνταν μηνιαίως.

Ο σκοπός των πειραμάτων αυτών είναι να αξιολογηθούν οι ιδιότητες φραγμού των επικαλύψεων με τον χρόνο, οι οποίες σχετίζονται με τη διαπερατότητά τους σε κάποιον ηλεκτρολύτη (εδώ 3.5% NaCl). Οι ιδιότητες φραγμού αξιολογήθηκαν στα καθορισμένα χρονικά διαστήματα με EIS. Παράλληλα, έγινε αξιολόγηση των οπτικών ιδιοτήτων (αποχρωματισμός και 60^{o} στιλπνότητα) και της σκληρότητας κατά König (ISO 1522).

Τα αποτελέσματα επιταχυνόμενης γήρανσης σε αλατονέφωση και UV ανέδειξαν την καλύτερη συμπεριφορά της πειραματικής σιλικόνης από άποψη σκληρότητας κατά τη διάρκεια και των δύο δοκιμών. Παράλληλα, το σύστημα αυτό παρουσίασε το μικρότερο αποχρωματισμό έπειτα από UV. Για τις υπόλοιπες περιπτώσεις, η απόδοσή του ήταν μέτρια. Η εμπορική σιλικόνη παρέμεινε σταθερή από άποψη σκληρότητας, έπειτα από αλατονέφωση, ενώ παράλληλα διατήρησε τη στιλπνότητά της έπειτα από UV, παρουσιάζοντας την καλύτερη συμπεριφορά σε αυτήν την ιδιότητα στο συγκεκριμένο πείραμα. Το ακρυλικό σύστημα δεν χαρακτηρίζεται από οπτικές ιδιότητες, συνεπώς δεν διατήρησε στιλπνότητα, ενώ εκδήλωσε και τον εντονότερο αποχρωματισμό, έπειτα και από τα δύο πειράματα. Παράλληλα παρουσίασε ρωγμάτωση του τελικού επιχρίσματος (topcoat checking) και αύξηση της σκληρότητας. Ως εκ τούτου, το σύστημα αυτό παρουσίασε τη χειρότερη συμπεριφορά από άποψη οπτικών ιδιοτήτων, ενώ από άποψη διατήρησης της σκληρότητάς του, η συμπεριφορά του ήταν μέτρια. Η πειραματική πολυουρεθάνη με 2% Econea παρουσίασε τη μεγαλύτερη αύξηση στη σκληρότητα έπειτα κι από τα δύο πειράματα και την μικρότερη μεταβολή στην στιλπνότητα έπειτα από αλατονέφωση. Για τις υπόλοιπες περιπτώσεις, η απόδοσή του ήταν μέτρια. Το αντιδιαβρωτικό χρώμα πολυουρεθάνης παρουσίασε διακυμάνσεις στις ιδιότητές του ανάμεσα στα διαφορετικά δοκίμια, αλλά γενικά παρουσίασε αύξηση της σκληρότητας, σε λιγότερο μικρότερο βαθμό από

την πειραματική πολυουρεθάνη. Επίσης, παρουσίασε την καλύτερη συμπεριφορά από άποψη αποχρωματισμού έπειτα από αλατονέφωση. Από άποψη ηλεκτρικών ιδιοτήτων όλα τα σύστηματα παρουσίασαν πλήρως χωρητική συμπεριφορά, η οποία είναι χαρακτηριστική ενός άθικτου, αναλλοίωτου χρώματος.

Οι παραπάνω παρατηρήσεις δεν επαληθεύτηκαν εξ ‘ ολοκλήρου κατά το πείραμα εμβάπτισης σε τεχνητό θαλασσινό νερό. Πιο συγκεκριμένα, η πειραματική σιλικόνη παρουσίασε την πιο σταθερή συμπεριφορά από άποψη σκληρότητας και στιλπνότητας, αλλά ήταν μέτρια από άποψη αποχρωματισμού. Η εμπορική σιλικόνη παρουσίασε μία ενδιάμεση απόδοση σε σχέση με τα υπόλοιπα συστήματα από άποψη σκληρότητας και στιλπνότητας και την καλύτερη συμπεριφορά από άποψη αποχρωματισμού. Η πειραματική σιλικόνη δεν παρουσίασε τόσο έντονη αύξηση στην σκληρότητα, όπως παρατηρήθηκε έπειτα από την έκθεση σε αλατονέφωση και UV. Γενικά, παρουσίασε ενδιάμεση απόδοση για όλες τις ιδιότητες. Το ακρυλικό σύστημα παρουσίασε τη χειρότερη απόδοση σε όλες τις ιδιότητες. Δεν παρατηρήθηκε «checking». Από άποψη ηλεκτρικών ιδιοτήτων, τα συστήματα σιλικόνης διατήρησαν χωρητική απόκριση καθ’ όλη τη διάρκεια του πειράματος. Το ακρυλικό και η πειραματική πολυουρεθάνη παρουσίασαν πλήρως χωρητικές αλλά και χωρητικές παρουσία αντίστασης πόρων αποκρίσεις ανά διαστήματα, οι οποίες δεν ήταν αντίστοιχες της διάρκειας εμβάπτισης. Παρόλα αυτά, οι τιμές της αντίστασης πόρων για το ακρυλικό σύστημα ήταν υψηλότερες από της πειραματικής πολυουρεθάνης, παρά το γεγονός ότι και τα δύο συστήματα παρουσίασαν παρεμφερείς τιμές έπειτα από 12 μήνες πειράματος, γεγονός που υποδηλώνει κάποια απώλεια στις ιδιότητες φραγμού. Παρόλα αυτά, όπως αναφέρθηκε και προηγουμένως, η μορφή των σημάτων παρουσίασε διακυμάνσεις κατά την περιοδική εξέταση.

Λαμβάνοντας υπόψη το σύστημα με την καλύτερη συμπεριφορά έπειτα από όλες τις μετρήσεις και στα τρία πειράματα, η πειραματική σιλικόνη παρουσίασε την καλύτερη συμπεριφορά 5 φορές, ακολουθούμενη από την εμπορική σιλικόνη με 3 φορές και την πειραματική και αντιδιαβρωτική πολυουρεθάνη με μία φορά η καθεμία.

Επιπλέον, η διαφορετική συμπεριφορά που παρατηρήθηκε από άποψη σκληρότητας για την πειραματική πολυουρεθάνη και από άποψη παρουσίας «checking» για το ακρυλικό σύστημα, υποδηλώνει ότι το πείραμα της εμβάπτισης εισάγει μικρότερες τάσεις στα εξεταζόμενα συστήματα σε σχέση με την αλατονέφωση και την έκθεση σε UV. Από την άλλη πλευρά, τα συστήματα σιλικόνης παρουσίασαν μικρής έκτασης, περιορισμένες μόνο στο τελικό επίχρισμα, φλύκταινες, οι οποίες δεν παρατηρήθηκαν κατά την αλατονέφωση ή την έκθεση σε UV. Πέραν αυτού, παρουσίασαν την καλύτερη συμπεριφορά κατά την 12-μηνη εμβάπτισή τους σε 3.5% NaCl.

2. Πειραματική διερεύνηση της επίδρασης της τραχύτητας στην υδροδυναμική αντίσταση πλοίου μέσω πειραμάτων αντίστασης σε επίπεδη πλάκα και σε μοντέλο πλοίου

Η συγκεκριμένη μελέτη είχε σαν σκοπό την υδροδυναμική αξιολόγηση επιφανειών με τραχύτητα και το κατά πόσο η επίδραση της τραχύτητας σε μικρή κλίμακα (εργαστηρίου) μπορεί να μεταφερθεί στην κλίμακα του πλοίου. Η τραχύτητα σε μεγάλη κλίμακα είναι πολύ βασική γιατί προκαλεί αύξηση στην υδροδυναμική αντίσταση του πλοίου και κατ’ επέκταση στην κατανάλωση καυσίμου. Τραχύτητα μπορεί να προκληθεί είτε από επικαθίσεις στην γάστρα του πλοίου (fouling) είτε από το εκάστοτε σύστημα βαφής. Σε εργαστηριακή κλίμακα η επίδραση της τραχύτητας αξιολογείται συνήθως με πειράματα αντίστασης σε επίπεδη πλάκα. Αυτό συμβαίνει επειδή η επίπεδη πλάκα, λόγω του σχήματός της, δεν έχει μεγάλη συνιστώσα υπόλοιπης αντίστασης, δηλαδή κυματισμού και μορφής, και έτσι οι μετρήσεις αφορούν σχεδόν εξ’ ολοκλήρου στην αντίσταση τριβής. Επιπλέον, από τη βιβλιογραφία υπάρχουν μέθοδοι προεκβολής της επίδρασης της τραχύτητας από την επίπεδη πλάκα σε κλίμακα εργαστηρίου σε μία επίπεδη πλάκα μήκους τάξης μεγέθους πλοίου. Η προεκβολή στην κλίμακα του πλοίου προϋποθέτει ότι η τραχύτητα που χαρακτηρίζει την υπό

μελέτη επιφάνεια έχει αναχθεί σε μία ομοιόμορφη τραχύτητα, η οποία περιγράφεται από το λεγόμενο ισοδύναμο ύψος ομοιόμορφης τραχύτητας (k_s). Η έννοια του όρου k_s είναι ότι η εκάστοτε τυχαία τραχύτητα μπορεί να περιγραφεί σαν ομοιόμορφη τραχύτητα με ύψος τραχύτητας τέτοιο που να προκαλείται η ίδια μείωση στο προφίλ ταχύτητας, για την περιοχή του τυρβώδους οριακού στρώματος που η ταχύτητα περιγράφεται από τον λογαριθμικό νόμο, όπως και με την αρχική τυχαία τραχύτητα. Αυτό είναι πολύ σημαντικό, γιατί έτσι μπορεί οποιαδήποτε τραχύτητα να μοντελοποιηθεί σε κώδικα CFD και να προβλεφθεί η επίδρασή της και στην κλίμακα του πλοίου.

2.1. Μελέτη επίδρασης ομοιόμορφης τραχύτητας με χρήση γυαλόχαρτων 40 και 80-grit

Το πρώτο στάδιο μελέτης της επίδρασης της τραχύτητας στην υδροδυναμική αντίσταση περιελάμβανε πειράματα σε επίπεδη πλάκα και σε μοντέλο πλοίου, καλυμμένα με γυαλόχαρτα 40 και 80-grit. Επειδή τα πειράματα επίπεδης πλάκας έγιναν με μία διάταξη που κατασκευάσθηκε από την αρχή για αυτό το σκοπό στο Εργαστήριο Ναυτικής και Θαλάσσιας Υδροδυναμικής (ΕΝΘΥ) του ΕΜΠ, ήταν σημαντικό να επαληθεύσουμε την αξιοπιστία των πειραματικών μετρήσεων, μέσω εξέτασης αρχικά επιφανειών με ομοιόμορφη τραχύτητα. Ο σκοπός λοιπόν των πειραμάτων αυτών ήταν να υπολογισθεί το k_s πειραματικά και να συσχετιστεί με το ονομαστικό ύψος τραχύτητας (R_a) του εκάστοτε γυαλόχαρτου.

Πριν από την μελέτη της επίδρασης της τραχύτητας στην αντίσταση της επίπεδης πλάκας, προηγήθηκε μία ενδελεχής μελέτη της αντίστασης της επίπεδης πλάκας σε λεία κατάσταση. Όπως αναφέρθηκε και προηγουμένως, η διάταξη με την επίπεδη πλάκα σχεδιάσθηκε και κατασκευάστηκε από την αρχή για αυτά τα πειράματα. Αξίζει να σημειωθεί ότι η διάσταση της πλάκας ήταν 2m × 1m × 3mm, ενώ οι ακμές της είχαν διαμορφωθεί με τέτοιο τρόπο, ώστε να θυμίζουν υδροτομές NACA, δηλαδή πομπέ μπροστά και τριγωνικές πίσω. Επίσης, άλλο ένα χαρακτηριστικό, που συνιστά και καινοτομία των εν λόγω πειραμάτων, είναι το πολύ μικρό πάχος της πλάκας, καθώς στην βιβλιογραφία το μικρότερο πάχος που έχει αναφερθεί είναι 3.2mm. Το μικρό πάχος της επίπεδης πλάκας κατέστησε αναγκαία τη χρήση εντατήρων, οι οποίοι θα διασφάλιζαν ότι η πλάκα δεν θα παρουσίαζε βέλος κάμψης κατά την τέλεση των πειραμάτων. Τρεις εντατήρες τοποθετήθηκαν κατά μήκος της πλάκας, διαμέτρου 0.8mm. Λόγω της αυξημένης πρόσθετης αντίστασης που προκλήθηκε από αυτή την προσθήκη, η οποία μπορεί να έφτανε και στο 48% της συνολικής μετρούμενης αντίστασης για τον μέγιστο αριθμό Reynolds (περίπου $4.2\ 10^6$), ήταν αναγκαίο να γίνεται αφαίρεση της αντίστασης των τριών συρμάτων (tension wires) εφεξής, ώστε τελικά να προκύπτει η αντίσταση τριβής της πλάκας. Στο σημείο αυτό αξίζει να σημειωθεί ότι στη διάταξη αυτή περίπου 5% της συνολικής αντίστασης οφειλόταν σε αντίσταση μορφής, όπως προέκυψε έπειτα από προσομοίωση σε κώδικα CFD. Το δεύτερο στάδιο μελέτης της επίπεδης πλάκας σε λεία κατάσταση περιελάμβανε την εξέταση διεγερτών τύρβης, προκειμένου να βρεθεί ο ιδανικός για διέγερση της ροής σε όλο το εύρος ταχυτήτων που μελετήθηκαν (0.25-2.5m/s). Η επιλογή του κατάλληλου διεγέρτη τύρβης είναι πολύ σημαντική, ώστε να προκύπτει ροή εφάμιλλη με εκείνη που παρατηρείται στο πλοίο, δηλαδή τυρβώδης. Πειράματα που διεξήχθησαν στην επίπεδη πλάκα χωρίς διεγέρτη έδειξαν ότι η ροή ήταν μεταβατική, συνεπώς ήταν αναγκαίο να τοποθετηθεί διεγέρτης. Με χρήση κατάλληλου λογισμικού της ITTC που διαθέτει το ΕΝΘΥ, με βάση το οποίο προτείνεται μία σειρά διεγερτών τύρβης συναρτήσει της θερμοκρασίας του νερού και των ταχυτήτων των πειραμάτων, εξετάστηκαν διεγέρτες τύρβης διαμέτρου 0.8, 0.9, 1, 1.128 και 1.3mm. Από τους διεγέρτες αυτούς, το σύρμα διαμέτρου 1.3mm διέγειρε αποτελεσματικά τη ροή σε όλο το εύρος ταχυτήτων. Όλοι οι διεγέρτες που εξετάστηκαν είχαν τοποθετηθεί σε απόσταση 5% του χείλους πρόσπτωσης.

Επιστρέφοντας στα πειράματα με τα γυαλόχαρτα, η αύξηση της αντίστασης λόγω της τραχύτητας ήταν 76% για το 40-grit και 45% για το 80-grit γυαλόχαρτο για ταχύτητες πάνω από 2m/s. Η μορφή των καμπυλών αντίστασης και για τα δύο γυαλόχαρτα ήταν χαρακτηριστική επιφανειών με ομοιόμορφη τραχύτητα, όπως παρουσιάζονται στο διάγραμμα του Schlichting για τις «sand roughened plates». Η απεικόνιση των καμπυλών αντίστασης στη μορφή που προτείνεται από τον Schlichting, δηλαδή $1000C_F$-Re, ανέδειξε ότι τα τέσσερα

τελευταία σημεία και από τα δύο γυαλόχαρτα, τα οποία αντιστοιχούν σε αριθμούς Reynolds $3\ 10^6 – 4.4\ 10^6$, σχηματίζουν ένα πλατό, το οποίο εκφράζει πλήρως τραχιά επιφάνεια (fully rough regime). Στην περίπτωση αυτή ο συντελεστής τριβής είναι ανεξάρτητος του αριθμού Reynolds, σχετίζεται μόνο με τον όρο ℓ/k_s, όπου ℓ είναι το μήκος της πλάκας και k_s το ισοδύναμο ύψος ομοιόμορφης τραχύτητας άμμου. Η τιμή του k_s που υπολογίστηκε και για τα δύο γυαλόχαρτα ήταν παραπλήσια της ονομαστικής τιμής τους, όπως αυτή προκύπτει από τον κατασκευαστή.

Ωστόσο, η τελική τιμή του k_s θα προκύψει μέσω του υπολογισμού της συνάρτησης τραχύτητας (roughness function). Η συνάρτηση τραχύτητας είναι η μείωση που προκαλείται στο προφίλ ταχύτητας λόγω της τραχύτητας, στην περιοχή εκείνη του τυρβώδους οριακού στρώματος, όπου ισχύει ο λογαριθμικός νόμος για το προφίλ ταχύτητας (log-law). Η «roughness function» υπολογίζεται μέσω της μεθοδολογίας του Granville και το διάγραμμα που την παρουσιάζει είναι το ΔU^+-k^+, όπου ΔU^+ είναι η συνάρτηση τραχύτητας και k^+ είναι ο «roughness Reynolds number», δηλαδή ο αριθμός Reynolds τραχύτητας που ορίζεται ως $k^+=k_sU_\tau/\nu$, όπου το k_s έχει ήδη οριστεί, U_τ είναι η ταχύτητα τριβής και ν η κινηματική συνεκτικότητα. Ανάλογα με το είδος της τραχιάς επιφάνειας που μελετάται, υπάρχει και αντίστοιχη «roughness function» που την περιγράφει. Για παράδειγμα, οι επιφάνειες με γυαλόχαρτα, που αναπαριστούν χονδρικά ομοιόμορφη τραχύτητα, περιγράφονται από την «roughness function» του Nikuradse (universal roughness function), ενώ οι επιφάνειες με τυχαία τραχύτητα (arbitrarily rough surfaces), και ιδιαιτέρως οι επιφάνειες που είναι βαμμένες με «antifouling» βαφές ακολουθούν την λεγόμενη «Colebrook-type roughness function». Με τη δεύτερη συνάρτηση τραχύτητας θα ασχοληθούμε στη συνέχεια. Εν προκειμένω, η συνάρτηση τραχύτητας για τα γυαλόχαρτα ήταν τύπου Nikuradse, το οποίο επιβεβαίωσε για ακόμα μία φορά την ορθότητα των πειραματικών μετρήσεων. Επειδή η πειραματική συνάρτηση τραχύτητας προέκυψε αριστερότερα της Nikuradse, απαιτούνταν πολλαπλασιασμός του αρχικού k_s με 1.7. Ο πολλαπλασιαστικός παράγοντας προκύπτει ως αποτέλεσμα της ανομοιογένειας που υπάρχει στους κόκκους του γυαλόχαρτου (polydispersity), αν και η έως τώρα εκτίμηση αφορούσε σε ομοιομορφία μεγέθους κόκκων (monodispersity). Αντίστοιχα, αν η τιμή R_t (total roughness height) χρησιμοποιούνταν σαν ύψος τραχύτητας, πιθανόν η πειραματική συνάρτηση τραχύτητας να έβγαινε δεξιότερα της Nikuradse, οπότε θα απαιτούνταν μείωση του αρχικά εκτιμώμενου k_s. Αξίζει εδώ να σημειωθεί ότι η μεταφορά της πειραματικής συνάρτησης τραχύτητας στην θεωρητική είναι αναγκαία, καθώς από τη θέση των πειραματικών σημείων πάνω στην θεωρητική καμπύλη μπορεί να εκτιμηθεί και η ένταση επίδρασης τραχύτητας στην ροή. Έτσι, στα συγκεκριμένα πειράματα, μόνο τα δύο τελευταία σημεία του γυαλόχαρτου 40-grit (δηλαδή στις δύο μεγαλύτερες ταχύτητες) παρατηρήθηκε συμπεριφορά πλήρως τραχιάς επιφάνειας (fully rough regime), ενώ όλα τα υπόλοιπα σημεία του 40-grit και όλα τα σημεία του 80-grit υπέδειξαν μεταβατική κατάσταση (transitionally rough regime). Τέλος, προεκβολή των τιμών της συνάρτησης τραχύτητας στην κλίμακα του πλοίου, μέσω μεθόδου που έχει προταθεί πάλι από τον Granville, υπέδειξε ότι το γυαλόχαρτο 40-grit μπορεί να οδηγήσει σε 6.66% υψηλότερη ολική αντίσταση (εκφρασμένη μέσω του συντελεστή ολικής αντίστασης C_T) από το 80-grit σε κατάσταση «heavy ballast (HB)» και 6.46% στην κατάσταση «full load departure (FLD)».

Η επίδραση της τραχύτητας μελετήθηκε με τον ίδιο τρόπο (δηλαδή με γυαλόχαρτα 40 και 80-grit) και σε μοντέλο πλοίου. Πριν από αυτό όμως, έγινε πλήρης ανάλυση της αντίστασης του μοντέλου σε λεία κατάσταση (smooth condition), ιδιαιτέρως έπειτα από προεκβολή στην κλίμακα του πλοίου χρησιμοποιώντας δύο βασικές μεθόδους, την Froude και την ITTC 78 και για δύο καταστάσεις φόρτωσης, τις HB και FLD. Η παραδοσιακή μέθοδος του Froude οδήγησε σε 15% μεγαλύτερο C_T σε σχέση με την ITTC 78 και για τις δύο καταστάσεις φόρτωσης, στον μεγαλύτερο αριθμό Reynolds. Αυτή η διαφορά προκύπτει από το γεγονός ότι η παραδοσιακή μέθοδος μεταφέρει στην κλίμακα του πλοίου όλες τις συνιστώσες της ολικής αντίστασης, πέραν της συνιστώσας τριβής, με βάση το νόμο του Froude, ενώ η δεύτερη μέθοδος εφαρμόζει αυτή την αρχή μόνο για την αντίσταση κυματισμού, ενώ η αντίσταση συνεκτικότητας προεκβάλλεται με βάση το νόμο του Reynolds. Επίσης, στη μέθοδο ITTC 78 έγινε χρήση δύο διαφορετικών τύπων για τον υπολογισμό του συντελεστή C_A (correlation allowance), του διορθωτικού συντελεστή που αναφέρεται στη διαφορά τραχύτητας ανάμεσα στο μοντέλο και το πλοίο και τη διαφορά στη ροή στην περιοχή της πλώρης. Ο τύπος

των Bowden-Davidson οδήγησε σε 5% υψηλότερο C_T και στις δύο καταστάσεις φόρτωσης, για τον υψηλότερο αριθμό Reynolds, σε σχέση με τον τύπο του Townsin.

Αναφορικά με τα πειράματα στο μοντέλο πλήρως καλυμμένο με γυαλόχαρτα, επιχειρήθηκε προεκβολή του C_T στην τραχιά κατάσταση στην κλίμακα του πλοίου, εφαρμόζοντας μία παραλλαγή της μεθόδου του Froude και κάνοντας χρήση του διαγράμματος του Schlichting για τις «sand roughened plates». Εδώ θα πρέπει να αναφερθεί ότι το ύψος τραχύτητας που προεκβάλλεται είναι ίδιο ανάμεσα στο πλοίο και το μοντέλο. Πιο συγκεκριμένα, η μεθοδολογία ακολουθεί το νόμο του Froude για την υπόλοιπη αντίσταση, αλλά αντί να χρησιμοποιηθεί ως καμπύλη συσχέτισης τριβής η ITTC 57 (friction correlation line), χρησιμοποιείται το διάγραμμα του Schlichting, όπου η αντίστοιχη γραμμή τριβής είναι η γραμμή σταθερού ℓ/k_s. Στην πρώτη εκδοχή της μεθόδου, η γραμμή ℓ/k_s, όπως προέκυψε από τα πειράματα της επίπεδης πλάκας παραμένει σταθερή για όλους τους αριθμούς Reynolds, τόσο σε κλίμακα μοντέλου όσο και σε κλίμακα πλοίου. Στην δεύτερη εκδοχή, η γραμμή ℓ/k_s από τα πειράματα επίπεδης πλάκας χρησιμοποιείται για τον υπολογισμό του C_F στην κλίμακα του μοντέλου, ενώ για την κλίμακα του πλοίου χρησιμοποιείται η γραμμή L_s/k_s, όπου L_s είναι το μήκος της ισάλου του πλοίου, για την εκάστοτε κατάσταση φόρτωσης. Η πρώτη εκδοχή της μεθόδου προέβλεψε τις μεγαλύτερες τιμές για το C_T, συγκριτικά με τα αποτελέσματα από την προεκβολή της πλάκας με τραχύτητα και της λείας γάστρας, ενώ η δεύτερη εκδοχή οδήγησε στις μικρότερες τιμές του C_T. Συνεπώς, οι δύο εκδοχές αυτής της μεθοδολογίας οδηγούν σε ένα άνω και ένα κάτω όριο για το C_T στην κλίμακα του πλοίου.

2.2. Μελέτη επίδρασης τραχύτητας επιφάνειας βαμμένης με υφαλόχρωμα

Σκοπός της παρούσας μελέτης ήταν ο προσδιορισμός της επίδρασης της τραχύτητας βαμμένων επιφανειών με αντιρρυπαντικά υφαλοχρώματα στην υδροδυναμική αντίσταση επίπεδης πλάκας. Για το σκοπό αυτό, πραγματοποιήθηκε βαφή της επίπεδης πλάκας με καθένα από τα συστήματα Exp. PU1 (πειραματική πολυουρεθάνη με 2% ακινητοποιημένη Econea), Exp. PU2 (πειραματική πολυουρεθάνη με μείγμα βιοκτόνων), Acrylic (εμπορικό υφαλόχρωμα τεχνολογίας SPC με Cu_2O και Zineb), Exp. Si (πειραματική σιλικόνη με 0.56% ακινητοποιημένη Econea) και Ref. Si (εμπορική σιλικόνη τεχνολογίας απελευθέρωσης ρύπων χωρίς βιοκτόνα). Όπως αναφέρθηκε και προηγουμένως, η συνάρτηση τραχύτητας που περιγράφει επιφάνειες με τυχαίο μοτίβο τραχύτητας, και ιδίως επιφάνειες βαμμένες με κάποιο antifouling χρώμα, περιγράφονται από την συνάρτηση τραχύτητας τύπου Colebrook, η οποία ορίζεται ως: $\Delta U^+=1/\kappa \ln(1+k^+)$, όπου $\kappa=0.41$, η σταθερά του Von Karman.

Τα πειράματα της επίπεδης πλάκας έδειξαν ότι τα συστήματα πολυουρεθάνης και σιλικόνης παρουσίασαν παρόμοια συμπεριφορά, παρουσιάζοντας διακυμάνσεις γύρω από τις τιμές αντίστασης λείας πλάκας. Η αντίσταση που προέκυψε από το ακρυλικό υφαλόχρωμα ήταν η μεγαλύτερη σε σχέση με τα υπόλοιπα συστήματα βαφής και ιδιαίτερα αυξημένη σε σχέση με την λεία πλάκα, σχεδόν για ολόκληρο το εύρος Reynolds. Η συνάρτηση τραχύτητας για το εκάστοτε σύστημα παρουσίασε πολύ καλή συσχέτιση με την τύπου Colebrook συνάρτηση τραχύτητας, με τις πολυουρεθάνες να εκδηλώνουν την μεγαλύτερη συσχέτιση, ακολουθούμενες από το ακρυλικό και τέλος από τις σιλικόνες, οι οποίες διέθεταν τα λιγότερα στατιστικώς σημαντικά πειραματικά σημεία. Παρόλα αυτά, από τη βιβλιογραφία έχει παρατηρηθεί ότι και οι σιλικόνες παρουσιάζουν συσχέτιση με την συνάρτηση τύπου Colebrook. Το ισοδύναμο ύψος ομοιόμορφης τραχύτητας ήταν κάποιος πολλαπλασιαστής του R_a (μέσου ύψους τραχύτητας), όπως παρατηρήθηκε και στα πειράματα με τα γυαλόχαρτα. Συνεπώς, και η τραχύτητα των βαμμένων επιφανειών μπορεί να περιγραφεί με ένα μόνο μέγεθος, όπως το μέσο ύψος τραχύτητας.

3. Δοκιμές πεδίου εμπορικών και πειραματικών υφαλοχρωμάτων στον κόλπο της Ελευσίνας

Στην παρούσα μελέτη πραγματοποιήθηκαν δοκιμές πεδίου (field tests) εμπορικών και πειραματικών υφαλοχρωμάτων στον κόλπο της Ελευσίνας. Τα πειράματα αυτά αφορούν σε εμβάπτιση βαμμένων χαλύβδινων δοκιμίων, διαστάσεων 100mm × 100mm × 6mm, σε βάθος 2.5m για συνολικό διάστημα ενός έτους. Τα πειράματα αυτά πραγματοποιήθηκαν με βάση τις οδηγίες ASTM D 3623 και ASTM D 6990. Συνολικά 6 δοκίμια ανά σύστημα βαφής «antifouling» εμβαπτίστηκαν στο πεδίο (Exp. PU1, Exp. PU2, Exp. Si, Ref. Si, Acrylic), καθώς και 3 δοκίμια βαμμένα με το αντιδιαβρωτικό χρώμα πολυουρεθάνης (PU), τα οποία χρησιμοποιήθηκαν ως αρνητική αναφορά (negative control) για το πειραματικό χρώμα Exp. PU1. Δηλαδή, τα δοκίμια αυτά, ακριβώς επειδή δεν μπορούν να εμποδίσουν την επικάθιση των θαλάσσιων οργανισμών, μπορούσαν να ρυπανθούν πολύ έντονα, παρέχοντας ενδείξεις της θαλάσσιας χλωρίδας και πανίδας της περιοχής εμβάπτισης. Κάθε δύο μήνες ένα δοκίμιο αποσυρόταν από την περιοχή και μεταφερόταν στο εργαστήριο για αξιολόγηση. Η αξιολόγηση περιελάμβανε υπολογισμό του ποσοστού κάλυψης της βαμμένης επιφάνειας από φυτικούς και ζωικούς θαλάσσιους οργανισμούς (foulers), το είδος των οργανισμών αυτών και τυχόν φυσική αλλοίωση των βαφών λόγω προσκόλλησης των οργανισμών. Η αξιολόγηση αυτή οδηγεί στη βαθμολόγηση του δοκιμίου, τόσο σε σχέση με την πυκνότητα των οργανισμών (fouling rating-F.R.), όσο και σε σχέση με τις αλλοιώσεις που μπορεί να έχουν προκληθεί από αυτούς ή από το περιβάλλον (physical damage rating-P.D.R.). Τα δοκίμια που αποσύρονταν από το πεδίο δεν ξαναχρησιμοποιούνταν. Η αξιολόγηση περιελάμβανε επίσης ηλεκτροχημική εξέταση των δοκιμίων με φασματοσκοπία ηλεκτροχημικής εμπέδησης (EIS), καθώς και μελέτη της σκληρότητας των βαφών (μέσω της δοκιμής απόσβεσης ταλάντωσης εκκρεμούς κατά König – ISO 1522), όπως και τη μεταβολή των οπτικών τους ιδιοτήτων, μέσω μετρήσεων αποχρωματισμού και στιλπνότητας 60^{o}.

Τα αποτελέσματα έδειξαν ότι η εμπορική βαφή σιλικόνης, η οποία βασίζεται στην απελευθέρωση ρύπων (foul release), δεν επέδειξε σταθερή αντι-επικαθιστική δράση, καθώς στην επιφάνεια των δοκιμίων έπειτα από 8, 10 και 12 μήνες παρατηρήθηκε πολύ έντονο «fouling», το οποίο οδήγησε σε ραγδαία πτώση του F.R., το οποίο έλαβε τιμές 9.55%, 10.8% και 6.61%, αντίστοιχα, καθιστώντας τη βαφή μη αποδοτική (θεωρώντας ότι η αποδοτική βαφή έχει F.R.≥80%). Ωστόσο, οι οργανισμοί που είχαν επικαθίσει, οι οποίοι ήταν κυρίως εκπρόσωποι της οικογένειας *serpulidae*, μπορούσαν να αφαιρεθούν πολύ εύκολα κάτω από τρεχούμενο νερό μικρής πίεσης. Αυτό οφείλεται στην μικρή επιφανειακή ενέργεια των σιλικονούχων χρωμάτων. Παρόλα αυτά, αν και οι οργανισμοί αφαιρέθηκαν εύκολα, παρατηρήθηκε πολύ έντονο «digging effect» στην επιφάνεια του δοκιμίου, δηλαδή οι οργανισμοί είχαν «σκάψει» τη βαφή, προκειμένου να προσκολληθούν ισχυρότερα, αν και τελικά αυτό δεν κατέστη δυνατό. Σε πραγματικές συνθήκες, η έκταση του «digging» θα είναι συνάρτηση του χρόνου που το πλοίο παραμένει αδρανές στο λιμάνι. Οι μετρήσεις σκληρότητας του δοκιμίου ήταν χαρακτηριστικές της μαλακής φύσης της σιλικόνης, γύρω στις 25 μονάδες κατά König, λόγω του ότι είναι ελαστομερές.

Η εμπορική ακρυλική βαφή, η οποία βασίζεται στην τεχνολογία του αυτολειαινόμενου συμπολυμερούς με βιοκτόνα Cu_2O+Zineb, παρουσίασε την καλύτερη συμπεριφορά κατά τη διάρκεια της στατικής εμβάπτισης στην Ελευσίνα. Ο δείκτης F.R. ήταν μεγαλύτερος του 94.93%, καθ' όλη τη διάρκεια του πειράματος. Τα δοκίμια δεν παρουσίασαν σχεδόν καθόλου προσκόλληση μακρο-οργανισμών. Η υψηλή αποδοτικότητα της βαφής αυτής προκύπτει από τον τρόπο δράσης της, που είναι η απελευθέρωση των βιοκτόνων (leaching). Η βαφή αυτή δεν διαθέτει καθόλου οπτικές ιδιότητες, παρουσιάζει μεγαλύτερη σκληρότητα από την εμπορική σιλικόνη (περίπου 50-70 μονάδες κατά König αλλά με διακυμάνσεις) και το βασικό της μειονέκτημα είναι η φθορά του τελικού επιχρίσματος (wearing of the topcoat), όπως και το φαινόμενο του «chipping», κατά το οποίο δημιουργούνται πολλαπλές εστίες «ξεφλουδίσματος» της βαφής. Το φαινόμενο αυτό παρατηρήθηκε μετά από 12 μήνες εμβάπτισης και ήταν τόσο εκτεταμένο που οδήγησε σε ραγδαία πτώση του P.D.R. στην τιμή του 22.12%.

Η πειραματική σιλικόνη με 0.56% ακινητοποιημένη Econea αποτέλεσε μία βελτιωμένη έκδοση της εμπορικής σιλικόνης. Το σύστημα αυτό παρουσίασε προσκόλληση μακρο-οργανισμών (macrofouling) μεγάλης ποικιλίας, όπως και η εμπορική σιλικόνη, καθιστώντας το μη αποδοτικό ανά διαστήματα, όπως παρατηρήθηκε έπειτα από 8 και 10 μήνες πειράματος, όπου η τιμή του F.R. έπεσε στο 69.46% και στο 38.97%, αντίστοιχα. Παρόλα αυτά, η μειωμένη απόδοση δεν ήταν τόσο έντονη όσο της εμπορικής σιλικόνης. Οι προσκολλημένοι οργανισμοί μπορούσαν εύκολα να απομακρυνθούν με τρεχούμενο νερό και μικρή πίεση, ενώ το «digging effect», από το οποίο υπέφερε η εμπορική σιλικόνη, ήταν μηδαμινό. Συνεπώς, σε πραγματικές συνθήκες, θα ήταν εύκολο για τους οργανισμούς να αποκολληθούν κατά τον πλου με ελάχιστη φυσική αλλοίωση. Τέλος, οι οπτικές ιδιότητες παρουσίασαν πολύ μικρές διακυμάνσεις, ενώ η σκληρότητα του συστήματος αυτού βρέθηκε παραπλήσια ή κάπως μικρότερη του αντίστοιχου εμπορικού.

Η πειραματική πολυουρεθάνη με 2% ακινητοποιημένη Econea δεν θα μπορούσε να χρησιμοποιηθεί σαν βαφή antifouling. Το σύστημα αυτό έχασε την αντιρρυπαντική του προστασία πολύ γρήγορα, αφού ήδη έπειτα από 6 μήνες το F.R. είχε πέσει στο 64.69%, ενώ έπειτα από 8, 10 και 12 μήνες, οι αντίστοιχες τιμές ήταν 12.14%, 3.39% και 12.38%. Η βασική διαφορά με τα υπόλοιπα συστήματα είναι ότι οι οργανισμοί που παρατηρήθηκαν, κυρίως βρυόζωα (bryozoans) και σκώληκες της οικογένειας *serpulidae,* ήταν πολύ έντονα προσκολλημένοι πάνω στη βαφή. Ακόμη και σε πραγματικές, δυναμικές συνθήκες, θα ήταν πολύ δύσκολο για αυτούς τους οργανισμούς να αποκολληθούν από τη γάστρα. Σε σχέση με τη φυσική αλλοίωση, «digging», αποχρωματισμός, αύξηση της σκληρότητας και μείωση της 60^{o} στιλπνότητας ήταν το γενικό μοτίβο που παρατηρήθηκε, καθ' όλη τη διάρκεια του πειράματος.

Η πειραματική πολυουρεθάνη με μείγμα βιοκτόνων παρουσίασε την χειρότερη απόδοση, αφού ήδη από τους πρώτους δύο μήνες πειράματος το F.R ήταν ίσο με 44.3% και παρουσίασε ακόμη μεγαλύτερη πτώση στα υπόλοιπα διαστήματα. Τα βασικά είδη οργανισμών που παρατηρήθηκαν ήταν βρυόζωα, άλγεις και τα ασβεστολιθικά κελύφη δακτυλιοσκωλήκων (spirorbinae). Όλοι οι οργανισμοί ήταν πολύ ισχυρά προσκολλημένοι πάνω στην βαφή, όμοια με το προηγούμενο σύστημα πολυουρεθάνης. Η φυσική αλλοίωση προήλθε κυρίως από «digging» των οργανισμών. Οι υπόλοιπες ιδιότητες ακολούθησαν το γενικό μοτίβο που περιγράφηκε για την προηγούμενη πειραματική πολυουρεθάνη. Οι τιμές της σκληρότητας δεν μπορούν να συγκριθούν με τα υπόλοιπα συστήματα, γιατί παρουσίασαν διακυμάνσεις.

Δεν παρατηρήθηκε απώλεια πιγμέντων για καμία από τις πειραματικές πολυουρεθάνες (softness rating equal to 10).

Συνεπώς, σε στατικές συνθήκες εμβάπτισης, το ακρυλικό σύστημα παρουσίασε την καλύτερη συμπεριφορά. Σε σχέση με τη φυσική αλλοίωση/ζημιά από τους οργανισμούς ή από φαινόμενα φθοράς κατά την εμβάπτιση, η πειραματική σιλικόνη παρουσίασε την καλύτερη συμπεριφορά. Ως εκ τούτου, σε πραγματικές συνθήκες, όπου οι οργανισμοί μπορούν να αφαιρεθούν εύκολα λόγω τριβής, η πειραματική σιλικόνη μπορεί να παρέχει αποδοτική αντιρρυπαντική προστασία μακροπρόθεσμα. Επιπλέον, η τεχνολογία του ακινητοποιημένου βιοκτόνου καθιστά τη βαφή αυτή μία φιλική προς το περιβάλλον πρόταση.

Ηλεκτροχημικά, οι ιδιότητες φραγμού της πειραματικής πολυουρεθάνης με μείγμα βιοκτόνων παρέμειναν σχεδόν ανεπηρέαστες κατά τη διάρκεια του πειράματος. Παραπλήσια συμπεριφορά παρουσίασε και η πειραματική σιλικόνη.

Λαμβάνοντας υπόψη όλες τις παρατηρήσεις, η πειραματική σιλικόνη μπορεί να αποτελέσει μία αποδοτική αντιρρυπαντική και αντιδιαβρωτική λύση για ναυπηγικές εφαρμογές, εάν τηρούνται και κάποιες προφυλάξεις, αναφορικά με την μαλακή ελαστομερή της σύνθεση.

4. Προσδιορισμός των μηχανικών ιδιοτήτων βαμμένων δοκιμίων και των φυσικών τους παραμέτρων

Οι δοκιμές που πραγματοποιήθηκαν στην εν λόγω έρευνα είχαν ως σκοπό να αξιολογήσουν τα συστήματα βαφής σε σχέση με τη διαπερατότητά τους σε νερό (water liquid transmission rate test- BS EN 1062-3), την πρόσφυση του πολυστρωματικού συστήματος με το μεταλλικό υπόστρωμα μέσω δοκιμών βαθείας κοίλανσης (cupping test- ISO 1520), την τάση για συλλογή ρύπων μέσω έκθεσης στην ατμόσφαιρα (dirt pick-up test- ASTM D 3719-00), καθώς και την εκδήλωση κιμωλίασης (chalking test- ASTM D 4214-98).

Σχετικά με τη δοκιμή διαπερατότητας σε νερό (water liquid transmission rate test), χρησιμοποιήθηκαν πυρότουβλα, των οποίων η μία από τις δύο μεγαλύτερες πλευρές βάφτηκε με το εκάστοτε πολυστρωματικό χρώμα, ενώ όλες οι υπόλοιπες επιφάνειες καλύφθηκαν με μονωτική ρητίνη. Τα τούβλα υποβλήθηκαν σε 4 κύκλους, κάθε ένας από τους οποίους περιελάμβανε κάποια ελαφριά θέρμανση των τούβλων για εξάλειψη της υγρασίας (conditioning), εμβάπτιση σε πόσιμο νερό και ξήρανση. Ζύγιση των τούβλων πραγματοποιήθηκε σε συγκεκριμένα διαστήματα και ο ρυθμός διαπερατότητας υπολογίστηκε μέσω συγκεκριμένης σχέσης που προτείνεται από την αντίστοιχη οδηγία. Τα συστήματα που μελετήθηκαν σε διαπερατότητα ήταν τα Ref. Si, Exp. Si, Acrylic, Exp. PU1, Exp. PU2 και PU. Όλα τα συστήματα παρουσίασαν μικρή διαπερατότητα, κλάσης III.

Για τη δοκιμή βαθείας κοίλανσης (cupping test) χρησιμοποιήθηκαν δοκίμια διαστάσεων 120mm × 60mm × 1mm για το Ref. Si και το Acrylic, ενώ δοκίμια διαστάσεων 200mm × 60mm × 1mm χρησιμοποιήθηκαν για τα συστήματα Exp. Si, Exp. PU1 και Exp. PU2. Χρησιμοποιήθηκαν 3 δοκίμια ανά σύστημα βαφής. Κατά τη βαθεία κοίλανση, η βαφή θεωρείται ότι έχει αστοχήσει από τη στιγμή που δημιουργείται η πρώτη ρωγμή κατά την κάμψη ή όταν το πολυστρωματικό σύστημα έχει αποκολληθεί από το μεταλλικό υπόστρωμα. Την καλύτερη συμπεριφορά εκδήλωσε το Ref. Si σύστημα, με μέσο βάθος κοίλανσης μέχρι την πρώτη ρωγμάτωση ίσο με 1.70mm, ακολουθούμενο από το Exp. PU1 με 1.64mm, το Acrylic με 1.55mm, το Exp. Si με 1.22mm και τελικά το Exp. PU1 με 0.84mm.

Η δοκιμή προσκόλλησης ρύπων (dirt pick-up test) στην επιφάνεια των βαφών πραγματοποιήθηκε με έκθεση δοκιμίων διαστάσεων 150mm × 250mm × 6mm για 61 ημέρες στην ατμόσφαιρα (weathering test). Τα δοκίμια τοποθετήθηκαν σε βάση κλίσης 45^{o} με νότιο προσανατολισμό. Η αξιολόγηση των βαφών γίνεται μέσω μετρήσεων αποχρωματισμού και με βάση τύπο που προτείνεται από την οδηγία ASTM D 3719-00. Σε αυτήν τη δοκιμή εξετάστηκαν οι βαφές Ref. Si, Exp. Si, Acrylic, Exp. PU1 και Exp. PU2, ενώ δύο δοκίμια ανά σύστημα βαφής εκτέθηκαν στο περιβάλλον. Τα αποτελέσματα έδειξαν την καλύτερη συμπεριφορά της Exp. PU1 βαφής με «dirt collection index (Dc)» 97.85%, ακολουθούμενη από το σύστημα Ref. Si με 100.65 %, το Exp. Si με 101.44%, το Exp. PU2 με 102.82% και το Acrylic με 118.14%.

Τέλος, η δοκιμή κιμωλίασης (chalking) αφορά στην αξιολόγηση των βαφών με βάση τη δημιουργία εύθρυπτης σκόνης στην επιφάνεια του τελικού επιχρίσματος, ως αποτέλεσμα έκθεσης πιγμέντων, λόγω μικρής πρόσφυσης με την πολυμερική μήτρα. Η κιμωλίαση μπορεί να είναι αποτέλεσμα αλλοίωσης των βαφών ή εγγενές χαρακτηριστικό τους, όπως στην περίπτωση του ακρυλικού χρώματος. Δύο δοκίμια ανά σύστημα βαφής εξετάστηκαν σε κιμωλίαση (Ref. Si, Exp. Si, Acrylic, Exp. PU1), με βάση τη «method D-TNO type method». Μόνο το ακρυλικό σύστημα παρουσίασε «chalking» No. 3, ενώ τα υπόλοιπα συστήματα δεν παρουσίασαν και αξιολογήθηκαν ως No. 2.

Συνεπώς, τα πειράματα αυτά ανέδειξαν ως καλύτερα συστήματα τα Ref. Si και Exp. PU1, τα οποία παρουσίασαν την καλύτερη συμπεριφορά από 2 φορές.

5. Γενικά συμπεράσματα

Από την ανάλυση που προηγήθηκε προκύπτει ότι την καλύτερη αντιδιαβρωτική συμπεριφορά σε κατάσταση με ελάττωμα (κρίνοντας από τις φάσεις σκωρίας στην περιοχή του ελαττώματος, δηλαδή των σχισμών) παρείχε το σύστημα Exp. PU1, ακολουθούμενο από το Exp. Si. Σε άθικτη κατάσταση, το Exp. Si σύστημα παρουσίασε την πιο σταθερή συμπεριφορά έπειτα από επιταχυνόμενη γήρανση. Από άποψη υδροδυναμικής συμπεριφοράς, τα δύο συστήματα πειραματικής πολυουρεθάνης και οι δύο σιλικόνες παρουσίασαν ίδια υδροδυναμική απόδοση σε κλίμακα εργαστηρίου, καθώς οι τιμές αντίστασης ήταν γύρω από τις αντίστοιχες της λείας πλάκας. Από άποψη αποτελεσματικότητας ενάντια στις επικαθίσεις ή στο κατά πόσο ισχυρά προσκολλούνται οι θαλάσσιοι οργανισμοί πάνω στη βαμμένη επιφάνεια, το ακρυλικό σύστημα θα ήταν ιδανικό σε στατική εμβάπτιση, ενώ το Exp. Si θα αποτελούσε μία πολύ αποδοτική λύση σε δυναμικές συνθήκες, συνδυάζοντας χαμηλή επιφανειακή ενέργεια (άρα εύκολη αποκόλληση των οργανισμών), πολύ μικρή φυσική αλλοίωση λόγω «digging» και όλα αυτά μαζί με ικανοποιητικές ιδιότητες φραγμού (συνεπώς διατήρηση χαμηλής διαπερατότητας για μεγαλύτερο χρονικό διάστημα), εφόσον τηρούνται κάποιες προφυλάξεις ως προς το χειρισμό και την ελικτικότητα του πλοίου, προκειμένου να ελαχιστοποιηθεί η πιθανότητα πρόκλησης μηχανικών αλλοιώσεων στη βαφή. Αντίθετα, κανένα από τα δύο πειραματικά συστήματα πολυουρεθάνης θα μπορούσε να εμποδίσει την επικάθιση των θαλάσσιων οργανισμών. Τέλος, τα συστήματα Ref. Si και Exp. PU1 παρουσίασαν την καλύτερη συμπεριφορά έπειτα από δοκιμές προσδιορισμού μηχανικών και φυσικών ιδιοτήτων. Από αυτές τις παρατηρήσεις προκύπτει ότι δεν υπάρχει το ιδανικό χρώμα. Προφανώς, εάν τα κύρια κριτήρια σύγκρισης είναι η αποτελεσματικότητα στην παρεμπόδιση των επικαθίσεων και η υδροδυναμική απόδοση, που αποτελούν κυρίαρχες παραμέτρους για την επιλογή ενός «antifouling» χρώματος, η πειραματική σιλικόνη θα ήταν η πιο κατάλληλη, φιλική προς το περιβάλλον επιλογή.

Contents

1 Rust morphology characterization of silicone-based marine antifouling paints after salt spray test on scribed specimens 3

1.1 Introduction . . . 3
1.2 Experimental methods and materials . . . 6
1.2.1 Coating systems examined . . . 6
1.2.2 Accelerated aging tests on scribed specimens . . . 7
1.2.3 SEM, XRD and Raman examination of rust samples . . . 7
1.3 Results and Discussion . . . 8
1.3.1 Observation of the scribed areas . . . 8
1.3.2 XRD examination of rust samples . . . 10
1.3.3 Raman spectra identification of rust samples . . . 12
1.3.3.1 Raman spectra identification of rust samples from scribed experimental silicone system (Paint A) . . . 12
1.3.3.2 Raman spectra identification of rust samples from scribed reference silicone system (Paint B) . . . 13
1.3.4 Identification of rust morphologies . . . 15
1.3.5 Correlation of the observed rust morphologies with paint efficiency . . . 16
1.4 Conclusions . . . 20

2 Rust morphology characterization of polyurethane and acrylic-based marine antifouling paints after salt spray test on scribed specimens 21

2.1 Introduction . . . 21
2.2 Experimental methods and materials . . . 23
2.2.1 Coating systems examined . . . 23
2.2.2 Salt spray tests-XRD, Raman and SEM examination of scribed samples . 23
2.3 Results and Discussion . . . 24
2.3.1 Observation of the scribed areas . . . 24
2.3.2 XRD examination of rust samples . . . 26
2.3.3 Raman spectra identification of rust samples . . . 29
2.3.3.1 Raman spectra identification of rust samples from scribed experimental polyurethane system (Paint A) . . . 29

2.3.3.2 Raman spectra identification of rust samples from scribed acrylic system (Paint B) . . . 31
2.3.4 Identification of rust morphologies . . . 33
2.3.5 Correlation of the observed rust morphologies with paint efficiency . . . 34
2.4 Conclusions . . . 39

3 Electrochemical impedance spectroscopy of scribed coated steel after salt spray testing 41
3.1 Introduction . . . 41
3.2 Experimental methods and materials . . . 44
3.2.1 Salt spray test and coating system . . . 44
3.2.2 Electrochemical examination setup . . . 44
3.2.3 Fitting of the experimental data . . . 46
3.2.4 Reproducibility and error estimation . . . 47
3.3 Results and discussion . . . 47
3.3.1 Impedance in scribed condition . . . 47
3.3.2 Linear polarization resistance method . . . 49
3.3.3 Semi-infinite diffusion impedance . . . 50
3.3.4 Finite-length diffusion impedance . . . 51
3.3.4.1 Restricted diffusion in its ideal form . . . 52
3.3.4.2 Modified restricted diffusion . . . 53
3.3.4.3 Anomalous linear restricted diffusion . . . 57
3.3.4.4 Transmissive diffusion in its ideal form . . . 59
3.3.4.5 Modified transmissive diffusion . . . 60
3.3.5 Modeling with generalized Warburg diffusion . . . 62
3.3.6 Orazem-Tribollet connection for the selected diffusion impedance models 63
3.3.7 Comparative overview of the results . . . 67
3.4 Conclusions . . . 70

4 Experimental investigation of roughness effect on ship resistance using flat plate and model towing tests 72
4.1 Introduction . . . 73
4.2 Experimental methods and materials . . . 77
4.2.1 Flat plate experimental setup . . . 77
4.2.2 Uncertainty estimates . . . 79
4.2.3 Ship model towing tests . . . 82
4.3 Results and discussion . . . 84
4.3.1 Flat plate towing tests . . . 84
4.3.1.1 Effect of tension wires on smooth plate resistance . . . 84
4.3.1.2 Effect of trip wires on smooth plate resistance . . . 85
4.3.1.3 Plate entirely covered with sandpapers . . . 86

4.3.1.4 Uniform sand roughness height (k_s) calculation from Schlichting diagram . . . 87
4.3.1.5 Roughness functions and correlation with Nikuradse results . . 89
4.3.2 Ship resistance calculation . . . 91
4.3.2.1 Model based extrapolation methods for smooth hull . . . 91
4.3.2.2 Comparison of flat plate and model based extrapolation methods for rough hull . . . 93
4.4 Conclusions . . . 94

5 Experimental investigation of paint roughness on ship resistance using flat plate towing tests 97
5.1 Introduction . . . 97
5.2 Experimental methods and materials . . . 99
5.2.1 Flat plate experimental setup . . . 99
5.2.2 Towing tank tests on painted flat plate . . . 99
5.3 Results and discussion . . . 100
5.3.1 Plate painted with AF paints on the whole surface–Resistance results . . 100
5.3.2 Roughness function calculation . . . 104
5.3.3 Effect of fouling on the resistance of a flat plate . . . 107
5.4 Conclusions . . . 109

6 Field tests of commercial and experimental antifouling paints in Elefsis Gulf110
6.1 Introduction . . . 111
6.2 Experimental methods and materials . . . 112
6.2.1 Painting systems examined . . . 112
6.2.2 Description of field tests in Elefsis . . . 112
6.2.3 Biofouling assessment . . . 114
6.2.4 Water quality measurements . . . 115
6.2.5 Electrochemical examination . . . 115
6.2.6 Coating hardness measurements . . . 115
6.2.7 Physical properties measurements . . . 115
6.3 Results and discussion . . . 116
6.3.1 Commercial Silicone and Arcylic AF systems . . . 116
6.3.1.1 After 2 months of immersion . . . 116
6.3.1.2 After 4 months of immersion . . . 119
6.3.1.3 After 6 months of immersion . . . 121
6.3.1.4 After 8 months of immersion . . . 125
6.3.1.5 After 10 months of immersion . . . 129
6.3.1.6 After 12 months of immersion . . . 134
6.3.1.7 Conclusions with regard to the field tests of reference silicone and acrylic paints . . . 138

6.3.2 Experimental Polyurethane (Exp PU1), Experimental Silicone (Exp Si) AF systems and Polyurethane (PU) anticorrosion system . . . 139
6.3.2.1 After 2 months of immersion . . . 139
6.3.2.2 After 4 months of immersion . . . 145
6.3.2.3 After 6 months of immersion . . . 151
6.3.2.4 After 8 months of immersion . . . 156
6.3.2.5 After 10 months of immersion . . . 161
6.3.2.6 After 12 months of immersion . . . 165
6.3.2.7 Conclusions with regard to the field tests of Exp PU1, Exp Si AF systems and the PU non-AF paint . . . 170
6.3.3 Experimental Polyurethane (Exp PU2) AF system . . . 171
6.3.3.1 After 2 months of immersion . . . 171
6.3.3.2 After 4 months of immersion . . . 172
6.3.3.3 After 6 months of immersion . . . 173
6.3.3.4 After 8 months of immersion . . . 174
6.3.3.5 After 10 months of immersion . . . 177
6.3.3.6 After 12 months of immersion . . . 179
6.3.3.7 Conclusions with regard to the field tests of the Exp PU2 AF system . . . 181
6.3.4 Electrochemical results . . . 183
6.3.4.1 Reference silicone system . . . 183
6.3.4.2 Acrylic system . . . 186
6.3.4.3 Experimental silicone system . . . 189
6.3.4.4 Experimental polyurethane (1) system . . . 191
6.3.4.5 Polyurethane system . . . 192
6.3.4.6 Experimental polyurethane (2) system . . . 194
6.3.5 Water titration results . . . 195
6.4 Conclusions . . . 198

7 Mechanical testing of experimental and commercial antifouling systems and electrochemical investigation thereof after accelerated aging tests on intact specimens 200
7.1 Introduction . . . 200
7.2 Experimental methods and materials . . . 204
7.2.1 Painting systems examined . . . 204
7.2.2 Experimental procedure . . . 204
7.2.3 Electrochemical examination . . . 205
7.2.4 Coating hardness and physical properties measurements . . . 205
7.2.5 Mechanical testing and determination of physical parameters . . . 205
7.3 Results and discussion . . . 207

7.3.1 Electrochemical measurements on intact specimens during a 9-week accelerated aging test in salt spray chamber . . . 207
7.3.1.1 Salt spray tests on reference silicone (Ref Si) system . . . 207
7.3.1.2 Salt spray tests on acrylic (Acrylic) system . . . 210
7.3.1.3 Salt spray tests on experimental silicone (Exp Si) system . . . 213
7.3.1.4 Salt spray tests on experimental polyurethane (Exp PU1) system 216
7.3.1.5 Salt spray tests on anticorrosive polyurethane (PU) system . . . 219
7.3.2 Conclusions with regard to the results after 9 weeks of salt spray examination . . . 222
7.3.3 Electrochemical measurements on intact specimens during a 9-week accelerated aging test in UV chamber . . . 222
7.3.3.1 UV tests on reference silicone (Ref Si) system . . . 222
7.3.3.2 UV tests on acrylic (Acrylic) system . . . 225
7.3.3.3 UV tests on experimental silicone (Exp Si) system . . . 227
7.3.3.4 UV tests on experimental polyurethane (Exp PU1) system . . . 230
7.3.3.5 UV tests on anticorrosive polyurethane (PU) system . . . 232
7.3.4 Conclusions with regard to the results after 9 weeks of UV examination . 234
7.3.5 Electrochemical measurements on intact specimens during a 12-month immersion in artificial seawater in laboratory conditions . . . 235
7.3.5.1 Reference silicone (Ref Si) system . . . 235
7.3.5.2 Acrylic system . . . 240
7.3.5.3 Experimental silicone (Exp Si) system . . . 246
7.3.5.4 Experimental polyurethane (Exp PU1) system . . . 250
7.3.6 Conclusions with regard to the results after 12 months of laboratory immersion test . . . 256
7.3.7 EIS testing of parameters for intact coatings . . . 257
7.3.8 Water quality measurements from laboratory immersion test . . . 258
7.3.9 Mechanical testing and determination of physical parameters . . . 258
7.3.9.1 Water-liquid transmission rate test (permeability) . . . 258
7.3.9.2 Cupping test . . . 263
7.3.9.3 Dirt pick-up test . . . 269
7.3.9.4 Chalking test . . . 272
7.4 Conclusions . . . 274

8 Conclusions of the PhD thesis **277**

9 Innovation of the PhD thesis **280**

10 Suggestions for further research **283**

11 Publications **284**

12 Curriculum Vitae **286**

13 Bibliography **292**

A Appendix of Chapter 3 **306**

A.1 Equivalent circuits and total impedance relations for Randles and Orazem Tribollet connections 306

A.2 Rest of diffusion impedance models examined for the experimental data 307

A.2.1 Results with regard to the restricted diffusion impedance mechanism . . 307

A.2.2 Results with regard to the anomalous ADIa diffusion impedance mechanism 309

A.2.3 Results with regard to the transmissive diffusion impedance mechanism . 310

A.2.4 Results with regard to the generalized Warburg impedance mechanism . 312

A.2.5 Fitting of the Bode plots for the selected models 313

A.2.6 Results based on the cast iron in drinking water problem 315

B Appendix of Chapter 3 **316**

B.1 Introduction 316

B.2 Results considering finite-length diffusion impedance theory 317

B.2.1 Results for specimen No. 2 317

B.2.2 Results for specimen No. 3 318

B.2.3 Results for specimen No. 4 319

B.2.4 Results for specimen No. 5 322

B.2.5 Results for specimen No. 7 323

B.2.6 Results for specimen No. 8 324

B.2.7 Summary of results 326

B.3 Results considering the porous electrode theory 326

B.3.1 Results for specimen No. 1 327

B.3.2 Results for specimen No. 2 329

B.3.3 Results for specimen No. 3 331

B.3.4 Results for specimen No. 4 333

B.3.5 Results for specimen No. 5 335

B.3.6 Results for specimen No. 6 337

B.3.7 Results for specimen No. 7 338

B.3.8 Results for specimen No. 8 340

B.3.9 Summary of results using the porous electrode theory 341

B.4 Difference in physical interpretation between finite length diffusion and porous electrode theory 341

B.4.1 Finite-length diffusion 341

B.4.2 Porous electrode theory 342

C Appendix of Chapter 6 **344**

C.1 Foulers dimensions measurements for Exp. Si, Exp. PU1 and PU specimens immersed for 2 months in Elefsis . . . 344

C.2 Foulers dimensions measurements for Exp. Si, Exp. PU1 and PU specimens immersed for 4 months in Elefsis . . . 346

C.3 Foulers dimensions measurements for Exp. Si, Exp. PU1 and PU specimens immersed for 6 months in Elefsis . . . 351

C.4 Foulers dimensions measurements for Exp. Si specimen immersed for 8 months in Elefsis . . . 357

C.5 Foulers dimensions measurements for Exp. Si specimen immersed for 10 months in Elefsis . . . 358

C.6 Foulers dimensions measurements for Exp. Si and Exp. PU1 specimens immersed for 10 months in Elefsis . . . 360

C.7 Foulers dimensions measurements for Exp. PU2 specimen immersed for 4 months in Elefsis . . . 363

C.8 Foulers dimensions measurements for Exp. PU2 specimen immersed for 6 months in Elefsis . . . 364

C.9 Foulers dimensions measurements for Exp. PU2 specimen immersed for 8 months in Elefsis . . . 365

C.10 Foulers dimensions measurements for Exp. PU2 specimen immersed for 10 months in Elefsis . . . 367

C.11 Foulers dimensions measurements for Exp. PU2 specimen immersed for 12 months in Elefsis . . . 367

Introduction

Antifouling marine paints constitute a crucial part of the maritime economy. This is because the quality of the applied painting system is directly related to the hydrodynamic efficiency of the ship in the as-painted condition, the vulnerability to fouling and the attachment strength of the foulers. A fouled hull may lead to increased fuel consumption and voyage costs. Biofouling on ship hulls has also adverse environmental effects, arising from biocide(s) leaching during ship voyaging. It is, hence, of paramount importance to formulate environmentally friendly antifouling paints, onto which the marine organisms would not be able to attach strongly.

To this purpose, the focus of the present thesis was the examination and evaluation of experimental, environmentally friendly, marine antifouling paints. The experimental formulations were developed during the Foul-X-Spel project (Grant agreement: 285552) and were based on immobilization of the biocide into the polymeric matrix. In this way, the biocide would act by contact and not through leaching into the sea.

Evaluation of the newly-developed paints was performed in terms of anticorrosion, hydrodynamic and antifouling efficiency, as well as, through examination of their mechanical and physical properties.

More specifically, in the first two chapters of the present thesis, the anticorrosion efficiency of the painting systems is presented, which was evaluated through salt spray tests on coated steel specimens with scribes. The morphology of the corrosion products in the area of the scribes was linked to the paint efficiency.

In the third chapter, a representative scribed specimen from the ones investigated in the first two chapters was selected and its corrosion behavior was examined, at specific intervals during the salt spray test, through electrochemical impedance spectroscopy (EIS). The obtained EIS spectra during the exposure were correlated with actual physical processes that affect the corrosion over time. For this reason, this study intended to clarify the type of diffusion impedance that best described dissolved oxygen diffusion at each interval, considered as the rate-determining step. Some supplementary imformation of this study is presented in Appendix A. In Appendix B the appropriate diffusion impedance models describing the EIS curves of the rest specimens are presented, while also the results considering the porous electrode theory for all specimens are also included.

In the fourth and fifth chapters, hydrodynamic investigation of roughness effect on ship resistance was performed, through towing tests on a flat plate. More specifically, in the fourth chapter, flat plate tests were performed in smooth and rough condition. The experiments on smooth flat plate included examination of a series of trip wires for flow stimulation, among

which the optimum was 1.3 mm. In rough condition, the plate was covered with sandpapers of 40 and 80-grit. The roughness functions were calculated and extrapolation to ship scale was performed. In the fifth chapter, flat plate tests in painted condition were performed and the theoretical roughness function describing the painted surfaces was determined. A comparison with regard to the hydrodynamic behavior of the tested antifouling paints was performed for the as-painted condition from the hydrodynamic resistance measurements.

In the sixth chapter, the antifouling assessment of the experimental paints is presented. To this purpose, static field tests were performed in Elefsis Gulf for 1 year. The specimens were immersed at 2.5 m depth and examined every two months, in terms of fouling density, types of foulers, electrochemical, mechanical and optical properties variations. Commercial paints were also immersed, for comparative purposes. Finally, a ranking among the different systems was performed. Some supplementary information of this champter is provided in Appendix C.

Finally, in the seventh chapter, the anticorrosion efficiency of the new products was evaluated through accelerated aging tests (salt spray, UV and immersion in artificial seawater) in intact state. The specimens were examined at frequent intervals, with regard to their electrochemical behavior, mechanical and optical properties. Also, standardized tests, regarding determination of their mechanical and physical properties were performed. All the tests were also conducted for the commercial painting systems, as well. Finally, a ranking among the different systems was attained.

Chapter 1

Rust morphology characterization of silicone-based marine antifouling paints after salt spray test on scribed specimens

Abstract

The experimental silicone formulation (Exp. Si) containing 0.56% immobilized Econea was examined in terms of its anticorrosion performance. The painting system was applied on steel specimens, then scribed with a sharp cutter and examined for 12 weeks in cyclic salt spray exposure. Identification of the rust morphologies was done with XRD, Raman spectroscopy, SEM and EDS methods. The observed paint swelling during the experiment caused the formation of large, coarse rust agglomerates without adherence, which detached frequently causing reinitiation of the corrosion process. This procedure was revealed by the oxyhydroxide nature of the corrosion products. The basic corrosion morphology observed was a mixture of akaganeite and goethite. The commercial, silicone-based, foul-release coating (Ref. Si) served as a reference. The experimental formulation exhibited superior anticorrosion performance overall, since the reference system presented higher enlargement of the scribed areas, increased substrate material loss, a highly inhomogeneous corrosion layer with voids and smaller (stable) goethite amounts in the rust areas containing mainly akaganeite/goethite mixture.

1.1 Introduction

Accelerated aging tests have long been considered a fast method to examine the anticorrosion performance of organic coatings [1–3]. Among these, salt spray test is one of the most widespread techniques, because it offers the potential to perform tests in more realistic conditions, by applying the relevant standards (e.g.ISO 14993:2001). The painted specimens can be examined in the chamber either intact, in order to study the barrier properties of the intact coat, or scribed, in order to examine the protection that the unscratched part of the paint provides [4, 5]. The second scenario offers the ability to assess the anticorrosion efficiency of

the painting system when it is flawed, which represents a common problem during the service life of a paint.

Determination of corrosion efficiency in scribed condition is also important for marine antifouling (AF) coatings. More specifically, the hull paint could be scratched either from natural or mechanical causes. In the first case, the fouling communities attaching onto the hull would dig into the paint in order to adhere more firmly [6], while in the second case paint defects could be created during ship handling or maneuvering. Hence, it is important to examine antifouling marine paints, not only in terms of their antifouling performance, but also in terms of their anticorrosion resistance by performing salt spray tests, which simulate the marine atmosphere [7].

Characterization of the performance of a paint, when it is scribed, can be performed by investigating the morphology of the corrosion products after the end of the salt spray test. In general, the most representative corrosion products of steel, when exposed to natural or artificial chloride containing environments are considered to be akaganeite (β-FeOOH), goethite (α-FeOOH), lepidocrocite (γ-FeOOH) and magnetite (Fe_3O_4) [8–10]. Formation of each of these oxides in salt spray conditions depends on the availability of dissolved hydrogen, oxygen and ions, which alternate among the dry, wet and salt fog conditions [11].

With regard to the nature of the corrosion products of steel, it is generally believed that magnetite forms at the interface of the metal substrate with the corrosion layer, where the conditions are more anoxic [12]. Presence of magnetite often denotes a high severity environment, while the higher the aggressiveness the more magnetite and less lepidocrocite is formed [13]. This is possibly due to the enhancement of magnetite production from lepidocrocite, through reaction of lepidocrocite with the ferrous ions from iron oxidation, and has been linked to high corrosion rates [14]. However, other study [15] suggests that magnetite, along with the rest of the iron oxides, is a more stable form than the oxyhydroxides and can be considered to provide protection to the steel substrate, reducing the corrosion rate.

Lepidocrocite is the most common corrosion product of steel found in a marine environment and forms, generally, in the outer layer of the rust, in contact with the environment [8]. Its presence decreases when the environmental conditions become more severe, in favor of formation of other phases, such as goethite or magnetite [13, 14]. Lepidocrocite has been linked to high corrosion rates, for painted mild steel exposed to marine atmosphere [15]. Salt spray tests have revealed that transformation of lepidocrocite to either of the aforementioned phases is favored during the drying process, while lepidocrocite itself forms during the wetting stage [11].

Goethite is the major corrosion product found in mild or severe chloride containing environments along with lepidocrocite and is considered the most stable of the oxyhydroxides [16]. Environments with high aggressiveness could promote formation of more crystalline structures or small particle goethite, which is believed to provide corrosion protection [13], since its stable structure inhibits chloride ions diffusion [17]. Chloride ions of certain concentration could accelerate transformation of lepidocrocite to goethite [15]. Usually, lepidocrocite transforms to goethite in the inner parts of the rust, leaving the lepidocrocite layer on the surface [18].

During a salt spray test, goethite is believed to form from lepidocrocite during the drying step of the cycle [14].

Akaganeite, a characteristic phase of severe marine atmospheres, requires high concentrations of chloride and ferrous ions to form, with the latter depending on relative humidity (RH) and time of wetness [19]. It is believed to form from oxidation of green rust (GR1) during dry conditions of natural exposure to marine atmosphere [20] and it is usually addressed at the steel/rust layer interface, after migration of the chloride ions through the rust layer [18]. Nevertheless, on the rust surface akaganeite can be formed through reaction of the ferrous ions, produced by corrosion, with chloride ions from the atmosphere [17]. During salt spray tests, formation of akaganeite is favored especially during the salt spray (fog) part of the cycle when the chloride ions are in abundance [13].

In general, akaganeite can adsorb an amount of chloride ions since they are part of its structure, however, above a threshold free chloride ions can attack the substrate and accelerate corrosion [18]. High akaganeite concentration has been linked to high corrosion rate and progressed corrosion state [21]. The same work highlighted also that the presence of akaganeite as the main corrosion product denotes intense and frequent detachment of large particle rust and exposure of the steel substrate to fresh attack. The same was also reported by Oh and Cook [22] after exposure of carbon steel specimens in marine environment. They assigned the presence of thick corrosion layers and increased chloride concentration to the increased amount of akaganeite noticed. Ma *et al.* [20] highlighted the importance of the porous, tunnel structure of β-FeOOH to the permeation of corrosive species, thus leading to corrosion acceleration, while they supported that the coexistence with more compact phases could restrict ion migration to the metallic substrate.

In accordance to the aforementioned analysis, the representative corrosion products of steel when exposed to salt spray conditions are presented in Table 1.1.

Table 1.1: Representative corrosion products of steel in salt spray conditions

Corrosion product	Location in rust layer	Salt spray step for formation
β-FeOOH	Outer rust layer-Rust/Substrate interface	Salt fog
γ-FeOOH	Outer rust layer	Humid
α-FeOOH	Inner rust layer	Dry
Fe_3O_4	Rust/Substrate interface	Dry

In the present chapter, the experimental silicone formulation containing 0.56% immobilized Econea was examined in terms of its anticorrosion properties, compared to the commercial silicone paint, serving as reference. The aim of this work was to compare the anticorrosion performance of the new formulation with the known efficiency of a reference paint of the same category. For this reason, steel specimens were painted with the silicone systems and then scribed manually with a sharp cutter. The specimens were examined for a total of 12 weeks in cyclic salt spray exposure, as per ISO 14993:2001, while periodic investigation was performed

every two weeks. After the end of the experiment, the rust morphology from each scribed painting system was assessed through SEM, XRD and Raman spectroscopy and was linked to the paint efficiency. The study presented in this chapter encompasses two innovative characteristics: the first is that it examines a state-of-the-art antifouling coating formulation with regard to its anticorrosive properties, while the second is that it links the nature of the corrosion products in the scratched areas with the paint efficiency.

1.2 Experimental methods and materials

1.2.1 Coating systems examined

The coat under investigation was the experimental antifouling (AF) silicone formulation containing 0.56% covalently bound Econea (Exp. Si). The experimental formulation was developed in the framework of the European FP7 collaborative project FOUL-X-SPEL (grant agreement 285552). Its innovative character arises from the immobilization of the biocide, which avoids the leaching effect commonly encountered in conventional biocide based AF painting systems. Biocide immobilization was provided by a newly developed functionalization method [23, 24]. It comprises the functionalization of the biocide with highly reactive isocyanate (NCO) functionality (Fig. 1.1).

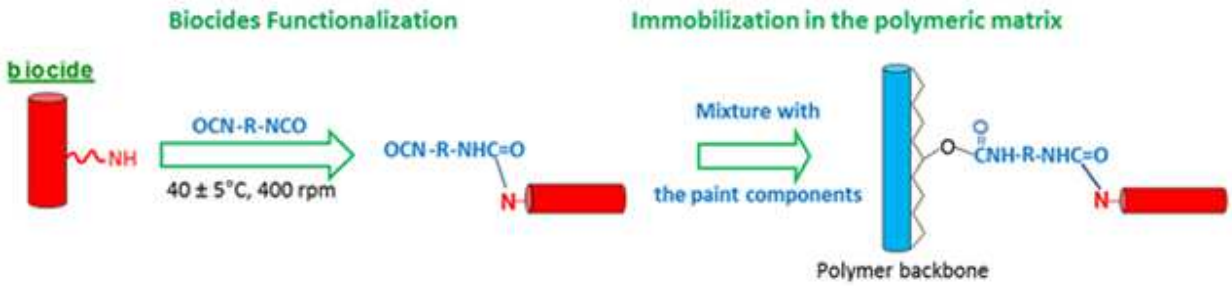

Figure 1.1: The newly developed functionalization method for biocide immobilization into the polymeric matrix.

The first step of this immobilization approach starts with biocide dissolution into a suitable solvent. In this case ethyl acetate p.a. from Sigma-Aldrich was suitable for Econea biocide. The prepared solution, which contained between 15 wt.% to 30 wt.% of biocide, was further added dropwise into aromatic diisocyanate (4,4 diphenyl diisocyanate-MDI), placed in a three necked round bottom ask, at 40 ± 5°C under mechanical agitation (about 400 rpm). The whole system was in inert atmosphere (nitrogen atmosphere), while the mixing of the two reactant components lasted about 7 to 10 hours, depending on the biocide content. The used content of the aromatic diisocyanate was calculated in order to obtain close stoichiometric reaction conditions between the NCO group of the diisocyanate and the NH groups of the biocide.

After completion of the mixing process the reaction mixture was left for one to two hours more, maintaining the above described conditions. Then, it was left to cool down to room temperature, promoting precipitation of the final product. Finally, the precipitate was filtrated

and further dried in a Butchi R-210/215 rotovapor for complete solvent removal. The obtained solid product, named Econea-NCO, was used as a biocide additive in the silicone matrix base. The optimum percentage of incorporated biocide into the silicone matrix was determined after examination of various matrix loading percentages and it was the one that satisfactorily improved the mechanical and antifouling characteristics [23] of the original unloaded paint.

The foul-release commercial silicone system (Ref. Si), based on hydrogel technology, was used as the reference system. For this chapter, the newly developed coating will be system (A), while the reference paint will be system (B). The coating systems were applied on a metallic Grade A steel substrate with dimensions 100 mm × 100 mm × 6 mm, according to manufacturer specifications. Each system consisted of three layers, namely a primer, a tie and a top coat layer with an average total thickness of 695 and 756 X'Om, respectively.

1.2.2 Accelerated aging tests on scribed specimens

Accelerated aging on scribed specimens included salt spray tests in a QFOG CCT1100 chamber, according to the ISO 14993:2001 standard for cyclic exposure to salt spray conditions. The conditions applied included 2 h salt mist at 35°C with 5% NaCl solution, 4 h dry conditions at 60°C and 2 h wet conditions at 50°C and relative humidity RH 95%. Two specimens from each coating system were scribed manually with a sharp cutter. On each specimen two diagonal scribes, perpendicular to each other, were made. The length of each scribe was 9 cm, while a 2 cm distance from the specimen's edges was kept. The scribe marks penetrated the coating until the metallic substrate was exposed. The scribed specimens were examined for a total duration of twelve weeks, while periodic examination of their condition was performed after 6, 8 and 12 weeks of experiment.

1.2.3 SEM, XRD and Raman examination of rust samples

After twelve weeks in the salt spray chamber, one scribed specimen from each painting system was transversely cut in three sections, in order to examine the amount of rust that spread beyond the scribes and beneath the coating. The observation of the cut sections was performed with a Leica MZ6 stereoscope. After the observation, rust samples collected from the cut specimens were observed with a JEOL JJM-6390 scanning electronic microscope (SEM), in order to capture the different morphologies of the corrosion products found in the rust. Finally, EDS analysis was performed, in order to identify the elements comprising the different rust morphologies.

Quantities of rust were also collected from the uncut scribed specimens. These rust amounts were then processed with mortar and pestle, in order to become a fine powder, and examined with a Siemens D5000 powder diffractometer using Cu-Kα radiation at 40 kV and 30 mA, in the 2θ range from 10° to 90°, 0.025° step size and 1 s/step counting time. Phase identification was performed by comparison to the ICDD-PDF Database, using the EVA Software. XRD measurements were performed, in order to identify rust phases with crystalline structure. The principle of the method is that is based on constructive interference of in-phase reflected X-Ray

beams from crystal atoms, according to Bragg's law: $n\lambda=2d\sin\theta$ ($n\lambda \leq 2d$), upon incidence of X-ray beams. The interpretation of the diffractograms is based on the position of the 2θ peaks, which represent a family of atomic planes of a specific crystal rust phase.

Validation of the corrosion products detected with SEM and XRD methods was attained using micro-Raman spectroscopy. The principle of the method is that is based on inelastic light scattering upon incidence of a monochromatic beam of light on molecules (frequency of scattered beam differs from frquency of incident beam). The intensity of the peaks in the spectrum is proportional to substance concentration, while the peak positions are characteristic of the chemical substance (vibrations, stretching etc.). The spectra were acquired on a Renishaw InVia Reflex Raman microscope, with a solid state laser excitation operating at 532 nm. The laser beam was focused on a 0.76 X'Om spot size using a 100X objective lens. The laser power applied was below 0.1 mW, while the acquisition time for each spectrum was 20 min. The spectra were obtained for every differently colored area found on each rust sample. The regions examined were of white, yellow, orange and black color. The measurements on each color were performed in various areas of the rust sample, in order to ensure reproducibility of the spectrum.

Many repetitions were performed with different percentages of laser power, in order to determine the optimum that would not cause phase transformation or intense fluorescence that could mask the signal (the latter was observed for laser power 0.01%). It was concluded that a suitable laser power would be at 0.1% of the maximum laser power, which corresponds to actual power reaching the sample smaller than 0.1 mW, after measurement with a power meter.

1.3 Results and Discussion

1.3.1 Observation of the scribed areas

The condition of system (A) before and after the salt spray test is presented in Fig. 1.2a. The average width in the as-scribed condition was 1.134 mm, while after the end of the test it became 1.979 mm, exhibiting an increase of 0.845 mm. For comparative reasons a macrograph of system (B) is presented in Fig. 1.2b, where the width increase was found to be 0.981 mm. In other words, the mean width increase of the scribed area for the reference system was 13.9% larger than the experimental system's, indicating that it would be harder for the corrosion products to form a corrosion layer with more compact nature and therefore the corrosion protection provided by the reference system was less sufficient.

A macrograph from the transversely cut areas of specimen (A) is presented in Fig. 1.3a. The macrograph was selected from the region where the paint exhibited the most intense swelling effect, in order to present the worst case. The maximum swelling value for this area was 2.596 mm. Moreover, the cross-sectional view revealed a close-packed corrosion layer buildup, which could account for the limited substrate material loss, manifested only as local small-scale cavities on the surface. The small-scale width and height increase, observed in the scratched areas of the experimental system, could account for the formation of a denser corrosion layer,

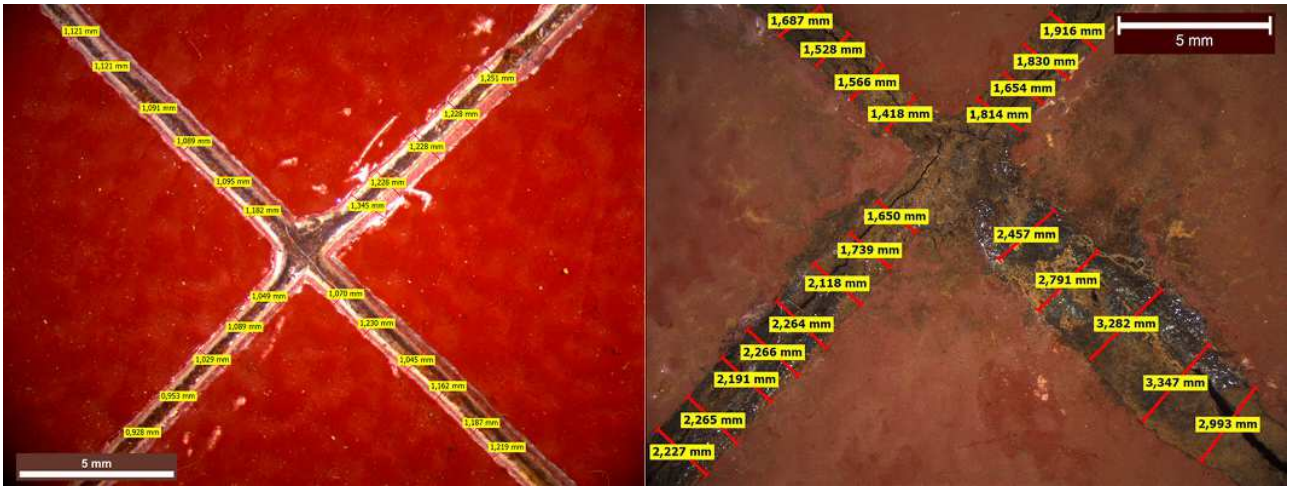

(a) Paint (A)

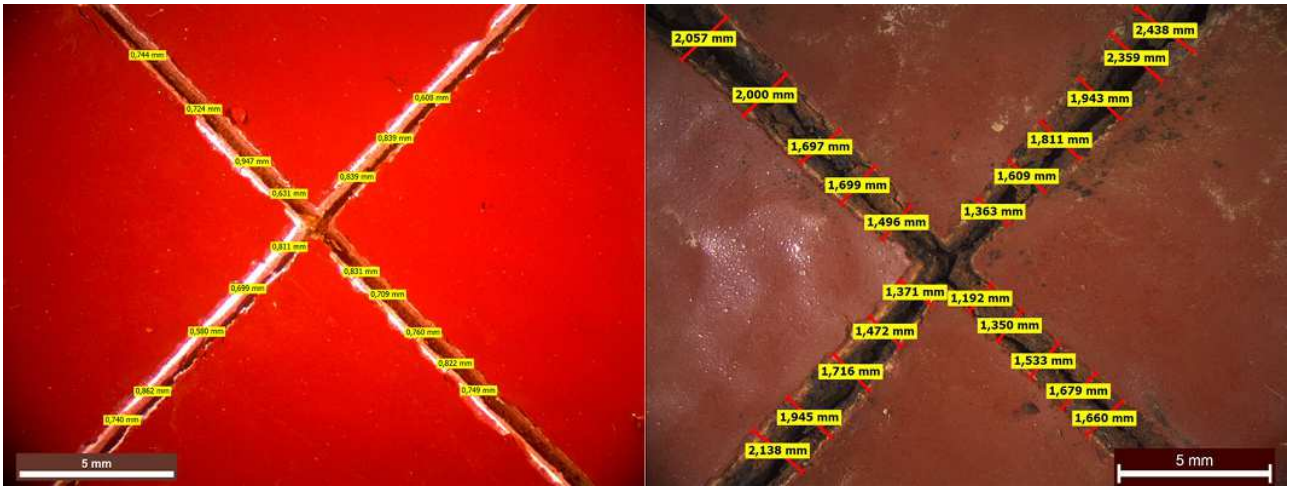

(b) Paint (B)

Figure 1.2: Surface views of scribed specimens before (left) and after 12 weeks (right) of experiment in the salt spray chamber.

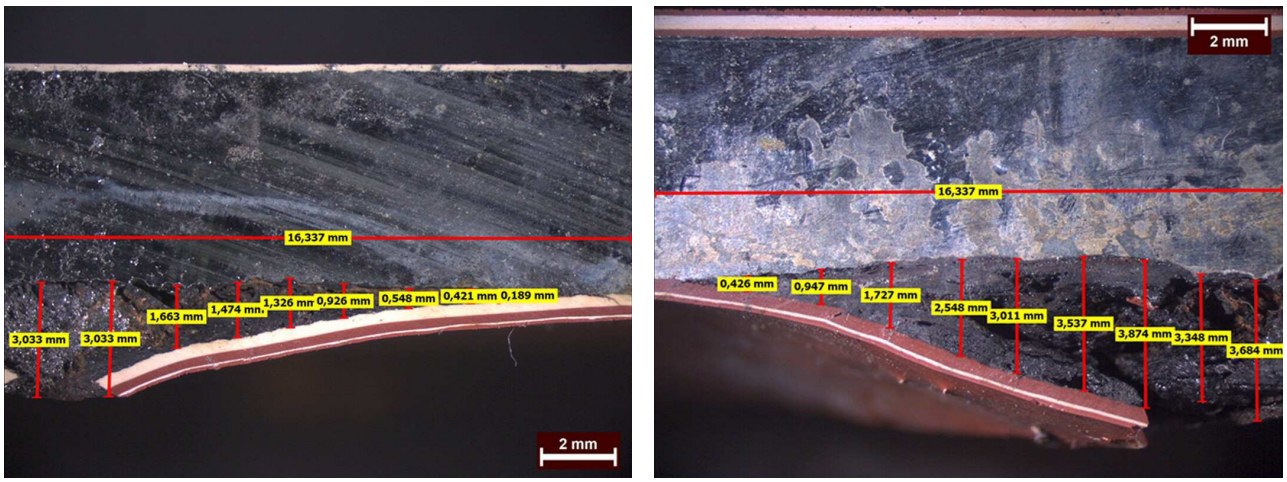

(a) Paint (A)

(b) Paint (B)

Figure 1.3: Optical macrographs of two cross sections of the scribed specimens after 12 weeks experiment in the salt spray chamber.

sealing the substrate more efficiently. On the contrary, system (B) exhibited a swelling value of 3.874 mm which, along with the higher width increase of the scribed areas, lead to significant substrate material loss and large rust quantities accumulation underneath the scribes with inhomogeneities and voids, thus denoting a more severe corrosion attack (Fig. 1.3b).

1.3.2 XRD examination of rust samples

The diffractogram of the rust samples collected from the scribed area of system (A) is presented in Fig. 1.4. The diffractogram was dominated by halite (NaCl) and magnetite (Fe_3O_4) response. The NaCl peaks could imply sodium and chloride ion precipitation from the aqueous solution, a process that could depend on the position of the samples [11]. Hence, rack inclination inside the salt spray chamber could affect the amount of deposited salt onto the specimens. Magnetite peaks were relatively broad and weak implying low crystallinity and hindering a more secure identification of the observed phases. The diffractogram of reference system (B) was similar to the experimental, however, magnetite exhibited higher crystallinity, while a maghemite (γ-Fe_2O_3) and two basic goethite peaks (α-FeOOH) were also apparent.

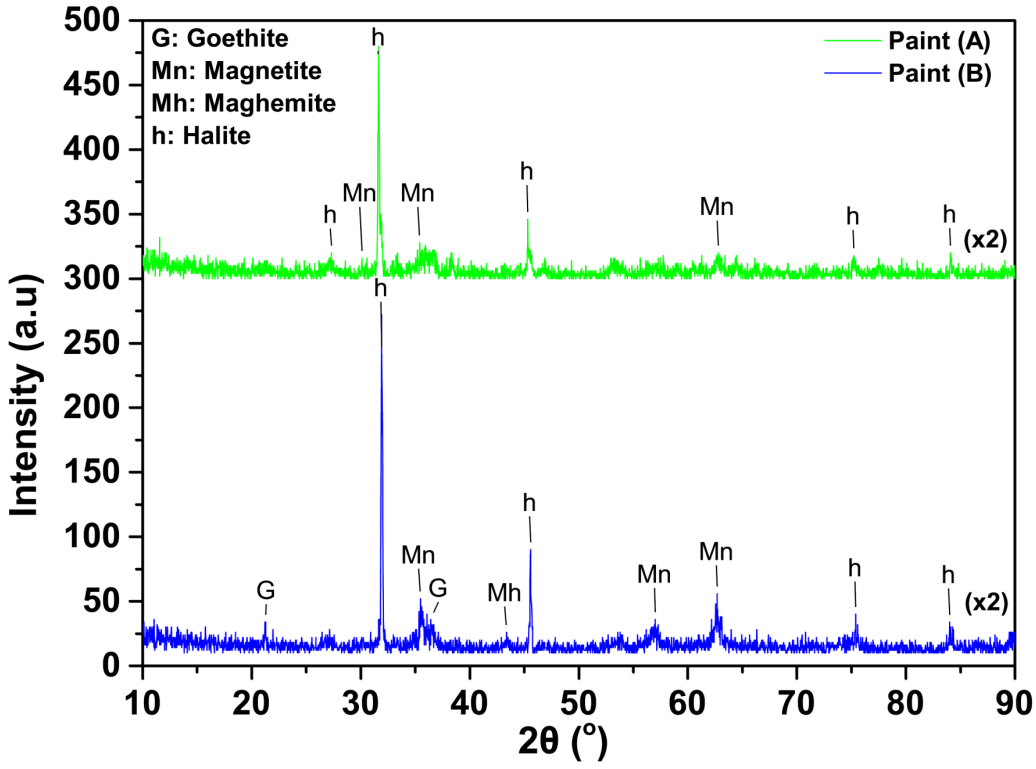

Figure 1.4: XRD graphs of the rust samples collected from the two silicone coatings after 12 weeks in the salt spray chamber.

With regard to the magnetite/maghemite peaks, it is very hard to identify their difference and usually they are not separated in an XRD graph [16]. However, in the diffractogram of system (B) the peaks at 35.48°, 57° and 62.67° were assigned to magnetite, while the peak at 43.47° could be attributed to maghemite traces. In the first case the peaks for maghemite could be expected around 35.8°, 57.2° and 63°, respectively, while in the second case the peak for magnetite would be expected around 43.1°, according to EVA software matching. Hence,

Table 1.2: 2θ positions for the phases observed in the XRD graph for each scribed system.

System	2θ (°)	Phases identified
A	30.1,35.42,62.8	Fe_3O_4
	31.6,45.3,75.2,84.1	NaCl
B	21.3,36.4	α-FeOOH
	35.48,57.0,62.67	Fe_3O_4
	31.9,45.57,75.4, 84.0	NaCl

magnetite would be expected to appear in slightly lower 2θ values than maghemite, especially above 35.55° [25]. However, maghemite 2θ value was not reported in Table 1.2, along with the rest of the phases, due to its trace amount.

The XRD graphs were characterized by the intense response of NaCl, followed by magnetite, while for the reference paint a small contribution of goethite was also noticed. Hence, the information provided by this method, with regard to the rust morphologies, was limited. Also, a safe comparison between the two systems was not feasible, since the diffractograms exhibited many similarities. As a result, Raman spectroscopy was performed, in order to gain a more thorough insight with regard to the nature of the formed corrosion products and draw a clearer conclusion, with regard to the anticorrosion efficiency of the painting system under investigation.

1.3.3 Raman spectra identification of rust samples

1.3.3.1 Raman spectra identification of rust samples from scribed experimental silicone system (Paint A)

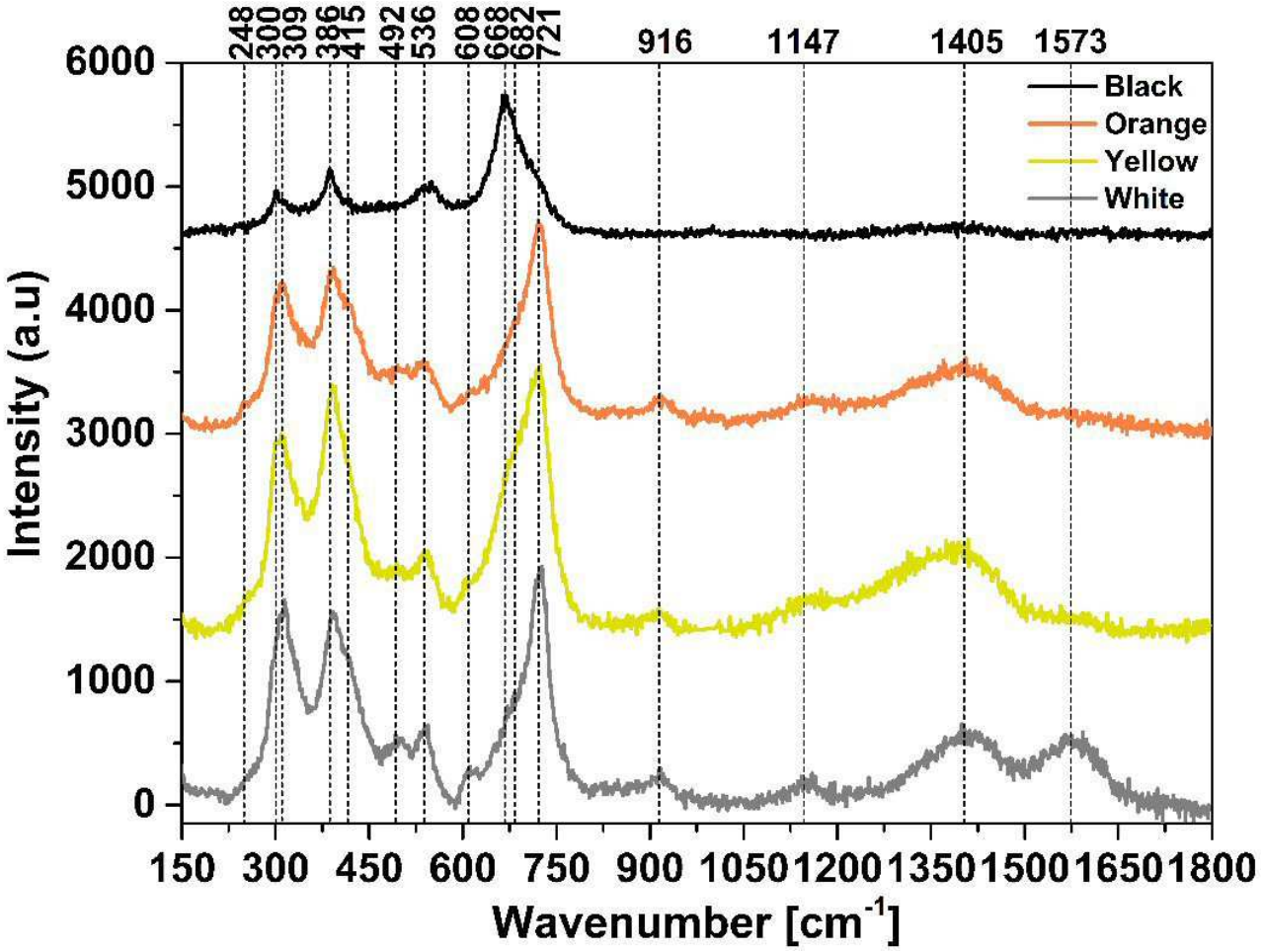

Figure 1.5: Raman spectra from rust areas of different color for scribed painting system (A)

The spectra from the white, yellow and orange regions were similar and could be identified as being mainly akaganeite (β-FeOOH), since the most intense peak was at 721 cm^{-1}, followed by the second characteristic peak of akaganeite at 309 cm^{-1} [18] (Fig. 1.5). The weak bands at 916, 1147 and 1405 cm^{-1} could also be attributed to akaganeite [19, 26, 27]. The strong peak at 386 cm^{-1} verified the existence of goethite, which contributed also to some common bands with akaganeite and could account for the high intensity of the second band of akaganeite at 309 cm^{-1} [18] (Table 1.4). Goethite presence was more intense in the yellow and orange spectra, since its peak was higher than the 309 cm^{-1} peak of akaganeite and slightly lower than akaganeite's main peak at 721 cm^{-1}. The differences in relative intensity of the two phases in each of the three graphs could indicate different relative concentrations [18]. Finally, the band at 1573 cm^{-1}, which appeared in the white spectrum, was probably due to burnt organic matter.

The black area spectrum revealed magnetite as the major phase, with an intense band at 668 cm^{-1} and contributions from the band at 300 cm^{-1} [26, 28, 29] and the hump at 550

cm^{-1} [30–32]. Goethite appeared also in the spectrum, with its strongest peak at 386 cm^{-1}, while some trace amounts of akaganeite were denoted by the hump at 721 cm^{-1}, at the flank of the strong magnetite band. The positions of the low intensity peaks of the spectrum were similar to the positions of the main peaks of the white, yellow and orange spectra analyzed before, hence, goethite could be designated as the second phase of the spectrum, while akaganeite would be ranked third, exhibiting the smallest amount.

Table 1.4: Raman bands for rust samples of scribed system (A)

Colour	Raman bands (cm^{-1})	Phases identified
White	314,391,415,492,536, 608,682,727,916,1147,1405	β-FeOOH
	314,391,415,682	α-FeOOH
Yellow	309,389,494,536,605 682,724,916,1147,1405	β-FeOOH
	309,389,682	α-FeOOH
Orange	309,393,413,536,608, 682,721,916,1147,1405	β-FeOOH
	248,309,393,413,682	α-FeOOH
Black	300,550,668	Fe_3O_4
	300,386,550,682	α-FeOOH
	300,386,536,721,1405	β-FeOOH

1.3.3.2 Raman spectra identification of rust samples from scribed reference silicone system (Paint B)

The white area spectrum of system (B) was totally different from system (A), since it consisted of lepidocrocite, as the major phase, followed by goethite and akaganeite mixture (Fig. 1.6). Lepidocrocite (γ-FeOOH) was predominant with the highest peak at 251 cm^{-1}, followed by goethite with maximum peak at 386 cm^{-1} and akaganeite contributions at 303, 386, 532 and the hump at 721 cm^{-1} [18]. The weak band with a center around 687 cm^{-1} could result from the synergistic contributions from α-FeOOH at 684 cm^{-1}, β-FeOOH at 721 cm^{-1} and γ-FeOOH at 651 cm^{-1}.

From the yellow area two characteristic spectra were obtained. The first spectrum ($Yellow_1$) exhibited the characteristic spectrum of akaganeite mixed with some goethite (388 cm^{-1}) and it was similar to the orange color spectrum of the same specimen, but with different intensities. These spectra were similar to the corresponding yellow and orange spectra of system (A) but with different intensities. The second spectrum ($Yellow_2$) presented the characteristic spectrum of lepidocrocite with the most intense peaks at 248 and 1307 cm^{-1}, accompanied by akaganeite and goethite mixture. Lepidocrocite was not found in any of the examined rust areas of the experimental system (A). Finally, the black color area presented the characteristic spectrum of magnetite with an intense band at 670 cm^{-1} accompanied by a weak broad band at 543

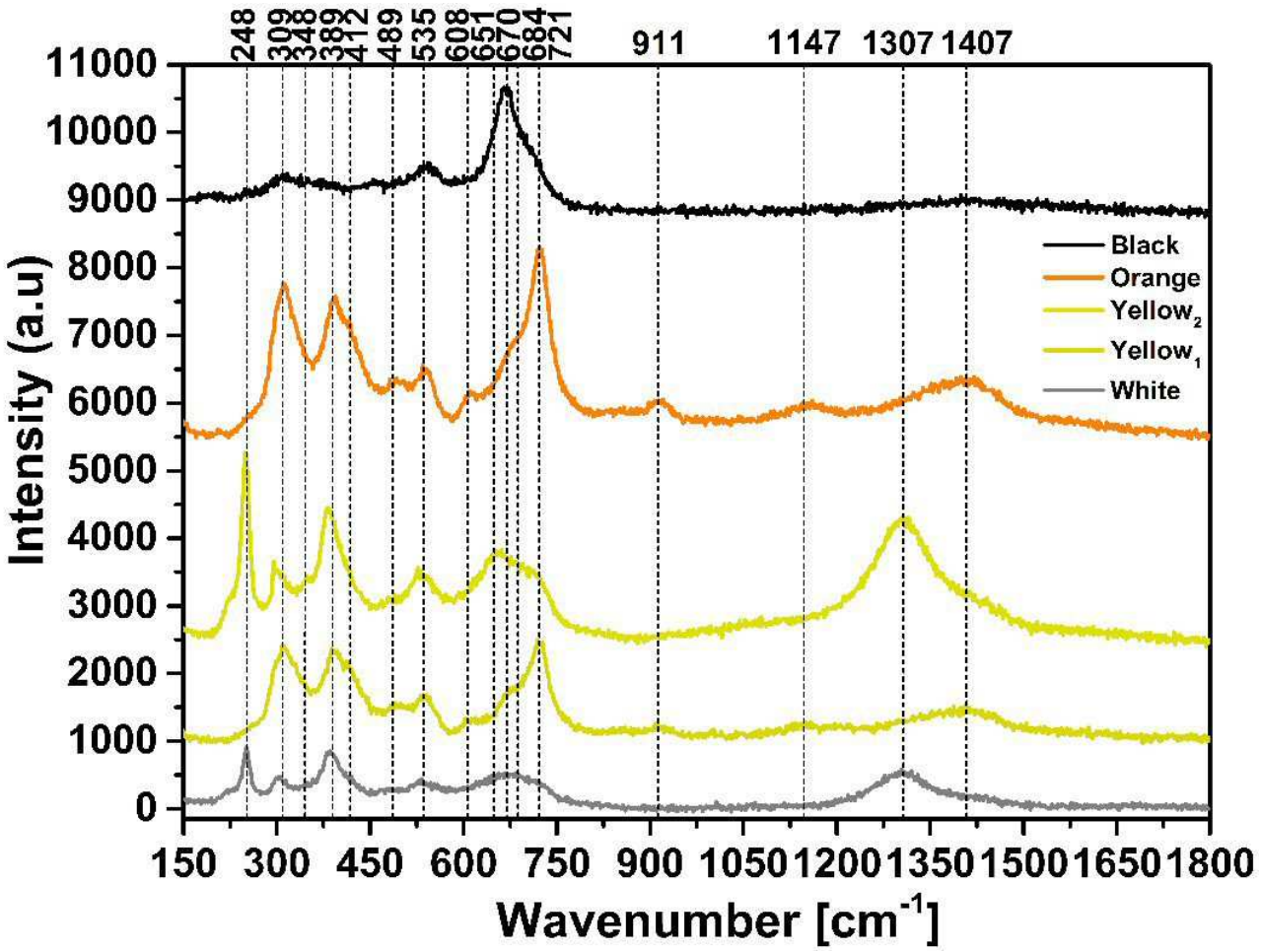

Figure 1.6: Raman spectra from rust areas of different color for scribed painting system (B).

cm^{-1} and a hump at 309 cm-1, similarly to the black spectrum of the experimental system (A). Akaganeite could contribute to the 309 and 721 cm^{-1} humps, however, due to its small fraction it was not included in Table 1.6.

Table 1.6: Raman bands for rust samples of scribed system (B)

Colour	Raman bands (cm^{-1})	Phases identified
White	251,314,386,651,1307	γ-FeOOH
	303,386,684	α-FeOOH
	303,386,532,721	β-FeOOH
$Yellow_1$	309,388,412,489,535,603, 684,721,911,1147,1407	β-FeOOH
	309,388,412,684	α-FeOOH
$Yellow_2$	248,348,383,527,651,1307	γ-FeOOH
	309,383,527,721	β-FeOOH
	295,383	α-FeOOH
Orange	309,389,417,489,535,608, 684,721,911,1147,1407	β-FeOOH
	309,389,417,684	α-FeOOH
Black	309,543,670	Fe_3O_4

1.3.4 Identification of rust morphologies

Raman spectroscopy revealed the presence of akaganeite, goethite, lepidocrocite and magnetite. The corrosion products were mainly of white, yellow, orange and black color, without necessarily implying presence of different phases, except for magnetite, which was found only in the black regions of rust. Each color consisted mainly of mixture of these phases, verifying the aggressiveness of the accelerated aging conditions [33]. In total, the different oxides and oxyhydroxides identified for each specimen were, as follows:

(a) System (A):Fe_3O_4,α,β-FeOOH

(b) System (B):Fe_3O_4,α,β,γ-FeOOH

With regard to the rust morphologies of scribed system (A), the structure presented in Figs. 1.7a and 1.7b in different magnifications could be assigned to goethite nuclei [34]. However, The EDS spectrum (Fig. 1.7c) taken from the marked point in Fig. 1.7b revealed a chloride percentage of 2.84 at.%, making also possible this structure to be akaganeite. The nuclei would grow to a flowery morphology.

SEM images of the rust morphologies found in other regions of the collected rust from system (A) revealed again a small area of flowery crystals, as presented in Fig. 1.8a. Moreover, the porous structure appearing in the center of Fig. 1.8b could be assigned to akaganeite [20]. The structure is surrounded by more compact rust parts, which could hinder permeation of chloride ions to the metallic substrate, in contrast to the porous akaganeite structure.

Finally, another morphology from scribed system (A) was the lamellar structure with cubic crystals aggregates presented in Figures 1.9a and 1.9b. EDS measurements were performed on the two points marked in Figure 1.9b and revealed presence of Fe, O, Cl and Na ions;

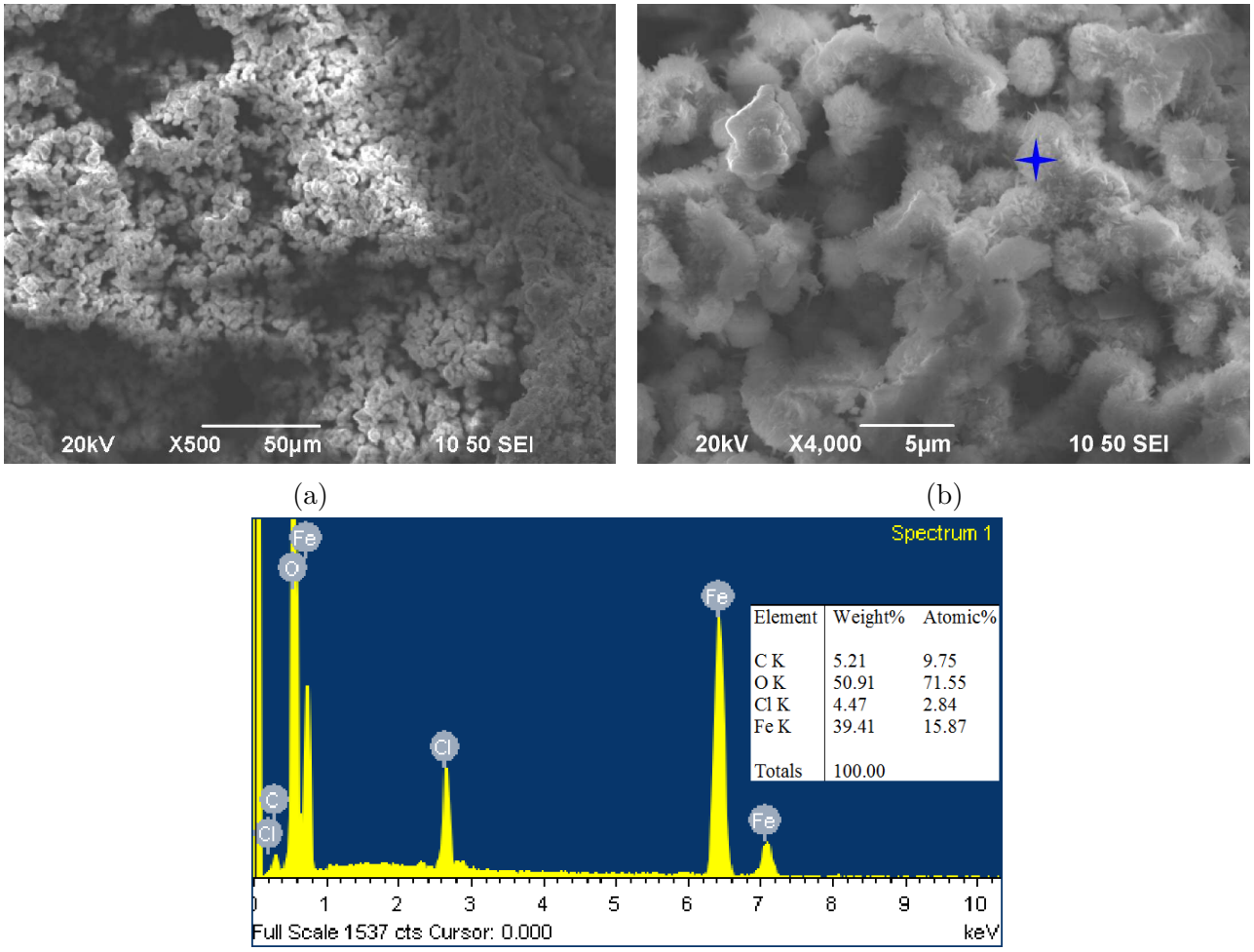

Figure 1.7: Electron micrographs from rust samples of scribed system (A) appearing nuclei of flowery morphology; a) nuclei (×500), b) nuclei (×4000) and c) EDS spectrum from (b)

hence, these cubes could be deposited NaCl crystals. Presence of Mn could be justified by its incorporation into the mild steel as alloying element. The EDS spectra are presented in Figures 1.9c and 1.9d.

The SEM rust morphologies of scribed system (B) are presented in Fig. 1.10. The first morphology observed is presented in Figs. 1.10a and 1.10b in different magnifications. This morphology consisted of wide and long rods, either found individually or connected together making leaf-type morphologies. The second morphology (Figs. 1.10c and 1.10d) was globular, and cotton-ball like in nature, hence it could be goethite [13, 35].

1.3.5 Correlation of the observed rust morphologies with paint efficiency

With regard to the experimental scribed system (A), Raman spectroscopy revealed that three of the four spectra (white, yellow, orange) were a mixture of akaganeite with goethite. The black rust region consisted mainly of magnetite, followed by a small amount of goethite and trace amounts of akaganeite. Hence, the majority of the corrosion products were oxyhydroxides in nature, with akaganeite being predominant, while magnetite was the only oxide and it was

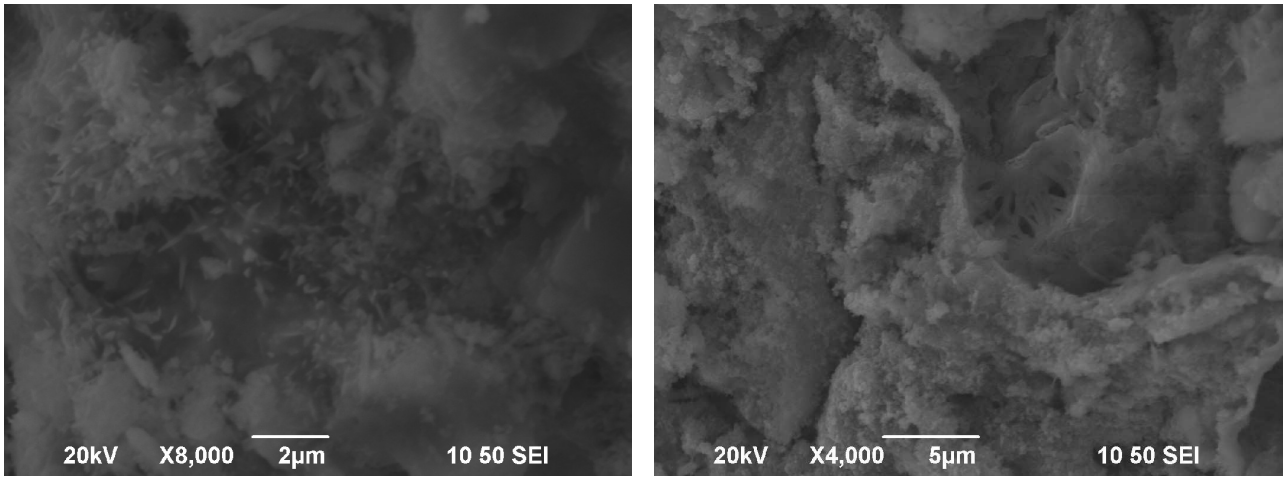

(a) (b)

Figure 1.8: Electron micrographs from rust samples of scribed system (A); a) flowery structure (×800), b) akaganeite (×4000)

restricted to the black rust areas. The nature of the corrosion products was similar for reference system (B), with the additional presence of lepidocrocite oxyhydroxide as the major phase in the white rust area and in a part of the yellow rust area. Systems (A) and (B) were expected to exhibit the same corrosion products, since the substrate was the same. Nevertheless, since the presence of specific corrosion products depends on the stage of the corrosion process, some corrosion products might not develop, due to the corrosion protection offered by the different coatings.

The rust morphology encountered in these systems denotes high vulnerability to corrosion attack [36] and it is an indicator of the degree of protection the corrosion products in the scribed areas of the examined silicone paints would provide.

The above observation is directly related to the paint behavior when flawed. The silicone paints exhibited intense swelling, which led to large coarse corrosion products that could become easily detached, leaving only hollows underneath the paint. In other words, there would be enough space for the corrosion products to fall off, leaving the steel substrate vulnerable to fresh attack. This process would repeat, whenever the newly developed corrosion layer detached the substrate. As a result, the corrosion layer would be formed and destroyed multiple times. Hence, during its formation stage, oxyhydroxides would appear, since they are the first phases to form during oxide layer buildup. If the time until the next detachment was adequate, the oxyhydroxides would have enough time to transform to more stable oxide forms [17], such as maghemite or hematite, which are considered to provide better protection against corrosion, compared to the oxyhydroxides [36]. However, Raman spectroscopy revealed mainly oxyhydroxides as corrosion products, thus denoting a continuous formation-detachment (spalling) process of the corrosion layer and frequent corrosion attack of the substrate.

In order to come to safer conclusions with regard to Raman spectroscopy, the absolute and relative intensities of the spectrum peaks should be taken into consideration, since they are proportional to concentrations. Therefore, with regard to the experimental system (A), for the

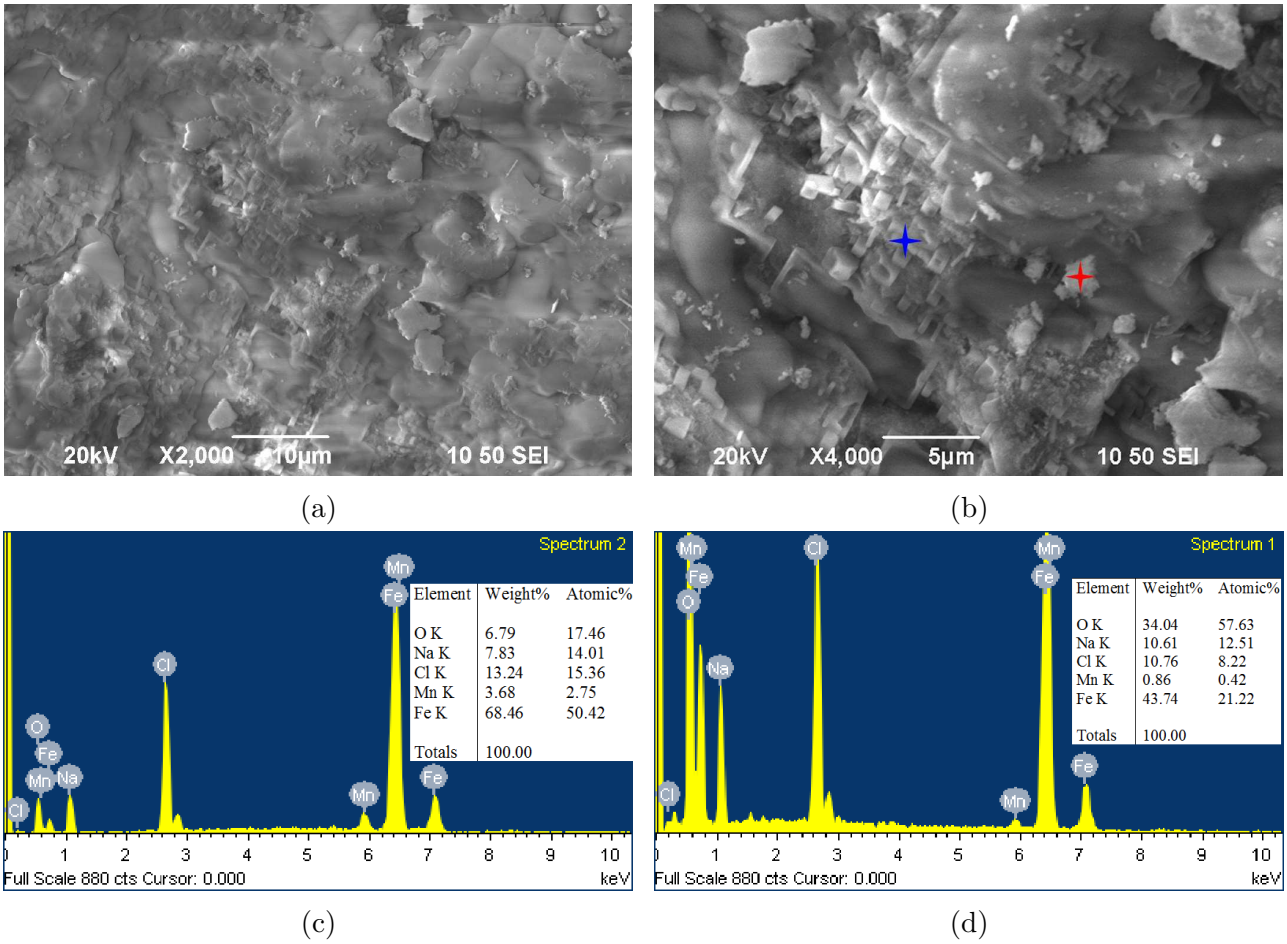

Figure 1.9: Electron micrographs exhibiting lamellar structure with scaled NaCl for system (A): a) ×2000 and b) ×4000; EDS measurements from c) left point on (b) and d) right point on (b)

white area spectrum the intensity of the highest peak was 1877, for the yellow area was 1637, for the orange area was 1559, while for the black spectrum was 1124. The respective values for the reference system were 773, 1444 (Yellow_1), 2759 and 1755. Since the white and black rust spectra of the two systems exhibited differences in the observed phases, a direct comparison could be made only between the yellow and orange spectra. More specifically, the maximum intensity of the yellow spectrum of system (A) was 1.13 times that of reference system (B), implying higher absolute concentrations. However, the ratio of akaganeite/goethite peaks at 724 cm^{-1} and 389 cm^{-1}, respectively, was close to 1.05 for both systems. A basic difference between the two spectra arises from the akaganeite/goethite ratio at 309 cm^{-1} and 389 cm^{-1} positions. For the experimental system this ratio was 0.88, while for the reference system it was 1.03. In other words, goethite contribution was more apparent for the experimental system than the reference paint. With regard to the orange spectra, the experimental system intensity was 0.56 times the reference, denoting the high concentration of akaganeite in the reference mixture. However, similarly to the aforementioned observation, the relative intensity between akaganeite and goethite was close to 1.1 for both systems. To this purpose, the main goethite peak was compared to the second characteristic akaganeite peak as in the yellow spectra and their ratio was found to be 0.97 for the experimental system and 1.03 for the reference system,

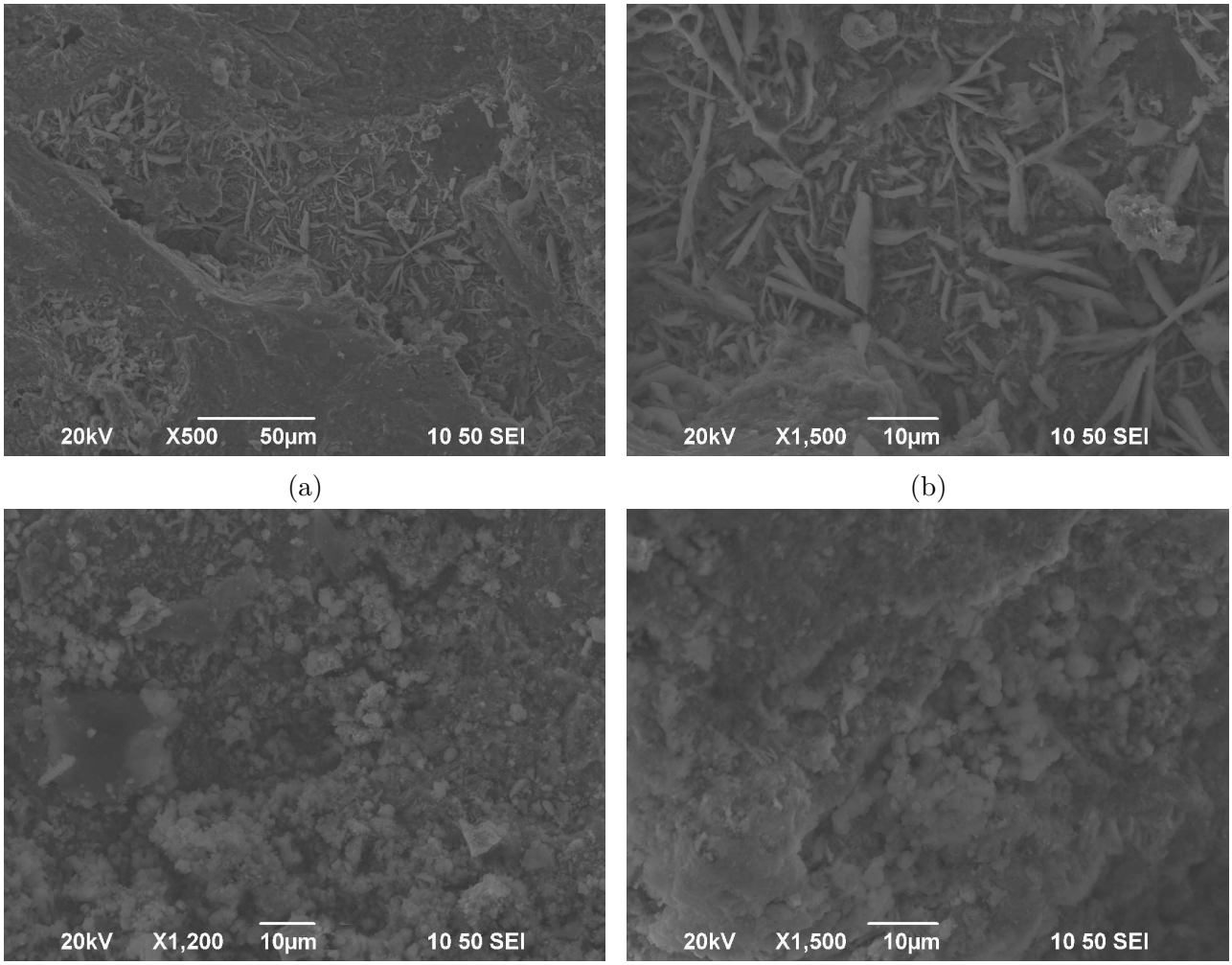

Figure 1.10: Electron micrographs of rust collected from scribed system (B); a) rod-type structure (×500), b) rod-type structure (×1500), c) globular morphology (×1200), d) globular morphology (×1500)

designating once more the presence of higher quantity of stable goethite in the experimental system compared to the reference counterpart.

With regard to the presence of lepidocrocite in the white spectrum and in a part of the yellow rust area of the reference system, its effect on the corrosion resistance is not feasible from the present study, since this phase was not encountered in any of the respective spectra of the experimental system. However, in the white spectrum of the reference system, lepidocrocite coexisted with akaganeite and goethite. Hence its presence could denote incomplete transformation to the more stable goethite. This fact, along with the presence of akaganeite could lead to higher corrosion attack and justify the inhomogeneities and voids found in the corrosion layer of this system (Fig. 1.3b).

From the aforementioned comparisons it could be concluded that for the spectra with common phases, i.e. in the yellow and orange areas, the protection provided by the experimental system was rather improved, since the relative amount of stable goethite in the akaganeite/goethite mixture was higher than the reference system. This observation, along with the more intense

macroscopic deterioration of the reference system in the scribed areas (Fig. 1.3), would classify the experimental silicone system as exhibiting superior anticorrosion performance overall, compared to the reference silicone system.

1.4 Conclusions

- The experimental silicone formulation (Exp. Si) was examined with regard to its anticorrosive properties during salt spray test. The scribed area of the painting system was characterized by limited material loss, which was manifested in the form of local valleys on the substrate surface, while the corrosion layer was close-packed. On the contrary, the reference silicone system (Ref. Si) exhibited extended material loss and a rather inhomogeneous corrosion layer with voids indicating more severe corrosion attack.

- The study presented in this chapter linked the nature of the corrosion products in the scratched areas with the paint efficiency. More specifically, the oxyhydroxide nature of the corrosion products verified the limited corrosion protection provided in the scribed areas by the silicone paints in general and was linked to the observed paint swelling during the experiment, which caused the formation of large, coarse rust agglomerates without adherence. The frequent detachment of these rust parts would reinitiate the corrosion process, thus, recreating a new corrosion layer, consisting mainly of the firstly forming oxyhydroxides, as observed in the current study.

- Rust morphology for the experimental silicone system included mainly akaganeite and goethite mixture for the white, yellow and orange rust areas and magnetite in the black rust areas. The reference silicone system exhibited similar morphologies, in addition to lepidocrocite in the white area and in a part of the yellow rust area.

- Comparison of the two systems in the yellow and orange rust areas, where the corrosion phases were similar, verified a rather improved corrosion protection for the experimental system, due to the relatively higher amount of stable goethite in the akaganeite/goethite mixture.

- The silicone experimental antifouling system provided better anticorrosion protection overall compared to the reference silicone system, combining satisfactory anticorrosion protection along with a newly developed antileaching mechanism for environmentally friendly antifouling protection.

Chapter 2

Rust morphology characterization of polyurethane and acrylic-based marine antifouling paints after salt spray test on scribed specimens

Abstract

The experimental polyurethane marine antifouling coating containing 2% immobilized Econea (Exp. PU1) was examined in terms of its anticorrosion performance. The novelty of the experimental formulation arises from the immobilization of the biocide, similarly to the experimental silicone formulation presented in Chapter 1. The painting system was applied on steel specimens, then scribed with a sharp cutter and examined for 12 weeks in cyclic salt spray exposure. Identification of the rust morphologies was performed with XRD, Raman spectroscopy, SEM and EDS methods. The absence of paint deformation during the experiment led to formation of compact corrosion products, firmly adherent to the substrate, allowing transformation to more protective forms, such as oxides (hematite, maghemite, magnetite) and the least harmful of the oxyhydroxides (goethite, feroxyhyte), found in mixture, ensuring sufficient corrosion protection. The unscratched part of the paint served as a barrier to corrosion product expansion beyond the scribed areas. The acrylic-based antifouling system (Acrylic) was also examined, for reasons of comparison. The experimental formulation exhibited superior anticorrosion performance overall, since the acrylic system presented extended material loss, blistering, checking and extensive substrate rust coverage beneath the multilayer coat, implying unsatisfactory corrosion protection.

2.1 Introduction

Marine structures, such as ships or platforms, are vulnerable to fouling, i.e. the accumulation of sea micro and macro flora and fauna on their surface [37]. In the case of ships, these organisms increase the surface roughness, thus, increasing friction resistance [38] and subsequently fuel consumption and total voyage cost [39, 40]. Heavy fouling could lead to paint failure and subsequent corrosion of the substrate, if not repelled or washed off of the submerged surface.

For this reason, the submerged metallic structures need to be efficiently protected both in terms of corrosion and fouling, by applying a multilayer coat, usually consisting of an anticorrosive primer and an antifouling topcoat, ensuring sufficient substrate protection.

The most commonly applied antifouling technologies are the ones exhibiting self-polishing (SP) or foul-release (FR) properties. The first category refers usually to acrylic copolymers combined with a common biocide, such as cuprous oxide [41] and some booster biocides [42]. The second category usually refers to cross-linked polydimethylsiloxane (PDMS), most commonly known as silicone paints [41] and usually they do not incorporate biocides. Polyurethane paints can also be used for antifouling purposes [43, 44] and are positioned between the main two categories. Some examples include fluorinated [45] and PDMS [46,47] polyurethanes, while Verborgt and Webb [48] suggested their use as SP coats, incorporating hydrolysable polyols.

Assessment of the anticorrosion efficacy of a multilayer marine painting system is as important as its antifouling performance. Usually, the corrosion resistance of organic coatings is examined through accelerated aging tests [1–3] and more specifically through salt spray tests [7]. When the painted specimens are examined in scribed condition, these tests can provide information with regard to the barrier properties provided by the unscratched part of the paint [4,5], which can be correlated to the protection provided by a flawed coating in real conditions. In the case of an antifouling painting system, the flaw could result from fouling attachment [6] or during ship handling or maneuvering.

Characterization of paint performance in scribed condition can be performed by investigating the morphology of the corrosion products after the end of the salt spray test. The basic corrosion products of mild steel when exposed to natural or artificial seawater are akaganeite (β-FeOOH), goethite (α-FeOOH), lepidocrocite (γ-FeOOH) and magnetite (Fe_3O_4) and have been described in previous work [49], which was presented in Chapter 1. Other phases, such as maghemite (γ-Fe_2O_3), hematite (α-Fe_2O_3) and feroxyhyte (δ-FeOOH), can also be formed either in natural [20, 33] or artificial salt spray environment [50]. Dubois *et al.* [21] reported that the corrosion products generally found on steel grades exposed to a marine environment form from the outermost to the innermost part of the rust layer in the following order: lepidocrocite, goethite, hematite (not always present), maghemite and possibly magnetite. Ma et al. [20] noticed that β-FeOOH decreased with the exposure time in favor of γ-Fe_2O_3 formation. A proposed mechanism suggests reduction of akaganeite (or lepidocrocite) to magnetite and then air oxidation of magnetite to maghemite [16]. Superparamagnetic maghemite, along with small particle goethite could create protective corrosion layers in inner rust layers [8].

Correlation of the corrosion products formed in the scribed areas of experimental and commercial antifouling silicone painted specimens, with paint performance, after 12 weeks of salt spray test was analyzed in Chapter 1 and published in [49]. The basic morphology of the corrosion products, a mixture mainly of akaganeite (β-FeOOH) and goethite (α-FeOOH), was a result of the deformation of the paint during the test (swelling), which made the products to loose adherence with the steel substrate frequently, leading to reinitiation of the corrosion process. The specific oxyhydroxide phases verified this argument and revealed the limited corrosion

protection provided by the silicone systems.

In the present chapter, the newly developed experimental polyurethane formulation containing 2% immobilized Econea (Exp. PU1) was examined in terms of its anticorrosion properties. Furthermore, the commercial, acrylic based antifouling coating, of the self-polishing copolymer (SPC) technology (Acrylic), was also examined for comprehensiveness reasons. This work continues and completes the work regarding the silicone based marine paints, in terms of corrosion products characterization after salt spray tests. The aim of this chapter is to provide a final ranking among all the examined painting systems of both works, with regard to their overall anticorrosion performance, by taking into account the observed rust composition and morphology. In order to ensure as thorough a comparison as possible, a wide range of different antifouling technologies, both experimental and commercial, were examined during these two studies.

The study presented in this chapter encompasses three innovative characteristics: the first is that it examines a state-of-the-art antifouling coating formulation with regard to its anticorrosive properties, the second is that it links the nature of the corrosion products in the scratched areas with the paint efficiency and the third is that it attempts a comparison among the most representative antifouling paint categories, in terms of their overall anticorrosion efficiency.

2.2 Experimental methods and materials

2.2.1 Coating systems examined

The coat under investigation was the experimental antifouling (AF) polyurethane (PU) formulation (Exp. PU1) containing 2% covalently bound Econea. The polyurethane coating was applied on top of an epoxy primer, used mainly to improve paint adhesion. The method of application of the coating material was by spraying, while the recoating interval was about 24 h. The innovative character of this paint arises from the immobilization of the biocide, similarly to the experimental silicone formulation. The immobilization process has been described in Sec. 1.2.1 of Chapter 1.

The commercial, acrylic based AF coating, of the self-polishing copolymer (SPC) technology, containing 21.6% Cu_2O and 7.1% Zineb as biocides was also examined. For this study, the newly developed polyurethane coating will be system (A), while the acrylic system will be system (B). The coating systems were applied on a metallic Grade A steel substrate with dimensions 100 mm $\times$ 100 mm $\times$ 6 mm, according to manufacturer specifications. Each system consisted of two layers, namely a primer and a top coat layer with an average total thickness of 522 and 580 X'Om, respectively.

2.2.2 Salt spray tests-XRD, Raman and SEM examination of scribed samples

Salt spray tests were performed on scribed specimens for 12 weeks, similarly with the procedure presented in Sec. 1.2.2 of Chapter 1. With regard to the XRD, Raman and SEM examination

of the scribed samples after the end of the test, the same procedure as the one presented in Sec. 1.2.3 of Chapter 1 was followed.

2.3 Results and Discussion

2.3.1 Observation of the scribed areas

The condition of experimental system (A) before and after the salt spray test is presented in Fig. 2.1a. The average width in the as-scribed condition was 1.108 mm, while after the end of the test the average width was 2.204 mm, exhibiting an increase of 1.096 mm. With regard to the acrylic system (B), the macrograph revealed a width increase of 0.660 mm.

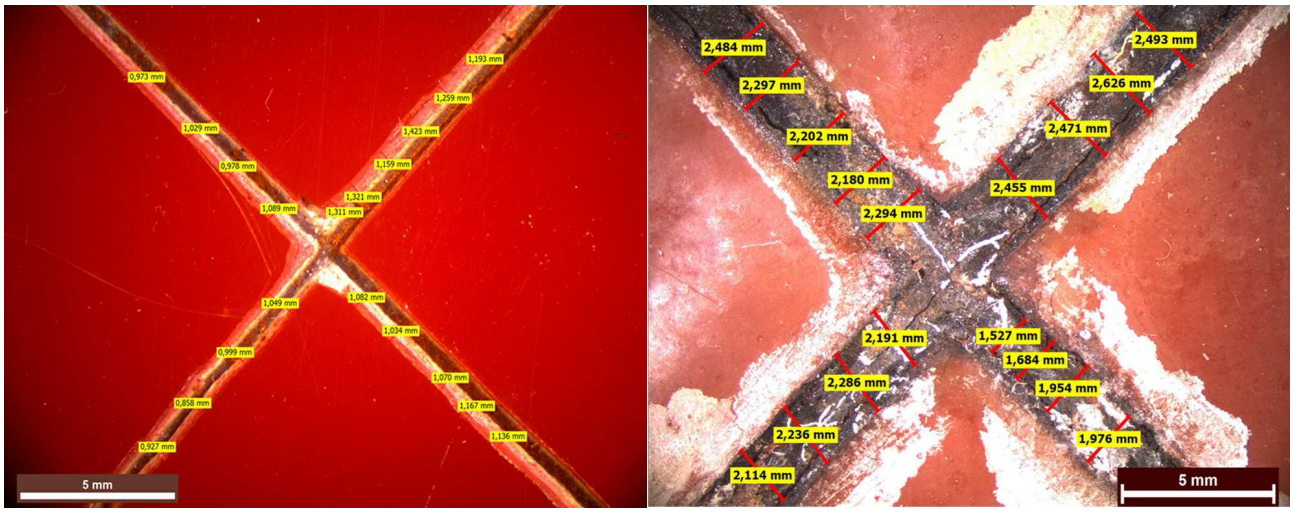

(a) Paint (A)

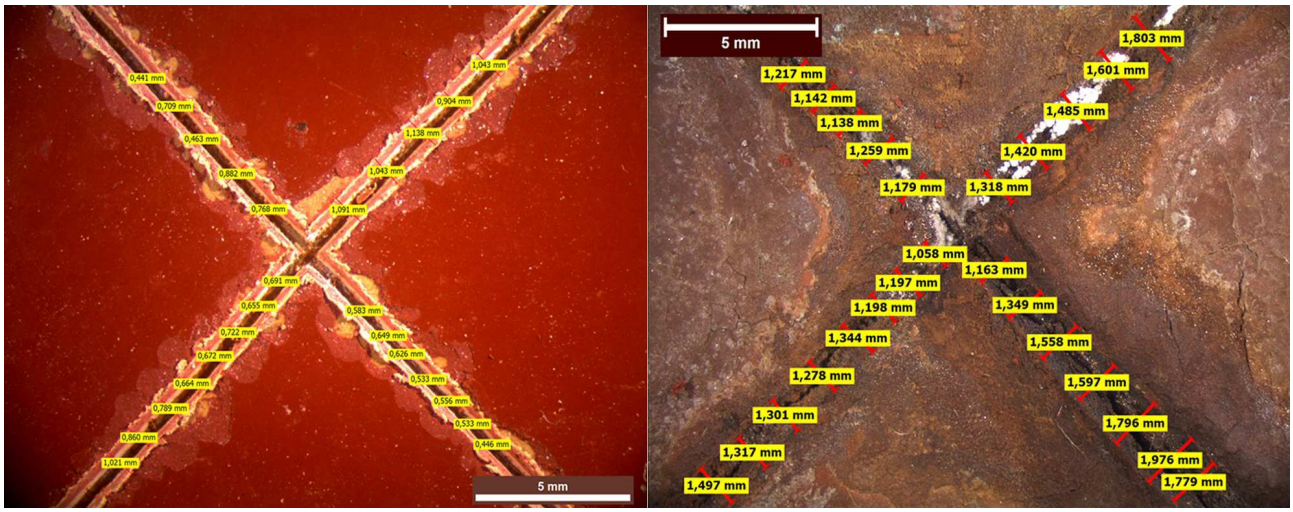

(b) Paint (B)

Figure 2.1: Surface views of scribed specimens before (left) and after 12 weeks (right) of experiment in the salt spray chamber.

Even though the mean width increase of the scribed area for the experimental system (A) was found larger than system's (B), the experimental system was slightly affected by accelerated aging overall, since it did not exhibit any degradation characteristics, but rather a slight swelling

along the scratched areas. On the contrary, the overall condition of the acrylic system was characterized by intense discoloration, blistering (ASTM D714) and checking (ASTM D660), verifying its lower performance. In Fig. 2.2, the areas in circles represent blisters. Blistering was apparent in various areas of the acrylic-based system, leading to local top layer cracking. Top coat micro-cracking (checking) was apparent as a self-induced phenomenon, as well (Fig.2.2c).

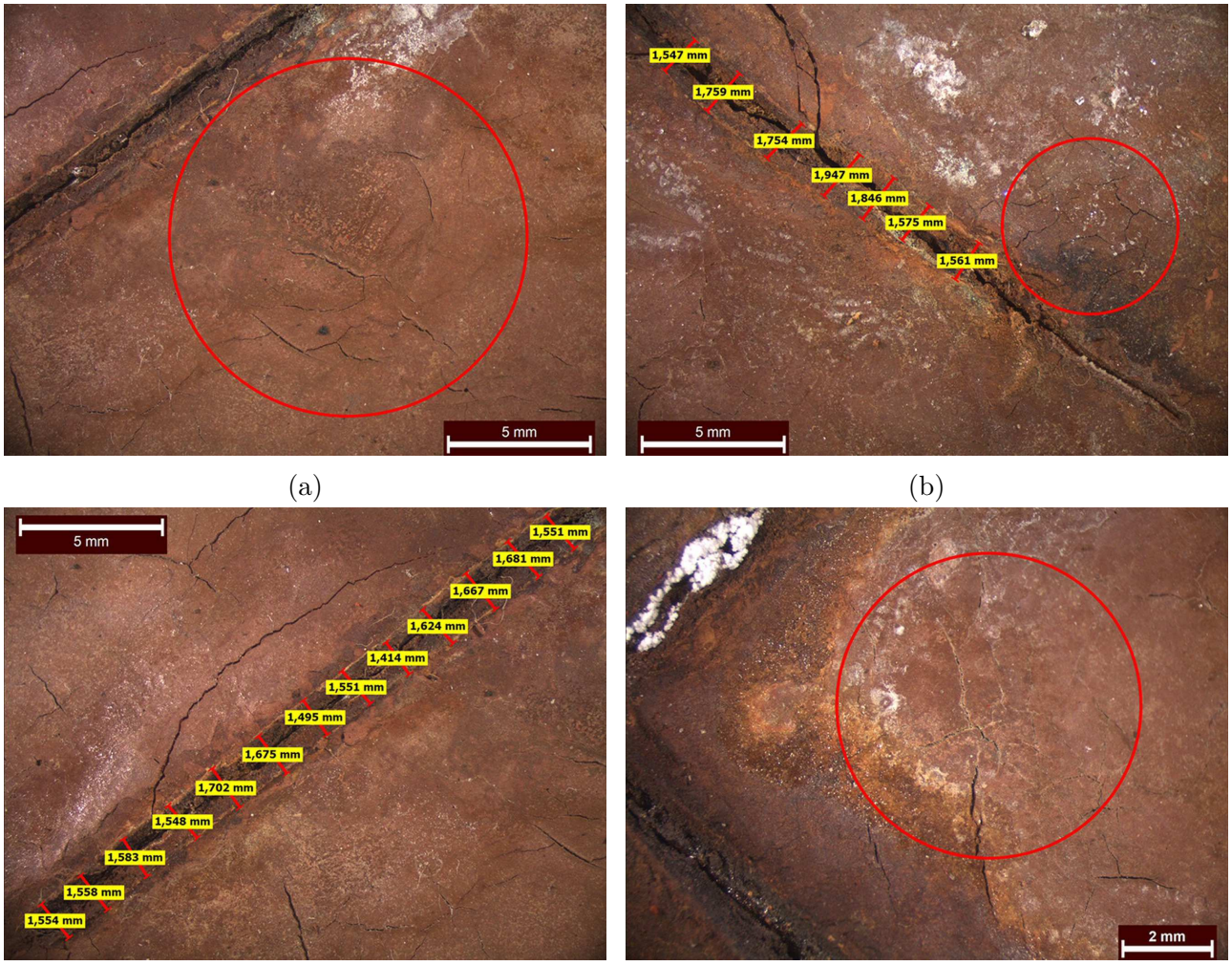

Figure 2.2: Surface views of system (B) after 12 weeks in the salt spray chamber; a) blister next to the down left scribe, b) blister next to the down right scribe, c) paint cracks, d) blister and cracks in the central specimen area

A macrograph from the transversely cut areas of system (A) is presented in Fig. 2.3a. The macrograph was selected from the region with the widest horizontal spread of the products beneath the scribes and the highest vertical corrosion product build-up, in order to present the worst case. The maximum vertical rust accumulation for this area was 1.387 mm, while the widest expansion beneath the unscratched part of the paint reached the value of 14.507 mm. Beyond this area the paint acted as a barrier and hindered further coverage of the metallic surface with rust. On the contrary, for system (B) the vertical rust accumulation was 1.845 mm, while horizontally the rust covered almost the entire metallic surface and the value of 24.432 mm presented in Fig. 2.3b is only a sample dimension, taken by the minimum magnification

of the stereoscope. Hence, the SPC acrylic-based system exhibited almost no barrier to rust accumulation and spreading, leading to substantial substrate material loss, thus, exhibiting characteristics of a severely degraded or failed coat.

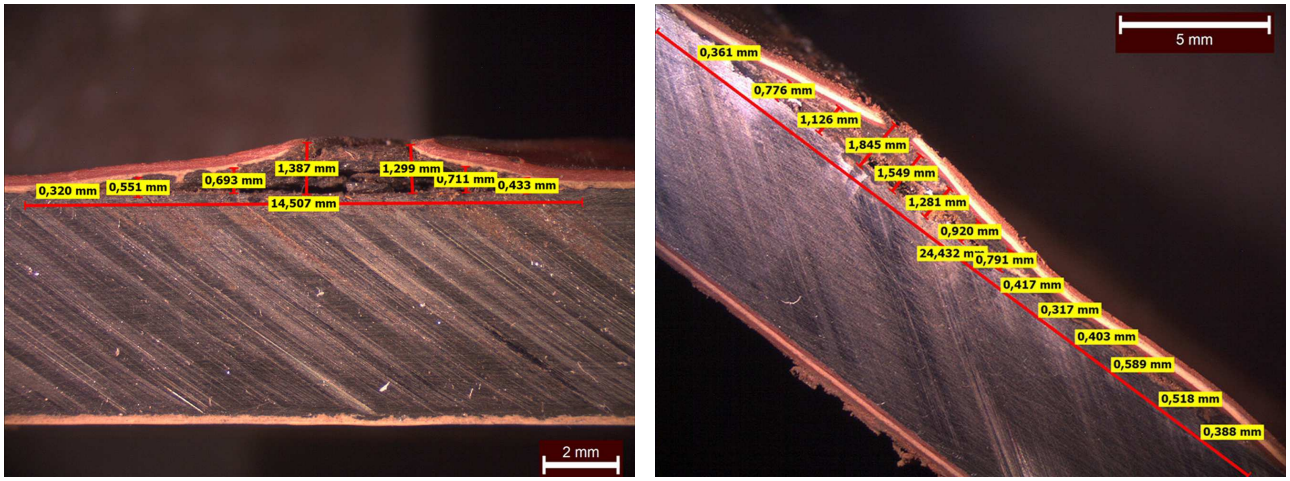

(a) Paint (A) (b) Paint (B)

Figure 2.3: Optical macrographs of two cross sections of the scribed specimens after 12 weeks experiment in the salt spray chamber.

Compared to the macroscopic observation results of the experimental silicone system from the previous chapter [49], the swelling effect exhibited by the experimental polyurethane system (A) of the present study was kept at a minimum. This could also be verified by the surface view of the PU system (Fig. 2.1a), where the swelling effect is hardly distinguishable even through stereoscopic observation. The minimum deformation of the PU system allowed the corrosion products to accumulate almost without any spalling, leading to effective substrate sealing. On the contrary, the paint swelling of the silicone system was manifested as obvious hollows underneath the paint, visible with the naked eye. For this reason, the corrosion products of the silicone system were characterized by frequent detachment, indicating insufficient substrate sealing and, thus, less effective corrosion protection.

In summary, the macroscopic observation from both studies revealed the satisfactory anti-corrosion protection provided by the polyurethane experimental system in scribed condition, since the paint did not exhibit any degradation characteristics, the corrosion products sealed the substrate effectively and the paint deformation was retained to a minimum level. The experimental silicone system of Chapter 1 [49] exhibited the second best performance, followed by the commercial silicone paint (also examined in Chapter 1) and finally the acrylic based system exhibited the least satisfactory performance with apparent and extensive macroscopic deterioration, characteristic of a severely degraded coat.

2.3.2 XRD examination of rust samples

In the XRD graph presented in Fig. 2.4, (H) stands for hematite, (M) for coexistence or presence of either magnetite (Mn)/maghemite (Mh), (G) for goethite, (A) for akaganeite, (L) for lepidocrocite, (F) for feroxyhyte and (h) for halite (NaCl).

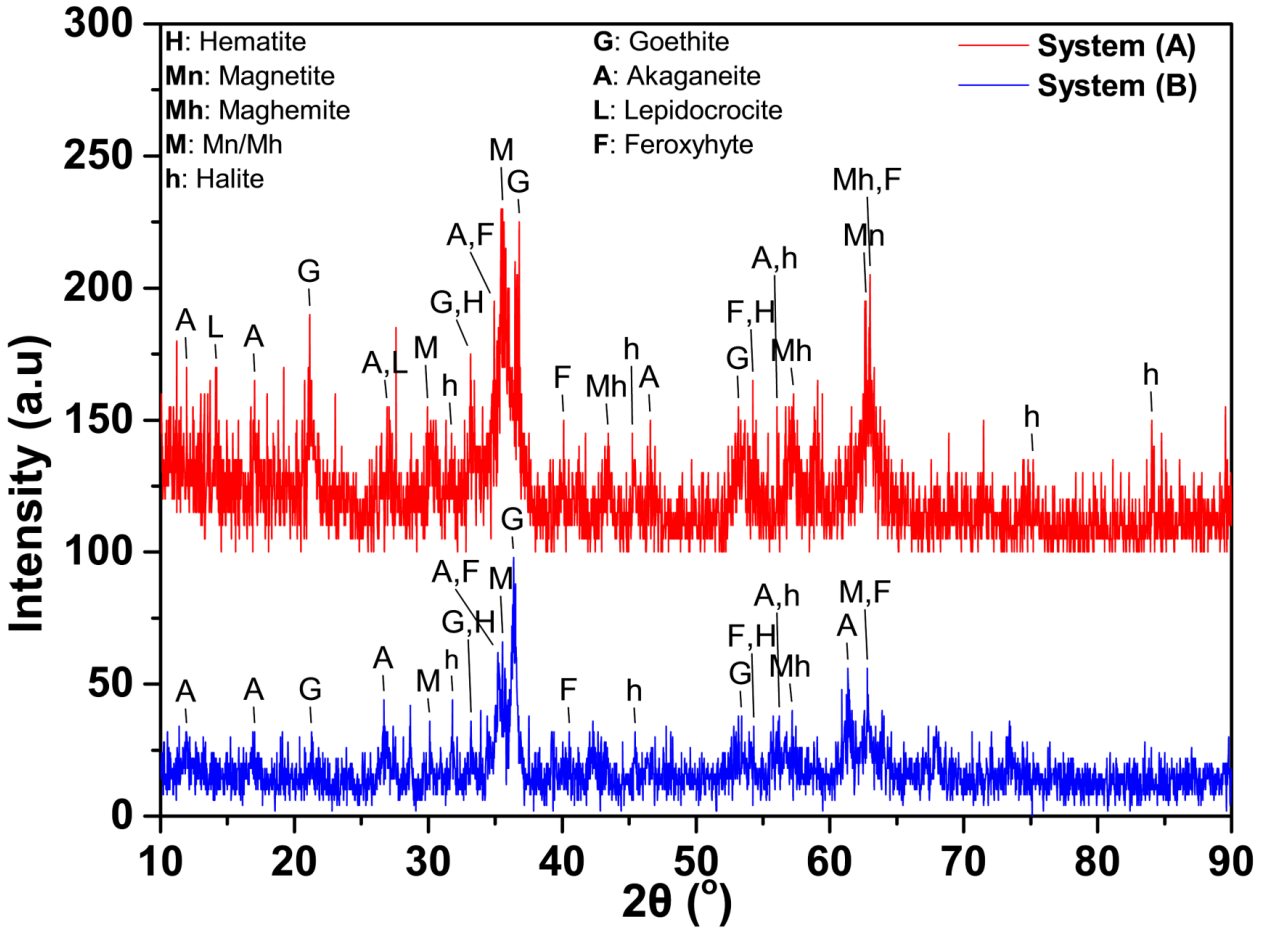

Figure 2.4: XRD graphs of the rust samples collected from scribed systems (A) and (B) after 12 weeks in the salt spray chamber.

The XRD graph of system (A) exhibited mainly goethite (α-FeOOH), akaganeite (β-FeOOH) and magnetite (Fe_3O_4)/maghemite (γ-Fe_2O_3) as main phases. Also, halite (NaCl) peaks appeared in the diffractogram. The peak at 35.2° could be attributed to both akaganeite and feroxyhyte (δ-FeOOH), since there were distinct peaks in other 2θ values of the graph that could justify existence of these phases. Since the peak at 35.2° is the most intense peak of the feroxyhyte spectrum, it is possible that the main contribution to this peak came from this phase. Also, the peaks at 33.2° and 54.3°, assigned to goethite and feroxyhyte, respectively, could also have contribution from hematite (α-Fe_2O_3), since they are the most intense peaks of its spectrum. Compared to the acrylic-based system (B), which exhibited similar phases, the diffractogram of system (A) exhibited also lepidocrocite (γ-FeOOH), which was noticed at 14.2° and 26.9° and more distinct peaks above 40°, such as those of maghemite and akaganeite at 43.45° and 46.6°, respectively. Moreover, above 60°, system (B) exhibited two peaks assigned to akaganeite and magnetite/maghemite at 61.3° and 62.8°, respectively, while for the experimental system (A) the more stable magnetite and maghemite/feroxyhyte peaks appeared at 62.62° and 63.0°, respectively. Finally, the diffractogram of system (B) presented lower crystallinity than system (A), especially at the positions of the maximum peaks, that is at 35.55°, 36.8° and 63.0°.

With regard to the magnetite/maghemite responses, it is very hard to identify their difference and usually they are not separated in an XRD graph [16]. However, in the diffractogram of system (A) the peak at 62.62° was assigned to magnetite, while the peak at 63.0° could be assigned to maghemite. This observation led in an effort to make separate identifications, when feasible. Hence, for the rust samples of the same system, the peaks at 43.45°, 57.27° and 63.0° were assigned to maghemite, when the corresponding magnetite peaks would be expected around 43.1°, 57.0° and 62.5°, according to EVA software matching. Hence, magnetite would be expected to appear in slightly lower 2θ values than maghemite, especially above 35.55°, as reported also by Kim *et al* [25]. A maghemite peak at 57.2° was also noticed for system (B), however the peak at 62.8° could not be differentiated. For the peaks around 30° and 35.5°, no separation was made, since both phases coincide. All the observed phases, as obtained from the XRD peaks, are presented in Table 1.

Compared to the XRD results of the scribed silicone system [49], the diffractogram of the experimental PU system exhibited a great variety of corrosion phases, both oxides and oxyhydroxides. On the contrary, the XRD graph obtained from the experimental scribed silicone system was dominated by halite peaks accompanied by some magnetite peaks, thus, hindering a more accurate assessment of its corrosion behavior.

Table 2.1: 2θ positions for the phases observed in the XRD graph for each specimen.

System	2θ (°)	Phases identified
A	21.2,33.2,36.8,53.2,	α-FeOOH
	11.8,17.0,26.9,35.0,	β-FeOOH
	46.6,56.0	
	14.2,26.9	γ-FeOOH
	35.0,40.1,54.3,63.0	δ-FeOOH
	30.0,35.55,43.45(Mh),	Fe_3O_4/
	57.27(Mh),62.62(Mn),63.0(Mh)	γ-Fe_2O_3
	33.2,54.3	α-Fe_2O_3
	31.7,45.25,56.0,	NaCl
	75.2,84.0	
B	21.3,33.2,36.4,53.2,	α-FeOOH
	11.8,16.9,26.7,35.2,	β-FeOOH
	56.2,61.3	
	35.2,40.52,54.3,62.8	δ-FeOOH
	30.1,35.55,42.3(Mn),	Fe_3O_4/
	57.2(Mh),62.8	γ-Fe_2O_3
	33.2,54.3	α-Fe_2O_3
	31.8,45.45,56.2	NaCl

2.3.3 Raman spectra identification of rust samples

The XRD graphs revealed a wide variety of rust morphologies for the polyurethane experimental system. Similar morphologies were observed for the acrylic system, as well. In order to ensure the existence of the various phases obtained by XRD and gain a more thorough insight with regard to the nature of the formed corrosion products for each system, Raman spectroscopy was performed, a valuable method for more precise determination of the corrosion behavior of the coating systems under investigation.

2.3.3.1 Raman spectra identification of rust samples from scribed experimental polyurethane system (Paint A)

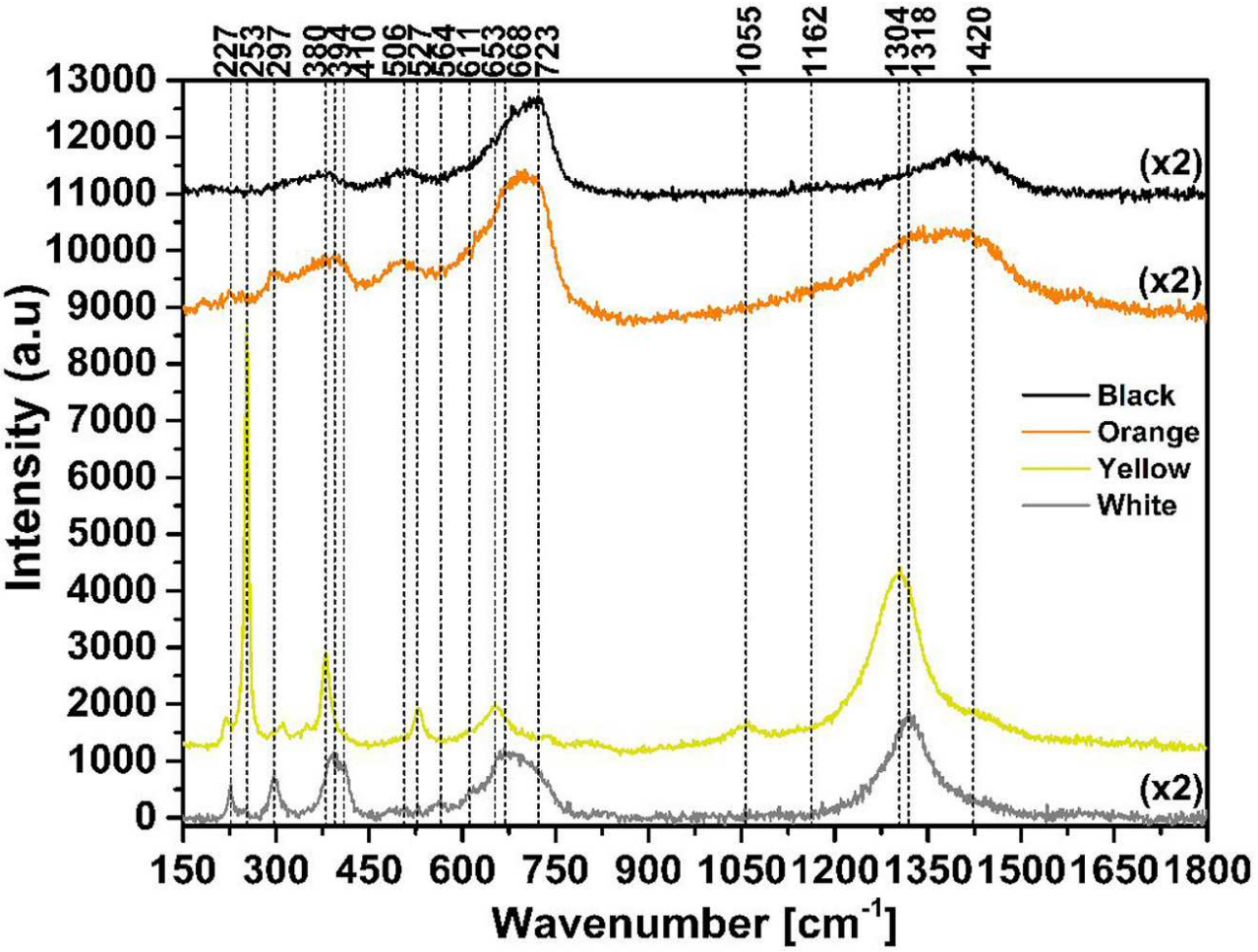

Figure 2.5: Raman spectra from rust areas of different color for scribed painting system (A)

The white area spectrum exhibited the most intense peak at 1320 cm^{-1} implying that the dominant phase was hematite [29]. Indeed, the narrow peaks at 227 and 297 cm^{-1} are characteristic of the hematite oxide. Also, a weak shoulder at 247 cm^{-1}, at the flank of the 227 cm^{-1} peak, as well as the intense band with full width at half maximum from 380 cm^{-1} to 415 cm^{-1} also imply hematite presence. The α-Fe_2O_3 spectrum includes also the weak shoulder at 611 cm^{-1} and contributes to the band which extends from 637 cm^{-1} to 730 cm^{-1} and includes magnetite. The magnetite phase was readily apparent from its characteristic band around

668 cm^{-1} and the weak broad band at 530 cm^{-1} [51]. The morphologies of the bands around 247, 297, 393 and the weaker bands around 483 and 564 cm^{-1} denote the presence of some goethite [30]. In the first band its contribution might be masked by the more intense hematite contribution, however, the morphology of the other bands indicate more clearly its presence. Finally, goethite contributes along with hematite to the magnetite broad band, but they are both masked by the stronger magnetite peak.

The intense hump following the magnetite peak with a center at around 711 cm^{-1} could be attributed to akaganeite. The morphology of the whole band underlines the predominance of magnetite, since its peak is apparent, however it seems that akaganeite has a strong presence, as well. Also, β-FeOOH contributes to the relatively narrow band at 300 cm^{-1} and to the broader band at 393 cm^{-1}. For the characterization of the hump three phases were examined: a) γ-Fe_2O_3, b) δ-FeOOH and c) β-FeOOH. The first phase could be apparent in trace amounts since the bands at 350 and 500 were not present, but at 1420 cm^{-1} a slight hump was noticed [52]. The second option was rejected because there were no contributions from higher wavenumbers, i.e. from 1160 and 1314 cm^{-1}, while the morphology of the spectrum was not similar to that obtained for feroxyhyte (see below description of orange area) [29, 53]. As a result, the only phase that matched the peaks at 305 and 393 cm^{-1} and could contribute at around 711 cm^{-1} would be akaganeite. It should be mentioned, however, that β-FeOOH is usually found around 723 cm^{-1} [18, 52], which could justify the asymmetry of the hump on the right side.

The yellow area exhibited the characteristic spectrum of lepidocrocite. Almost all of the peaks noticed in the graph are attributed to this phase with the 253 cm^{-1} peak being the most intense followed by the peak at 1304 cm^{-1} [28]. The weak bands at 742 and 1430 cm^{-1} could be attributed to maghemite traces and, thus, they were not reported in Table 2.3. Finally, the band at 818 cm^{-1} is probably attributed to a phase other than the oxides and oxyhydroxides addressed in this work and was not identified.

The orange area spectrum presented a more complicated morphology. The basic band of the spectrum had a center at 700 cm^{-1}, without exhibiting a sharp peak. The second most important band was the area extending from 1284 to 1462 cm^{-1}, which could be decomposed to two bands with centers at 1318 and 1420 cm^{-1}, accordingly. Also, the spectrum contained two distinct, weak, broad bands at 394 and 506 cm^{-1} and a very weak hump at 1162 cm^{-1}. These observations could reveal that this spectrum is a combination of γ-Fe_2O_3 and δ-FeOOH [29, 53]. The 350 cm^{-1} band of maghemite is included in the broad 394 cm^{-1} band. The band at 1318 cm^{-1} could be attributed to both feroxyhyte and hematite. With regard to δ-FeOOH, the morphology and position of the identified peaks, along with the upward trend of the curve from wavenumber 1100 cm^{-1} and beyond consolidate this assumption [53]. With regard to α-Fe_2O_3, many of the bands of the spectrum and especially at 227, 245 and 401 cm^{-1} could be assigned to hematite, as well. As a result, these phases could share the band at 1318 cm^{-1}. Finally, a small amount of goethite appears at 297 cm^{-1} and contributes also to the 393 cm^{-1} peak, since goethite spectrum presents a peak at 386 cm^{-1}. In general, goethite is found around 386 cm^{-1} [26, 31], but it has also been positioned above 390 cm^{-1} [28, 54]. Hence, due to the

presence of two phases in this band, there could be a slight shift towards higher wavenumbers, but still identify it as goethite.

The black region spectrum was characteristic of maghemite. The largest peak appeared at 723 cm^{-1}, followed by weaker bands at 367, 506 and 1420 cm^{-1}. The morphology of the spectrum implied that γ-Fe_2O_3 was the only oxide present in this area. The broad and slightly shifted to the right shape of the band at 367 cm^{-1} denotes the presence of some goethite with a peak at 386 cm^{-1}. However, since its presence was denoted only by this peak, meaning that the amount of this phase was small, it was not included in Table 2.3 along with the rest of the observed morphologies.

Table 2.3: Raman bands for rust samples of scribed system (A)

Colour	Raman bands (cm^{-1})	Phases identified
White	227,247,297,410, 494,611,660,1320	α-Fe_2O_3
	530,668	Fe_3O_4
	247,297,393,483, 564,680	α-FeOOH
	305,393,711	β-FeOOH
Yellow	219,253,311,350,380, 527,653,1055,1304	γ-FeOOH
Orange	350,506,700,1425	γ-Fe_2O_3
	394,506,680,1162,1318	δ-FeOOH
	227,245,295,401,507, 613,659,1318	α-Fe_2O_3
	245,297,382,682	α-FeOOH
Black	367,506,723,1420	γ-Fe_2O_3

2.3.3.2 Raman spectra identification of rust samples from scribed acrylic system (Paint B)

The white area spectrum of system (B) was very similar to the orange color spectrum of system (A), for wavenumbers below 1162 cm^{-1}. Indeed, the same phases were identified with some slight variations in the wavenumbers. More specifically, the peak at 1314 cm^{-1} was predominant, followed by the 693 cm^{-1} band. This fact suggested hematite to be the predominant oxide in the white rust area, followed by maghemite. Except for the maximum peak at 1314 cm^{-1}, hematite could also have contributions from its second more intense peak at 409 cm^{-1}, as well as from the peaks at 222, 240 and 295 cm^{-1}. Maghemite contributions could also come from the 494 and 1432 cm^{-1} bands. In addition, feroxyhyte was readily apparent from the asymmetric peak at 399 cm^{-1} and from the positive slope of the curve close to 1160 cm^{-1} (at 1137 cm^{-1}), as well as, from the peak at 1314 cm^{-1} [29]. Finally, goethite could participate in the formation of the broad band with center at 399 cm^{-1}, by contributing at 386 cm^{-1}, while

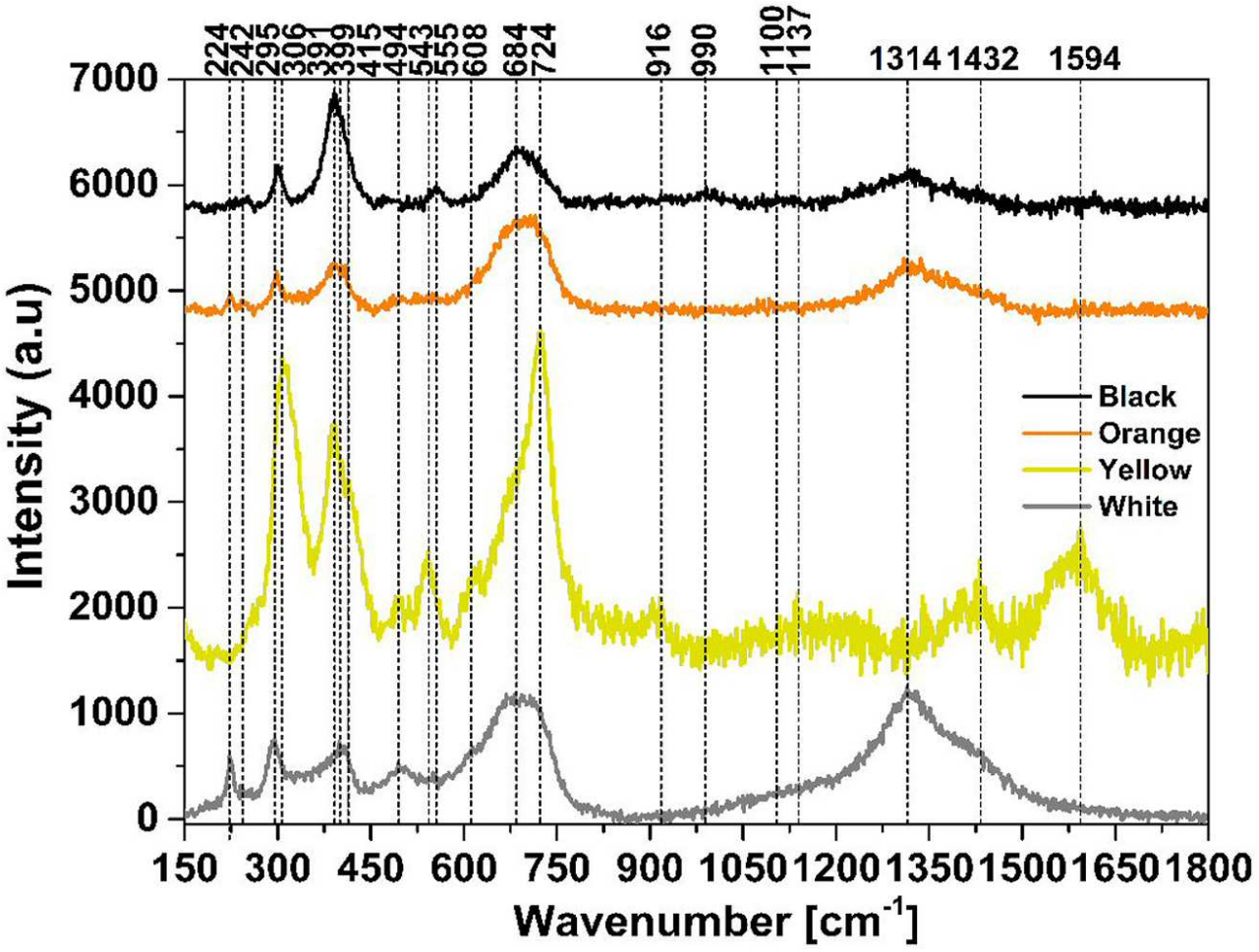

Figure 2.6: Raman spectra from rust areas of different color for scribed painting system (B)

its presence could also affect formation of some other bands of the spectrum, as presented in Table 2.5.

The yellow area exhibited the spectrum of akaganeite as a major phase, followed by goethite. Akaganeite presented its characteristic peaks at 306 and 724 cm^{-1}. Also, the weak bands at 916, 1137 and 1397 cm^{-1} could be attributed to akaganeite [19,26,27]. The intense peak at 391 cm^{-1} denotes the presence of goethite [18], which contributed also to some common bands with akaganeite [18], as presented in Table 2.5. Above 916 cm^{-1} the spectrum exhibited very broad bands with multiple peaks, which could be recognized as three independent bands: a) one that extended from 990 to 1286 cm^{-1}, b) another from 1286 to 1492 cm^{-1} and c) a third band from 1494 to 1699 cm^{-1}. The center for each band, irrespectively of the fluctuations presented in each one of them were around 1137, 1397 and 1594 cm^{-1}, respectively. The first two bands around 1160 and 1390 cm^{-1} could be attributed to akaganeite [27], while the band at 1594 cm^{-1} could be attributed to burnt organic matter [32].

The orange area spectrum presented a more complicated morphology. The most intense band of the spectrum was the band with a center around 693 cm^{-1}, including contributions from magnetite, maghemite and akaganeite. Maghemite and magnetite were found only as contributions to the 693 cm^{-1} band, since no other characteristic bands [52] or humps [51,55] of their spectrum were apparent. Akaganeite contribution included also the peak at 391 cm^{-1}.

The smooth convexity of the maximum band of the spectrum and the fact that the center of the band was around 700 cm^{-1}, could imply maghemite as the major component. However, the lack of sufficient amount of peaks per phase in this spectrum did not allow for a more accurate characterization of the main peak. The rest of the peaks at 242, 298 and 391 cm^{-1} could be attributed to goethite, which also contributed as a secondary phase in the biggest band of the spectrum at around 684 cm^{-1} [28, 32]. Finally, the bands at 224, 242 cm^{-1}, a contribution at 409 cm^{-1} (as part of the 391 cm^{-1} band) and the band at 1314 cm^{-1} could be assigned to hematite.

The black spectrum indicated the existence of goethite with the maximum peak at 391 cm^{-1}, followed by peaks at 299 and 684 cm^{-1} [32]. The weak band at 990 cm^{-1} could also be part of the goethite spectrum [28, 29, 56]. Another weak band at 1100 cm^{-1} and a slightly stronger band with a well-shaped peak at 1323 cm^{-1} could also be assigned to goethite [27,32], exhibiting, however some deviation from the reference values of 1120 and 1255 cm^{-1} [28], which could also be attributed to lepidocrocite traces [29]. In Table 2.5, the bands at 990, 1100 and 1323 cm^{-1} were presented as part of the goethite spectrum, with some reservation about the 1323 cm^{-1} peak, because it could be attributed to hematite traces [29]. Finally, the band at 251 cm^{-1} was possibly due to trace amounts of lepidocrocite and was not presented in Table 2.5.

Table 2.5: Raman bands for rust samples of scribed system (B)

Colour	Raman bands (cm^{-1})	Phases identified
White	222,240,295,409,494, 608,659,1314	α-Fe_2O_3
	494,700,1432	γ-Fe_2O_3
	399,494,680,1137,1314	δ-FeOOH
	240,295,386,684	α-FeOOH
Yellow	306,391,415,494,543,608, 684,724,916,1137,1397	β-FeOOH
	306,391,415,684	α-FeOOH
Orange	700	γ-Fe_2O_3
	662	Fe_3O_4
	391,720	β-FeOOH
	242,298,391,684	α-FeOOH
	224,242,409,1314	α-Fe_2O_3
Black	299,391,555,684, 990,1100,1323	α-FeOOH

2.3.4 Identification of rust morphologies

Raman spectroscopy revealed the presence of oxyhydroxides, such as goethite, akaganeite, lepidocrocite and feroxyhyte and oxides, such as magnetite, maghemite and hematite. The corrosion products were mainly of white, yellow, orange and black color, without necessarily implying

presence of different phases. Each color consisted mainly of mixture of these phases, verifying the aggressiveness of the accelerated aging conditions [33]. In total, the different oxides and oxyhydroxides identified for each specimen are, as follows:

(a) System (A):α,γ-Fe_2O_3,Fe_3O_4,α,β,γ,δ-FeOOH

(b) System (B):α,γ-Fe_2O_3,Fe_3O_4,α,β,δ-FeOOH

The SEM rust morphologies of scribed system (A) are presented in Fig. 2.7. Figures 2.7a and 2.7b present typical flowery structures from two different areas of the observed rust parts, thus, denoting oxyhydroxide presence [13, 15]. The morphology presented in Figs.2.7c and 2.7d could be rod-type goethite [35, 57]. Finally, the morphology presented in Figs. 2.7e and 2.7f is a compact structure consisting of globular, nano-scale grains and could be assigned to magnetite [58]. The globular morphologies have also been assigned to goethite [13, 35].

With regard to the rust morphologies of scribed system (B), in Figs. 2.8a and 2.8b a structure with irregularly shaped grains is presented. The grains would grow in a variety of shapes towards the vertical direction, making compact structures. However, the structure presents cracks at few locations on the left side of Figure 2.8a. At the lower side of the same figure, rust agglomerates are presented. The open porous structure presented either alone in Figure 2.8c, or mixed with a flowery structure in Fig. 2.8d could be akaganeite [20].

A very characteristic rust morphology from system (B) is presented in Fig. 2.9. This morphology presents characteristic wide, leaf type formations. The structure in the form of wide plates appears to interconnect with some nest formations [13, 33, 59], which could be protective goethite [60].

Finally, another rust morphology of system (B) appears in Figure 2.10. More specifically, this structure consists of large rust parts, while the EDS measurement performed on the marked point of Fig. 2.10a revealed presence mainly of iron and oxygen, while 1.16 at.% Cl and 8.94 at.% C were also found. Hence, this spectrum could imply presence of an oxide or oxyhydroxide, other than akaganeite, due to the low chloride content.

2.3.5 Correlation of the observed rust morphologies with paint efficiency

With regard to the experimental antifouling polyurethane scribed system (A), Raman spectroscopy revealed a variety of oxides and oxyhydroxides. More specifically, the white area spectrum exhibited hematite as the main oxide, followed by magnetite, goethite and akaganeite. The yellow area was pure lepidocrocite, the orange area spectrum exhibited maghemite as the main phase followed by feroxyhyte, hematite and goethite, while the black area was mainly maghemite. The same variety of phases, except for lepidocrocite, was noticed for the acrylic SPC system (B), but in different combinations. For the white area spectrum, in particular, the main oxide was hematite followed by maghemite, feroxyhyte and goethite. In the yellow area spectrum akaganeite was the predominant phase mixed with goethite. The orange area spectrum revealed predominance of maghemite, followed by magnetite, akaganeite, goethite

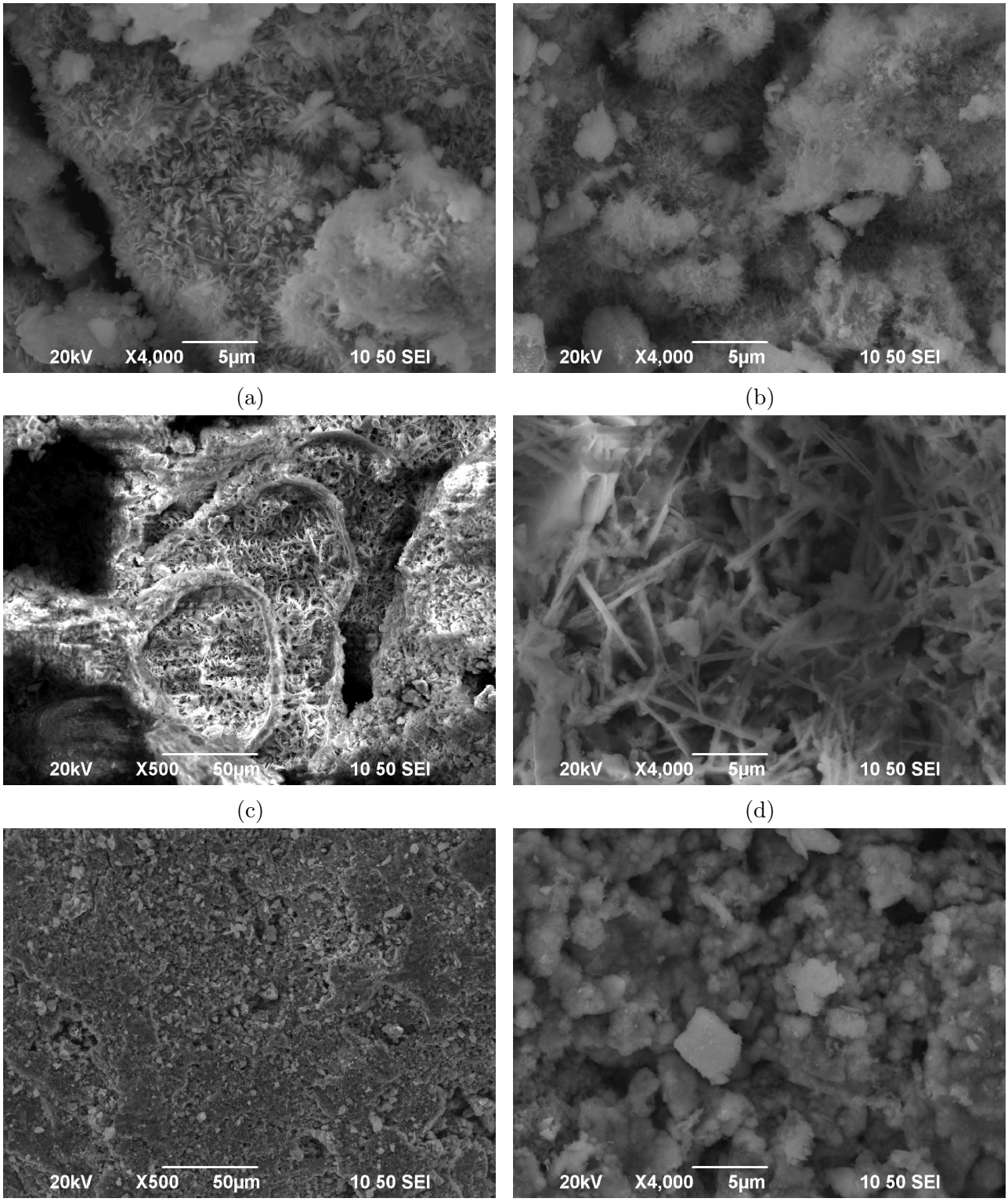

Figure 2.7: Electron micrographs of rust collected from scribed system (A); a) flowery structure (×4000), b) flowery structure from another area (×4000), c) thin microrods (×500), d) thin microrods (×4000), e) morphology exhibiting globular grains (×500), f) morphology exhibiting globular grains (×4000)

and hematite, while the black area was mainly goethite. In other words, for three of the four spectra of system (A) oxide phases were predominant (hematite in white area and maghemite in orange and black areas), while the oxyhydroxide lepidocrocite was predominant only in the

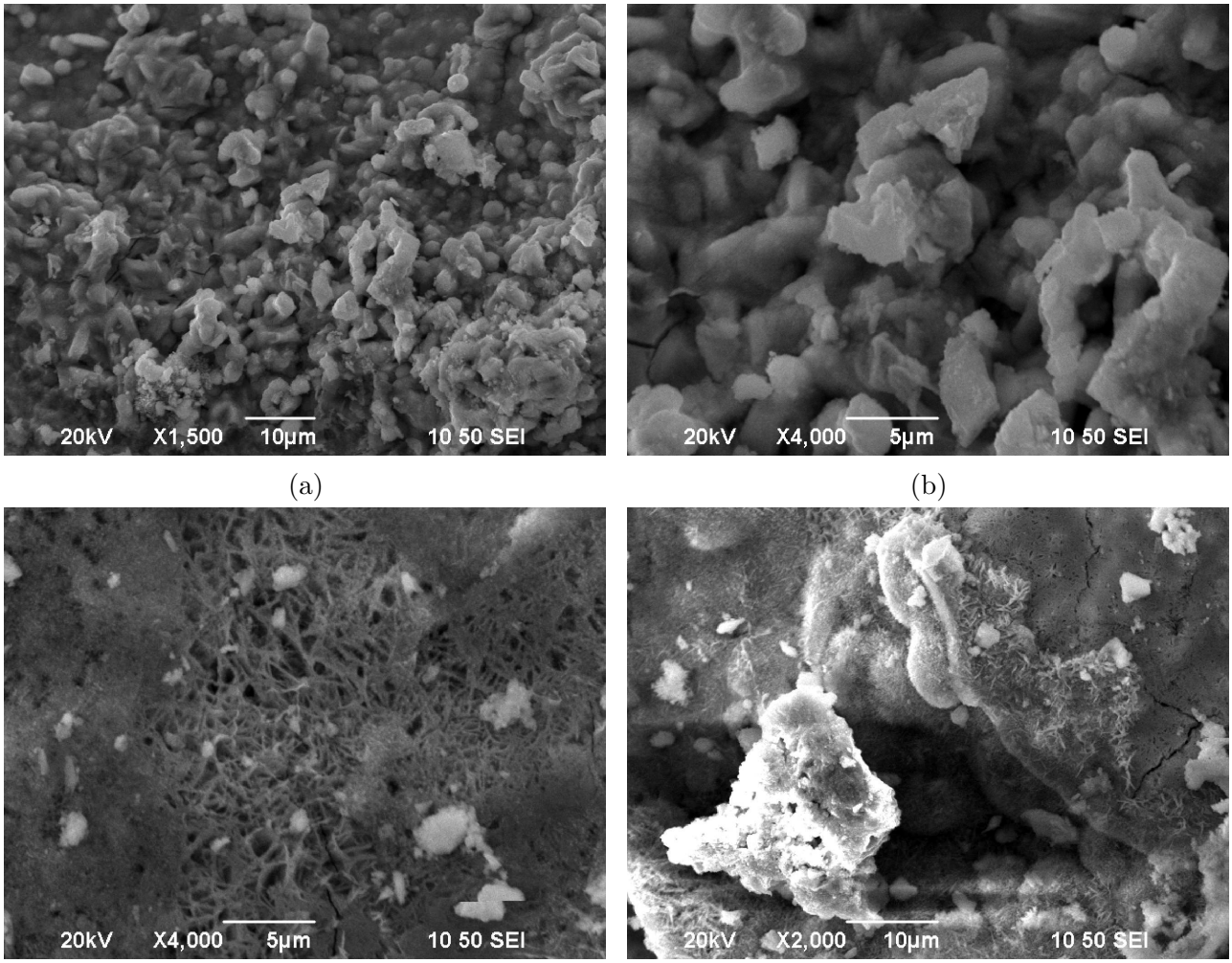

Figure 2.8: Electron micrographs of rust collected from scribed system (B); a) irregular shaped structure (×1500), b) irregular shaped structure (×4000), c) open structure (×4000), d) open structure mixed with flowery morphology (×2000)

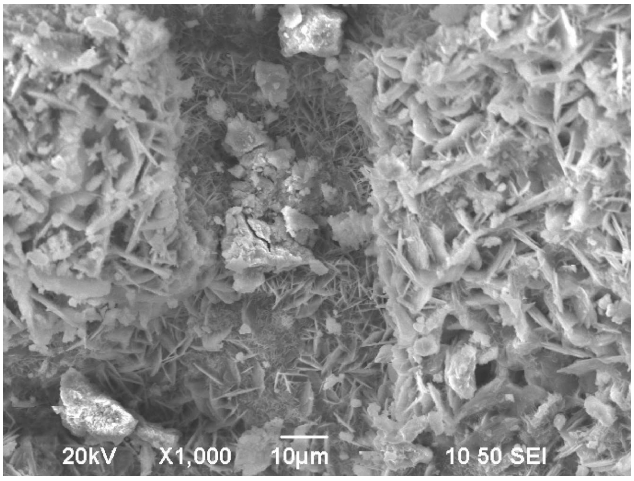

Figure 2.9: Electron micrograph from rust sample of system (B) presenting wide plate formations

yellow region. With regard to system (B), oxide phases were predominant in two of the four spectra. More specifically, hematite and maghemite were the main phases in the white and

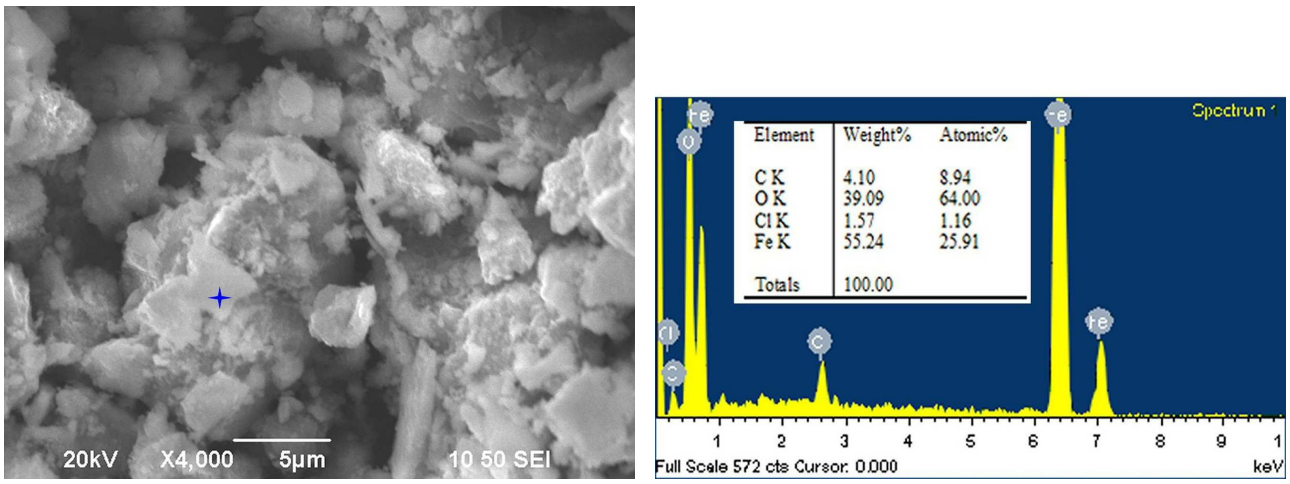

(a) (b)

Figure 2.10: Electron micrographs of rust collected from scribed system (B); a) compact rust parts (×4000), b) EDS spectrum from the marked point in (a)

orange areas, respectively, while the oxyhydroxides akaganeite and goethite were abundant in the yellow and black areas, correspondingly.

With regard to lepidocrocite presence in experimental system (A), this oxyhydroxide usually forms in the outer layer of the rust [22], in contact with the environment and is quite common during marine exposure of carbon steel [8]. Thus, the observed high purity lepidocrocite in the yellow Raman spectrum of experimental system (A) was probably incorporated in the surface rust layer. Lepidocrocite is considered more aggressive than small particle goethite, which is considered protective [13, 17] and less aggressive than akaganeite, which is linked to very high corrosion rates [21, 59]. As an oxyhydroxide, lepidocrocite is quite unstable and usually transforms to other forms, such as goethite or magnetite [13, 14], which were also observed in both examined painting systems. The latter phases are mostly abundant in inner rust layers [16, 18], eventually limiting γ-FeOOH presence on the outer rust. In either case, comparison of the corrosion performance between the two painting systems cannot be based solely on the presence of the pure lepidocrocite spectrum, since the corrosion rate depends on the total composition of the rust layer [17].

Antifouling systems (A) and (B) were expected to exhibit the same corrosion products, since the substrate was the same. Nevertheless, since the presence of specific corrosion products depends on the stage of the corrosion process, some corrosion products might not develop, due to the corrosion protection offered by the different coatings. The rust composition encountered in these systems denotes sufficient protection against further corrosion attack and it is an indicator of the degree of protection the corrosion products in the scribed areas of the examined systems would provide. The composition and combination of corrosion products for the experimental system denoted its superior performance compared to the acrylic-based system, due to the more intense presence of corrosion protective oxides [17] as major phases and the less intense presence of corrosion threatening oxyhydroxides [36]. In addition, system (B) was greatly affected by the exposure, since it exhibited intense blistering, discoloration (possibly implying

chemical alterations) and checking, either self-induced or caused by blistering. Moreover, as mentioned earlier, the rust spread beyond the scribes covering almost the entire surface of the metallic substrate making the traditional SPC antifouling technology practically unsuitable for anticorrosion purposes.

The nature of the corrosion products is directly related to the paint behavior when flawed. The experimental system exhibited very slight deformation along the scribe lines, which was mainly originated by the accumulation of corrosion products in the vicinity of the scribes. As a result, compact rust structures were formed, firmly attached to the surface of the steel and the paint, which sealed the scribed areas effectively and hindered further corrosion progression. The adherence of the rust layer onto the metallic substrate, along with its compact structure, would lead to minimum oxide spalling. This, in turn, would provide adequate time for the initially formed oxyhydroxides to transform to more stable oxide forms, such as maghemite or hematite, which provide better protection against corrosion [17], compared to the oxyhydroxides [36]. The variety of the corrosion products observed in this investigation, where oxides (e.g. hematite, maghemite) and less harmful oxyhydroxides (goethite, feroxyhyte) were predominant, verify the limited deformation of the experimental painting system during accelerated aging, which favored formation of more stable rust morphologies. It should be noted that the goethite oxyhydroxide is considered as the most stable form among the oxyhydroxides [16, 36], while the presence of feroxyhyte, even in small amounts, is important, since it is considered as an oxyhydroxide that provides protection to the substrate [61].

With regard to the silicone paints [49], it was found that the oxyhydroxide form of the corrosion products was a result of the intense swelling that the silicone systems exhibited during accelerated aging and caused the formation of large, coarse rust agglomerates without adherence. This led to a continuous alternation among corrosion layer detachment, corrosion attack, formation of a new corrosion layer, a procedure that was revealed by the rust phases and verified the limited corrosion protection provided in the scribed areas by the silicone paints in general. The above observations corroborate the better anticorrosion performance of the experimental polyurethane system (A) of the present study, compared to the silicone painted scribed specimens. The nature of the corrosion products observed in these two investigations was totally different. In the first study, the majority of the corrosion products were oxyhydroxides, with predominance of akaganeite, denoting vulnerability to corrosion attack [36]. On the contrary, in this study a mixture of mainly oxides and the most stable of the oxyhydroxides were predominant ensuring sufficient corrosion protection.

In summary, the main observation of the present study is that the variety of the rust phases formed during accelerated aging of the antifouling polyurethane experimental system (A), with predominance of oxides and the least harmful of the oxyhydroxides, was indicative of a compact oxide layer sufficiently sealing the substrate, since the observed phases require sufficient time to form from the initial oxyhydroxide phases. The observed morphologies were a result of the paint behavior in the scribed areas, where the absence of intense swelling or deformation along the scribe lines favored the formation of solid and compact oxide layers that would not spall,

hence there would be sufficient time for the metastable forms to transform to more protective phases, such as oxides.

A final ranking between the examined paints in the present study would designate the anticorrosion properties provided by the experimental polyurethane system (Exp. PU1) in flawed condition as being more than satisfactory, while, on the contrary, the general deterioration of the acrylic system on the surface and under the coating would rank it as unsatisfactory for severe corrosive conditions. The experimental system exhibited hardly any deterioration characteristics providing adequate corrosion protection. As a result, the experimental formulation exhibited better anticorrosion performance overall compared to the acrylic paint. Finally, a total comparison among all the examined antifouling systems in both investigations would rank as first the experimental polyurethane system, second the experimental silicone system, third the commercial silicone system and last the commercial SPC acrylic based system. Hence, the newly developed experimental systems surpassed the known anticorrosion efficiency of commercial products, however, between the two experimental systems, the polyurethane coating exhibited superior performance.

2.4 Conclusions

- The experimental antifouling polyurethane formulation (Exp. PU1) was examined with regard to its anticorrosive properties during salt spray test. The newly developed experimental system was not deformed or degraded during aging, only exhibited a slight swell in the close vicinity of the scribes, due mainly to local rust accumulation beneath the coat, without extending, though, far beyond the scribed area. On the contrary, the acrylic-based antifouling system exhibited extended material loss, blistering, checking and extensive substrate rust coverage beneath the multilayer coat, implying insufficient barrier properties of the unscratched part of the paint.

- This study linked the nature of the corrosion products in the scratched areas with paint efficiency. More specifically, the presence of mixture of the more protective oxides with the least harmful of the oxyhydroxides verified the sufficient corrosion protection provided by the polyurethane system and was linked to the absence of paint deformation during the experiment, which allowed formation of compact corrosion products, efficiently sealing the substrate. This, in turn, provided sufficient time for transformation of the firstly formed and thermodynamically metastable oxyhydroxides to the more corrosion protective phases observed in this study, hindering further corrosion progression.

- Rust morphology for the experimental polyurethane system included hematite oxide as major phase in the white rust area and maghemite in the orange and black rust areas. The yellow area exhibited lepidocrocite. The acrylic-based system exhibited hematite as major phase in the white area, mixture of akaganeite-goethite in the yellow area, maghemite in the orange area and goethite in the black rust area, indicating its inferior corrosion properties, compared to the experimental system.

- The polyurethane experimental antifouling system provided better anticorrosion protection overall compared to the traditional self-polishing copolymer technology, combining satisfactory anticorrosion protection along with a newly developed antileaching mechanism for environmentally friendly antifouling protection.

- Compared to the overall anticorrosion efficiency of the silicone systems presented in Chapter 1, the experimental polyurethane system would be ranked in the first position, followed by the experimental silicone system, the commercial silicone system and finally the commercial SPC acrylic based system. Hence, the newly developed experimental systems surpassed the known anticorrosion efficiency of commercial products, however, between the two experimental formulations, the polyurethane coating exhibited superior performance.

Chapter 3

Electrochemical impedance spectroscopy of scribed coated steel after salt spray testing

Abstract

In the present study, the electrochemical behavior of scribed coated steel examined for 12 weeks in salt spray conditions (Chapters 1 and 2) was investigated at 6, 8 and 12-week intervals. The impedance curves of the scribed specimens examined in salt spray (two scribed specimens for each of the systems Exp. Si, Ref. Si, Exp. PU1 and Acrylic) exhibited similar trends (Appendix B). For this reason, this study focused on the investigation of one scribed coated specimen, which was selected to be one scribed specimen painted with the Exp. PU1 system. During this investigation, various representative models of finite length diffusion impedance were examined, in order to find the optimum description for dissolved oxygen diffusion at each interval. Modified restricted diffusion fitted the experimental data after 6 and 8 weeks,and modified restricted or modified transmissive could fit the data after 12 weeks, accompanied by a decrease in corrosion resistance. Oxygen would diffuse through the porous corrosion layer and reduce on the magnetite layer, lying on top of the electrode surface.

3.1 Introduction

The use of painting systems is important for protection of metallic structures from their environment. The appropriate painting system should withstand the specific environmental conditions and provide long-lasting protection. This is why it is of paramount importance to assess the corrosion resistance of coated metals. For most applications, salt spray testing is considered as one of the most widespread methods for accelerated corrosion testing [62]. Salt spray results have been correlated with results from atmospheric exposure in subtropical environments [63], enhancing their validity. The painted specimens can be examined into the chamber either intact, in order to study the barrier properties of the intact coat, or scribed, in order to examine the protection that the unscratched part of the paint provides. The second scenario offers the ability to assess the anticorrosion efficiency of the painting system when it is flawed,

which represents a common problem during the service life of a paint and commonly leads to failure [64].

Oxygen diffusion plays a very important role in the corrosion rate of coated and uncoated carbon steel. For uncoated steel or coated steel with large scribes, the limiting diffusion rate of oxygen could be the predominant corrosion rate if the rust layer morphology can facilitate corrosion, as in the case of presence of both lepidocrocite oxyhydroxide (γ-FeOOH) and magnetite oxide (Fe_3O_4), during immersion of steel in 3% NaCl solution [65]. These corrosion products are also representative of steel exposure in natural or artificial chloride containing environments [8–10] and have been reported, among other phases, during 12 weeks of cyclic salt spray exposure (ISO 14993:2001) of painted steel specimens with large scribes [49, 66]. Reduction of lepidocrocite to magnetite is attained through reaction of the former with the ferrous ions from oxidation and is promoted during immersion in 3% NaCl solution or in cyclic exposure conditions (alternation of dry, wet and salt mist steps) during a salt spray test, hence in slightly acidic environments [65]. In this way, magnetite presence is enhanced, which, in turn can provide a large cathodic area for oxygen reduction, leading to increased corrosion rates [14].

In order to evaluate the protective properties of a painting system or depict the corrosion process of a corroded metal beneath a coating, electrochemical impedance spectroscopy (EIS) is usually applied, because it comprises an electrochemical method that does not disturb the system during the measurement and it is also applicable to very thick coatings [62]. The indication for a freshly degraded coating is usually a well-resolved semicircle in the Nyquist plot, appearing in the high frequency (HF) range, which accounts for the barrier properties of the coating, *i.e.* capacitance and pore resistance [67]. In a later stage of degradation the impedance graphs usually become more complicated, depicting, in a general case, a second arc in the mid frequency (MF) range, accounting for the double layer capacitance and charge transfer resistance and a diffusion tail with an angle of -45° in the low frequency (LF) range, accounting for Warburg diffusion processes [64], usually attributed to mass transport of dissolved oxygen. Finally, for coatings with extensive porosity, a -45° diffusion line would appear in the HF range upon immersion in the electrolyte, due to their high permeability, while the familiar LF diffusion tail would appear to designate severe degradation [68].

Unfortunatelly, the above description is not valid for more complex systems, such as scribed samples after salt spray testing, since corrosion products accumulate on the scribed areas affecting the diffusion process and giving rise to complex impedance graphs. In such a case, a proper expression for diffusion impedance, *i.e.* the difficulty for the electroactive species to travel through the diffusion layer and reach the reaction site, would arise by taking into consideration both the morphology of the scribed area covered by the corrosion products and the physicochemical characteristics of these products.

Indeed, impedance graphs exhibiting a shape similar to modified restricted finite-length diffusion (to be discussed in Sec. 3.3.4) have been obtained during salt spray testing of painted steel specimens with scribes after 30 days of exposure [69]. More specifically, the HF diffusion branch exhibited an angle equal to -20°, while the LF branch exhibited a CPE response. The

authors suggested that this behavior was attributed to a more "confined environment" caused by the corrosion products, possibly implying hindering of dissolved oxygen diffusion through the corrosion layer. A blocking effect to oxygen transport caused by the corrosion products has also been reported by van der Weijde *et al.* [70], during investigation of cathodic delamination of painted steel panels with small defects. Finally, a restricted diffusion character has also been reported by Tansuğ *et al.* [71] after 24 h and 192 h of mild steel immersion in 3.5% NaCl solution of pH 8. The authors attributed this characteristic on accumulation of non protective corrosion products, which decreased the rate of diffusion.

On the other hand, transmissive finite-length diffusion (to be discussed in Sec. **??**) has been proposed by Jüttner *et al.* [72] to describe oxygen diffusion through a porous 3D oxide layer, covering a steel electrode. More specifically, in their study they defined the total mass transport impedance as the sum of the diffusion impedances taking place in the Nernst layer, within a sub-layer inside the Nernst diffusion layer and finally through the pores of the oxide layer. Each of these three diffusion impedances was expressed as finite-length transmissive impedance.This type of diffusion is usually chosen to describe oxygen diffusion through the corrosion layer, during steel corrosion [73], while its physical meaning is that the whole concentration gradient is developed within the thickness of the corrosion layer [74]. Hence, in this case the diffusion layer thickness (L_{D}) would approximate the thickness of the corrosion products (δ), assuming them as a porous layer that covers the electrode. Apparently, this observation also holds for restricted diffusion, if a more enclosed space has been created by the corrosion products and some impermeability to dissolved oxygen diffusion has been developed. Transmissive diffusion has also been proposed by Bonnel *et al.* [75] to describe diffusion impedance of oxygen during immersion experiments of carbon steel in 3% NaCl solution (pH 6.2), using a rotating disk electrode (RDE). The mass transport of dissolved oxygen, as reported by Bonnel *et al.* [75] was of two types: the first type included convective diffusion in the liquid phase, where the Nernst diffusion layer applies (outside the porous layer), while the second type referred to dissolved oxygen diffusion through the porous oxide layer. The circuit proposed during this investigation was similar to the one proposed by Orazem and Tribollet [76] for iron dissolution and oxygen reduction reaction (ORR) (presented in Sec. 3.3.6), with the cathodic diffusion impedance being of the transmissive type.

Another approach for the interpretation of the impedance spectra of corroded steel is based on porous electrodes [77]. A characteristic example of application of porous electrode theory is the problem of cast iron in drinking water [76, 78, 79]. The corrosion products layer covering the cast iron electrode consisted of red rust (goethite and hematite), black magnetite and a layer of green rust (Fe^{2+} and Fe^{3+} in mixture) and carbonates. The authors supported that the black rust layer consisted of macropores, was in direct contact with the metal and it was an electronic conductor, thus could not be separated during EIS measurements by the electrode response. The macropores of the black rust layer were filled with red rust, which is an electronic insulator but ionic conductor [76] and, finally, the pore walls of black rust were covered circumferentially by green rust and carbonates. The EIS response for this problem

consisted of two capacitive loops, the HF loop arising from the presence of green rust and carbonates and the cathodic charge-transfer process (making basically two loops) and a LF loop, which accounted for diffusion and the anodic process. The observed semicircles were depressed, a characteristic that arises from the presence of black rust [76]. Finally, the diffusion related LF loop exhibited an angle of -22.5°, in absence of free chlorine, even from the beginning of immersion, implying semi-infinite pores as per de Levie, while in presence of free chlorine a -45° line was observed at initial stages of immersion, which progressively decreased to -22.5°.

In the present chapter, the individual EIS spectra obtained for mild coated steel with scribes after 6, 8 and 12 weeks of salt spray exposure are presented. The experimental data were analyzed, in order to interpret oxygen diffusion, which is considered to determine the overall corrosion rate. To this purpose, several diffusion impedance models were examined for assessing their ability to represent the experimental data. The parameters of the mathematical expressions of these models were calculated with a regression analysis specially developed for this procedure. The obtained EIS spectra from the regression models were evaluated based on the success of the equivalent circuit fitting and the values of the determined physicochemical parameters. The aim of the present work is to suggest a methodology for interpreting EIS spectra of complex systems and the specific paradigm of corrosion of painted steel with scribes was used for demonstrating this procedure.

3.2 Experimental methods and materials

3.2.1 Salt spray test and coating system

The accelerated aging test was the procedure described in Chapters 1 and 2, while the examined scribed coated system was one of the two samples painted with the Exp. PU1 paint, which was analyzed in Sec. 2.2.1 of Chapter 2. The condition of the specimen during the exposure period is presented in Fig. 3.1.

After the end of the experiment and the completion of the electrochemical examination, the specimen was cut in transverse sections and the thickness of the corrosion layer was measured, with the aid of a stereoscope. The average thickness was 1.4 mm.

3.2.2 Electrochemical examination setup

Corrosion behavior of scribed coated steel during salt spray test was evaluated by electrochemical impedance spectroscopy (EIS) and linear polarization resistance (LPR) measurements. EIS is a non-destructive technique, which is based on a small amplitude, sinusoidal potential perturbation of the electrochemical system, around the open circuit potential value. The small amplitude perturbation causes a linear response of the current. The impedance is the ratio of the phasor of the potential to the phasor of the current. With this method, the electrical characteristics of the system are obtained, as a response to the AC perturbation. The impedance response is depicted as a spectrum from frequencies around 10^{5} to 0.01 Hz. In this way, responses of different electrical characteristics (corresponding to certain physical processes) are

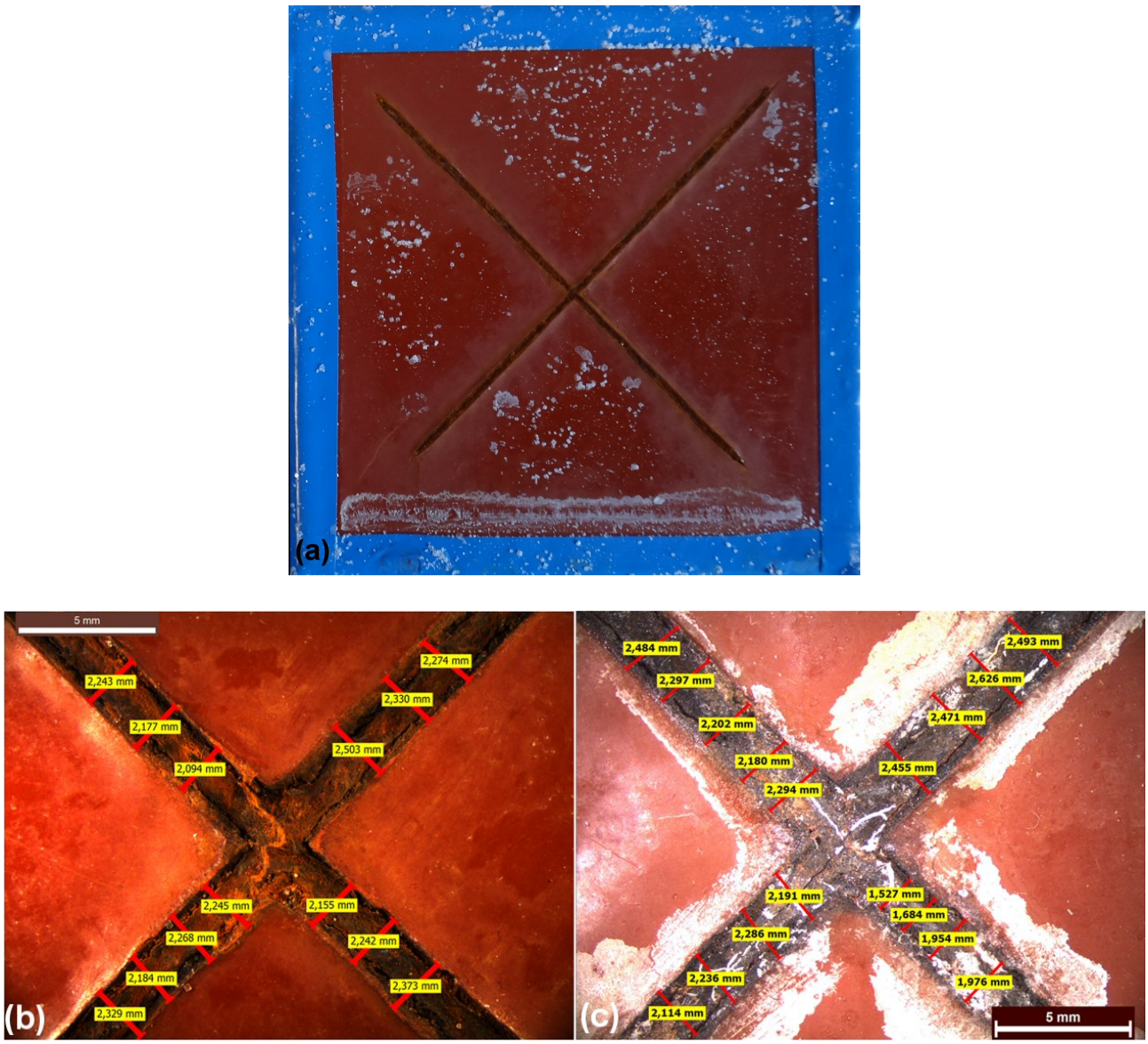

Figure 3.1: a) Photo of the scribed specimen after 6 weeks of experiment and surface views after b) 8 and c) 12 weeks of experiment in the salt spray chamber

depicted, depending on the frequency regime. The small perturbation around the DC potential value ensures that the system is not polarized. Also, the AC characteristic of the measurement enables the capture of electrical characteristics of high impedance systems with no measurable OC potential (insulators), such as coated steel with paint of large thickness. The physical processes are represented using equivalent electrical circuits (e.g. series and/ or parallel connections of resistors and capacitors). The LPR method is a DC technique, which provides a measure of the corrosion resistance of the electrochemical system. It is based on small scale polarization of the system around the OC potential value, usually ±20 mV versus the corrosion potential. The small polarization and slow scan rate ensure a linear response in the V-I plot, hence, Ohm's law can be applied in a small region around I=0 (corresponding to the corrosion potential) and the obtained resistance is a representative value of system's corrosion resistance.

The measurements were performed in a three electrode flat cell using the scribed coated

specimen as a working electrode, a platinum mesh as counter electrode and a saturated calomel electrode (SCE) as a reference. The electrolytic solution consisted of 3.5% NaCl in naturally aerated deionized water. Measurements were performed at room temperature. The exposed scratched area was 0.783 cm^2. A Solatron 1260 impedance/phase gain analyzer was used, combined with a PAR 263A potentiostat. The perturbation amplitude was ± 10 mV and was applied versus the open circuit potential. The maximum starting frequency for the EIS measurements was 10^5 Hz and the minimum was 10^{-2} Hz, with 10 points per decade. It should be noted that, in the high-frequency range only the points with a physical meaning for each curve were kept. The highest frequency was 3162 Hz for the 6-week curve, 39811 Hz for the 8-week curve and 10000 Hz for the 12-week curve. For frequencies above these thresholds, a positive phase angle was recorded, which could not be correlated with any physical processes, regarding the investigated system and they could be attributed to experimental artifacts. As a result, the curves could not all initiate from the same high-frequency. The impedance spectra were obtained via the Zplot software.

Normalization of the resistance was performed versus the geometrical surface of the exposed scratched area, that is 0.783 cm^2. The aim of the study was to assess the corrosion behavior of the exposed scratched area overall at each interval and not to determine the corrosion rate of the exposed metallic substrate underneath the corrosion products. In other words, the focus of the present investigation was on the change of corrosion resistance over time for a damaged area as a whole, *i.e.* macroscopically, without focusing on the corrosion rate variations arising from changes of the active area beneath the pores of the corrosion layer microscopically.

For the LPR method only the PAR 263A potentiostat was required. The polarization was set at ± 20 mV versus the corrosion potential, while the scanning rate was set to 0.166 mV/sec, in order to avoid charging of the double-layer. The LPR measurements were obtained through the PowerSuite software.

3.2.3 Fitting of the experimental data

In the present work, certain models - equivalent circuits, that could potentially fit the experimental data, were tested. The mathematical expression of total impedance for each of these equivalent circuits is dependent on several parameters, which have to be adjusted in order for the models to express the frequency response of the measured data as good as possible. Calculation of these parameters was carried out through the formulation and solution of an optimization problem. The aforementioned parameters are assumed to be the independent (or decision) variables of the optimization problem. The objective function (OF) to be minimized is the sum of the distances between each point on the complex plane representing each of the measured data ($Z_{\mathrm{exp},i}$) and the corresponding point representing the expression of the model equation at the same frequency ($Z_{\mathrm{fit},i}$). The optimization problem was solved using a Particle Swarm Optimization algorithm.

$$\mathrm{OF} = \sum_{i=1}^{n} |Z_{\mathrm{fit},i} - Z_{\mathrm{exp},i}| \tag{3.1}$$

where $Z_{\mathrm{fit},i} = Z_{\mathrm{fit},i}(\vec{X}, \omega_i)$, with $\vec{X}$ being the vector containing all the parameters for fitting and ω_i the angular frequency corresponding to data point i.

3.2.4 Reproducibility and error estimation

The analysis presented in the following sections is focused on the determination of the appropriate diffusion impedance mechanism for a painted steel specimen with scribes after 6, 8 and 12 weeks of exposure in the salt spray chamber. It should be mentioned that the selected diffusion impedance mechanism for each examination interval was verified through repeatability tests on painted steel specimens with scribes of similar dimensions, examined simultaneously with the specimen described herein. The results from the repeatability measurements are presented in Appendix B of this chapter.

Estimation of the goodness of fit (through calculation of chi-squared and sum of squares values) and the uncertainties of the physicochemical parameters was attained through complex non-linear least squares (CNLLS) fitting procedure. For all the examined models (both in this chapter and the Appendix B) the results as obtained from the PSO and the CNLLS methods are presented. The goodness of fit values, along with the physical interpretation of the obtained parameters, were crucial for the selection of the appropriate diffusion impedance mechanism for all the examined specimens.

3.3 Results and discussion

3.3.1 Impedance in scribed condition

In order to properly model the experimental impedance graphs of a corroding system, it is first important to determine its electrochemical behavior, *i.e.* type, sequence, sites and number of anodic and cathodic reactions, as well as the species that dissolve or reduce. However, in complicated systems, such as corrosion of painted steel with scribes after salt spray test, this might not be such an easy task to accomplish. The difficulty in interpreting such systems lies on the wide variety of iron corrosion products, which either form from scratch or transform to/from other phases, while these phases can be found either alone or in mixture in various positions across the corrosion layer [49, 66]. Hence, iron corrosion is a dynamic process affected by a large number of variables. In such cases, the shape of the impedance curves could provide crucial information, with regard to the basic mechanism that controls the corrosion rate of the system.

The experimental curves in the as-scribed condition are presented in Fig. 3.2. As can be seen from the plot, a one time-constant curve was obtained, with the charge-transfer resistance (R_{ct}) being 936.80±0.49% Ω cm^2 and the double-layer capacitance parameters (treated as a

contant phase element-presented in Sec. 3.3.3) being 7.71 $10^{-4}\pm0.51\%$ F s^{n-1} cm^{-2} for the CPE-Q and $0.539\pm0.14\%$ for the CPE exponent n.

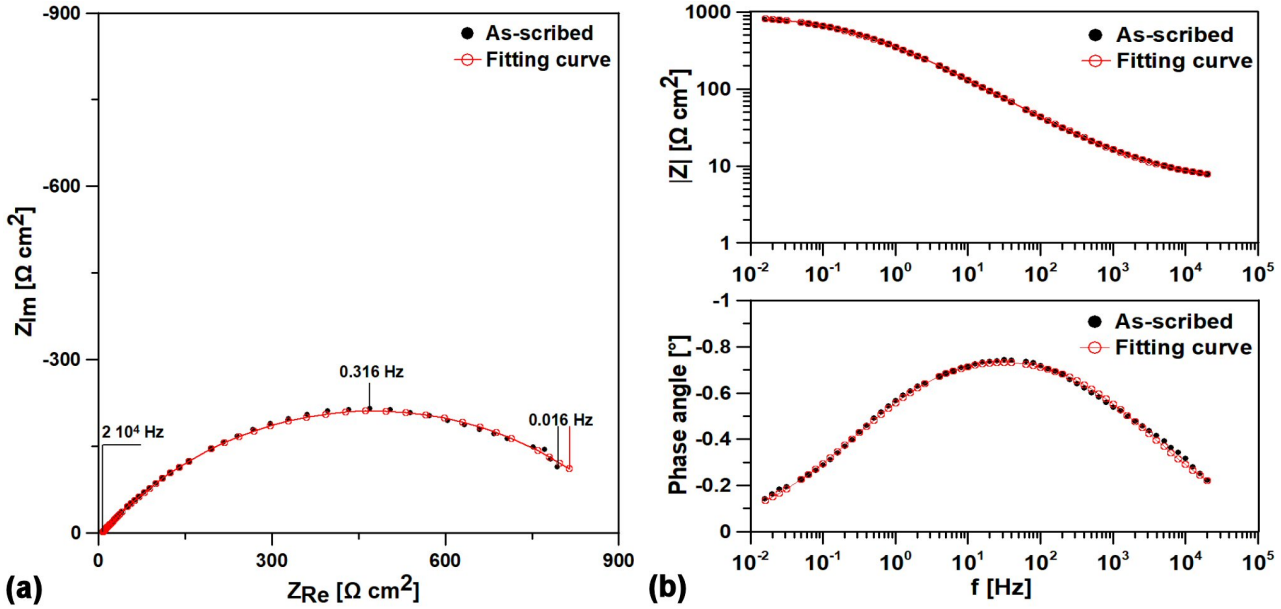

Figure 3.2: a) Nyquist and b) Bode plots of painted steel with scribes in the as-scribed condition

The experimental curves are presented in Fig. 3.3. The difference in the electrolyte resistance between the three curves of the Nyquist plot (Fig. 3.3a) could be attributed to the change of the active surface, during the experiment. Indeed, the electrolyte resistance, R_e , could be given as:

$$R_e = \varrho \frac{l}{S} \tag{3.2}$$

where ϱ is the specific resistance of the electrolyte [Ω cm], l is the distance between the electrode surface and the reference electrode [cm], while S is the exposed surface of the electrode to the electrolyte [cm^2]. Since resistivity is characteristic of the electrolyte and the distance between the exposed area and the reference electrode is also fixed in a three electrode flat cell, the electrolyte resistance could be affected only by changes on the exposed surface. These changes could result, for example, either from corrosion products accumulation on the steel surface creating some blocking effect (decrease of S) or from corrosion acceleration (increase of S).

In order to come to safer conclusions with regard to the theory that best interprets the observed EIS spectra, various models were examined, as proposed from the literature and are presented in the following sections.

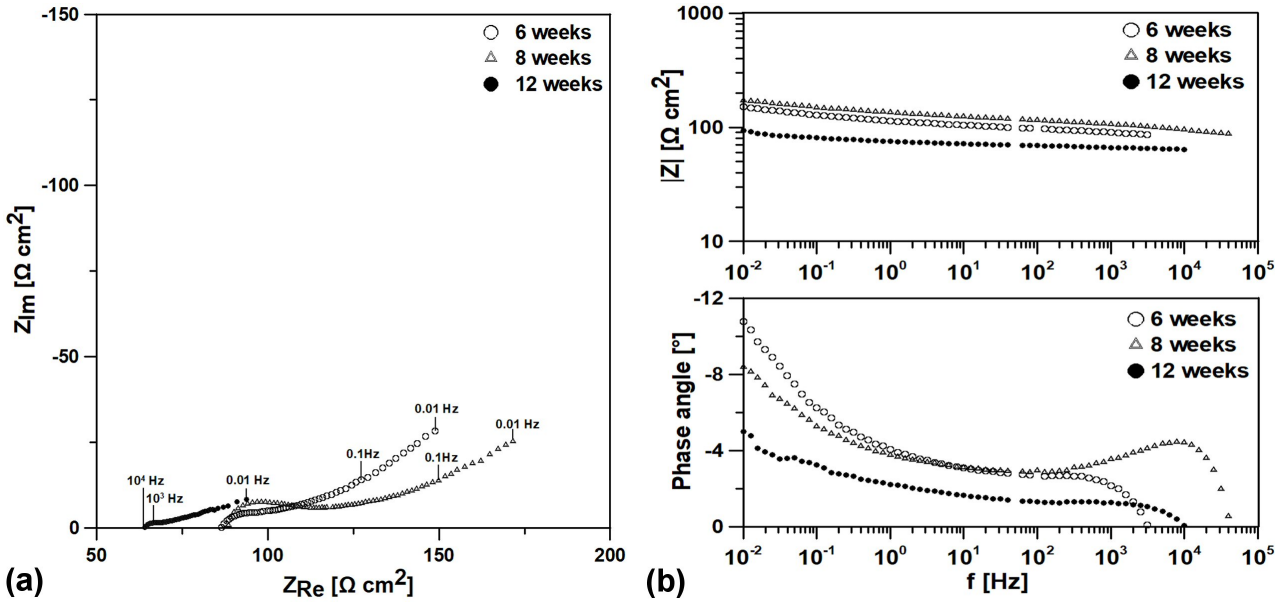

Figure 3.3: a) Nyquist and b) Bode plots of the examined scribed specimen after 6, 8 and 12 weeks of experiment in the salt spray chamber

3.3.2 Linear polarization resistance method

Linear polarization resistance method was performed after 6, 8 and 12 weeks of experiment. The obtained curves are presented in Fig. 3.4.

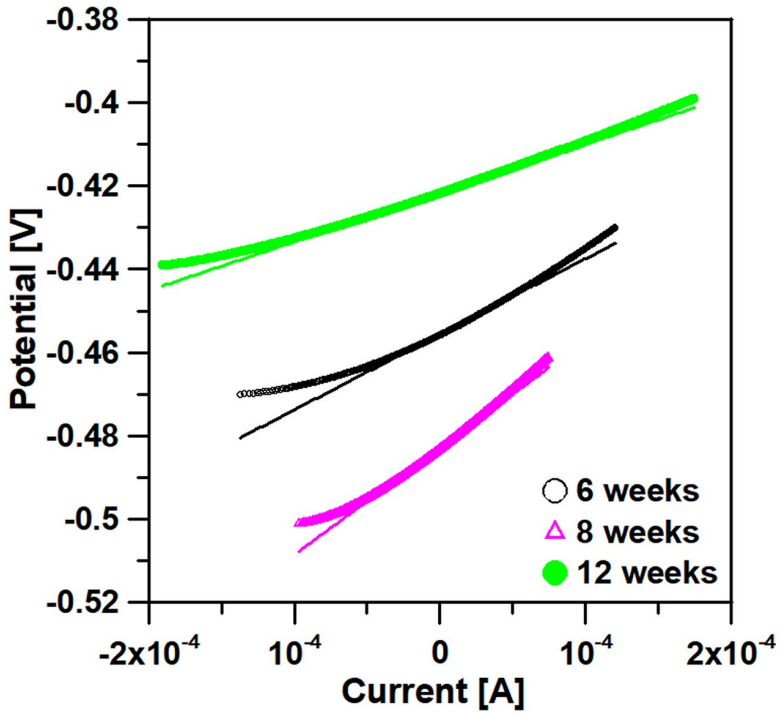

Figure 3.4: Linear polarization resistance curves for the experimental data after 6, 8 and 12 weeks of exposure in the salt spray chamber

The resistance obtained from the LPR method (R_{LPR}), defined as [73]:

$$\mathrm{R_{LPR}} = \Big[\frac{\Delta E}{\Delta i}\Big]_{(E-E_{corr})\to 0} \tag{3.3}$$

was calculated from the slope of the obtained curve (V/I), according to Ohm's law, for the range $\pm 2\ 10^{-5}$ A for the 6 and 8-week curves and in the range $\pm 5\ 10^{-5}$ A for the 12-week curve.The corresponding values of the resistance $\mathrm{R_{LPR}}$ are presented in Table 3.1. Comparison of $\mathrm{R_{LPR}}$ with $|Z(\omega \to 0)|$ from the Bode plot, Fig. 3.3b, revealed a similar trend, as presented in Table 3.1.

Table 3.1: Comparison of resistance values obtained from the low-frequency impedance magnitude and the LPR method

Weeks	$\lvert Z(\omega \to 0)\rvert$ [Ω cm^2]	R_{LPR} [Ω cm^2]
6	151.59	133.35
8	173.42	207.66
12	94.14	93.22

As can be seen from Table 3.1, the obtained values using the two methods are in good agreement. In the present study, where the lowest frequency for EIS measurements was 10^{-2} Hz and the LPR was performed with a scan rate of 0.166 mV/s, a very good correlation between the two methods was attained, possibly because the scan rate applied corresponded to a frequency equal to or slightly smaller than the low frequency limit of the impedance measurements.

3.3.3 Semi-infinite diffusion impedance

If the diffusion layer (L_{D}) for oxygen has an infinite thickness within the examined frequency range, the diffusion is semi-infinite and the corresponding impedance is called Warburg impedance [80]. The physical meaning behind this type of diffusion impedance is that unrestricted diffusion commences on a planar electrode surface and that the concentration gradient starting with its lowest value onto the electrode surface, reaches its (maximum) bulk value in infinite. The Warburg impedance is defined as [81, 82]:

$$Z_{\mathrm{W}} = \frac{(1-j)\sigma}{\sqrt{\omega}} = \frac{\sqrt{2}\sigma}{\sqrt{j\omega}} = \frac{\sigma'}{(j\omega)^{1/2}} \tag{3.4}$$

where σ is the Warburg coefficient and can be obtained from the slope of the plot Z_{Re} or Z_{Im} vs $\omega^{-1/2}$ [82]. Lasia [82] defines a mass-transfer coefficient given as $\sigma' = \sqrt{2}\sigma$. In the case of a Redox process and semi-infinite diffusion, the Warburg coefficient (σ) is given by the following formula:

$$\sigma = \frac{RT}{z^2F^2\sqrt{2}}\Big[\frac{1}{\sqrt{D_{\mathrm{Ox}}}C_{\mathrm{Ox}}(0) + \sqrt{D_{\mathrm{Red}}}C_{\mathrm{Red}}(0)}\Big] \tag{3.5}$$

where R is the gas constant (8.314 J mol^{-1} K^{-1}), T is the absolute temperature [K], z is the number of transferred electrons per diffusing species, F is the Faraday constant (96500 C mol^{-1}), $C_{\mathrm{Ox}}(0)$ is the surface concentration of oxidant species [mol cm^{-3}], $C_{\mathrm{Red}}(0)$ is the

surface concentration of reductant species [mol cm^{-3}], D_{Ox} is the diffusion coefficient of oxidant species [cm^2 s^{-1}] and D_{Red} is the diffusion coefficient of reductant species [cm^2 s^{-1}].

Apparently, the real and imaginary parts of the Warburg impedance are equal. Hence, in a Nyquist plot the Warburg impedance appears as a straight line, with a slope corresponding to -45°. A corroding system exhibiting this type of diffusion is usually represented by a Randles cicuit where the faradaic impedance, composed by a series connection of the charge transfer resistance R_{ct} and the diffusion impendace Z_{W}, is in parallel to the double layer capacitance C_{dl}. This connection is in series with the electrolyte resistance R_{e}. The Randles connection is presented in Appendix A, Fig. A.1. For the present case, $Z_{\mathrm{D}} = Z_{\mathrm{W}}$. In the high frequency (HF) range, a semi-circle appears, either perfect or depressed, depending on whether C_{dl} is ideal or behaves as a constant phase element, with $Z_{\mathrm{CPE}} = 1/[Q(j\omega)^n]$. The time constants for the two processes are defined as [81, 82]:

$$\tau_{\mathrm{ct}} = R_{\mathrm{ct}} C_{\mathrm{dl}} \qquad \text{for the charge-transfer process} \tag{3.6}$$

$$\tau_{\mathrm{D,Inf}} = R_{\mathrm{ct}}^2 / 2\sigma^2, \qquad \text{for the semi-infinite diffusion process} \tag{3.7}$$

In the case of an overlap between the kinetic and the diffusion process, extrapolation of the Warburg tail to the real axis would intersect it at $R_{\mathrm{e}} + R_{\mathrm{ct}} - 2\sigma^2 C_{\mathrm{dl}}$ [81]. Finally, in the case of a CPE for double-layer the kinetic time constant becomes [83]:

$$\tau_{\mathrm{ct,CPE}} = [R_{\mathrm{ct}} Q]^{1/n} \tag{3.8}$$

3.3.4 Finite-length diffusion impedance

The finite-length diffusion theory assumes a diffusion layer of finite thickness. For the particular case of corrosion of scribed steel examined herein, the thickness of the diffusion layer is correlated with the actual thickness of the corrosion layer. Compared to semi-infinite linear diffusion, the concentration gradient is developed within the pores of the porous layer of corrosion products, while the diffusion time constant becomes [81]:

$$\tau_{\mathrm{D,FD}} = L_{\mathrm{D}}^2 / D \tag{3.9}$$

D is the diffusion coefficient for dissolved oxygen, which usually ranges between 10^{-5} cm^2/s [82] to 1.9 10^{-5} cm^2/s [65].

Moreover, in this case the Warburg coefficient should be modified accordingly [84], for a corrosion process involving one type of diffusing species:

$$\sigma_{\mathrm{f}} = \frac{RT}{z^2 F^2 \sqrt{2}} \left[\frac{1}{\sqrt{D_{\mathrm{f}}} C_{\mathrm{f}}} \right] \tag{3.10}$$

where, as proposed in the work of Dawson and John [84], D_{f} is the diffusion coefficient through the pores of the film and C_{f} is the concentration, which depends on the concentration gradient through the film pores.

3.3.4.1 Restricted diffusion in its ideal form

In the present model, diffusion impedance was considered to be linear restricted diffusion in its ideal form [81, 82, 85]:

$$Z_{\mathrm{D,res}}(\omega) = \frac{\sigma'}{(j\omega)^{1/2}} \coth\sqrt{\frac{j\omega L_{\mathrm{D}}^2}{D}} = R_{\mathrm{D}} \frac{\coth\sqrt{j\omega\tau_{\mathrm{D,FD}}}}{\sqrt{j\omega\tau_{\mathrm{D,FD}}}} \tag{3.11}$$

where R_{D} is a diffusion related resistance, defined as [82]:

$$R_{\mathrm{D}} = \frac{\sigma' L_{\mathrm{D}}}{\sqrt{D}} \tag{3.12}$$

From Eq. (3.12) the mass transfer coefficient can be derived, as follows:

$$\sigma' = \frac{R_{\mathrm{D}}}{\sqrt{\tau_{\mathrm{D,FD}}}} \tag{3.13}$$

The high frequency part of restricted diffusion impedance is a semi-infinite Warburg impedance with a slope equal to -45°, given by the following formula [80, 86]:

$$Z_{\mathrm{D,res}}(\omega) = \frac{R_{\mathrm{D}}}{\sqrt{\frac{j\omega L_{\mathrm{D}}^2}{D}}} \tag{3.14}$$

At low frequencies, the impedance branch becomes a line parallel to the imaginary axis, exhibiting a purely capacitive behavior with an angle of -90°. The characteristic diffusion frequency from the high-frequency Warburg behavior to the low-frequency imaginary branch is equal to $\omega_{\mathrm{D,FD}} = D/L_{\mathrm{D}}^2$ [81]. The low frequency impedance is represented by a series connection of $R_{\mathrm{D}}/3$ with a pseudocapacitance C_{D}, defined as [80]:

$$C_{\mathrm{D}} = \frac{z^2 F^2 C^* L_{\mathrm{D}}}{RT} \tag{3.15}$$

where C^* is the bulk concentration of the diffusing species. The original definition of Eq. (3.15) included the active electrode area (A) in the numerator. However, in the present study all parameters are normalized, hence the area was not included.

Another definition for C_{D} has been proposed by Lasia [82],

$$C_{\mathrm{D}} = \frac{L_{\mathrm{D}}}{\sqrt{D}\sigma'} \tag{3.16}$$

In the LF range $\lim_{x\to 0}\left(\frac{\coth(x)}{x}\right) \approx \frac{1}{3} + \frac{1}{x^2} + \ldots$, hence the diffusion impedance becomes,

$$Z_{\mathrm{D,res}}(\omega) = \frac{R_{\mathrm{D}}}{3} + \frac{1}{j\omega C_{\mathrm{D}}} \tag{3.17}$$

For the present model, the total impedance assuming Randles connection and CPE for double layer is given by Eq. A.1, with $Z_{\mathrm{D}} = Z_{\mathrm{D,res}}$. In the LF range, the total impedance becomes,

$$Z_{\mathrm{tot}}(\omega) = \left(R_{\mathrm{e}} + R_{\mathrm{ct}} + \frac{R_{\mathrm{D}}}{3}\right) + \frac{1}{j\omega C_{\mathrm{D}}} \tag{3.18}$$

For the purpose of the present model, Eq. (A.1) was used as total impedance, while diffusion impedance was given by Eq. (3.11). This model was not suitable for the experimental data. This is verified by the goodness of fit values, chi-squared and sum of squares (Table A.3), which were larger than the values for the finally selected diffusion impedance models, which will be presented in the following sections. For this reason, the results for this model are presented in the Appendix section A.2.1. The characteristic of this model was that the high-frequency semicircle, describing the charge-transfer process, was barely approached (Fig. A.3). This observation could be verified especially by the very small values of the CPE-exponent n, which was found smaller than 0.3 for all curves (Table A.1). Moreover, with regard to the CNLLS results (Table A.2), the $\tau_{\mathrm{D,FD}}$ and R_{D} values after 12 weeks exhibited uncertainty 223% and 107%, respectively, meaning that the diffusion related components of this model were statistically insignificant.

The $\tau_{\mathrm{ct,CPE}}$ and σ' values (Tables A.1 and A.2) were calculated from the mean values of the corresponding parameters, according to Eqs. (3.8) and (3.13), respectively. The value of $\tau_{\mathrm{ct,CPE}}$ was used in comparison to the $\tau_{\mathrm{D,FD}}$ time constant, in order to have an indication of how much faster the charge-transfer process is compared to the diffusion process. The mass-transfer (or the Warburg) coefficient is a parameter that is apparent in both semi-infinite and finite-length diffusion impedance mechanisms but, to the authors' knowledge, is not generally analyzed in the literature. As can be seen from Eqs. (3.10) and (3.13), its value depends on the diffusion coefficient inside the pores (D_{f}), concentration gradient inside the pores (C_{f}), diffusion-related resistance (R_{D}) and diffusion layer thickness (L_{D}), hence, it would be very hard to estimate what are the exact parameter(s) in each model that could affect its value. To this purpose, calculation of σ' was performed for comprehensiveness reasons. The observations reported in this paragraph apply for all the diffusion impedance mechanisms presented in this chapter.

3.3.4.2 Modified restricted diffusion

In the present model, diffusion impedance was considered to be linear modified restricted diffusion, given by the following equation [81, 82]:

$$Z_{\mathrm{D,mod-res}}(\omega) = R_{\mathrm{D}} \frac{\coth\left(\frac{j\omega L_{\mathrm{D}}^2}{D}\right)^{\phi/2}}{\left(\frac{j\omega L_{\mathrm{D}}^2}{D}\right)^{\phi/2}} = R_{\mathrm{D}} \frac{\coth\left(j\omega\tau_{\mathrm{D,FD}}\right)^{\phi/2}}{\left(j\omega\tau_{\mathrm{D,FD}}\right)^{\phi/2}} \tag{3.19}$$

where ϕ is a dispersion parameter [81], which can take values between zero and unity [82]. This model is different from the restricted diffusion of Ho *et al.* [85] in that it predicts two CPE responses, for the high-frequency (HF) and low-frequency (LF) diffusion impedance parts correspondingly, deviating from the Warburg slope (-1) and the purely capacitive reponse at the respective frequency regimes. According to Cabanel *et al.* [86], modified restricted diffusion impedance could be separated in the HF and LF regime. For the HF regime,

$$Z_{\mathrm{D,mod-res}}(\omega) = \frac{R_{\mathrm{D}}}{(\omega\tau_{\mathrm{D,FD}})^{\phi/2}}(\cos(\phi\pi/4) - j\sin(\phi\pi/4)) = \frac{R_{\mathrm{D}}}{(j\omega\tau_{\mathrm{D,FD}})^{\phi/2}} \tag{3.20}$$

and for the LF regime,

$$Z_{\mathrm{D,mod-res}}(\omega) = \frac{R_{\mathrm{D}}}{3} + \frac{R_{\mathrm{D}}}{(\omega\tau_{\mathrm{D,FD}})^{\phi}}(\cos(\phi\pi/2) - j\sin(\phi\pi/2)) = \\ = \frac{R_{\mathrm{D}}}{3} + \frac{R_{\mathrm{D}}}{(j\omega\tau_{\mathrm{D,FD}})^{\phi}} \tag{3.21}$$

Taking into consideration Eq. (A.1), with $Z_{\mathrm{D,mod-res}}$ as diffusion impedance and Eq. (3.21) for the LF limit of this impedance, the total impedance of the corroding system in the LF region, assuming modified restricted diffusion impedance, becomes,

$$Z_{\mathrm{tot}}(\omega) = \left(R_{\mathrm{e}} + R_{\mathrm{ct}} + \frac{R_{\mathrm{D}}}{3}\right) + \frac{1}{(j\omega)^{\phi}Q_{\mathrm{D}}} \tag{3.22}$$

where $Q_{\mathrm{D}} = (\tau_{\mathrm{D,FD}})^{\phi}/R_{\mathrm{D}}$

For the purpose of the present model, Eq. (3.19) was taken into consideration for diffusion impedance, which predicts a $-\phi\pi/4$ angle in the HF part of the diffusion branch and a $-\phi\pi/2$ angle at low frequencies [81, 86]. The total impedance, assuming Randles connection, is given by Eq. (A.1).

Table 3.2: PSO fitting results and derived parameters for the painted scribed specimen after 6, 8 and 12 weeks of experiment in the salt spray chamber, assuming modified restricted diffusion, Randles connection and CPE for double-layer

Parameter	Unit	6 weeks	8 weeks	12 weeks
$\tau_{\mathrm{D,FD}}$	[s]	78.30	281.27	8.11 10^{5}
R_{D}	[Ω cm^2]	88.38	112.61	184.72
ϕ		0.450	0.288	0.368
R_{ct}	[Ω cm^2]	7.37	9.25	0.97
n		0.698	0.749	0.793
Q	[F s^{n-1} cm^{-2}]	2.87 10^{-4}	1.78 10^{-5}	1.36 10^{-4}
σ'	[Ω cm^2 s$^{-1/2}$]	9.99	6.71	2.05 10^{4}
$\tau_{\mathrm{ct,CPE}}$	[s]	1.47 10^{-4}	8.89 10^{-6}	1.28 10^{-5}

Table 3.3: CNLLS fitting results and derived parameters for the painted scribed specimen after 6, 8 and 12 weeks of experiment in the salt spray chamber, assuming modified restricted diffusion, Randles connection and CPE for double-layer

Parameter	Unit	6 weeks	8 weeks	12 weeks
$\tau_{\mathrm{D,FD}}$	[s]	100.50±23.4%	239.00±71.3%	7.67 10^{5}±1.3 10^{6}%
R_{D}	[Ω cm^2]	94.96±8.9%	110.20±17.3%	206.90±2.4 10^{5}%
ϕ		0.481±7.7%	0.308±13.7%	0.384±4.3%
R_{ct}	[Ω cm^2]	8.56±23.1%	13.49±26.7%	0.67±87.0%
n		0.737±5.6%	0.728±3.5%	0.943±9.0%
Q	[F s^{n-1} cm^{-2}]	2.46 10^{-4}±39.0%	1.96 10^{-5}±30.8%	4.31 10^{-5}±85.3%
σ'	[Ω cm^2 s$^{-1/2}$]	9.47	7.13	0.24
$\tau_{\mathrm{ct,CPE}}$	[s]	2.33 10^{-4}	1.22 10^{-5}	1.54 10^{-5}

With regard to the results presented in Tables 3.2 and 3.3, the fitting values refer to parameters $\tau_{D,FD}$, R_D, R_{ct}, n, Q and ϕ, while the calculated parameters are σ' and $\tau_{ct,CPE}$.

Table 3.4: Chi-squared and sum of squares values, as indicators of goodness of fit for the modified restricted diffusion impedance mechanism

Parameter	6 weeks	8 weeks	12 weeks
χ^2	$3.12\ 10^{-5}$	$3.62\ 10^{-5}$	$3.22\ 10^{-5}$
Sum of Squares	$3.19\ 10^{-3}$	$4.57\ 10^{-3}$	$3.67\ 10^{-3}$

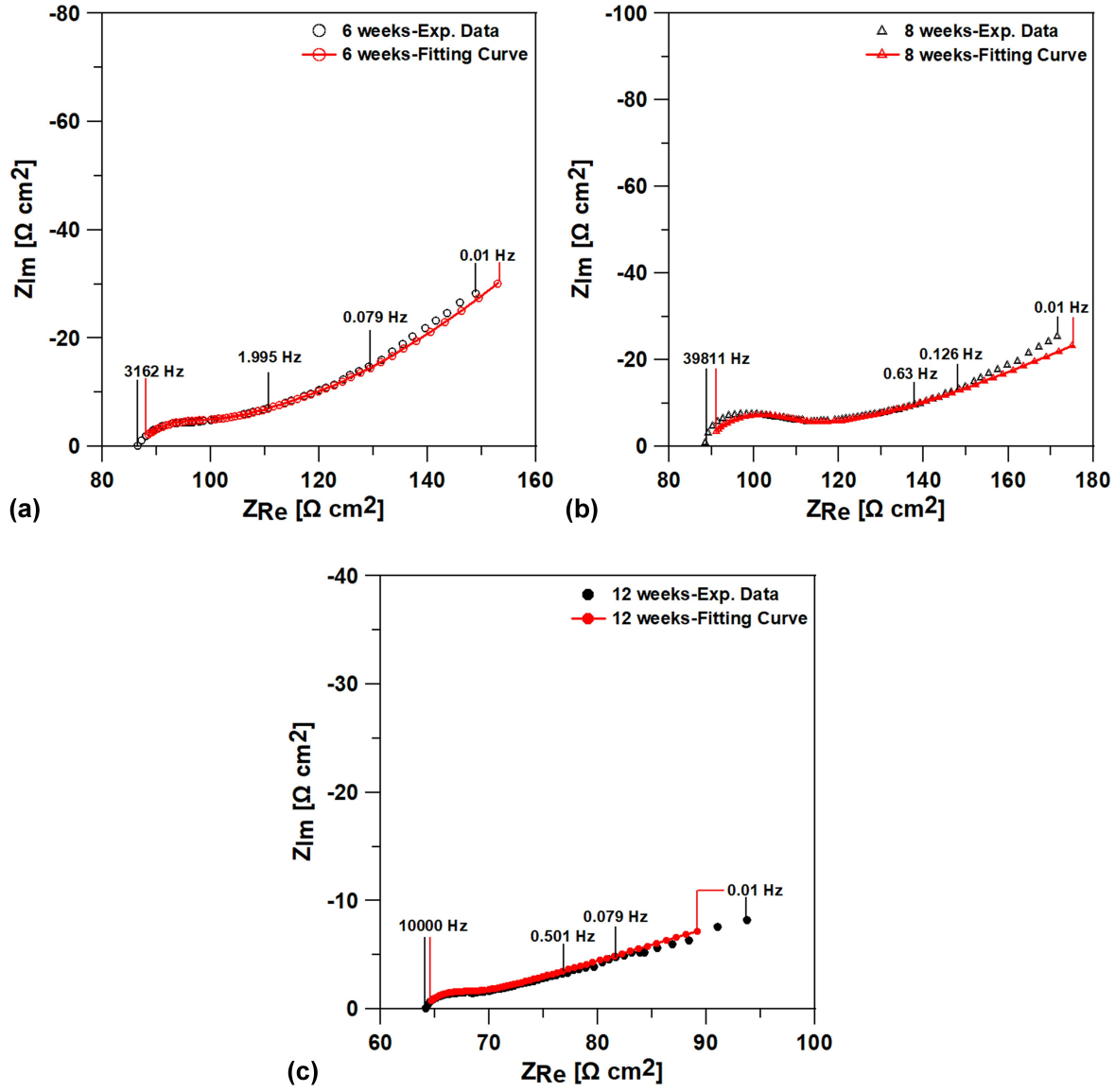

Figure 3.5: Fitting curves for the painted scribed specimen after a) 6, b) 8 and c) 12 weeks of experiment in the salt spray chamber, assuming modified restricted diffusion, Randles connection and CPE for double-layer

The goodness of fit results (Table 3.4) indicated that this model provided the best fit for the 6 and 8-week curves, compared to the rest of the diffusion impedance mechanisms examined throughout this study. However, this is not the case for the 12-week curve, since the goodness

of fit values were found larger than the finally selected model (presented in a following section), while the uncertainties of the $\tau_{D,FD}$ and R_D parameters were $\pm 1.3\ 10^6$ and $\pm 2.4\ 10^5$, respectively, implying that this model was unsuitable for these data.

With regard to the results after 6 and 8 weeks, it can be seen from Tables 3.2 and 3.3 that the results provided by the two methods per interval were in close proximity. More specifically, the results from the PSO procedure were within the uncertainty range of the calculated parameters of the CNLLS regression analysis for the respective examination period. This is a very important finding in favor of the PSO algorithm, which is much less dependent on initial guesses and does not require any weighting factors for minimization of the objective function.

This type of diffusion impedance is not very common in corrosion studies. Transmissive type diffusion impedance is usually encountered (e.g. [74, 75, 87]). However, since modified restricted diffusion impedance suggests finite-length diffusion, two basic assumptions shall be common between the two types of finite-length diffusion impedance mechanisms: a) that the concentration gradient develops inside the pores of the corrosion layer and b) there is some hindrance to dissolved oxygen diffusion through the porous layer [74]. This type of diffusion impedance, along with the modified transmissive type presented in a following section, could be attributed to nonuniform diffusion or existence of multiple paths [82]. With respect to the low-frequency CPE behavior, and borrowing the observations from ion inserion experiments through thin film electrodes, this characteristic could result from modification of the "terminal impedance" Z_f, assuming that the diffusion impedance is represented as a transmission line with distributed resistance and capacitance elements with Z_f being the impedance of the boundary [88]. According to Bisquert *et al.* [88], in the ideally restricted case $Z_f = \infty - j\infty$ (open circuit), while in the modified restricted case Z_f corresponds to a CPE. However, in the same work it is reported that the LF CPE response could also result from a purely reflecting boundary with porosity or roughness.

The CPE-restricted diffusion proposed by Bisquert *et al.* [88] includes a Warburg behavior at the HF branch of diffusion impedance and the CPE is observed only in the LF part. In our case, the type of restricted impedance observed included a non-Warburg behavior in the HF part of the difffusion impedance branch, while a doubling exponent for jω between the HF and LF parts of the diffusion branch was observed, as has also been reported by Cabanel *et al.* [86] and it is confirmed by the slope ratio equal to 2, between the two frequency regimes, in the $\log(-Z_{Im})$ vs $\log(f)$ plot (Fig. 3.6). According to the same work, this behavior arises from the non-ideal behavior of the electrochemical systems. Indeed, the curves corresponding to 6 and 8 weeks of experiment exhibited two-sloped curves with a ratio equal to 2.03 and 2.44, respectively, Fig. 3.6a and 3.6b, satisfying this theory.

With regard to the values of the obtained parameters after 6 and 8 weeks, the higher value of R_D compared to the corresponding R_{ct} denotes a faster kinetic process, which becomes more profound by comparison of the characteristic time constants for both processes. The difference between the kinetic and mass-transfer time constants was more obvious in the 8-week data, where the HF semicircle was better resolved. Another characteristic of the obtained parameters

is that there is no statistically significant difference between the two intervals for almost all parameters containing error estimates, except for the CPE pre-factor Q. This means that there was not a significant change in the corrosion layer between the two periods such that could affect the diffusion and charge-transfer processes. Despite the increase in R_{LPR} after 8 weeks (Table 3.1), the overlapping of almost all the parameter values between the two intervals, as is deduced by the corresponding uncertainties, did not imply a change in the corrosion protection provided by the oxide layer for this period.

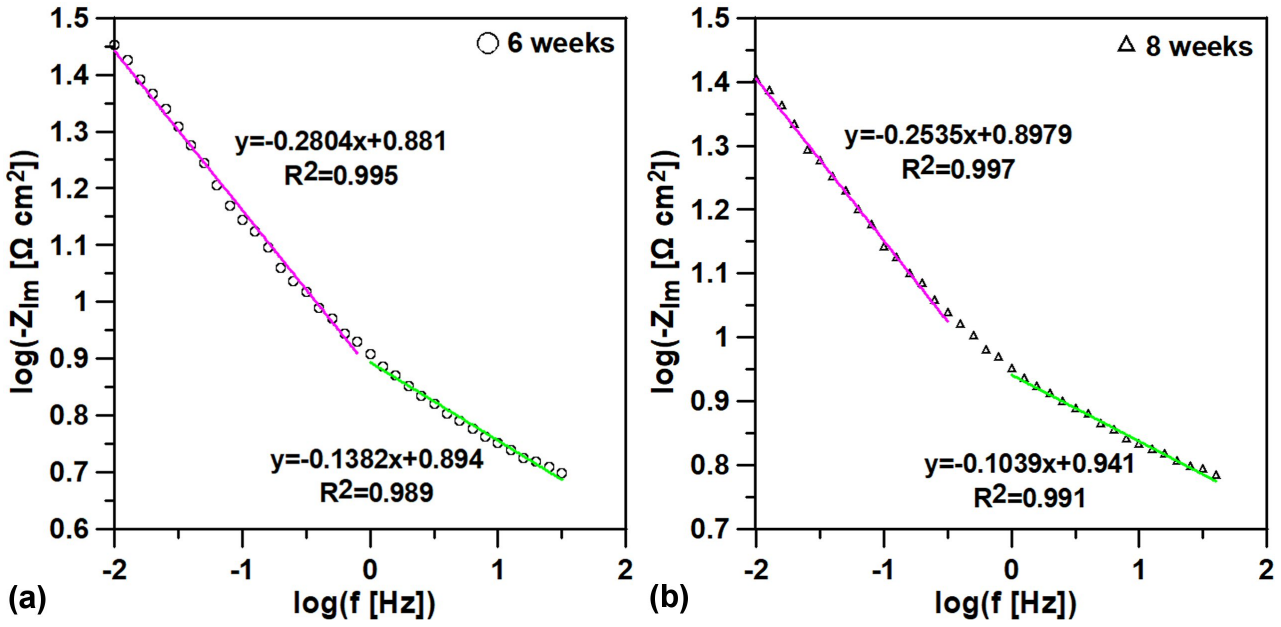

Figure 3.6: Plots of $\log(-Z_{\mathrm{Im}})$ vs $\log(f)$, as proposed by Cabanel *et al.* [86], for the EIS experimental data after a) 6 and b) 8 weeks of experiment in the salt spray chamber

3.3.4.3 Anomalous linear restricted diffusion

With regard to the present investigation, anomalous diffusion Ia with reflecting boundary (ADIa) [89] was applied, in order to fit the experimental data. This type was selected because it exhibits an angle smaller than -45° in the HF diffusion branch and a CPE behavior in the LF range. This type of impedance is characterized by a power law dependence of frequency, departing from the ordinary Warburg dependence of 1/2 and could describe cases where there is structural complexity of the substrate of diffusion [89]. In terms of transmission line representation, this case could be represented using a series of distributed resistance and CPE elements, considering an open circuit at the end of the transmission line (reflecting boundary) [89]. The formula for the diffusion impedance, applied in the present model, is the following,

$$Z_{\mathrm{D,AD}}(\omega) = R_{\mathrm{D}} \frac{\coth\left(\frac{j\omega}{\omega_{\mathrm{D,AD}}}\right)^{\gamma/2}}{\left(\frac{j\omega}{\omega_{\mathrm{D,AD}}}\right)^{\gamma/2}} \tag{3.23}$$

where $\omega_{\mathrm{D,AD}} = (D/L^2_{\mathrm{D,AD}})^{1/\gamma}$. The dffusion time constant now becomes:

$$\tau_{\mathrm{D,AD}} = (L^2_{\mathrm{D,AD}}/D)^{1/\gamma} \tag{3.24}$$

where D has units [cm^2 s$^{-\gamma}$] and γ is a power-law exponent, with $\gamma \leq 1$.

Hence, Eq.(3.23) finally becomes:

$$Z_{\mathrm{D,AD}}(\omega) = R_{\mathrm{D}} \frac{\coth\left[(j\omega)^{\gamma/2}\sqrt{L^2_{D,AD}/D}\right]}{(j\omega)^{\gamma/2}\sqrt{L^2_{D,AD}/D}} \tag{3.25}$$

In the HF and LF diffusion branch, respectively, the impedance becomes,

$$Z(\omega) = R_{\mathrm{D}}\Big(\frac{\omega_{\mathrm{D,AD}}}{j\omega}\Big)^{\gamma/2} \qquad \text{if } \omega > \omega_{\mathrm{D,AD}} \tag{3.26}$$

$$Z(\omega) = \frac{1}{3}R_{\mathrm{D}} + \frac{Q_{\mathrm{AD}}}{(j\omega)^{\gamma}} \qquad \text{if } \omega < \omega_{\mathrm{D,AD}} \tag{3.27}$$

where $Q_{\mathrm{AD}} = R_{\mathrm{D}}\omega^{\gamma}_{\mathrm{D,AD}}$.

The LF impedance is described by an equivalent circuit similar to the one proposed for modified restricted diffusion. Also, as can be seen from Eq. (3.27), the power-law exponent γ becomes double in the LF part. Similar behavior has been reported by Cabanel *et al.* [86] for modified restricted diffusion, where the ratio of the two-sloped curve presented in the $\log(-Z_{\mathrm{Im}})$ vs $\log(f)$ plot is near to two (Fig. 3.6).

The obtained fitting parameters assuming diffusion ADIa were similar to the modified restricted model, especially with regard to the 6 and 8-week data, which were efficiently described by the modified restricted type of diffusion. For this reason, the results are presented in the Appendix section A.2.2 and more specifically in Table A.4 and Fig. A.4, respectively.

Even though the results were similar between the two diffusion impedance mechanisms, some differences do exist. More specifically, taking into consideration Eq. (3.19) for modified restricted and Eqs. (3.23) and (3.24) for ADIa diffusion, the following equation is valid with regard to the value of the diffusion layer thickness, L_{D}, as calculated for the two models:

$$L^{\phi}_{\mathrm{D}_{\mathrm{mod-res}}} = L_{\mathrm{D,AD}}\mathrm{D}^{\frac{\phi-1}{2}} \tag{3.28}$$

For the two models it is that the diffusion related exponents are equal, ϕ=γ and that they both exhibit similar time constants. However, according to Eq. (3.28) and for an indicative diffusion coefficient equal to 1.9 10^{-5} cm^2/s, the diffusion layer thickness in the case of anomalous diffusion would be 0.12 mm after 6 weeks and 0.10 mm after 8 weeks of experiment, while the corresponding indicative values using the modified restricted model would be 0.38 and 0.72 mm, respectively. Hence, there is a difference in the estimated diffusion layer thickness between the two models. However, at this point, this difference could not be used as a criterion of choice between the two options, due to the range of uncertainties in the modified restricted model (reported in the previous paragraph) and the difficulty for estimating uncertainties for the present model.

3.3.4.4 Transmissive diffusion in its ideal form

In the present model, diffusion impedance was considered to be linear transmissive diffusion in its ideal form [81, 82]:

$$Z_{\mathrm{D,trans}}(\omega) = \frac{\sigma'}{(j\omega)^{1/2}} \tanh \sqrt{\frac{j\omega L_{\mathrm{D}}^2}{D}} = R_{\mathrm{D}} \frac{\tanh \sqrt{\frac{j\omega L_{\mathrm{D}}^2}{D}}}{\sqrt{\frac{j\omega L_{\mathrm{D}}^2}{D}}} = R_{\mathrm{D}} \frac{\tanh \sqrt{j\omega \tau_{\mathrm{D,FD}}}}{\sqrt{j\omega \tau_{\mathrm{D,FD}}}} \tag{3.29}$$

Definition of R_{D} is the same as in Eq. (3.12). At high frequencies, the impedance exhibits a Warburg behavior, similarly to restricted diffusion impedance (Eq. (3.14)). At low frequencies, where $\lim_{x\to 0} \frac{\tanh x}{x} = 1$, the diffusion impedance becomes,

$$Z_{\mathrm{D,trans}} = R_{\mathrm{D}} \tag{3.30}$$

At low frequencies, the impedance takes the form of a semicircle, intersecting the real axis at R_{D}. The semicircle can be represented by a parallel connection of the diffusion related resistance R_{D} with a limiting differential capacitance $C_{\mathrm{D}}/3$ [80]. The corresponding formula for R_{D}, except for Eq. (3.12), is $R_{\mathrm{D}} \approx L_{\mathrm{D}}^2/(DC_{\mathrm{D}})$, where C_{D} is given by Eq. (3.15) and (3.16). In the presence of a charge-transfer reaction coupled with the diffusion impedance, the system would be described by a Randles circuit (Eq. (A.1) with $Z_{\mathrm{D}} = Z_{\mathrm{D,trans}}$) and the overall impedance at $\omega \to 0$ would be [80, 82]:

$$Z_{\mathrm{tot}} = R_{\mathrm{e}} + R_{\mathrm{ct}} + R_{\mathrm{D}} \tag{3.31}$$

Hence, at low frequencies the total impedance equals the polarization resistance.

The fitting curves could not efficiently describe the experimental ones, when transmissive diffusion was used as diffusion impedance and for this reason the results are presented in the Appendix section A.2.3. This became apparent from the large goodness of fit values (Table A.7), which were the largest among the rest examined models for the 6 and 8-week curves. The large errors (above 100%) for the $\tau_{\mathrm{D,FD}}$ parameter for both intervals and for R_{D} after 8 weeks consolidate this argument (Table A.6). Moreover, for these curves, the sum of R_{D}+R_{ct} was much larger than their corresponding R_{LPR} values (Table 3.1).

The same observations apply for the 12-week curve, as well. The goodness of fit values were larger than the selected model for this curve, which will be presented in a following paragraph. Moreover, even though the uncertainty ranges of the parameters could not provide enough information to exclude this model (Table A.6), it becomes apparent from the very small value of the CPE-exponent n that the charge-transfer process was barely approached (Fig. A.5c), which was observed for the rest curves, as well. Moreover, the small diffusion related time constant $\tau_{\mathrm{D,FD}}$, indicated a diffusion layer thickness equal to 0.15 mm (assuming D=1.9 10^{-5} cm^2/s), one order of magnitude smaller than the actual corrosion layer thickness, as observed through stereoscopic observation, which was measured around 1.4 mm. From the above observations it becomes apparent that transmissive diffusion impedance could not describe any of the experimental curves.

3.3.4.5 Modified transmissive diffusion

For the present model, the equation applied is presented as follows [82],

$$Z_{\mathrm{D,mod-trans}}(\omega) = R_{\mathrm{D}} \frac{\tanh\left(\frac{j\omega L_{\mathrm{D}}^2}{D}\right)^{\phi/2}}{\left(\frac{j\omega L_{\mathrm{D}}^2}{D}\right)^{\phi/2}} = R_{\mathrm{D}} \frac{\tanh(j\omega\tau_{\mathrm{D,FD}})^{\phi/2}}{(j\omega\tau_{\mathrm{D,FD}})^{\phi/2}} \tag{3.32}$$

The parameter ϕ is the dispersion parameter, as defined in modified restricted diffusion impedance.

Table 3.5: PSO fitting results and derived parameters for the painted scribed specimen after 6, 8 and 12 weeks of experiment in the salt spray chamber, assuming modified transmissive diffusion, Randles connection and CPE for double-layer

Parameter	Unit	6 weeks	8 weeks	12 weeks
$\tau_{\mathrm{D,FD}}$	[s]	3.56 10^3	3.40 10^5	4.01 10^2
R_{D}	[Ω cm^2]	300.95	421.82	46.82
ϕ		0.601	0.350	0.400
R_{ct}	[Ω cm^2]	16.62	15.02	1.97
n		0.540	0.694	0.731
Q	[F s^{n-1} cm^{-2}]	1.30 10^{-3}	3.44 10^{-5}	2.74 10^{-4}
σ'	[Ω cm^2 s$^{-1/2}$]	5.04	0.72	2.34
$\tau_{\mathrm{ct,CPE}}$	[s]	8.24 10^{-4}	1.84 10^{-5}	3.39 10^{-5}

Table 3.6: CNLLS fitting results and derived parameters for the painted scribed specimen after 6, 8 and 12 weeks of experiment in the salt spray chamber, assuming modified transmissive diffusion, Randles connection and CPE for double-layer

Parameter	Unit	6 weeks	8 weeks	12 weeks
$\tau_{\mathrm{D,FD}}$	[s]	1.76 10^3±1112.8%	3.47 10^5±83982%	4.71 10^2±77.3%
R_{D}	[Ω cm^2]	253.00±355.9%	464.90±15469%	51.82±14.5%
ϕ		0.632±4.1%	0.368±3.7%	0.432±5.8%
R_{ct}	[Ω cm^2]	17.60±8.8%	15.62±8.2%	2.53±30.4%
n		0.566±5.1%	0.762±3.2%	0.747±9.2%
Q	[F s^{n-1} cm^{-2}]	1.18 10^{-3}±25.0%	1.77 10^{-5}±27.1%	2.73 10^{-4}±69.9%
σ'	[Ω cm^2 s$^{-1/2}$]	6.03	0.79	2.39
$\tau_{\mathrm{ct,CPE}}$	[s]	1.06 10^{-3}	2.14 10^{-5}	5.87 10^{-5}

Table 3.7: Chi-squared and sum of squares values, as indicators of goodness of fit for the modified transmissive diffusion impedance mechanism

Parameter	6 weeks	8 weeks	12 weeks
χ^2	5.58 10^{-5}	6.85 10^{-5}	3.01 10^{-5}
Sum of Squares	5.69 10^{-3}	8.64 10^{-3}	3.43 10^{-3}

With regard to the results presented in Tables 3.5 and 3.6, the fitting values refer to parameters $\tau_{\mathrm{D,FD}}$, R_{D}, R_{ct}, n, Q and ϕ, while the calculated parameters are σ' and $\tau_{\mathrm{ct,CPE}}$.

For this model, the uncertainty ranges for the $\tau_{D,FD}$ and R_D parameters after 6 and 8 weeks were quite above 100%, indicating that this model was not appropriate for these curves (Table 3.6). The goodness of fit values for these curves were larger than the modified resricted model and smaller than the restricted and transmissive models.

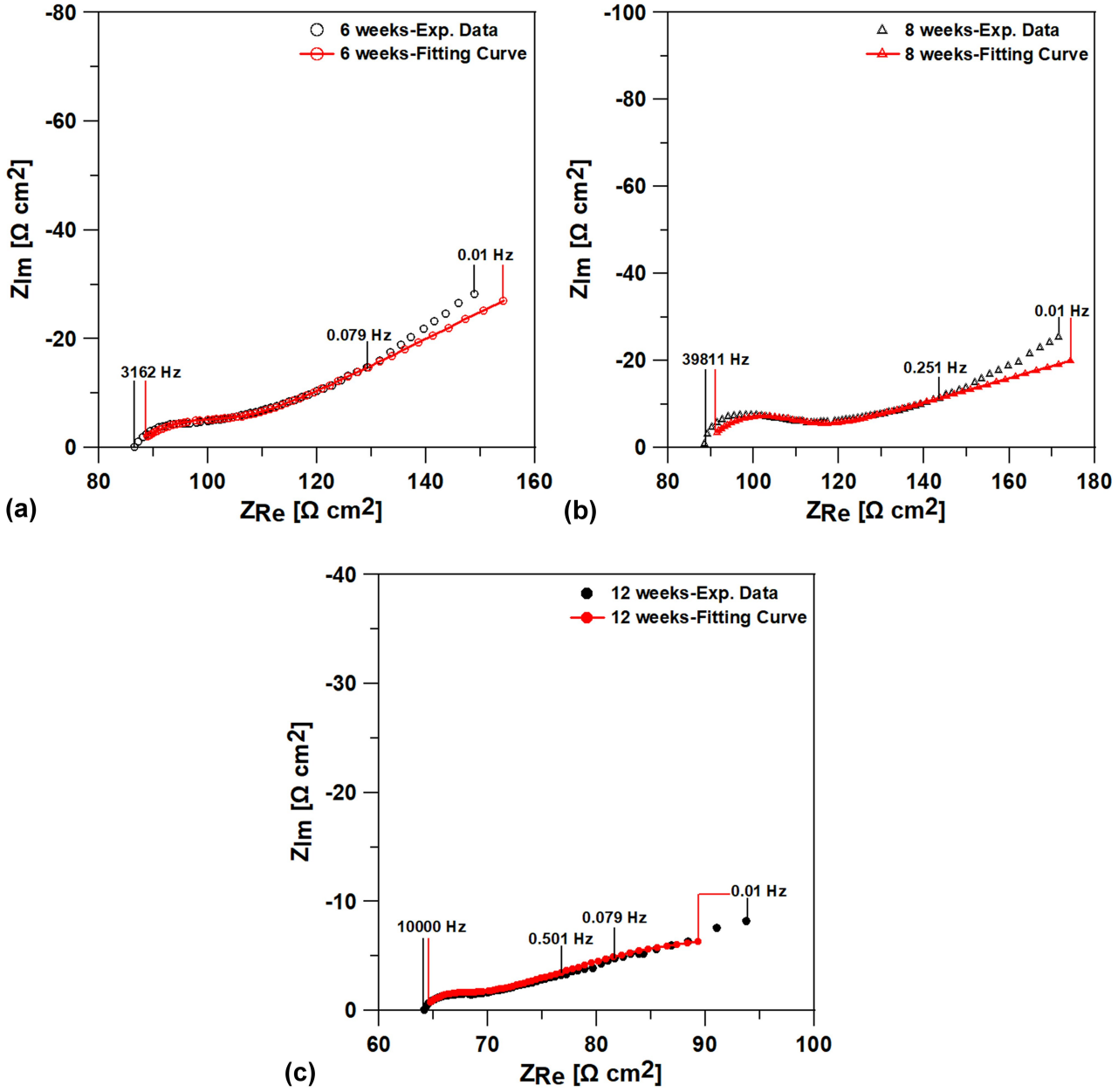

Figure 3.7: Fitting curves for the painted scribed specimen after a) 6, b) 8 and c) 12 weeks of experiment in the salt spray chamber, assuming modified transmissive diffusion, Randles connection and CPE for double-layer

With regard to the 12-week curve, the goodness of fit values were found the smallest of all the examined models. With regard to the calculated parameters, assuming an indicative diffusion coefficient equal to 1.9 10^{-5} cm^2/s, the diffusion layer thickness would be around 0.87 mm, close to the measured mean value of 1.4 mm. Moreover, the low frequency resistance value, as given in Eq. (3.31), would be equal to 112.93 Ω cm^2, very close to the value determined

through LPR, which was around 94 Ω cm^2 (Table 3.1). Finally, the kinetic branch (the HF semicircle) was also well described.

3.3.5 Modeling with generalized Warburg diffusion

The 12-week curve reminded of Warburg diffusion in the frequency range 100 Hz–0.01 Hz, however, its deviation from the Warburg angle of -45° would not allow the use of Eq. (3.4) for fitting. Ni and Lu [90] have proposed the use of Eq. (3.33) for similar graphs, treating this type of diffusion as a CPE,

$$Z_{\mathrm{D,CPE}}(\omega) = \frac{A_{\mathrm{D}}}{(j\omega)^{n_{\mathrm{D}}}} \tag{3.33}$$

In this equation, A_{D} has similar dimensions to Warburg coefficient σ, modified however to account for the deviation from the ideal Warburg behavior [Ω cm^2 s$^{-n_{\mathrm{D}}}$]. The term "generalized Warburg" is proposed in the work of Kendig *et al.* [91], even though Lasia [82] uses this term for the modified restricted and transmissive cases. In either case, in this paragraph a modification of the classic Warburg is assumed, where the CPE exponent n_{D} is allowed to take values between 0 and 1. Ni and Lu [90] correlated the value of the exponent with the direction of the oxidants. More specifically, for $n_{\mathrm{D}} = 0.5$, the diffusion direction is parallel to their concentration gradient and Warburg diffusion is obtained. For $n_{\mathrm{D}} < 0.5$, infinite tangential diffusion is obtained and a slope smaller than -45° appears in the Nyquist graph. Finally, for $0.5 < n_{\mathrm{D}} < 1$, the diffusion is hindered by obstacles (possibly oxide growth) and becomes finite-length, while the slope of the diffusion tail is again smaller than unity. A generalized Warburg impedance with the same formula as Eq. (3.33) has also been proposed by Kendig *et al.* [91]. However, these authors did not recognize three regimes for n_{D}, but only two; the Warburg ($n_{\mathrm{D}} = 0.5$) and the generalized-Warburg ($n_{\mathrm{D}} \neq 0.5$) behavior. According to the authors [91], the latter behavior could arise either from tangential or heterogeneous penetration of the electrolyte towards the metal/coat interface.

In the LF region, the diffusion impedance would exhibit a behavior similar to classic Warburg, meaning that its value would constantly increase [84]. Hence, the total impedance at LF ($\omega \to 0$), assuming Eq. (A.1) for the equivalent circuit would be:

$$Z_{\mathrm{tot}}(\omega) = R_{\mathrm{e}} + R_{\mathrm{ct}} + Z_{\mathrm{D,CPE}}(\omega) \tag{3.34}$$

The goodness of fit values presented in Table A.10 for the 6 and 8-week data were close to the values obtained for the modified transmissive model. The corresponding values for the 12-week data were close to the modified restricted model. The best goodness of fit values for the 6 and 8-week curves were obtained for the modified restricted model, while for the 12-week curve for the modified transmissive model. Hence, it seems that this model was not suitable for any of the experimental curves, in terms of goodness of fit values and this is why the results are presented in the Appendix section A.2.4.

The uncertainty estimates obtained for this model (Table A.9) could not be used as an indicator of the suitability of the model for the curves, since similar ranges were obtained for the corresponding parameters, except for the R_{ct} and Q values after 12 weeks, which exhibited a wider range than the corresponding uncertainties after 6 and 8 weeks.

With regard to the obtained parameters, the Q factor for the 6-week data was equal to 1.390 10^{-3} F s^{n-1} cm^{-2}, one order of magnitude higher than the corresponding value from the modified restricted model, indicating that the present model could not approach the HF part of the experimental curve as efficiently. Moreover, the R_{ct} value was around double the value from the modified restricted model. With regard to the 8-week data, the parameters related to the double-layer (n,Q) were found similar to the modified restricted model. The A_D value, representing the modulus of the CPE diffusion impedance, was found larger after 8 weeks, probably indicating that the accumulated corrosion products hindered oxygen diffusion more efficiently than after 6 weeks. However, the R_{ct} value remained more or less constant between the two intervals. This in turn would mean that the concentration of the oxidant at the electrode surface would not change during this period, which contradicts the greater impedance for dissolved oxygen diffusion (expressed through A_D), which would result in smaller concentration, since the flux would decrease. Hence, in terms of physical interpretation, this model would not be suitable for the 6 and 8-week curves.

Finally, with regard to the 12-week curve, the goodness of fit values would serve as a criterion for selection, since the parameter values obtained in this model, as well as their uncertainties, did not provide much information as per the suitability of the present model. More specifically, the R_{ct} value was around 1.35 Ω cm^2, smaller than the corresponding values after 6 and 8 weeks, as obtained from the modified restricted model. Moreover, the diffusion impedance magnitude at 0.01 Hz would be 25.08 Ω cm^2 much smaller than the corresponding R_D values after 6 and 8 weeks (the impedance magnitude and not A_D is used here for comparison with R_D, because they have similar units). The small values of the kinetic and diffusion related resistances after 12 weeks (compared to the corresponding parameters after 6 and 8 weeks), could imply corrosion acceleration, expressed as infinite tangential diffusion (n_D <0.5), suggesting that the corrosion layer could not serve as an obstacle any longer. However, the slightly better goodness of fit values for the modified transmissive case would make it the model of preference. In either case, corrosion acceleration was observed after 12 weeks.

3.3.6 Orazem-Tribollet connection for the selected diffusion impedance models

So far, the experimental data were modelled based on the Randles equivalent circuit. However, as observed from the fitting parameters, this circuit encompasses the individual anodic and cathodic charge-transfer resistances in a total corrosion resistance, termed as R_{ct}. Hence, in order to get an insight with regard to the individual values of these resistances, the circuit proposed by Orazem and Tribollet [76] for iron dissolution and ORR was used. This circuit consists of three parallel branches, the first being the CPE for double-layer, the second being

the charge transfer resistance for the anodic reaction ($R_{\mathrm{ct,Fe}}$) and the third being the faradaic cathodic impedance ($R_{\mathrm{ct,O_2}} + Z_{\mathrm{D}}$). The whole connection is in series with the electrolyte resistance R_{e}. This circuit is based on the anodic and cathodic impedances of the corrosion process being connected in parallel and is presented in Appendix A, Fig. A.2. For this circuit, the total impedance formula is given by Eq. A.2.

The circuit proposed by Orazem and Tribollet [76] was applied for the selected diffusion impedance models for the data after 6, 8 and 12 weeks of experiment, *i.e.* modified restricted diffusion after 6 and 8 weeks and modified transmissive diffusion after 12 weeks.

In the HF range, the diameter of the obtained semicircle would be equal to $R_{\mathrm{ct,Fe}}R_{\mathrm{ct,O_2}}/(R_{\mathrm{ct,Fe}}+R_{\mathrm{ct,O_2}})$, as proposed by Bonnel *et al.* [75]. Since this value corresponds to the total charge-transfer resistance of the system, the R_{ct} value obtained from the Randles circuit was used for each case.

In the LF range, diffusion impedance is given by Eq. (3.21), when modified restricted diffusion is the selected mechanism for mass transfer, while the total impedance of the system is given by Eq.(A.2). Hence, the total impedance of the system as $\omega \to 0$ becomes,

$$Z_{\mathrm{tot}}(\omega) = R_{\mathrm{e}} + \frac{R_1 R_2 + R_{\mathrm{ct,Fe}} K_2^2}{R_2^2 + K_2^2} - j\frac{R_{\mathrm{ct,Fe}} R_2 K_2 - R_1 K_2}{R_2^2 + K_2^2} \tag{3.35}$$

where,

$$R_1 = R_{\mathrm{ct,Fe}}[R_{\mathrm{ct,O_2}} + \frac{R_{\mathrm{D}}}{3} + K_1] \tag{3.36}$$

$$R_2 = R_{\mathrm{ct,Fe}} + R_{\mathrm{ct,O_2}} + \frac{R_{\mathrm{D}}}{3} + K_1 \tag{3.37}$$

$$K_1 = \frac{R_{\mathrm{D}}}{(\omega\tau_{\mathrm{D,FD}})^{\phi}}(\cos(\phi\pi/2) \tag{3.38}$$

$$K_2 = \frac{R_{\mathrm{D}}}{(\omega\tau_{\mathrm{D,FD}})^{\phi}}(\sin(\phi\pi/2) \tag{3.39}$$

When diffusion is of the modified transmissive type, in the LF range it is given by Eq. (3.30). Hence, the total impedance of the system as $\omega \to 0$, according to Eq. (A.2), becomes:

$$Z_{\mathrm{tot}} = R_{\mathrm{e}} + \frac{R_{\mathrm{ct,Fe}}(R_{\mathrm{ct,O_2}} + R_{\mathrm{D}})}{R_{\mathrm{ct,Fe}} + R_{\mathrm{ct,O_2}} + R_{\mathrm{D}}} \tag{3.40}$$

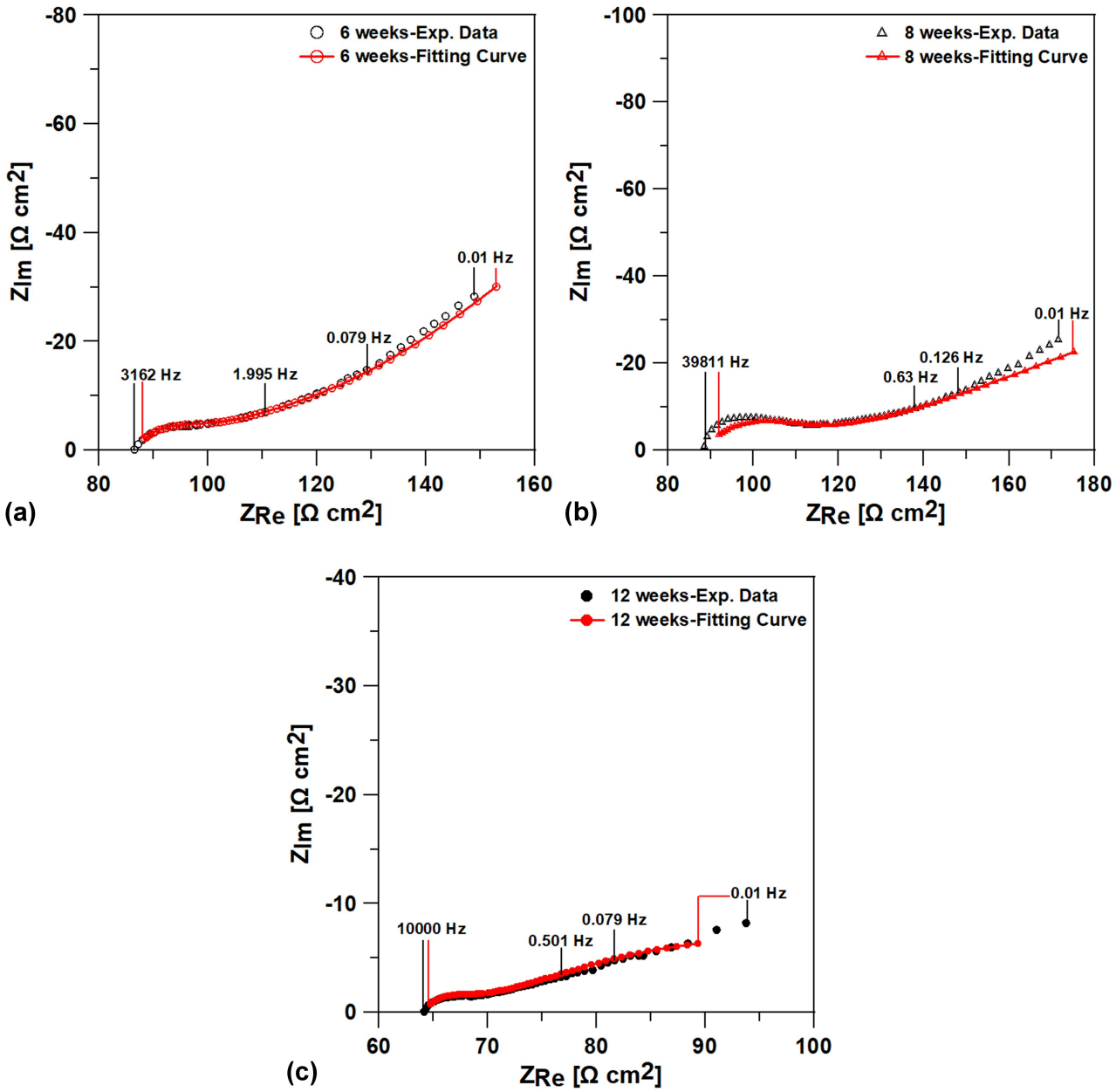

Figure 3.8: Fitting curves for the painted scribed specimen after 6, 8 and 12 weeks of experiment in the salt spray chamber, assuming Orazem-Tribollet connection for the selected diffusion impedance models; a) 6w-modified restricted, b) 8w-modified restricted and c)12w-modified transmissive

Table 3.8: PSO fitting results and derived parameters for the painted scribed specimen after 6, 8 and 12 weeks of experiment in the salt spray chamber, assuming Orazem-Tribollet connection for the selected diffusion impedance models

Parameter	Unit	6 weeks	8 weeks	12 weeks
		Mod. Res.	Mod. Res.	Mod. Trans.
$\tau_{D,FD}$	[s]	78.74	80.29	472.20
R_D	[Ω cm^2]	88.54	98.26	51.58
ϕ		0.451	0.281	0.409
$R_{ct,Fe}$	[Ω cm^2]	3.49 10^7	872.09	499.80
R_{ct,O_2}	[Ω cm^2]	7.42	9.20	1.97
n		0.697	0.663	0.740
Q	[F s^{n-1} cm^{-2}]	2.90 10^{-4}	4.18 10^{-5}	2.50 10^{-4}
σ'	[Ω cm^2 s$^{-1/2}$]	9.98	10.97	2.37
$\tau_{ct,CPE}$	[s]	1.49 10^{-4}	6.95 10^{-6}	3.38 10^{-5}

Table 3.9: CNLLS fitting results and derived parameters for the painted scribed specimen after 6, 8 and 12 weeks of experiment in the salt spray chamber, assuming Orazem-Tribollet connection for the selected diffusion impedance models

Parameter	Unit	6 weeks	8 weeks	12 weeks
		Mod. Res.	Mod. Res.	Mod. Trans.
$\tau_{D,FD}$	[s]	101.00±22.7%	268.30±88.1%	371.00±85.4%
R_D	[Ω cm^2]	95.32±8.8%	112.10±20.1%	64.77±92.0%
ϕ		0.488±7.7%	0.286±15.7%	0.127±37.1%
$R_{ct,Fe}$	[Ω cm^2]	3.95 10^{18}±2531.5%	1.09 10^9±1.57 10^7%	153.50±257.5%
R_{ct,O_2}	[Ω cm^2]	9.29±21.6%	8.32 ±49.5%	3.823±67.4%
n		0.714±5.7%	0.836±3.4%	0.683±13.5%
Q	[F s^{n-1} cm^{-2}]	2.92 10^{-4}±38.2%	7.34 10^{-6}±34.2%	5.23 10^{-4}±98.7%
σ'	[Ω cm^2 s$^{-1/2}$]	9.48	6.84	3.36
$\tau_{ct,CPE}$	[s]	1.85 10^{-4}	1.01 10^{-5}	4.22 10^{-5}

Table 3.10: Chi-squared and sum of squares values, as indicators of goodness of fit for the Orazem-Tribollet equivalent circuit for the selected diffusion impedance mechanisms

Parameter	6 weeks	8 weeks	12 weeks
χ^2	3.16 10^{-5}	4.02 10^{-5}	3.02 10^{-5}
Sum of Squares	3.19 10^{-3}	5.02 10^{-3}	3.41 10^{-3}

As can be seen from Figs. 3.5a and 3.8a, as well as from Tables 3.2 and 3.8, the fitting results for the 6-week data were similar, when using Randles or the Orazem-Tribollet equivalent circuit. Moreover, the results obtained from the PSO procedure were within the uncertainty range of the parameters of the CNLLS procedure (Table 3.10). However, application of the latter connection caused the R_{ct,O_2} value to tend to zero, leading $R_{ct,Fe}$ to a very large value with an error much larger than 100%. It was the presence of the constraint $R_{ct,Fe}R_{ct,O_2}/(R_{ct,Fe} + R_{ct,O_2}) = R_{ct}$, that hindered R_{ct,O_2} from approaching zero, thus, becoming identical to R_{ct}. As a result, the Orazem-Tribollet [76] connection could not efficiently describe the experimental data after 6

weeks of experiment, hence, the individual values of $R_{ct,Fe}$ and R_{ct,O_2} could not be considered as trustworthy.

With regard to the 8-week data, the fitting values of $\tau_{D,FD}$ and n differed between the two connections (Tables 3.2 and 3.8). However, as can be seen from the CNLLS results in Table 3.10, the obtained values were closer to the PSO results of Table 3.2, with some variations concerning the charge-transfer related parameters n and Q. Similarly to the observations reported for the 6-week data, the $R_{ct,Fe}$ tended to an infinite value with a correspondingly increasing error. Hence, once more, this connection would not be a trustworthy representation of the physical processes related to modified restricted diffusion impedance.

As regards the 12-week data, even though the proposed impedance mechanism could favor the use of this circuit, the results presented in Table 3.10 indicated that the anodic charge transfer resistance was not a statistically significant parameter. Moreover, for this curve, the uncertainties of all parameters were larger compared to the previously examined curves.

Finally, the goodness of fit values for this equivalent circuit (Table 3.10) were similar to the ones obtained from the Randles connection for the 6 and 12-week data, denoting the importance of examining also the uncertainty ranges of the obtained parameters for selection of the appropriate diffusion impedance mechanism and/or equivalent circuit.

3.3.7 Comparative overview of the results

The values of the objective function (OF) from the PSO procedure for each model and for each experimental curve are presented in Table 3.11. It should be noted that the value of the OF could provide information only for the quality of the fitting curve and not for the suitability of the model, similarly to the goodness of fit values (chi-squared and sum of squares) from the CNLLS procedure. However, the models with the smallest OF were the ones eventually selected. For example, the values of the OF for the 6 and 8-week data were the smallest for the modified restricted and anomalous diffusion models, which gave similar results, in terms of fitted parameters. Similarly, with regard to the values of the 12-week data, the value of the OF was the smallest for the modified transmissive model, which was eventually the most suitable.

Table 3.11: Objective function values from the PSO procedure for all examined models for the experimental data after 6, 8 and 12 weeks of experiment in the salt spray chamber, assuming Randles connection

Fitting Model	6 weeks	8 weeks	12 weeks
Restricted	52.625	129.840	37.030
Mod. Restricted	30.878	51.555	21.378
Anomalous	30.836	51.555	21.379
Gen. Warburg	46.004	71.522	21.378
Transmissive	59.593	135.895	33.527
Mod. Transmissive	45.989	71.524	20.346

With regard to the diffusion impedance mechanism that was appropriate for the 6 and 8-week curves, modified restricted diffusion impedance gave similar results to anomalous (ADIa)

diffusion [89], however, there was a difference in the calculated diffusion layer thickness (Eq 3.28). The feasibility for error analysis of the results from the modified restricted case made it the mechanism of choice for these intervals. After 12 weeks, modified transmissive diffusion was the selected mechanism. The Bode plots for the selected models are presented in the Appendix section A.2.5.

The selected diffusion impedance mechanisms for this specimen were validated, especially for the 6 and 8 weeks of experiment, from the repeatability measurements. The results from these measurements are presented in Appendix B. With regard to the results from the 12-week curves, modified transmissive or modified restricted diffusion could be possible after 12 weeks of exposure in the salt spray chamber. Moreover, it was concluded that Randles connection could best describe the experimental curves of all intervals. Even though the parallel branches suggested by Orazem and Tribollet [76] for separation of the anodic and cathodic reactions in a corrosion process seem more appropriate, it was observed that this circuit was not suitable for the experimental data presented here and in Appendix B.

For the specimen examined in the present study, in particular, it was observed that after 8 weeks no statistically significant differences were observed between similar parameters, hence, it was assumed that the porous corrosion layer covering the electrode did not exhibit structural changes that could affect the diffusion and charge-transfer processes. After 12 weeks, though, there was a decrease in both R_{D} and R_{ct} values, which could be considered as statistically significant, compared to the uncertainty ranges of these parameters for the rest intervals. This decrease, which was also depicted in the LPR measurement, could imply corrosion acceleration after 12 weeks. This result could be verified by the respective values of σ', which had the (indicative) value 9.99, 6.71 and 2.34 Ω cm^2 s$^{-1/2}$, after 6, 8 and 12 weeks, respectively. Apparently, the increase of $\mathrm{L_D}$ after 12 weeks (0.87 mm estimation from the model and 1.4 mm actual mean measurement) compared to the estimated values after 6 and 8 weeks (0.38 mm and 0.72 mm as estimated from the respective model), along with the decrease in R_{D} could lead to this result (Eq. (3.13)). Also, from Eq. (3.10), it becomes apparent that the decrease of σ' is related to an increase in the oxidant concentration inside the pores of the corrosion layer, which could be correlated with the smaller diffusion impedance observed after 12 weeks. Even though σ' depends on various parameters, a conclusion that could be drawn is that an obvious decrease in mass transfer coefficient could possibly imply easier diffusion and, hence, corrosion. This finding was verified for the rest repeatability measurements presented in the Appendix B.

With regard to the morphology of the corrosion layer, the corrosion products observed through XRD and Raman investigation of rust samples of the scribed specimen under study, after 12 weeks of experiment, were magnetite (Fe_3O_4), maghemite (γ-Fe_2O_3), hematite (α-Fe_2O_3), feroxyhyte (δ-FeOOH), goethite (α-FeOOH) and lepidocrocite (γ-FeOOH) (presented in detail in [66]), revealing presence of red and black rust, as in the problem of cast iron in drinking water [76, 78, 79]. The physical model presented in the cast iron problem could be correlated (even partially) with the observed rust morphology of the scribed specimen under

study. Hence, the EIS response for the present experimental data could refer to the metal-magnetite structure, which could possibly serve as the available area for reduction reaction. On top of this layer there would be the red rust layer (which does not affect the kinetics), possibly along with maghemite and feroxyhyte, while the outer rust layer would consist of lepidocrocite [65]. From another perspective, the corrosion products layer could be treated as being two layers: the magnetite conducting layer covering the electrode and the layer including all the other corrosion products (oxides and oxyhydroxides) through which diffusion occurs [69]. A simple physical model presenting the structure of the corrosion layer and the diffusion of dissolved oxygen is presented in Fig. 3.9. The model is based on the one proposed by Jüttner *et al.* [**?**, 72].

The basic difference between the theory adopted in the present investigation and the theory of porous electrode lies primarily on the fact that the porous electrode theory assumes magnetite to be a macroporous layer filled with red rust, while in the present study, magnetite and red rust are treated as consecutive layers with porous structure. Another major difference is that the pore walls of a porous electrode are electroactive, while for a porous oxide layer are inert [76]. Indicative PSO fitting results for the 6-week curve, making use of the equivalent circuit proposed in the cast iron in drinking water problem, are presented in Appendix section A.2.6. It was found that this model was not suitable for either of the experimental data, presented herein or in the Appendix B.

Another finding of the present study was that most of the parameters obtained from the PSO algorithm were in most cases within the uncertainty range of the parameters obtained using the CNLLS procedure, especially for the impedance models that actually fitted the experimental data. This enhances the use of an alternative algorithm for regression of impedance spectra, which is much less dependent on initial guesses and does not require weighting factors. Verification of this observation depends on the quality of the impedance signals, as well. These two methods could also be used supplementally. The PSO algorithm provides indicative and representative values of the parameters, the uncertainty ranges of which could be estimated using the CNLLS procedure. The goodness of fit values obtained from the two methods were in agreement, hence, either could be used.

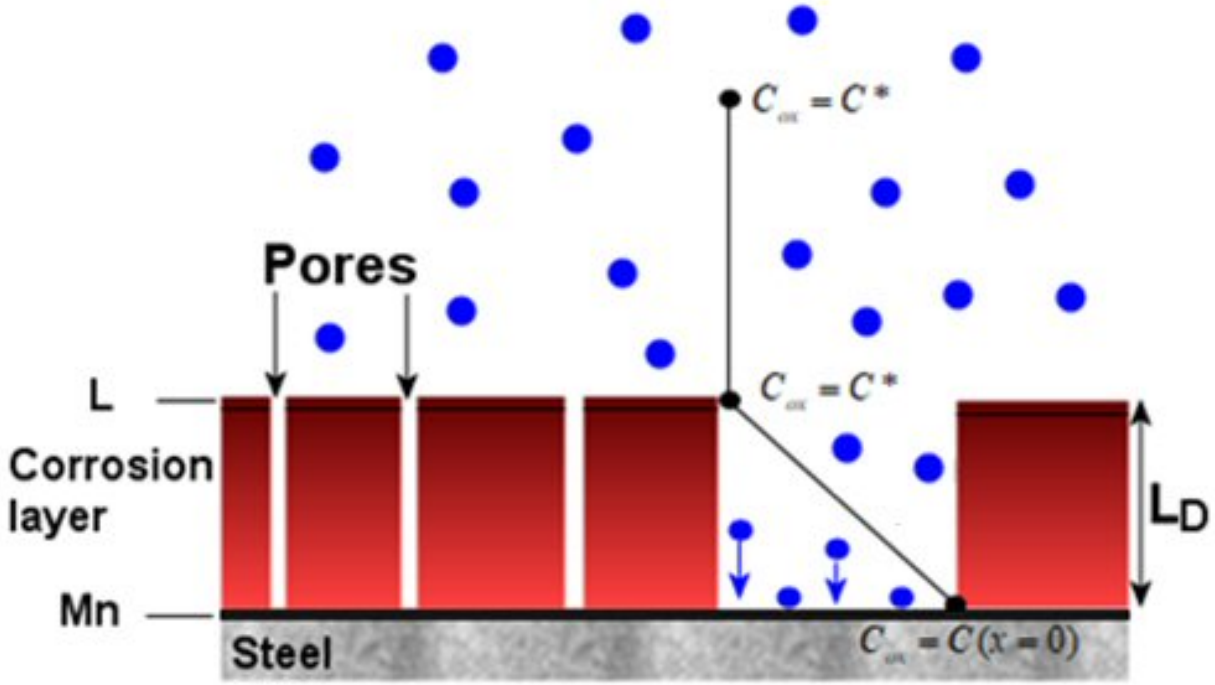

Figure 3.9: A general physical model presenting the corrosion layer structure and oxygen diffusion through its pores. L: lepidocrocite; Mn: magnetite, all the rest phases lie in between.

3.4 Conclusions

In the present study, coated steel in scribed condition was examined in a salt spray chamber using cyclic corrosion conditions, for a total of 12 weeks. Periodic examination was performed after 6, 8 and 12 weeks of experiment and included EIS and LPR measurements. The aim was to correlate the impedance graphs with actual physical processes that affect the development of corrosion over time. Considering diffusion as the mass transport of dissolved oxygen, this study intended to clarify the type of diffusion impedance that best described this procedure at each examination interval, considering it as the rate-determining step.

- Finite-length diffusion impedance described mass transport of dissolved oxygen after 6, 8 and 12 weeks of experiment, implying that the concentration gradient would be developed inside the pores of the corrosion products layer, covering the electrode.
- The selected model for each curve exhibited minimum gooness of fit values for both PSO and CNLLS procedures, a diffusion layer thickness compatible to the corrosion products layer, as observed by stereoscopic observations and kinetic parameters that could be ascribed to a charge transfer/ double layer time constant.
- Modified restricted diffusion described mass transport of oxygen after 6 and 8 weeks of experiment, while, after 12 weeks diffusion impedance could be either modified restricted

or modified transmissive. A decrease in corrosion resistance after 12 weeks was observed for all the examined specimens.

- The porous electrode theory, as adopted in cast iron in drinking water model, could not efficiently describe the experimental data.

Chapter 4

Experimental investigation of roughness effect on ship resistance using flat plate and model towing tests

Abstract

In the present Chapter, the hydrodynamic resistance of a flat plate is presented, which was studied in two conditions, namely smooth and with homogenous roughness, which was provided by sandpapers of 40 and 80-grit sizes. The aim of the present study was to examine the effect of roughness in laboratory scale and in ship scale, using appropriate extrapolation methods. Resistance data from model towing tests in both conditions were also processed and extrapolation to ship scale was performed, based on common and newly proposed extrapolation methods.

Towing tests on a thin flat plate of 3 mm thickness and extrapolation to ship scale was attempted. A newly designed experimental setup was constructed for the examination of the thin plate. The experiments on smooth flat plate included examination of a series of trip wires for flow stimulation, among which the optimum was 1.3 mm. In rough condition, the plate was covered with sandpapers of 40 and 80-grit. Both calculated roughness functions exhibited Nikuradse behavior, verifying the validity of the experiments. The equivalent sand roughness height was 1.7 times the average sandpaper roughness, as calculated by the Schlichting diagram for sand roughened plates. Both roughness functions indicated transitionally rough regime, except for the last two data of the rougher sandpaper that lay on the fully rough regime. The results were extrapolated to ship scale using Granville method.

Also, resistance results from ship model towing tests from another study in smooth and rough condition [92] were analysed. Extrapolation of smooth model results in ship scale revealed that the traditional Froude method predicts higher resistance coefficient compared to the ITTC 78 method. Rough model results were extrapolated to ship scale by applying a newly proposed extrapolation method, using Schlichting resistance formula for rough plates as the friction correlation line, according to Froude method and for two length scales, namely the plate and ship length. The two versions of the proposed extrapolation method provided an upper and lower limit for the predicted rough hull total resistance coefficient.

4.1 Introduction

Marine structures, such as ships or platforms, are vulnerable to corrosion [93] and biofouling [6], which cause their surface to be rough. Corrosion could be stimulated by the aggressiveness of the sea environment itself or it could result from extensive biofouling on the submerged part of the metallic surface. When it comes to ships, the ship bottom area is threatened by both factors with adverse structural, environmental, hydrodynamic and economic effects. It is noteworthy that even small scale fouling (slime) can cause increase in skin friction [38], while intense fouling could cause a 40% increase in fuel consumption and a 77% increase in total voyage cost [39,40]. It is, thus, of paramount importance to estimate the additional drag induced by the surface roughness in large scale marine applications.

The most widespread method to assess the total resistance coefficient of rough large scale surfaces is to perform laboratory towing tests on rough flat plates and calculate the roughness function (ΔU^+) [94]. The roughness function expresses a downward shift in the log-law region of the mean velocity profile [95], arising from increased momentum deficit, due to roughness [96,97]. The roughness function is a function of the roughness nature and roughness Reynolds number k^+ [96]. For the case of uniform sand roughened surfaces, if $k^+<5$, the flow is considered to be hydraulically smooth, if $5<k^+<70$, the flow is transitionally rough, while if $k^+>70$, the flow is completely rough. For each of these regimes, the additional drag induced by the roughness is null, considerable and predominant, respectively [95,98–100]. Finally, in the fully rough regime the friction coefficient is independent of Reynolds number [97].

The roughness function and roughness Reynolds number can be calculated through iteration via the indirect methodology proposed by Granville [101], which is based on total drag measurements of rough flat plates and has been extensively analyzed in various studies [102,103]. A very important parameter in this methodology is the roughness scaling length. In general, surfaces are said to exhibit k-type behavior when the roughness function scales on roughness height (k), which could be for instance the maximum peak to trough height (R_t) or the average roughness height (R_a), while for surfaces with sharp rough elements of shallow angle, the slope is the main scaling length [96].

For uniformly rough surfaces the equivalent sand roughness height (k_s) is the roughness value that collapses the experimental roughness function data onto the Nikuradse universal roughness function in the fully rough regime [95,100] and it is usually a multiple of the roughness height, k. In Nikuradse [98] experiments the k_s value coincided with the diameter of the grains. For sandpapers, this value has been proposed to be equal to $0.75R_t$ [104].

Arbitrarily rough surfaces, such as surfaces painted with epoxy or antifouling coatings, exhibit Colebrook-type roughness functions, which can be usually described as follows [96,103, 105–107]:

$$\Delta U^+ = \frac{1}{\kappa}\ln(1+k^+) \tag{4.1}$$

where κ is the Von Karman constant.

A suitable roughness height for the collapse has been proposed to be $0.39\mathrm{R}_a$ for epoxy painted surfaces [104, 108] and $0.17\mathrm{R}_a$ for antifouling coatings [107]. Determination of the appropriate roughness height for collapse of either sandpapers or surfaces with engineering roughness on the respective universal roughness function is important, for the complete and accurate characterization of a rough surface. Changes in the value of the selected roughness height (k), in order to attain the collapse, will not affect the value of the roughness function, only the value of the roughness Reynolds number [103].

The value of the calculated roughness function can be applied in the similarity law proposed by Granville [94], in order to predict the added frictional resistance component in ship scale ($\Delta\mathrm{C}_{Fs}$), which is then added to the smooth hull total resistance coefficient, as calculated by applying the Froude method [109]. The traditional Froude method along with the Hughes method are considered as the two main extrapolation methods from smooth model towing tests. The latter method has also been suggested by Internatinal Towing Tannk Conference (ITTC) [110] and is currently known as ITTC 78 [111–113]

The Froude method is based on the following hypothesis:

$$\mathrm{C_T}(\mathrm{Re}, \mathrm{Fn}) = \mathrm{C_F}(\mathrm{Re}) + \mathrm{C_R}(\mathrm{Fn}) \tag{4.2}$$

where C_T refers to the total resistance coefficient, C_F refers to the friction resistance coefficient of a flat plate with the same length as the model or the ship, depending on the scale of interest, and $\mathrm{C}C_R$ is the residual resistance coefficient. The Froude hypothesis assumes that the residual resistance is only a function of Froude number (Fn) and not a function of both Reynolds (Re) and Froude number. In other words, the difference between C_T and C_F is more or less constant and independent of Reynolds number for geometrically similar ship models at the same Froude number. Hence, C_R is kept constant between the model and the ship during the extrapolation process.

With regard to the friction coefficient (C_F), the Schoenherr friction line was adopted by the American Towing Tank Conference (ATTC) in 1947 and is defined as:

$$\frac{0.242}{\sqrt{\mathrm{C_F}}} = \log_{10}(\mathrm{ReC_F}) \tag{4.3}$$

The disadvantage of this line is that iterations are required in order to calculate the value of C_F for a given Reynolds number. In order to avoid this, the ITTC 57 friction correlation line was introduced, which is defined as follows:

$$\mathrm{C_F}(\mathrm{Re}) = \frac{0.075}{(\log_{10}\mathrm{Re} - 2)^2} \tag{4.4}$$

The two lines coincide at ship scale Reynolds numbers. However, in model scale the ITTC 57 line calculates a bit higher resistance, in order to avoid ship power overestimation [110].

The ITTC 78 method is based on Hughes's proposed extrapolation method which takes into consideration the form factor, k [111, 114]. More specifically, the Hughes hypothesis is, as follows:

$$C_T(Re, Fn) = C_F(Re) + C_R(Re, Fn) \tag{4.5}$$

Where,

$$C_R(Re, Fn) = C_{FORM}(Re, Fn) + C_W(Fn) \tag{4.6}$$

and also that,

$$C_{FORM}(Re, Fn) = kC_F(Re) \tag{4.7}$$

Hence,

$$C_R(Re, Fn) = kC_F(Re) + C_W(Fn) \tag{4.8}$$

Finally,

$$\begin{aligned} C_T(Re, Fn) = C_F(Re) + kC_F(Re) + C_W(Fn) \Rightarrow \\ C_T(Re, Fn) = (1 + k)C_F(Re) + C_W(Fn) \Rightarrow \\ C_T(Re, Fn) = C_V(Re) + C_W(Fn) \end{aligned} \tag{4.9}$$

In Hughes's approach the residuary resistance is considered as a function of both the Reynolds and Froude number and is divided into the form resistance (C_{FORM}) and the wavemaking resistance (C_W). Furthermore, according to Hughes's hypothesis, the form resistance, which is related to the different distribution of tangential stresses and vertical pressures compared to the flat plate, due to the shape of the hull and accounts also for the fact that the wave resistance is also dependent on Reynolds number, is presented solely as a function of Reynolds number. Hence, the total resistance is a sum of the viscous resistance (C_V), which incorporates both friction and viscous pressure resistance components [110] and the wavemaking resistance. The latter is kept constant between the model and the ship during extrapolation.

The calculation of the form factor, k, can be performed using Prohaska's method in the Froude range 0.12 to 0.20 (or 0.22) [114, 115]. If the wave resistance coefficient is defined as [115]:

$$C_W = a \cdot Fn^n, 4 \leqslant n \leqslant 6 \tag{4.10}$$

Then,

$$\frac{C_T}{C_F} = (1 + k) + a \cdot \frac{Fn^n}{C_F} \tag{4.11}$$

For small values of Froude number the curve C_T/C_F versus Fn^n/C_F is linear and the intersection of the curve with the C_T/C_F axis (at Fn=0) equals to 1+k, hence the form factor can be determined [115]. The value of the exponent n depends on the hull form, with fuller hulls being better described with n>4 [115].

Extrapolation to ship scale usually requires the addition of a correlation allowance (C_A), which traditionally in the Froude method has the value of 0.0004 [110]. This allowance accounts for differences between the model and the ship in terms of roughness and flow characteristics close to the bow. In ITTC 78 method this allowance was first given by the Bowden-Davidson formula, defined as follows:

$$\Delta C_{F,B-D} = \left(105\left(\frac{k_s}{L}\right)^{1/3} - 0.64\right) \times 10^{-3} \tag{4.12}$$

If roughness measurements were lacking, the value of ks=150 μm could be used as ship roughness. In later versions of the ITTC 78 method, the roughness allowance was separated from the correlation allowance [112, 113]. The roughness allowance has been suggested to be calculated by the Townsin formula, which incorporates also a correction for Reynolds number [110]:

$$\Delta C_{F,T} = 0.044\left[105\left(\frac{k_s}{L}\right)^{1/3} - 10 \times Re^{-1/3}\right] + 0.000125 \tag{4.13}$$

While, the correlation factor (C_A) is given by the following equation:

$$C_A = (5.68 - 0.6\log_{10}Re) \times 10^{-3} \tag{4.14}$$

The sum $\Delta C_{F,T}$+C_A should equal the value of the formerly applied Bowden-Davidson correlation allowance including roughness effects ($\Delta C_{F,B-D}$) [112, 113].

One of the major subjects that necessitate the use of correlation allowance is the difference in the laminar part of the flow close to the bow between the model and the ship. The extrapolation process is widely affected by the similarity of the flow regimes between model and ship scale. Extrapolation of frictional resistance implies turbulent flow at both scales, which is usually not the case for the model [116]. The smaller the model is, the bigger the problem of laminar flow becomes. In order to eliminate the extent of laminar flow on the model and ensure similar flow characteristics at the two scales, the use of turbulence stimulators is usually recommended [117]. Some common examples of turbulent stimulators are the trip wires [118] and sand grains in the form of sandpapers [96, 103]. Less common are small pins and Hama strips [116].The stimulators are usually placed 5% aft the model's or plate's fore perpendicular or leading edge, respectively [118]. The selection of the suitable type and size of a stimulating device is not an easy task and may require multiple experiment repetitions with various types and/or sizes until sufficient flow stimulation is attained. As proposed by Joubert and Matheson [117], a suitable stimulator generates higher resistance values at low speeds and lower resistance values at high speeds.

In the present study, flat plate towing tests in smooth and rough condition were performed and extrapolation to ship scale was attempted. The novelty of the experiments lies on the very thin plate used for the experiments, which had a thickness of 3 mm. For this reason, a whole new experimental setup was designed and constructed for the performance of these experiments. The experiments on the flat plate in smooth condition included examination of

the resistance induced by the tension wires providing structural support and alignment and investigation of a series of trip wires, in order to find the optimum that provided sufficient flow stimulation. In rough condition, the plate was covered with sandpapers of 40 and 80-grit and the roughness functions were found to be in agreement with Nikuradse behavior, verifying that the newly developed experimental setup provided trustworthy results. The results were then extrapolated to ship scale using Granville's similarity method.

Also, data from ship model towing tank tests in smooth and rough condition [92] were extrapolated to ship scale. The ship model towing experiments were performed in heavy ballast and full load departure condition for smooth and rough hull [92]. The smooth hull total resistance coefficient results were extrapolated to ship scale using both Froude and ITTC 78 method. The novelty was that a detailed presentation of both methods was attempted for a wide speed range and in both loading conditions, in order to better illustrate their differences in practice. The results from the rough condition were extrapolated to ship scale by applying a newly proposed extrapolation method, using Schlichting formula for sand roughened plate as a friction correlation line. The procedure was performed in two versions. In the first version the length scale used for the extrapolation was the length of the plate, while in the second version the plate length was used in model scale and the ship length was used in ship scale. Finally, a comparison among the selected extrapolation methods from both rough plate and rough model towing tests was performed and their differences on the calculated rough hull total resistance coefficient were estimated.

4.2 Experimental methods and materials

The tests were carried out in the Towing Tank of Laboratory of Ship and Marine Hydrodynamics (LSMH) of the National Technical University of Athens, which has a length of 91 m, a width of 4.55 m and a water depth of 3 m. The towing tank is equipped with a running carriage that can achieve a maximum speed of 5.5 m/s or 10.7 knots.

Before initiation of each experiment, the tank water level was checked, in order to ensure consistent measuring conditions. Moreover, during the experiments the tank water temperature was measured and proper corrections were made for density and viscosity.

4.2.1 Flat plate experimental setup

A flat plate made of aluminium for marine applications with dimensions 2 m $\times$ 1 m $\times$ 3 mm was used for the resistance tests. The plate length is a crucial parameter for the flat plate tests, in order to ensure high Reynolds numbers and turbulent flow at most of the plate's length. The length of the plate is limited by the dimensions of the towing tank. Another limitation is introduced by the maximum weight that the resistance dynamometer can handle. The maximum load of 50 kg for the Kempf and Remmers R35 dynamometer that was used for the present tests did not allow the use of a steel plate. For this reason, a plate made of aluminium was used, even though its higher elasticity caused some deflection during the

experimemnts. To this purpose, the plate was reinforced longitudinally with two aluminium square hollow sections of dimensions 2.1 m × 5 cm × 5 cm, placed at the top of each side and vertically using three tension wires with diameter 0.8 mm. Each tension wire was stretched at both sides of the plate passing through a through hole, while a controllable tensor system allowed adjustment of the wire tension, if needed.

For the purpose of plate alignment a rotary table with precision higher than 0.1° was fitted on top of a stiffener at the fore side of the plate, allowing micrometric position control. The whole system was attached to the resistance dynamometer on the towing carriage and the plate was submerged at 79.45 cm (fore - 79.8 cm, aft - 79.1 cm). The plate was towed multiple times at constant speed, until a position was found where the dynamometer strain gages received minimum deformation. The rotary table was locked in this position and the alignment was completed. A schematic of the experimental setup is presented in Fig. 4.1.

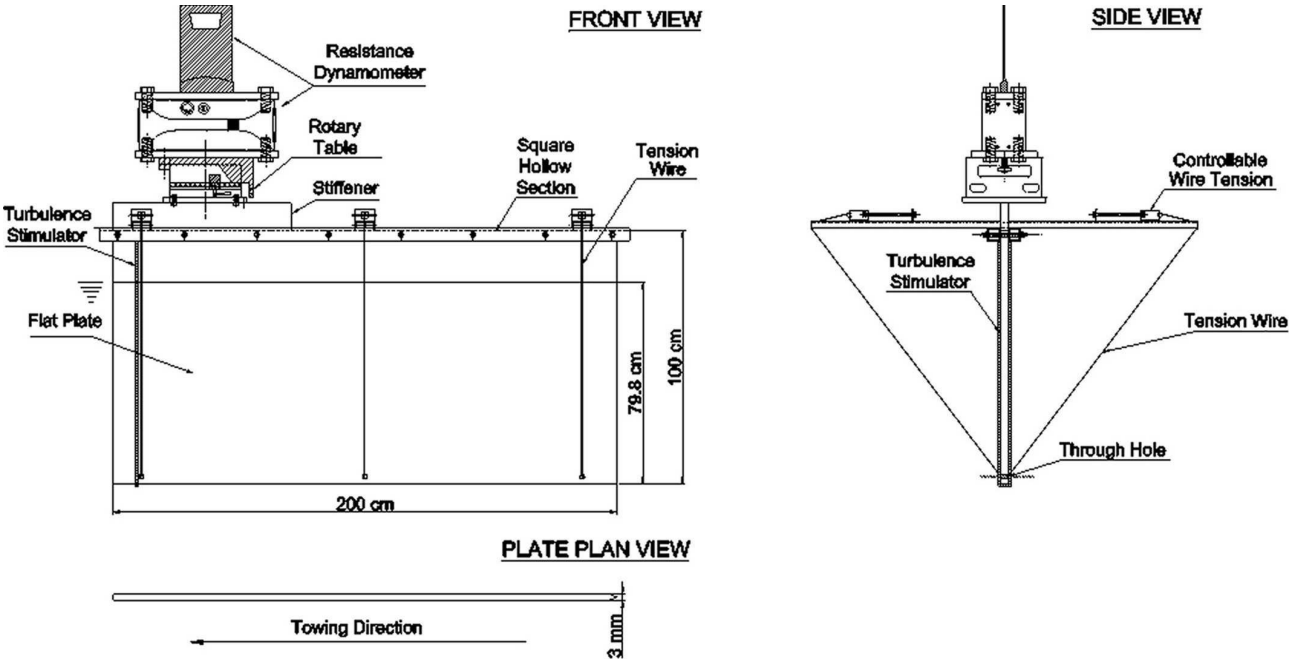

Figure 4.1: Front, plan and side view of the flat plate experimental setup

The dynamometer used for the experiments was a Kempf and Remmers R35 resistance dynamometer, with average load range towards the x-direction equal to 20 kg and maximum load equal to 50 kg. The signal was received by strain gages in full bridge arrangement for high precision measurements. The data were gathered at a sampling rate of 100 Hz and were digitized using a 12-bit A/D converter. A ±2.5 V and ±5 V voltage range, corresponding to 25 s and 15 s of recording time, was used for the measurements, depending on the load of each speed. Usually, the big range was used for speeds above 1.75 m/s.

The use of the tension wires (three on each side) was crucial for the successful performance of the resistance measurements, since they provided structural support to the thin aluminium plate and ensured that it was kept aligned. The added resistance induced by each wire was measured with a naval steel blade with dimensions 119 cm × 7.6 cm × 1 cm, appropriately processed to gain a NACA airfoil shape and cold galvanized, in order to ensure cathodic corrosion protection

(Fig. 4.2). The angle of the wire adapted in the perimeter of the blade and its wetted length were equal to the corresponding values of the plate's wires. The tension wire resistance was subtracted from the measured flat plate towing resistance ever since, in order to obtain the net flat plate frictional resistance coefficient.

All the tests were performed in fresh water and covered a speed range from 0.25 m/s (Re 4 $\times$ 10^5) to 2.5 m/s (Re 4.2 $\times$ 10^6) with a step of 0.25 m/s. The smooth plate runs were performed with and without trip wires for comparative reasons. A series of trip wires of different diameters were examined, in order to find the optimum that ensured completely turbulent flow in the whole range of measurements. The selected range included diameter values as proposed by ITTC, depending on water temperature and speed range. In total, five different trip wires were used, namely of 0.8, 0.9, 1, 1.128 and 1.3 mm diameter. Each wire was attached on both sides of the plate, at the fore part, located longitudinally from the trailing edge distance equal to 5% of plateb••s total length. Finally, each trip wire extended in height above the waterline level, in order to ensure stimulation at the whole flow front.

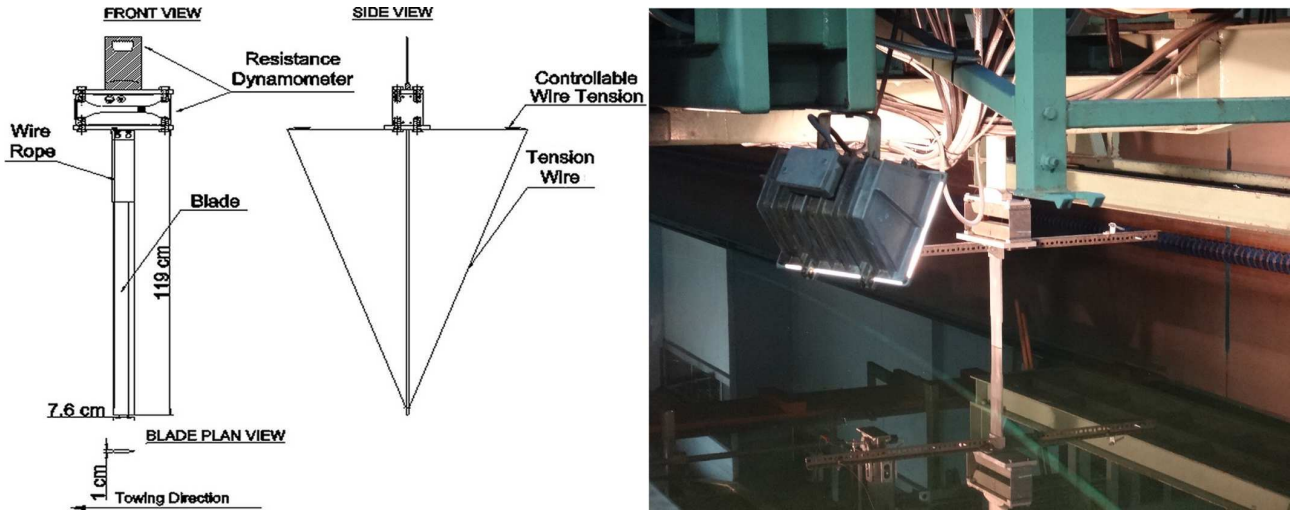

Figure 4.2: a) Front, plan and side view of the blade experimental setup and b) blade tank tests for determination of its resistance without the tension wire

After examination of the smooth condition, the plate was covered with sandpapers of 40 and 80-grit, in order to examine the roughness effect on the friction resistance coefficient.

4.2.2 Uncertainty estimates

Uncertainty estimates on the flat plate towing tank tests were performed according to ITTC [119] procedure. Estimation of the uncertainties related to carriage speed, applied force, temperature-density-viscosity and total resistance coefficient was performed.

The carriage speed is measured via an encoder wheel, which is connected to the carriage. In order to calculate the speed, the following equation was used.

$$V = \frac{c\pi D}{2500\Delta t} \tag{4.15}$$

where, c=pulse count

D= wheel diameter

Δt=AD card time base

The uncertainty of the pulse count includes four components. With regard to the bias of the encoder calibration, the optical encoder is factory calibrated with a rated accuracy of ± 0.2 pulses on every update. Hence, $B_{C1}= 0.2$ pulses. With regard to the speed data acquisition error, the speed data were converted to the PC by two 12-bit conversions. The AD boards are accurate by 1.5 pulses, as determined by the calibration sheet of the manufacturer. Therefore, the bias is $B_{C2}=B_{C3}=1.5$ pulses. The data reduction bias error was assumed by ITTC to be $B_{C4}= 0.25$ pulses.

The time base of the speed circuitry is related to the clock speed of its oscillator module, which is up to 300 kHz, giving an accuracy of 6×10^{-6} s on every update. However, for the present calculations, the smaller accuracy suggested by ITTC was used, in order to avoid underestimation. Hence, $B_{\Delta t}=1.025 \times 10^{-5}$ s. The wheel diameter was considered accurate within $B_D= 0.000115$ m. The total speed bias is given by the following equation:

$$B_V = \sqrt{\left(\frac{\partial V}{\partial c}B_c\right)^2 + \left(\frac{\partial V}{\partial D}B_D\right)^2 + \left(\frac{\partial V}{\partial \Delta t}B_{\Delta t}\right)^2} \tag{4.16}$$

From the total 17 tests performed on the plate, the raw speed data were gathered and the mean values, along with the total speed bias error (B_V) were calculated for the speed range 1.5 m/s to 2.5 m/s (Table 4.1). The bias error ranged from 0.078% to 0.074% in the examined speed range.

Table 4.1: Uncertainty estimation for the flat plate towing tank tests

Average speed (m/s)	Average resistance (N)	Speed bias (B_V) (m/s)	Resistance bias (B_R) (N)
1.247	14.910	1.00E-3	9.55E-2
1.498	21.455	1.12E-3	9.55E-2
1.751	28.854	1.34E-3	9.55E-2
2.003	37.760	1.51E-3	9.55E-2
2.254	47.133	1.68E-3	9.55E-2
2.506	56.680	1.86E-3	9.55E-2

With regard to the force term, the uncertainty estimation includes four components. The first component is related to the tolerance of the dynamometer calibration weights (B_{RX1}), which was equal to 0.003%. The second component arises from the assumption of the linearity of the load cell, where the calibration data are approximated with a linear regression curve fit [119], which introduces a precision error (SEE- standard error of estimate), given by the following formula [120]:

$$SEE = \sqrt{\frac{\sum_{i=1}^{N}(Y_i - (aX_i + b))^2}{N - 2}} \tag{4.17}$$

In Eq. (4.17), N is the number of calibration data, Y_i is the actual measured force (N), whilethe equation in parenthesis is the linear curve fit for force (N), with X_i being the ouput voltage (V). The precision error was equal to 0.0408 N, corresponding to a bias component equal to B_{RX2}=0.0815 N. The alignment of the experimental apparatus (smooth plate together with the load cell versus the dynamometer) to the mid-section of the carriage was performed via a laser sheet. The total misalignment of the plate at each edge was found equal to ±1 mm, corresponding to a maximum 2 mm deviation from the load cell or 0.057°. The total apparatus misalignment was assumed less than 0.25° (B_{RX3}=0.25°). Nevertheless, with the aid of the high precision rotary table positioned at the fore part of the plate (Fig. 4.1), with accuracy higher than 0.1°, the position of minimum drag of the plate was determined. This procedure was necessary, in order to eliminate the effect of other factors affecting the final alignment (e.g. plate shape). The fourth component (B_{RX4}) is the AD conversion bias error in voltage, which was found equal to B_{RX3}=0.04972 N. With regard to the fifth component, the tests consisted of fixed trim and draught conditions. Hence, B_{RX5} can be assumed to be zero. The final bias error for each measured resistance is presented in Table 4.1. The total bias limit in resistance ranged from 0.640% (at 1.25 m/s) to 0.168% (at 2.5 m/s) of the average measured resistance.

During each test, the temperature was measured using a mercury-in-glass thermometer with an accuracy of ±0.1°C. With regard to the density bias error calculations, this error consists of three components. The first component is related to the calibration and is equal to $B_{\rho 1}$=0.0133 kg/m^3. The second component is related to the conversion of temperature to density and is equal to $B_{\rho 2}$=0.0769 kg/m^3. The third component is zero ($B_{\rho 3}$=0), since, the density was calculated according to the measured temperature. Hence, the total bias limit for density is B_ρ= 0.078 kg/m^3. Finally, with regard to the viscosity, the first component of the bias limit is related to the calibration and is equal to $B_{\nu 1}$=3.199 × 10^{-9} m^2/s. The second component is related to the difference of the viscosity values given by the table in ITTC [121] and the fitting curve of the temperature/density data and was found equal to $B_{\nu 2}$= -9.01 × 10^{-10} m^2/s. Hence, the total bias limit for viscosity is B_ν=3.323 × 10^{-9} m^2/s. With regard to error estimation of the wetted surface, in flat plate towing tests no wetted surface changes are considered. Hence, no wetted surface error is taken into consideration.

Following the ITTC [119] guidelines, the total bias limit for total resistance coefficient (B_{CT}) of the smooth plate is presented in Table 4.2. The total C_T bias ranged from 0.658% to 0.224% of the value of C_T.

Table 4.2: Total uncertainty limit for total resistance coefficient of the experimental setup

Average speed	Average C_T	B_{CT}	P_{CT}	U_{CT}
1.247	0.0061	3.99E-5	1.28E-5	4.19E-5
1.498	0.0060	2.84E-5	1.15E-5	3.06E-5
1.751	0.0059	2.17E-5	1.59E-5	2.69E-5
2.003	0.0059	1.75E-5	5.54E-8	1.75E-5
2.254	0.0058	1.47E-5	5.42E-6	1.57E-5
2.506	0.0057	1.28E-5	3.93E-5	4.13E-5

The precision limit of total resistance coefficient is given by the following formula:

$$P_{\overline{C_T}} = \sqrt{\frac{KSDev\overline{C_T}}{\sqrt{M}}} \tag{4.18}$$

In Eq. (4.18), K is a coverage factor usually taken equal to two [119, 120, 122] and M is the number of test repetitions. The largest value of the precision limit error (P_{CT}) was at 2.5 m/s and was 0.690% of C_T. The high speed error can be partially justified as small deflections occurred at this speed. These variations could also arise from the limited test repetitions. Hence, more repeatability tests would cause a significant decrease in P_{CT}. This is the main reason that tests were not conducted at higher speeds, although it was desirable to achieve even higher Reynolds numbers.

Finally, the expanded uncertainty of C_T (Fig. 4.3), as proposed by Delen and Bal [122] is given by the following equation:

$$C_T = \overline{C_T} \pm U_{C_T} \tag{4.19}$$

where U_{C_T} is the total uncertainty.

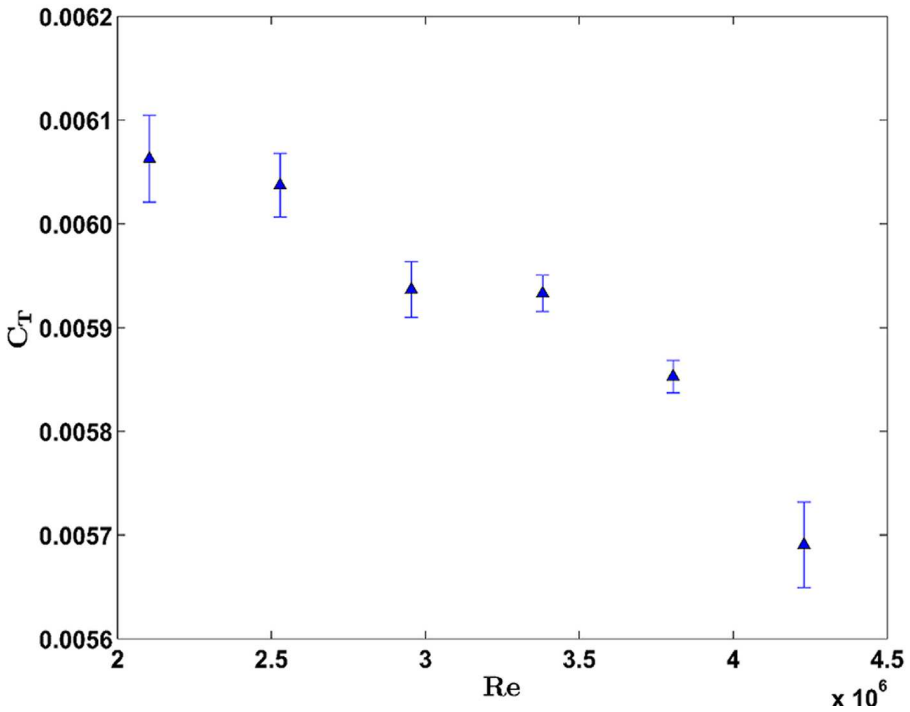

Figure 4.3: C_T values with error bars for the speed range 1.25 m/s -b•“ 2.5 m/s. (Bias error ranged from ±0.658% at lowest Reynolds number to ±0.224% at highest Reynolds number, for the presented data. Precision uncertainty ≤ ±0.690%)

4.2.3 Ship model towing tests

The model towing tests were performed during the Diploma Thesis of Korfiatis [92]. The model used for the resistance measurements was a bulk carrier at scale 1/35, while the general particulars for both the model and the ship are presented in Table 4.3.

Table 4.3: General particulars for ship and model for heavy ballast and full load departure conditions

Particulars	Symbol	Units	Heavy ballast		Full load departure	
			Ship	Model	Ship	Model
Waterline length	L_{W_L}	m	179.880	5.139	183.200	5.234
Waterline breadth	B_{W_L}	m	23.700	0.677	23.700	0.677
Mean draft	T_m	m	7.250	0.207	10.150	0.290
Displacement	Δ	t	25996	591.500	37290	848.500
Trim	t	$^\circ$	0.000	0.000	0.000	0.000
Wetted surface	S	m^2	5720.900	4.670	6883.900	5.620
Block coefficient	C_B		0.820	0.820	0.820	0.820
Water plane coefficient	C_W		0.872	0.872	0.872	0.872
Prismatic coefficient	C_P		0.825	0.825	0.825	0.825

The dynamometer used for the experiments was a Kempf and Remmers R47 resistance dynamometer, with average load range towards the x-direction equal to 25 kg and maximum load equal to 37.5 kg. A $\pm$10 V voltage range was used for the measurements. The sensors and digitization of data was similar to the R35 dynamometer used for the flat plate towing tests. The dynamometer was attached longitudinally at the center of buoyancy (LCB) and vertically at the center line (CL).

The towing tests were performed for two different loading conditions, namely heavy ballast and full load departure. For every loading condition the hull was examined smooth and covered with 40 and 80–grit sandpapers (Fig. 4.4b), respectively. The towing tests were performed for 13 speeds ranging from Froude number (Fn) 0.072–0.20, according to Froude similarity between ship and model scale. In Fig. 4.4a, the plate covered with sandpapers is also presented.

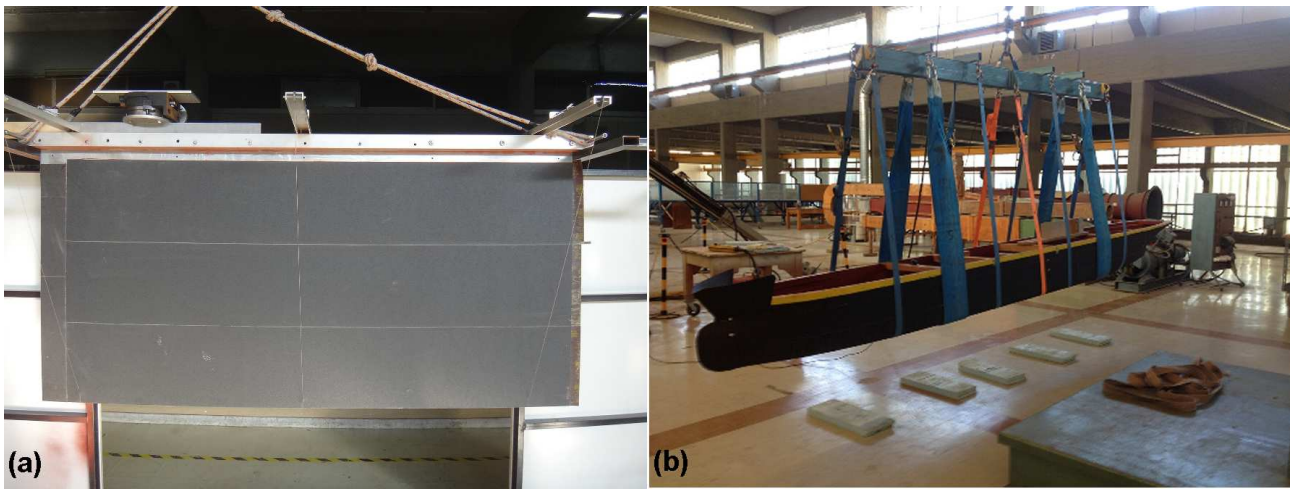

Figure 4.4: a) Flat plate and b) ship model entirely covered with sandpaper

4.3 Results and discussion

4.3.1 Flat plate towing tests

4.3.1.1 Effect of tension wires on smooth plate resistance

The effect of tension wires on total resistance is presented in Figure 5a. As can be seen from the graph, the tension wires resistance accounted for 48% of the total measured resistance at 2.5 m/s. The tension wire resistance, if not subtracted, would cause a significant increase in smooth plate total resistance coefficient, as presented in Figure 5b. More specifically, the increase in resistance coefficient was around 28% at 0.25 m/s and reached a maximum value of 45% at 2.5 m/s.

ITTC (2002) [119] guidelines for uncertainty estimation of the measured total resistance coefficient (Fig. 4.5b) were applied for the six highest Reynolds numbers. The overall error ranged from 0.691% (at Reynolds number 2.09×10^6) to 0.268% (at Reynolds number 3.78×10^6) of the measured CT. An exception to this trend was the measurement corresponding to the highest Reynolds number (4.20×10^6), which exhibited an overall error of 0.726% and could be attributed to small plate deflections, as mentioned in previous paragraph. The same uncertainty percentages are applied for total resistance (Fig. 4.5a), as proposed by ITTC (2014) [123]. Determination of smooth plate resistance was attained through uncertainty propagation, after subtraction of the tension wires drag from the experimental total resistance. The overall uncertainty in plate total resistance ranged from 1.304% (at Reynolds number 2.09×10^6) to 0.518% (at Reynolds number 3.78×10^6), while for the largest Reynolds number it was 1.440% of plate's total resistance. Finally, the overall uncertainty percentages for the last six data of the resistance coefficient were similar to the uncertainties of the total resistance [123], while the error bars are presented in magnification in the inset graph of Fig. 4.5b.

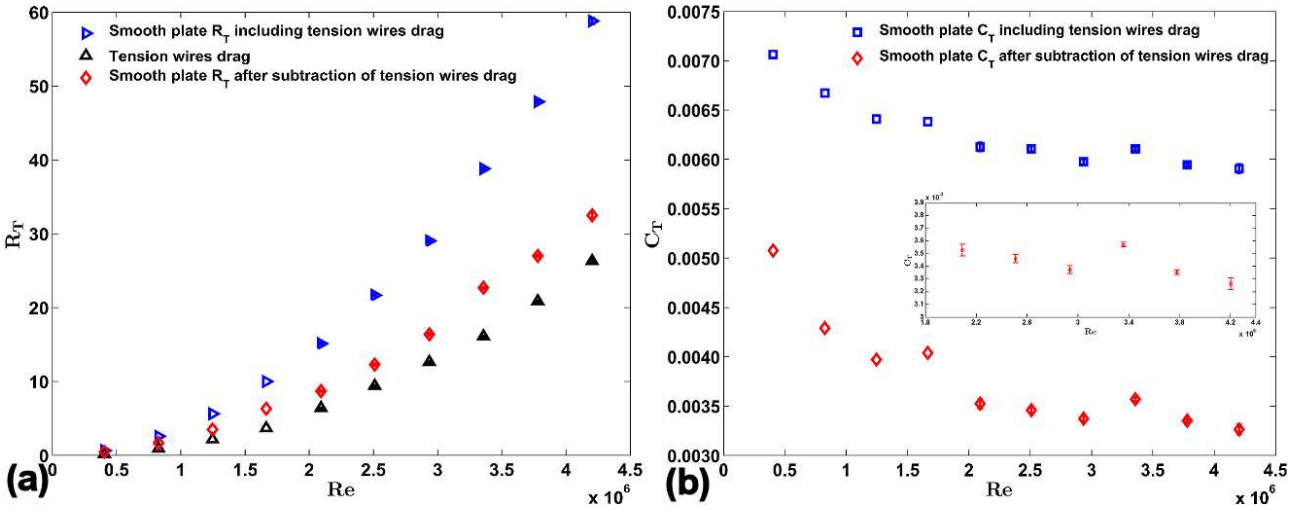

Figure 4.5: Smooth plate a) total resistance and b) total resistance coefficient before and after subtraction of tension wires resistance. Error bars presented for the six highest Reynolds numbers. (Overall uncertainty in C_T before subtraction of tension wires drag: $\leq 0.726\%$; after subtraction of tension wires drag: $\leq 1.440\%$, with the error bars presented in magnification in inset graph)

4.3.1.2 Effect of trip wires on smooth plate resistance

Resistance measurements were performed on the smooth plate using various trip wires of different diameter, in order to determine the optimum turbulent stimulator in the entire Reynolds range (Liarokapis *et al.* [124]). Wires of 0.8, 0.9, 1, 1.128 and 1.3 mm in diameter were tested progressively. The total resistance coefficient curves for each wire are presented in Fig. 4.6a. The four values appearing in the frame correspond to resistance values at 0.25 m/s and imply transitional flow. Despite these data, however, the curves corresponded to turbulent flow. The best stimulation was attained with the wire of 1.3 mm in diameter, as it seemed to behave better at low speeds. Following the instructions of ITTC, the 0.8 mm trip wire was supposed to stimulate properly for speeds higher than 0.8 m/s, while the 1.3 mm stimulator for speeds higher than 0.4 m/s. On the other hand, using bigger trip wire diameters would restrain the highest speeds of the experiments (i.e. for 13.6°C a trip wire of 1.6 mm diameter stimulates efficiently the flow up to 1.5 m/s, according to ITTC). Nevertheless, the selected trip wire was closest to the Schoenherr line (4%) for the entire speed range (Fig. 4.6b). The fitted curve for these data was used as the smooth plate friction line.

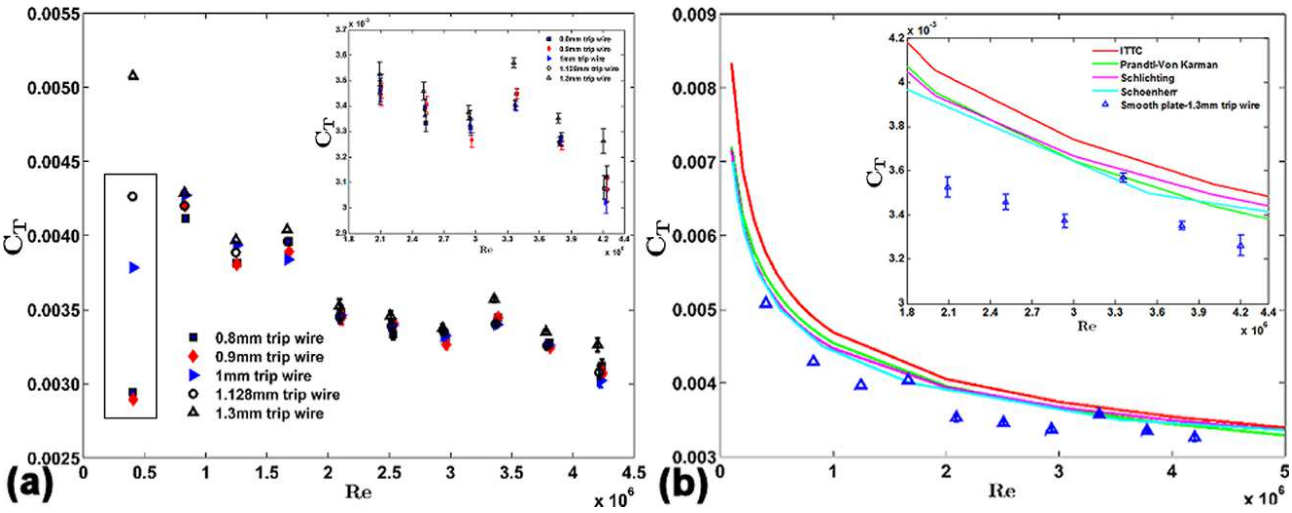

Figure 4.6: Smooth plate total resistance coefficient for a) all the tested trip wires and b) for the optimum turbulence stimulator. The experimental data for the six highest Reynold numbers are presented with error bars. The inset graphs present these data in magnification. (Overall uncertainty $\leq 1.501\%$ for all trip wires, calculated for the six highest Reynolds numbers)

From a physical point of view, as the diameter of a trip wire increases, an increase in friction resistance is expected. In strictly statistical terms, though, the error bars could mask this difference and cause confusion, especially in lack of a sufficient amount of repeatability tests. However, calculation of the statistical differences of total resistance coefficients between the selected trip wire (1.3 mm) and either of the other examined stimulators revealed that they were statistically significant especially in the higher Reynolds numbers, which are of most significance. The statistical differences between the 1.3 mm wire with the 0.8 mm and 1.128 mm stimulators, respectively, are presented in Fig. 4.7.

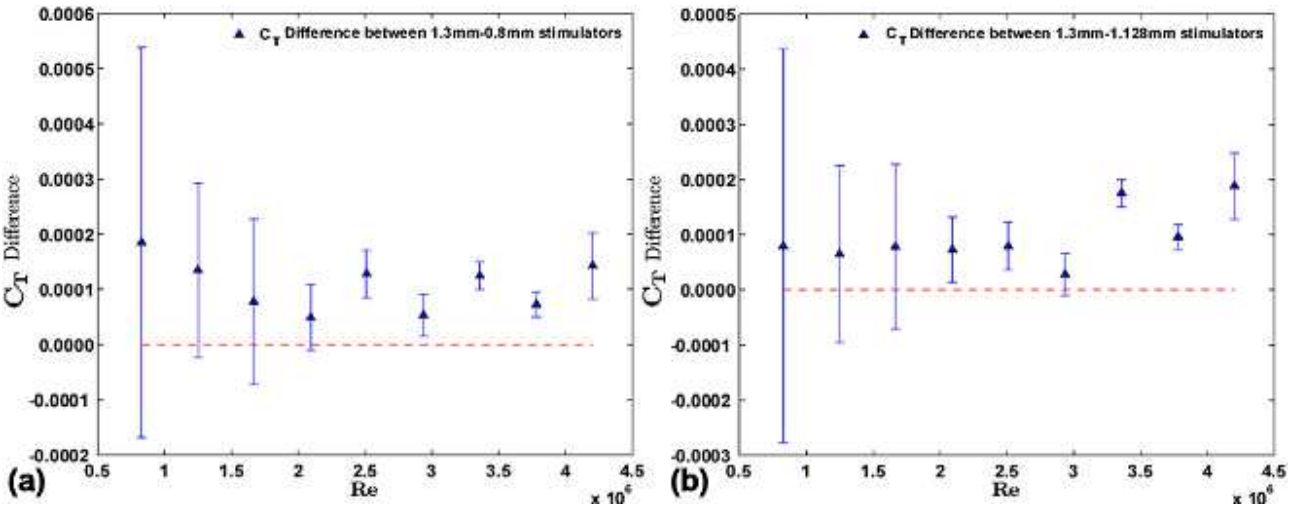

Figure 4.7: Calculation of the difference between the total resistance coefficient of the 1.3 mm trip wire with a) the 0.8 mm wire (uncertainty range: 20.24%–71.50%) and b) the 1.128 mm stimulator (uncertainty range: 14.30%–81.77%), for the examined speed range. (Uncertainty ranges refer to the statistically significant differences)

As can be seen from Fig. 4.7, the calculated differences exhibited uncertainties with positive lower limit, for Reynolds numbers of 2.1×10^6 and higher, which correspond to fully turbulent flow. The positive value of the lower uncertainties in this Reynolds range is a strong indicator of statistical significance, implying that the C_T values of these trip wires could not be equal. The above argument could be further supported by comparing the values of the C_T differences with their respective uncertainties (for the positive uncertainties). More specifically, with regard to the first couple (Fig. 4.7a), the calculated differences were found to be 1.40 (at Reynolds=2.93×10^6) to 4.94 (at Reynolds=3.36×10^6) times larger than their respective uncertainties, ensuring that for the measured C_T values we could be over 68% (over one standard deviation) confident that are actually different. Similarly, for the second couple (Fig. 4.7b), the C_T differences were 1.22 (at Reynolds=2.1×10^6) to 6.99 (at Reynolds=3.36×10^6) times larger than their uncertainties, implying a confidence level that initiates above 68%. Similar findings were noticed for the other two couples, 1.3 mm–0.9 mm and 1.3 mm–1.0 mm, as well. The former exhibited statistically significant differences for Reynolds numbers of 2.1×10^6 and higher, while the latter for Reynolds numbers of 1.66×10^6 and higher. As a result, it could be concluded that, in the higher Reynolds numbers, the experimental C_T values obtained during flat plate tests with various trip wires were actually different and could not be attributed to chance.

4.3.1.3 Plate entirely covered with sandpapers

The sandpaper experiments caused a significant increase in measured total resistance compared to the smooth plate (Fig. 4.8a). The added resistance for the 40-grit sandpaper was around 26 N at 2.5 m/s and around 16 N for the 80-grit sandpaper at the same speed. The total increase in resistance compared to the smooth plate is presented in Fig. 4.8b. As can be seen from the

graph, the resistance increase was apparent until 2 m/s and then it was stabilized at 76% for the 40-grit and at 45% for the 80-grit sandpaper.

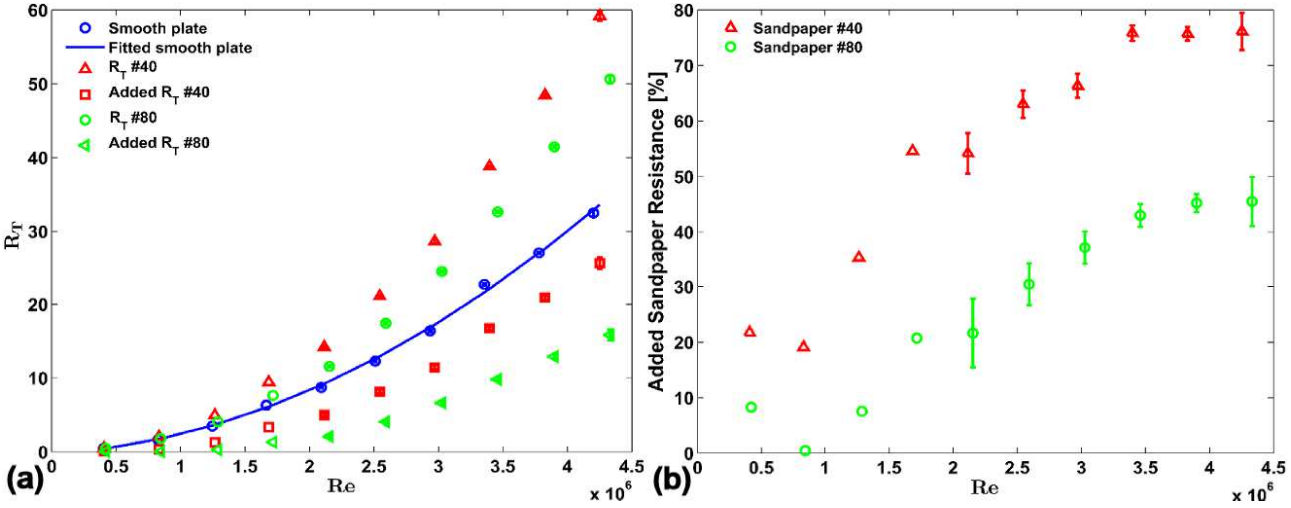

Figure 4.8: a) Total frictional resistance of the flat plate covered with sandpapers (overall uncertainty range: 0.40%–1.17%) and added sandpaper resistance (uncertainty range; 40-grit: 1.11%–3.41%, 80-grit: 1.56%–6.02%) and b) percentage increase of frictional resistance due to the sandpapers (uncertainty range; 40-grit: 1.23%–3.65%, 80-grit:1.64%–6.16%)

Overall uncertainty estimation for added sandpaper resistance is presented in Fig. 4.8a, for the six highest Reynolds numbers. The percentage uncertainty in total resistance was similar for smooth and rough condition, since the experimental setup and the environmental factors were not altered. The uncertainty for added resistance of the examined sandpapers was calculated through uncertainty propagation method for differences. For the 40-grit sandpaper the added resistance uncertainty ranged from 1.11% (at Reynolds 3.83×10^6) to 3.41% (at Reynolds 2.11×10^6), while for the 80-grit sandpaper it ranged from 1.56% (at Reynolds 3.83×10^6) to 6.02% (at Reynolds 2.11×10^6). Finally, the uncertainties of the percentages in Fig. 4.8b were calculated making use of the uncertainty propagation method, as well. For the 40-grit sandpaper the uncertainty ranged from 1.23% to 3.65%, at the same Reynolds numbers as the previously reported for Fig. 4.8a for the same grit, while for the 80-grit sandpaper the uncertainty ranged from 1.64% to 6.16%, for the same Reynolds numbers as for Fig. 4.8a, as well.

4.3.1.4 Uniform sand roughness height (k_s) calculation from Schlichting diagram

In order to proceed with the calculation of the roughness function for each of the examined sandpapers, it was crucial to calculate a proper roughness length scale. To this purpose, firstly, the total resistance coefficient for each sandpaper-grit was plotted against the Reynolds number, along with the smooth plate for comparative reasons (Fig. 4.9a). The shape of both rough curves followed Nikuradse's resistance formula for rough pipes, exhibiting the characteristic dip of the transitionally rough regime of uniformly rough surfaces [95, 97, 98], with the 40-grit sandpaper displaying the inflection at an earlier stage. The behavior of the sandpapers

indicated their homogenous roughness nature, hence, their roughness scale could be described by the uniform sand roughness height, k_s, as defined in Nikuradse [98] and Schlichting [99].

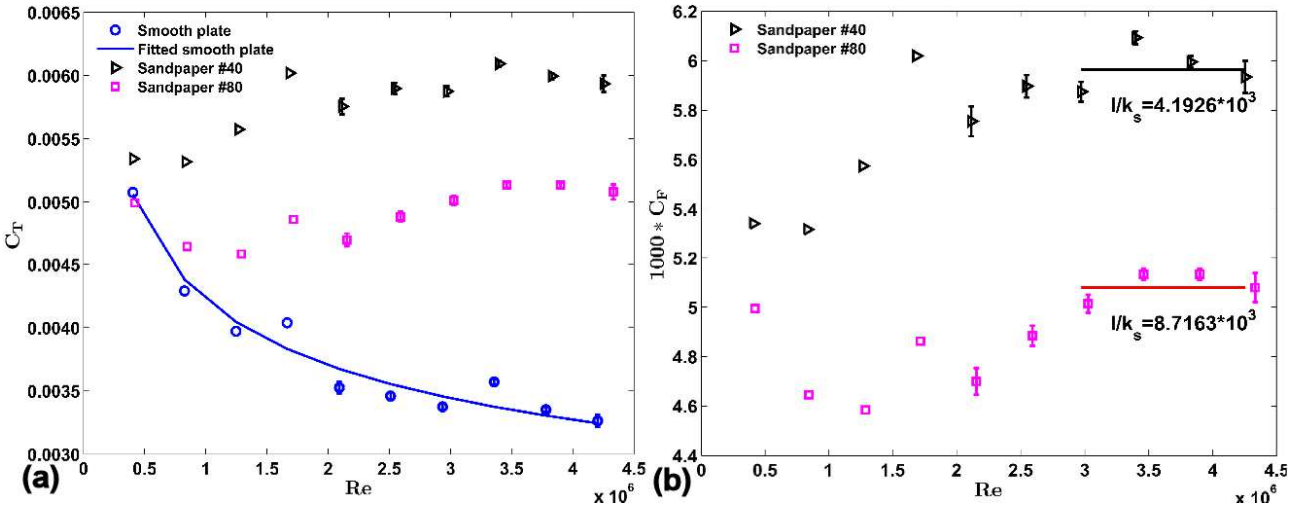

Figure 4.9: a) Total resistance coefficient for both examined sandpapers and b) k_s calculation from Schlichting resistance formula for sand-roughened plate (Overall uncertainty in C_T: $\leq$ 0.726% for smooth condition and $\leq$ 1.17% for rough condition, calculated for the six highest Reynolds numbers)

The plateau-like behavior of the last four data (Fig. 4.9a) made it possible to apply Schlichting's [99] diagram for the resistance formula of sand-roughened plate in the fully rough regime, in order to calculate the value of k_s (Fig. 4.9b). The k_s values for the 40 and 80-grit sandpapers, as calculated by the respective l/k_s values, where l the length of the plate, were 477 X'Om and 229 X'Om, lying in close proximity to the nominal average particle diameter values (R_a) of 425 X'Om and 201 X'Om, respectively. Hence, despite the difference between the mono-disperse nature of Nikuradse sand and the poly-disperse nature of the sandpapers [108], the results verified the homogenous roughness pattern of the sandpapers.

Statistical validity of the experimental data presented in Fig. 4.9 was confirmed through calculation of the differences between the total resistance coefficients of the smooth plate with each rough condition, as well as between the two rough conditions. The procedure was similar to the one followed for the trip wires and the results are presented in Fig. 4.10.

As can be seen from Fig. 4.10, the uncertainties obtained for the differences in C_T between the smooth condition and plate covered with 40-grit sandpaper were all positive. Moreover, the calculated C_T difference ranged from 2.87 (at lowest Reynolds number) to 94.21 (at Reynolds 3.78×10^6) times the value of the corresponding uncertainties, indicating a confidence interval initiating from almost three standard deviations, hence larger than 99.7%. Consequently, it is almost certain that the observed values could not be equal. Same observations hold for the differences between the smooth plate and the 80-grit sandpaper. In this case, the C_T difference ranged from 3.54 (at Reynolds 8.26×10^5) to 68.01 (at Reynolds 3.78×10^6) times the values of their uncertainties, indicating once more a certainty about these experimental data being different. Only the difference corresponding to the lowest Reynolds number exhibited a lower boundary limit equal to zero, hence there is a possibility that these two values were

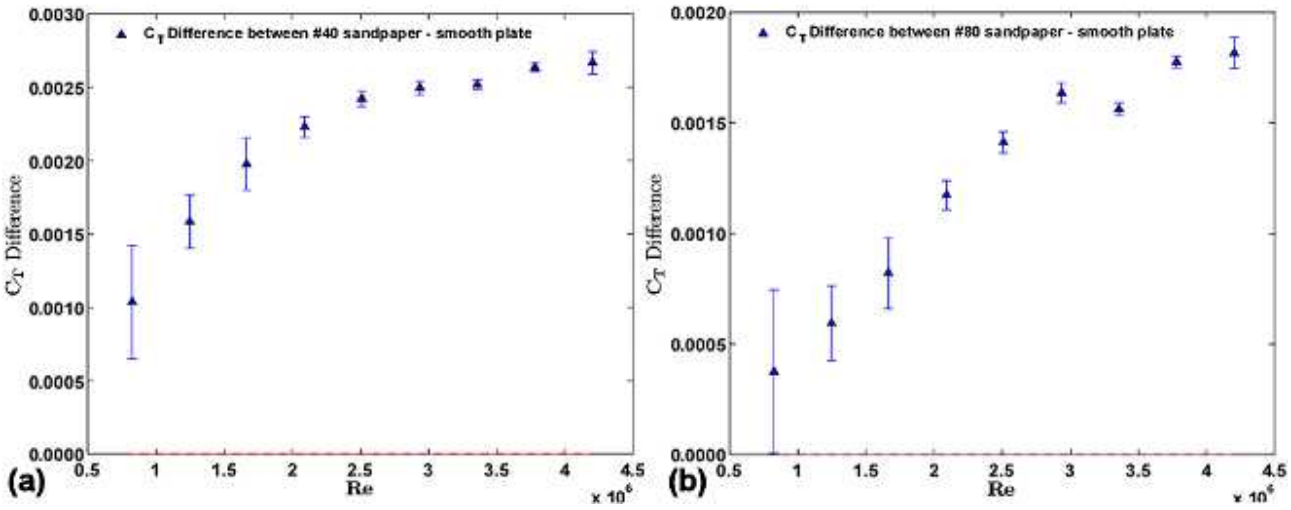

Figure 4.10: Calculation of the difference between the total resistance coefficient of the smooth plate with a) the 40-grit sandpaper (uncertainty range: 1.06%–37.30%) and b) the 80-grit sandpaper (uncertainty range: 1.47%-28.22%), for the examined speed range. (Uncertainty ranges refer to the statistically significant differences)

equal. Finally, all the differences between the two rough conditions exhibited positive lower boundaries for the whole examined Reynolds range (corresponding to carriage speed ≥ 0.5 m/s) with minimum confidence over 68%.

4.3.1.5 Roughness functions and correlation with Nikuradse results

The calculated k_s was used in Granville's [101] equations for the calculation of roughness function (ΔU^+) and roughness Reynolds number (k^+). The procedure is presented in Fig. 4.11a. For comparison, the Nikuradse data [98] for the corresponding roughness heights k_s=200 X'Om and k_s=400 X'Om, along with the Prandtl-Karman equation for smooth pipes, as presented in Granville [101], are also showed. The fitted lines of the experimental data were used to better represent the similarity of the corresponding curves between the experimental and the Nikuradse data. Uncertainty propagation method was performed, in order to obtain the overall uncertainties of the last six data after applying Granville method. The error for the smooth condition ranged from 0.26% to 0.72%, for the 40-grit condition from 0.20% to 0.55% and for the 80-grit condition from 0.21% to 0.58%, of the calculated y-value depicted in Fig. 4.11a. The same procedure was followed for estimation of the roughness functions of 40 and 80-grit sandpapers presented in Fig. 4.11b. The total uncertainty in ΔU^+ for the former ranged from ± 0.090 to ± 0.250 and for the latter from ± 0.096 to ± 0.266. The average values from both sandpapers made an overall uncertainty in ΔU^+ of ± 0.171 or 2.9%.

The experimental roughness functions exhibited a Nikuradse behavior (Fig. 4.11b) [103]. Both functions lay on the same line, similarly to Nikuradse roughness functions and indicated transitionally rough regime, as was noticed in Fig. 4.9a. This was also verified by the maximum k^+ value which was found to be equal to 48 and, according to Schlichting [99], denotes this regime. Nevertheless, the asymptote of the universal roughness function, which denotes fully rough regime, initiates above the value of 70, supporting the aforementioned hypothesis.

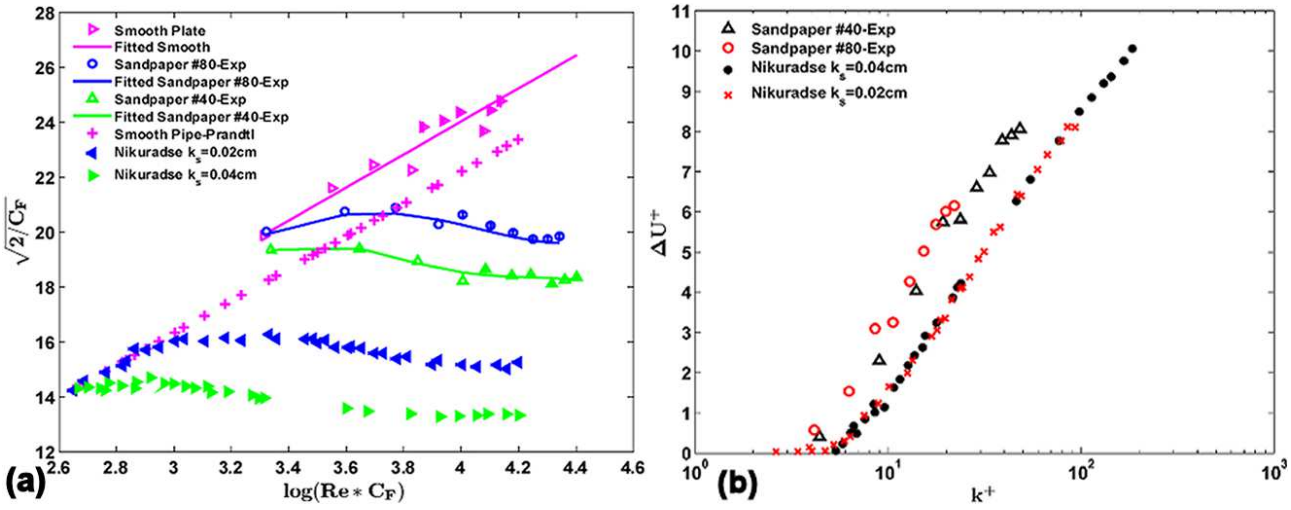

Figure 4.11: a) Granville method for calculation of roughness functions for experimental and Nikuradse (1933) data of similar k_s (mean overall uncertainties for last six data; smooth: 0.47%, 40-grit: 0.37%, 80-grit: 0.40%) and b) the calculated roughness functions (mean overall uncertainty in ΔU^+ for last six data of both conditions: ± 0.171)

However, the experimental functions were on the left side of Nikuradse universal roughness function and a factor of 1.7 would collapse the data on the Nikuradse curve (Fig. 4.12). Similar behavior has been reported by Schultz and Flack [96] for sharp roughness elements of steep slope. The distance between the experimental and Nikuradse universal roughness function could be attributed to the poly-dispersity of the sandpapers [108]. As a result, the average particle size used for the calculations could be an underestimation of the actual roughness pattern of the sandpaper, hence, this factor accounts for the grains of higher size. A factor of 0.75 has been proposed by Schultz and Myers [103] when the maximum roughness height (R_t) is used as the characteristic roughness length scale, because in this case the roughness pattern is overestimated.

The factor of 1.7 collapsed well the experimental roughness function data on the universal roughness function for both regimes, even though this is not always guaranteed [95]. The collapse on the Nikuradse curve revealed that the last two points of the 40-grit sandpaper lay on the fully rough regime, since they exhibited k^+ values of 74 and 82, respectively, in contrast to the observations made before their transfer. This fact suggests that a proper comparison for the two sandpaper grits can be performed only if both lie onto the Nikuradse curve. From the comparison it became apparent that the 80-grit sandpaper lay entirely on the transitionally rough regime, in accordance to the observations before transfer. The difference between the two sandpapers became even more obvious through the last five data from each curve, since the rougher sandpaper lay clearly ahead the smoother grit.

The above observations suggest that, in order to draw right conclusions with regard to the proper roughness length scale (k_s) and the flow regime of different roughness patterns, it is important to collapse their roughness functions onto the Nikuradse curve. Also, from the same study it became apparent that even though the shape of the friction resistance curves (Fig. 4.9a) implied uniform roughness, which in turn led us use Schlicting's diagram for uniform roughness

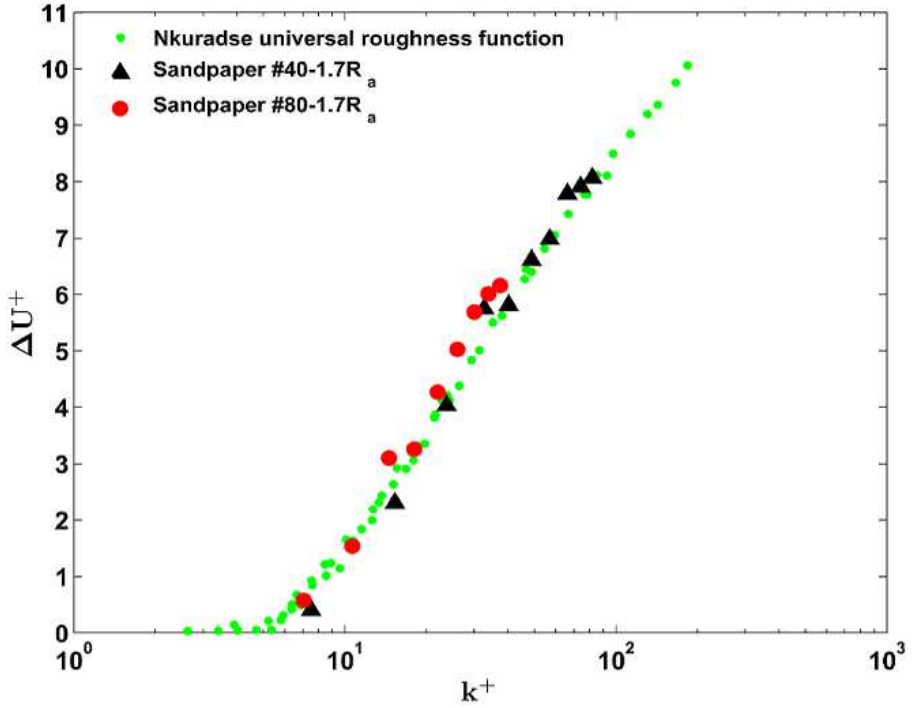

Figure 4.12: Collapse of the experimental data on uniform sand roughness function for the final value of k_s=1.7R_a (mean overall uncertainty in ΔU^+ for last six data: $\pm$0.171)

assuming fully rough regime and, finally, calculate a k_s similar to the nominal R_a value of the sandpaper, it was finally proven that the equivalent sand roughness height was 1.7 times the initial estimation of k_s. Since the initial estimation of k_s was driven by the assumption of uniform roughness, it was somehow expected to end up to the equivalent sand roughness height of the sandpaper. As a result, the poly-dispersity of surfaces that are commonly considered as uniformly rough should always be kept in mind, even if the data imply mono-dispersity.

4.3.2 Ship resistance calculation

4.3.2.1 Model based extrapolation methods for smooth hull

The smooth model towing tests were performed for Froude number values of 0.072 to 0.20 in heavy ballast (HB) (Fig. 4.13a) and full load departure (FLD) (Fig. 4.13b) conditions [92]. For each loading condition the total ship resistance coefficient ($C_{T,S}$) was calculated using two methods, namely the Froude [109, 110] and ITTC 78 method [111].

The data referring to the model tests were derived from the Diploma Thesis of Korfiatis [92]. Uncertainty analysis concerning model testing in the Laboratory of Ship and Marine Hydrodynamics (LSMH) of NTUA has been previously investigated [125] and was found to be up to 2% of C_T for a speed of 1.5 m/s.

With regard to the ITTC 78 method, Prohaska's method was applied in the Froude range of 0.12 to 0.20, in order to determine the form factor, k [111, 114]. As a result, the first four measurements were excluded from form factor calculation, since they corresponded to Froude numbers smaller than 0.12. Due to the full hull form of the model (C_B >0.8), the quantity of C_T/C_F was plotted versus Fn^6/C_F, in order to avoid a concave shape of the curve [115]. The

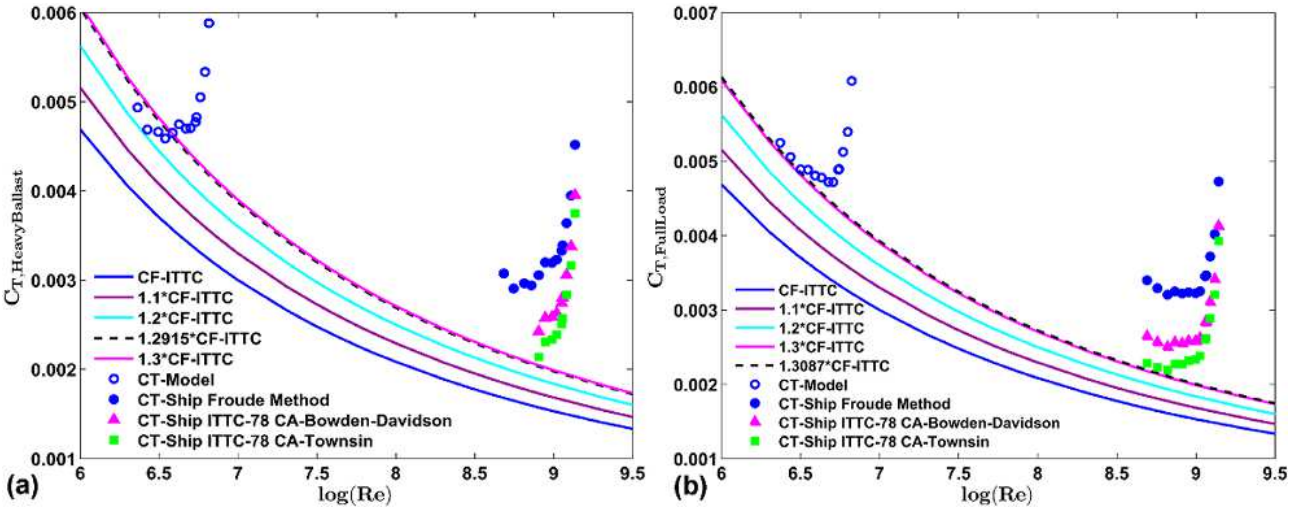

Figure 4.13: Froude method for smooth hull total resistance coefficient for a) heavy ballast and b) full load departure conditions (overall uncertainty in model C_T at 1.5 m/s $\leq$ 2%)

value of 1+k was found to be 1.2915 and 1.3087 for each condition, respectively. As regards the methodology for the HB condition, the first four measurements lay below the Prohaska linear fitting curve, leading to negative wavemaking resistance coefficient (C_W) values. As a result, these measurements could not be extrapolated to ship scale (Fig. 4.13a). Finally, for the calculation of the correlation allowance including roughness effects (ΔC_F), a value of k_s=150 X'Om was used for the average hull roughness. The ITTC 78 method was repeated using Townsin's formula for ΔC_F [112, 113].

The model total resistance coefficient ($C_{T,M}$) curve exhibited the highest values due to the significantly higher friction coefficient values of the ITTC 57 correlation friction line in the lower Reynolds numbers. With regard to the Froude and ITTC 78 methods, the traditional extrapolation seems to overestimate the $C_{T,S}$, because it assumes that all the non-frictional parts of total resistance scale according to Froude's law, while the latter method assumes that only for the wavemaking resistance, while for the viscous resistance assumes scaling according to Reynold's law [110]. Moreover, as can be observed from Fig. 4.13b, the ITTC 57 correlation friction line for the selected 1+k value for the FLD condition is tangential to the inflection point of the $C_{T,M}$ curve. Similar behavior, but not as profound has been observed for the HB condition, as well (Fig. 4.13a). Finally, when applying the roughness allowance proposed by Townsin the $C_{T,S}$ curve is tangential to the friction correlation line for the selected value of 1+k, similarly to the model $C_{T,S}$ curve. On the other hand, using the Bowden-Davidson correlation allowance the curve lies higher, representing a rougher condition.

With regard to the model resistance in the two loading conditions, an average increase of 3.11% in $C_{T,M}$ was noticed in the FLD condition compared to the HB. With regard to HB condition in ship scale, the Froude method led to 24.05% higher resistance than the ITTC 78 method for the first point of extrapolation (Re=8.03×10^8) and 14.29% for the last point at Reynolds 1.36×10^9. For the FLD condition, the difference was 28.42% at Reynolds 4.91×10^8 and 14.51% at the highest Reynolds value of 1.39×10^9. With regard to the two versions of ITTC 78 in HB condition, the common methodology using Bowden-Davidson formula for ΔC_F

led to 13.20% higher estimation of $C_{T,S}$ compared to Townsin's for the extrapolation point corresponding to Reynolds 8.03×10^8 and 5.49% for the point of highest Reynolds number. In the FLD condition, the corresponding differences ranged from 15.92% at Reynolds 4.91×10^8 to 5.09% at Reynolds 1.39×10^9. The calculated $C_{T,S}$ values for the FLD condition, using the common ITTC 78 method, were in average 1.82% higher than the respective values in the HB condition, for similar Froude values. On the contrary, by applying the Froude method, the FLD $C_{T,S}$ values were on average 2.55% higher than the HB condition.

4.3.2.2 Comparison of flat plate and model based extrapolation methods for rough hull

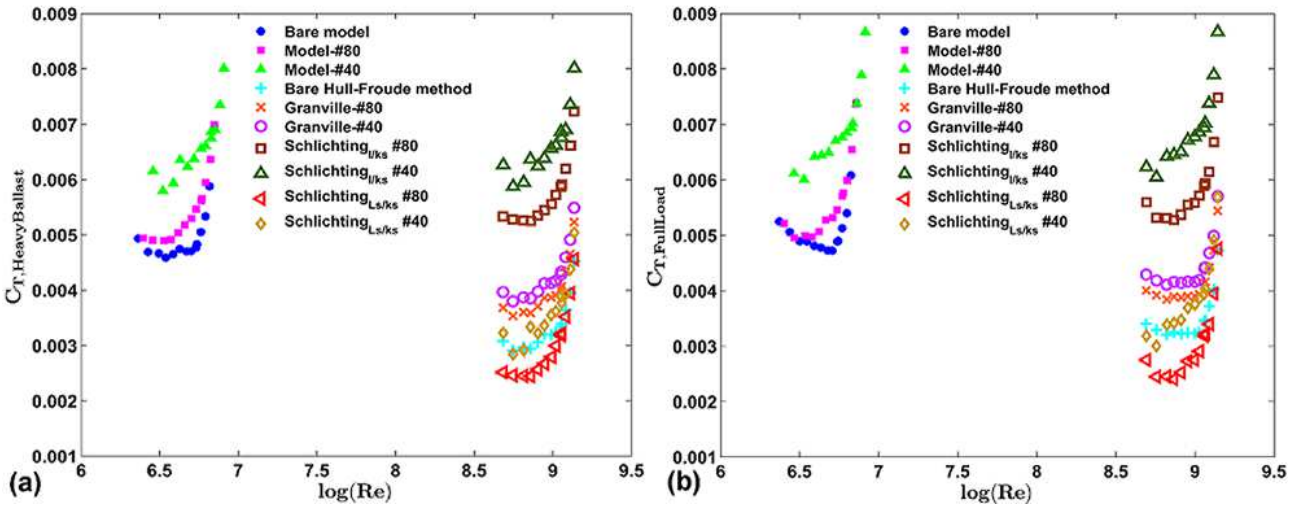

Figure 4.14: Comparison of flat plate and model based extrapolation methods in calculated ship resistance for rough hull for a) heavy ballast and b) full load departure conditions (overall uncertainty in model C_T at 1.5 m/s $\leq$ 2%)

In Fig. 4.14 three extrapolation methods are presented, based on the resistance data from rough flat plate and rough model towing tests. All methods considered the same roughness height between plate, model and the ship for each rough condition. The first method included prediction of ship total drag coefficient from rough flat plate towing tests based on Granville's similarity law analysis [94], which is described also in Schultz [109]. The other two methods are proposed herein and were based on Schlichting [99] resistance formula for sand roughened plates and are a variation of Froude method. More specifically, the methodology follows Froude law for residual resistance, but, instead of using ITTC 57 friction correlation line for C_F, the Schlichting diagram is used, where the correlation line is the line of constant l/k_s. In the first version of the method the line of l/k_s as calculated from flat plate towing tests (Fig. 4.9b) is kept constant in both model and ship Reynolds numbers. In the second version, the line of l/k_s from flat plate towing tests was used for calculation of C_F in model scale, while the extrapolation in ship scale was based on the line of L_s/k_s, where L_s the ship length for each loading condition (Table 4.3).

The results from all the extrapolation methods applied, for both the HB and FLD conditions are presented in Fig. 4.14a and 4.14b, respectively. As can be seen from the graphs,

the Schlichting method using constant l/k_s in both scales predicted the highest values of $C_{T,S}$, followed by Granville method and, finally, the second version of Schlichting method predicted the lowest values. With regard to the 40-grit sandpaper in HB condition, the $C_{T,S}$ values predicted using the first method were in average 55.68% higher than Granville's, 85.12% higher than Schlichting's second version and 99.64% higher than smooth hull $C_{T,S}$ as calculated using Froude method. The respective values for the 80-grit sandpaper in the same loading condition were 44.37%, 94.65% and 73.50%, respectively. With regard to the 40-grit sandpaper in FLD condition, the respective values were 56.24%, 79.67% and 98.30%, while for the 80-grit sandpaper were 40.22%, 96.20% and finally 67.12%. The two versions of Schlichting method provided an upper and lower limit for $C_{T,S}$, even though the $C_{T,S}$ values corresponding to 80-grit sandpaper roughness height exhibited values smaller than the smooth hull, when applying the second version of Schlichting method.

The extrapolation methods could also be characterized by the difference between the 40 and 80-grit $C_{T,S}$ results, compared to the initial differences in laboratory scale. More specifically, with regard to the flat plate tests, the 40-grit C_F was in average 19.76% higher than the 80-grit. This difference was translated as 6.66% higher $C_{T,S}$ in HB condition and 6.46% in FLD condition, by using Granville's method. With regard to the respective differences in $C_{T,M}$ in model scale, the 40-grit sandpaper was 20.94% higher than the 80-grit in HB and 23.80% in FLD condition. The corresponding differences in $C_{T,S}$ for the first version of Schlichting method were 15% and 18.63%, that is around 5% smaller difference in both loading conditions, whereas the second version for the HB condition was closer to the initial difference in laboratory scale with 20.86% difference, while for the FLD condition the difference was 29.47%, that is 5.67% higher than the laboratory scale.

4.4 Conclusions

The main objective of the present investigation was to gain an insight with regard to the resistance components of rough surfaces in large scale. To this purpose, flat plate and model towing tank tests on rough surfaces were performed in the laboratory and extrapolation to ship scale was attempted. The results from the rough flat plate were extrapolated according to Granville method, while the results from the rough model were extrapolated based on Schlichting's formula for sand roughened plate. With these experiments, data were provided with regard to the resistance components in rough condition, in order to get an insight of ship's C_F, and, finally be able to estimate ship's C_P. In order to ensure trustworthy results from the flat plate tests in rough condition, a thorough examination of the flat plate setup in smooth condition was initially performed and presented also in this study.

- Flat plate tests on a very thin plate of 3 mm thickness were performed. The novelty arising from the very small thickness of the plate required the design and construction of a whole new experimental setup presented in this study.

- With regard to the flat plate towing tests, the tension wires resistance was significant and accounted for 48% of total measured resistance at 2.5 m/s necessitating its subtraction for correction purposes ever since. From the series of trip wires examined, the 1.3 mm trip wire was found to satisfactorily stimulate the flow in the whole examined speed range.

- With regard to the rough plate experiments, the resistance increase compared to the smooth plate was 76% for the 40-grit and at 45% for the 80-grit sandpaper for speeds over 2 m/s. The shape of the friction resistance curves for both sandpapers was indicative of uniformly rough sand surfaces in the transitionally rough regime, in accordance to Nikuradse experiments. These results verified the validity of the experimental data and hence, of the newly designed experimental setup. This allowed the use of Schlichting's resistance formula for sand roughened plates, in order to make an initial estimation of the equivalent sand roughness length scale, which was similar to the nominal average particle diameter of the sandpaper. The roughness functions exhibited a Nikuradse behavior, while a factor of 1.7 collapsed the data onto the universal roughness function revealing that the last two data of the 40-grit roughness function lay on the fully rough regime and that the equivalent sand roughness height was 1.7 times the nominal average roughness, designating the polydispersity of the sandpapers.

- With regard to the model towing tests on smooth hull, a detailed presentation of the Froude and ITTC 78 methods was performed for two loading conditions. The Prohaska's method in ITTC 78 methodology required the use of sixth power, in order to calculate the form factor, due to the full hull form of the model. However, for the heavy ballast condition the first four data could not be extrapolated to ship scale. The traditional Froude method led to around 15% higher total resistance coefficient compared to the ITTC 78 method for both heavy ballast and full load conditions, at the highest Reynolds number, which is attributed to the different scaling background of the methods.

- A comparison of the most commonly applied formulas for correlation allowances in both extrapolation methods was presented. The Bowden-Davidson formula for correlation allowance led to approximately 5% higher total resistance coefficient in both loading conditions and at the highest Reynolds number, compared to Townsin's formula for roughness allowance.

- With regard to the model towing tests in rough condition, a newly proposed extrapolation method based on Schlichting diagrams of sand roughened plates was applied. This method, when using plate's l/k_s as friction correlation line predicted the highest total resistance coefficient in ship scale, followed by the Granville method, while, the Schlichting method using l/k_s in laboratory scale and L_s/k_s in ship scale predicted the smallest resistance coefficient. Granville's method predicts an added frictional resistance component due to roughness, which is added to the smooth hull total resistance coefficient, while the

proposed method predicts the total resistance coefficient by applying Froude methodology in rough condition. The two versions of the newly proposed methodology based on Schlichting diagrams provided an upper and lower limit in the predicted ship resistance coefficient.

Chapter 5

Experimental investigation of paint roughness on ship resistance using flat plate towing tests

Abstract

Flat plate tests in painted condition were performed and extrapolation to ship scale was attempted. In total, all the five different experimental and commercial antifouling (AF) systems of silicone, polyurethane and acrylic formulation were examined (Ref. Si, Exp. Si, Acrylic, Exp. PU1, Exp. PU2). The towing tank tests were performed in the range of 0.75-2.5 m/s, with a step of 0.25 m/s. The silicone and polyurethane formulations exhibited similar hydrodynamic behavior, fluctuating around the smooth condition, whereas the acrylic system exhibited the highest resistance increase of all. Roughness function calculation was based on R_a and correlation with the Colebrook-type roughness function was feasible for all systems, when the proper multiplication factor was applied to R_a.

5.1 Introduction

Marine structures, such as ships or platforms, are vulnerable to biofouling, i.e. the attachment of marine fauna and flora on the submerged part of their surface [6]. When it comes to ships, the ship bottom area is threatened by biofouling with adverse structural, environmental, hydrodynamic and economic effects. It is noteworthy that even small scale fouling (slime) can cause an increase in skin friction drag [38], while intense fouling could cause 40% increase in fuel consumption and 77% increase in total voyage cost [39, 40]. Fouling effect on drag is more profound in lower speeds, where the frictional resistance is predominant [109]. For these reasons, application of an efficient antifouling (AF) and anticorrosion protection painting system is required, which will provide a hydrodynamically smooth surface, leading to minimized drag and fuel consumption [126].

Among the most commonly applied antifouling systems are the tin-free biocide-containing self-polishing copolymers (SPC-chemically active AFs) and the foul release systems (FRS-non-toxic AFs) [127]. In the former category the biocide is mixed into the polymeric matrix and

both are released into the water via hydrolysis. Representatives of this category are acrylic copolymers as a matrix and cuprous oxide (Cu_2O) as a biocide. The latter category contains no biocides and its AF protection arises from the low surface tension between paint and fouling agent. Polydimethylsiloxane (PDMS) silicone elastomers are widely used for this purpose [103, 128].

Examination of the roughness effect of a freshly painted flat plate on friction resistance has been performed by Schultz [107] and Candries [102, 129]. Both studies concluded that the FR systems exhibited lower frictional resistance overall than the examined SPC systems, while all systems presented higher roughness and friction resistance than the unpainted smooth plate. The maximum increase in resistance of a freshly painted plate, compared to the unpainted condition could reach up to 8% [107].

The roughness effect of a freshly painted or fouled plate can be expressed through calculation of the roughness function (ΔU^+) [101] ,which was also analyzed in Chapter 4. The value of the roughness function can then be applied in the similarity law proposed by Granville [94], in order to predict the added frictional resistance component in ship scale (ΔC_{F_s}), which is then added to the bare hull total resistance coefficient (C_T), as calculated by applying the Froude method [109]. The roughness function expresses a downward shift in the log–law region of the mean velocity profile [95], arising from increased momentum deficit, due to roughness [96, 97]. The roughness function is a function of the roughness nature and roughness Reynolds number k^+ [96].

A very important parameter in this methodology is the roughness length scale, k. For uniformly rough surfaces, such as sandpapers, the equivalent sand roughness height (k_s) is the appropriate roughness length scale to be specified, because for this value the experimental roughness function data collapse onto the Nikuradse universal roughness function in the fully rough regime [95, 100], while for arbitrarily rough surfaces, such as painted surfaces, the appropriate length scale is the one that collapses the data onto the Colebrook-type roughness function [103] (presented in Eq. 4.1).

In the present study, towing tests on a flat plate painted with each one of the commercial and experimental antifouling systems examined in this thesis (Ref. Si, Exp. Si, Acrylic, Exp. PU1 and Exp. PU2) were performed and the resistance coefficient for each case was calculated for Reynolds numbers 1.26×10^6 – 4.2×10^6. The aim of the present study was to examine if there would be any differences in flat plate resistance using different painting systems. Another purpose of this study was to calculate the roughness function of each painting system and determine potential correlation with common theoretical roughness functions, such as the Colebrook-type roughness function. Correlation with theoretical roughenss functions is crucial in terms of CFD modelling of the effect of arbitrary roughness in ship scale.

5.2 Experimental methods and materials

5.2.1 Flat plate experimental setup

The experimental setup for the flat plate towing tests has been presented in Sec. 4.2.1 of Chapter 4.

5.2.2 Towing tank tests on painted flat plate

During these tests, the plate was painted with each one of the commercial and experimental antifouling systems examined in this study, namely the Ref. Si, Exp. Si, Acrylic, Exp. PU1 and Exp. PU2 formulations. For comparative purposes smooth plate experiments were also performed. During both experiments in smooth and painted condition a flow stimulator of diameter 1 mm was applied at the fore part of the plate, at distance equal to 5% of plate's total length.

Application of each coat was performed with a 2.2 mm nozzle spray gun, under 8 bar pressure, according to manufacturer's specifications from an expertice technician. The polyurethane (PU) topcoats were applied on top of a primer. With regard to the silicone coatings, their application necessitated the use of a tie-coat, in order to attain adequate adhesion between the elastomeric topcoat and the aluminium surface. After application of each coat, thickness and roughness measurements were performed at both sides of the plate. The roughness measurements were performed with a TR100 Surface Roughness Tester, using a cutoff length of 2.5 mm and measuring the average surface roughness (R_a). Thickness measurements were performed with a Wilson-Wolpert WCG 200/210 thickness gauge. Twenty five measurements per side were performed and their average values are presented in Table 5.1.

Table 5.1: Mean roughness and thickness measurements of the painting systems

System	Thickness (μm)	Roughness (R_a) (μm)
Exp .PU1	107.40	0.94
Exp. PU2	146.80	1.37
Acrylic	195.38	2.15
Exp. Si	59.90	1.87
Ref. Si	92.16	1.55
Smooth plate		0.41

The roughness distribution of the coating systems is presented in Fig. 5.1. The box plot of Fig. 5.1a was constructed, in order to compare the roughness range of the different systems and gain an insight with regard to the roughness values with the highest frequency. The frequency polygon of Fig. 5.1b was constructed after selecting six classes to classify the 50 roughness measurements of each coating system.

With regard to the boxplot of Fig. 5.1a, the values within the limits of the box represent the 50% of the measurements, while the horizontal black line inside each box represents the median of each data set. The lower and upper quartiles correspond to 25% and 75% of the

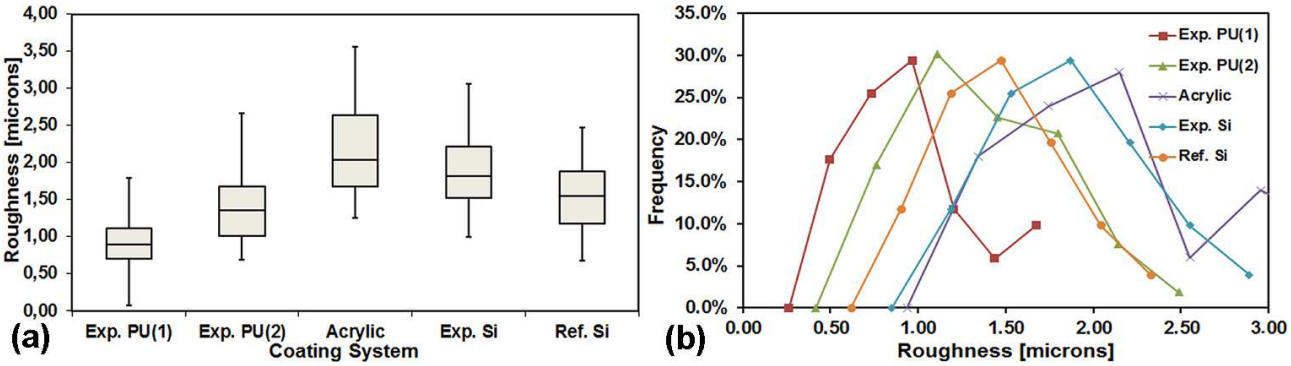

Figure 5.1: a) Box plot and b) frequency polygon presenting the roughness distribution of the examined coating systems

observed measurements, respectively. The box plot can provide an insight with regard to the distribution of the roughness measurements. With regard to the experimental PU1, PU2 and the acrylic systems, the 50% of the data above the median exhibited wider distribution than the data below this value. This implied a slight positive skew in the respective histograms of these systems (Fig. 5.1b). The silicone systems exhibited a more symmetrical behavior. However, in either case, the smooth shape of the roughness histograms, consisting of one main peak, without long tail-ends and plateaus, indicated the successful application of the painting systems using a spray gun [102]. The condition of the plate after examination of the experimental PU2 and the acrylic system is presented in Figs. 5.2a and 5.2b, respectively.

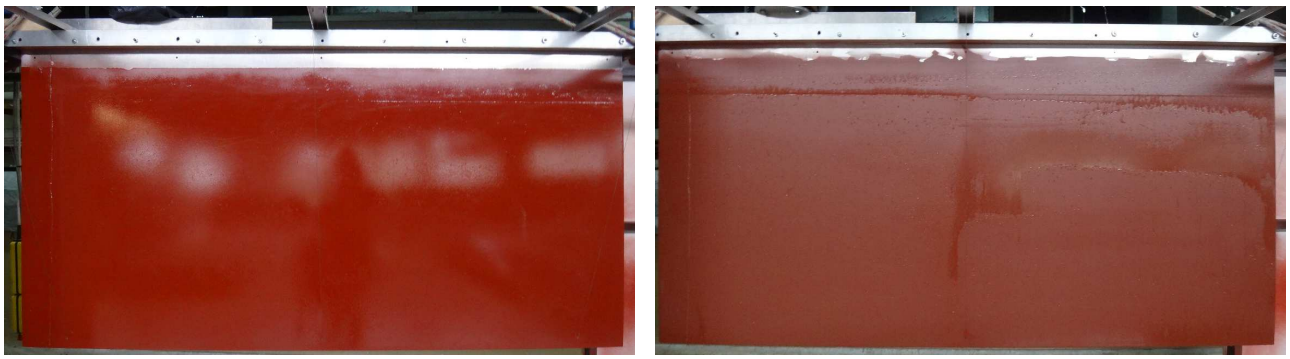

Figure 5.2: Plate painted with a) the experimental polyurethane (2) and b) the acrylic self-polishing copolymer painting schemes

5.3 Results and discussion

5.3.1 Plate painted with AF paints on the whole surface–Resistance results

The results for total resistance coefficient for the examined AF systems are presented in Fig. 5.3. It should be mentioned that all the presented points lay on the turbulent region. The measurements at 0.25 m/s and 0.5 m/s were omitted, since they corresponded to transitional rather than turbulent flow. With regard to the smooth plate, a curve similar to Schoenherr's line was used to fit the data.

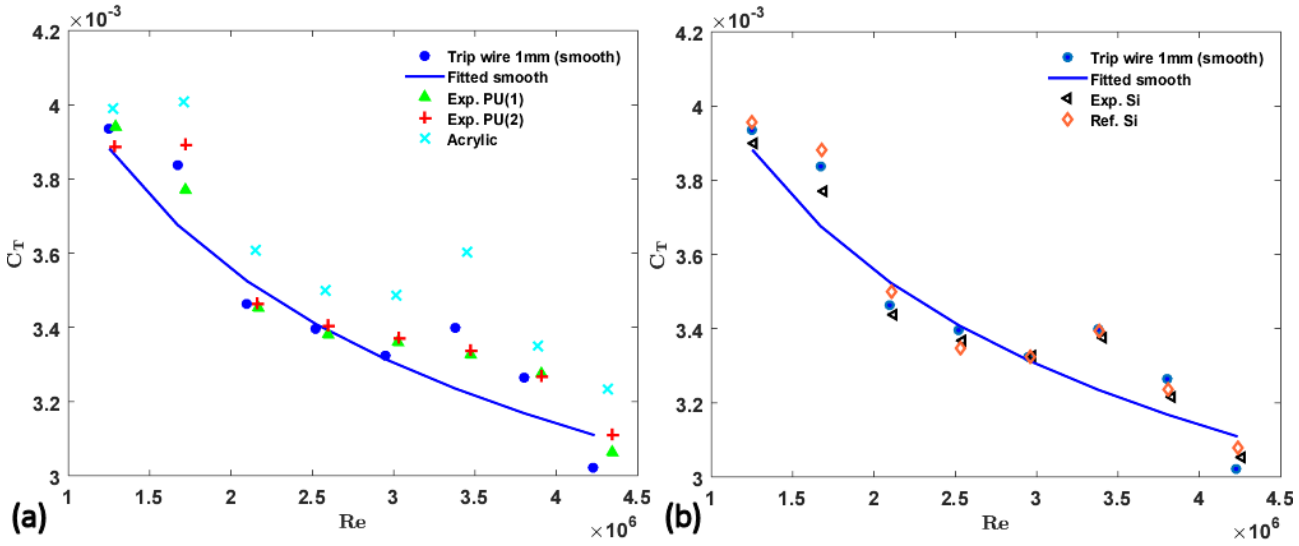

Figure 5.3: Total resistance coefficient versus Reynolds number for a) the polyurethane and acrylic based coatings and b) the silicone based coating systems (Uncertainty range for last six data:0.53%–1.50% for all conditions)

The resistance measurements of the polyurethane experimental systems indicated that hardly any effect in resistance was caused by any of the systems (Fig.5.3a). More specifically, Exp. PU1 formulation exhibited C_T values smaller than the unpainted plate at 1 m/s (-1.74%), 1.25 m/s (-0.31%), 1.5 m/s (-0.42%) and at 2 m/s (-2.15%). With regard to the Exp. PU2 paint, resistance values smaller than the unpainted condition were measured at 0.75 m/s (-1.23%) and at 2 m/s (-1.87%). Finally, the acrylic system exhibited resistance increase at the whole Reynolds range, which ranged from 1.42% at 0.75 m/s to 7.06% at 2.5 m/s.

The resistance measurements of the silicone systems revealed also a smoother nature, compared to the unpainted (smooth) plate (Fig. 5.3b). The biggest differences were recorded for the speed 1 m/s (-1.75%) and 2.25 m/s (-1.46%). On the other hand, at 2.5 m/s the coating exhibited resistance 1.03% higher than the unpainted plate. The reference silicone system exhibited smaller resistance than the smooth condition at 1.5 m/s (-1.44%), at 2 m/s (-0.19%) and at 2.25 m/s (-0.85%). At 1.75 m/s the resistance coefficient was the same as the smooth condition. The C_T defferences between each paint with the smooth condition are presented in Table 5.2.

From Table 5.2 it can be observed that the increase in total resistance coefficient of the AF paints, compared to the smooth condition, was rather low for most of the coatings. This is not the case for the acrylic system, though, for which the observed resistance increases could be considered as significant [107] for almost the whole Reynolds range. For the rest systems the highest positive increase was noticed for the highest Reynolds number and for the experimental PU1 system was 1.41%, for the experimental PU2 system was 2.92%, for the experimental silicone was 1.03%, while for the reference silicone was 1.91%. The highest increase in total resistance coefficient was obtained for the acrylic system and it was 7.06% (obtained at the highest Reynolds number). Even though all the AF coated surfaces exhibited the highest resistance at the highest Reynolds number, the roughness effect did not increase accordingly

Table 5.2: C_T differences [%] between painted and smooth condition, for all examined painting schemes

Velocity (m/s)	Exp. PU1	Exp. PU2	Acrylc	Exp. Si	Ref. Si
0.75	0.12	-1.23	1.42	-0.91	0.54
1.00	-1.74	1.44	4.43	-1.75	1.16
1.25	-0.31	0.01	4.22	-0.71	1.04
1.50	-0.42	0.25	3.05	-0.80	-1.44
1.75	1.13	1.41	4.94	0.12	0.00
2.00	-2.15	-1.87	5.94	-0.75	-0.19
2.25	0.38	0.15	2.64	-1.46	-0.85
2.50	1.41	2.92	7.06	1.03	1.91

with increasing Reynolds number, as has also been reported by Schultz [107]. This can be verified by the shape of the experimental curves presented in Fig. 5.1. Similar behavior has also been observed by Candries [102], during experiments on a 2.55 m flat plate painted with foul-release (FR) and self-polishing copolymer (SPC) painting schemes. The shape of the curve for the SPC painted plate in that study was even more similar to the curves obtained in the present work.

In order to come to safer conclusions with regard to the validity of the total resistance coefficient values for each painting system, the statistical differences were measured, according to the procedure followed in Chapter 4. It should be noted that the differences presented in Figs. 5.4– 5.6 are the absolute differences.

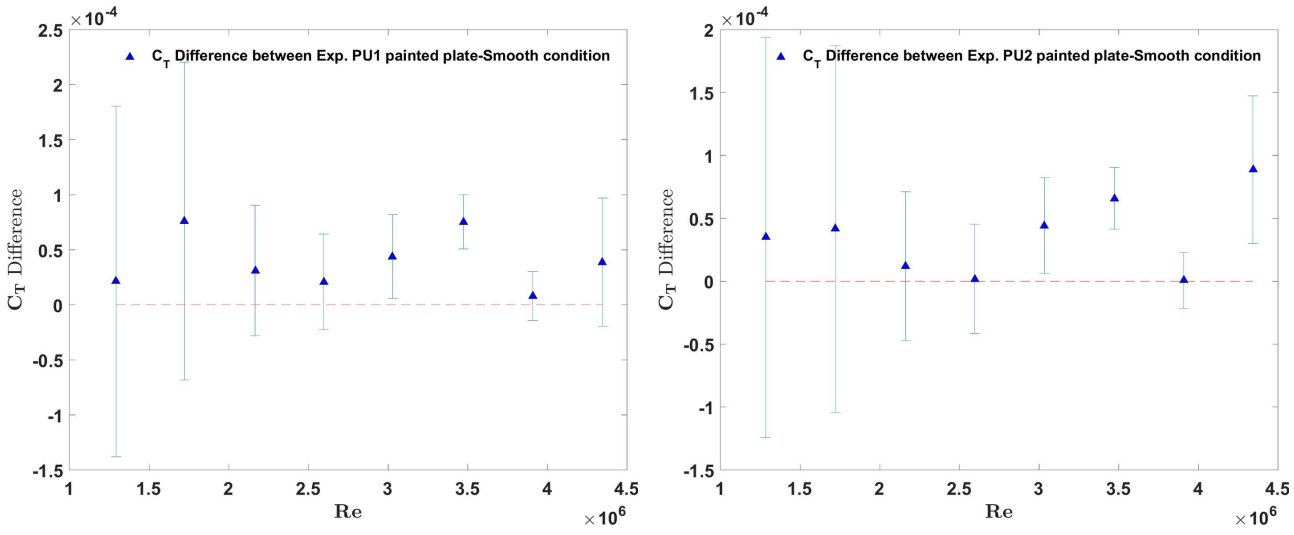

Figure 5.4: Absolute values of statistical differences between the total resistance coefficient of the smooth plate with the a) Exp. PU1 (uncertainty range: 32.53%–86.94%) and b) Exp. PU2 (uncertainty range: 37.30%–85.99%) painted conditions (Uncertainty ranges refer to the statistically significant differences.)

As can be seen from Figs. 5.4a and b, the statistically significant C_T values for the Exp. PU1 system were the values at 1.75 m/s (+1.13%) and 2 m/s (-2.15%). For the Exp. PU2 system, the values at 1.75 m/s (+1.41%), 2 m/s (-1.87%) and 2.5 m/s (+2.92%) could be

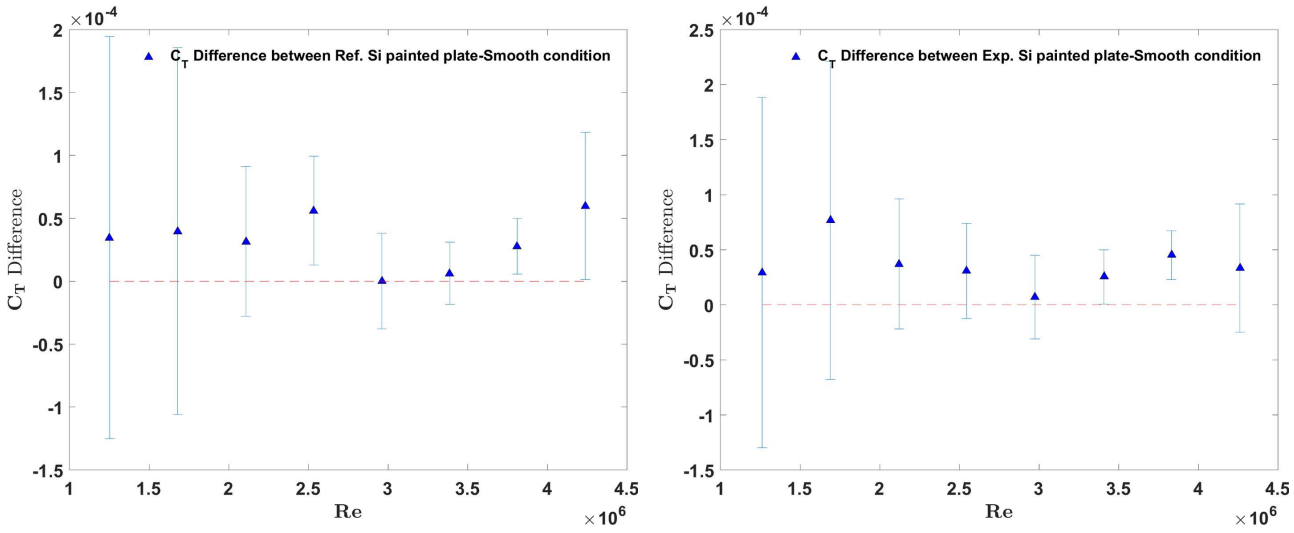

Figure 5.5: Absolute values of statistical differences between the total resistance coefficient of the smooth plate with the a) Ref. Si (uncertainty range: 76.93%–97.73%) and b) Exp. Si (uncertainty range: 48.94%–97.18%) painted conditions (Uncertainty ranges refer to the statistically significant differences.)

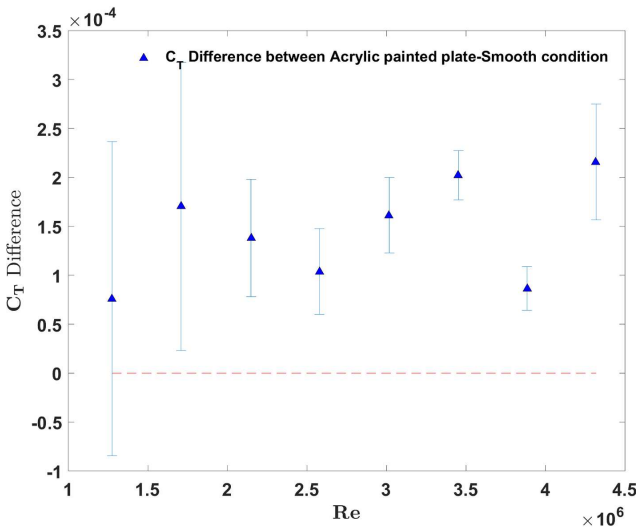

Figure 5.6: Absolute values of statistical differences between the total resistance coefficient of the smooth plate with the acrylic painted condition (uncertainty range: 12.42%–86.44%) (Uncertainty ranges refer to the statistically significant differences.)

considered as real experimental values and not as experimental error. A closer look at both figures reveals that the stastically significant values follow the same trend for the polyurethane systems, with the Exp. PU2 system exhibiting an extra value at 2.5 m/s. With regard to the silicone systems, the Ref. Si painted plate exhibited C_T values beyond the experimental error at 1.5 m/s (-1.44%), 2.25 m/s (-0.85%) and 2.5 m/s (+1.91%) (Fig. 5.5a), whereas the Exp. Si at 2 m/s (-0.75%) and 2.25 m/s (-1.46%) (Fig. 5.5b). Finally, the acrylic painted plate exhibited statistically significant values for almost all speeds, except for the value at 0.75 m/s, ensuring that the rest of the measurements were actually different from the smooth condition.

The differences observed between the different painting systems were quite small (except for the acrylic system) and were very close to the values of the unpainted condition. The generally

good hydrodynamic characteristics of the FR silicone systems are usually attributed to the inherent surface properties of these paints, which exhibit a longer surface waveform [107]. The better hydrodynamic behavior of the FR systems compared to the SPC technology observed in the present study has also been reported by Candries [102]. Apparently, the large mean roughness value of the SPC acrylic system compared to the polyurethane and silicone systems could play a major role in this finding. Moreover, the leaching nature of the SPC formulation (constantly altering the surface texture) and probably the specific surface texture of the SPC system, could also account for the large C_T differences compared to the rest of the painting systems.

5.3.2 Roughness function calculation

In order to calculate the roughness function for each of the coating systems it is important for the resistance in the painted condition to be larger than the smooth condition. The results from the comparison of C_T values between the two conditions (smooth and painted) did not reveal a stable pattern, rather a behavior exhibiting fluctuations around the smooth condition.

However, comparison of the experimental data for each painted condition with the fitted smooth curve (blue line in Fig. 5.3) would result in an average increase of 3.01% for the Exp. PU1 system, 3.97% for the Exp. PU2 system, 1.27% for the Exp. Si, 2.76% for the Ref. Si and finally 6.15% for the acrylic system (all percentages refer to statistically significant differences between the fitted smooth condition and the individual C_T points of each painted ccondition). Hence, the comparison of the experimental data with the smooth fitted line results in a mean resistance increase for all the painted surfaces, without altering the observations made in the previous section, with regard to the hydrodynamic characteristics provided by each paint category. Under this assumption, the statistically significant differences for each painted condition with the smooth plate are presented in Figs. 5.7–5.9.

For the calculation of the roughness functions, the overall method of Granville [101] was applied. The roughness functions were calculated for the points in painted condition which exhibited statistically significant differences with the smooth condition and did not exhibit large error bars. However, it should be noted that statistically significant differences were calculated also for points with smaller C_T than the smooth condition, as is the case of the 1.5 m/s data for the reference silicone paint (Fig. 5.8a) and the 1.25 m/s data for the exprimental silicone paint (Fig. 5.8b). For the calculation of the roughness function, though, only the points with larger C_T values than the smooth condition were used.

The initial calculation of the roughness Reynolds number was based on the measured R_a values (Table 5.1). However, in order to examine correlation with the Colebrrok–type roughness function, which commonly describes antifouling coatings, a multiplication factor was applied, which was not the same for all painting systems. More specifically, the value of $3.48R_a$ would lead to a variance equal to R^2=0.900 for the Exp. PU1 system, the value $2.48R_a$ would lead to a variance equal to R^2=0.886 for the Exp. PU2 system, with a value equal to $2.44R_a$ for the acrylic system the Colebrook–type function would match the data with a variance equal to

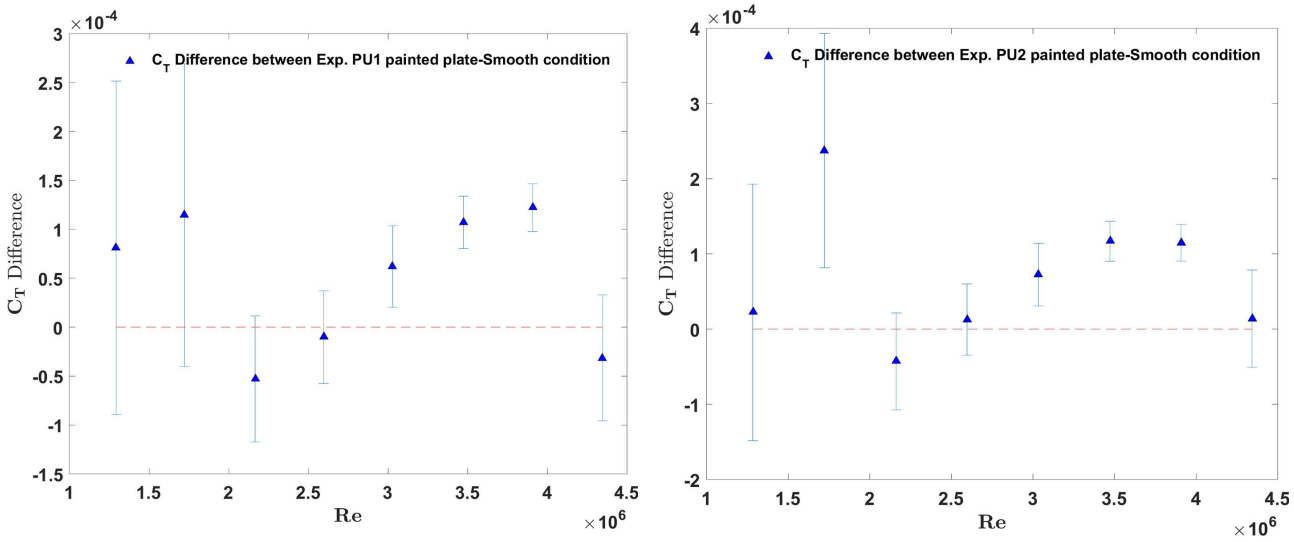

Figure 5.7: Statistical differences between the total resistance coefficient of the fitted smooth plate with the a) Exp. PU1 (uncertainty range: 19.86%–67.05%) and b) Exp. PU2 (uncertainty range: 21.16%–65.67%) painted conditions (Uncertainty ranges refer to the statistically significant differences.)

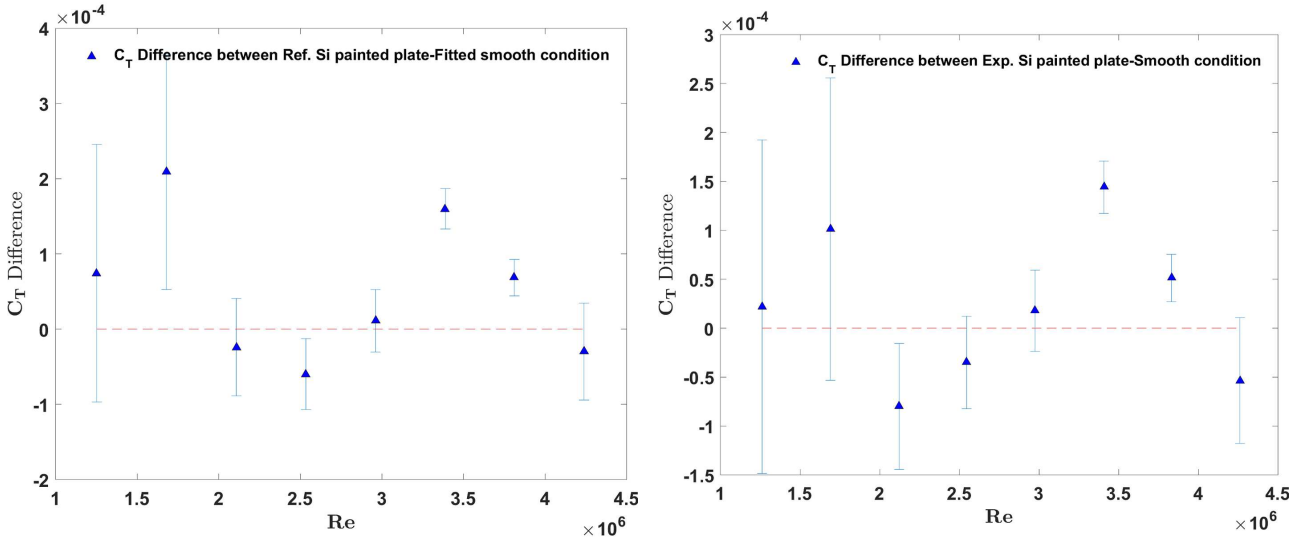

Figure 5.8: Statistical differences between the total resistance coefficient of the smooth plate with the a) Ref. Si (uncertainty range: 16.77%–78.96%) and b) Exp. Si (uncertainty range: 18.61%–80.43%) painted conditions (Uncertainty ranges refer to the statistically significant differences.)

0.724, for the Ref. Si painted plate the value of $3R_a$ would lead to R^2=0.622, whereas for the Exp. Si painted plate the value of $1.63R_a$ would lead to R^2=0.711. The calculated roughness functions are presented in Fig. 5.10.

The roughness functions exhibited very good correlation with the Colebrook-White law, for most of the painting systems, indicating that the appropriate roughness length scale could consist of only one scaling parameter, such as the average roughness (R_a) or the peak to trough roughness height (R_t) [95]. The best correlation was attained for both experimental polyurethane formulations, followed by the acrylic system, the experimental silicone system and finally the reference silicone system, for which a variance equal to 62.2% was obained.

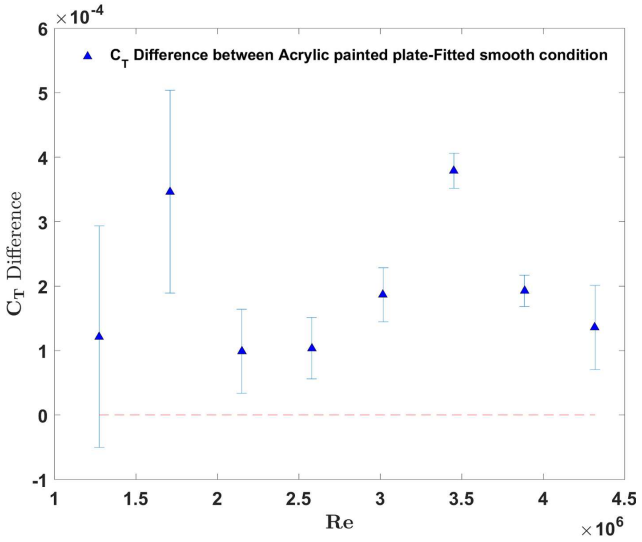

Figure 5.9: Statistical differences between the total resistance coefficient of the smooth plate with the acrylic painted condition (uncertainty range: 7.19%–65.88%) (Uncertainty ranges refer to the statistically significant differences.)

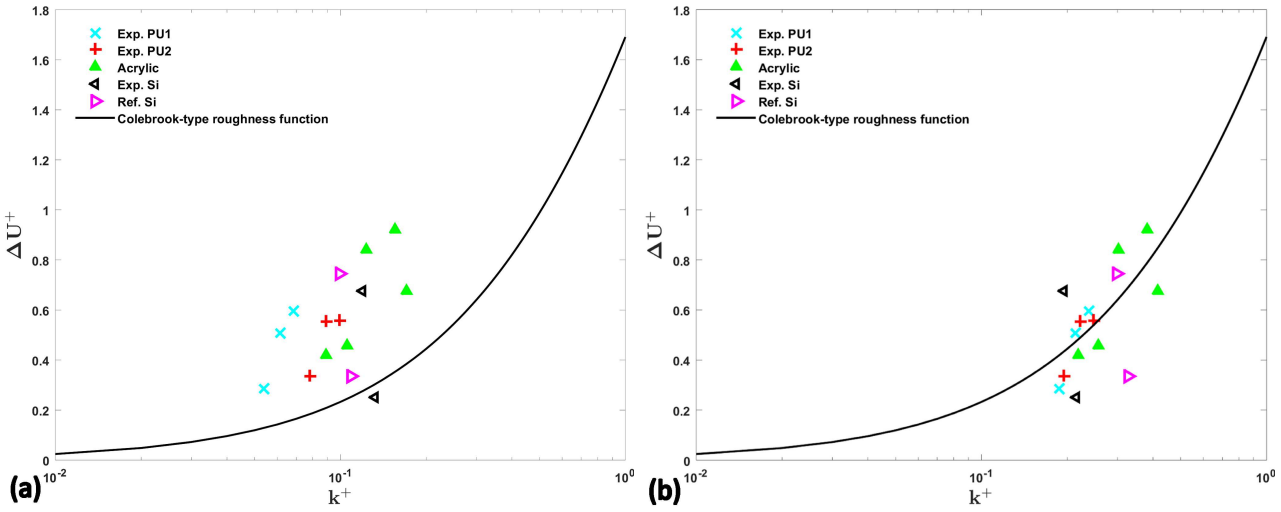

Figure 5.10: Calculated roughness functions for all painted systems for the points with C_T larger than the smooth condition; a) original position of points and b) after transfer on the Colebrook–type roughness function (mean overall uncertainty in ΔU^+: Exp. PU1:±0.162, Exp. PU2:±0.114, Acrylic:±0.246, Exp. Si:±0.135, Ref. Si:±0.095)

For the rest of the systems, the Colebrook–type roughness function would fit the experimental roughness functions with a variance larger than 71.1%.

As can be seen from Fig. 5.10, the points referring to the roughness function of the silicone systems exhibited variarions, with respect to the polyurethane systems, hence, a comparison would be hard among the systems. However, these silicone systems are expected to exhibit Colebrook-type behavior [130], as well. In addition, the shape of the roughness function for the acrylic and the polyurethane-based systems has also been reported elsewhere [130].

5.3.3 Effect of fouling on the resistance of a flat plate

The aim of this study was to examine the increase in resistance caused by the attached foulers first in laboratory and then in ship scale. To this purpose towing tank tests on the flat plate covered with 5%, 10% and 15% artificial fouling were performed. Each artificial fouling unit had dimensions 10 cm×10 cm×4 mm and it was made of ABS plastic. The goal of this study was to represent as real fouling conditions as possible. In order to achieve this task, the fouling schemes observed on painted specimens of dimensions 10 cm×10 cm×6 mm, during their 1 year static immersion in Elefsis Gulf were examined and a representative fouling pattern was created. The field tests in Elefsis were performed for all the antifouling systems presented so far in this Chapter and are presented in more detail in Chapter 6. The fouling condition of two specimens covered with high density fouling is presented in Fig. 5.11.

Figure 5.11: Fouling condition of a) Exp. PU1 painted specimen after 8 months and b) Ref. Si painted specimen after a 12-month static immersion in Elefsis Gulf

In order to design the artificial fouling unit, first some representative foulers were selected, which are presented in Fig. 5.12a. These foulers were observed on almost all the painting systems examined for 1 year in Elefsis, hence they could be found on the hull of a ship remaining idle in Elefsis. These foulers were 3D scanned and their geometry was digitized to an .stl file. Then, the artificial unit was designed in Rhinoceros 5 with dimensions 10 cm×10 cm×4 mm (Fig. 5.12b) [131], with the selected height being representative of the height of the observed macrofoulers, such as barnacles. At the final stage, the designed sample was printed in a Makerbot Replicator 2X 3D printer.

The plate with 3 lines of fouling (15% coverage) is presented in Fig. 5.13. The fouling lines were positioned at the aft-part of the plate, while at the fore part a turbulence stimulator of 1.128 mm in diameter was placed at distance equal to 5% of plate's leading edge. Each artificial fouling unit was glued onto the plate. In order to reduce the form resistance caused by the

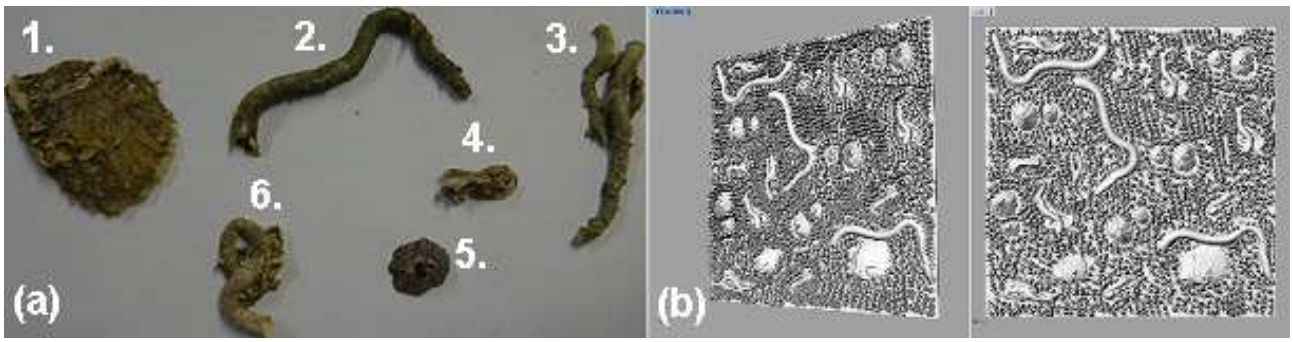

Figure 5.12: a) Representative foulers selected from Elefsis field test for creation of artificial fouling unit; 1) clam, 2),3),6) various sizes of *polychaetes* tubes, 4) calcareous tube of a *serpulid*, possibly the *serpulinae* sub-family and 5) barnacle; b) the artificial fouling unit in Rhinoceros 5

height of the samples (4 mm), a wedge was placed in front of the fouling samples, with an angle equal to 30°, a height equal to 4 mm and a length equal to 6.93 mm. The width of the wedge was equal to the width of the plate. Some first results regarding the total resistance values (R_t) for each coverage are presented in Fig. 5.14. **Detailed analysis of the results is the aim of future work**.

Figure 5.13: Plate covered with 15% artificial fouling at the aft-part

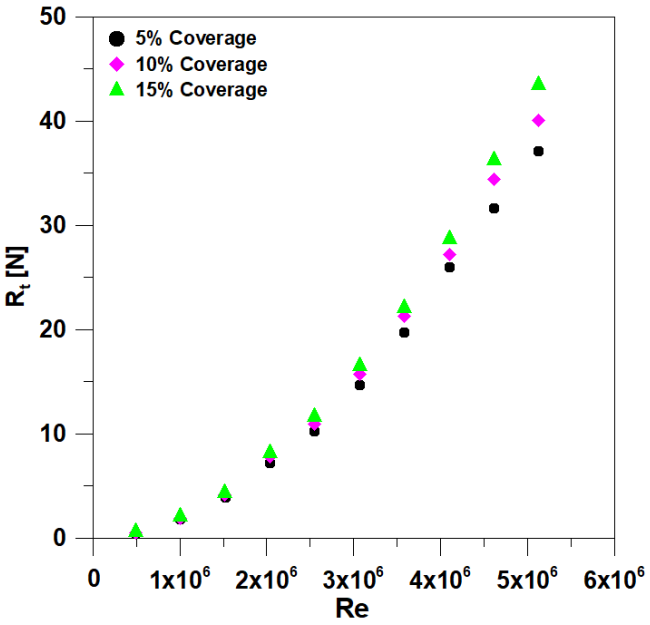

Figure 5.14: Total resistance results for all the coverages examined with artificial fouling

5.4 Conclusions

- The silicone and polyurethane formulations exhibited similar hydrodynamic behavior, fluctuating around the smooth condition, whereas the acrylic system exhibited the highest resistance increase of all.
- The roughness functions exhibited very good correlation with the Colebrook-White law, for most of the painting systems, indicating R_a as the appropriate roughness length scale.
- Best correlation with the Colebrook-type roughness function was attained for the experimental polyurethane formulations, followed by the acrylic, the experimental silicone and, finally, the reference silicone system.

Chapter 6

Field tests of commercial and experimental antifouling paints in Elefsis Gulf

Abstract

In the present Chapter, all the painting systems examined throughout this thesis (reference silicone, acrylic-based, experimental silicone, experimental polyurethane 1, experimental polyurethane 2 and anticorrosive polyurethane) were investigated in terms of antifouling performance. To this purpose, static immersion tests were performed in Elefsis Gulf for one year. Six (6) specimens per painting system were immersed (for the polyurethane system three (3) specimens were immersed and the examination was performed for six months). All systems were applied on top of a Grade A steel substrate. Every two months, one specimen from each painting system was removed from site and examined the laboratory, in terms of fouling density, types of foulers, physical damage, optical and mechanical characteristics and electrochemical behavior. The specimens that were removed from site were not re-immersed. The acrylic-based system exhibited only incipient fouling throughout the test, but its self-polishing nature caused intense erosion. The reference silicone system exhibited variety of foulers, which were easily detached, causing, however, extensive digging effect, especially in the summer period (June-September). The experimental silicone system exhibited improved characteristics overall compared to its commercial counterpart. The experimental polyurethane systems would be unsuitable for antifouling purposes, exhibiting intense fouling, already from the first months of immersion, which was strongly adherent. In terms of electrical properties, generally all systems exhibited a capacitive response. Only the reference silicone system after 10 months of immersion could be described by a Randles circuit, exhibiting corrosion. In conclusion, the experimental silicone formulation was proven to be the most efficient system, since it exhibited the best antifouling and physical damage behavior in the long run, compared to the rest of the systems, quite stable optical and mechanical characteristics and hardly any electrochemical degradation.

6.1 Introduction

Field tests are considered as the most important tests when examining antifouling paints, because the painting systems are examined under real conditions, that is into the marine environment. The paints are then ranked, according to their fouling efficiency and physical condition after the end of the test [132]. Field tests can be either static or dynamic. In the former case, the specimens are immersed in site and remain still throughout the entire testing period, until they are removed from site and examined in the laboratory. The latter case could include stripes of the paint of interest directly onto the ship hull, in order to assess its effectiveness against the fouling communities encountered during the ship route. Another type of dynamic tests includes painted specimens subjected to erosion using seawater of high velocity (ASTM D 4938 [133]) or using painted panels adjusted on a rotating drum, being immersed in seawater (ASTM D 4939 [134]). These tests simulate the erosion conditions encountered during ship voyaging. Static and dynamic tests could also be performed in succession. First, the severity of the fouling and types of foulers are estimated and then the amount of fouling removed under shear forces in seawater is assessed [135]. The former test simulates a ship in port, while the latter a ship in motion [136].

The main advantage of the static tests is that the paint is allowed to become heavily fouled without disturbance. This means that the paint may suffer severe fouling, so its performance is estimated in the most difficult conditions. For this reason, water temperature and salinity are crucial when selecting an immersion site [137]. Short-term static tests (less than a month) with a large number of replicates could also be performed in the 'proof-of-concept phase' of new products, for preliminary review of their antifouling and mechanical integrity in the field [138]. Short term static tests (45 days) have been performed by Abdel-Gaber *et al.* [139], during investigation of a vinyl chloride-vinyl acetate copolymer based paint, incorporating Lupine seeds extract, in Egypt. The authors reported the antifouling character of ZnO, when used as a pigment in the paint, in contrast to TiO2 pigment, which enhanced fouling growth. Five-year tests have been performed on "flexible" (hardness 40 Shore A) and "rigid" (hardness 90 Shore A) polyurethane paints in Brest Estuary, France by Davies and Evrard [43]. The authors observed that the fouling layer could be easily removed when wet, however, barnacles were more strongly attached and have dug the paint. Static tests can be performed in parallel in many places of the world, in order to examine the efficiency of a specific antifouling paint under different climate, salinity and pollution conditions.

Another advantage of the static tests is that they are much easier to perform if some precautions are followed. The precautions refer to factors such as the safety of the immersion site, for instance if it is exposed to heavy winds and waves, if it is located in open sea or in contact with the sea, or, finally, if there is a possibility that the specimens hit one another or the installation (e.g. a wall). Also, the specimens should be immersed in more than 0.5 m depth but no more than 3 m (as described in ASTM D 3623 standard for shallow submergence [140]) and be rigidly and tightly hung. Generally, static tests are easier and cheaper to perform than dynamic tests.

Either static or dynamic, field tests constitute the basic method for assessing the efficacy of an antifouling coat. They provide an insight into the paint's behavior against micro and macrofoulers, which in turn provides valuable knowledge for continuous improvement of the antifouling technology, in terms of fouling defense and environmental protection.

6.2 Experimental methods and materials

6.2.1 Painting systems examined

All the commercial and experimental systems were studied in the field. The systems are presented in Table 6.1 (also presented in Abstract). All systems were multilayered and applied on top of a Grade A steel substrate of dimensions 100 mm × 100 mm × 6 mm. The total thickness of the systems was around 600 μm. Application of the painting systems was performed by expertice technicians in Estaleiros Navais de Peniche in Portugal. The ready painted samples were then sent to NTUA for examination using the various methods presented in the present study.

Table 6.1: Painting systems examined in the field

Painting system	Abbreviated name	Characteristics/ Type of action	Biocides
Silicone-based	Ref. Si	Commercial/ Foul-release	No biocides
Acrylic-based	Acrylic	Commercial/ Self polishing Copolymer(SPC)	5%≤Zineb≤10% 10%≤Cu_2O≤25%
Silicone-based	Exp. Si	Experimental	0.56% immobilized Econea
PU-based	Exp. PU (or Exp. PU1)	Experimental	2% immobilized Econea
PU-based	Exp. PU2	Experimental	Mixture of biocides
PU-based	PU	Newly developed anti-corrosive	No biocides

6.2.2 Description of field tests in Elefsis

The field tests were conducted in Elefsis Gulf, according to the ASTM D-3623 standard for shallow submergence. The site of immersion is presented in Fig. 6.1, while its climatic and geographical characteristics are presented in Table 1. Six specimens per AF system and three from the anticorrosive system were submerged in the site. Every two months one specimen per system was removed from site and examined in the laboratory, while the rest of the specimens were photo recorded. The specimen that was removed from site was not re-immersed. The last specimen from each AF painting system was removed after one year of exposure, while from the anticorrosion system after six months.

Figure 6.1: The immersion site in Elefsis

Table 6.2: Elefsis exposure site characteristics

Country	City	Lat./Lon.	Climate	Exposure Type
Greece	Elefsis	38°3'18"N 23°32'14"E	Temperate	Specimens hung using a 2mm thick trawl

The ecosystem in the immersion site was a channel in communication with the open sea, with temperate climate. The choice of this specific site was made after detailed considerations and designing of the field test. In order for a static field test to succeed, there are some parameters that need to be fulfilled: a) the area to be in contact with the open sea (if not a site at open sea is offered), b) to be protected from heavy winds and waves, c) the structure of immersion to be rigid enough to hold the panels and d) the structure of immersion to be as wide as possible in order to allow a safe distance between the panels. In other words, there should be some control and protection of the whole process, in order to guarantee the safety of the samples and that they are not going to experience any physical damage caused by non experimental factors.

All specimens were immersed in 2.5 m depth (as mentioned in ASTM D 3623, shallow submergence refers to an immersion depth ranging from 0.3 m-3 m) hung vertically by a 2 mm thick trawl. The retrieved panels were transferred to the laboratory into containers filled with water from site, in order to keep the attached foulers alive for longer and be able to capture them during stereoscopic observation.

6.2.3 Biofouling assessment

Biofouling assessment of the retrieved specimens was performed by calculating the fouling resistance index (FR), combining both ASTM D 3623 and ASTM D 6990 standards. More specifically, as mentioned in paragraph 11.1.3 of D 6990-03 guideline, the fouling resistance should be calculated by subtraction of the fouled area by 100, when macrofouling is present. However, in standard ASTM D 3623, a penalty of 5% is proposed, when macrofouling appears on the specimen. Hence, in the present investigation, all the macrofoulers were subtracted from 95%, according to the covered area and not by separating colonial and solitary forms (as proposed in ASTM D 3623). This procedure has also been suggested by Redfield *et al.* [141].

With regard to the biological slime, it may refer to germinal fouling, such as algal spores, diatomaceous or bacterial layers. Generally, in ASTM D 3623 standard the presence of slime does not affect the fouling rating. Only incipient fouling causes a penalty of 5%. In ASTM D 6990 standard, however, it is reported that a painted surface free from macrofouling but with microfouling, referred as adherent slime, shall be ranked with 99%. In the present study, the slime was treated as having no impact on the fouling rating.

As per the presence of silt, in ASTM D 6990 silt refers to sedimentary material consisting of mineral particles, being in size between those of sand and clay. It will be observed throughout this investigation that some specimens were covered with sand, clay and/or silt, which was referred as silt. The silt coverage percentage was reported before water rinse of the specimens, as proposed in ASTM D 6990 standard practice. Whenever possible, the surface covered by larger macrofoulers was excluded from silt coverage calculation.

The fouling communities were identified through visual examination via a Leica MZ6 stereoscope. Measurements of characteristic lengths (e.g. tubeworm diameters) were performed with the Leica Application Suite (LAS) software platform. The observed species were mainly slime and algae, as regards the flora, and barnacles, bryozoans (encrusting or/and filamentous), serpulid tubeworms, mussels and amphipods, as regards the fauna. Characteristics of these organisms have been presented in the work of Almeida *et. al* [126]. With regard to the amphipods (which were also observed in the present study), in ASTM D 6990 standard it is stated that the surface coverage percentage by mud tube-building amphipods shall be reported but not included in the fouling rating.

Classification and rating of physical deterioration (PDR) was based on guidelines proposed by ASTM D 6990-05 standard. Finally, the overall performance rating would be the smallest rating between the fouling resistance rating and the physical damage rating.

According to standards ASTM D 3623 and D 6990, a negative control is suggested to be used for comparison. The negative control is an inert surface susceptible to heavy fouling and indicates the degree of fouling expected if no AF protection is provided. The polyurethane coating system, which was anticorrosive, was used as a negative control for the experimental polyurethane antifouling formulation, Exp. PU1. Apart from the negative control, the same standards suggest the use of a reference, which is an AF paint of known efficiency, which could also be used for comparative purposes with the systems under investigation. For the present

study, the commercial silicone AF system could serve as a reference for the experimental silicone system.

Finally, a 1 cm distance from the specimens' edges should be kept when examining the fouling density, because the edges are more prone to physical damage. Whenever possible, this guideline was followed.

6.2.4 Water quality measurements

Water quality measurements were conducted every two months. Along with the samples that were retrieved from site, water samples were also collected and analyzed in the laboratory. Conductivity measurements were performed with a Thermo Scientific Orion 3 Star conductivity benchtop meter and pH measurements were performed with a Metrohm 744 pH meter. Finally, the volumetric chloride content of the seawater was calculated through titration, according to the Mohr method.

6.2.5 Electrochemical examination

Coating degradation during immersion was evaluated by electrochemical impedance measurements. EIS measurements were performed in a three electrode flat cell using the coated specimen as a working electrode, a platinum mesh as counter electrode and a saturated calomel electrode (SCE) as a reference, similarly to the setup presented in Chapter 3. The electrolytic solution consisted of 3.5% NaCl in naturally aerated deionized water. Measurements were performed at room temperature. The total exposed area was 10.75 cm^2. A Solatron 1260 impedance/ phase gain analyzer was used, combined with a PAR 263A potentiostat. The perturbation amplitude was ± 10 mV. All measurements initiated at 10^5 Hz, with 10 points per decade. The impedance spectra were obtained via the Zplot softwate.

6.2.6 Coating hardness measurements

Hardness measurements were performed for all painted samples before and at the end for their immersion period. These measurements reflect the hardness of the coat (or the vehicle), that is resistance to deformation. Five measurements per sample were performed, located at a distance of 2 cm from one another. The measurements were performed according to standard ISO 1522 [142], based on the König pendulum damping test. Pendulum damping measurements were performed with an Erichsen R299/300 König pendulum.

6.2.7 Physical properties measurements

Gloss measurements were performed with a HORIBA gloss checker, the IG-331 model, with measurement capabilities at 20° and 60°. Since the primary aim of an antifouling system is protection, rather than aesthetic appearance, these coatings do not have a measurable gloss at 20°, hence all gloss measurements were taken at 60°. This means that the glossmeter will transmit a concentrated beam of light at 60° and measure the percent of the beam reflected.

The discoloration index (DE) of the specimens was determined using the colorimetry technique, according to the CIE L*a*b color model. Each one of the L, a, b represents a different color axis. The L axis is for lightness, the a for red (if positive)-green (if negative) and, finally, the b axis represents yellow (if positive)-blue (if negative). Optical examination is very important, since, if we know each coating's chemical composition and the degree of discoloration, we could assess whether any chemical alterations have commenced on the painted surface.

6.3 Results and discussion

In the present section, the results from the fouling assessment and physical damage of the Ref. Si and Acrylic painted specimens are presented together, since the specimens painted with these coatings were immersed simultaneously. Similarly, the antifouling performance of the Exp. Si, Exp. PU1 and PU painted specimens is presented, which were immersed simultaneously in Elefsis. Finally, the fouling analysis of the Exp. PU2 painted specimens is presented.

6.3.1 Commercial Silicone and Arcylic AF systems

6.3.1.1 After 2 months of immersion

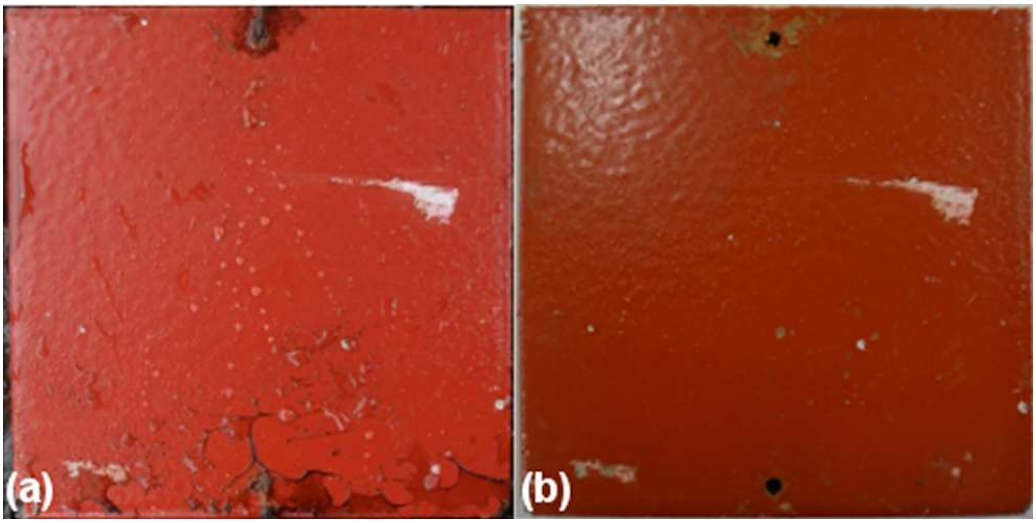

Figure 6.2: Surface condition of Ref. Si specimen from Pair 1 that remained immersed for 2 months in Elefsis: a) after 2 months, during removal from site and b) after gentle cleaning with rinsing water

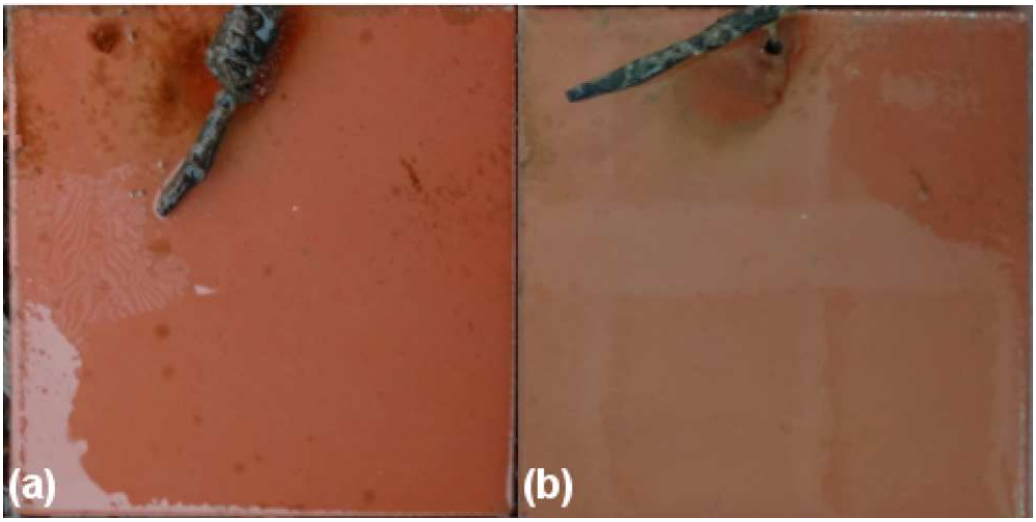

Figure 6.3: Surface condition of Acrylic specimen from Pair 1 that remained immersed for 2 months in Elefsis: a) after 2 months, during removal from site and b) after gentle cleaning with rinsing water

Table 6.3: Antifouling performance calculation of Ref. Si specimen from Pair 1 (2 months immersion), according to ASTM D 3623 and ASTM D 6990 guidelines

Fouling Examination	Ref. Si
Fouling on surface	No silt, slime, algal spores or other micro or macro fouling was observed.
Fouling Resistance (F.R.) [%]	100
Physical Condition of Antifouling Film	• The specimen had physical damage before immersion; this is why it was the first to be immersed, in order for the damage not to affect the fouling rating. • Discoloration index (DE) before immersion: 3.21 • DE after 2 months immersion: 3.11 • König pendulum hardness: 31.2 • 60° gloss before immersion: 11 • 60° gloss after 2 months immersion: 11.5
Physical Damage Rating (P.D.R.) [%]	100
Overall Performance (O.P.) [%]	100

Table 6.5: Antifouling performance calculation of Acrylic specimen from Pair 1 (2 months immersion), according to ASTM D 3623 and ASTM D 6990 guidelines

Fouling Examination	Acrylic
Fouling on surface	Only slime was apparent, especially on the upper left side of the specimen (6.5%).
Fouling Resistance (F.R.) [%]	100
Physical Condition of Antifouling Film	• No physical damage was caused. • The specimen exhibited discoloration which is attributed to the self-polishing nature of the paint. • Discoloration index (DE) before immersion: 0.70 • DE after 2 months immersion: 9.46 • König pendulum hardness: 69.6 • 60° gloss before immersion: 14 • 60° gloss after 2 months immersion: 3.25
Physical Damage Rating (P.D.R.) [%]	100
Overall Performance (O.P.) [%]	100

As can be seen from Tables 6.3 and 6.5, no physical damage caused by fouling was observed on any of the examined specimens. With regard to the optical characteristics of the paints, the discoloration index (DE) values refer to the difference between the color of each examined specimen and a reference that serves as a calibration for all the subsequent measurements. For every paint category examined in the present investigation a different color reference has been saved in the colormeter.

Discoloration was more apparent on the acrylic-based specimen, due to its leaching nature, which makes the acrylic matrix to become depleted from biocides and pigments. This leaching nature was also apparent as chalking (ASTM D 4214 [143]) before immersion, which was ranked as No. 3, according to the TNO method. This characteristic of the acrylic paint justifies the abrupt gloss drop after 2 months of immersion. On the contrary, the foul-release silicone system exhibited stable characteristics in terms of color and 60° gloss after 2 months of immersion, implying that it was hardly affected by the experiment. Finally, the König pendulum hardness measurements revealed the much harder nature of the acrylic vehicle, compared to the elastomeric silicone formulation.

6.3.1.2 After 4 months of immersion

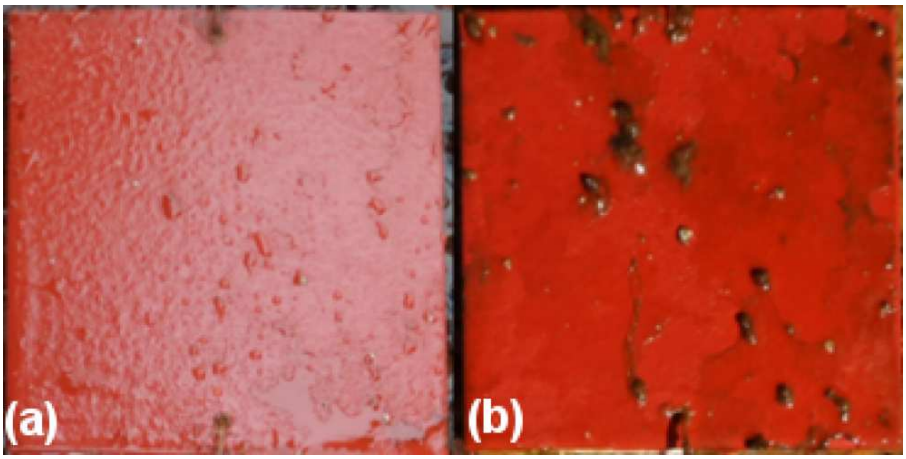

Figure 6.4: Surface condition of Ref. Si specimen from Pair 2 that remained immersed for 4 months in Elefsis: a) after 2 months and b) after 4 months, when it was removed from site

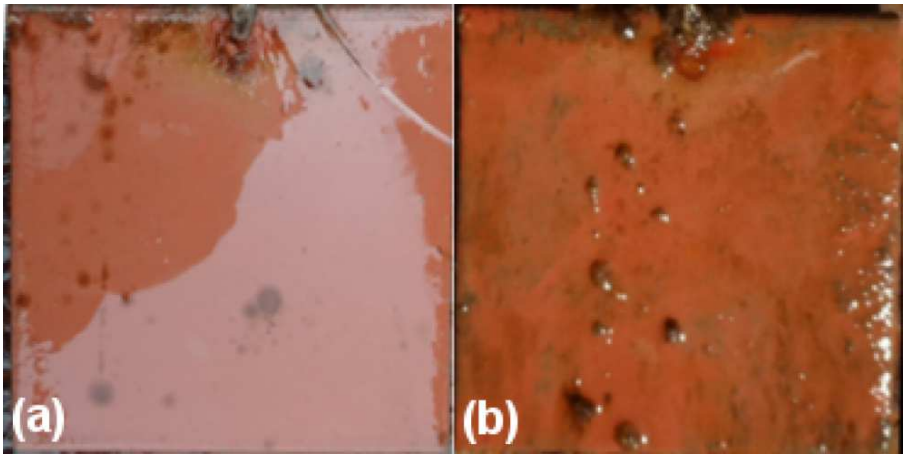

Figure 6.5: Surface condition of Acrylic specimen from Pair 2 that remained immersed for 4 months in Elefsis: a) after 2 months and b) after 4 months, when it was removed from site

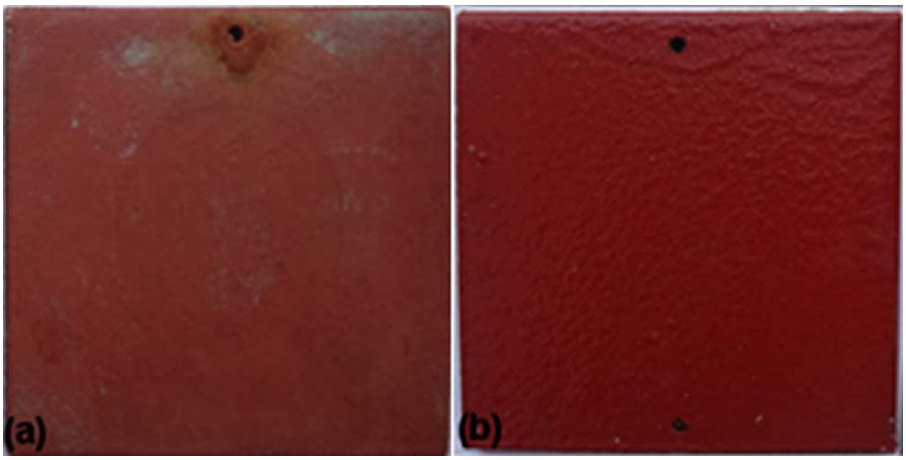

Figure 6.6: Surface condition of a) Acrylic and b) Ref. Si specimens from Pair 2 after surface cleaning with rinsing water in the laboratory

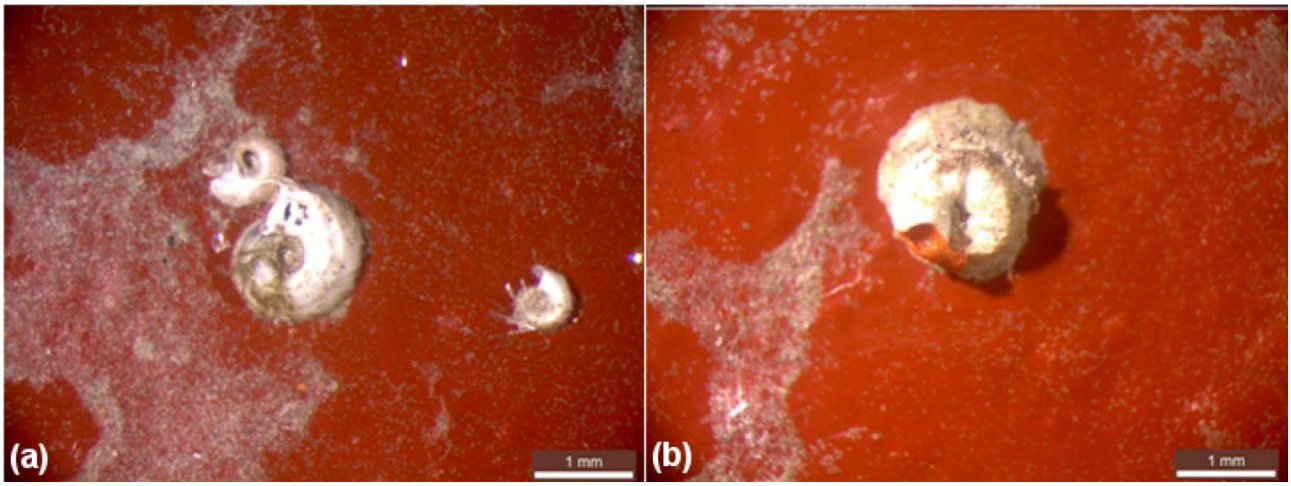

Figure 6.7: Stereoscopic observation of Ref. Si specimen after 4 months of immersion in Elefsis with samples of spirorbinae attached on the coated surface; a) dextral and sinistral and d) a dextral spirorbis with ascending coiling

Table 6.7: Antifouling performance calculation of Ref. Si specimen from Pair 2 (4 months immersion), according to ASTM D 3623 and ASTM D 6990 guidelines

Fouling Examination	Ref. Si
Fouling on surface	Polychaetes (PC)- *Spirorbinae*: 29, diameter 1–4 mm Total area: A=181.43 mm^2 Silt: 60%, light layer
Fouling Resistance (F.R.) [%]	95-1.81=93.19
Physical Condition of Antifouling Film	• Slight digging effect caused by 6 individuals of total surface equal to: 13.14 mm^2 (0.1314%) • DE before immersion: 2.65 • DE after 4 months immersion: 2.32 • König pendulum hardness: 25.8 • 60° gloss before immersion: 17 • 60° gloss after 4 months immersion: 18.25
Physical Damage Rating (P.D.R.) [%]	100-(0.1314)≈99.87
Overall Performance (O.P.) [%]	93.19

Table 6.9: Antifouling performance calculation of Acrylic specimen from Pair 2 (4 months immersion), according to ASTM D 3623 and ASTM D 6990 guidelines

Fouling Examination	Acrylic
Fouling on surface	PC- *Spirorbinae*:3, mean diameter: 1.67 mm Total area: A=6.57 mm^2 Light layer of slime and silt uniformly covering the surface (81%)
Fouling Resistance (F.R.) [%]	95-0.066≈94.93
Physical Condition of Antifouling Film	• Some discoloration, arising from the self-polishing nature of the paint. It was not considered as physical damage. • DE before immersion: 0.6 • DE after 4 months immersion: 8.52 • König pendulum hardness: 37.6 • 60° gloss before immersion: 17 • 60° gloss after 4 months immersion: 3.25
Physical Damage Rating (P.D.R.) [%]	100
Overall Performance (O.P.) [%]	94.93

With regard to the physical damage of the paints, slight digging was caused on the silicone specimen by 6 of the 10 *spirorbinae*, possibly due to the soft nature of the specific system. The system retained its gloss and color characteristics after 4 months of immersion, while the hardness measurements revealed once more its soft nature. Wih regard to the acrylic specimen, no digging or other kind of physical damage was observed. In terms of hardness, the present specimen was found softer (37.6), compared to the hardness value (69.6) after 2 months of immersion. However, since the examined specimens are different, it is possible that some differences exist, which could arise from the painting procedure.

6.3.1.3 After 6 months of immersion

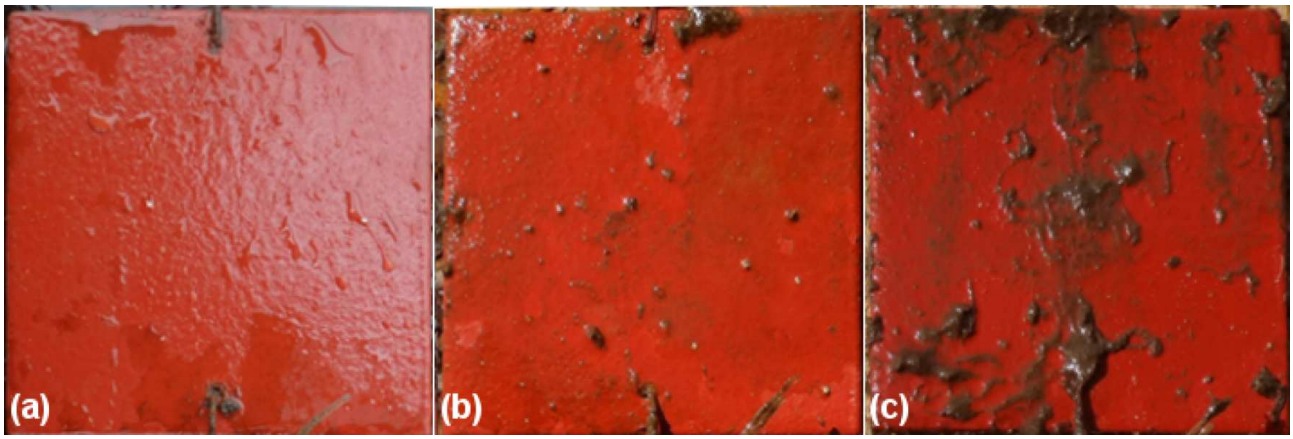

Figure 6.8: Surface condition of Ref. Si specimen from Pair 3 that remained immersed for 6 months in Elefsis: a) after 2 months, b) after 4 months and c) after 6 months, when it was removed from site

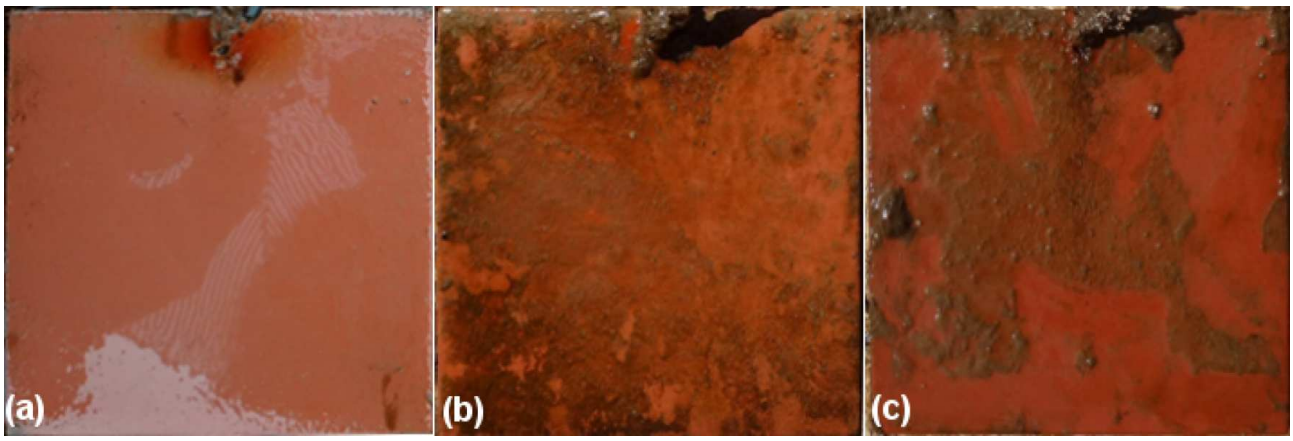

Figure 6.9: Surface condition of Acrylic specimen from Pair 3 that remained immersed for 6 months in Elefsis: a) after 2 months, b) after 4 months and c) after 6 months, when it was removed from site

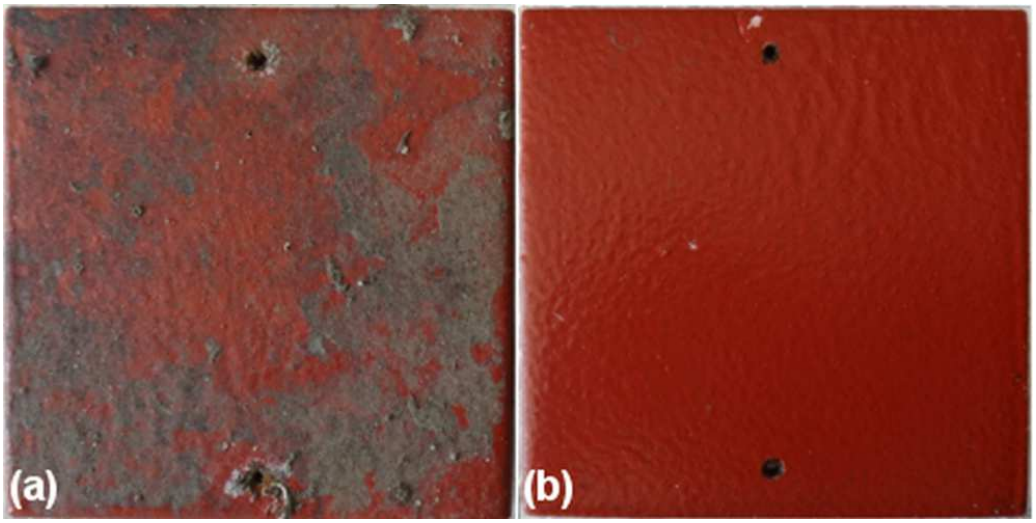

Figure 6.10: Surface condition of Ref. Si specimen after 6 months of immersion: a) as dried condition and b) after gentle cleaning with rinsing water

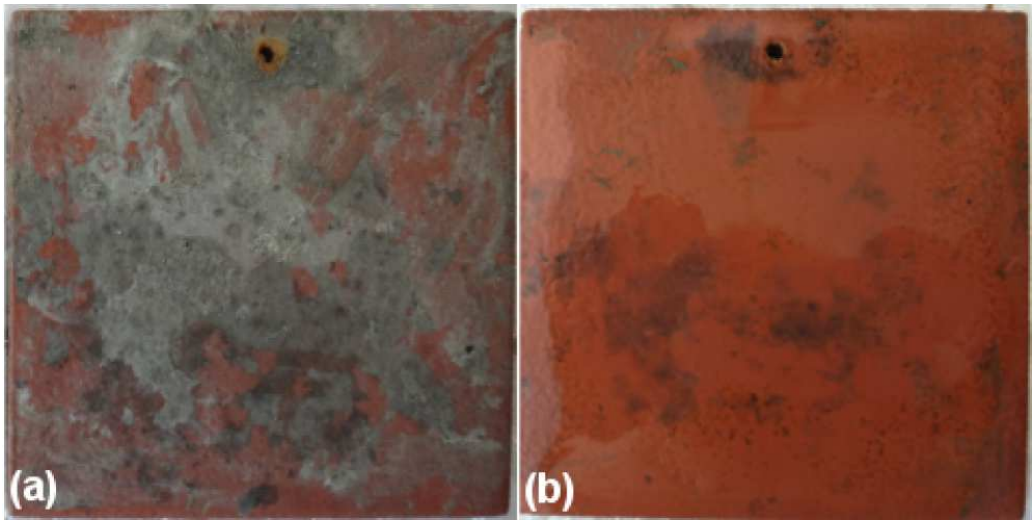

Figure 6.11: Surface condition of Acrylic specimen after 6 months of immersion: a) as dried condition and b) after gentle cleaning with rinsing water

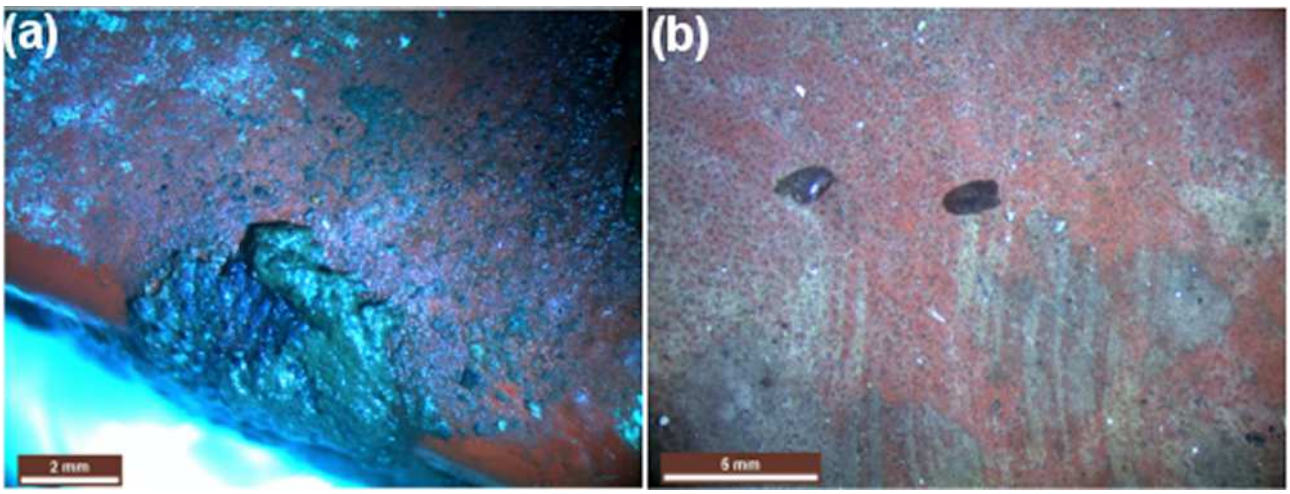

Figure 6.12: Stereoscopic observation of a) Ref. Si (possibly cheilostomata bryozoans colony) and b) Acrylic specimen (2 mussels) after 6 months of immersion

Table 6.11: Antifouling performance calculation of Ref. Si specimen from Pair 3 (6 months immersion), according to ASTM D 3623 and ASTM D 6990 guidelines

Fouling Examination	Ref. Si
Fouling on surface	PC-*Spirorbinae*:18, 0.361 to 1.383 mm in diameter Diameters of the observed spirorbinae [mm]: 0.828, 1.270, 0.584, 0.723, 0.924, 0.361, 0.421, 1.007, 0.615, 1.202, 1.077, 0.516, 0.612, 0.716, 1.383, 1.199, 0.632 and 0.771. Total area: A= 10.85 mm^2 (0.109%) PC-*Serpulidae*: 4, non-ringed tubeworms, 2.96 to 10.44 mm^2 in surface, isolated (Table 6.15) Encrusting Bryozoans (EB): 7.926 mm^2 (0.0793%), considering only the part covering the top of the painted surface (Fig. 6.12a). Silt: 30%, layer of moderate thickness
Fouling Resistance (F.R.) [%]	95-(0.109+0.272+0.079)=94.54
Physical Condition of Antifouling Film	• Digging effect was caused by individuals of PC-*spirobinae*: 10, 0.824 mm mean diameter. Total digging area=5.34 mm^2 (0.0534%) • DE before immersion: 2.37 • DE after 6 months immersion: 1.56 • König pendulum hardness: 25.3 • 60° gloss before immersion: 15.5 • 60° gloss after 6 months immersion: 16.5
Physical Damage Rating (P.D.R.) [%]	100-(0.0534)≈99.95
Overall Performance (O.P.) [%]	94.54

Table 6.13: Antifouling performance calculation of Acrylic specimen from Pair 3 (6 months immersion), according to ASTM D 3623 and ASTM D 6990 guidelines

Fouling Examination	Acrylic
Fouling on surface	Mollusks-*(Mol)*: 2, mussels found solitary (Fig. 6.12b) A_1=1.912 mm × 1.029 mm=1.967mm^2 (0.0197%) A_2=1.470 mm × 0.880 mm=1.294 mm^2 (0.0129%) Silt: 60%, layer of moderate thickness, mixed with slime (Fig. 6.11a)
Fouling Resistance (F.R.) [%]	95-(0.0197+0.0129)≈94.97
Physical Condition of Antifouling Film	• Paint wearing, leading to exposure of the underneath coat: A=396.62 mm^2 (3.9662%) • Discoloration and black stains (Fig. 6.11b). • DE before immersion: 0.48 • DE after 6 months immersion: 7.63 • König pendulum hardness: 78.5 • 60° gloss before immersion: 14 • 60° gloss after 6 months immersion: 1 • Softness rating (ASTM D 6990-05): 4, 'moderate amount of pigment transferred to a cotton swab'
Physical Damage Rating (P.D.R.) [%]	100-3.9662≈96.03
Overall Performance (O.P.) [%]	94.97

Table 6.15: Cacluclation of surfaces for the four non-ringed tubeworms observed on Ref. Si specimen of Pair 3, after 6 months exposure in Elefsis

Mean length (mm)	Mean width (mm)	Mean surface (mm^2)
2.993	0.989	2.960
10.562	0.989	10.446
5.865	1.000	5.865
3.015	2.629	7.926
Total surface		27.197

With regard to the physical damage of the silicone system, 10 of the 18 *spirorbinae* had left their stain on the paint. The pendulum hardness of the paint remained in similar levels as after 4 months immersion. As regards the acrylic system, some paint wearing was observed, which led to exposure of the undercoat, of surface 396.62 mm^2. This behavior could be characterized either as wearing (ASTM D 16-03), which is related to paint loss as a result of environmental exposure, or as erosion (ASTM D 662-93), in terms of paint wearing, which causes exposure of the underneath layer or the substrate and could result from chalking. However, erosion is usually related to wearing due to interaction with moving water, hence, the "wearing" term was used. Moreover, the change in color and gloss were profound. The pendulum hardness

for this specimen was measured to be 78.5, higher than the values after 2 (69.6) and 4 (37.6) months of immersion.

6.3.1.4 After 8 months of immersion

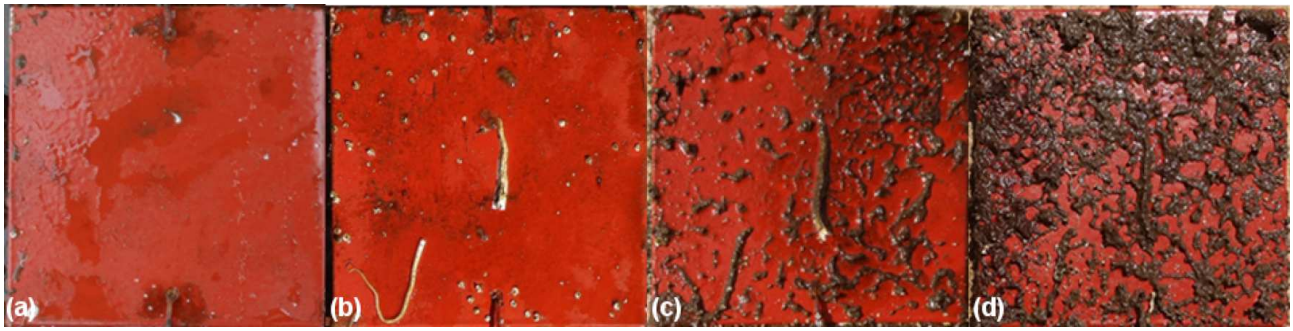

Figure 6.13: Surface condition of Ref. Si specimen from Pair 4 that remained immersed for 8 months in Elefsis after: a) 2, b) 4, c) 6 and d) 8 months, when it was removed from site

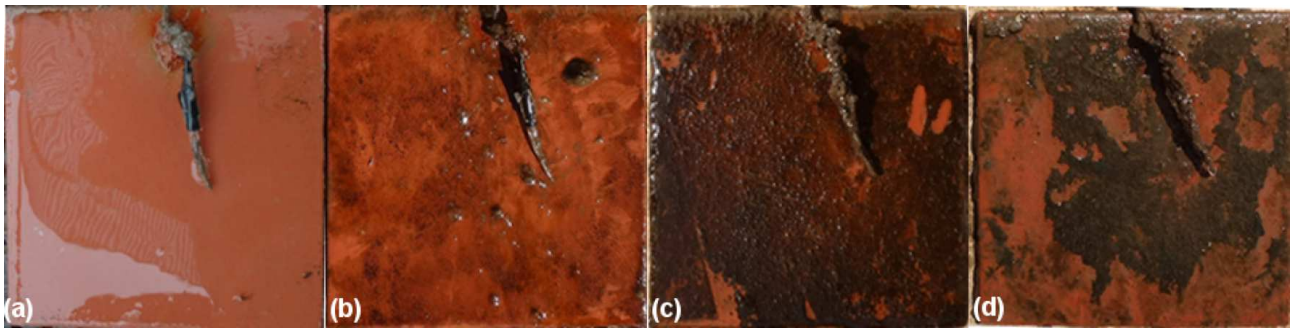

Figure 6.14: Surface condition of Acrylic specimen from Pair 4 that remained immersed for 8 months in Elefsis after: a) 2, b) 4, c) 6 and d) 8 months, when it was removed from site

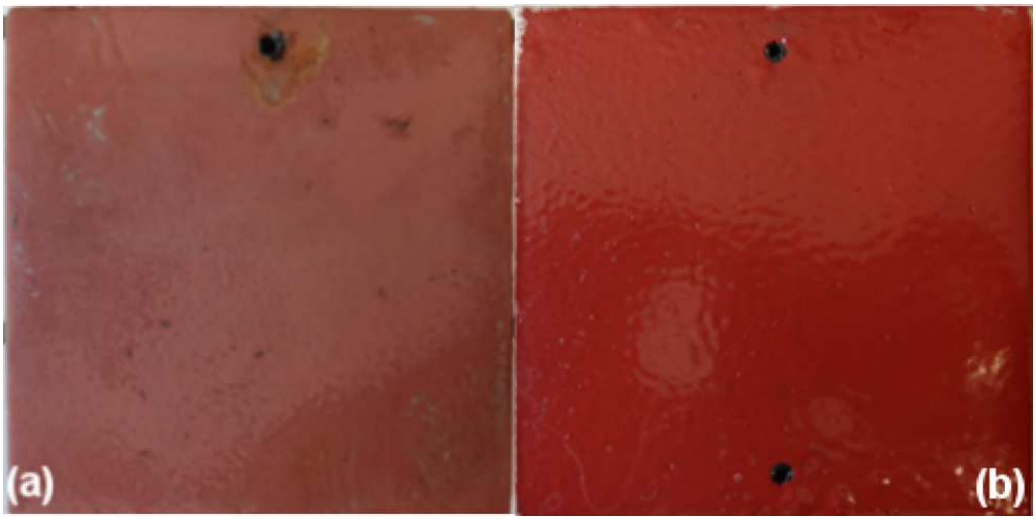

Figure 6.15: Surface condition after cleaning for the a) Acrylic and b) Ref. Si specimens after 8 months of immersion

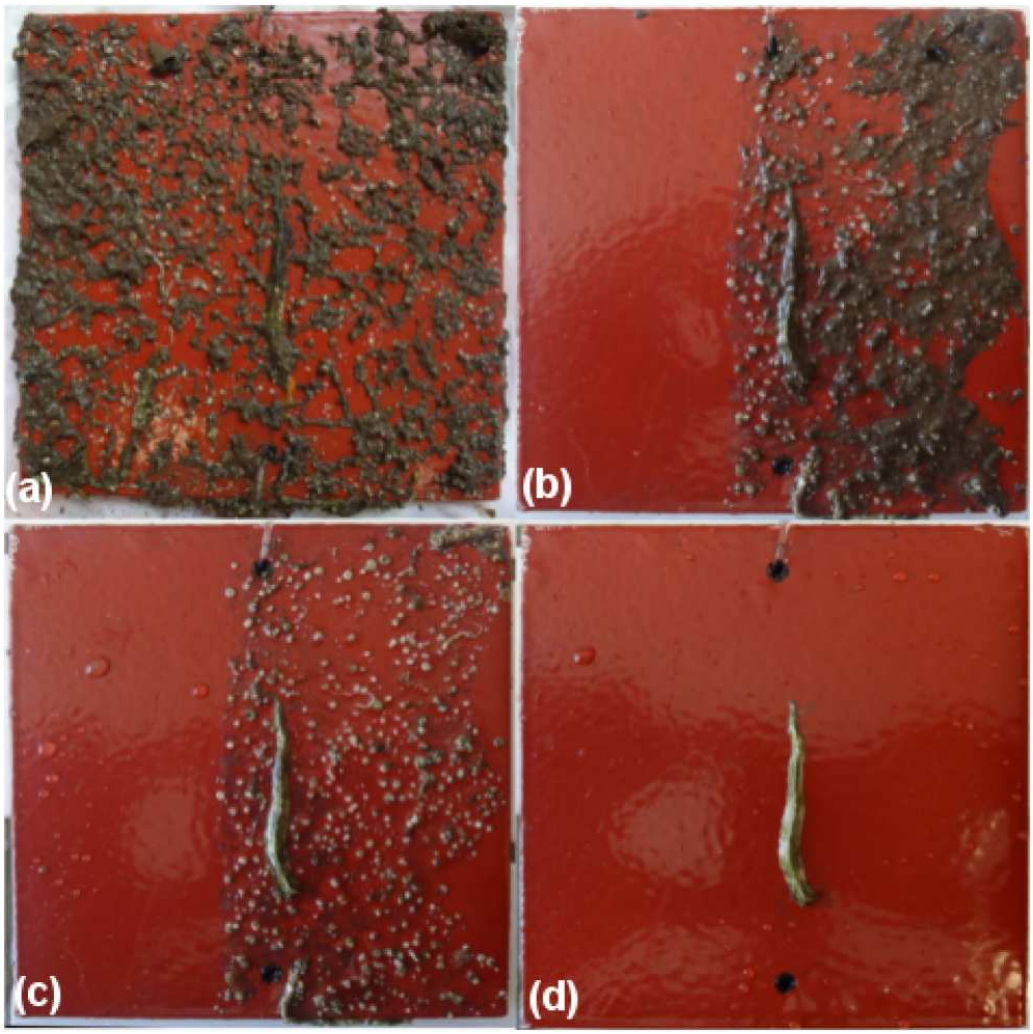

Figure 6.16: Cleaning process of Ref. Si specimen after 8 months of immersion in Elefsis. The foulers were easily removed from the specimen under flowing water with gentle finger pressure, verifying the low surface tension of the FR paint

As can be seen in Fig. 6.16a-d, the cleaning process of the foul-release silicone system was very easy, since the foulers adhered loosely onto the painted surface. This is a result of the low surface tension of the hydrogel surface of the silicone system. Despite the low surface tension, however, physical damage caused by the majority of the attached hard macro-foulers (e.g. tubeworms) can be seen in Fig. 6.15b. The print of some foulers onto the coated surface is readily apparent and is a result of these foulers "digging" into the coat, in order to adhere more firmly. Even though strong attachment is not possible on foul-release systems, some physical deterioration was caused, possibly due to the elastomeric nature of the polydimethylsiloxane (PDMS), which is not characterized by mechanical integrity. This is why this type of AF systems is characterized as being soft compared to the traditional self-polishing AF technology, which is generally quite hard, thus more efficient against digging.

Table 6.16: Antifouling performance calculation of Ref. Si specimen from Pair 4 (8 months immersion), according to ASTM D 3623 and ASTM D 6990 guidelines

Fouling Examination	Ref. Si
Fouling on surface	PC-*Serpulidae*:15, non-ringed tubeworms of cylindrical cross-section, of similar dimensions, found in various positions over the coated surface. Mean area per individual: 10.988 mm × 0.587 mm=6.45 mm^2 (0.0645%) Total area: A=96.75 mm^2 (0.9675%) PC-*Serpulidae*:2, non-ringed tubeworms of cylindrical cross-section, larger than the previous ones (Fig. 6.16b, lower left side, covered with mud, green in color and Fig. 6.16c, lower central region). Their mean areas are: A_1=10.6 mm × 1.8 mm=19.08 mm^2 (0.1908%) A_2=11.8 mm × 2.1 mm=24.78 mm^2 (0.2478%) PC-*Serpulinae*:1, non-ringed tubeworm, the largest of all, attached onto the central specimen region (Fig 6.16d), of triangular cross-section, similar to *pomatoceros triqueter*. Mean area is: A=51mm × 4mm=204 mm^2 (2.04%) The area of this cell was 2% of the specimen's area. Hence, for FR calculation, the area was subtracted. PC-*Spirorbinae*: Heavy fouling, of diameters 0.446-3.394 mm. Dense population with uniform coverage (Fig. 6.13d, Fig. 6.16a) Mol: 2, mussels found as secondary fouling, attached onto a mud agglomeration and not directly onto the surface. Hence, not considered for the calculation of the FR index. Silt: 73%, as presented in Fig. 6.16a. The observed silt was dense but not uniform.
Fouling Resistance (F.R.) [%]	9.55
Physical Condition of Antifouling Film	• Extensive digging caused by the attached calcareous cells on the surface (Fig. 6.15b). • Total area of digging:A= 3234.6 mm^2 (32.35%) • DE before immersion: 2.66 • DE after 8 months immersion: 2.62 • König pendulum hardness: 32 • 60° gloss before immersion: 35.25 • 60° gloss after 8 months immersion: 30.75
Physical Damage Rating (P.D.R.) [%]	100-(32.35)=64.65
Overall Performance (O.P.) [%]	9.55

Table 6.18: Antifouling performance calculation of Acrylic specimen from Pair 4 (8 months immersion), according to ASTM D 3623 and ASTM D 6990 guidelines

Fouling Examination	Acrylic
Fouling on surface	Medium severity biological slime and some incipient fouling covering the area in a wide extent, mixed with silt (72%) (Fig. 6.14d).
Fouling Resistance (F.R.) [%]	95
Physical Condition of Antifouling Film	• Top coat loss, due to leaching. Exposure of the undercoat: A=1139.15 mm^2 (11.391%) • Discoloration of the paint. • DE before immersion: 0.58 • DE after 8 months immersion: 8.02 • König pendulum hardness: 59 • 60° gloss before immersion: 14 • 60° gloss after 8 months immersion: 1
Physical Damage Rating (P.D.R.) [%]	100-11.391≈88.61
Overall Performance (O.P.) [%]	88.61

With regard to the silicone painted specimen, many of the attached foulers could be removed from the specimens with gentle finger pressure under running water, without breaking or leaving remainders of their calcareous shells on the silicone surface. However, extensive digging effect was noticed, affecting an area around 3234.6 mm^2 and causing a sharp drop to P.D.R. The heavy fouling observed on the Ref Si painted specimen after 8 months could be attributed to the increased temperature encountered during July, when these organisms reproduce and grow faster.

With regard to antifouling performance of the acrylic-based specimen (Table 6.18), the biofilm covering the paint after 8 months (Fig. 6.14d) did not extend over the whole surface, as after 6 months of immersion (Fig. 6.14c). This was probably attributed to the leaching effect of the paint. The "fingerprints" on the specimen after 6 months are probably attributed to some kind of fish that came in contact with the specimen. Finally, its pendulum hardness (59) compared to the silicone specimen (32) revealed the harder nature of the SPC technology. Hence, compared to the silicone system, the acrylic paint appeared to be harder after 8 months of immersion, with less fouling and physical damage.

6.3.1.5 After 10 months of immersion

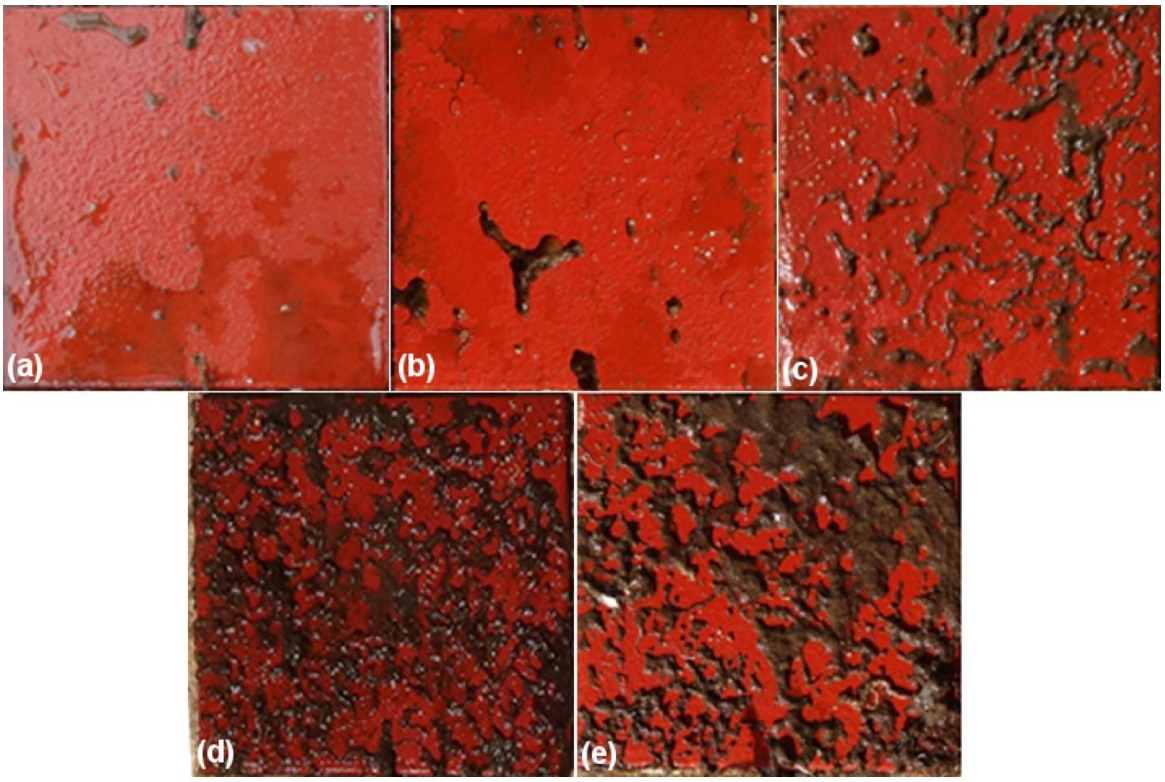

Figure 6.17: Surface condition of Ref. Si specimen from Pair 5 that remained immersed for 10 months in Elefsis after: a) 2, b) 4, c) 6, d) 8 and e) 10 months, when it was removed from site

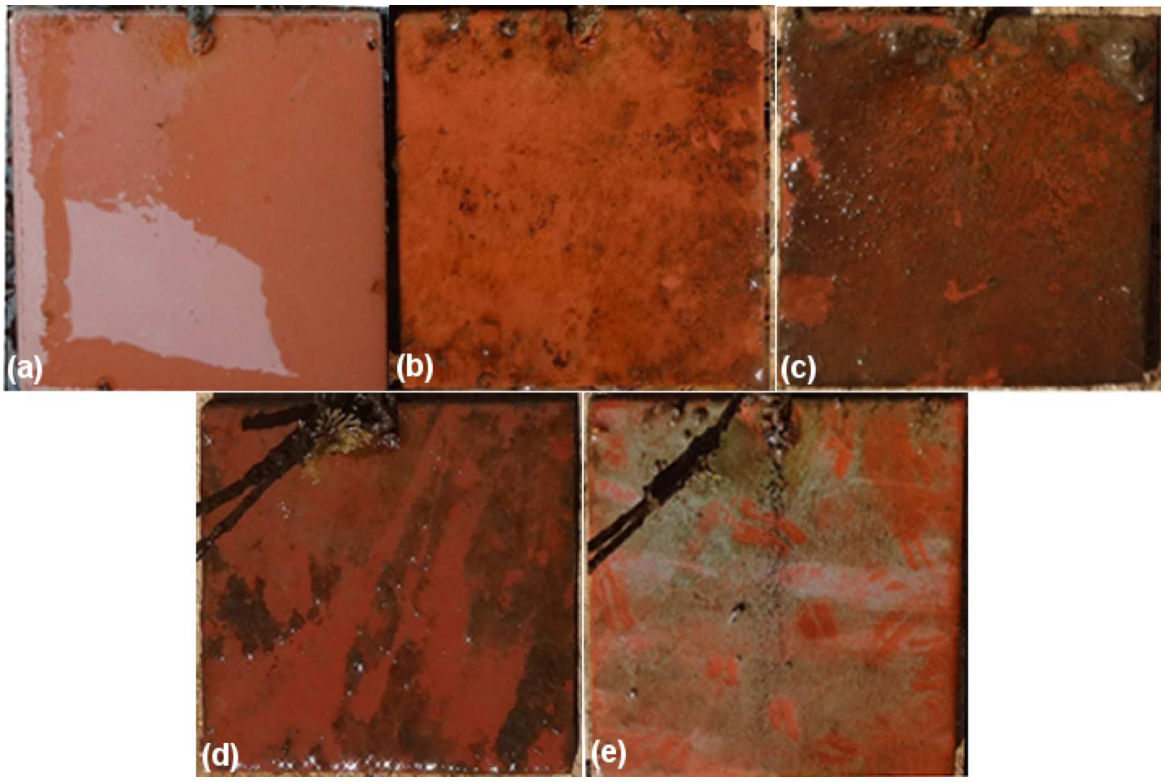

Figure 6.18: Surface condition of Acrylic specimen from Pair 5 that remained immersed for 10 months in Elefsis after: a) 2, b) 4, c) 6, d) 8 and e) 10 months, when it was removed from site

From Figs. 6.17 and 6.18 it can be seen that the silicone system tended to accumulate silt on its surface, in contrast to the acrylic-based SPC system which did not exhibit such a problem. The acrylic-based antifouling coating exhibited only slime and some incipient fouling throughout its 10-month sea immersion. Apparently, the self-polishing nature of this system is quite effective against macro-fouling, allowing fouling only from biofilms and micro-foulers. With regard to the silicone system, even though the silt along with the attached macro-foulers could be easily removed under running water using finger pressure (Fig. 6.19b), the accumulation of all these organisms would negatively affect the final fouling rating of the paint, leading to small values. Moreover, physical damage caused by the attached foulers (digging) was also observed on the silicone specimen. On the other hand, the hard SPC coat did not exhibit digging but other forms of physical damage, such as wearing, which could be attributed to the continuous release of biocide, making the acrylic matrix depleted.

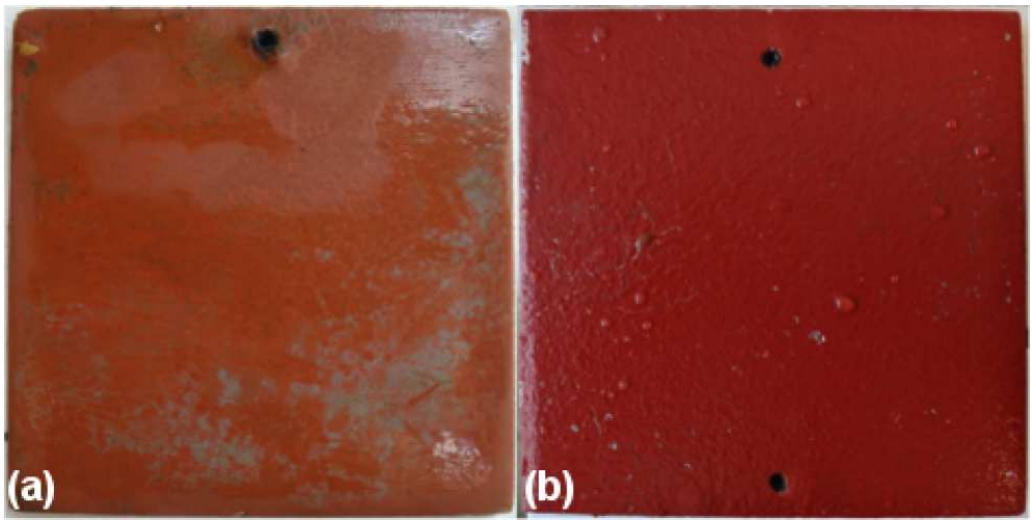

Figure 6.19: Surface condition of a) Acrylic and b) Ref. Si specimen after 10 months of immersion in Elefsis after gentle cleaning with rinsing water

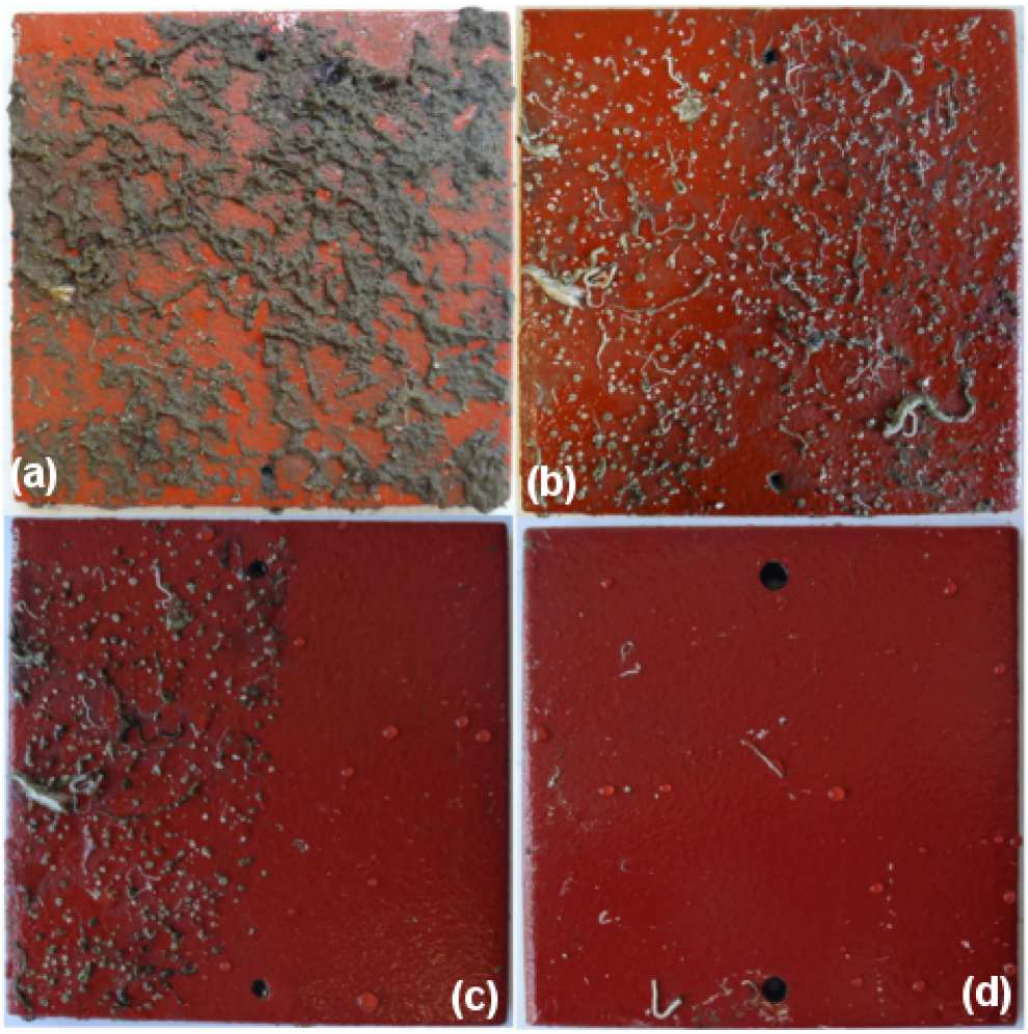

Figure 6.20: Cleaning process of the Ref. Si specimen after 10 months of immersion in Elefsis. The foulers were easily removed from the specimen under flowing water with gentle finger pressure, verifying the low surface tension of the FR paint

Figure 6.21: Stereoscopic observation of Ref. Si specimen after 10 months of immersion in Elefsis with representative species of the *serpulidae* family: a) *spirorbinae*, all dextral, b) a serpulid similar to *pomatoceros triqueter*

As can be seen from Fig. 6.21, the attached foulers onto the silicone specimen after 10

months immersion in Elefsis included mainly representatives of the phylum *Annelida*, class *Polychaeta* and Family *Serpulidae*. In Fig. 6.21a, some representatives of the *spirorbinae* subfamily are presented, all exhibiting dextral (counter-clockwise) coiling (dexiospira). From closer observation two types were identified, namely, *spirorbis spirillum* (mainly smooth tube) and *spirorbis pagenstecheri* (tube exhibiting three longitudinal ridges) [144]. The former species creates ascending tubes which were also observed in Fig. 6.21a. In Fig. 6.21b some representatives of the *serpulidae* family are presented, with the triangular tube reminding of *pomatoceros triqueter* [144]. This species is characterized by its triangular cross-sectional area and its central longitudinal ridge with teeth. It is important to note that the operculum of this species (the lid that seals the entrance of the tube, inside which the organism is protected) is closed, meaning that possibly a living organism was lying inside, during stereoscopic observation.

Table 6.20: Antifouling performance calculation of Ref. Si specimen from Pair 5 (10 months immersion), according to ASTM D 3623 and ASTM D 6990 guidelines

Fouling Examination	Ref. Si
Fouling on surface	PC-*Spirorbinae*:Heavy fouling, 0.735-1.446 mm in diameter, uniformly covering the painted surface (Fig. 6.20b). PC-*Serpulidae*: 160, non-ringed tubeworms of cylindrical cross-section and of similar dimensions. Mean average area per individual=6.08mm × 1.25 mm=7.6 mm^2 (0.076%) Mean total area A=1216 mm^2 (12.16%) PC-*Serpulidae*: 11, non-ringed tubeworms of cylindrical cross-section lying adjacent to the larger foulers, as in Fig. 6.21b. a)Adjacent to the *pomatoceros triqueter* tube: A_1=5mm × 0.875mm=4.375 mm^2 (0.04375%) A_2=21.43mm × 0.53mm=11.358 mm^2 (0.1136%) A_3=10.714mm × 0.53mm=5.678 mm^2 (0.0568%) A_4=2.38mm × 0.595mm=1.416 mm^2 (0.0142%) A_5=11.31mm × 0.42mm=4.750 mm^2 (0.0475%) b) Randomly dispersed onto the entire surface: A_6=20.00mm × 0.60mm=12.000 mm^2 (0.1200%) A_7=12.00mm × 0.60mm=7.200 mm^2 (0.0720%) A_8=12.60mm × 0.72mm=9.072 mm^2 (0.0907%) A_9=16.20mm × 0.46mm=7.452 mm^2 (0.0745%) A_{10}=12.63mm × 0.75mm=9.472 mm^2 (0.0947%) A_{11}=7.58mm × 0.50mm=3.790 mm^2 (0.0379%) Mean total area A=76.563 mm^2 (0.7656%) PC-*Serpulinae*: 2, non-ringed tubeworms, of triangular cross-section, similar to pomatoceros triqueter, lying on the left side of the painted specimen, close to its edges (Fig. 6.20b, Fig. 6.21b).Mean area is: A_1=13mm × 2.5mm=32.5 mm^2 (0.325%) A_2=10.83mm × 1.31mm=14.19 mm^2 (0.142%)

	Silt: 74%, thick layer of silt, without homogenous coverage of the surface.
Fouling Resistance (F.R.) [%]	10.80
Physical Condition of Antifouling Film	• The great amount of tubeworms observed left their stain on the specimen's surface causing a digging effect. The total area of digging was A=3338 mm^2 (33.38%). • DE before immersion: 2.56 • DE after 10 months immersion: 2.62 • König pendulum hardness: 23.4 • 60° gloss before immersion: 13.75 • 60° gloss after 10 months immersion: 12
Physical Damage Rating (P.D.R.) [%]	100-(33.38)=66.62
Overall Performance (O.P.) [%]	10.80

Table 6.21: Antifouling performance calculation of Acrylic specimen from Pair 5 (10 months immersion), according to ASTM D 3623 and ASTM D 6990 guidelines

Fouling Examination	Acrylic
Fouling on surface	PC-*Spirorbinae*: 12, 1.52 mm mean diameter Mean area per individual: 1.814 mm^2 Total mean area: 21.768 mm^2 (0.2177%) Slime: A uniform and moderately dense layer covering almost 75% of the specimen area. Fish-prints are apparent.
Fouling Resistance (F.R.) [%]	95-0.2177≈94.78
Physical Condition of Antifouling Film	• Wearing: A=3469.02 mm^2 (34.690%) • Flaking: at the top left side of the specimen (not included in the PDR, because it was close to specimen's edge) • DE before immersion: 0.71 • DE after 10 months immersion: 6.05 • König pendulum hardness: 35.2 • 60° gloss before immersion: 17 • 60° gloss after 10 months immersion: 1
Physical Damage Rating (P.D.R.) [%]	100-34.690≈65.31
Overall Performance (O.P.) [%]	65.31

After 10 months, the silicone specimen was mainly affected by fouling, dropping its overall rating to 10.80%, while the acrylic-based specimen was mainly affected by wearing, dropping its overall rating to 65.31%. Flaking referred to the missing paint parts at the top left side (Fig.. 6.19a) of the specimen (ASTM D 772-93 [145]). Despite its physical deterioration, though, the acrylic system exhibited better performance overall compared to the silicone specimen,

which, as mentioned previously, is mainly attributed to its efficiency against macrofouling attachment.

6.3.1.6 After 12 months of immersion

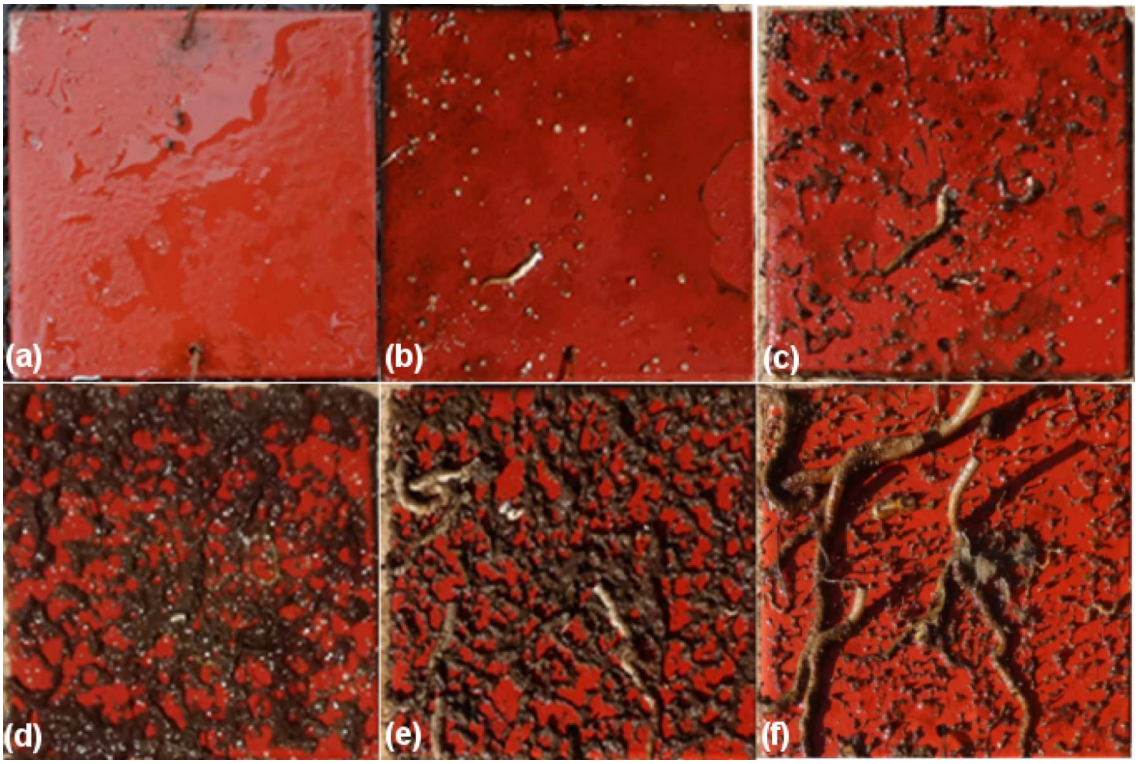

Figure 6.22: Surface condition of the Ref. Si specimen from Pair 6 that remained immersed for 12 months in Elefsis after: a) 2, b) 4, c) 6, d) 8, e) 10 and f)12 months, when it was removed from site

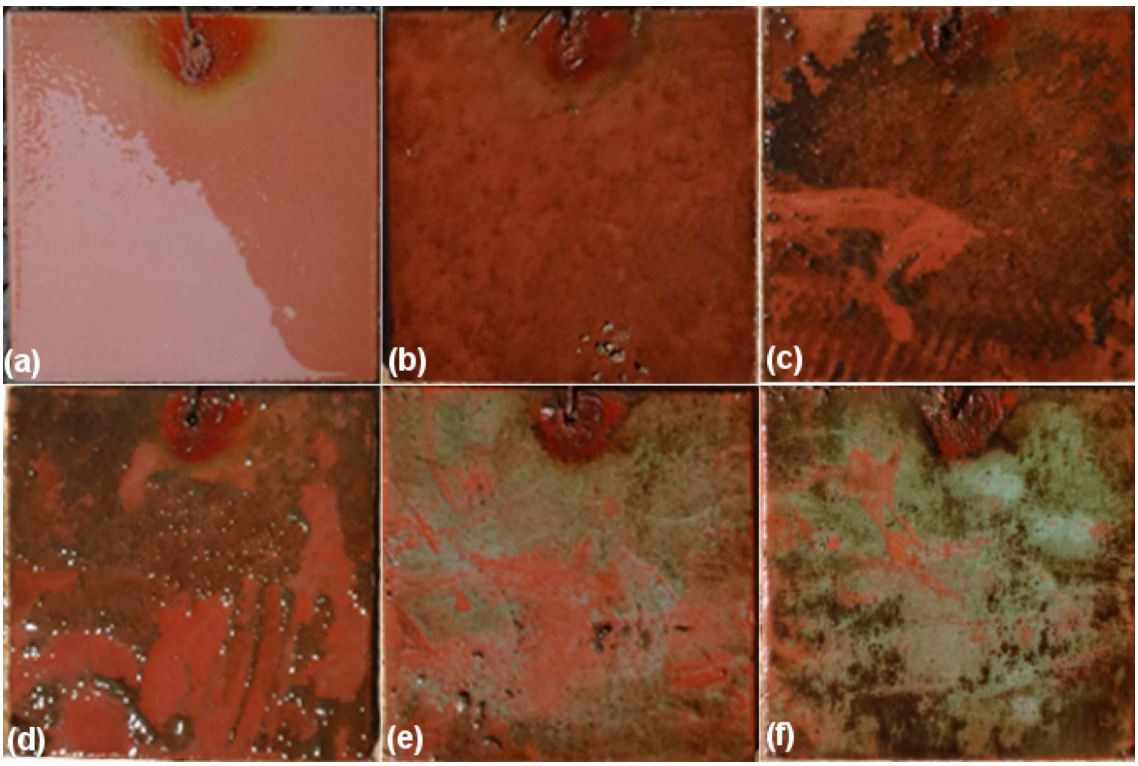

Figure 6.23: Surface condition of Acrylic specimen from Pair 6 that remained immersed for 12 months in Elefsis after: a) 2, b) 4, c) 6, d) 8, e) 10 and f)12 months, when it was removed from site

Figure 6.24: Surface condition of dried a) Acrylic and b) Ref. Si specimens after 12 months immersion in Elefsis

Surface condition after drying in the laboratory revealed some chipping (ASTM D 16-03 [146]) of the topcoat for the acrylic-based paint (Fig. 6.24a). Chipping effect becomes apparent as small pieces detaching the layer and could be attributed to wear during service.

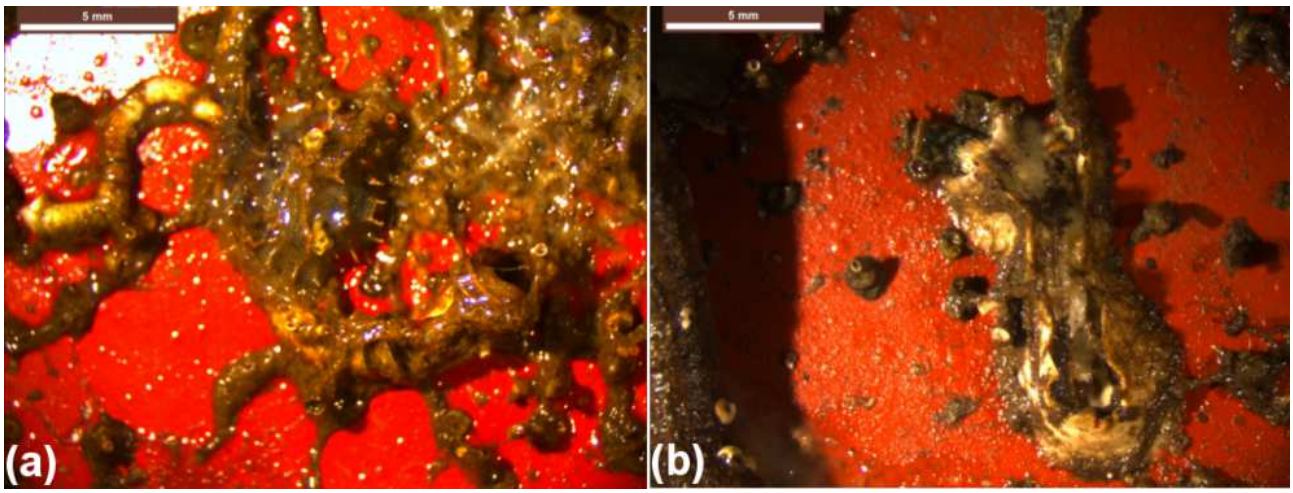

Figure 6.25: Stereoscopic observation of Ref. Si specimen after 12 months immersion in Elefsis depicting serpulids: a) possibly *mercierella enigmatica* and b) tube similar to *pomatoceros triqueter*

In Fig. 6.25a many organisms appear, but all of them surround the tube of interest. The characteristic of this tube is the multiple transverse flanges appearing on the opening of the tube and on various locations along it. The tube diameter was around 2 mm and it was partly above the surface. These characteristics could imply *mercierella enigmatica*. This organism can be found in harbors and estuaries and has been distributed worldwide through shipping [144].

With regard to Fig. 6.25b, this serpulid exhibited an operculum with a brown crown consisting of five branches, each projecting with two "toothed edges". The tube exhibited a longitudinal ridge with teeth, while a sharp tooth projected at the mid-top of the opening reminding of *pomatoceros triqueter* tube. Also some irregular coiling was observed. The tube was "dirty white" [144], while some mauve marks were observed circumferentially the tube opening. Finally, the branchial filaments exhibited black and white bands, while further inside a red abdomen was observed.

Table 6.23: Antifouling performance calculation of Ref. Si specimen from Pair 6 (12 months immersion), according to ASTM D 3623 and ASTM D 6990 guidelines

Fouling Examination	Ref. Si
Fouling on surface	PC-*Spirorbinae*: Heavy fouling, of 0.393-2.946 mm in diameter, uniformly covering the painted surface (Fig. 6.24b). PC-*Serpulidae*: 6, non-ringed tubeworms of cylindrical cross-section, standing on their one side over the painted surface, of the largest dimensions (Fig. 6.22f). A_1=85.0 × 3.0 =255 mm^2 (2.55%) A_2=55.0 × 3.0 =165 mm^2 (1.65%) A_3=77.0 × 3.0 =231 mm^2 (2.31%) A_4=55.0 × 3.0 =165 mm^2 (1.65%) A_5=70.0 × 3.0 =210 mm^2 (2.10%) A_6=77.0 × 4.0 =308 mm^2 (3.08%) Mean total area: A=1334 mm^2 (13.34%)

	PC-*Serpulidae*: 7, non-ringed tubeworms of cylindrical cross-section, of the shortest dimensions. A_1=21.0 × 1.5 =31.5 mm^2 (0.315%) A_2=12.0 × 1.0 =12.0 mm^2 (0.120%) A_3=23.0 × 2.0 =46.0 mm^2 (0.460%) A_4=11.0 × 1.0 =11.0 mm^2 (0.110%) A_5=15.0 × 1.0 =15.0 mm^2 (0.150%) A_6=26.0 × 1.0 =26.0 mm^2 (0.260%) A_7=8.0 × 1.0 =8.0 mm^2 (0.080%) Mean total area: A=149.5 mm^2 (1.495%) PC-*Serpulinae*: 2, non-ringed tubeworms, of triangular cross-section, one appearing in Fig. 6.25b.Mean area is: A_1=48.0 × 4.0 =192.0 mm^2 (1.92%) A_2=31.0 × 2.0 =62.0 mm^2 (0.62%) Mean total area: A=254 mm^2 (2.54%) Silt: not observed this time
Fouling Resistance (F.R.) [%]	6.61
Physical Condition of Antifouling Film	• The great amount of tubeworms observed left their stain on the specimen's surface causing a digging effect. The total area of digging was A=5583 mm^2 (55.83%). • DE before immersion: 1.98 • DE after 12 months immersion: 2.30 • König pendulum hardness: 28 • 60° gloss before immersion: 21.33 • 60° gloss after 12 months immersion: 21.25
Physical Damage Rating (P.D.R.) [%]	100-(55.83)=44.17
Overall Performance (O.P.) [%]	6.61

Table 6.24: Antifouling performance calculation of Acrylic specimen from Pair 6 (12 months immersion), according to ASTM D 3623 and ASTM D 6990 guidelines

Fouling Examination	Acrylic
Fouling on surface	*Amphipods*: 3, 1.8-2.19 mm in length (1.8, 2, 2.19 mm respectively) *Filamentous bryozoans (FB)*: 3.2mm × 0.6mm=1.92 mm^2 (0.0192%) Slime: 95%, thick layer, uniformly covering the surface, mixed with some silt (Fig. 6.23f).
Fouling Resistance (F.R.) [%]	95-0.0192≈94.98
Physical Condition of Antifouling Film	• Extensive chipping: A=7788.19 mm^2 (77.882%) • DE before immersion: 0.75 • DE after 12 months immersion: 17.73 • König pendulum hardness: 36.8 • 60° gloss before immersion: 14

	• 60° gloss after 12 months immersion: 1
Physical Damage Rating (P.D.R.) [%]	100-77.882≈22.12
Overall Performance (O.P.) [%]	22.12

After 12 months, the population of *spirorbinae* was still quite dense, similarly to 8 and 10-month intervals. The dense fouling dropped the F.R. of the silicone painted specimen to 6.61%. The heavy fouling caused a further drop to the P.D.R. value which became 44.17%. With regard to the acrylic painted specimen, the F.R. remained close to 95%, providing efficient antifouling protection. With regard to physical damage, though, extensive chipping was observed, covering almost the entire surface of the acrylic-based specimen and dropping the final rating to 22.12%.

6.3.1.7 Conclusions with regard to the field tests of reference silicone and acrylic paints

Table 6.25: Summary of antifouling and physical damage rating for the Ref. Si and Acrylic systems during the 12-month immersion experiment in Elefsis

Months	Ref. Si			Acrylic		
	FR [%]	PDR [%]	OP[%]	FR [%]	PDR [%]	OP[%]
2	100	100	100	100	100	100
4	93.19	99.87	93.19	94.93	100	94.93
6	94.54	99.95	94.54	94.97	96.03	94.97
8	9.55	64.65	9.55	95	88.61	88.61
10	10.80	66.62	10.80	94.78	65.31	65.31
12	6.61	44.17	6.61	94.98	22.12	22.12

As can be observed from Table 6.25, the silicone system was severely affected by fouling attachment especially after 8 months, dropping its F.R. to around 10% and making this paint to be insufficient for antifouling protection, assuming that an efficient system would always be ranked above 80% [141, 147]. However, its main characteristic is that the attached foulers were loosely adherent, hence, they could be removed under running water. Even though hardly any shell remainders were observed on the painted specimen, the digging effect was apparent. The physical damage rating decreased after 8 months, exhibiting value equal to 64.65%. The acrylic system, on the other hand, exhibited very good antifouling behavior. However, after 10 months it started to exhibit physical damage, which progressed almost abruptly in the final interval, leading to a PDR of 22.12% after 12 months of immersion.

From these observations, the mode of action for each antifouling category becomes apparent. The silicone system seems to be more prone to *spirorbinae* attachment and it serves as a friendly environment for growth of *serpulidae* tubes. As a result, the fouling rating drops easily, however, in dynamic conditions, these organisms would be easily detached. Apparently, it is not possible to predict the severity and extent of digging effect in real conditions, since it depends on many factors. The static immersion test in Elefsis Gulf revealed that the organisms were easily

removed from the paint, however, digging effect was apparent. In real conditions, a service speed close to 10 m/s along with small idle periods would be an ideal combination for a foul release coating to remain free from fouling [135]. With regard to the disadvantages of the foul-release system, its elastomeric nature would be prone to mechanical damage, hence, extra precautions should be taken, especially during ship maneuvering.

The acrylic-based system, which is based on the SPC technology, was quite efficient against fouling attachment and growth but its physical properties became abruptly deteriorated after a time regime, due to wearing, flaking and chipping. In the present investigation, the physical damage expanded to the immediate underneath layer, without, however, revealing the substrate. This characteristic makes the overall rating to drop quite sharply after a period of immersion which, for the present investigation, was after a year of exposure. Moreover, it should be mentioned that the SPC technology is based on biocide(s) leaching, which could be considered as a drawback, from an environmental point of view.

6.3.2 Experimental Polyurethane (Exp PU1), Experimental Silicone (Exp Si) AF systems and Polyurethane (PU) anticorrosion system

6.3.2.1 After 2 months of immersion

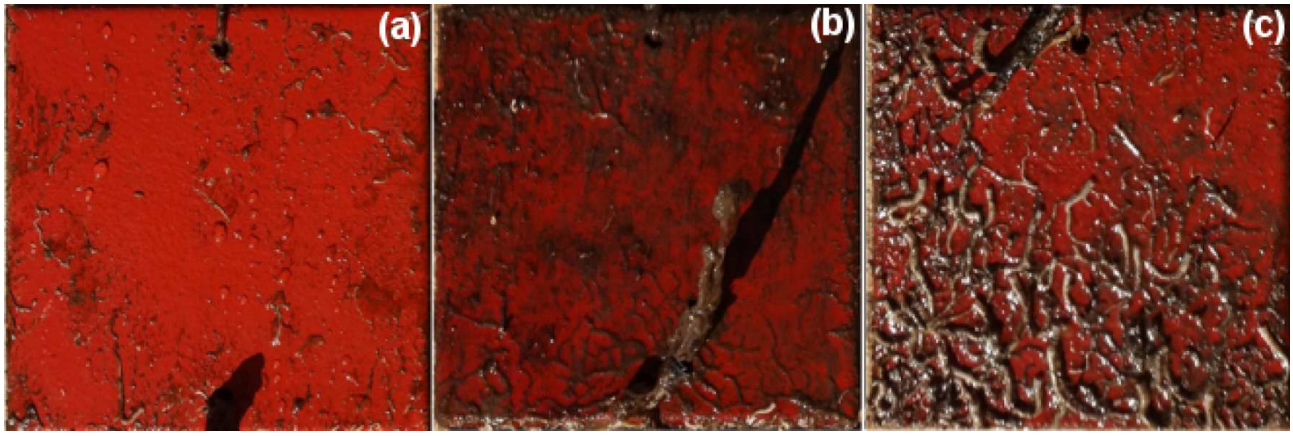

Figure 6.26: Surface condition of the a) Exp Si, b) Exp PU1 and c) PU painted specimens from Pair 1 that remained immersed for 2 months in Elefsis, when they were removed from site

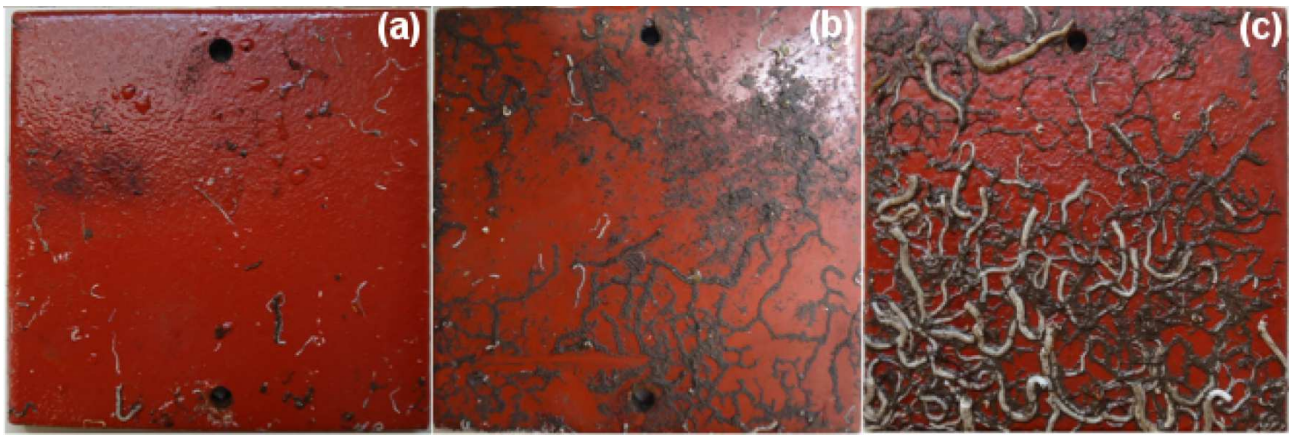

Figure 6.27: Surface condition of dried a) Exp Si, b) Exp PU1 and c) PU painted specimens after 2 months immersion in Elefsis

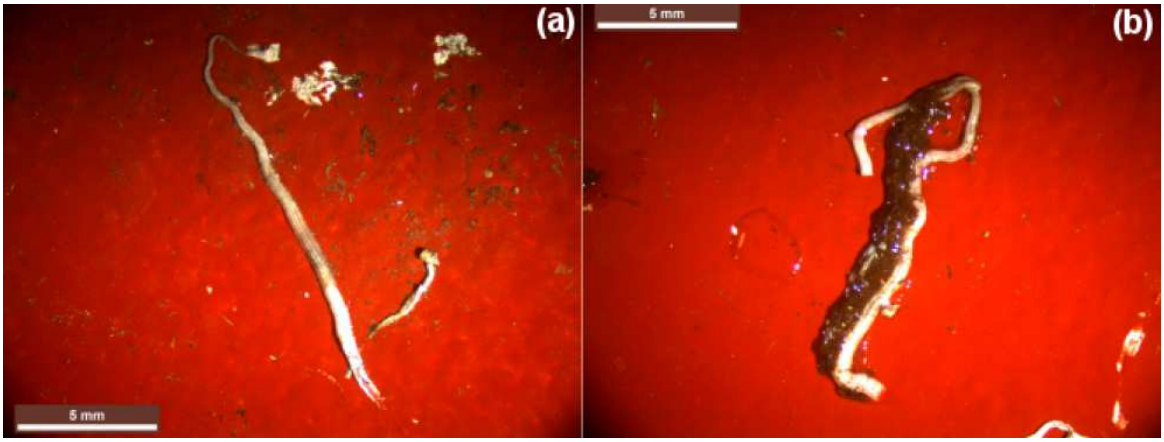

Figure 6.28: Stereoscopic observation of the Exp Si specimen after 2 months of immersion in Elefsis; a), b) calcareous shells of *polychaetes*

In Fig. 6.28, the cells of three tubeworms are presented. In Fig. 6.28a, the calcareous cell of a *polychaeta* is presented with conical tube shape and a longitudinal flat ridge on the top. In Fig. 6.28b the cells of two other *polychaetes* are presented, which have a circular cross-section and do not exhibit a ridge.

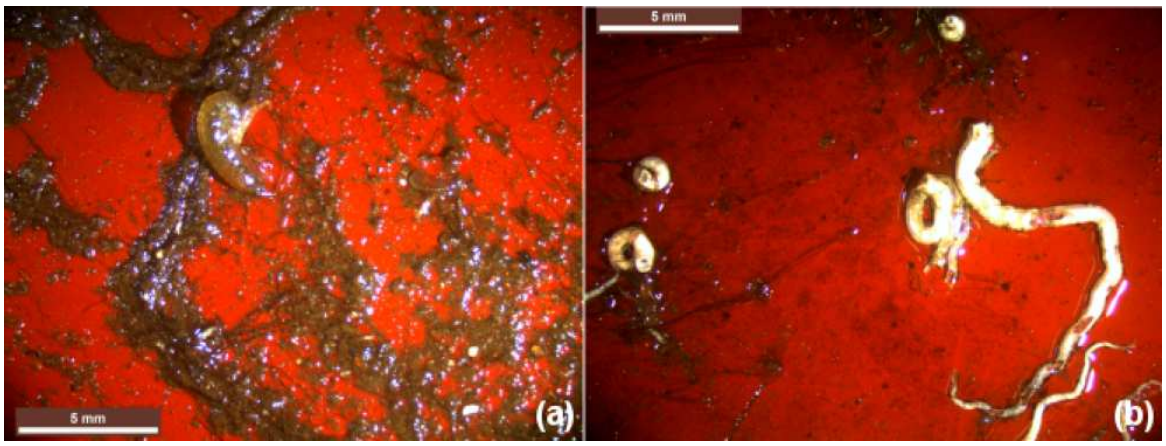

Figure 6.29: Stereoscopic observation of Exp. PU1 specimen after 2 months immersion in Elefsis; a) amphipod and b) *serpulidae spirorbinae* (dextral and sinistral) and a tube of the *serpulidae* family

In Fig. 6.29a, an amphipod is presented, probably of the *corophiidae* family. This crustacean family is usually encountered in small depths and muddy habitats. The same organism was also found on the surface of the PU painted specimen (Fig. 6.30). In Fig. 6.29a,b "black-hair" algae was noticed, covering the surface of the specimen.

With regard to Fig. 6.29b, two calcareous cells of the*spirorbinae* sub-family with sinistral coiling are presented, on the left side of the specimen. Sinistral coiling has also been encountered on the reference silicone specimen after two months immersion. The tubes had a diameter of 1.250 mm and 1.745 mm, respectively, while their tube was smooth, without apparent transverse or longitudinal ridges and it was dirty white in color. Various genes could be related to these characteristics, such as *S. borealis* [144] and *S. militaris* or *S. pseudomilitaris* [148].

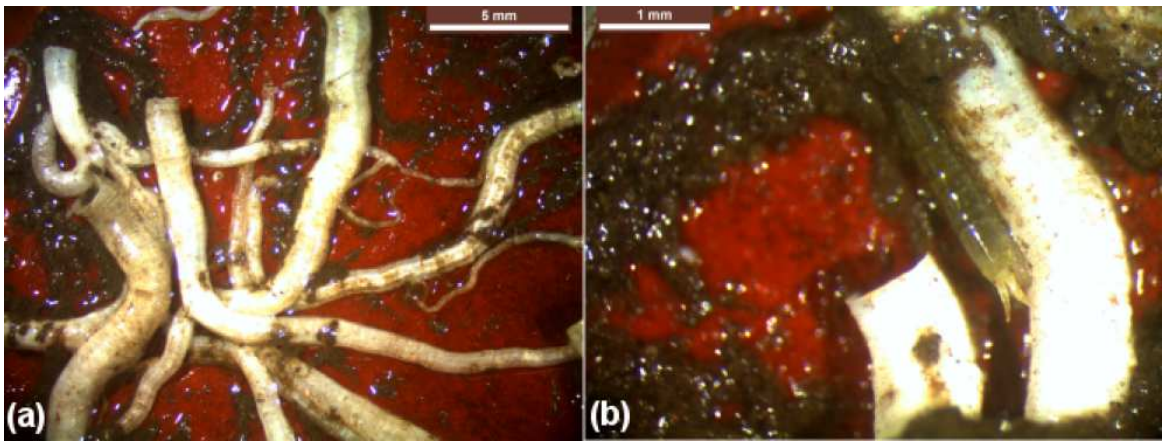

Figure 6.30: Stereoscopic observation of PU painted specimen after 2 months of immersion in Elefsis; a) a great amount of interconnected tubeworms among which many amphipods existed; b) a moving amphipod along a tube

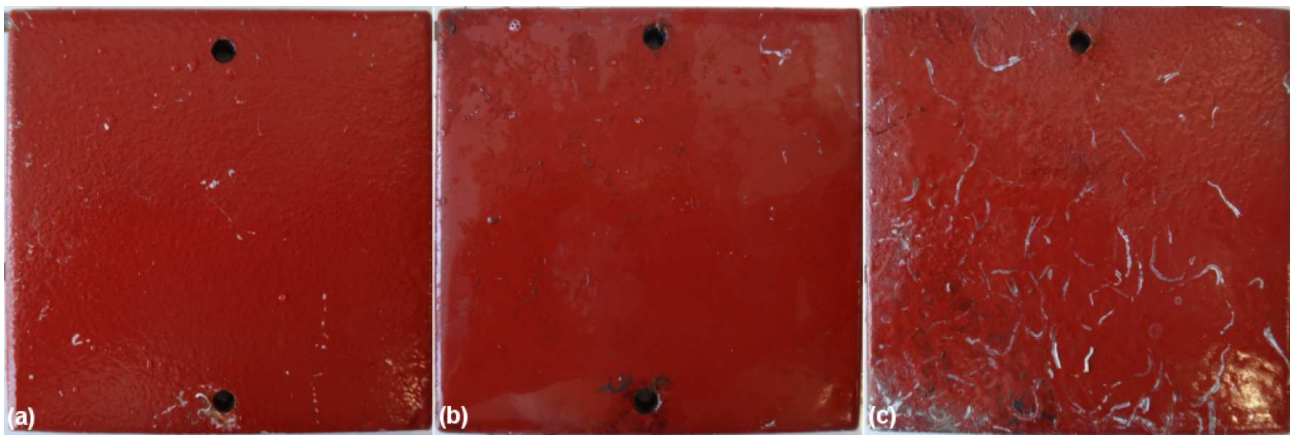

Figure 6.31: Surface condition of a) Exp Si, b) Exp PU1 and c) PU painted specimens immersed for 2 months in Elefsis after thorough cleaning

Table 6.26: Antifouling performance calculation of Exp. Si specimen from Triplet 1 (2 months immersion), according to ASTM D 3623 and ASTM D 6990 guidelines

Fouling Examination	Exp. Si
Fouling on surface	PC-*Serpulidae*: 32, non-ringed tubeworms, found at various locations across the painted surface. The mean area covered by the organisms is presented in Table C.1. Total area: A=161.15 mm^2 (1.611%) PC-*Spirorbinae*: 5, 1-2 mm in diameter (2 individuals with 1mm diameter, 2 individuals with 1.5 mm and 1 individual with 2mm diameter) A_1=0.785 mm^2 A_2=0.785 mm^2 A_3=1.767 mm^2 A_4=1.767 mm^2 A_5=3.141 mm^2 Total area: A=8.245 mm^2 (0.082%) Silt: 24.2%
Fouling Resistance (F.R.) [%]	95-(1.611+0.082)=93.31
Physical Condition of Antifouling Film	• Prints of the organisms attached onto the paint. A=1.38% • DE before immersion: 0.57 • DE after 2 months immersion: 0.87 • König pendulum hardness before immersion: 14.2 • König pendulum hardness after 2 months immersion: 16.6 • 60° gloss before immersion: 18 • 60° gloss after 2 months immersion: 17.5
Physical Damage Rating (P.D.R.) [%]	100-1.38≈98.62
Overall Performance (O.P.) [%]	93.31

Table 6.27: Antifouling performance calculation of Exp. PU1 specimen from Triplet 1 (2 months immersion), according to ASTM D 3623 and ASTM D 6990 guidelines

Fouling Examination	Exp. PU1
Fouling on surface	PC-*Serpulidae*: 10, no-ringed tubeworms, 1.20 to 12.60 mm^2 mean area. Calcareous tubes of circular cross-section, found individually on the painted surface. The mean areas of the 10 cells are presented in Table C.2. Total mean area A=46.37 mm2 (0.464%) PC-*Amphipods*: 2, found solitary on the coated surface A_1=2.381 × 0.8=1.905 mm^2 (0.0190%) A_2=2.892 × 1.0=2.892 mm^2 (0.0289%) PC-*Spirorbinae*:94, 82 of which with 1 mm mean diameter, homogenously dispersed across the painted surface. The mean area of coiled tubes with a diameter other than 1 mm is reported below. A1= 2.27 mm^2 (0.0227%) A2= 1.33 mm^2 (0.0133%) A3= 4.91 mm^2 (0.0491%) A4= 0.28 mm^2 (0.0028%) A5= 1.77 mm^2 (0.0177%) A6= 0.45 mm^2 (0.0045%) A7= 3.14 mm^2 (0.0314%) A8= 5.03 mm^2 (0.0503%) A9= 1.84 mm^2 (0.0184%) A10=1.81 mm^2 (0.0181%) A11=1.77 mm^2 (0.0177%) A12=0.78 mm^2 (0.0078%) Total mean area A= 89.78 mm^2 (0.898%) Black Algae *(Al-b)*: 6%, black algae with length of filaments around 5-10 mm, homogeneously covering the surface. Silt: 35%, not uniform layer of silt, moderate thickness
Fouling Resistance (F.R.) [%]	95-(0.464+0.898+6)=87.64
Physical Condition of Antifouling Film	Digging and remainders of shells/organisms that were strongly adherent onto the paint: A=1.362% • Softness rating: 10, "no pigment transferred to a cotton swab" • DE before immersion: 0.74 • DE after 2 months immersion: 0.96 • König pendulum hardness before immersion: 22.2 • König pendulum hardness after 2 months immersion: 31.2 • 60° gloss before immersion: 77.25 • 60° gloss after 2 months immersion: 54.5
Physical Damage Rating (P.D.R.) [%]	100-1.362=98.64
Overall Performance (O.P.) [%]	87.64

Table 6.28: Antifouling performance calculation of PU specimen from Triplet 1 (2 months immersion), according to ASTM D 3623 and ASTM D 6990 guidelines

Fouling Examination	PU
Fouling on surface	PC-*Amphipods*: 2, found solitary on the coated surface A_1=5.0 × 0.7=3.5 mm^2 (0.035%) A_2=2.0 × 0.3=0.6 mm^2 (0.006%) PC-*Serpulidae*: calcareous tubes of circular cross-section, other than spirorbinae, making a network of interconnected tubes of area A=44.16% PC-*Spirorbinae*:38, 0.6-2.5 mm in mean diameter, found solitary A=60.413 mm^2 (Table C.3) (0.604%) Silt: 35%, not uniform layer of silt, moderate thickness
Fouling Resistance (F.R.) [%]	95-(44.16+0.6041)=50.23
Physical Condition of Antifouling Film	Almost all foulers with calcareous shells caused a digging effect on the painted surface, hence the affected area was taken equal to the area of the foulers: A=4476.413 mm^2 (44.764%) • Softness rating: 10, "no pigment transferred to a cotton swab" • DE before immersion: 0.47 • DE after 2 months immersion: 0.64 • König pendulum hardness before immersion: 57.67 • König pendulum hardness after 2 months immersion: 52.67 • 60° gloss before immersion: 23 • 60° gloss after 2 months immersion: 20.5
Physical Damage Rating (P.D.R.) [%]	100-44.76=55.24
Overall Performance (O.P.) [%]	50.23

As can be seen from Figs. 6.26c and 6.27c and from Table 6.28, the overall performance of the polyurethane painted specimen, which was not an antifouling paint, was the worst of all. A large amount of the painted surface was covered by large interconnected tubes (44.16%) dropping its AF performance to 50.23%. Apparently, its PDR was not satisfactory either, since the tubes left their stains on the paint (Fig. 6.31c) leading to a PDR equal to 55.24%. On the contrary, the experimental polyurethane formulation exhibited values equal to 87.64% and 98.64%, correspondingly, verifying an efficient AF protection. However, the experimental silicone formulation exhibited the best characteristics of all, with ratings equal to 93.31% and 98.62%, respectively. The observed macrofoulers were mainly *polychaetes*, which could be *spirorbinae* or not. The largest amount of *spirorbinae* was encountered on the Exp PU1 specimen (94), followed by the PU (38) and the Exp Si (5) specimens. With regard to *serpulidae* worms, other than *spirorbinae*, 32 individuals were found on the Exp Si specimen and 10 individuals on the Exp PU1 specimen. The Exp PU1 specimen was also covered by black-algae, which covered around 6% of the specimen's surface. Silt coverage ranged between 24-35% for all specimens.

After 2 months, "digging" was caused on the experimental silicone painted specimen by the attached foulers and accounted for 1.38% of the painted surface (Table 6.26). Compared to the reference silicone system, the foulers on the experimental silicone system were also easily removed under running water, however, their digging effect was quite faint and could be characterized mainly as prints of the attached organisms onto the paint. König hardness exhibited 16.9% increase compared to the initial condition, while the discoloration index increased 0.3 units or 52.6%. Gloss value exhibited 0.5 units decrease, remaining almost stable.

With regard to the Exp. PU1 painted specimen, digging and remainders of shells/organisms that were strongly adherent onto the paint accounted for damage covering 1.36% of the painted surface (Table 6.27). Some discoloration was measured (29.73%) and gloss loss (29.45%), implying deterioration of the optical characteristics of the painting system. The König pendulum hardness increased by 40.5%, in accordance with the observations for the experimental silicone system (Table 6.28), where the coating hardness exhibited an increase, compared to the initial condition, during all the examination intervals. Finally, the softness rating was equal to 10, meaning that no pigment loss was detected.

Finally, with regard to polyurethane painted specimen, almost all the attached foulers caused a digging effect on the paint. Hence, the affected area was taken equal to the area of the foulers, that is 44.76% (Table 6.28). The optical properties indicated some deterioration, with the DE index increasing by 36.2% and the gloss decreasing by 10.9%. The König hardness exhibited a slight decrease (8.7%).

6.3.2.2 After 4 months of immersion

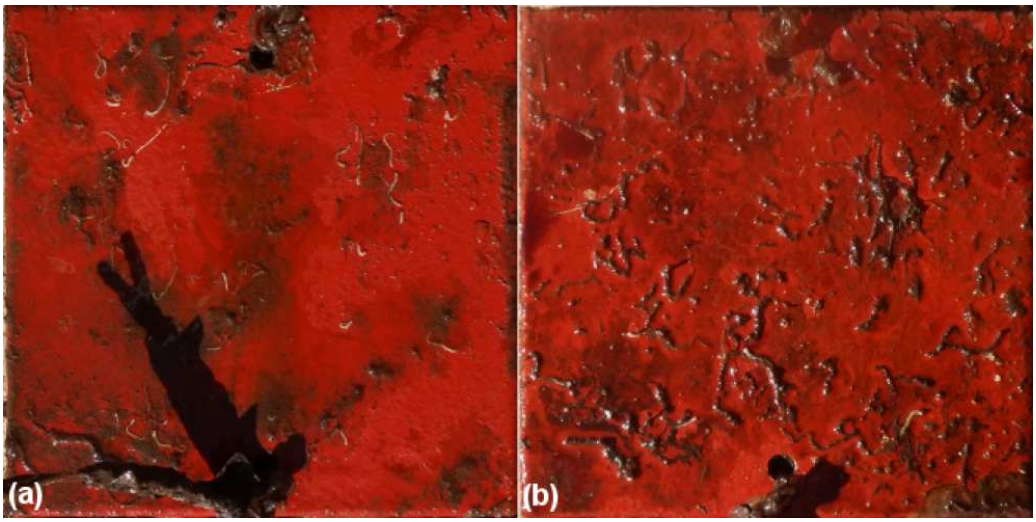

Figure 6.32: Surface condition of Exp Si specimen from Pair 2 that remained immersed for 4 months in Elefsis: a) after 2 months, b) after 4 months, when it was removed from site.

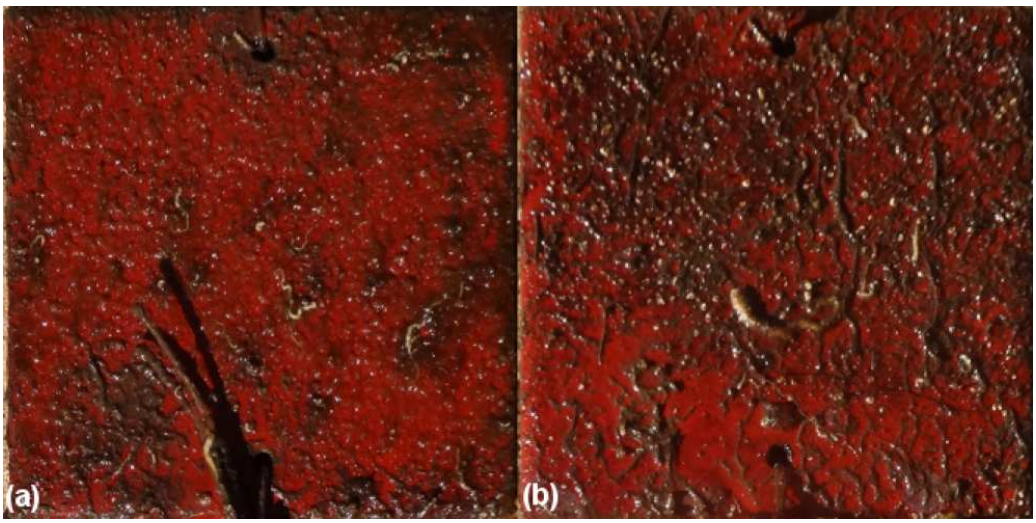

Figure 6.33: Surface condition of Exp PU1 specimen from Pair 2 that remained immersed for 4 months in Elefsis: a) after 2 months, b) after 4 months, when it was removed from site.

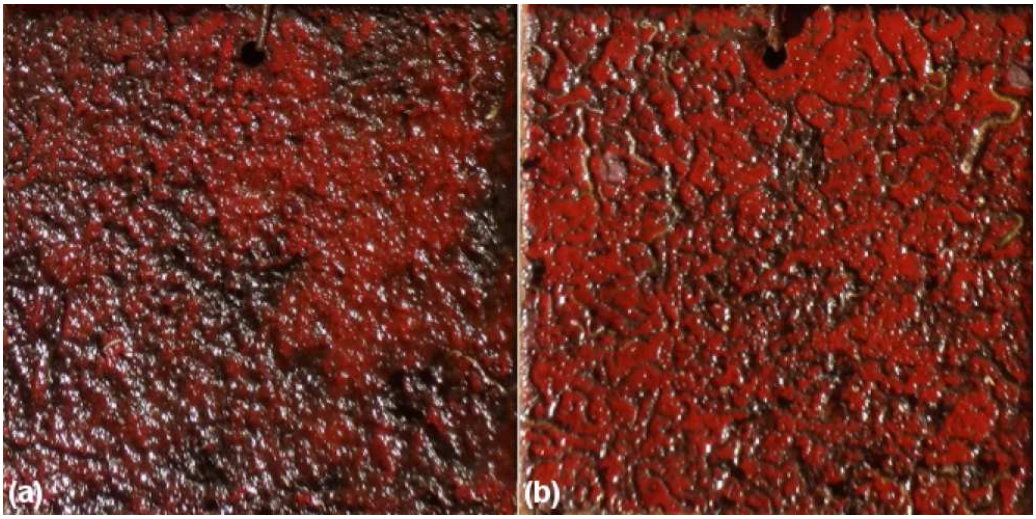

Figure 6.34: Surface condition of PU specimen from Pair 2 that remained immersed for 4 months in Elefsis: a) after 2 months, b) after 4 months, when it was removed from site.

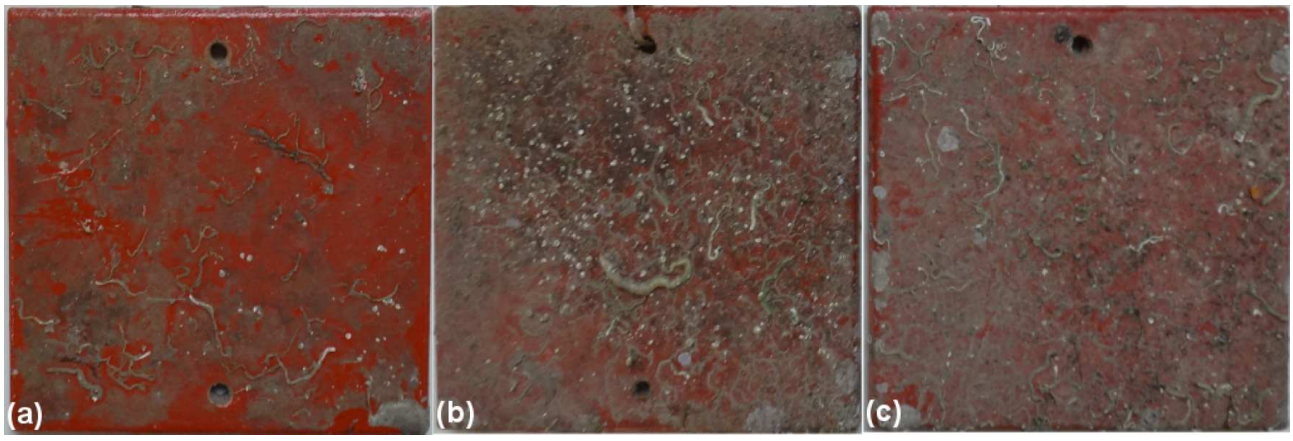

Figure 6.35: Surface condition of dried a) Exp Si, b) Exp PU1 and c) Polyurethane specimens after 4 months immersion in Elefsis

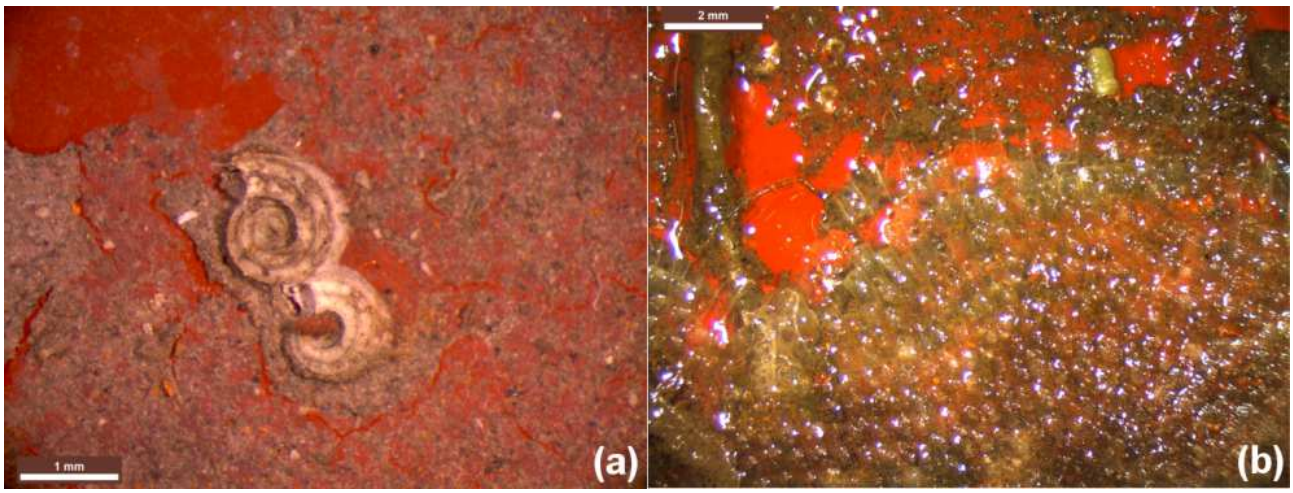

Figure 6.36: Stereoscopic observation of Exp Si specimen after 4 months immersion in Elefsis; a) two dextral *spirorbinae* and b) bryozoans at the lower right side of the specimen

With regard to Fig. 6.36a, the longitudinal ridges on the presented tubes are characteristic of *S. pagenstecheri*. The encrusting bryozoans appearing in Fig. 6.36b could be *bryozoans cheilostomata* [149].

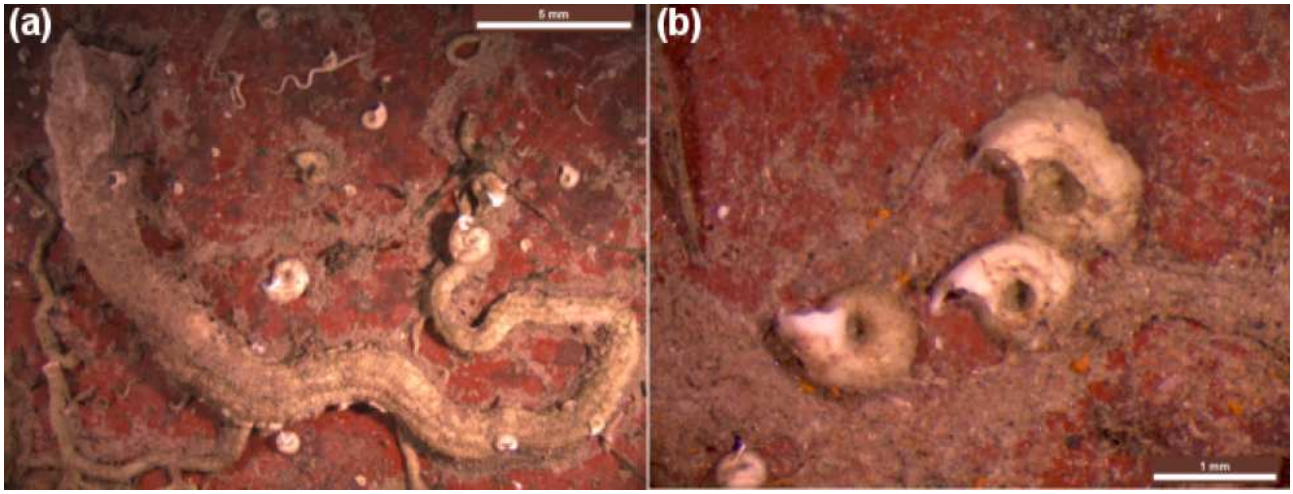

Figure 6.37: Stereoscopic observation of Exp PU1 specimen after 4 months immersion in Elefsis; a) the biggest shell observed in the specimen and b) sinistral and dextral *spirorbinae*

Figure 6.38: Stereoscopic observation of PU specimen after 4 months immersion in Elefsis; a) white area full of *spirorbinae* spores, b) the biggest biomineralising *polychaeta* of the specimen and c) various white interconnecting cells

In Fig. 6.38a, a white area full of *spirorbinae* spores is presented. These spores were found at various locations of the present specimen. Similar areas were encountered on Exp PU1 specimen, as well. In Fig. 6.38b the largest *polychaeta* of the specimen is presented. Its length was 32.605 mm, while its diameter at the opening was 1.821 mm. The tube exhibited three longitudinal ridges, it was funnel shaped, while its color was dirty white, except for the front area, which was white. Finally, in Fig. 6.38c various interconnected tubes are presented, white in color, with intense coiling, which could be *salmacina dysteri* [144].

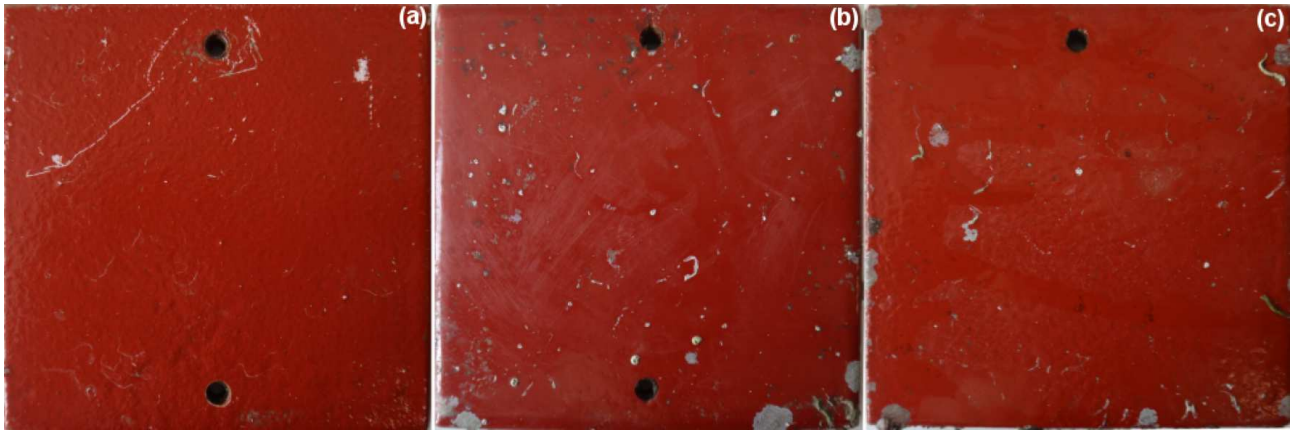

Figure 6.39: Surface condition of a) Exp Si, b) Exp PU1 and c) Polyurethane specimens immersed for 4 months in Elefsis after thorough cleaning

Table 6.29: Antifouling performance calculation of Exp. Si specimen from Triplet 2 (4 months immersion), according to ASTM D 3623 and ASTM D 6990 guidelines

Fouling Examination	Exp. Si
Fouling on surface	PC-*Serpulidae*: 37, non-ringed tubeworms, 1.827-40.298 mm^2. More details about their surface are presented in Table C.4. Total area: A=306.985 mm^2 (3.070%) PC-*Spirorbinae*: 23, 0.404-1.552 mm, at random locations over the painted surface. More details about their surface are presented in Table C.5. Total area: A=19.441 mm^2 (0.194%) *FB*: 21.077 mm^2 (0.211%) *EB*: 78.352 mm^2 (0.783%) Silt: 76.18%, small thickness and inhomogeneous coverage of the surface
Fouling Resistance (F.R.) [%]	95-(3.070+0.194+0.211+0.783)≈90.74
Physical Condition of Antifouling Film	Prints of the organisms attached onto the paint. A=242.92 mm^2 It should be noted that the prints were quite faint and no actual digging was observed. • DE before immersion: 0.60 • DE after 4 months immersion: 0.73 • König pendulum hardness before immersion: 17.75 • König pendulum hardness after 4 months immersion: 20.6 • 60° gloss before immersion: 23.25

	• 60° gloss after 4 months immersion: 28.75
Physical Damage Rating (P.D.R.) [%]	100-2.429≈97.57
Overall Performance (O.P.) [%]	90.74

Table 6.30: Antifouling performance calculation of Exp. PU1 specimen from Triplet 2 (4 months immersion), according to ASTM D 3623 and ASTM D 6990 guidelines

Fouling Examination	Exp. PU1
Fouling on surface	PC-*Serpulidae*: 24, non-ringed tubeworms, 0.411-104.017 mm^2 mean surface. All surfaces are presented in detail in Table C.6. Total mean area A=255.526 mm^2 (2.555%) PC-*Spirorbinae*:452, 0.591-1.0282 mm in diameter, dispersed over the entire specimen surface. More details are presented in Table C.7. Total mean area A=218.304 mm^2 (2.183%) *Barnacle(Barn)*: 1, A=0.833 × 0.625=0.521 mm^2 (0.0052%) *FB*: 0.134%, A=13.375 mm^2 *White surface including spirorbinae spores*: 182.5 mm^2 (1.825%), possibly encrusting bryozoans Silt: 76.92%, small thickness but extensive coverage
Fouling Resistance (F.R.) [%]	95-(2.555+2.183+0.0052+0.134+1.825)≈88.30
Physical Condition of Antifouling Film	Digging and remainders of shells/organisms, that were strongly adherent onto the paint: A= 594.099 mm^2 Softness rating: 10, "no pigment transferred to a cotton swab" • DE before immersion: 0.53 • DE after 4 months immersion: 0.92 • König pendulum hardness before immersion: 31.6 • König pendulum hardness after 4 months immersion: 57.6 • 60° gloss before immersion: 79 • 60° gloss after 4 months immersion: 24.5
Physical Damage Rating (P.D.R.) [%]	100-5.941≈94.06
Overall Performance (O.P.) [%]	88.30

Table 6.32: Antifouling performance calculation of PU specimen from Triplet 2 (4 months immersion), according to ASTM D 3623 and ASTM D 6990 guidelines

Fouling Examination	PU
Fouling on surface	PC-*Spirorbinae*: 239, 0.5-1.044 mm in diameter, dispersed over the entire specimen surface. More details are presented in Table C.8. Total mean area A=101.772 mm^2 (1.018%)

	PC-*Serpulidae*: : 67, non-ringed tubeworms, 0.5-52.168 mm2 mean surface. All surfaces are presented in detail in Table C.9. Total mean area A=462.465 mm^2 (4.625%) *White surface including spirorbinae spores*:1.618% (A=161.768 mm^2), found at various locations across the painted surface, which could be encrusting bryozoans. The calculated surfaces are presented in Table C.10. *Barnacle(Barn)*: 1, A=5.71 × 3.66=20.899 mm^2, located at the thickness dimension of the specimen, hence not included in the FR rating. *Amphipod*: 1, A=1.91 × 0.30=0.570 mm^2 (0.006%) Silt: 92.52%, moderately thick, extended but inhomogeneous coverage of the surface.
Fouling Resistance (F.R.) [%]	95-(1.018+4.625+1.618+0.21)≈87.53
Physical Condition of Antifouling Film	Digging and remainders of shells/organisms, that were strongly adherent onto the paint: A= 694.621 mm^2 Softness rating: 10, "no pigment transferred to a cotton swab" • DE before immersion: 0.51 • DE after 4 months immersion: 1.026 • König pendulum hardness before immersion: 56.33 • König pendulum hardness after 4 months immersion: 77 • 60° gloss before immersion: 32.25 • 60° gloss after 4 months immersion: 23.75
Physical Damage Rating (P.D.R.) [%]	100-6.946≈93.05
Overall Performance (O.P.) [%]	87.53

After 4 months of immersion, the AF Exp PU1 specimen exhibited similar antifouling performance with the non-antifouling PU painted specimen. The FR for the former was 88.30%, while for the latter 87.53%. The PDR values were also similar, being 94.06% and 93.05%, respectively. The Exp Si specimen exhibited the best performance of all, scoring 90.74% and 97.57%, respectively. The observed foulers were *spirorbinae*, with the largest population encountered on the Exp PU1 specimen (452), followed by the PU specimen (239) and the Exp Si specimen (23). Encrusting and filamentous bryozoans were found on all specimens. The largest amount was found on Exp PU1 specimen, which was around 1.825% and it was possibly white encrusting bryozoans. Finally, one barnacle was observed on the surface of each polyurethane system. Other non-*spirorbinae* worms (PC-*serpulidae*) were also found on all specimens, with the largest population encountered on the polyurethane painted specimen (67). Finally, silt covered the surface of all specimens, ranging between 76-92.5%.

With regard to physical damage, the prints of the attached foulers on the Exp. Si painted specimen accounted for 2.43% of the surface. The hardness of the vehicle exhibited 16% increase, while DE increased 21.67%. With regard to the Exp. PU1 painted specimen, a similar trend as after 2 months of immersion was observed also after 4 months. The digging effect increased to 5.94%, leading to a P.D.R. value equal to 94.06%, hence, the physical damage was

not extensive after 4 months of immersion. With regard to the rest of the properties, discoloration was once more apparent (73.58% increase), while the gloss loss was more profound than the previous interval (around 69%). Finally, the coating hardness increased by 82.3%, becoming almost double and approaching the hardness values of the acrylic-based system. As regards the PU painted specimen, the digging effect was much smaller (6.95%), compared to the value after 2 months, while the variation of the rest of the properties reminded of the Exp. PU1 system trend with discoloration (102%), gloss drop (26.36%) and hardness increase (36.7%). Hence, after 4 months, the polyurethane paint was found to be the hardest of all (77), followed by the AF polyurethane (57.6) and the experimental silicone (20.6). Finally, no pigment transfer was observed for either of the polyurethane formulations (softness rating equal to 10).

6.3.2.3 After 6 months of immersion

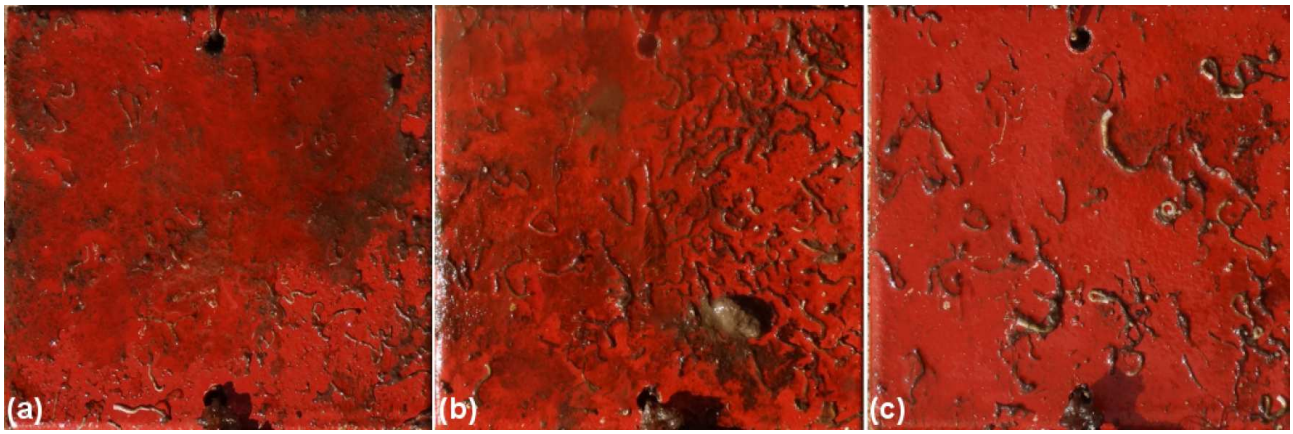

Figure 6.40: Surface condition of Exp Si specimen from Triplet 3 that remained immersed for 6 months in Elefsis: a) after 2 months, b) after 4 months and c) after 6 months, when it was removed from site.

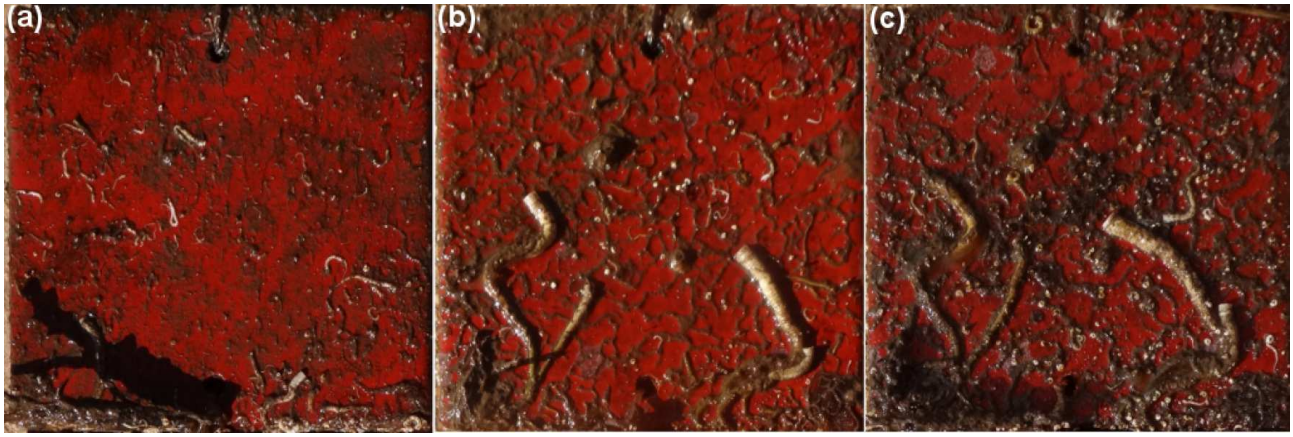

Figure 6.41: Surface condition of Exp PU1 specimen from Triplet 3 that remained immersed for 6 months in Elefsis: a) after 2 months, b) after 4 months and c) after 6 months, when it was removed from site.

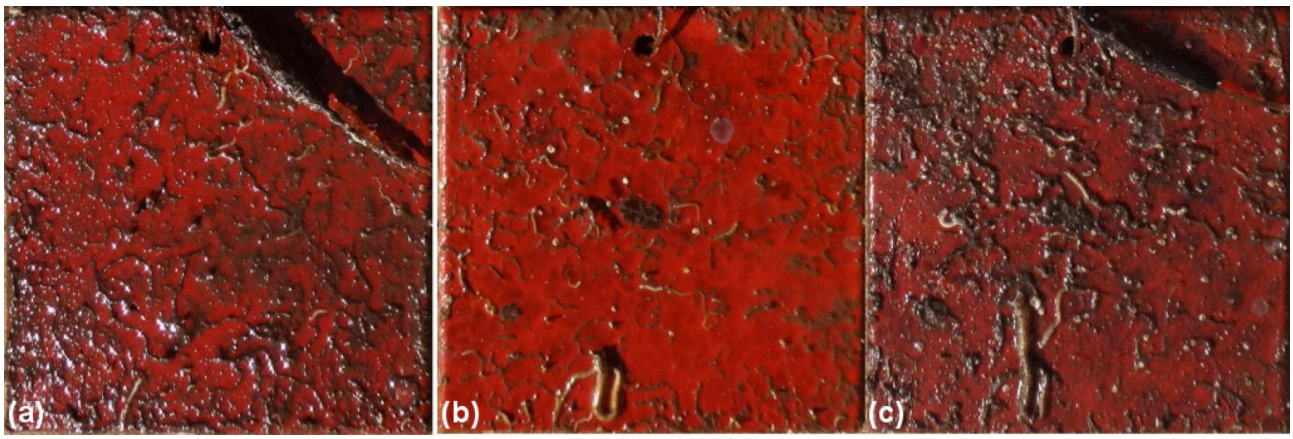

Figure 6.42: Surface condition of PU specimen from Triplet 3 that remained immersed for 6 months in Elefsis: a) after 2 months, b) after 4 months and c) after 6 months, when it was removed from site.

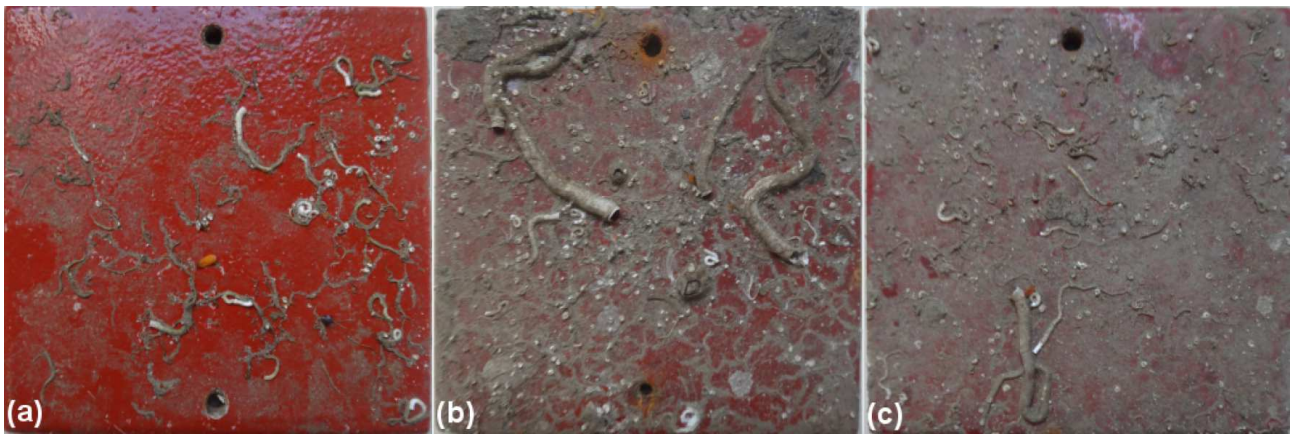

Figure 6.43: Surface condition of dried a) Exp Si, b) Exp PU1 and c) Polyurethane specimens after 6 months immersion in Elefsis

Table 6.33: Antifouling performance calculation of Exp. Si specimen from Triplet 3 (6 months immersion), according to ASTM D 3623 and ASTM D 6990 guidelines

Fouling Examination	Exp. Si
Fouling on surface	PC-*Serpulidae*: 46, 2.276-76.922mm2. More details about their surface are presented in Table C.11. Total area: A=692.256 mm^2 (6.922%) PC-*Spirorbinae*: 337, 1.011-2.166 mm, at random locations over the painted surface. More details about their surface are presented in Table C.12. Total area: A=321.552 mm^2 (3.215%) *Mol*: 1, A=2.719 × 2.400=6.526 mm^2, one black mussel-like organism (Fig. 6.43a) *Amphipods*: 4, 0.342-1.236 mm^2, found randomly on the painted surface. Their surfaces are analyzed in Table C.13. Total area: A=3.100 mm^2 (0.031%)

	Silt: 57.59%, a light-thickness layer of silt inhomogeneously covering the painted surface.
Fouling Resistance (F.R.) [%]	95-(6.922+3.215+0.065)≈84.80
Physical Condition of Antifouling Film	• Prints of the organisms attached onto the paint. A_1=422.748 mm^2.The prints of the organisms were quite faint. No actual digging was observed. • Some physical damage possibly caused by the elastomeric nature of the paint, due to wearing, and not due to the attached foulers, was in the form of flaking and occupied a surface equal to A_2=349.380 mm^2. • DE before immersion: 0.90 • DE after 6 months immersion: 0.45 • König pendulum hardness before immersion: 12.60 • König pendulum hardness after 6 months immersion: 14.67 • 60° gloss before immersion: 19.0 • 60° gloss after 6 months immersion: 21.5
Physical Damage Rating (P.D.R.) [%]	100-7.721≈92.28
Overall Performance (O.P.) [%]	84.80

Table 6.34: Antifouling performance calculation of Exp. PU1 specimen from Triplet 3 (6 months immersion), according to ASTM D 3623 and ASTM D 6990 guidelines

Fouling Examination	Exp. PU1
Fouling on surface	PC-*Serpulidae*: 4, 133.451-337.801 mm^2, the biggest on the surface, as appearing in Fig. 6.43b. More details about their surface are presented in Table C.14. Due to their very large dimensions, they will be treated as a colony and not as solitary forms. Hence, for the FR calculation, their surface will be deducted. Total area: A=889.983 mm^2 (8.900%) PC-*Serpulidae*: 79, 1.361-47.620 mm^2, the rest of the calcareous tubes observed on the painted surface. It should be noted that most of them were of cylindrical cross-section (no serpulinae forms detected). More information about the mean calculated areas are presented in Table C.15. Total area: A=549.291mm^2 (5.493%) *PC-Spirorbinae*: 489, 0.058-2.232 mm, at random locations over the painted surface. More details about their surface are presented in Table C.16. Total area: A=854.341 mm^2 (8.543%) *Amphipods*: 9, 0.480-1.792 mm^2 (Table C.17) Total area: A=9.86 mm^2 (0.099%) *Barn*:3, 22.50-59.85 mm^2 A_1=5.387 × 5.387=29.020 mm^2 A_2=8.080 × 7.407=59.848 mm^2

	A_3=4.500 × 5.000=22.500 mm^2 Total area: A=111.368 mm^2 (1.114%) *White surface including spirorbinae spores*:1.041%, found in the middle and close to the specimen edges. A larger magnification of this area revealed a surface similar to bryozoans. A_1=2.564 × 2.308=5.918 mm^2 A_2=1.600 × 1.760=2.816 mm^2 A_3=7.742 × 8.064=62.431 mm^2 A_4=5.600 × 5.880=32.928 mm^2 Total area: A=104.093 mm^2 *Mol*:4, possibly clams found on various locations on the specimen, with the largest located at the lower right edge of the specimen. A_1=17.845 × 9.428=168.243 mm^2 A_2=1.203 × 0.800=0.962 mm^2 A_3=0.352 × 0.850=0.299 mm^2 A_4=3.708 × 5.617=20.828 mm^2 Total area: A=190.332 mm^2 (1.903%) *FB*: 1.228% *EB*: 2.092%, white in color, located at the upper left side of the specimen, while a small portion was also spotted at the center of the painted surface. A_1=15.825 × 12.795=202.481 mm^2 A_1=2.258 × 2.958=6.679 mm^2 Total area: A=209.160 mm^2 Silt: 61.668%, which is the silt covering the specimen apart from the large tubes.
Fouling Resistance (F.R.) [%]	95-(8.9+5.493+8.543+1.114+1.041+1.903+1.228+2.092)≈64.69
Physical Condition of Antifouling Film	• Digging and remainders of shells/organisms, strongly adherent onto the paint. A=1078.034 mm^2. • Softness rating: 10, no pigment transfer • DE before immersion: 0.27 • DE after 6 months immersion: 0.74 • König pendulum hardness before immersion: 25.8 • König pendulum hardness after 6 months immersion: 50.3 • 60° gloss before immersion: 78.25 • 60° gloss after 6 months immersion: 49.25
Physical Damage Rating (P.D.R.) [%]	100-10.78=89.22
Overall Performance (O.P.) [%]	64.69

Table 6.35: Antifouling performance calculation of PU specimen from Triplet 3 (6 months immersion), according to ASTM D 3623 and ASTM D 6990 guidelines

Fouling Examination	PU
Fouling on surface	PC-*Serpulidae*: 45, 0.201-220.363 mm^2. More details about their surface are presented in Table C.18. Total area: A=687.792 mm^2 (6.878%) *PC-Spirorbinae*: 324, 0.070-3.015 mm, at random locations over the painted surface. More details about their surface are presented in Table C.19. Total area: A=254.963 mm^2 (2.550%) *Amphipods*: 1, A=6.88 × 0.88=6.054 mm^2 (0.061%) *Mol*: 2, solitary forms on the specimen surface A_1 (black mussel)=0.996 × 0.724=0.721 mm^2 A_2 (clam-like organism)=1.106 × 1.407=1.556 mm^2 Total area: A=2.277 mm^2 (0.023%) *EB*: 0.689%, of the *Cheilostomata* order, white and transparent/grey in color, located on the right and middle side of the specimen, respectively. A_1 (transparent/grey)=10.555 × 5.025=53.039 mm^2 A_2 (white)=15.904 mm^2 Total area: A=68.943 mm^2 (0.689%) *FB*: 0.525%, Located on the middle-right area of the painted surface (A=15 × 3.5=52.5 mm^2) Silt: 84.026%, a layer of moderate thickness, with variations on thickness and coverage over the specimen surface.
Fouling Resistance (F.R.) [%]	95-(6.878+2.550+0.023+0.689+0.525)≈84.34
Physical Condition of Antifouling Film	• Digging and remainders of shells/organisms, strongly adherent onto the paint. A=836.43mm^2. • Softness rating: 10, no pigment transfer • DE before immersion: 0.50 • DE after 6 months immersion: 1.35 • König pendulum hardness before immersion: 60.50 • König pendulum hardness after 6 months immersion: 75.17 • 60° gloss before immersion: 37.0 • 60° gloss after 6 months immersion: 26.8
Physical Damage Rating (P.D.R.) [%]	100-8.364≈91.64
Overall Performance (O.P.) [%]	84.34

After 6 months of immersion in Elefsis the overall performance of the non-AF polyurethane coating was better than the experimental polyurethane formulation. Even though both systems exhibited a decrease in the FR, compared to 4 months, the decrease was more profound for the AF polyurethane coat which was rated with 64.69%, compared to the 84.34% of the polyure-

thane system. The PDR values were 89.22% and 91.64%, correspondingly. After 6 months of immersion the anticorrosive polyurethane system was better overall than the AF experimental polyurethane formulation. These findings can be verified from Figs. 6.41 and 6.42, where the fouling of the experimental polyurethane system appears to be more severe. The experimental silicone formulation was rated with FR 84.80% and PDR 92.28%, respectively, exhibiting the best behavior overall. The types of the observed foulers were similar to the ones after 4 months, in addition to some mussels observed on the two experimental formulations.

With regard to the pysical damage after 6 months, the prints of the organisms on theExp. Si painted specimen covered area equal to 422.75 mm^2. Some physical damage caused possibly by the elastomeric nature of the paint, was attributed to wearing and affected area equal to 349.38 mm^2. The hardness of the coat exhibited 16.43% increase, similarly to the observations after 2 and 4 months of immersion. The gloss value exhibited small increase after 6 months, similarly to the finding after 4 months, while the discoloration index exhibited 50% decrease. With regard to the Exp. PU1 painted specimen, the physical damage caused by digging expanded to 10.78% of the painted surface. With regard to the rest of the properties, a behavior similar to previous intervals was observed. DE increased 174%, 60° gloss dropped by 37%, while the hardness of the coat increased by 95%. As regards the PU painted specimen, the digging effect affected a larger area, but still quite small, compared to the condition after 2 months, equal to 8.36%. The optical properties exhibited the same behavior as in the previous interval, with the corresponding changes being equal to 170%, 27.58% and 24.25%, respectively. The anticorrosive polyurethane system exhibited the highest hardness, compared to the rest of the systems (as was also reported after 4 months of experiment). Finally, no pigment transfer was observed for either of the polyurethane formulations.

6.3.2.4 After 8 months of immersion

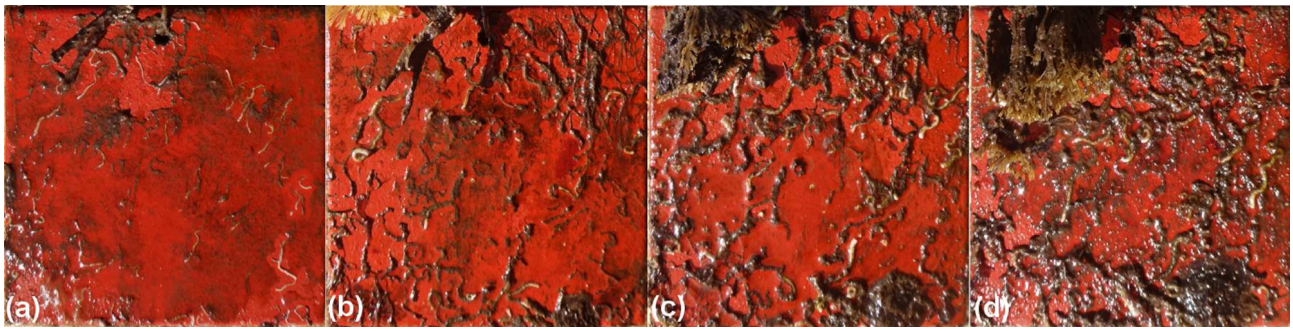

Figure 6.44: Surface condition of Exp Si specimen from Pair 4 that remained immersed for 8 months in Elefsis: a) after 2 months, b) after 4 months and c) after 6 months, d) after 8 months, when it was removed from site.

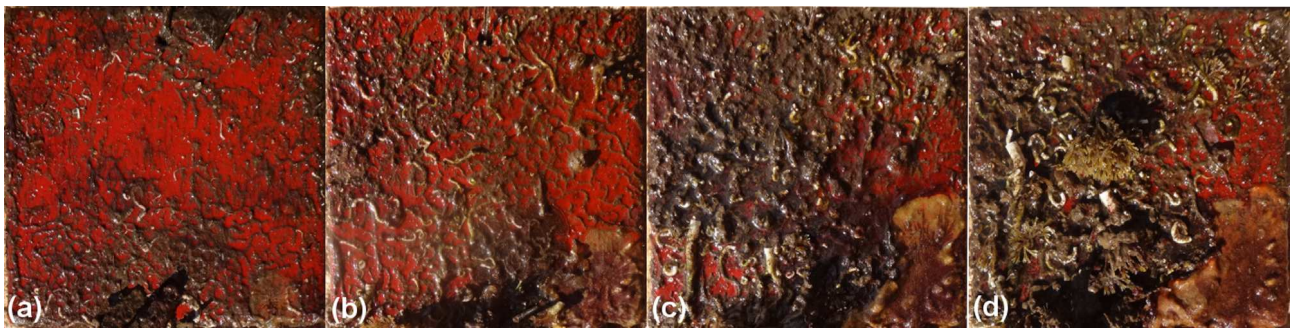

Figure 6.45: Surface condition of Exp PU1 specimen from Pair 4 that remained immersed for 8 months in Elefsis: a) after 2 months, b) after 4 months and c) after 6 months, d) after 8 months, when it was removed from site.

As can be seen from Fig. 6.45, fouling progressively covered almost the entire surface of the specimen after 8 months of immersion. An area equal to 19.445 cm^2 was covered by encrusting bryozoans, especially the "rust"-colored *cheilostomata*. Also, in Fig. 6.45d, filamentous bryozoans can be seen. The rest foulers were *serpulidae* and *spirorbinae*. Due to the high density coverage of the surface with fouling, the fouling rating dropped to 12.14%. The two types of bryozoans are presented in Fig. 6.46.

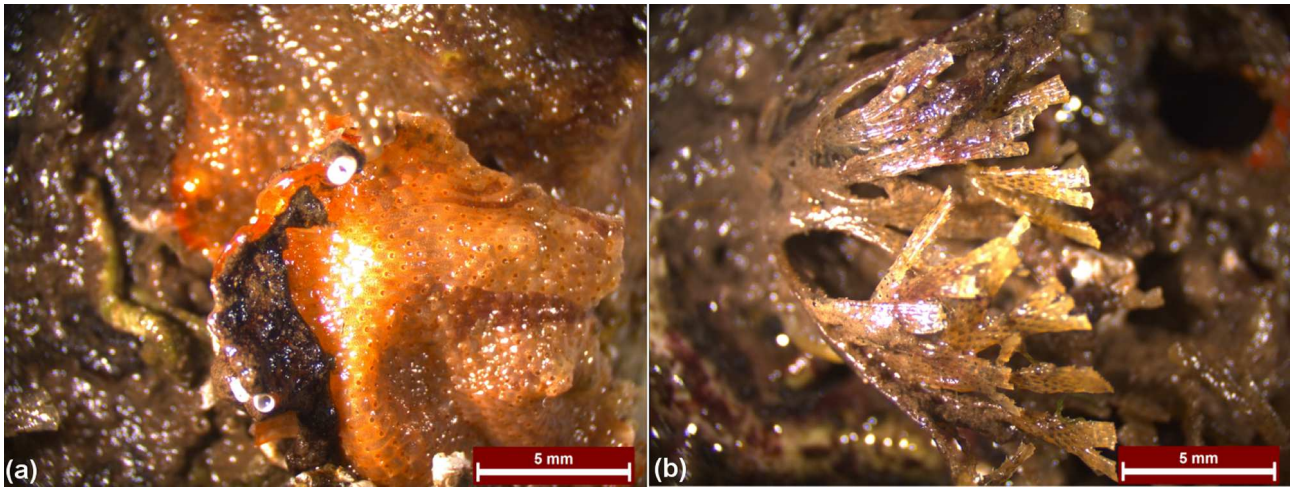

Figure 6.46: Stereoscopic observation of Exp PU1 specimen after 8 months of immersion; a) encrusting bryozoans *cheilostomata* and b) bushy bryozoans

The retrieved specimen was transferred to the laboratory immersed in water from site. Indeed, the foulers remained alive upon arrival to the laboratory, as can be seen from Fig. 6.47a. In Fig. 6.47b, the same specimen during inspection in the stereoscope is presented, while, finally, in Fig. 6.47c, the final condition of the specimen is presented, with the less adherent foulers having been removed.

Figure 6.47: Surface condition of Exp PU1 specimen after 8 months immersion in Elefsis; a) in the laboratory, immersed in water from site, b) during drying and c) after total cleaning and removal of less adherent foulers

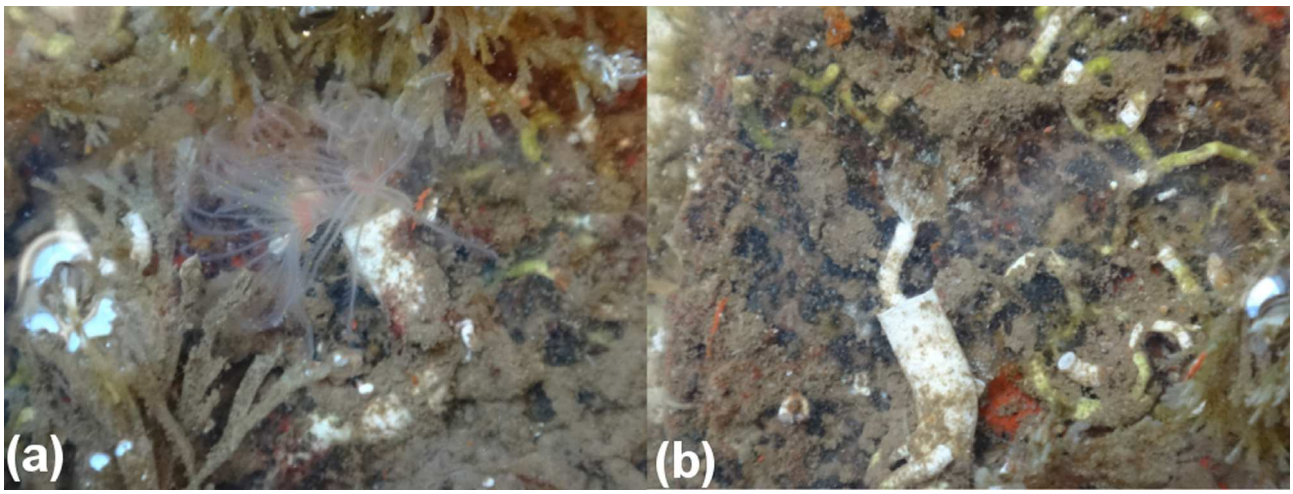

Figure 6.48: Representatives of *serpulidae* family on Exp PU1 specimen after 8 months immersion in Elefsis; a) *protula* and b) *hydroides* genera

In Fig. 6.48 two representatives of the *serpulidae* family are presented. In Fig. 6.48a, an organism, possibly of the *protula* genus is presented, while in Fig. 6.48b a representative of the *hydroides* genus, of the *serpulinae* sub-family is presented. The first organism exhibited similar characteristics with the one presented in Fig. 6.49. The second organism was identified by its characteristic operculum, which becomes apparent as a bending stalk, on the right side of the filaments. The operculum exhibits a funnel stalk, in the middle of which a crown bearing brown spines is presented.

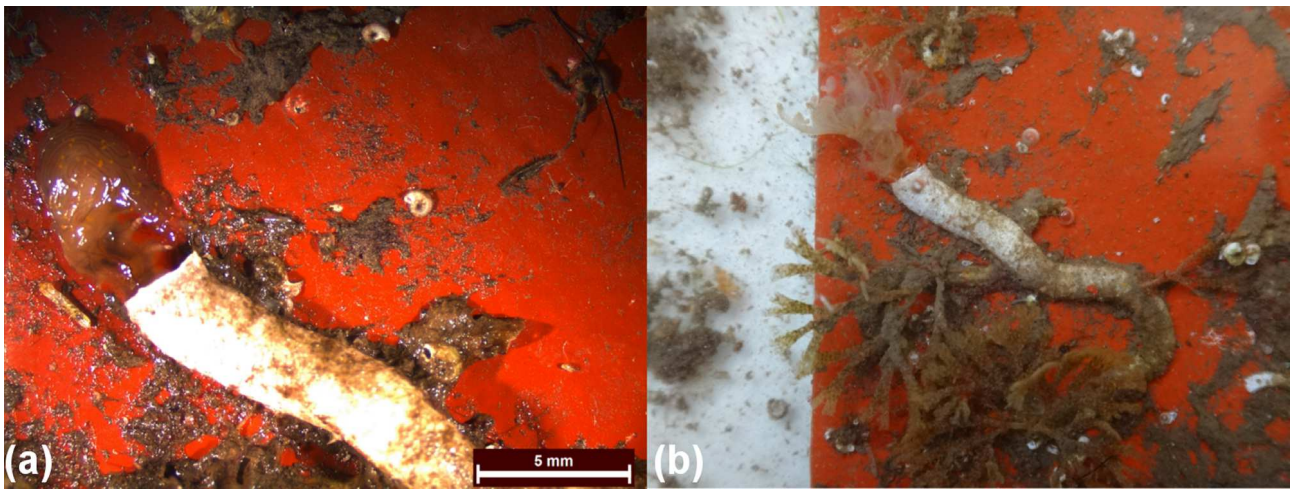

Figure 6.49: Representative of *serpulidae* family on Exp Si specimen after 8 months immersion in Elefsis; a) before and b) after blossom

In Fig. 6.49, a representative of the *serpulidae* family is presented. This organism exhibited a smooth tube, funnel-shaped, white in color especially in the half distal part and dirty-white to brown for the latter half part. Two representatives of this species were found on the specimen, with a diameter of 3.158 mm and 2.885 mm, respectively. The length of the tubes was 44.211 mm and 37.500 mm, correspondingly, while both tubes were prostrate. The organisms exhibited colorless branchial filaments with yellow dots and faint red stripes. When blossomed, the dots appeared along each branchial filament, while a faint red stripe appeared at the lower part of the filaments. The large dimensions and the morphology of the tubes could imply the *protula* genus, which has global distribution [144].

Table 6.37: Antifouling performance calculation of Exp. Si specimen from Pair 4 (8 months immersion), according to ASTM D 3623 and ASTM D 6990 guidelines

Fouling Examination	Exp. Si
Fouling on surface	PC-*Serpulidae*: 47, 4.429-139.618 mm^2. It should be noted that they were mainly of cylindrical cross-section (no *serpulinae* forms detected). More information about the mean calculated areas are presented in Table C.20. Total area: A=1626.465 mm^2 (16.265%) PC-*Spirorbinae*: : 141, 0.526-2.105 mm, at random locations over the painted surface. More details about their surface are presented in Table C.21. Total area: A=229.216 mm^2 (2.292%) *Barn*: 1, 5.263×4.737=24.931 mm^2 (0.249%) *Mol*: 1, a very large clam covering the upper left side of the painted surface. A=421.204 mm^2 (4.212%) *FB*: 2.521%, found at three locations on the painted surface. A_1=7.895×12.632=99.730 mm^2 A_2=4×(10.526×5.263)/2=110.797 mm^2

	A_3=7.895×5.263=41.551 mm^2 Silt: 14.588%, not uniform coverage of the surface and not of uniform thickness
Fouling Resistance (F.R.) [%]	95-(16.265+2.292+0.249+4.212+2.521)≈69.46
Physical Condition of Antifouling Film	• Prints of the organisms attached onto the paint. A=1319.15 mm^2. • DE before immersion: 0.41 • DE after 8 months immersion: 1.56 • König pendulum hardness before immersion: 9.33 • König pendulum hardness after 8 months immersion: 11 • 60° gloss before immersion: 15.25 • 60° gloss after 8 months immersion: 14.75
Physical Damage Rating (P.D.R.) [%]	100-13.192≈86.81
Overall Performance (O.P.) [%]	69.46

Table 6.38: Antifouling performance calculation of Exp. PU1 specimen from Pair 4 (8 months immersion), according to ASTM D 3623 and ASTM D 6990 guidelines

Fouling Examination	Exp. Si
Fouling on surface	Extensive coverage with fouling. Main representatives: encrusting and bushy bryozoans, barnacles, a great variety of *serpulidae* and *spirorbinae*, as well as amphipods. The encrusting bryozoans covered a great amount of the painted surface, above which secondary fouling-mainly *serpulidae* worms-appeared. The surface that was not covered with bryozoans (encrusting or bushy) and secondary foulers, was full of *spirorbinae*. The total area that was free of fouling was A=1213.91 mm^2
Fouling Resistance (F.R.) [%]	12.14
Physical Condition of Antifouling Film	• Digging and remainders of shells/organisms, strongly adherent onto the paint. A=2278.488 mm^2. • Softness rating:10, no pigment trnasfer. • DE before immersion: 0.482 • DE after 8 months immersion: 2.364 • König pendulum hardness before immersion: 44.33 • König pendulum hardness after 8 months immersion: 52.67 • 60° gloss before immersion: 53 • 60° gloss after 8 months immersion: 27
Physical Damage Rating (P.D.R.) [%]	100-22.785≈77.22
Overall Performance (O.P.) [%]	12.14

After 8 months of immersion, the experimental polyurethane formulation was almost fully

fouled, exhibiting An FR equal to 12.14%. A large amount of the surface was covered by encrusting bryozoans *cheilostomata*, of rusty color. The PDR was 77.22%, remaining in relatively high levels, compared to the extent of the fouling. The experimental silicone formulation retained its fouling resistance to higher levels, scoring an FR of 69.46% and a PDR of 86.81%, exhibiting better performance overall after 8 months immersion.

With regard to the physical damage of the specimens, a larger surface of "fouling-prints" was observed on the Exp. Si painted specimen (13.19%). The hardness of the coat exhibited increase equal to 17.9%, similar to the previous observations. Discoloration index increased (2.8%) and gloss value decreased (3.3%), a combination of changes that could indicate some initial signs of deterioration. With regard to the Exp. PU1 specimen, digging increased after 8 months and affected area equal to 22.78%, discoloration increased by 391.67%, while gloss dropped by 49%, remaining, however, higher than the less affected silicone painted specimen (15.25 GU before experiment and 14.75 GU after 8 months). Also, the hardness values verified the harder nature of the Exp. PU1 system, which had a value equal to 52.67 after 8 months, while the Exp Si system a value of 11. Apparently, both systems became a bit harder after immersion, which was noticed also for the examined specimens after 2, 4 and 6 months (the only exception was the hardness for the non-AF PU system after 2 months immersion, which exhibited a slight decrease). Finally, the softness rating for the Exp PU1 paint was once more equal to 10, since no pigment loss was observed.

6.3.2.5 After 10 months of immersion

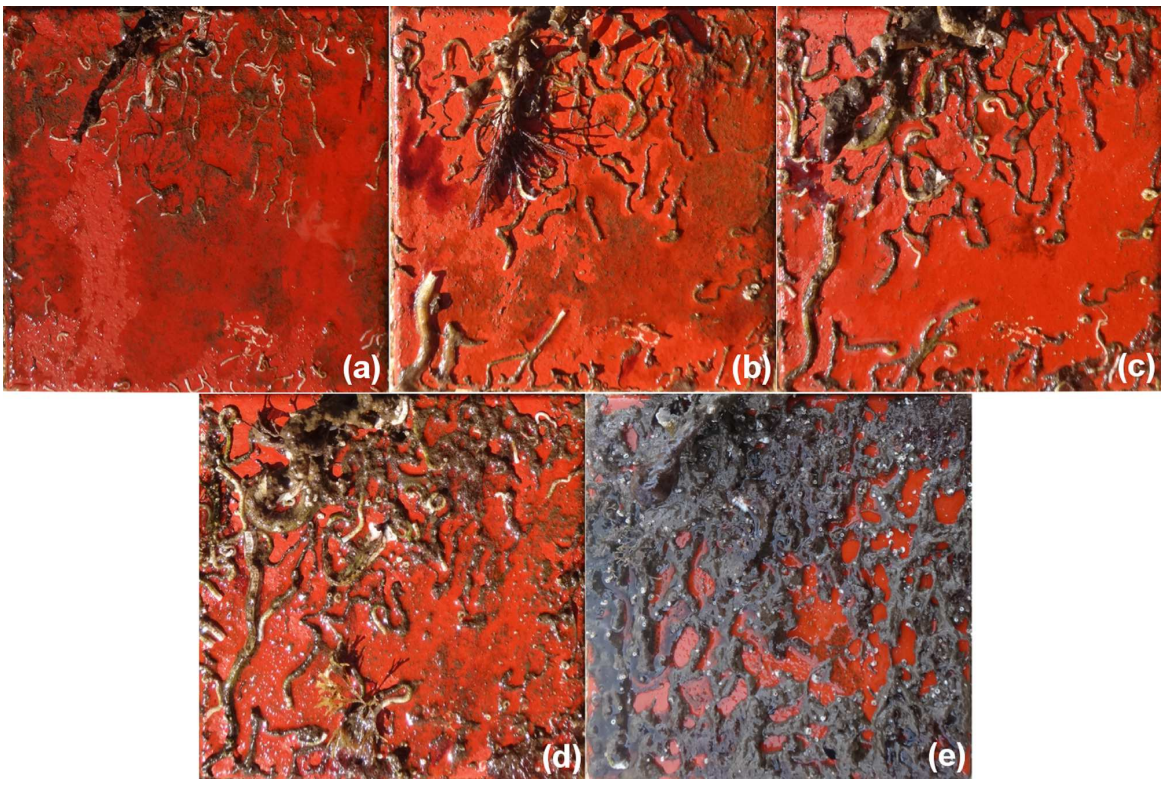

Figure 6.50: Surface condition of Exp Si specimen from Pair 5 that remained immersed for 10 months in Elefsis: a) after 2 months, b) after 4 months and c) after 6 months, d) after 8 months and e) after 10 months, when it was removed from site.

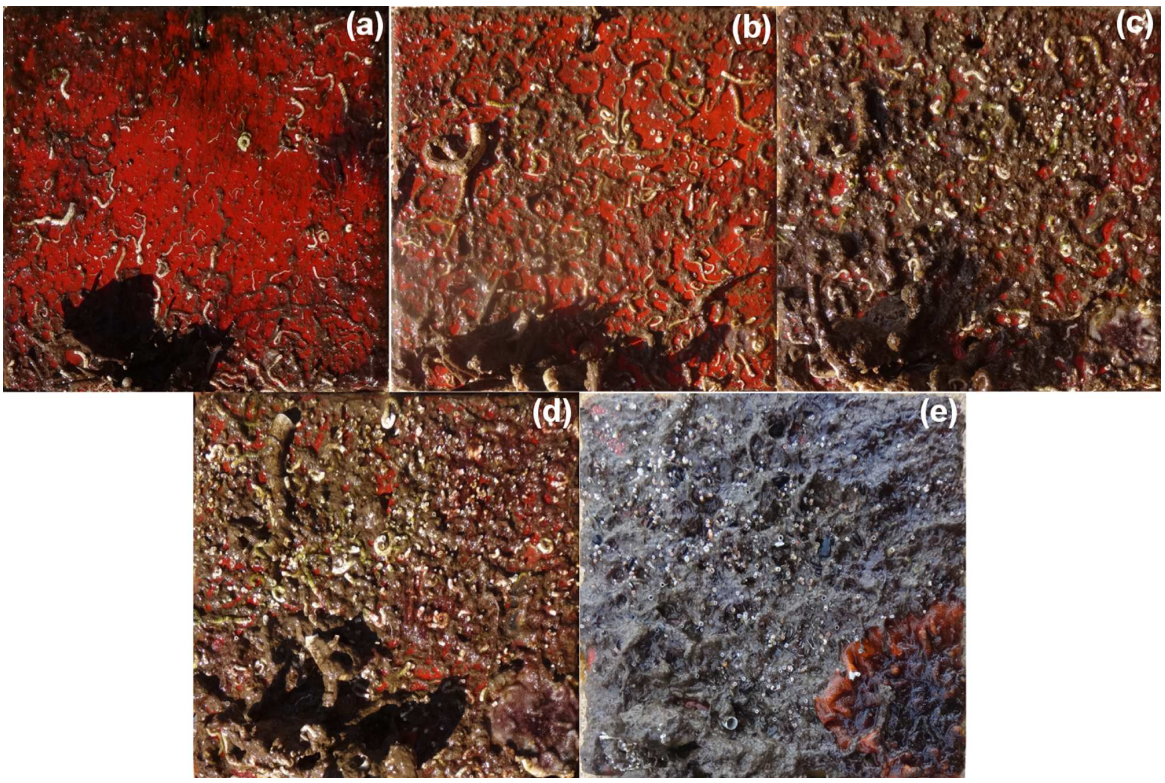

Figure 6.51: Surface condition of Exp PU1 specimen from Pair 5 that remained immersed for 10 months in Elefsis: a) after 2 months, b) after 4 months and c) after 6 months, d) after 8 months and e) after 10 months, when it was removed from site.

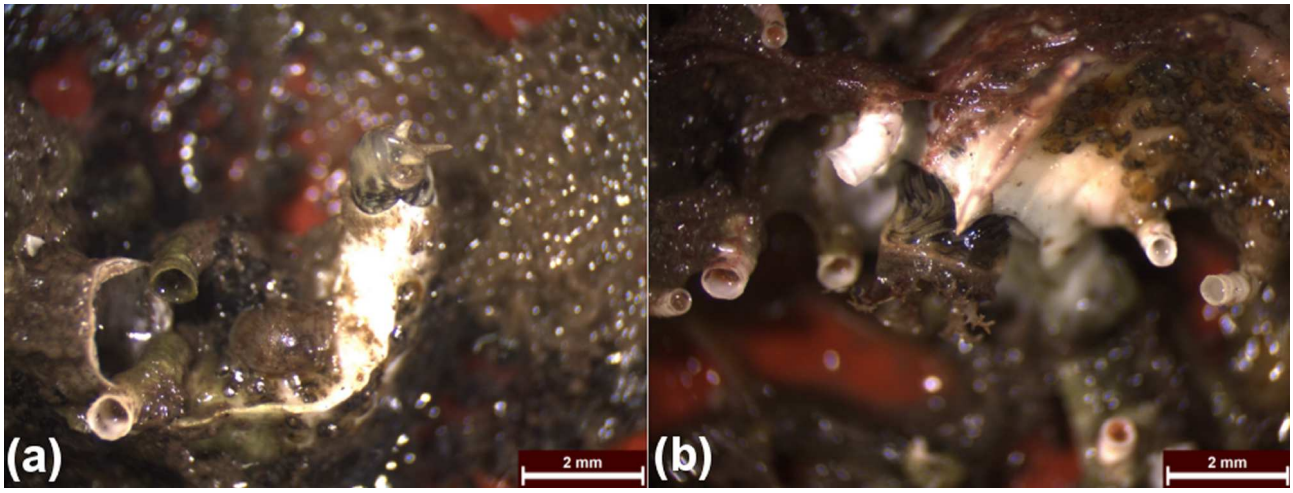

Figure 6.52: Stereoscopic observation of Exp. Si specimen after 10 months of immersion, presenting representatives of the *serpulidae* family

In Fig. 6.52a, a *pomatoceros triqueter* is presented [150]. This organism can be easily identified by its characteristic operculum, bearing three distinct projections, and its triangular-sectioned tube, with a prominent longitudinal ridge on top. A similar tube, but much larger in dimension, is presented in Fig. 6.52b. The operculum of the organism reminded of *spirobranchus tetraceros* [151], however the shape of its tube was similar to pomatoceros.

Table 6.39: Antifouling performance calculation of Exp. Si specimen from Pair 5 (10 months immersion), according to ASTM D 3623 and ASTM D 6990 guidelines

Fouling Examination	Exp. Si
Fouling on surface	PC-*Serpulidae*: 30, 11.394-450.273 mm^2, found on various locations over the painted surface. More details about their surface are presented in Table C.22. Total area: A=1874.903 mm^2 (18.749%) PC-*Spirorbinae*: 156, 0.521-2.604 mm, found mainly as colonies on various locations over the painted surface. More details about their surface are presented in Table C.23. Total area: A=172.448 mm^2 (1.724%) *Barn*: 1, 2.604×1.982=5.161 mm^2 *Mol*: 1, mussel of dimensions 5.208×3.204=16.686 mm^2 *Foulers (general)*: 35.34%, this surface refers to mixture of various kinds of foulers, consisting mainly of *serpulidae* tubes and *spirorbinae* colonies, which could not be identified individually. Silt: 15.54%, not uniform coverage of the surface and not of uniform thickness. The small percentage of the silt is justified by the fact that the covered macrofoulers could be easily distinguished (Fig. 6.50) in the silt and were excluded from the coverage calculation.
Fouling Resistance (F.R.) [%]	95-(18.749+1.724+0.052+0.167+35.34)≈38.97
Physical Condition of Antifouling Film	• Prints of the organisms attached onto the paint. A=886.644 mm^2 (8.866%). • Physical damage caused as a result of erosion/wear: 766.861 mm^2 (7.669%) • DE before immersion: 0.79 • DE after 10 months immersion: 1.51 • König pendulum hardness before immersion: 18.8 • König pendulum hardness after 10 months immersion: 24.2 • 60° gloss before immersion: 20.75 • 60° gloss after 10 months immersion: 17.5
Physical Damage Rating (P.D.R.) [%]	100-(8.866+7.669)≈83.47
Overall Performance (O.P.) [%]	38.97

Table 6.40: Antifouling performance calculation of Exp. PU1 specimen from Pair 5 (10 months immersion), according to ASTM D 3623 and ASTM D 6990 guidelines

Fouling Examination	Exp. PU1
Fouling on surface	Extensive coverage with fouling. Some representatives of the observed foulers are presented below: PC-*Serpulidae*: 1, the biggest tube of the specimen with an area A=4×75=300 mm^2 (3%) PC-*Spirorbinae*: 2.8%, a colony of spirorbinae occupying a surface of A=14×20=280 mm^2 *Barn*: 10, 0.839-3.489 mm on average, for the bigger inner diameter of the barnacle shells. Average barnacle height around 5 mm. *EB*: 14.52%, the large orange bryozoans surface on the lower right side of the specimen (A=1452.20 mm^2). *Bristle worm*: 1, A=2×35=70 mm^2 (0.7%) The encrusting bryozoans covered a great amount of the painted surface, above which secondary fouling-mainly *serpulidae* worms-appeared. The surface that was not covered with bryozoans and secondary foulers, was full of *spirorbinae*. The total area that was free of fouling was A=339.338 mm^2
Fouling Resistance (F.R.) [%]	3.39
Physical Condition of Antifouling Film	• Digging and remainders of shells/organisms, strongly adherent onto the paint. A=1621.997 mm^2 (16.22%). • Softness rating: 10, no pigment transfer • DE before immersion: 0.82 • DE after 10 months immersion: 0.85 • König pendulum hardness before immersion: 30.67 • König pendulum hardness after 10 months immersion: 46.4 • 60° gloss before immersion: 72 • 60° gloss after 10 months immersion: 33.5
Physical Damage Rating (P.D.R.) [%]	100-16.22=83.78
Overall Performance (O.P.) [%]	3.39

After 10 months of immersion, the fouling on the Exp PU1 specimen covered almost the entire surface, leaving a free surface equal to 3.39%. However, the physical damage of the paint was not as profound, since a PDR equal to 83.78% was measured. This is attributed to the fact that the phydical damage rating was performed after thorough cleaning of the specimens. For the first time, a bristle worm was observed on the surface of the Exp PU1 specimen, covering 0.7% of the specimen area. The silicone specimen exhibited an FR equal to 38.97% and a PDR equal to 83.47%, being superior overall, but inefficient, in terms of antifouling performance. In terms of hardness, both systems became harder after immersion, with the polyurethane

having a higher value (46.4 compared to 24.2). In terms of optical characteristics, gloss drop was more abrupt for the Exp PU1 system compared to the silicone (33.5 GU versus 17.5 GU). No discoloration was observed for the polyurethane formulation, while for the silicone system discoloration increased by 0.72 units, implying a slight change in color. Finally, no pigment transfer was observed for the Exp PU1 system after 10 months of immersion in Elefsis.

6.3.2.6 After 12 months of immersion

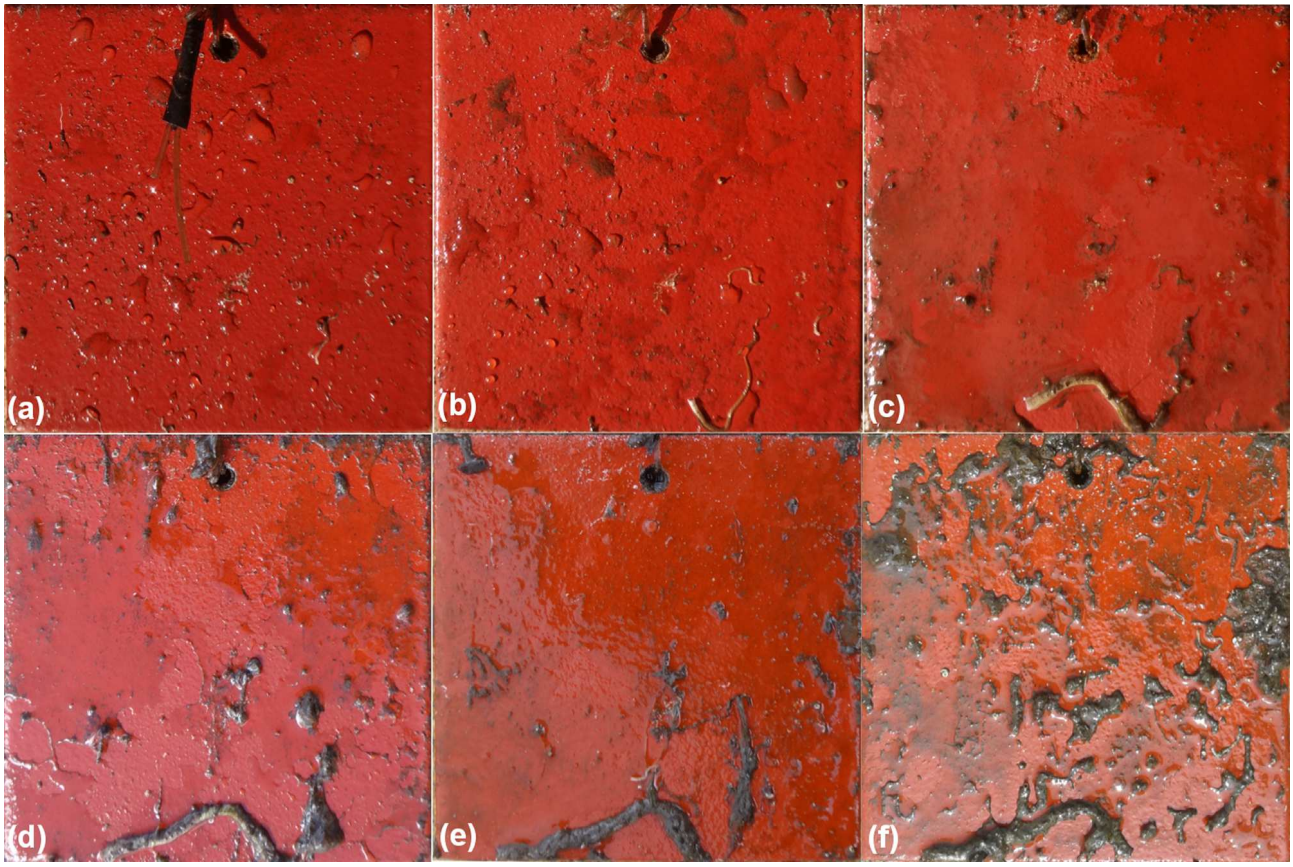

Figure 6.53: Surface condition of Exp Si specimen from Pair 6 that remained immersed for 12 months in Elefsis: a) after 2 months, b) after 4 months and c) after 6 months, d) after 8 months, e) after 10 months and f) after 12 months, when it was removed from site

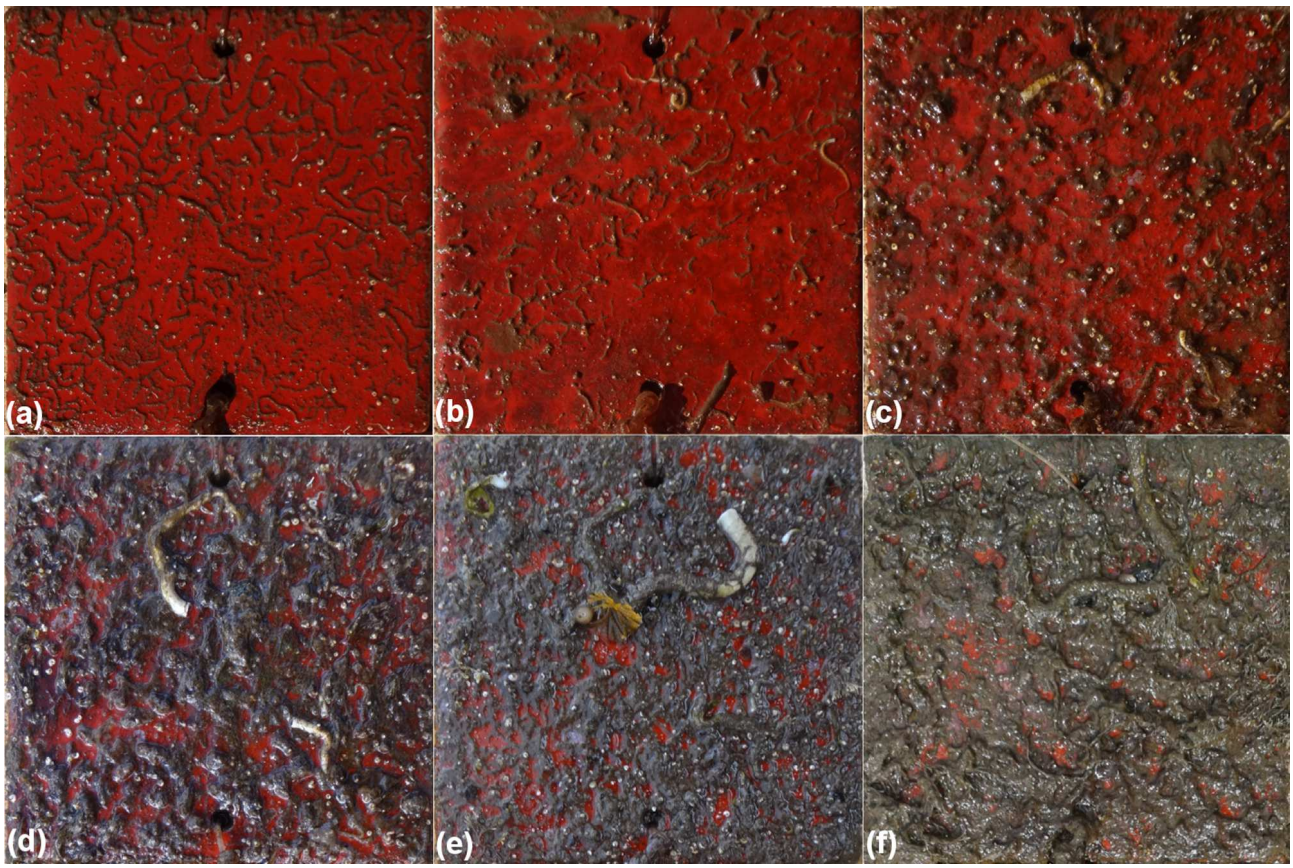

Figure 6.54: Surface condition of Exp PU1 specimen from Pair 6 that remained immersed for 12 months in Elefsis: a) after 2 months, b) after 4 months and c) after 6 months, d) after 8 months, e) after 10 months and f) after 12 months, when it was removed from site

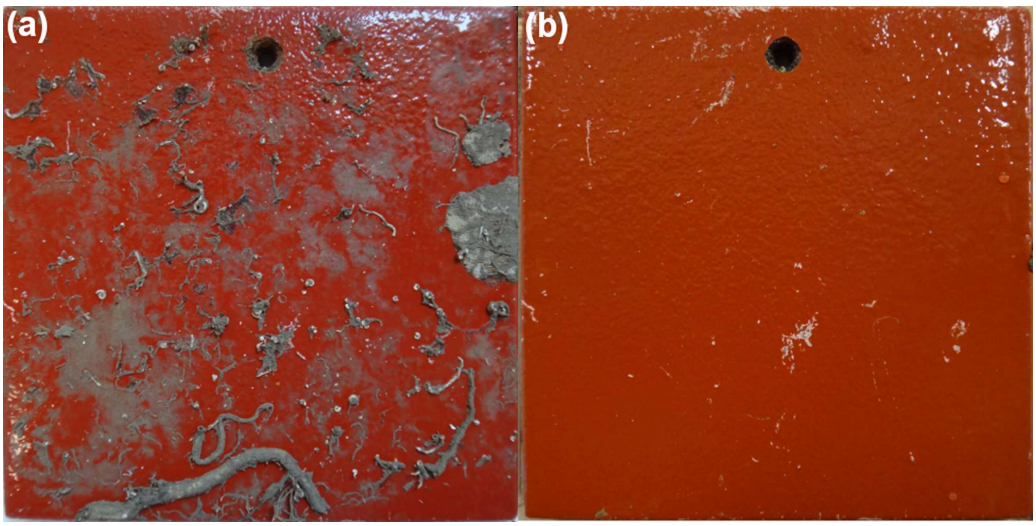

Figure 6.55: Surface condition of Exp Si specimen from Pair 6 that remained immersed for 12 months in Elefsis; a) after gentle wash and b) after complete removal of the foulers

Figure 6.56: Surface condition of Exp PU1 specimen from Pair 6 that remained immersed for 12 months in Elefsis; a) as dried, b) after gentle wash and b) after complete removal of the foulers

As can be seen from Fig. 6.56a, the specimen was covered with an intense layer of silt, mixed with a great amount of filamentous bryozoans. The silt covered the areas where encrusting bryozoans were observed, hence, gentle cleaning was mandatory, in order to reveal these areas (Fig. 6.56b). The surface of the specimen after thorough cleaning is presented in Fig. 6.56c.

Table 6.42: Antifouling performance calculation of Exp. Si specimen from Pair 6 (12 months immersion), according to ASTM D 3623 and ASTM D 6990 guidelines

Fouling Examination	Exp. Si
Fouling on surface	PC-*Serpulidae*: 52, non-ringed tubeworms, 0.719-133.702 mm^2, found on various locations over the painted surface (Table C.24). Total area: A= 560.631 mm^2 (5.606%) PC-*Spirorbinae*: 175, 0.222- 2.083 mm, found mainly as colonies on various locations over the painted surface (Table C.25). Total area: A= 86.822 mm^2 (0.868%) *Amphipod*: 1, of dimensions 1.832×0.550=1.008 mm^2 *Mol*: 1, mussel of dimensions 2.602×3.861=10.046 mm^2 *EB*: 2.946%, encrusting bryozoans were observed on the mid-right side of the painted surface. A_1=8.681×8.293=71.992 mm^2 A_2=14.385×15.483=222.723 mm^2 Silt: 63.37%, light layer of silt, not uniform coverage of the surface.
Fouling Resistance (F.R.) [%]	95-(5.606+0.868+2.946+0.100)=85.48
Physical Condition of Antifouling Film	• Prints of the organisms attached onto the paint. A=39.836 mm^2 (0.398%). • Physical damage caused as a result of wear: 343.146 mm^2 (3.431%) • DE before immersion: 0.724

	• DE after 12 months immersion: 0.666 • König pendulum hardness before immersion: 20 • König pendulum hardness after 12 months immersion: 23 • 60° gloss before immersion: 19.5 • 60° gloss after 12 months immersion: 20.75
Physical Damage Rating (P.D.R.) [%]	100-3.83=96.17
Overall Performance (O.P.) [%]	85.48

Table 6.43: Antifouling performance calculation of Exp PU1 specimen from Pair 6 (12 months immersion), according to ASTM D 3623 and ASTM D 6990 guidelines

Fouling Examination	Exp. PU1
Fouling on surface	PC-*Serpulidae*: 8, non-ringed tubeworms, 21.789- 599.655 mm^2. A few but quite large tubes were observed after 12 months of exposure. More details about their dimensions are presented in Table C.26. Total area: A= 968.74 mm^2 (9.687%) PC-*Spirorbinae*: 27.72%, 1.093-2.186 mm, extensive coverage of the surface with spirorbinae, either mature forms, found solitary or in colonies, or colonies of larvae. *Barn*: 1, 9.836×9.290=91.376 mm^2 (0.914%) *EB*: 44.303%, extensively covering the painted surface (Fig. 6.56b). Their dimensions are presented in Table C.27. Silt: 32.72%, covering the surface covered by bryozoans. The silt was mixed with filamentous bryozoans, which were secondary foulers, hence, not included in the fouling rating assessment. Due to the large amount of silt, the fouling rating was based on Fig. 6.56b.
Fouling Resistance (F.R.) [%]	95-(9.687+44.303+0.914+27.72)=12.38
Physical Condition of Antifouling Film	• The physical damage of the paint was mainly attributed to digging and remainders of calcareous shells and organisms(especially bryozoans) (Fig. 6.56b). A= 2673.017 mm^2 (26.730%). • Some damage caused by black stains (possibly remainders of foulers, silt and algae, Fig. 6.56c) was: A= 429.046 mm^2 (4.290%) • Softness rating: 10, no pigment transfer • DE before immersion: 0.582 • DE after 12 months immersion: 2.014 • König pendulum hardness before immersion: 23.17 • König pendulum hardness after 12 months immersion: 23 • 60° gloss before immersion: 71.5 • 60° gloss after 12 months immersion: 43
Physical Damage Rating (P.D.R.) [%]	100-(26.730+4.290)=68.98
Overall Performance (O.P.) [%]	12.38

After 12 months of immersion, the fouling for the Exp PU1 specimen was as severe as after 8

months of immersion. The FR was 12.38% and included mainly large serpulidae tubes, a large amount of encrusting bryozoans (44.30% coverage), as well as, a great amount of spirorbinae, homogenously covering the surface, giving a coverage percentage of 27.72%. The physical damage was the lowest, compared to the previous intervals, giving a ranking equal to 68.98%. The experimental silicone system exhibited a remarkable behavior (FR 85.48%), which could be compared with the fouling ratings of the first 6 months of immersion. The same observation also holds for the PDR which was 96.17%, ranked between the values after 4 and 6 months immersion.

Hardness value remained the same for the Exp PU1 system and slightly increased (from 20 before immersion to 23 after 12 months) for the Exp Si specimen. The gloss value exhibited a drop for the polyurethane system but remained at higher levels compared to the Exp Si system (43 GU versus 20.75 GU), which remained unaffected. Discoloration increased 1.432 units for the polyurethane and remained more or less unaffected for the silicone system. Finally, after 12 months of immersion the softness rating for the experimental polyurethane formulation was granted a ranking equal to 10.

In summary, the experimental silicone formulation exhibited effective antifouling protection after 2,4,6 and 12 months of immersion, since the F.R. was above 84.80%. However, after 8 and 10 months the dense fouling settlement made the paint become ineffective. The painted surface facilitated mainly ringed tubeworms and serpulid tubeworms of cylindrical cross section. Compared to the reference silicone formulation, the experimental system exhibited better antifouling behavior overall. With regard to the physical damage, it was mainly attributed to digging and some wearing of the topcoat. The P.D.R. value remained above 83.47% during the whole immersion period. The optical characteristics exhibited variations from interval to interval, hence, the paint was slightly affected. The hardness of the coat increased after all intervals, remaining, however, at similar or somewhat lower levels than the reference silicone formulation.

The Exp. PU1 system did not exhibit satisfactory behavior in terms of antifouling protection, since it became largely affected after 6 months of experiment with strongly adherent foulers. Variety of foulers, especially serpulid worms (e.g. *spirorbinae*, *protula*, *hydroides*) and bryozoans (both encrusting and filamentous) were observed. Physical damage rating was above 68.98% for all intervals, as calculated after specimens' cleaning, and it was mainly atributed to digging. Discoloration and 60° gloss drop were observed for all intervals, implying some deterioration of physical properties. In terms of mechanical integrity, the coating was found harder compared to the initial condition, after each interval, except for the 12-month examination, during which no change in hardness was observed. The softness rating was always equal to 10, meaning that there was no pigment loss for this paint.

Finally, With regard to the behavior of the anticorrosive polyurethane formulation, its antifouling behavior was unsatisfactory after two months of immersion, however, after 4 and 6 months it was above 80%. The F.R. index after 6 monhts was better for the reference formulation than its antifouling counterpart (64.69%). The physical damage was mainly atrributed

to digging of the strongly attached foulers. The optical and mechanical properties followed the trend of the experimental polyurethane formulation, with discoloration, 60° gloss drop and increase of coating hardness. The hardness of the polyurethane painted specimens exhibited the largest values compared to the previous systems. Apparently, the limited amount of specimens painted with the PU system did not allow a complete comparison with the Exp. PU1 formulation, which was immersed for one year. In either case, the PU formulation is an anticorrosive system, not intended for antifouling purposes. Finally, it should be mentioned that the softness rating was always equal to 10, meaning that there was no pigment loss for this paint, either.

6.3.2.7 Conclusions with regard to the field tests of Exp PU1, Exp Si AF systems and the PU non-AF paint

Table 6.44: Summary of antifouling and physical damage rating for the Exp Si, Exp PU1 and PU systems during the 12-month immersion experiment in Elefsis

Months	Exp. Si			Exp. PU1			PU		
	FR [%]	PDR [%]	OP[%]	FR [%]	PDR [%]	OP[%]	FR [%]	PDR [%]	OP[%]
2	93.31	98.62	93.31	87.64	98.64	87.64	50.23	55.24	50.23
4	90.74	97.57	90.74	88.30	94.06	88.30	87.53	93.05	87.53
6	84.80	92.28	84.80	64.69	89.22	64.69	84.34	91.64	84.34
8	69.46	86.81	69.46	12.14	77.22	12.14	-	-	-
10	38.97	83.47	38.97	3.39	83.78	3.39	-	-	-
12	85.48	96.17	85.48	12.38	68.98	12.38	-	-	-

The 12-month immersion of Exp Si, Exp PU1 and PU painted specimens revealed the better behavior of the Exp Si formulation, compared to the polyurethanes overall. The experimental AF silicone system retained a FR larger than 80% for the first 6 months and after 12 months of experiment, exhibiting a drop only after 10 months of immersion. Its PDR was always above 83.47%, implying an excellent behavior against fouling attachment. The organisms were easily removed under running water of low pressure, usually leaving a print, with almost any digging. Even though the PDR calculation includes some wear of the paint, which is expected to be high for an elastomeric paint, it was eventually proven that the paint was less affected than expected, during the field test. The paint allowed loose attachment and growth of *serpulidae* worms of various genera. *Spirorbinae* were also apparent. The mean hardness value of the paint was around 17.71 and exhibited only small increases, during the experiment. Finally, the optical characteristics did not exhibit sharp changes. The discoloration index changes were smaller than +1.15, while the highest gloss drop was 3.25 GU, with the mean gloss value being around 18.91 GU.

With regard to the AF experimental polyurethane formulation and its anticorrosive reference, after 2 months the reference paint was granted a very low rating, since a very big part of the surface was covered with a large network of tubes. As can be seen from Table 6.44, the FR was 50.23%, while for the AF formulation was 87.64%. After 4 months, the two systems exhibited similar behavior. Finally, after 6 months their difference was profound, with the

experimental formulation having an overall rating of 64.69%, while the anticorrosive system had a rating of 84.34%. The unsatisfactory efficiency of the Exp PU1 system after 8, 10 and 12 months of experiment revealed its limited antifouling performance. Even though the PDR was retained at high levels ranging from 68.98% (after 12 months) to 98.55% (after 2 months), it should be mentioned that the organisms were strongly attached onto the painted surface and it was very hard to remove them, even with high water or finger pressure (usually there were remainders from the calcareous tubes). However, in order to be able to assess the physical damage of the paint, the foulers were removed from the specimen. From the above observations it could be concluded that the Exp PU1 formulation could not be used for antifouling purposes.

6.3.3 Experimental Polyurethane (Exp PU2) AF system

6.3.3.1 After 2 months of immersion

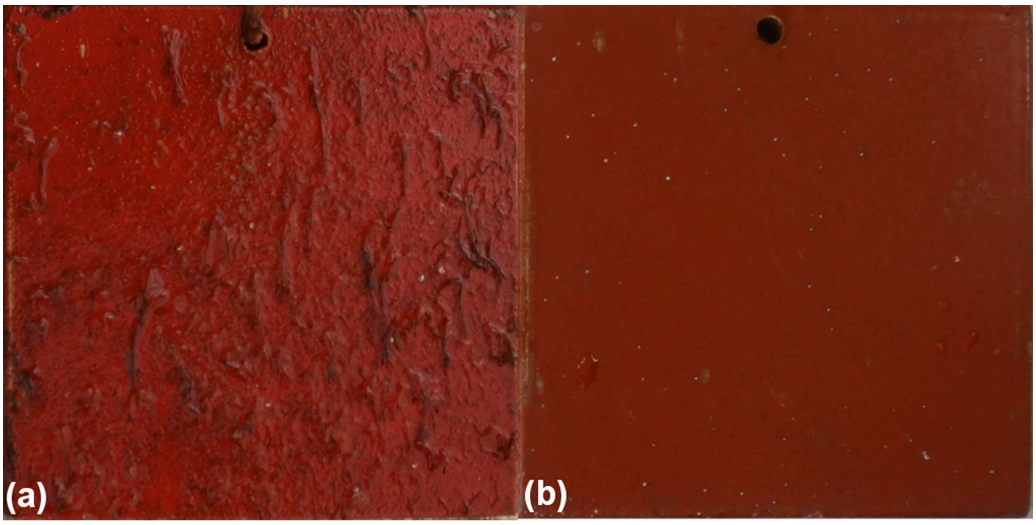

Figure 6.57: Surface condition of Exp PU2 specimen after 2 months immersion in Elefsis; a) at site and b) after thorough cleaning

Table 6.45: Presentation of antifouling performance calculation of Exp PU2 paint after 2 months of immersion, according to ASTM D 3623 and ASTM D 6990 guidelines

Fouling Examination	Exp. PU2
Fouling on surface	PC-*Spirorbinae*: 114, 0.227- 1.111 mm (Table 6.46) Total area: A= 70.923 mm2 (0.709%) *Amphipods*: 8, 0.929-2.980 mm, in length *Al-FB*: 49.99%, filamentous algae and/or bryozoans extensively covering the painted surface. Silt: 50%,not uniform coverage of the surface and not of uniform thickness.
Fouling Resistance (F.R.) [%]	95-(49.99+0.709)≈44.30
Physical Condition of	• Paint digging: A=42.421 mm^2 (0.424%)

Antifouling Film	• Some damage of the paint noticed during inspection: A= 41.171 mm^2 (0.412%) • Softness rating: 10, no pigment transfer • DE before immersion: 1.522 • DE after 2 months immersion: 1.593 • König pendulum hardness before immersion: 22.80 • König pendulum hardness after 2 months immersion: 26.63 • 60° gloss before immersion: 59 • 60° gloss after 2 months immersion: 28.5
Physical Damage Rating (P.D.R.) [%]	100-(0.424+0.412)≈99.16
Overall Performance (O.P.) [%]	44.30

Table 6.46: Mean diameter, number of individuals and total surface area covered by the 114 *spirorbinae* found on the surface of the Exp PU2 specimen after 2 months immersion in Elefsis

Mean diameter (mm)	Number of individuals	Mean area (mm^2)
0.402	1	0.127
0.590	1	0.273
0.455	4	0.650
0.318	1	0.079
0.227	1	0.040
0.385	1	0.116
1.000	1	0.785
0.753	61	27.165
1.111	43	41.686
Total area		70.923

6.3.3.2 After 4 months of immersion

Figure 6.58: Surface condition of Exp PU2 specimen after 4 months immersion in Elefsis; a) after 2 months, b) after 4 months, when it was removed from site and c) after thorough cleaning

Table 6.47: Presentation of antifouling performance calculation of Exp PU2 paint after 4 months of immersion, according to ASTM D 3623 and ASTM D 6990 guidelines

Fouling Examination	Exp. PU2
Fouling on surface	PC-*Spirorbinae*: 155, 0.563-2.147 mm in diameter, found on various locations over the painted surface (Table C.28). Total area: A= 214.692 mm^2 (2.147%) *Amphipods*: 2, 0.963-3.148mm, in length *Al-FB*: 85.316%, filamentous algae and/or bryozonas extensively covering the painted surface. Silt: 12.53%, almost uniform coverage of the painted surface with a thick layer of silt
Fouling Resistance (F.R.) [%]	95-(85.316+2.147)≈7.54
Physical Condition of Antifouling Film	• Paint digging: A=214.692 mm^2 (2.147%). • Some black "stains" observed during inspection (probably remainders of algae/bryo): A= 423.453 mm^2 (4.235%) • Softness rating: 10, no pigment transfer • DE before immersion: 1.296 • DE after 4 months immersion: 0.686 • König pendulum hardness before immersion: 22.80 • König pendulum hardness after 4 months immersion: 20.83 • 60° gloss before immersion: 52 • 60° gloss after 4 months immersion: 32
Physical Damage Rating (P.D.R.) [%]	100-(2.147+4.235)≈93.62
Overall Performance (O.P.) [%]	7.54

6.3.3.3 After 6 months of immersion

Figure 6.59: Surface condition of Exp PU2 specimen after 6 months immersion in Elefsis; a) after 2 months, b) after 4 months, and c) after 6 months, when it was removed from site

Table 6.48: Presentation of antifouling performance calculation of Exp PU2 paint after 6 months of immersion, according to ASTM D 3623 and ASTM D 6990 guidelines

Fouling Examination	Exp. PU2
Fouling on surface	PC-*Spirorbinae*: 403, 0.157-2.959 mm in diameter, found on various locations over the painted surface (Table C.29). Total area: A= 438.994 mm^2 (4.390%) PC-*Serpulidae*: 8, 0.505-13.725 mm^2, found mainly as solitary forms over the painted surface (Table C.30). Total area: A= 21.388 mm^2 (0.214%) *Al-FB*: 65.119%, filamentous algae and/or bryozonas extensively covering the painted surface. *Amphipods*: 2, 2.029 -2.048 mm, in length *Mol*: 1, mussel of dimensions 5.008×2.093=10.482 mm^2 (0.105%) Silt: 25.7%, a medium thickness silt layer without uniform coverage of the painted surface
Fouling Resistance (F.R.) [%]	95-(65.119+4.390+0.214+0.105)=25.17
Physical Condition of Antifouling Film	• Paint digging. A=51.555 mm^2 (0.516%) • Some black "stains" observed during inspection (probably remainders of algae/bryo): 623.506 mm^2 (6.235%) • Softness rating: 10, no pigment transfer • DE before immersion: 1.098 • DE after 6 months immersion: 1.646 • König pendulum hardness before immersion: 10.8 • König pendulum hardness after 6 months immersion: 18 • 60° gloss before immersion: 44.25 • 60° gloss after 6 months immersion: 9.25
Physical Damage Rating (P.D.R.) [%]	100-(0.516+6.235)≈93.25
Overall Performance (O.P.) [%]	25.17

6.3.3.4 After 8 months of immersion

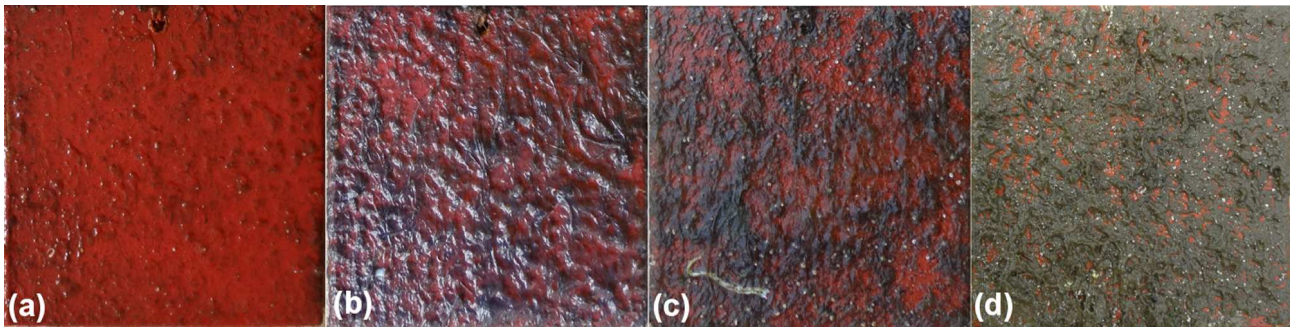

Figure 6.60: Surface condition of Exp PU2 specimen after 8 months immersion in Elefsis; a) after 2 months, b) after 4 months, c) after 6 months and d) after 8 months, when it was removed from site

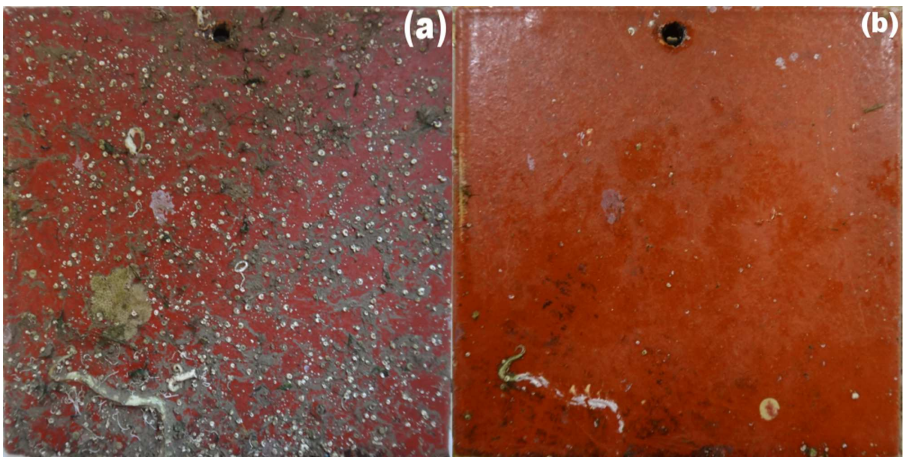

Figure 6.61: Surface condition of Exp PU2 specimen after 8 months immersion in Elefsis; a) dried, after gentle removal of the silt and b) after thorough cleaning

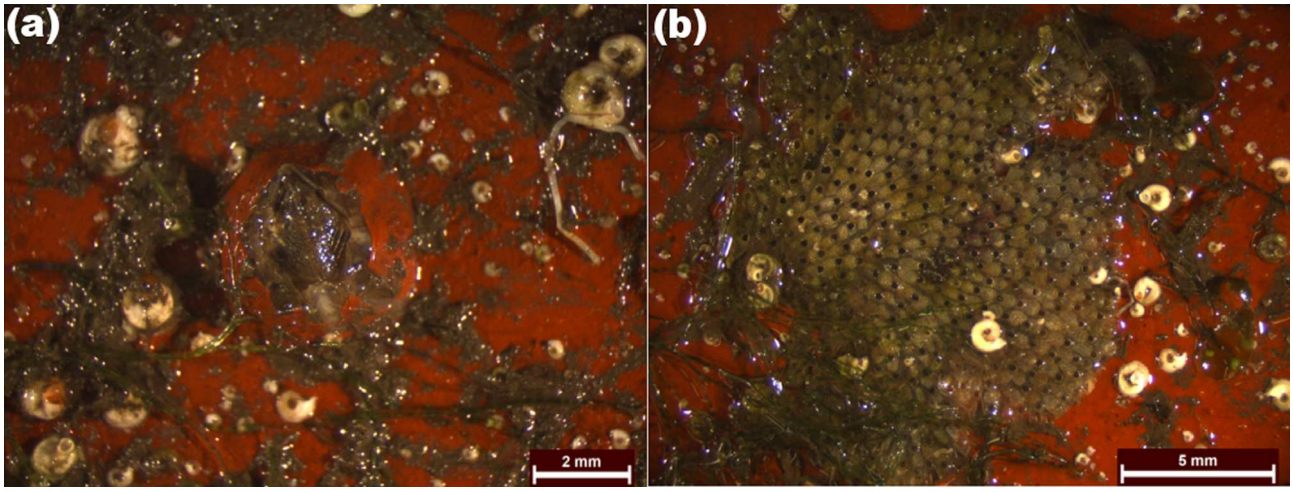

Figure 6.62: Stereoscopic observation of Exp PU2 specimen after 8 months immersion in Elefsis; a) barnacle, having been colored with the paint and b) encrusting bryozoans on the painted surface

Table 6.49: Presentation of antifouling performance calculation of Exp PU2 paint after 8 months of immersion, according to ASTM D 3623 and ASTM D 6990 guidelines

Fouling Examination	Exp. PU2
Fouling on surface	Heavily fouled surface with spirorbinae, bryozoans (both filamentous and encrusting) and some serpulid-tubes. The surface free from fouling was 14.66%. Stereoscopic observation of the observed fouled area allowed measurement of an amount of the representative species, which are presented right below. PC-*Spirorbinae*: 876, 0.111-2.813 mm in diameter, homogenously covering the painted surface (Table C.31). Total area: A=305.971 mm^2 (3.060%) PC-*Serpulidae*: 14, 0.463-191.248 mm^2, found mainly as solitary forms over the painted surface (Table C.32). Total area: A=297.256 mm^2 (2.973%)

	FB and EB: 3.032%, found on various locations on the painted surface (Table C.33) *Amphipods*: 4, found solitary on different positions of the painted surface A_1=2.784×0.385= 1.072 mm^2 A_2=1.820×0.259= 0.471 mm^2 A_3=2.218×0.370= 0.821 mm^2 A_4=1,167×0.294= 0.343 mm^2 Total area: A=2.707 mm^2 (0.027%) *Barn*: 2, found solitary on different positions of the painted surface A_1=3.967×3.818=15.146 mm^2 A_2=2.627×3.780= 9.930 mm^2 Total area: A=25.076 mm^2 (0.251%) Silt: 43.52%, light silt layer, not homogenous coverage of the painted surface
Fouling Resistance (F.R.) [%]	14.66
Physical Condition of Antifouling Film	• Digging of serpulid-tubes and bryozoans: A=464.94 mm^2 (4.649%) • Digging of spirorbinae: 155.88 mm^2 (1.559%) • Damage/black "stains": 167.78 mm^2 (1.678%) • Softness rating: 10, no pigment transfer • DE before immersion: 1.456 • DE after 8 months immersion: 2.24 • König pendulum hardness before immersion: 18 • König pendulum hardness after 8 months immersion: 17 • 60° gloss before immersion: 34.25 • 60° gloss after 8 months immersion: 4.5
Physical Damage Rating (P.D.R.) [%]	100-(4.649+1.559+1.678)≈92.11
Overall Performance (O.P.) [%]	14.66

6.3.3.5 After 10 months of immersion

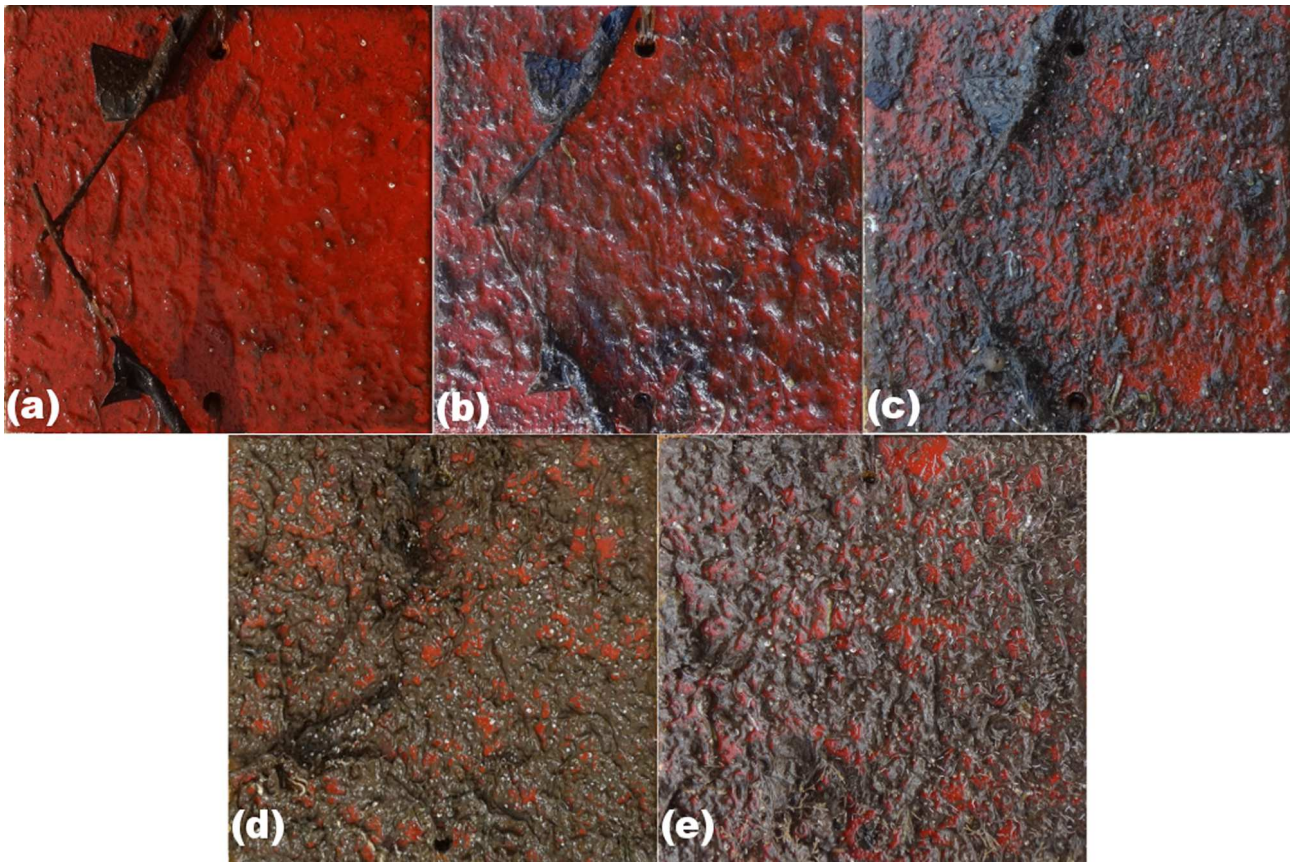

Figure 6.63: Surface condition of Exp PU2 specimen after 10 months immersion in Elefsis; a) after 2 months, b) after 4 months, c) after 6 months, d) after 8 months and e) after 10 months, when it was removed from site

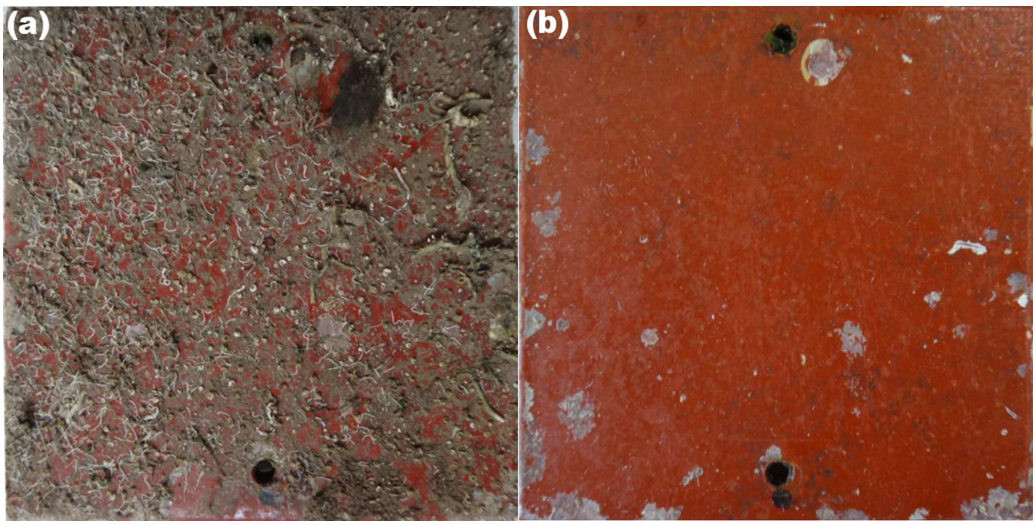

Figure 6.64: Surface condition of Exp PU2 specimen after 10 months immersion in Elefsis; a) dried and b) after thorough cleaning

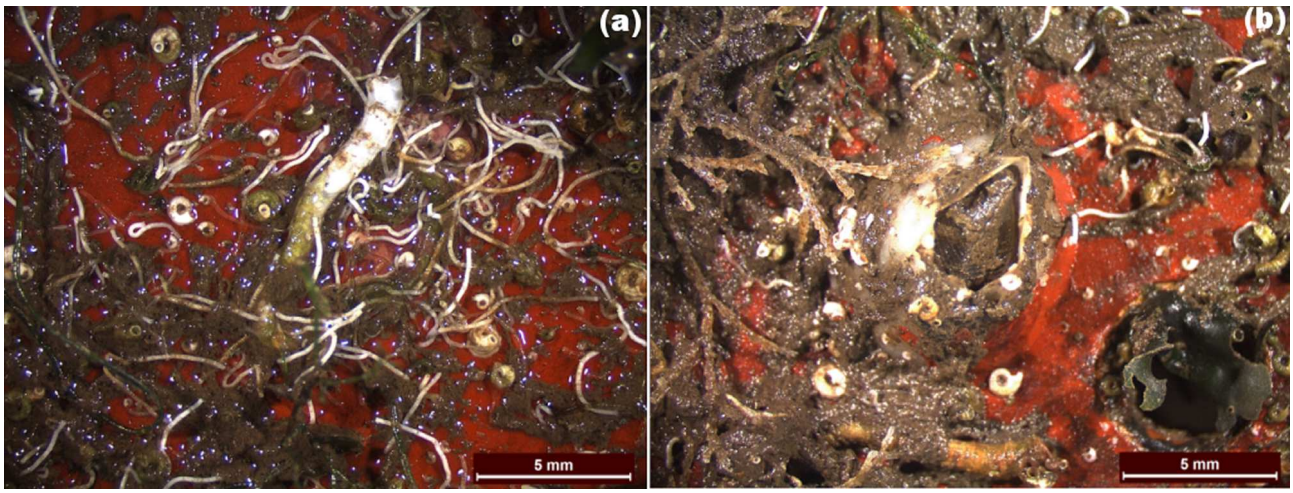

Figure 6.65: Stereoscopic observation of Exp PU2 specimen after 10 months immersion in Elefsis; a) interconnecting network probably of *salmacina dysteri* and b) a barnacle, having been colored with the paint

Table 6.50: Presentation of antifouling performance calculation of Exp PU2 paint after 10 months of immersion, according to ASTM D 3623 and ASTM D 6990 guidelines

Fouling Examination	Exp. PU2
Fouling on surface	Heavily fouled surface with spirorbinae, bryozoans (both filamentous and encrusting) and a great amount of small interconnected white tubes, possibly *salmacina dysteri*. The surface free from fouling was 6.67%. Stereoscopic observation of the observed fouled area allowed measurement of an amount of the representative species, which are presented right below. PC-*Spirorbinae*: 467, 0.472-1.764 mm in diameter, homogenously covering the painted surface (Table C.34). Total area: A≈220.616 mm^2 (2.206%) PC-*Serpulidae*: 6, 2.442- 12.302 mm^2, found mainly as solitary forms over the painted surface (Table C.35). Total area: A=35.814 mm^2 (0.358%) *FB and EB*: 4.708%, found on various locations on the painted surface *Amphipods*: 1, 2.649×0.306=0.811 mm^2 *Barn*: 1, 7.147×4.354=31.118 mm^2 (0.311%) *Mol*: 5, 2.043-113.560 mm^2, clams of various sizes found solitary on the painted surface Total area: A=281.411 mm^2 (2.814%) Silt: 60.87%, medium silt layer, not homogenous coverage of the painted surface
Fouling Resistance (F.R.) [%]	6.67
Physical Condition of Antifouling Film	• Digging of bryozoans/tubes/other foulers: 1695.114 mm^2 (16.951%) • Prints of spirorbinae: 221.764 mm^2 (2.218%) • Damage/black "stains": 481.338 mm^2 (4.813%)

	• Softness rating: 10, no pigment transfer • DE before immersion: 1.68 • DE after 10 months immersion: 1.09 • König pendulum hardness before immersion: 32 • König pendulum hardness after 10 months immersion: 55.20 • 60° gloss before immersion: 52.25 • 60° gloss after 10 months immersion: 16.4
Physical Damage Rating (P.D.R.) [%]	100-(16.951+2.218+4.813)≈76.02
Overall Performance (O.P.) [%]	6.67

6.3.3.6 After 12 months of immersion

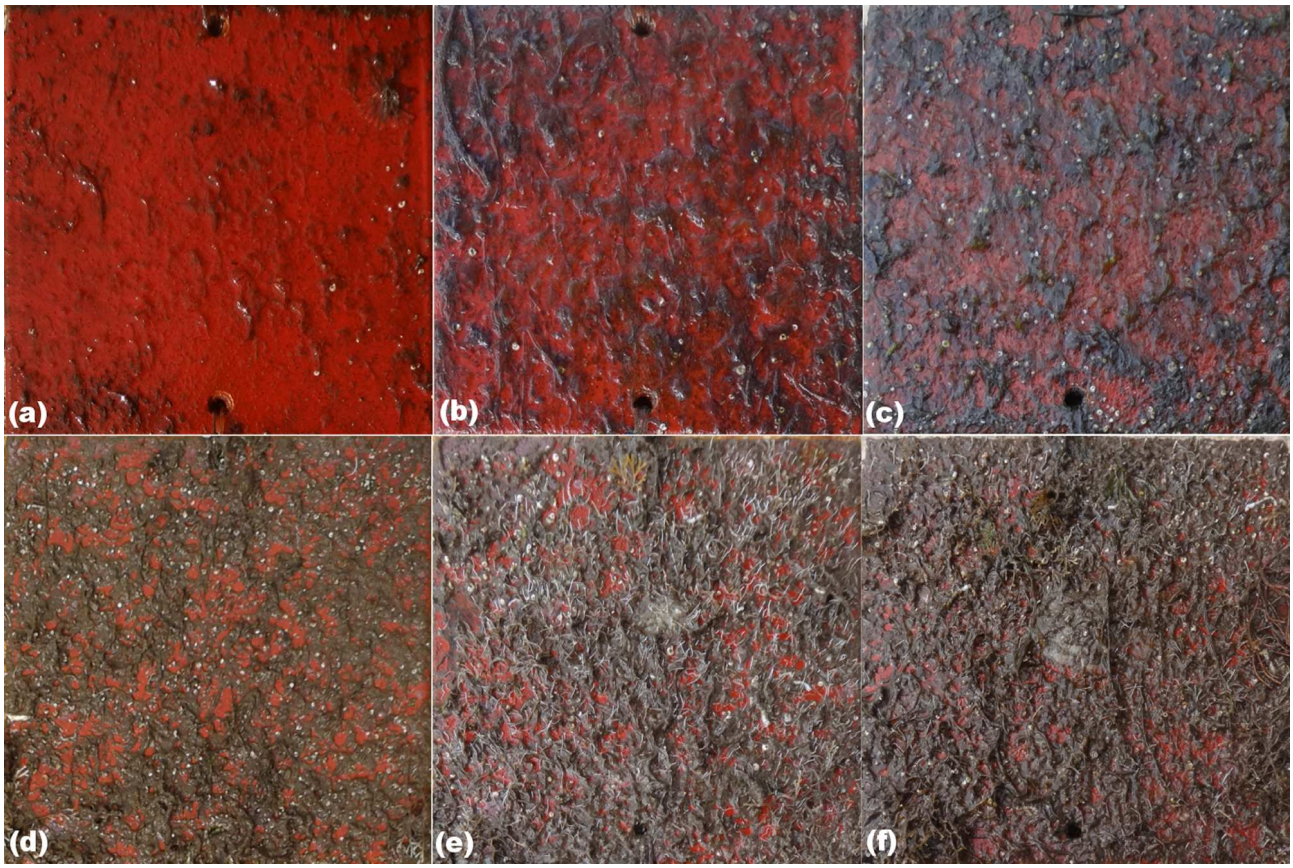

Figure 6.66: Surface condition of Exp PU2 specimen after 12 months immersion in Elefsis; a) after 2 months, b) after 4 months, c) after 6 months, d) after 8 months, e) after 10 months and f) after 12 months, when it was removed from site

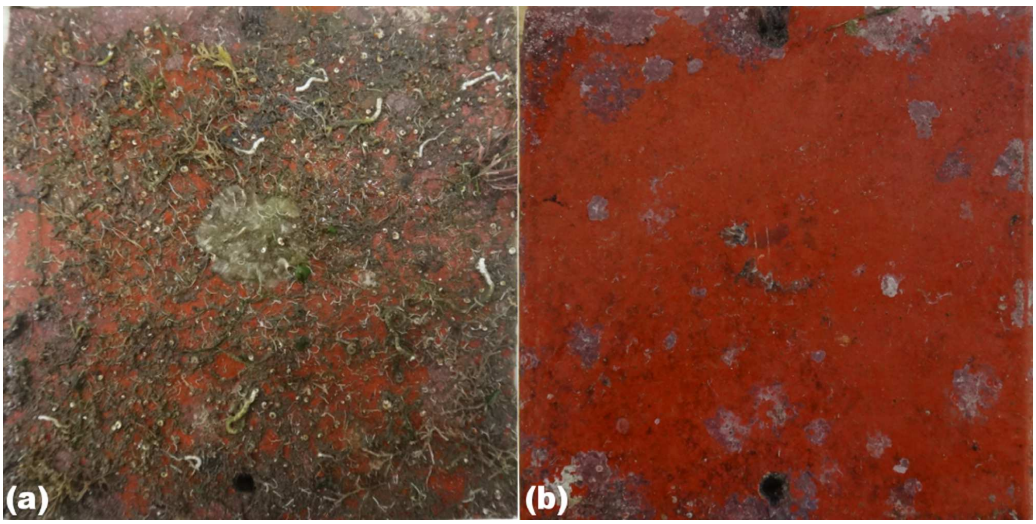

Figure 6.67: Surface condition of Exp PU2 specimen after 12 months immersion in Elefsis; a) dried and b) after thorough cleaning

Table 6.51: Presentation of antifouling performance calculation of Exp PU2 paint after 12 months of immersion, according to ASTM D 3623 and ASTM D 6990 guidelines

Fouling Examination	Exp. PU2
Fouling on surface	Heavily fouled surface with *spirorbinae*, bryozoans (mainly filamentous and a small amount of encrusting) and a great amount of small interconnected white tubes, possibly *salmacina dysteri*. The surface free from fouling was 12.31%. Stereoscopic observation of the observed fouled area allowed measurement of an amount of the representative species, which are presented right below. PC-*Spirorbinae*: 275, 0.528-1.106 mm in diameter, homogenously covering the painted surface (Table C.36). Total area: A≈177.966 mm^2 (1.780%) PC-*Serpulidae*: 7, 8.884-28.498 mm^2, found mainly as solitary forms over the painted surface (Table C.37). Total area: A=126.02 mm^2 (1.260%) PC-*Serpulidae*: 3.21%, colony of *salmacina dysteri* *FB and EB*: 14.63%, found on various locations on the painted surface *Barn*: : 1, 2.671×2.844=7.596 mm^2 (0.076%) Silt: 71.58%, medium silt layer, not homogenous coverage of the painted surface
Fouling Resistance (F.R.) [%]	12.31
Physical Condition of Antifouling Film	• Digging of bryozoans: 2532.042 mm^2 (25.320%) • Digging of *serpulidae* tubes: 1003.11 mm^2 (10.031%) • Digging of *spirorbinae*: 70.907 mm^2 (0.709%) • Damage/black "stains"/other foulers: 70.1 mm^2 (0.701%) • Softness rating: 10, no pigment transfer • DE before immersion: 1.68

	• DE after 12 months immersion: 1.26 • König pendulum hardness before immersion: 17.8 • König pendulum hardness after 12 months immersion: 28.4 • 60° gloss before immersion: 41 • 60° gloss after 12 months immersion: 3.75
Physical Damage Rating (P.D.R.) [%]	100-(25.320+10.031+0.709+0.701)≈63.24
Overall Performance (O.P.) [%]	12.31

6.3.3.7 Conclusions with regard to the field tests of the Exp PU2 AF system

Table 6.52: Summary of antifouling and physical damage rating for the Exp PU2 system during the 12-month immersion experiment in Elefsis

Months	Exp PU2		
	FR [%]	PDR [%]	OP[%]
2	44.30	99.16	44.30
4	7.54	93.62	7.54
6	25.17	93.25	25.17
8	14.66	92.11	14.66
10	6.67	76.02	6.67
12	12.31	63.24	12.31

The main foulers observed onto the surface of the Exp PU2 painted specimens were filamentous algae/bryozoans, spirorbinae and encrusting bryozoans. More specifically, after 2 months immersion, extensive coverage with algae/bryozoans was observed, which covered around half of the specimen's surface. As a result, the FR dropped to 44.3% (Table 6.52). The PDR was kept quite high, due to the limited amount of spirorbinae (114). In accordance to previous observations of the optical and mechanical properties of the antifouling paints, DE increased by 4.66%, gloss dropped by 51.69%, while the coat became harder after 2 months of immersion, since the König hardness increased by 16.8%. No pigment transfer to a cotton swab was observed for the Exp. PU2 painted specimen after 2 months of immersion in Elefsis (softness rating equal to 10).

After 4 months, the filamentous algae/bryozoans covered almost the entire surface, reaching a percentage equal to 85.32% (Table 6.47). As a result, the FR dropped to 7.54%. Apparently, the surface was nearly completely fouled. Once more, the PDR was quite high, due to the small amount of spirorbinae (155) and the small amount of "black stains" (probably remainders of algae/bryo), leading to a PDR value of 93.62%. However, the attached foulers were strongly adherent. The color and hardness values decreased after 4 months, deviating from the observed trend, so far. However, the 60° gloss exhibited 38.46% drop. The softness rating remained unaffected.

After 6 months, along with the algae/bryozoans and the 403 spirobinae, 8 serpulidae tubes were also observed. The distribution of the foulers was such that the FR was equal to 25.17%.

At this point, it should be mentioned that the foulers were strongly adherent onto the paint and it was quite hard to remove them even with high water/finger pressure, as has also been reported for the rest polyurethane systems. However, for the PDR analysis, the specimens were thoroughly cleaned and the analysis was based on the quality of the washed surface. As a result, the PDR value after 6 months was 93.25%. Some "black stains" were noticed, covering a surface equal to 6.24%. The rest of the properties followed the common rule of increase in discoloration (50%) and hardness (66.67%) and decrease in gloss (79.1%), while once more, the softness rating was equal to 10.

After 8 months of immersion, the variety of the attached macrofoulers increased and included *spirorbinae* (876), *serpulidae* of other genera (14), barnacles (2) and filamentous and encrusting bryozoans, covering around 3.03% of the painted surface. The characteristic of these foulers was their intense digging into the paint, as was observed for a barnacle, the cell of which had been colored circumferentially with the paint (Fig. 6.62a). Also, some amphipods were observed, however, since these organisms do not attach onto the paint, they are not taken into consideration during fouling rating calculation. The fouling rating was again quite low (Table 6.52), due to the wide extent of fouling coverage (Fig. 6.61a). The gloss value after 8 months decreased by 86.86%, while discoloration increased by 53.42%, exhibiting close values with the previous interval. The König hardness remained stable and so did the softness rating. The P.D.R. value, as calculated through stereoscopic observation of the stains and damages after the cleaning process of the specimen, was found equal to 92.11%.

After 10 months of immersion the fouling rating dropped to 6.67%, meaning that the surface was basically completely fouled. The types of organisms were similar to the specimen that was retrieved from site after 8 months, however, a large population of *salmacina dysteri* tubes was observed (Fig. 6.65a). The hardness increased (72.5%) and gloss decreased (68.61%), however, discoloration decreased. At this point, the PDR exhibited a significant drop being equal to 76.02%. The softness rating remained unaffected.

After one year of exposure, the types of foulers were similar to the ones observed after 10 months, with the population of bryozoans covering a larger surface, equal to 14.63%. The fouling rating was 12.31%, while the PDR continued to decrease, reaching a value equal to 63.24%. Similarly to the previous interval, discoloration decreased, while hardness increased (59.55%) and 60° gloss decreased (90.85%), following these properties (gloss and hardness) the common trend, as has been developed in the present study. No pigment loss was observed after 12 months of experiment.

With regard to the mechanical characteristics of the examined specimens, the König pendulum hardness had a mean value of 22.93, while the largest increase was observed after 10 months of experiment, when the hardness increased 23.2 units (from 32 before immersion it became 55.2 after 10 months of experiment). In terms of optical characteristics, the gloss values exhibited wide variations. The mean gloss value before immersion was 47.13 GU and the largest decrease was observed after 12 months of experiment, where a sharp decrease of 37.25 GU was measured, since the gloss value dropped from 41 GU before immersion to 3.75 at the

end of the experiment. However, the discoloration index was not affected as much, exhibiting a maximum difference in DE equal to +0.78.

The antifouling performance of the Exp PU2 system could not be described as satisfactory. The painted surface became fouled almost immediately, with large amounts of algae/bryozoans and *spirorbinae*. The variety and population of foulers increased constantly throughout the experiment, almost totally covering it, already after 4 months of immersion. Intense digging effect with coloring of the foulers was also observed. The foulers were strongly attached and it was very hard to be removed by traditional means (high water/finger pressure). As a result, it could be stated that the Exp PU2 system would not be an appropriate paint for antifouling protection.

6.3.4 Electrochemical results

6.3.4.1 Reference silicone system

Table 6.53: Electric properties of the specimens painted with the Ref Si system, during their immersion in Elefsis

Months	Coating Capacitance [F]
Before	$8.057\ 10^{-10}$
2	$2.604\ 10^{-10}$
4	$2.063\ 10^{-10}$
6	$1.675\ 10^{-10}$
8	$3.152\ 10^{-10}$
12	$3.416\ 10^{-10}$

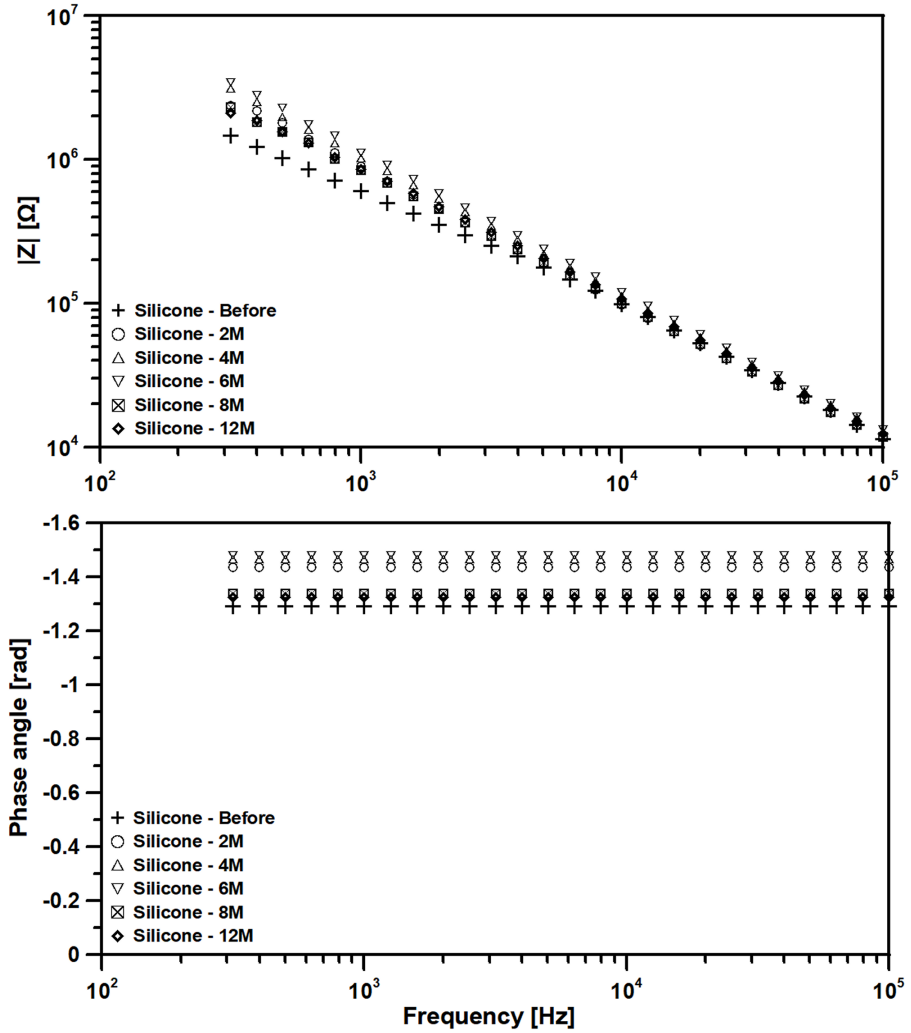

Figure 6.68: Bode plot of the Ref. Si painted specimens during the 12-month immersion in Elefsis. The presented curves exhibited purely capacitive characteristics.

As can be seen from Fig. 6.68, the Bode plot was typical of a capacitive response, implying an intact coat [68]. The magnitude graph exhibited straight lines with slopes around -0.9, implying a perfect coat. The phase angle plots were straight lines around the value -$\pi/2$, which is the phase shift of the capacitor. The obtained capacitance values were characteristic of a thick, high-impedance coating (Table 6.53). As a result, no electrochemical degradation was detected for the specimens that were immersed for 2, 4, 6, 8 and 12 months in Elefsis.

On the contrary, the specimen that remained immersed for 10 months, exhibited an open circuit potential equal to -0.510 V vs SCE and the obtained impedance spectra had the shape presented in Fig. 6.69. More specifically, the Nyquist plot exhibited a semicircle in the high frequency range, implying a kinetic time-constant, while in the mid-frequency range a diffusion tail appeared, which exhibited a slope increase in the low frequency region of the spectrum. In other words, the diffusion related branch could be considered to be separated in two constant phase elements (CPE). This behavior has also been reported during salt spray examination of painted steel samples with scribes, after 6 and 8 weeks of experiment, as presented in Chapter 3.

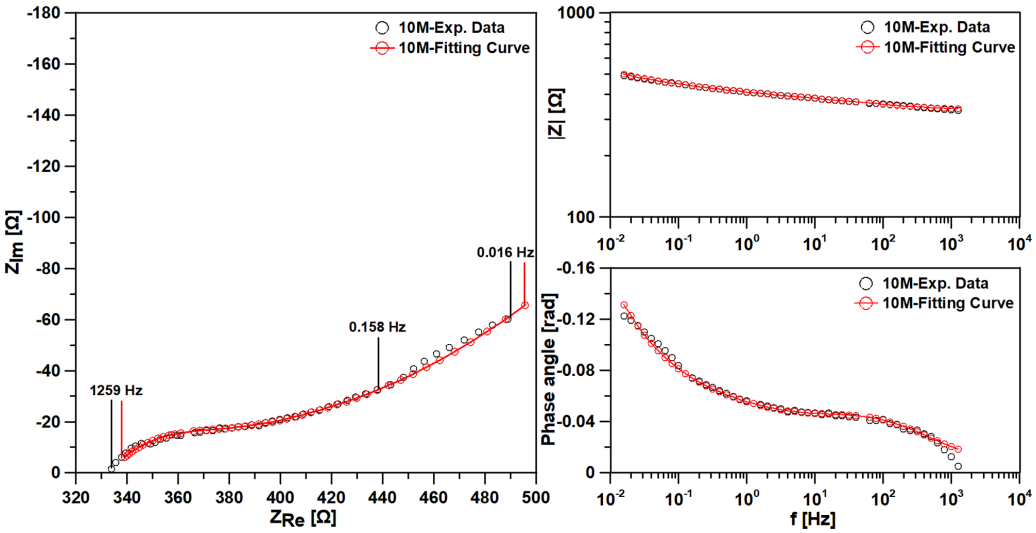

Figure 6.69: EIS graphs of the specimen painted with the Ref. Si system, that remained immersed for 10 months in Elefsis

The diffusion process, related to the mass transport of dissolved oxygen through the pores of the corrosion products layer, could be described using the modified restricted diffusion model proposed by Diard *et al.* [81] and Lasia [82]. This type of diffusion impedance generally implies that the corrosion products layer provides some protection to the substrate. However, this observation could be verified only through comparative analysis of the obtained parameters in the course of time. The equation providing the modified restricted diffusion impedance is given by Eq. (3.19). A Randles circuit was used to fit the total impedance, which is presented in Fig. A.1, while the expression for total impedance is given by Eq. (A.1).

The parameters presented in Table 6.54 were obtained from the regression analysis. The diffusion related time constant ($\tau_{D,FD}$) was found equal to 93.6 s. Assuming a representative diffusion coefficient for dissolved oxygen equal to 1.9 10^{-5} cm^2/s [65], the diffusion layer thickness (L_D) becomes equal to 0.42 mm, around half the actual thickness value of the multi-layer coat, which was measured 864.5 μm, using a portable KTA-Tator Elektro-Physik eXacto coating thickness gauge, the FN type. This means that the amount of corrosion products was not thick enough to cover the whole coating thickness. The diffusion related resistance (R_D), representing the difficulty for the oxygen molecules to travel through the corrosion layer, was equal to 243.56 Ω, one order of magnitude larger than the charge-transfer resistance (R_{ct}), which was equal to 27.88 Ω. Hence, the charge-transfer process was quicker. This can be verified through comparison of the diffusion related ($\tau_{D,FD}$) and kinetic ($\tau_{ct,CPE}$) time constants. Apparently, the time needed for the oxidant molecules to travel through the diffusion layer is five orders of magnitude larger than the time needed for electron exchange. The kinetic time constant is given by Eq. (3.8) and the diffusion related time constant is given by Eq. (3.9). Finally, the CPE parameters n and Q could be ascribed to a double layer.

Linear polarization resistance method provided a polarization resistance value equal to 541.601 Ω, close enough to the polarization resistance value of 500.065 Ω obtained from the fitting results. The obtained LPR curve is presented in Fig. 6.70.

Table 6.54: Fitting results and derived parameters for the specimen painted with the Ref Si system, that remained immersed for 10 months in Elefsis, assuming modified restricted diffusion, Randles connection and CPE for double-layer

Parameter	Unit	Value
$\tau_{\mathrm{D,FD}}$	[s]	93.602
R_{D}	[Ω]	243.556
ϕ		0.465
R_{ct}	[Ω]	27.881
n		0.671
Q	[F s^{n-1}]	2.648 10^{-4}
$\tau_{\mathrm{ct,CPE}}$	[s]	6.653 10^{-4}

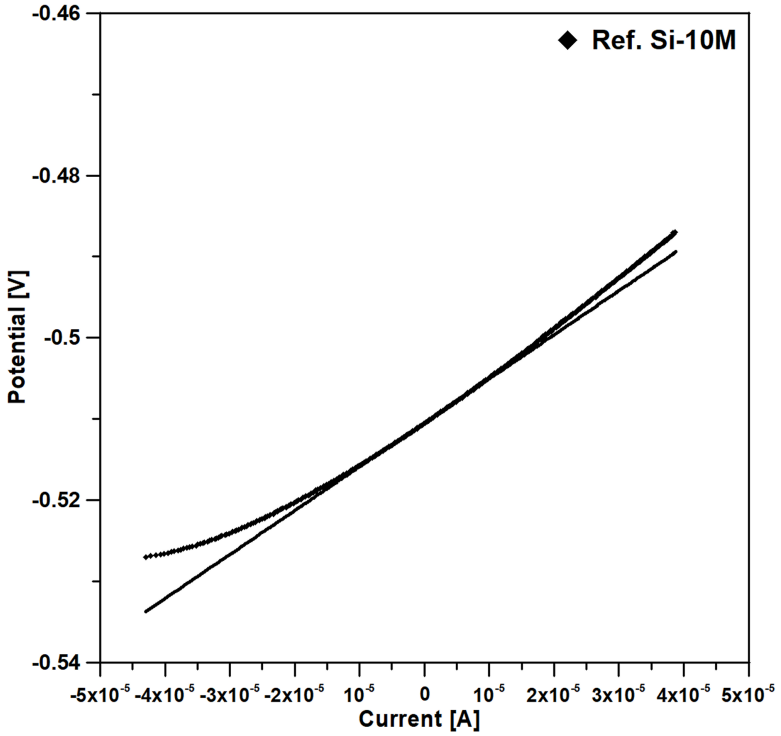

Figure 6.70: Linear polarization resistance examination of the specimen painted with the Ref Si system, that remained immersed for 10 months in Elefsis.

6.3.4.2 Acrylic system

The specimens that were painted with the acrylic system and remained immersed for 2, 4 and 6 months, exhibited purely capacitive characteristics, with the capacitance values being in the range of 10^{-10} F (or 10^{-11} F/cm^2). The respective signals are presented in Fig. 6.71. The deviation of the EIS signal corresponding to 2 month-immersion from the ideal slope of -1 was attributed to the quality of the signal, which exhibited more intense noise in the high-frequency range, compared to the other responses.

Table 6.55: Electric properties of the specimens painted with the Acrylic system, that remained immersed for 2, 4 and 6 months in Elefsis

Months	Coating Capacitance [F]
Before	$2.214\ 10^{-10}$
2	$2.302\ 10^{-9}$
4	$2.814\ 10^{-10}$
6	$2.662\ 10^{-10}$

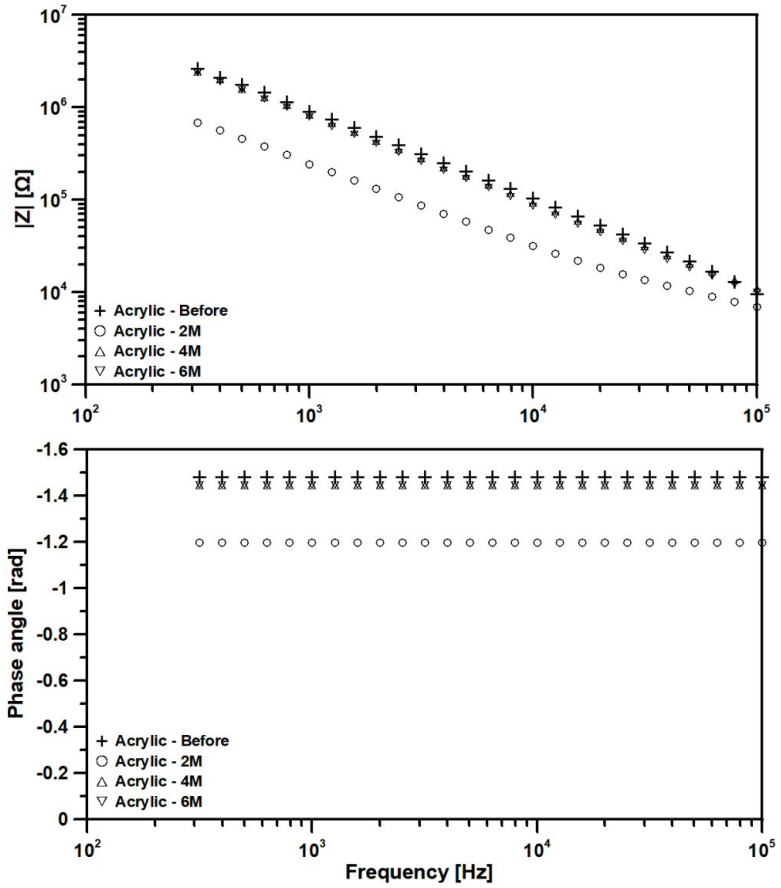

Figure 6.71: Bode plot of the Acrylic painted specimens that remained immersed for 2, 4 and 6 months in Elefsis. The presented curves exhibited purely capacitive characteristics.

The specimen that remained immersed for 8 months exhibited a two time-constant behavior, as can be seen from Fig. 6.72. The parameters obtained from the regression analysis (Table 6.56) indicated that the high-frequency, better resolved semicircle accounted for the coating time-constant, while the low-frequency depressed semicircle accounted for the charge-transfer process at the metal/coat interface. The values of R_{pore} and R_{ct} were equal to $3.66\ 10^5\ \Omega\ \text{cm}^2$ and $3.34\ 10^5\ \Omega\ \text{cm}^2$, respectively, smaller than $10^6\ \Omega\ \text{cm}^2$, indicating loss of barrier properties and corrosion susceptibility [152]. Finally, the polarization resistance (R_{p}), defined as $R_{\text{e}} + R_{\text{pore}} + R_{\text{ct}}$, had a value of $8.34\ 10^5\ \Omega\ \text{cm}^2$ at the lowest frequency (0.025 Hz).

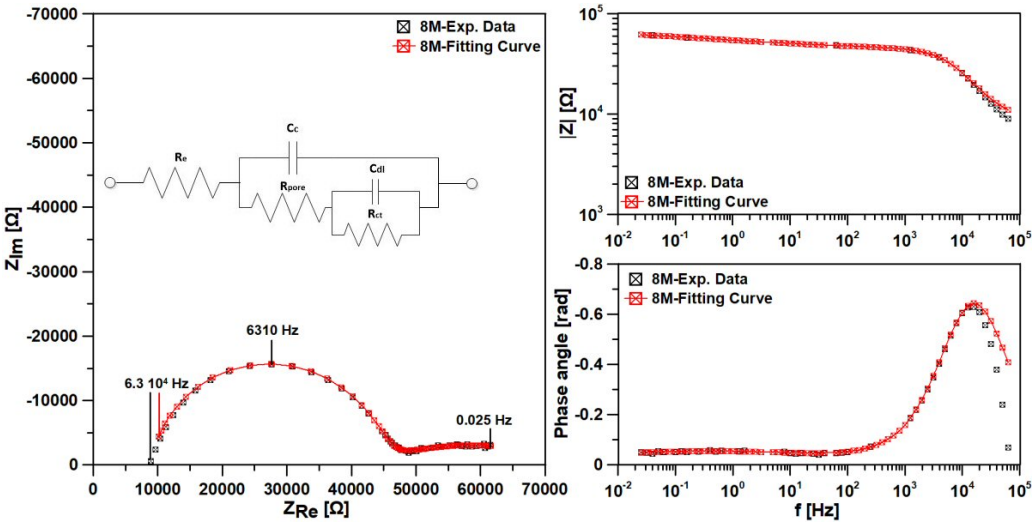

Figure 6.72: EIS graph for the specimen painted with the Acrylic system, that remained immersed for 8 months in Elefsis.

Table 6.56: Fitting results and derived parameters for the specimen painted with the Acrylic system, that remained immersed for 8 months in Elefsis, assuming a two time-constants model

Parameter	Unit	Value
n_c		0.914
Q_c	[F s^{n-1}]	1.653 10^{-9}
R_{pore}	[Ω]	3.406 10^4
n		0.248
Q	[F s^{n-1}]	3.457 10^{-5}
R_{ct}	[Ω]	3.107 10^4
$\tau_{ct,CPE}$	[s]	1.333

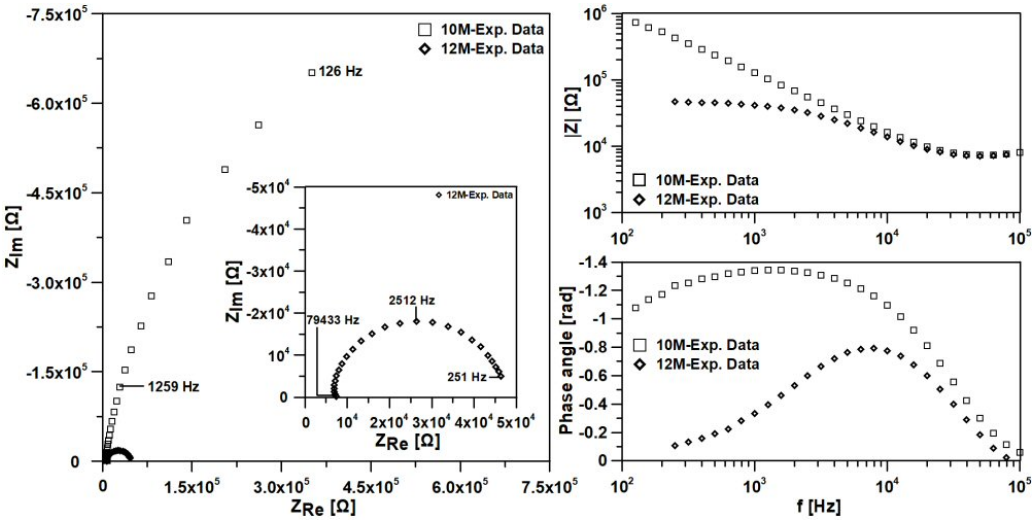

Figure 6.73: EIS graphs for the specimens painted with the Acrylic system, that remained immersed for 10 and 12 months in Elefsis.

Table 6.57: Electric properties of the specimens painted with the Acrylic system, that remained immersed for 10 and 12 months in Elefsis

Months	Coating Capacitance [F]	Coating Resistance [Ω]
10	$3.271\ 10^{-9}$	$1.949\ 10^{6}$
12	$1.555\ 10^{-9}$	$4.144\ 10^{4}$

The specimens that remained immersed for 10 and 12 months, respectively, exhibited the impedance graphs presented in Fig. 6.73. The Nyquist plot corresponding to 12 months of immersion is also presented as inset graph in Fig. 6.73. Both responses corresponded to a one time-constant circuit, consisting of the parallel connection of the coating capacitance and the pore resistance (Table 6.57). These two graphs are characteristic of the gradual deterioration of an organic coating. More specifically, after 10 months the R_{pore} was equal to $2.09\ 10^{7}\ \Omega\ \text{cm}^2$, indicating satisfactory protection [153]. However, the specimen that remained immersed for 12 months exhibited an R_{pore} equal to $4.45\ 10^{5}\ \Omega\ \text{cm}^2$, exhibiting a plateau, implying barrier properties deterioration and increase of permeability [154], even for frequencies above 100 Hz. Generally, as a coating degrades, coating resistance (R_{pore}) decreases [155], due to easier permeation of the electrolyte. Under this prism, coating capacitance could also increase for the same reason, since, water ingress increases the dielectric value. However, the present specimens exhibited similar coating capacitances, being $3.04\ 10^{-10}\ \Omega\ \text{cm}^2$ after 10 months and $1.45\ 10^{-10}\ \Omega\ \text{cm}^2$ after 12 months.

6.3.4.3 Experimental silicone system

Table 6.58: Electric properties of the specimens painted with the Exp. Si system, during their 12-month immersion in Elefsis

Months	Coating Capacitance [F]	Coating Resistance [Ω]
Before	$3.572\ 10^{-10}$	-
2	$3.447\ 10^{-10}$	$4.497\ 10^{5}$
4	$3.730\ 10^{-10}$	-
6	$3.472\ 10^{-10}$	-
8	$6.356\ 10^{-10}$	-
10	$3.182\ 10^{-10}$	-
12	$4.518\ 10^{-10}$	-

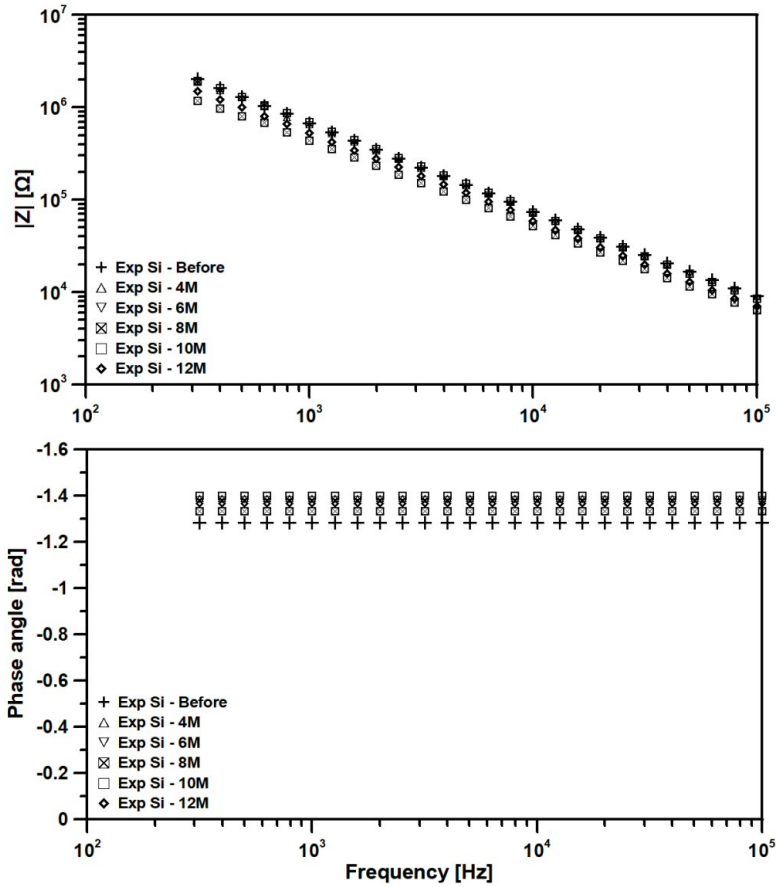

Figure 6.74: Bode plot of the Exp. Si painted specimens that remained immersed for 4, 6, 8, 10 and 12 months in Elefsis. The presented curves exhibited purely capacitive characteristics.

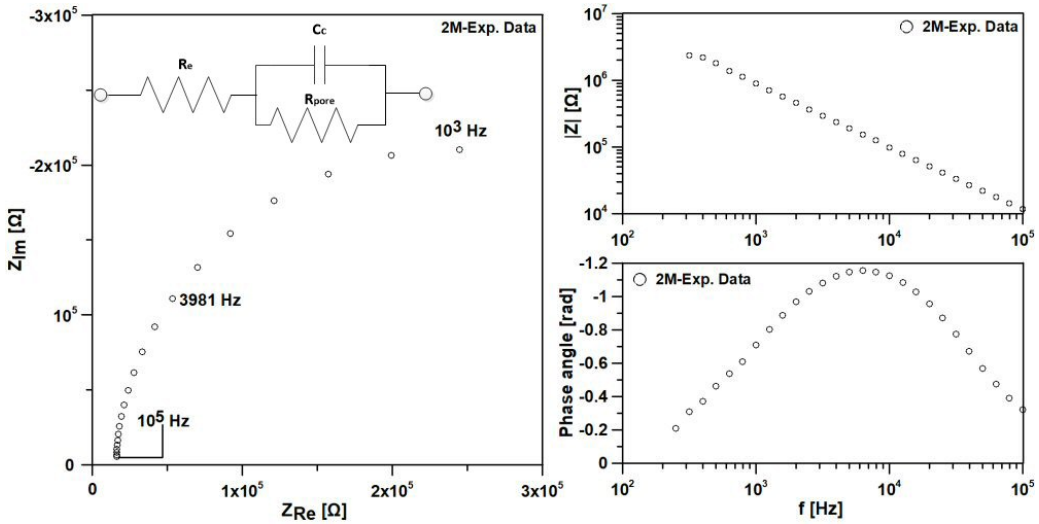

Figure 6.75: EIS graph for the specimen painted with the Exp. Si system, that remained immersed for 2 months in Elefsis.

The specimens that remained immersed for 4, 6, 8, 10 and 12 monhts exhibited a purely capacitive behavior (Fig. 6.74). The largest capacitance value was equal to 6.36 10^{-10} F (or 5.91 10^{-11} F/cm^2), corresponding to impedance magnitude $|Z(\omega \to 1)|$ equal to 1.69 10^{10} Ω cm^2, implying a rather efficient protection [152]. The only specimen that exhibited some initial degradation characteristics was the one that remained immersed for 2 months in Elefsis. The

EIS response of this specimen could be described by a one time-constant circuit, with the coating capacitance being in parallel to the coating resistance (Fig. 6.75). The values of the parameters are presented in Table 6.58. The value of the pore resistance (4.83 10^6 Ω cm^2) was close to the threshold of 10^6 Ω cm^2 [152], arising some thoughts with regard to its long-term anticorrosion efficiency.

6.3.4.4 Experimental polyurethane (1) system

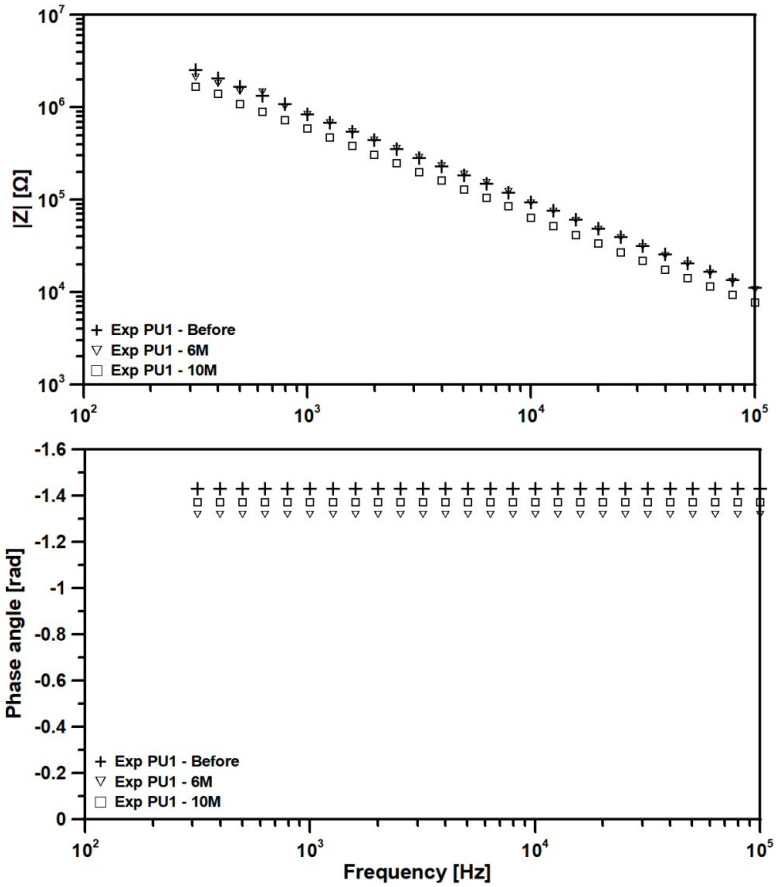

Figure 6.76: EIS graph for the specimens painted with the Exp. PU1 system, that remained immersed for 6 and 10 months in Elefsis.

Table 6.59: Electric properties of the specimens painted with the Exp. PU1 system, during their 12-month immersion in Elefsis

Months	Coating Capacitance [F]	Coating Resistance [Ω]
Before	2.624 10^{-10}	-
2	3.929 10^{-10}	5.505 10^5
4	3.821 10^{-10}	5.316 10^5
6	2.811 10^{-10}	-
8	3.619 10^{-10}	3.253 10^5
10	3.967 10^{-10}	-
12	4.602 10^{-10}	1.022 10^6

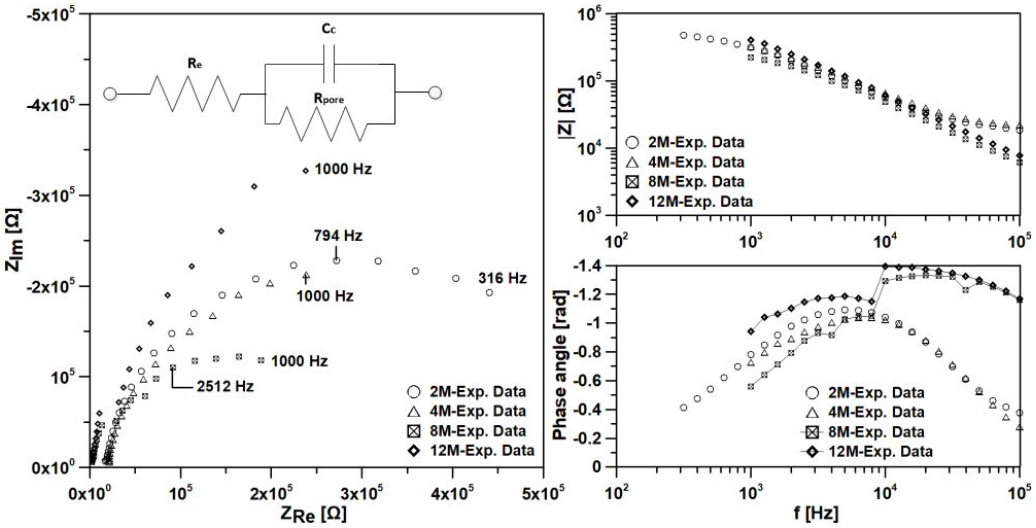

Figure 6.77: EIS graph for the specimens painted with the Exp. PU1 system, that remained immersed for 2, 4, 8 and 12 months in Elefsis.

The painted specimens that retained their barrier properties were the ones that were immersed for 6 and 10 months in Elefsis (Fig. 6.76). Similarly to previous observations, the coating capacitance was in the range of 10^{-10} F (Table 6.59), with the largest value calculated for the specimen that remained immersed for 10 monhts in Elefsis (3.967 10^{-10} F or 4.26 10^{-11} F/cm^2), corresponding to magnitude at $\omega \rightarrow 1$ equal to 2.34 10^{10} Ω cm^2 . With regard to the specimens that remained immersed for 2, 4, 8 and 12 monhts (Fig. 6.77), they could be described by a one-time constant circuit. The R_{pore} values for the corresponding periods were 5.92 10^6, 5.71 10^6, 3.49 10^6 and 1.10 10^7 Ω cm^2, respectively. Hence, the barrier properties for the first three specimens could be considered to be slightly above the margin of efficient protection (10^6 Ω cm^2, according to [152]) or even beneath it (10^7 Ω cm^2, as mentioned in [153]). However, the barrier properties of the specimen that remained immersed for 12 months could be considered as satisfactory and implied an efficient coating.

6.3.4.5 Polyurethane system

The PU painted specimens that were immersed for 2 and 6 months did not exhibit any degradation characteristics (Fig. 6.78). The specimen that was examined for 4 months in the field exhibited some degradation, which was at initial stage, since only the high-frequency part of the semicircle was depicted during EIS (Fig. 6.79). The obtained parameters are presented in Table 6.60. After 4 months, the capacitance exhibited some increase, compared to the previous interval, being equal to 1.04 10^{-9} F (or 9.67 10^{-11} F/cm^2), while the R_{pore} was equal to 9.55 10^5 Ω or 1.03 10^7 Ω cm^2, implying an efficient coating [152, 153].

Table 6.60: Electric properties of the specimens painted with the PU system, during their 6-month immersion in Elefsis

Months	Coating Capacitance [F]	Coating Resistance [Ω]
Before	$2.710\ 10^{-10}$	-
2	$7.868\ 10^{-10}$	-
4	$1.042\ 10^{-9}$	$9.545\ 10^{5}$
6	$2.425\ 10^{-10}$	-

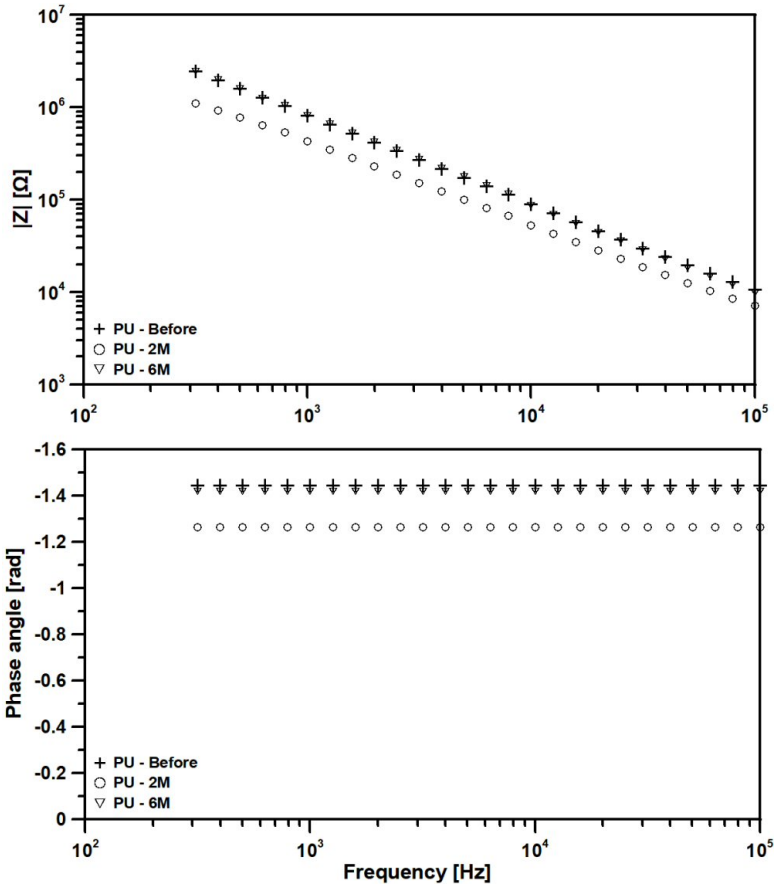

Figure 6.78: EIS graph for the specimenS painted with the PU system, that remained immersed for 2 and 6 months in Elefsis.

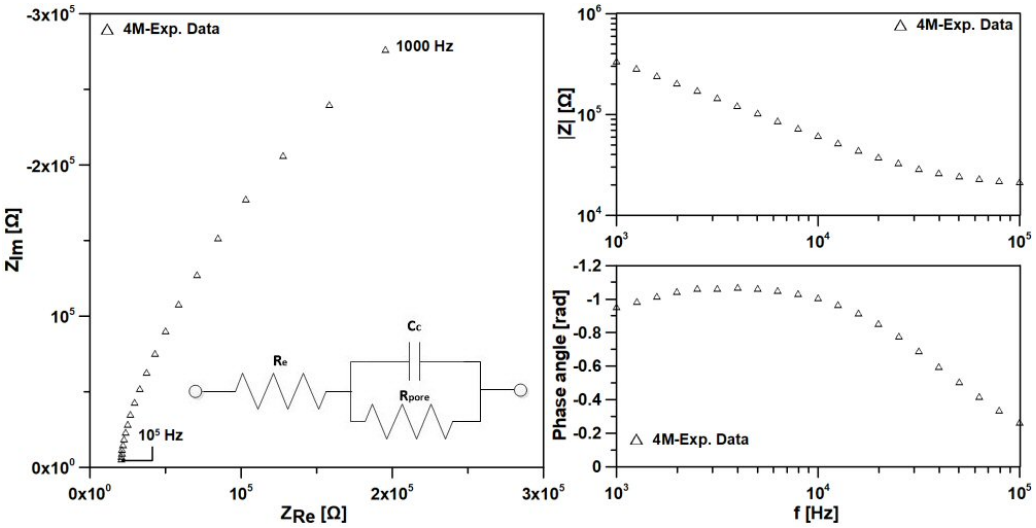

Figure 6.79: EIS graph for the specimen painted with the PU system, that remained immersed for 4 months in Elefsis.

6.3.4.6 Experimental polyurethane (2) system

Five of the six specimens painted with the experimental polyurethane formulation (2) exhibited a purely capacitive behavior throughout the testing period, despite the heavy fouling (Figure 6.80). The capacitance of the metal/electrolyte system, with the coating serving as the dielectric, was in the order of 10^{-10} F, corresponding to an intact coat with an efficiently protective character (Table 6.61). Only the curve corresponding to 4 months of immersion exhibited deviation from the ideal behavior (Figure 6.81), compared to the rest of the curves, exhibiting a poorly resolved semicircle, due to the large value of the R_{pore} (2.73 10^7 Ω cm^2).

Table 6.61: Electric properties of the specimens painted with the Exp. PU2 system, during their immersion in Elefsis

Months	Coating Capacitance [F]	Coating Resistance [Ω]
Before	3.159 10^{-10}	-
2	2.943 10^{-10}	-
4	1.197 10^{-9}	2.544 10^6
6	2.294 10^{-10}	-
8	5.585 10^{-10}	-
10	4.553 10^{-10}	-
12	2.504 10^{-10}	-

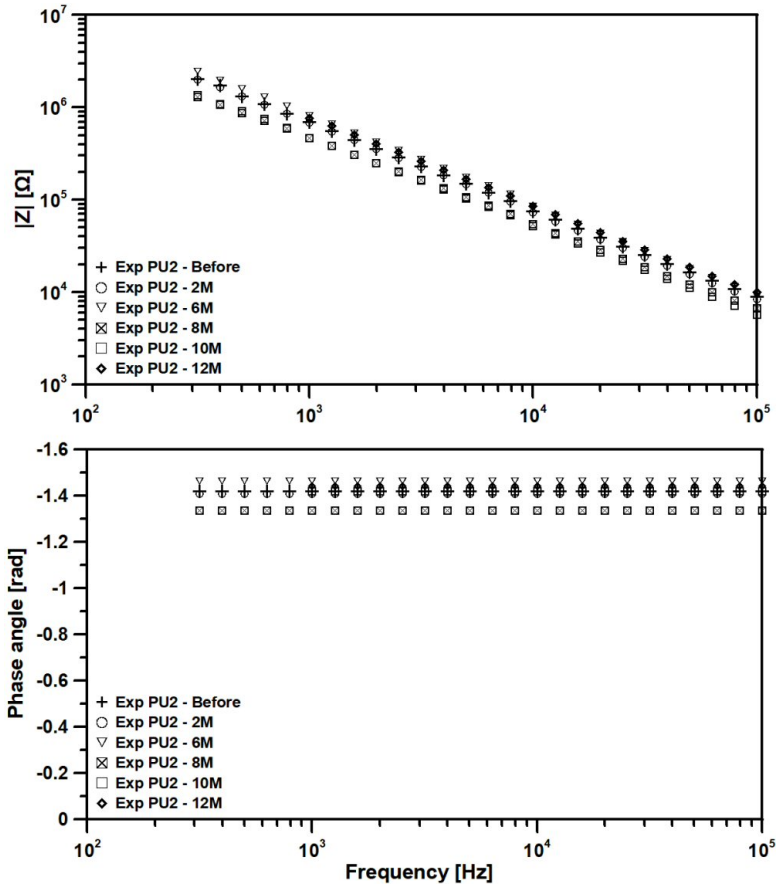

Figure 6.80: Bode plot of the Exp. PU2 system during the 12-month immersion in Elefsis. All curves exhibited purely capacitive characteristics.

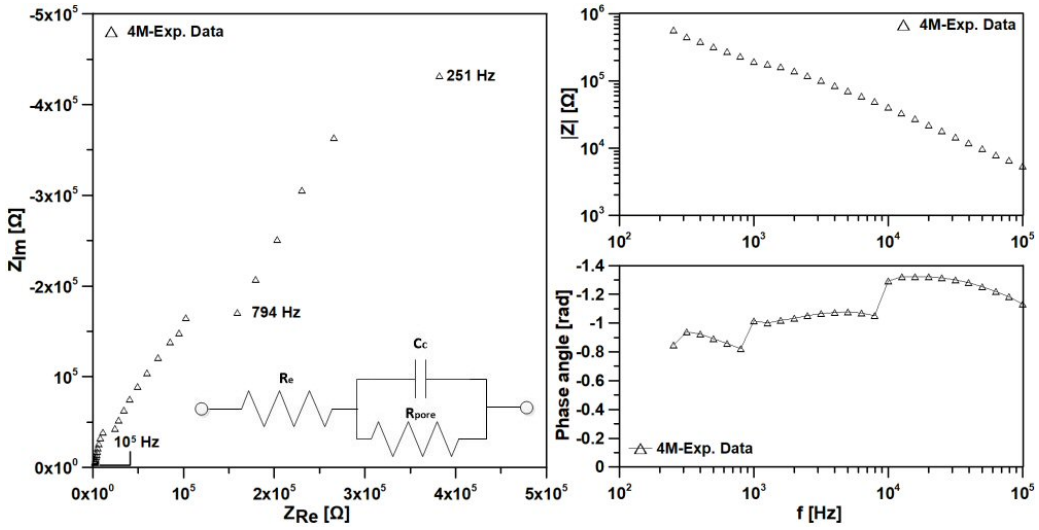

Figure 6.81: EIS graph for the specimen painted with the Exp. PU2 system, that remained immersed for 4 months in Elefsis.

6.3.5 Water titration results

The titration procedure was performed, in order to calculate the molarity of chloride ions into the sea water taken from Elefsis. The Mohr's method was applied for determination of the Cl^- concentration. According to this procedure, in order to calculate a substance of unknown

concentration (here the chloride ions, called the analyte), we should first use a standard solution (the titrant) of known concentration, which will react with the NaCl of the seawater to produce a solid precipitate. In the Mohr's method the titrant is $AgNO_3$ in concentration of 0.1M. The precipitation reaction is the following:

$$AgNO_3(aq) + NaCl(aq) \rightarrow AgCl(s) + NaNO_3(aq) \tag{6.1}$$

The method stops when all the Ag^+ ions have reacted with the Cl^- ions of the solution, to form AgCl precipitate. In order to visually be able to determine the equivalence point (the point at which the moles of the titrant are equal to the moles of the analyte in the sample), we usually use a potassium chromate indicator (K_2CrO_4), which is yellow in color. The potassium chromate reacts with the silver (I) ions, according to the following reaction:

$$K_2CrO_4(aq) + 2AgNO_3(aq) \rightarrow Ag_2CrO_4(aq) + 2KNO_3(aq) \tag{6.2}$$

As soon as the Ag^+ ions have reacted with all the Cl^- ions of the seawater, they start to react with the indicator, turning the solution to light orange. This is when the experiment stops. More specifically, firstly the seawater is diluted with distilled water because the chloride concentration is too big to measure. The diluted seawater sample is placed into a conical flask and then 1 ml or 2 ml of the indicator are added, turning the solution into transparent yellow (Fig. 6.82a). The sample is placed under the burette presented in Fig. 6.82, which contains the 0.1M $AgNO_3$.

By the moment the first drop of the titrant ($AgNO_3$) from the burette reaches the analyte, it obtains a milky white color (Fig. 6.82b). At the endpoint, the maximum quantity of AgCl precipitates has been created and the solution obtains a slight orange color (Fig. 6.82c). If the process continues beyond the endpoint, the solution turns into dark orange, due to the production of Ag_2CrO_4 molecules (Fig. 6.82d).

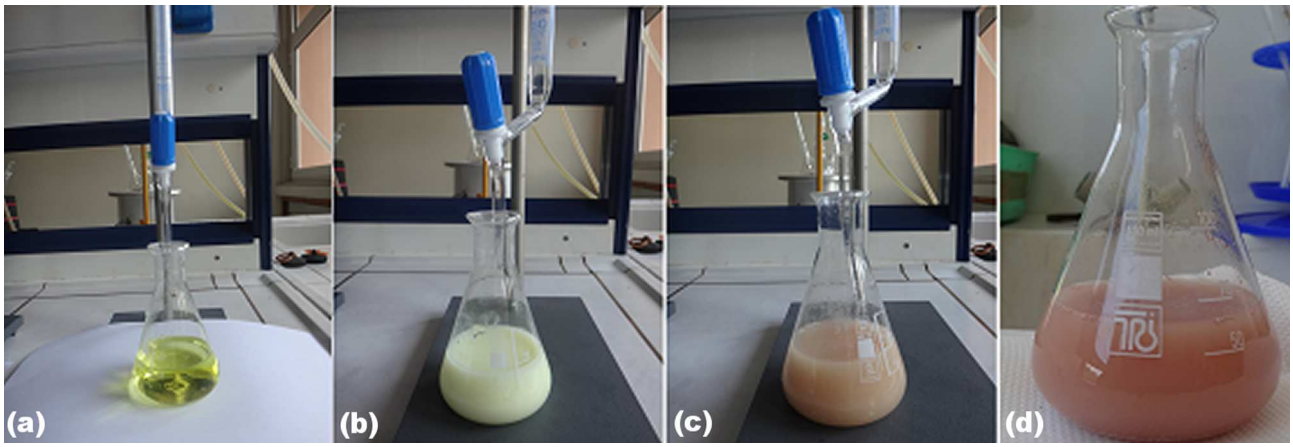

Figure 6.82: Titration steps; a) before initiation of the titration, b) during the titration procedure, c) endpoint of titration and d) excess of AgCl in the solution beyond the endpoint

The solution used for the titration was a two-times diluted seawater sample taken from Elefsis. The procedure followed was:

1. 20 ml seawater diluted to 100 ml distilled H_2O
2. 10 ml from the above diluted seawater diluted again to 50ml H_2O, containing 1 ml of the indicator (to color the solution yellow). This solution was the sample used for titration.
3. The procedure was repeated three times for each sample and the mean value was calculated.

In order to calculate the molarity of Cl^- ions in the original undiluted seawater sample, the following procedure was applied [156] (example presented for seawater sample taken after 10 months immersion in Elefsis):

1. Calculation of the amount of Cl^- ions into the 50 ml solution which was titrated

$$n_{Cl^-} = \frac{0.1\text{mol}Ag^+}{1\text{L}Ag^+} \times 0.0111\text{L}Ag^+ \times \frac{0.1\text{mol}Cl^-}{1\text{mol}Ag^+} = 1.11\ 10^{-3}\ \text{mol} \tag{6.3}$$

2. Calculation of Cl^- concentration in the diluted solution

$$c_{Cl^-} = \frac{n_{Cl^-}}{V_{\text{solution}}} = \frac{1.11\ 10^{-3}\,\text{mol}}{0.050\quad\text{L}} = 0.0222\ \text{M} \tag{6.4}$$

3. Calculation of Cl^- concentration in the original undiluted seawater

$$c_{Cl^-} = 25 \times 0.0222 = 0.555\ \text{M} \tag{6.5}$$

The sample was diluted two times by five times each. Hence, it was finally diluted twenty-five times its original concentration. The obtained Cl^- concentrations, during the 24-month experiment in Elefsis, are presented in Table 6.62 .

Table 6.62: Water characteristics for the total of 24 months immersion in Elefsis

Months	pH	Conductivity (mS/cm)	Average $AgNO_3$ (ml)	Cl^- concentration (M)
2	9.67	37.1	10.0	0.500
4	8.28	49.1	13.7	0.685
6	8.22	48.8	11.3	0.565
8	7.88	49.2	11.2	0.560
10	8.06	48.4	11.1	0.555
12	8.13	42.2	10.1	0.503
14	8.28	33.7	9.50	0.475
16	8.30	45.2	9.43	0.472
18	8.42	45.2	8.47	0.423
20	8.35	48.8	13.00	0.650
22	8.41	47.2	12.33	0.617
24	8.33	47.0	13.73	0.687

The titration measurements revealed that the mean chloride content of the seawater was 0.558 M. The mean pH value was 8.19, while the average conductivity was 44.99 mS/cm.

6.4 Conclusions

- The commercial, foul-release, silicone-based formulation (Ref Si) did not exhibit a consistent antifouling behavior, since it could facilitate dense fouling, dropping the F.R. index quite sharply, thus, becoming ineffective. However, the attached foulers, mainly serpulid representatives, could be easily removed under running water, due to the low surface tension of the paint, causing, though, intense digging. In real conditions, the severity of digging would depend on the idle periods of the ship. The hardness measurements revealed the soft nature of the elastomeric system.

- The commercial, self-polishing, acrylic-based system exhibited the best antifouling behavior overall, with F.R. values close to 95%, with almost any macrofoulers attached. Its efficiency arises from the mode of action, based on leaching. This paint does not retain any optical properties, it is harder than the commercial silicone formulation but suffers wearing and chipping, as a result of leaching.

- The experimental silicone formulation with 0.56% immobilized Econea (Exp. Si) was an improved version of the commercial silicone system. This system could also facilitate macrofouling attachment of great variety, which could make it inefficient on occasion, but not as severely as the reference silicone formulation. The foulers could be easily removed under running water, while the digging effect was minimized, compared to the commercial silicone system. Hence, in real conditions, it would be easy for the organisms to detach from the hull with minimum physical damage. Finally, the optical properties were only slightly affected, while, in terms of hardness, it was found somewhat softer than its commercial counterpart.

- The experimental polyurethane formulation with 2% immobilized Econea (Exp. PU1) would not be suitable for antifouling purposes. This system lost its antifouling efficiency quickly after immersion, becoming progressively more heavily fouled with serpulid-worms and bryozoans, strongly adherent onto the paint. Even in dynamic conditions, it would be very difficult for these foulers to become detached. In terms of physical damage, digging, discoloration, gloss drop and hardness increase were observed as a general trend, during immersion.

- The experimental polyurethane formulation with mixed biocides (Exp. PU2) would be rather unsuitable for antifouling protection, since it became heavily fouled even from the first two months of immersion. Bryozoans, algae and *spirorbinae* were the main foulers. The foulers were strongly attached, similarly to the Exp. PU1 formulation. Physical damage was mainly attributed to digging. The rest of the properties exhibited the trend reported for the previous experimental polyurethane system. The hardness of the coat exhibited variations.

- No pigment loss or other manifestations of physical damage (e.g. wearing, chipping, flaking etc.) were observed for either of the polyurethane formulations.
- In terms of antifouling protection in static immersion, the acrylic-based system exhibited the best behavior. In terms of physical damage, the experimental silicone system was the best candidate. As a result, in real conditions, where the foulers would be easily removed due to friction, the experimental silicone formulation would provide a long-lasting efficient behavior. Moreover, the immobilized biocide makes this formulation an environmentally friendly solution.
- Electrochemically, the Exp. PU2 system retained its barrier properties almost unaffected throughout the test. The second best behavior was exhibited by the experimental silicone system, if a comparison among the antifouling paints is to be made.
- Taking into consideration the aforementioned observations, the experimental silicone formulation would be an efficient antifouling and anticorrosive solution for marine applications, if some precautions are followed, concerning its soft elastomeric nature.

Chapter 7

Mechanical testing of experimental and commercial antifouling systems and electrochemical investigation thereof after accelerated aging tests on intact specimens

Abstract

In the present chapter, accelerated aging tests in a salt spray and a climatic chamber, as well as, immersion tests in artificial seawater in laboratory conditions were performed for selected painting systems in intact condition. The performance of the systems was assessed through K*ö*nig pendulum hardness, 60° gloss, discoloration (DE) and EIS measurements. The experimental silicone formulation exhibited the best behavior, followed by the reference silicone, while the experimental polyurethane (Exp PU1) and the anticorrosive polyurethane systems were ranked in the last position exhibiting the best behavior only one time, during all three tests. From the results obtained from all these tests, it was concluded that the immersion test imposes smaller stresses on the painting systems compared to the accelerated aging tests. Moreover, the mechanical and physical properties of the systems were determined through water liquid transmission rate test, cupping, chalking and dirt pick-up standardized practices. In these tests, the reference silicone system and the experimental polyurethane system (Exp PU1) exhibited the best behavior.

7.1 Introduction

In order for an organic coating to be efficient and suitable for the service conditions it is intended to, it should withstand the specific environmental stresses it is subjected to, retaining its barrier properties, adhesion, physical, chemical and mechanical characteristics. Assessment of the effective performance of a painting system is usually performed through accelerated aging tests. These tests impose larger stresses on the examined paint than it would normally encounter in the field and could include continuous immersion in an electrolyte, exposure to salt

spray or UV conditions and/or increased temperatures with variations. Under these conditions, penetration of the electrolyte through the coating becomes faster and, as a result, the corrosion process starts and progresses faster [1]. Apparently, the selection of the right aging test or combination of those depends on the service conditions that the paint will encounter. During accelerated aging tests the failure mechanism remains the same but the failure commences faster [1].

Since oxygen, water (or generally a conducting electrolyte), UV radiation and temperature are the most important parameters for a coating's degradation, a proper accelerated aging test could involve most or all of them as imposed stresses. The ASTM D 5894-96 [157] standard practice combines exposure in a UV chamber (as proposed in ASTM G 154-06 standard [158] for UV exposure of non-metallic materials) with a Prohesion chamber, based on alternation of fog/dry cycles. Due to the intervals with absent UV radiation, this procedure was proven to be less damaging after 27 weeks of experiments than a 24-week UV exposure, during aging of high gloss polyurethane coatings [3]. More specifically, the authors observed as a major degradation indication the intense pigment exposure on the surface, leading to void and cracks in the bulk of the coat. On the contrary, through the UV/Prohesion test, pigment loss was hardly detected. The same trend was observed in gloss loss, while blistering was observed after both experiments, with the ones observed after UV exposure being larger and fewer than after the UV/Prohesion test.

UV aging is a very common accelerated aging method and it is used as a simulation method of the stresses induced from UV radiation from sunlight for coatings intended for outdoors. UV light along with oxygen lead to "photo-oxidation" or "photodegradation" [159]. Incorporation of water effect is often assured through a step including condensation. UV aging has been reported to cause blistering to epoxy varnish paints after 35 days of exposure, causing coating resistance drop and loss of adhesion [160]. Also, an epoxy primer/ epoxy topcoat paint exhibited intense chalking after 4500 h of UV aging and topcoat degradation, which became apparent through a measurable coating resistance. On the contrary, an epoxy primer/polyester-urethane topcoat paint was hardly deteriorated and retained its capacitive behavior during the course of the experiment [161]. A drawback of these tests is that the failure mode induced by the usually applied short wavelength UV source could be different from the one observed during natural weathering [162]. This is because the higher intensity UV sources have a larger potential to break chemical bonds, which might not be the case during an outdoor weathering test, where the sunlight intensity depends on season, location and atmosphere quality [163].

Salt spray test is one of the most widespread techniques, because it offers the potential to perform tests combining increased temperature, salt spray-simulating marine atmosphere- and humidity. The painted specimens can be examined into the chamber either intact, in order to examine the barrier properties of an intact coat, or scribed, in order to investigate the barrier properties of the unscratched part and possible corrosion products accumulation and expansion beneath the unscratched paint [7, 164]. One of the most common standards is the ASTM B 117 [165] standard practice for continuous salt fog at 35°C. Paint assessment of painted samples

after the end of the test is usually based on visual inspection, with an emphasis on blistering dimensions and their density [166]. Currently, the standard ISO 14993:2001 [167] has been widely applied, because it combines cyclic corrosive conditions, based on alternation of salt fog, dry and humid steps at different temperatures, thus better representing conditions that could be encountered in the field.

If temperature is the main parameter that affects a coating's performance, thermal cycling tests could be applied. These tests are based on alternation of temperature steps and can be combined with continuous immersion of the painted samples in an electrolyte, in order to draw conclusions with regard to their barrier and adhesion properties. These tests are ideal for coatings that are intended to work at temperatures higher than their glass transition temperature [168]. Increase of temperature would cause increased water penetration through the coating, leading to faster physical and chemical aging [162]. The same authors proposed reversibility of film damage after cooling to room temperature, as an accredited criterion for assessment of barrier properties and adhesion performance of the examined paint. Thermal cycling without immersion in an electrolyte, but including intervals with UV radiation have been performed at NTUA [169]. The painting systems were multilayer (primer and topcoat) with alkyd, vinyl-chloride, polyurethane and aspartic polyurethane as topcoats. Also, an antifouling system was examined. The specimens were exposed to UV aging (ASTM G 154-06) for 240 h and then to thermal cycling for 480 h. Three temperatures were examined, namely 25°C, 45°C and 65°C. Each thermal cycle lasted 120 h and included five steps of 24 h each. Each step included alternation of UV lamp on and off every 4 hours, starting with the lamp off. The succession of steps was 25°C, 45°C, 65°C, 45°C and finally 25°C. The vinyl-chloride system was electrochemically more largely affected, since there was exposure of the primer coat and corrosion spots on the iron peaks exposed outside the paint. Chemical degradation was also observed for this system, with a larger effect on the 879.4, 1541 and 1699 cm^{-1} transmittance peaks, hence implying chemical modification of the epoxy resin [170]. Finally, the antifouling system exhibited intense pigment loss and a cohesion mode of detachment, 5% top coat and 95% primer, during the pull-off test (ISO 4624:2002 [171]).

Immersion test in artificial seawater (NaCl) at room or elevated temperatures [43] comprises also another common aging procedure. This test is directly related to EIS measurements and aims at depicting electrolyte uptake gradually, until substrate corrosion initiates. This test has been performed by Abdel-Gaber *et al.* [139], during investigation of a vinyl chloride-vinyl acetate copolymer based paint, containing lupine seed extract. The authors performed the test for a duration of 33 days. Even though two time constants were already apparent after 24 days of exposure, the lupine extract acted as an inhibitor, leading to higher coating and double-layer resistances and capacitances, respectively, compared to the unloaded paint. However, this type of tests generally requires a long immersion period, in order to differentiate high performance paints, which could range from 10 weeks to 1 year, without ensuring that a measurable change in barrier properties would be feasible [162].

Assessment of paint performance should be performed at frequent intervals during testing and should include measurement of as many characteristics of the painting system as possible, such as physical characteristics (e.g. gloss, color), electrical characteristics (e.g. through electrochemical impedance spectroscopy), mechanical characteristics (e.g. König pendulum hardness) and any chemical alterations (e.g. through FTIR).

A subject of extended conversation is whether accelerated aging tests can be correlated with natural exposure tests. In the work of Deflorian *et al.* [172], the authors performed a 10 month natural weathering test in Trento, Italy, between August and May on two polyester paints with different thicknesses. Also, various accelerated aging tests, such as salt spray, UV and thermal cycling tests were performed. The authors reported that UV aging could not be correlated with natural exposure, in contrast to the salt spray and thermal aging tests, which could be correlated with natural weathering results for painted samples of small thickness (around 45 μm). The authors highlighted the importance to clarify the relative effect of each meteorological parameter (UV radiation intensity, precipitation, humidity etc) on coating degradation and the synergistic effect of combination of different accelerated aging tests on polymer degradation. In this way, a tailor made accelerated aging protocol could be applied, simulating specific environmental conditions encountered in the field of interest.

Electrochemical impedance spectroscopy (EIS) has been proven to be a very valuable tool in the examination of coated steel, since it is a non-destructive method that can be applied even on thick coatings, when no current can flow. With EIS, progressive degradation of the barrier properties of a painting system can be captured if performed at frequent intervals during aging. During a weathering test, barrier properties are largely affected by coating thickness, with lower thickness coatings being more affected. This is because their smaller thickness allows the electrolyte to permeate easier through the coat and reach the substrate, usually leading to blister formation and subsequent decrease of coating resistance [172].

At initial stages of immersion, an intact coat of good quality would exhibit only an imaginary component in a Nyquist plot, corresponding to the response of a capacitor, where the coating serves as the dielectric. The dielectric values for an organic coating are usually between 3-8 [173], while more strict limits have also been reported, ranging between 3-4 [1]. The magnitude of the impedance of a perfect capacitor is $|Z_c|=1/(\omega C)$, meaning that for $\omega=1$ the capacitance would be given by the following equation: $C=10^{-log|Z_c|}$. The plates of the capacitor are the electrolyte and metallic substrate, correspondingly. The impedance magnitude plot would exhibit a straight line with a slope equal to -1, while the phase angle plot would be $-\pi/2$, corresponding to the phase shift of a capacitor.

As degradation progresses, straight lines will continue to appear in the impedance magnitude plot with the same slop (-1), transferred however towards lower frequencies, implying initiation of electrolyte penetration and increase of coating capacitance [173]. By the time some water ingress has commenced, a plateau will appear at lower frequencies, representing the sum of the electrolyte resistance R_e and the coating pore resistance R_{pore}. At this point, the phase angle plot would exhibit an inclination towards zero, which is the phase shift of the resistor, while

in the Nyquist plot a semicircle would appear, with a diameter equal to R_{pore}, corresponding to the time constant CR_{pore}, where C is the coating capacitance [174]. At this point, water infiltration has started, which would preferentially proceed through the interconnections of the hydrophylic regions of the coat, which allow permeation of large amounts of electrolyte [175]. Another approach suggests that infiltrated water forms inclusions inside the polymer, mostly filling void areas of the polymer, while some water paths between inclusions allow diffusion of water inside the polymer coating [176].

At the final stage of degradation the electrolyte approaches the film/substrate interface and reaches the metallic substrate. Corrosion initiates at the base of the pathway (anodic region), while cathodic reactions occur in the periphery (cathodic region). The cathodic reactions lead to cathodic delamination blistering of the coating, with the corrosion products located in the center of the blister [175]. At this stage, usually a third plateau appears in the low frequency region of the impedance magnitude plot, corresponding to the sum of the electrolyte resistance, the pore resistance and the polarization resistance [173, 177, 178].

In the present study, cyclic salt spray (ISO 14993:2001 [167]), UV aging (ASTM G 154-06 [158]) and immersion in 3.5% NaCl solution at room temperature were performed for four antifouling and one anticorrosive system, namely the Ref. Si, Acrylic, Exp. Si and Exp. PU1. Also, the anticorrosive polyurethane formulation (PU) was examined. Duration of the salt spray and UV tests was 9 weeks, while immersion in 3.5% NaCl solution lasted 1 year. Assessment of the paints was performed at frequent intervals through König pendulum hardness (ISO 1522:2006 [142]) measurements, gloss, color and EIS. In parallel, mechanical testing of these systems was performed and included cupping (ISO 1520:2006 [179]), chalking (ASTM D 4214-98 [143]), dirt pick-up (ASTM D 3719-00 [180]) and water-liquid transmission rate tests (BS EN 1062-3:1999 [181]).

7.2 Experimental methods and materials

7.2.1 Painting systems examined

The painting systems examined are presented in Table 7.1. All systems were multilayered and applied on top of a Grade A steel substrate of dimensions 100 mm × 100 mm × 6 mm. The total thickness of the systems was around 500-600 μm.

7.2.2 Experimental procedure

Accelerated aging tests on intact specimens included salt spray and UV tests. The former experiments were performed in a QFOG CCT1100 chamber, according to the ISO 14993:2001 standard for exposure to cyclic corrosive conditions. The aging steps were 2 h salt mist at 35°C, 4 h dry conditions at 60°C and 2 h wet conditions (RH 98%) at 50°C. Photo-oxidation was performed in a Angelantoni ACS Global Test System 600, according to the ASTM G 154-06 standard Cycle No. 2, which suggests 4 h with lamp on at 60°C (dry day), followed by 4 h with lamp off at 50°C and RH 98% (humid night). The light source radiated in the UVB+UVC

Table 7.1: Painting systems examined in either/both accelerated aging and mechanical testing

Painting system	Abbreviated name	Characteristics/ Type of action	Biocides
Silicone-based	Ref. Si	Commercial/ Foul-release	No biocides
Acrylic-based	Acrylic	Commercial/ Self polishing Copolymer(SPC)	10%≤Cu_2O≤25% 5%≤Zineb≤10%
Silicone-based	Exp. Si	Experimental	0.56% immobilized Econea
PU-based	Exp. PU (or Exp. PU1)	Experimental	2% immobilized Econea
PU-based	Exp. PU2	Experimental	Mixture of biocides
PU-based	PU	Newly developed anti-corrosive	No biocides

range. Both experiments were performed for a total of 9 weeks, while two specimens per coating system were examined. Examination of specimens was performed at 4, 6 and 9-week intervals, with an exemption of the reference silicone and acrylic painted specimens exposed to UV, which were examined at 6 and 9-week intervals.

With regard to the laboratory immersion experiments, two specimens per painting system were examined. The specimens painted with the same system were simultaneously immersed in a plastic container filled with 0.5 L of 3.5% NaCl solution. The total duration of the experiment was 12 months, while periodic examination was performed every month, unless declared otherwise.

7.2.3 Electrochemical examination

Coating degradation during immersion was evaluated by electrochemical impedance measurements, similarly to the procedure presented in Sec. 6.2.5 in Chapter 6.

7.2.4 Coating hardness and physical properties measurements

Coating hardness measurements were performed according to the procedure presented in Sec. 6.2.6 in Chapter 6 and physical properties measurements were presented in Sec. 6.2.7 of Chapter 6.

7.2.5 Mechanical testing and determination of physical parameters

Water liquid transmission rate test was performed on all the painting systems presented in Table 7.1. This test aims at determining the permeability of the paint to water liquid, according to the BS EN 1062-3 standard. The examined paint is applied on one of the two bigger sides of a firebrick, while the rest sides are covered with insulating resin. The bricks are then subjected to 4 cycles, each one of which involves conditioning, immersion in potable water and drying steps. Weighing of the painted specimens is performed at specific intervals and the transmission rate is calculated through a proposed formula. Finally, a ranking for each paint is performed, regarding their overall permeability to water liquid.

The cupping test (ISO 1520:2006) gives valuable results with regard to the adhesion strength of a multilayer painting system. Coated specimens with dimensions 120 mm × 60 mm × 1mm for the reference paints (reference silicone and acrylic) and of dimensions 200 mm × 60 mm × 1 mm for the new paints (experimental silicone, experimental polyurethane (1) and experimental polyurethane (2)) were subjected to deep drawing using a spherical punch of 33 mm diameter, which was drawn from a blank of 64 mm diameter. The punch was moving via a manually controlled rotor. The total depth of the drawing was easily readable through a graduated ruler on the cupping tester body. The whole test was performed at a slow rate (rotation at 0.1 mm steps), in order to capture the gradual loss of adhesion of each system. Three specimens per painting system were examined, while on each specimen the experiment was performed once. The tests were performed with a Sheen Ref-760 cupping tester. The paint is considered to have failed as soon as the first crack appears during drawing or the multilayer coat has detached from the metallic substrate.

Dirt pick-up test was performed on the reference paints and on both the experimental polyurethane and the experimental silicone paint, according to the ASTM D 3719-00 standard. This method provides a tool for quantifying the dirt collection of paints during outdoor exposure for 61 days. The prerequisite for a successful dirt pick-up determination is the specimens to be placed at a 45° angle to the horizontal and facing the equator. For this test, two panels per painting system were examined, with dimensions 150 mm × 250 mm × 6 mm. Assessment of dirt collection onto the painted surface was made through colorimetry measurements. The discoloration index of the specimens was determined using the colorimetry technique, according to the CIE L*a*b color model.

Finally, chalking tests were performed, according to the ASTM D 4214-98 standard. As mentioned in the standard, chalking is defined as "the formation on a pigmented coating of a friable powder evolved from the film itself at or just beneath the surface". In other words, when the paint degrades, the pigment particles loose their adherence to the film and can be removed just by wiping the surface. The shorter time is needed for a paint to chalk, the sooner the paint will fail.

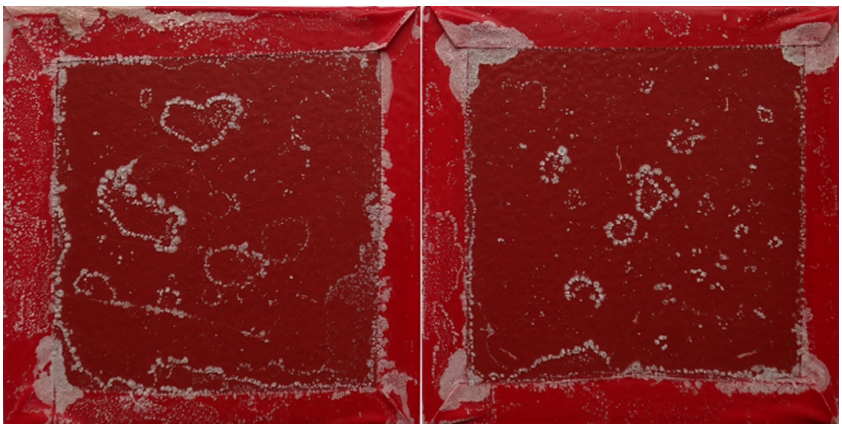

(c) After 9 weeks

Figure 7.1: Surface condition of the specimens painted with the Ref Si system during their 9-week examination in the salt spray chamber. Left: specimen (A), Right: specimen (B)

7.3 Results and discussion

7.3.1 Electrochemical measurements on intact specimens during a 9-week accelerated aging test in salt spray chamber

7.3.1.1 Salt spray tests on reference silicone (Ref Si) system

(a) After 4 weeks

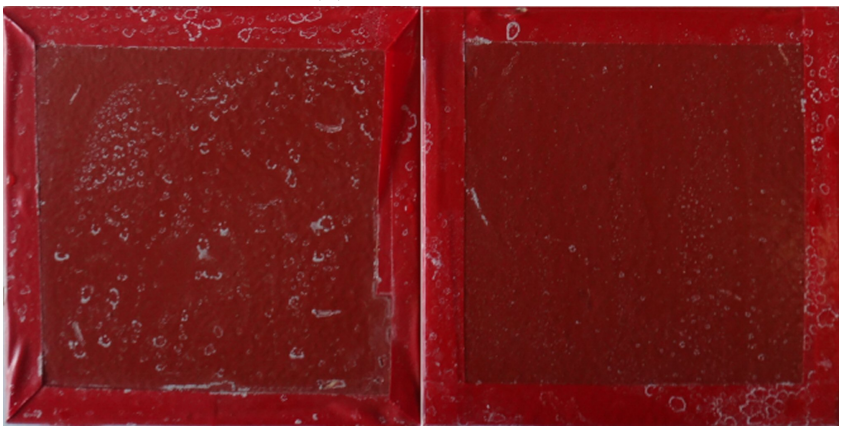

(b) After 6 weeks

Table 7.2: König pendulum hardness measurements for specimens painted with the Ref Si system during their 9-week examination in the salt spray chamber

Duration (Weeks)	Ref Si (A)	Ref Si (B)
Before	25.00	31.00
4	21.80	24.60
6	22.00	26.80
9	27.40	30.80

Table 7.3: 60° gloss measurements for specimens painted with the Ref Si system during their 9-week examination in the salt spray chamber

Duration (Weeks)	Ref Si (A)	Ref Si (B)
Before	28.00	13.00
4	28.50	15.50
6	26.00	13.25
9	21.50	10.00

Table 7.4: Discoloration (DE) measurements for specimens painted with the Ref Si system during their 9-week examination in the salt spray chamber

Duration (Weeks)	Ref Si (A)	Ref Si (B)
Standard sample: L=36.43, a=32.64, b=11.68, C=34.66, H=19.69		
Before	0.58	0.68
4	1.27	1.37
6	1.63	1.74
9	1.12	1.12

After 9 weeks of experiment in the salt spray chamber, the König hardness of the reference silicone system remained more or less constant, ranging between 25 and 30. Generally, the smaller the oscillations number till total damping is (till an angle of 3°), the softer the coat will be. Silicone based paints exhibit small number of oscillations, due to their elastomeric nature, being considered as soft paints. Gloss loss was in the order of 23% for both specimens. Finally, discoloration index exhibited fluctuations, however, taking into consideration the value after 9 weeks of experiment, a 93% increase was observed for specimen (A) and a 76% increase for specimen (B). As can be seen from Table 7.4, the discoloration was quite small for the silicone system.

At this point, it should be noted that the gloss and color measurements are largely affected by the selected measurement points onto the specimen surface. If there are flaws on the painted surface, e.g. scratches etc., the results could be misleading. For this reason, care should be taken when selecting the points of measurement, in order to more accurately represent the condition of the painted surface, during the course of the experiment.

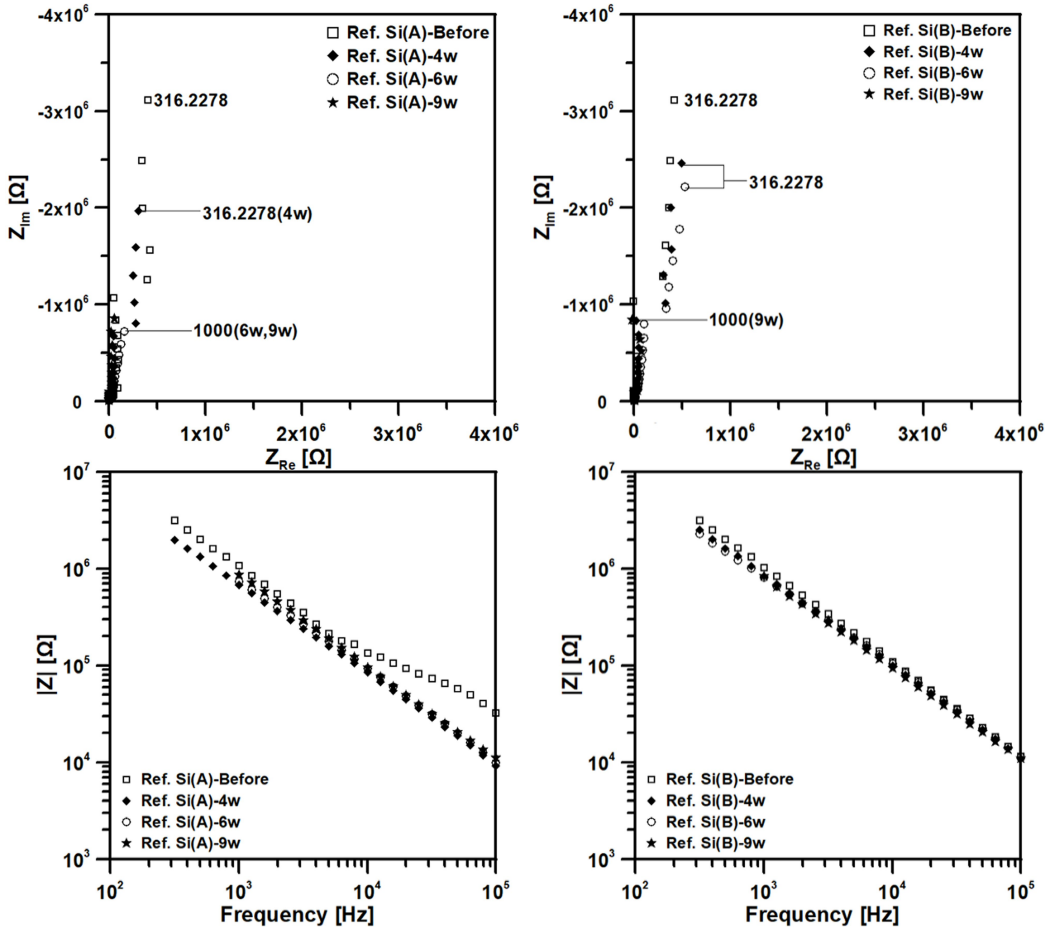

Figure 7.2: Nyquist and impedance magnitude plots for the specimens painted with the Ref Si system, during their 9-week examination in the salt spray chamber. Left: specimen (A), Right: specimen (B)

Table 7.5: Electric properties of specimens painted with the Ref Si system, during their accelerated aging in salt spray chamber

Duration (Weeks)	Coating capacitance (F)-Ref Si (A)	Coating capacitance (F)-Ref Si (B)
Before	7.335 10^{-10}	1.816 10^{-10}
4	3.829 10^{-10}	2.792 10^{-10}
6	3.240 10^{-10}	3.439 10^{-10}
9	2.805 10^{-10}	2.903 10^{-10}

EIS data revealed the pure capacitive nature of the silicone painted specimens after 9 weeks of experiment in the salt spray chamber. This becomes apparent through the pure imaginary component of the Nyquist plot and the straight line in the impedance magnitudde plot, exhibiting a slope close to -1. The shape of the "Before" curve for specimen (A) could be attributed to experimental artifacts. The capacitance value was in the order of 10^{-10} F for both specimens, revealing their high impedance character. Apparently, their large thickness (around 510 μm) served as the most important parameter in retaining their barrier properties intact after 9 weeks of salt spray.

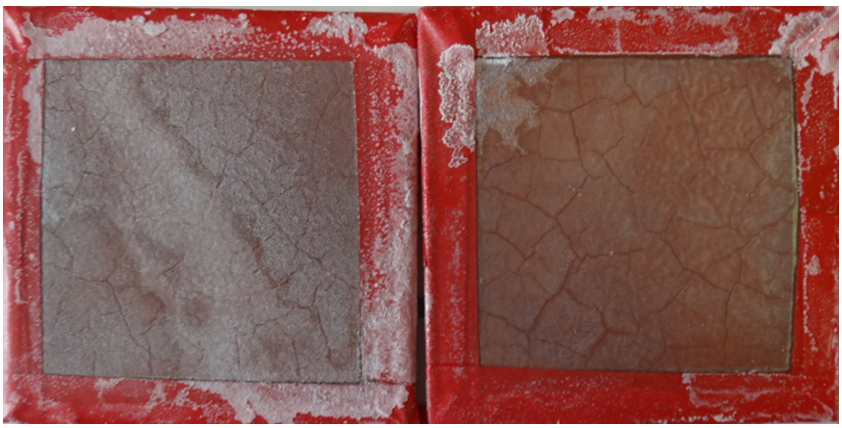

(c) After 9 weeks

Figure 7.3: Surface condition of the specimens painted with the Acrylic system during their 9-week examination in the salt spray chamber. Left: specimen (A), Right: specimen (B)

7.3.1.2 Salt spray tests on acrylic (Acrylic) system

(a) After 4 weeks

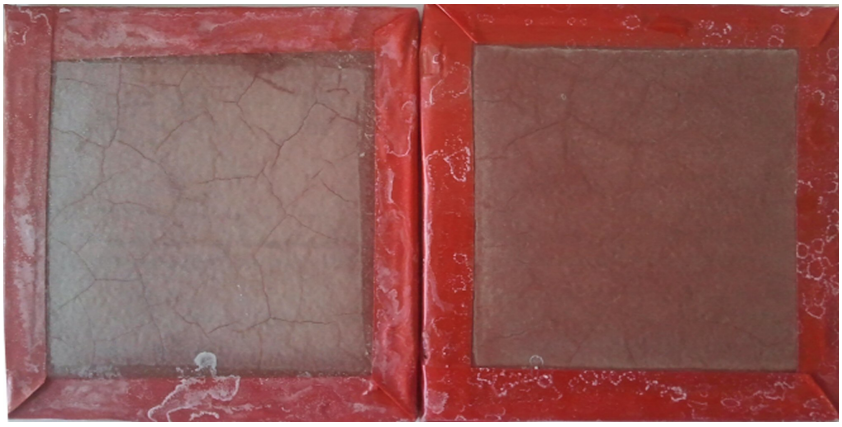

(b) After 6 weeks

Table 7.6: König pendulum hardness measurements for specimens painted with the Acrylic system during their 9-week examination in the salt spray chamber

Duration (Weeks)	Acrylic (A)	Acrylic (B)
Before	68.00	79.00
4	69.40	97.60
6	85.80	106.80
9	87.80	98.60

Table 7.7: 60° gloss measurements for specimens painted with the Acrylic system during their 9-week examination in the salt spray chamber

Duration (Weeks)	Acrylic (A)	Acrylic (B)
Before	9.00	17.00
4	5.00	7.00
6	4.00	5.00
9	2.50	2.00

Table 7.8: Discoloration (DE) measurements for specimens painted with the Acrylic system during their 9-week examination in the salt spray chamber

Duration (Weeks)	Acrylic (A)	Acrylic (B)
Standard sample: L=37.22, a=23.26, b=8.48, C=24.76, H=20.03		
Before	0.47	0.47
4	9.23	9.40
6	9.36	9.74
9	10.58	11.81

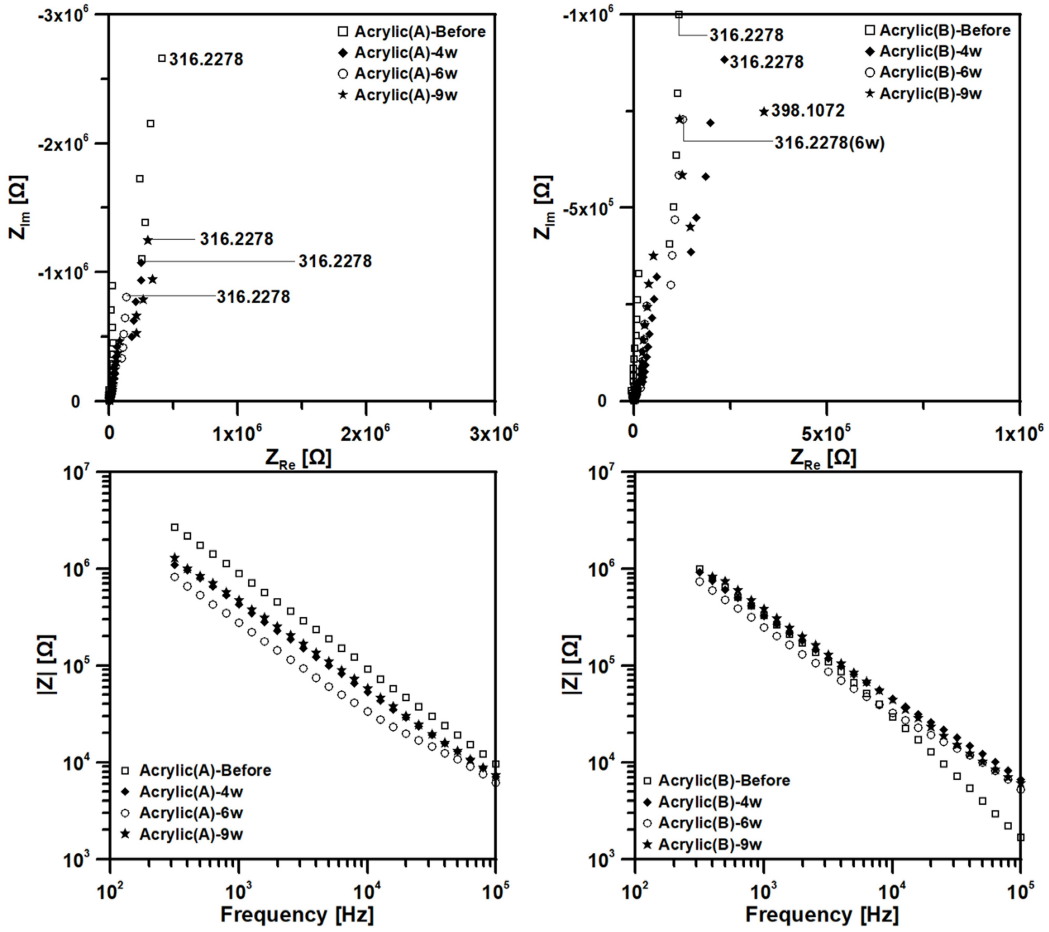

Figure 7.4: Nyquist and impedance magnitude plots for the specimens painted with the Acrylic system, during their 9-week examination in the salt spray chamber. Left: specimen (A), Right: specimen (B)

Table 7.9: Electric properties of specimens painted with the Acrylic system, during their accelerated aging in salt spray chamber

Duration (Weeks)	Coating capacitance (F)-Acrylic (A)	Coating capacitance (F)-Acrylic (B)
Before	$2.007\ 10^{-10}$	$2.167\ 10^{-10}$
4	$8.014\ 10^{-10}$	$1.371\ 10^{-9}$
6	$1.667\ 10^{-9}$	$1.862\ 10^{-9}$
9	$6.614\ 10^{-10}$	$7.408\ 10^{-10}$

The main characteristic of the acrylic system is the checking effect that was noticed in a wide extent after 6 weeks and especially after 9 weeks of experiment (Fig. 7.3). The type of checking was of the mosaic type, the ASTM No. 3 rank (ASTM D 660-93 [182]). The KöG'Anig hardness of the paint exhibited an increase during the experiment which ranged from 25% (specimen B) to 29% (specimen A). The initial hardness of the coat was in the range 68 to 79, revealing its harder nature compared to the silicone elastomer. Gloss is not a property that characterizes this system. Finally, intense discoloration was observed, due to leaching, which exposes pigments and biocides.

The acrylic system exhibited satisfactory electrical characteristics during the salt spray test. A capacitive behavior was observed, with some fluctuations in the capacitance values, which could arise either from the quality of the measured signal or from differences in physical properties of the polymer.

7.3.1.3 Salt spray tests on experimental silicone (Exp Si) system

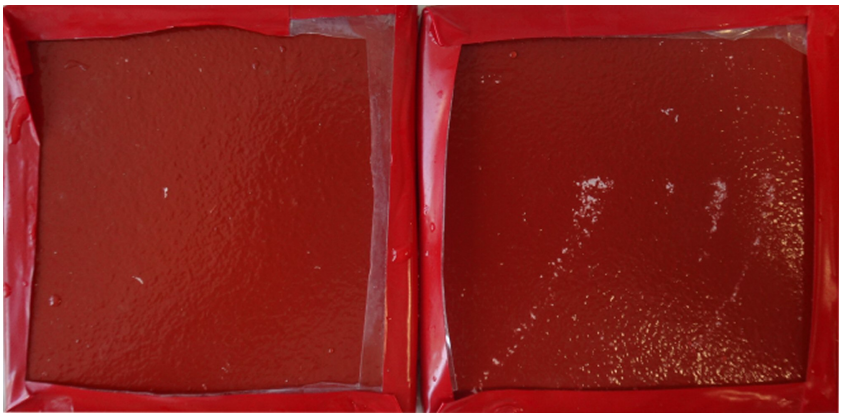

(a) After 4 weeks

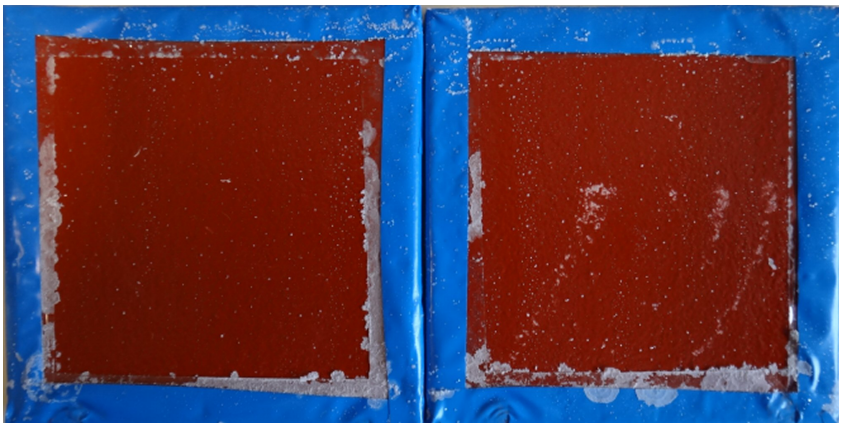

(b) After 6 weeks

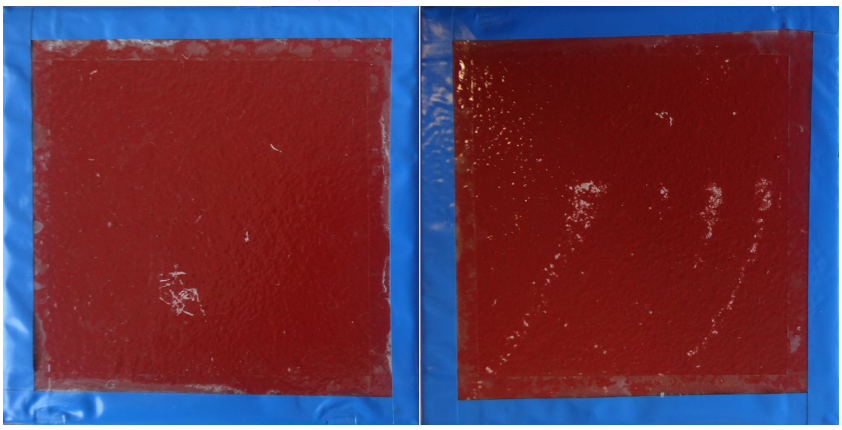

(c) After 9 weeks

Figure 7.5: Surface condition of the specimens painted with the Exp Si system during their 9-week examination in the salt spray chamber. Left: specimen (A), Right: specimen (B)

Table 7.10: König pendulum hardness measurements for specimens painted with the Exp Si system during their 9-week examination in the salt spray chamber

Duration (Weeks)	Exp Si (A)	Exp Si (B)
Before	20.60	18.67
4	20.33	15.50
6	18.00	18.40
9	20.60	16.80

Table 7.11: 60° gloss measurements for specimens painted with the Exp Si system during their 9-week examination in the salt spray chamber

Duration (Weeks)	Exp Si (A)	Exp Si (B)
Before	22.25	14.25
4	22.25	18.50
6	18.75	18.50
9	22.75	20.25

Table 7.12: Discoloration (DE) measurements for specimens painted with the Exp Si system during their 9-week examination in the salt spray chamber

Duration (Weeks)	Exp Si (A)	Exp Si (B)
Standard sample: L=35.71, a=35.04, b=12.52, C=37.21, H=19.66		
Before	0.81	0.69
4	0.61	0.51
6	0.62	0.77
9	0.49	0.53

The surface of the experimental silicone painted specimens after the end of the test was hardly affected. This can be verified by the almost no gloss change for specimen (A) and the 42% gloss change for specimen (B). Specimen (A) was the least affected of the two, since it exhibited also a very small variation in the König pendulum hardness values, remaining stable. The same is also true for specimen (B), which exhibited also small variations remaining more or less stable. The elastomeric nature of the PDMS experimental paint is apparent by the small hardness values, which ranged around the value of 20. Color change was -39.5% for specimen (A) and -23.2% for specimen (B). EIS results revealed their capacitive nature, as observed for the rest of the paints so far.

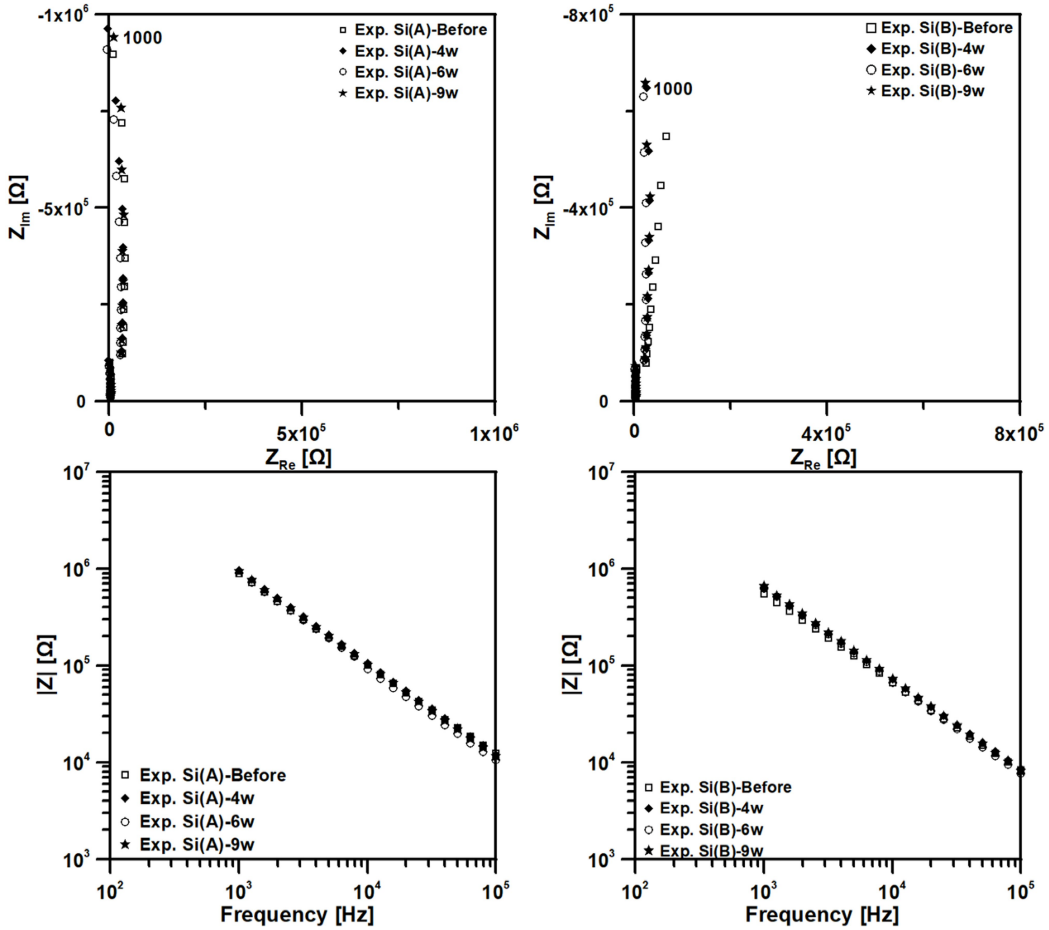

Figure 7.6: Nyquist and impedance magnitude plots for the specimens painted with the Exp Si system, during their 9-week examination in the salt spray chamber. Left: specimen (A), Right: specimen (B)

Table 7.13: Electric properties of specimens painted with the Exp Si system, during their accelerated aging in salt spray chamber

Duration (Weeks)	Coating capacitance (F)-Exp Si (A)	Coating capacitance (F)-Exp Si (B)
Before	$2.854\ 10^{-10}$	$5.056\ 10^{-10}$
4	$2.282\ 10^{-10}$	$2.453\ 10^{-10}$
6	$2.028\ 10^{-10}$	$3.108\ 10^{-10}$
9	$2.216\ 10^{-10}$	$3.221\ 10^{-10}$

7.3.1.4 Salt spray tests on experimental polyurethane (Exp PU1) system

(a) After 4 weeks

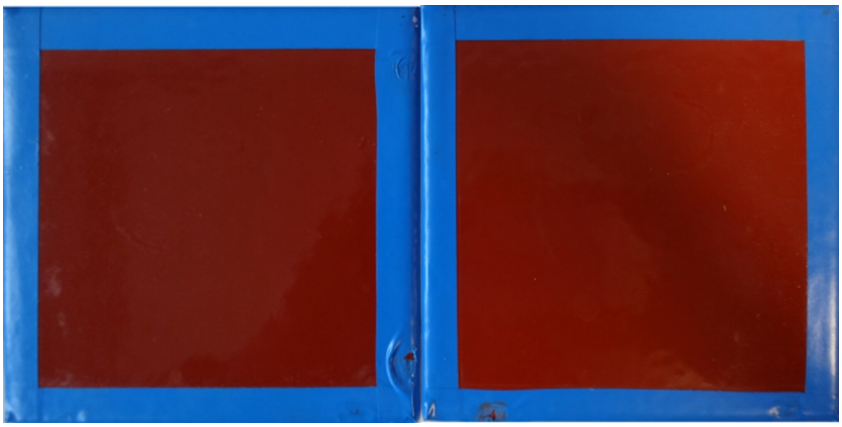

(b) After 6 weeks

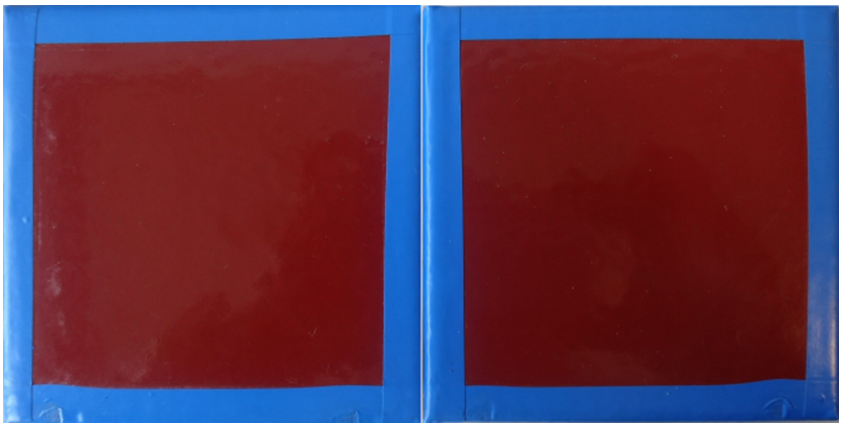

(c) After 9 weeks

Figure 7.7: Surface condition of the specimens painted with the Exp PU1 system during their 9-week examination in the salt spray chamber. Left: specimen (A), Right: specimen (B)

Table 7.14: König pendulum hardness measurements for specimens painted with the Exp PU1 system during their 9-week examination in the salt spray chamber

Duration (Weeks)	Exp PU1 (A)	Exp PU1 (B)
Before	31.67	28.83
4	86.50	75.17
6	95.00	91.20
9	104.80	102.40

Table 7.15: 60° gloss measurements for specimens painted with the Exp PU1 system during their 9-week examination in the salt spray chamber

Duration (Weeks)	Exp PU1 (A)	Exp PU1 (B)
Before	80.00	86.75
4	68.75	59.50
6	76.25	77.25
9	76.00	83.50

Table 7.16: Discoloration (DE) measurements for specimens painted with the Exp PU1 system during their 9-week examination in the salt spray chamber

Duration (Weeks)	Exp PU1 (A)	Exp PU1 (B)
Standard sample: L=35.92, a=28.75, b=8.26, C=29.91, H=16.03		
Before	0.70	0.70
4	0.49	0.62
6	0.68	1.77
9	0.38	0.60

Experimental polyurethane system was not largely affected in terms of color. Color change exhibited variations during the experiment and exhibited a 45.7% decrease for specimen (A) and 14.3% decrease for specimen (B), after the end of the test. A profound increase in hardness was observed for both specimens. More specifically the hardness of specimen (A) after 9 weeks was 3.3 times its initial value, while for specimen (B) was 3.55 times larger. The initial hardness values for this system were close to the silicone based paints. However, the increase after the test led to hardness values around 100. Gloss exhibited variations, however a constant drop was observed leading finally to a decrease equal to 5% for specimen (A) and 3.75% for specimen (B). It should be noted that the experimental polyurethane system has exhibited the highest gloss value so far and the smallest gloss decrease, compared to the rest of the paints. In terms of hardness, it exhibited initial values similar to the silicone system but, after the test the obtained hardness values were comparable to the acrylic system. This is attributed to the fact that the initially harder acrylic system exhibited a 1.25 to 1.5 times increase in hardness during the test, while the experimental polyurethane system exhibited an increase of around 3 times

its initial value. Finally, in terms of barrier properties, both specimens retained their capacitive behavior, while all the obtained EIS signals were of good quality.

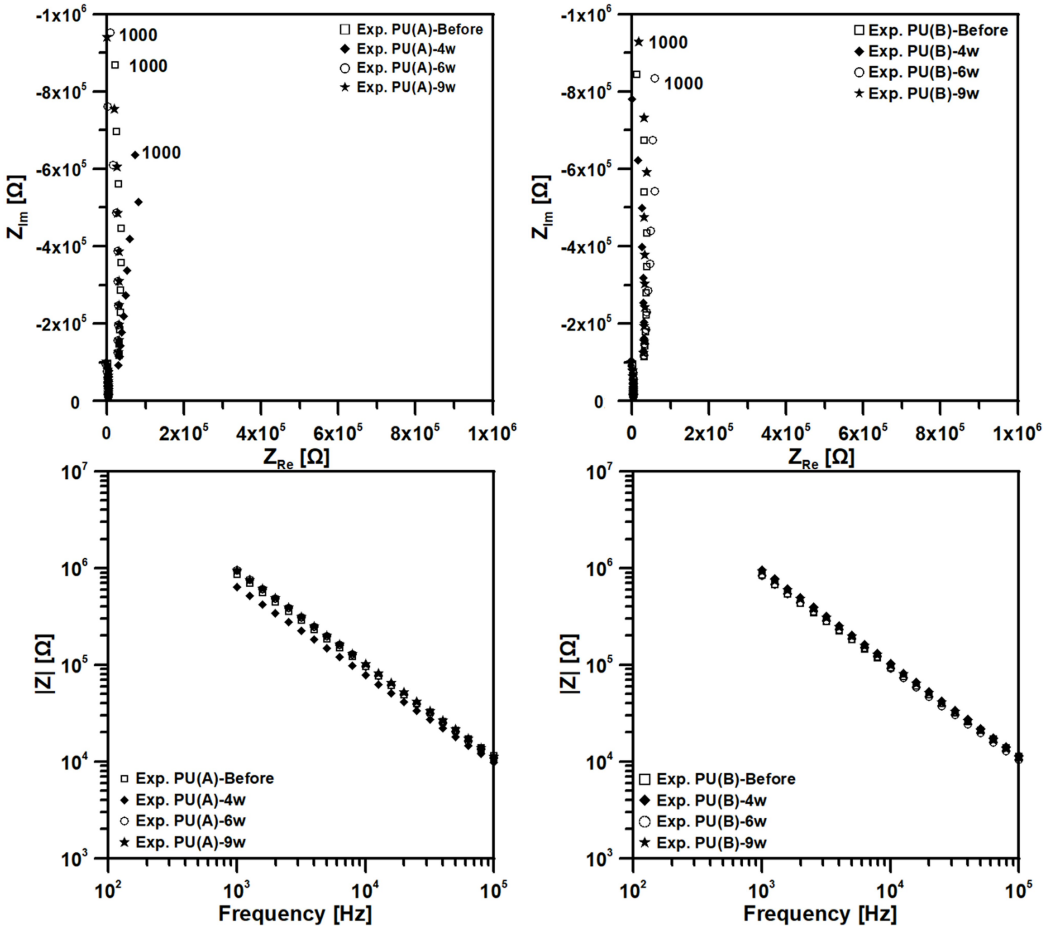

Figure 7.8: Nyquist and impedance magnitude plots for the specimens painted with the Exp PU1 system, during their 9-week examination in the salt spray chamber. Left: specimen (A), Right: specimen (B)

Table 7.17: Electric properties of specimens painted with the Exp PU1 system, during their accelerated aging in salt spray chamber

Duration (Weeks)	Coating capacitance (F)-Exp PU1 (A)	Coating capacitance (F)-Exp PU1 (B)
Before	$2.684\ 10^{-10}$	$2.922\ 10^{-10}$
4	$4.544\ 10^{-10}$	$2.096\ 10^{-10}$
6	$1.906\ 10^{-10}$	$2.395\ 10^{-10}$
9	$2.106\ 10^{-10}$	$2.153\ 10^{-10}$

7.3.1.5 Salt spray tests on anticorrosive polyurethane (PU) system

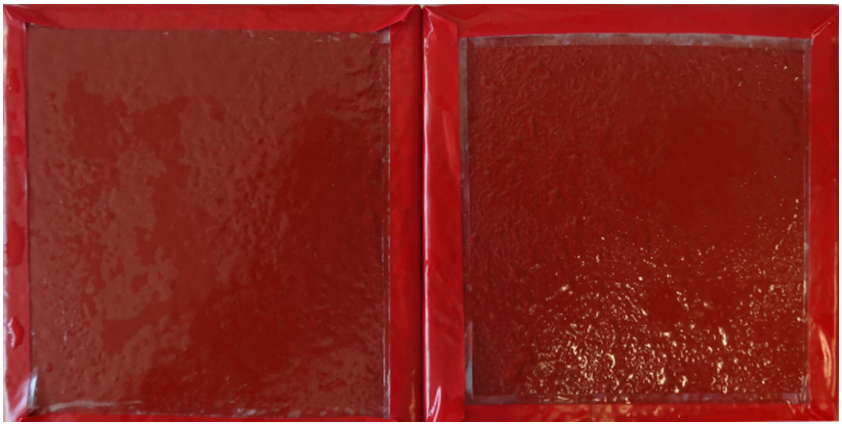

(a) After 4 weeks

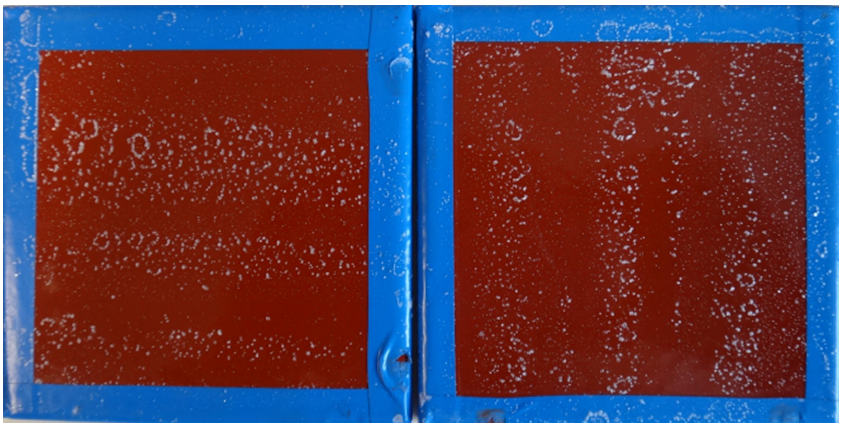

(b) After 6 weeks

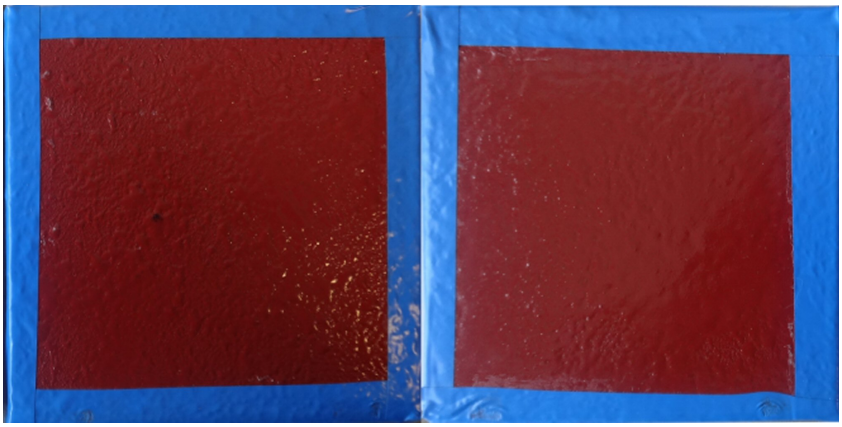

(c) After 9 weeks

Figure 7.9: Surface condition of the specimens painted with the PU system during their 9-week examination in the salt spray chamber. Left: specimen (A), Right: specimen (B)

Table 7.18: König pendulum hardness measurements for specimens painted with the PU system during their 9-week examination in the salt spray chamber

Duration (Weeks)	PU (A)	PU (B)
Before	56.17	33.40
4	82.83	69.50
6	85.40	78.60
9	93.80	79.00

Table 7.19: 60° gloss measurements for specimens painted with the PU system during their 9-week examination in the salt spray chamber

Duration (Weeks)	PU (A)	PU (B)
Before	40.50	12.00
4	33.50	10.00
6	38.50	11.25
9	33.25	16.00

Table 7.20: Discoloration (DE) measurements for specimens painted with the PU system during their 9-week examination in the salt spray chamber

Duration (Weeks)	PU (A)	PU (B)
Standard sample: L=36.29, a=28.49, b=8.90, C=29.85, H=17.36		
Before	0.61	0.49
4	0.50	0.42
6	0.50	0.44
9	0.59	0.61

Table 7.21: Electric properties of specimens painted with the PU system, during their accelerated aging in salt spray chamber

Duration (Weeks)	Coating capacitance (F)-PU (A)	Coating capacitance (F)-PU (B)
Before	$2.613\ 10^{-10}$	$2.065\ 10^{-10}$
4	$4.156\ 10^{-10}$	$2.453\ 10^{-10}$
6	$2.537\ 10^{-10}$	$2.691\ 10^{-10}$
9	$2.537\ 10^{-10}$	$2.415\ 10^{-10}$

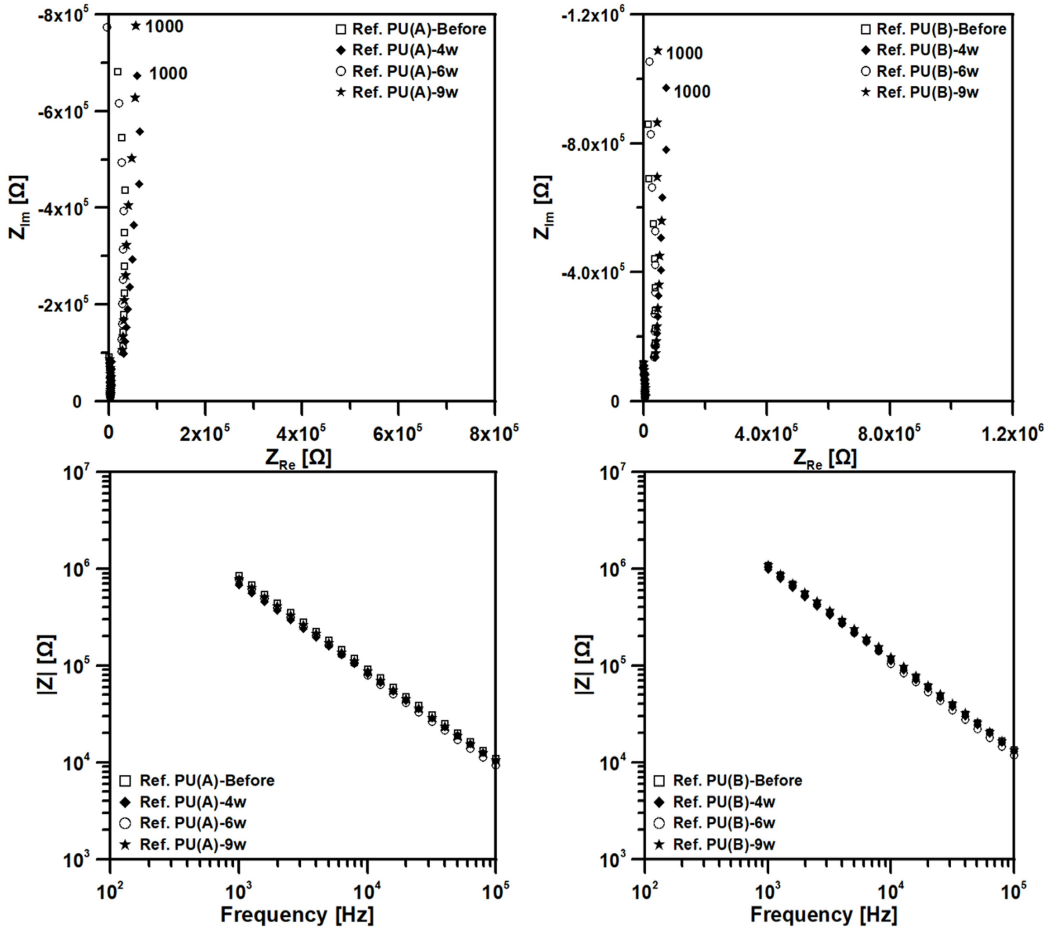

Figure 7.10: Nyquist and impedance magnitude plots for the specimens painted with the PU system, during their 9-week examination in the salt spray chamber. Left: specimen (A), Right: specimen (B)

The newly developed anticorrosive polyurethane formulation exhibited variations in König pendulum hardness and gloss values between the two specimens. The surface structure was not homogenous enough to obtain similar results. More specifically, the initial hardness value for specimen (A) was equal to 56.17, ranking it below but close to the acrylic system. Specimen (B), though, exhibited a value equal to 33.40, slightly higher than the experimental polyurethane system. Similar deviations between the two specimens were also observed for the 60° gloss. More specifically, specimen (A) exhibited a value equal to 40.5, larger than the silicone system and smaller than the experimental polyurethane formulation. However, specimen (B) exhibited initial gloss value equal to 12, close to the values observed for reference silicone and experimental silicone specimen (B). With regard to the change of properties during the test, hardness increase was observed, similarly to the acrylic and experimental polyurethane formulation. The increase for specimen (A) was 67%, while the increase for specimen (B) was 136.53%, revealing again inhomogeneity of properties between the two specimens. Gloss decreased 17.9% for specimen (A) and increased 33.33% for specimen (B). Color of both specimens exhibited variations but remained more or less stable. Finally, impedance measurements revealed good barrier properties, since both specimens retained their pure capacitive behavior, similarly to the rest of the specimens examined so far.

7.3.2 Conclusions with regard to the results after 9 weeks of salt spray examination

The experimental polyurethane formulation exhibited the highest increase in König hardness, followed by the anticorrosive polyurethane, the acrylic and finally the silicone paints, which exhibited a stable behavior. In terms of color change, the acrylic system exhibited the highest discoloration, followed by the reference silicone formulation, the experimental polyurethane, the experimental silicone and finally the anticorrosive polyurethane, which exhibited stable color characteristics. Gloss could not be perceived as a characteristic property for the acrylic system. Also, this system suffered from checking. With regard to the rest of the systems, experimental silicone was affected most (one of the two specimens), followed by the anticorrosive polyurethane, the reference silicone and finally the experimental polyurethane formulation. The barrier properties of all systems remained unaffected, during the exposure. The results exhibited variations among the examined painting systems, hence, no system could be selected as the best overall after 9 weeks in salt spray. A ranking between the different systems (taking into consideration the worst values obtained for each coating system) in terms of hardness, gloss and discoloration would be as follows:

- König hardness: Exp.PU (greatest variation)<PU<Acrylic<Ref.Si=Exp.Si (most stable behavior)
- 60° gloss: Acrylic<Exp.Si<PU<Ref.Si<Exp.PU
- DE: Acrylic<Ref.Si<Exp.PU<Exp.Si<PU

7.3.3 Electrochemical measurements on intact specimens during a 9-week accelerated aging test in UV chamber

7.3.3.1 UV tests on reference silicone (Ref Si) system

(a) After 6 weeks

(b) After 9 weeks

Figure 7.11: Surface condition of the specimens painted with the Ref Si system during their 9-week examination in the climatic chamber. Left: specimen (A), Right: specimen (B)

Table 7.22: König pendulum hardness measurements for specimens painted with the Ref Si system during their 9-week examination in the climatic chamber

Duration (Weeks)	Ref Si (A)	Ref Si (B)
Before	24.00	29.67
6	18.80	18.00
9	20.83	23.17

Table 7.23: 60° gloss measurements for specimens painted with the Ref Si system during their 9-week examination in the climatic chamber

Duration (Weeks)	Ref Si (A)	Ref Si (B)
Before	22.00	27.00
6	23.00	29.25
9	21.00	28.50

Table 7.24: Discoloration (DE) measurements for specimens painted with the Ref Si system during their 9-week examination in the climatic chamber

Duration (Weeks)	Ref Si (A)	Ref Si (B)
Standard sample: L=35.59, a=34.00, b=12.90, C=36.36, H=20.77		
Before	2.26	2.56
6	0.52	0.55
9	0.77	0.70

After UV aging, a slight decrease in hardness of both reference silicone painted specimens was observed. The decrease was 13.2% for specimen (A) and 21.9% for specimen (B). Gloss remained more or less stable. Color difference was intense for both specimens exhibiting a

decrease of 65.93% for specimen (A) and 72.66% for specimen (B). EIS data revealed, once more, a capacitive character of the paint for both specimens.

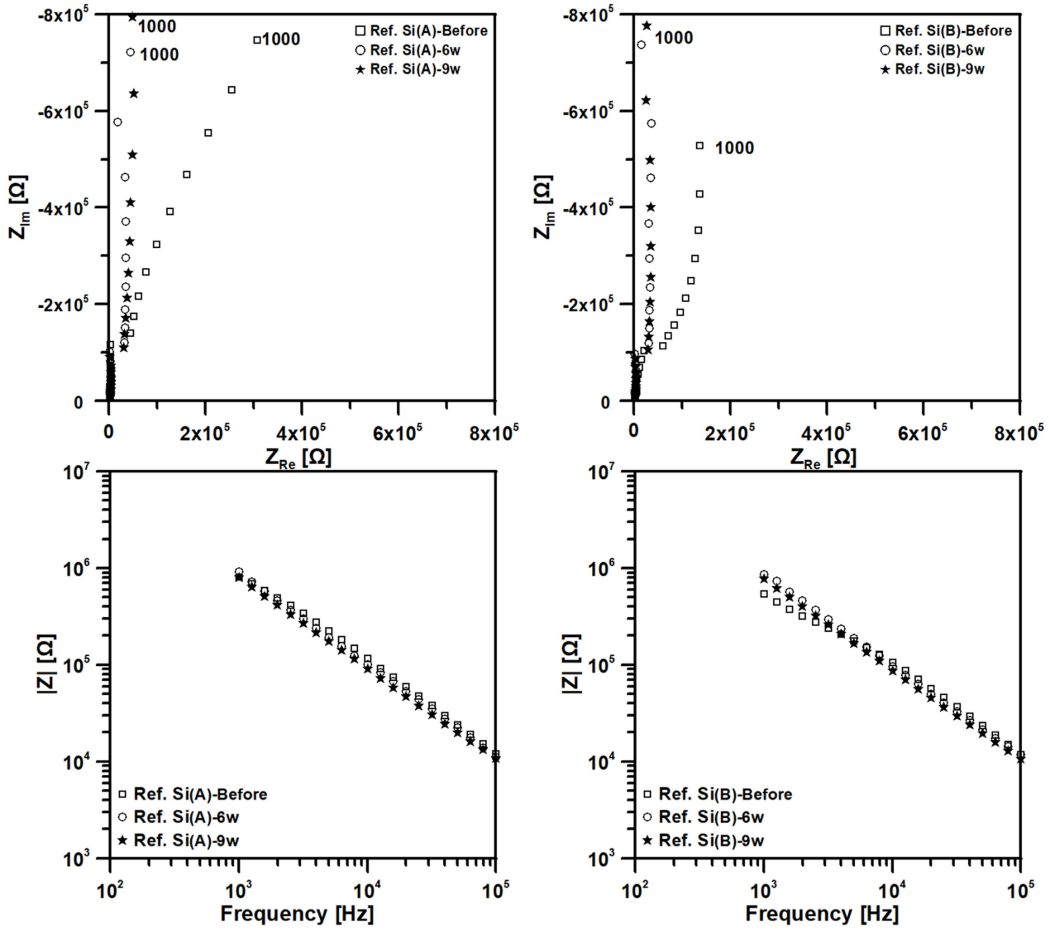

Figure 7.12: Nyquist and impedance magntude plots for the specimens painted with the Ref Si system, during their 9-week examination in the climatic chamber. Left: specimen (A), Right: specimen (B)

Table 7.25: Electric properties of specimens painted with the Ref Si system, during their 9-week examination in the climatic chamber

Duration (Weeks)	Coating capacitance (F)-Ref Si (A)	Coating capacitance (F)-Ref Si (B)
Before	2.725 10^{-10}	9.160 10^{-10}
6	2.590 10^{-10}	2.611 10^{-10}
9	3.093 10^{-10}	3.197 10^{-10}

7.3.3.2 UV tests on acrylic (Acrylic) system

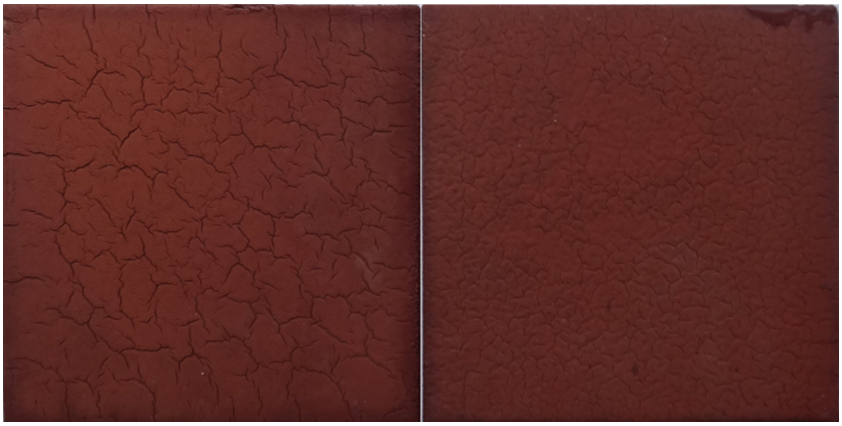

(a) After 6 weeks

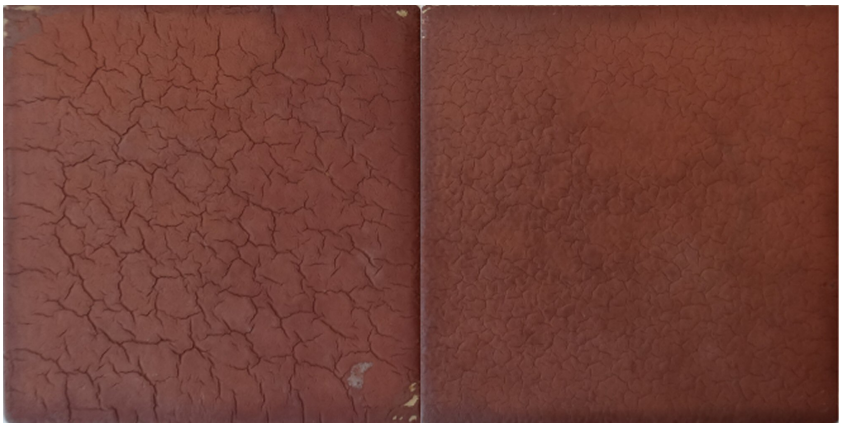

(b) After 9 weeks

Figure 7.13: Surface condition of the specimens painted with the Acrylic system during their 9-week examination in the climatic chamber. Left: specimen (A), Right: specimen (B)

Table 7.26: König pendulum hardness measurements for specimens painted with the Acrylic system during their 9-week examination in the climatic chamber chamber

Duration (Weeks)	Acrylic (A)	Acrylic (B)
Before	67.67	83.00
6	82.80	83.80
9	81.50	88.50

Table 7.27: 60° gloss measurements for specimens painted with the Acrylic system during their 9-week examination in the climatic chamber

Duration (Weeks)	Acrylic (A)	Acrylic (B)
Before	12	14
6	1	1
9	1	1

Table 7.28: Discoloration (DE) measurements for specimens painted with the Acrylic system during their 9-week examination in the climatic chamber

Duration (Weeks)	Acrylic (A)	Acrylic (B)
Standard sample: L=37.78, a=22.66, b=8.70, C=24.27, H=21.01		
Before	0.46	0.39
6	5.99	6.26
9	7.37	8.00

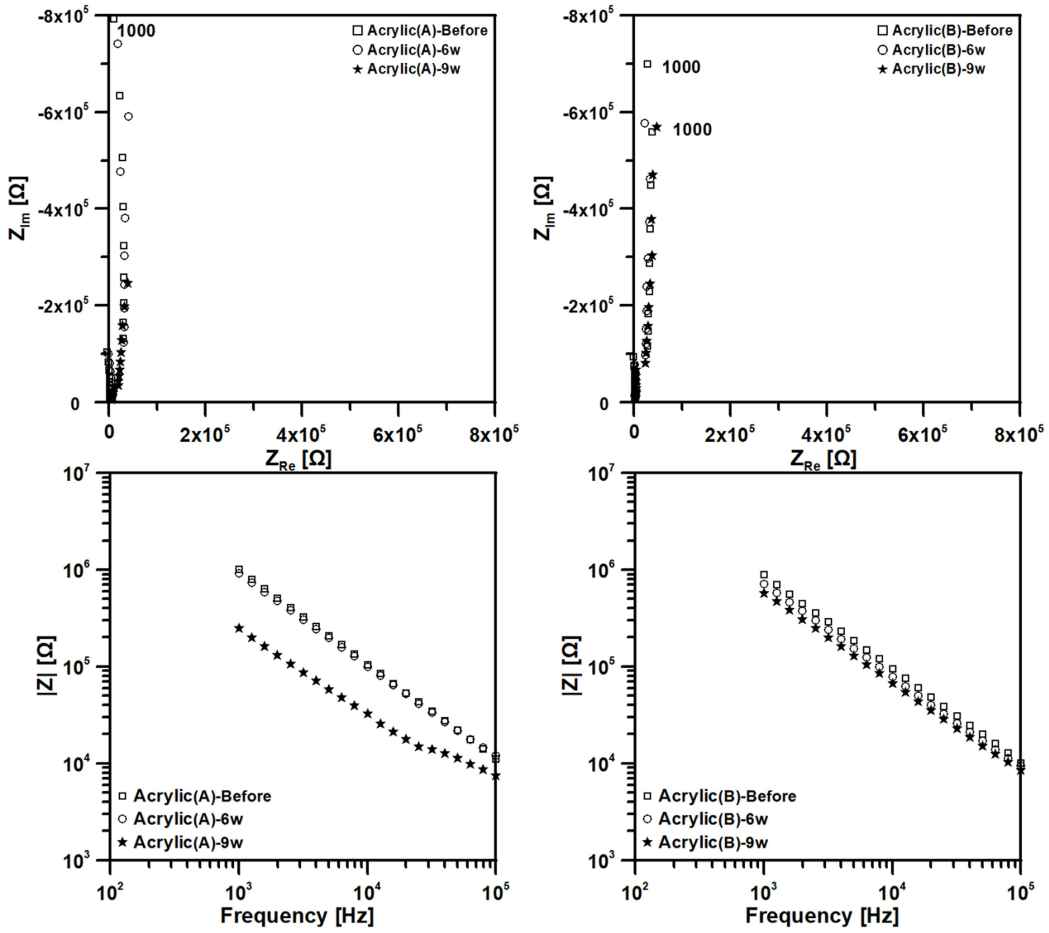

Figure 7.14: Nyquist and impedance magnitude plots for the specimens painted with the Acrylic system, during their 9-week examination in the climatic chamber. Left: specimen (A), Right: specimen (B)

Table 7.29: Electric properties of specimens painted with the Acrylic system, during their accelerated aging in the climatic chamber

Duration (Weeks)	Coating capacitance (F)-Acrylic (A)	Coating capacitance (F)-Acrylic (B)
Before	$1.893\ 10^{-10}$	$2.253\ 10^{-10}$
6	$2.433\ 10^{-10}$	$3.118\ 10^{-10}$
9	$1.465\ 10^{-10}$	$4.624\ 10^{-10}$

The acrylic system exhibited once more checking effect (Fig. 7.11), which was of the shrinkage type (ASTM D 660-93). For specimen (A), the grading would be No. 3 in the ASTM rank, while for specimen (B) No. 2, since the latter specimen exhibited smaller and denser cracks. König hardness exhibited small increase during the test, 20.44% for specimen (A) and 6.63% for specimen (B). The increase was smaller for this system after UV aging, compared to the salt spray test. Gloss was almost zero, while intense discoloration, arising from the leaching character, was the main characteristic, ranging from 16 to 20.5 times the initial color value. No electrochemical degradation was observed for either of the acrylic painted specimens. The capacitance values were in the order of 10^{-10} F, implying an undamaged coating.

7.3.3.3 UV tests on experimental silicone (Exp Si) system

(a) After 4 weeks

(b) After 6 weeks

Figure 7.15: Surface condition of the specimens painted with the Exp Si system during their 9-week examination in the climatic chamber. Left: specimen (A), Right: specimen (B)

Table 7.30: König pendulum hardness measurements for specimens painted with the Exp Si system during their 9-week examination in the climatic chamber

Duration (Weeks)	Exp Si (A)	Exp Si (B)
Before	23.40	25.00
4	21.60	24.40
6	22.40	23.40
9	18.50	20.50

Table 7.31: 60° gloss measurements for specimens painted with the Exp Si system during their 9-week examination in the climatic chamber

Duration (Weeks)	Exp Si (A)	Exp Si (B)
Before	21.60	28.20
4	21.75	26.00
6	22.75	27.50
9	26.50	32.75

Table 7.32: Discoloration (DE) measurements for specimens painted with the Exp Si system during their 9-week examination in the climatic chamber

Duration (Weeks)	Exp Si (A)	Exp Si (B)
Standard sample: L=35.71, a=35.04, b=12.52, C=37.21, H=19.66		
Before	0.76	0.82
4	1.09	1.01
6	0.62	0.69
9	0.62	0.58

Table 7.33: Electric properties of specimens painted with the Exp Si system, during their accelerated aging in the climatic chamber

Duration (Weeks)	Coating capacitance (F)-Exp Si (A)	Coating capacitance (F)-Exp Si (B)
Before	$3.421\ 10^{-10}$	$3.459\ 10^{-10}$
4	$4.125\ 10^{-10}$	$3.418\ 10^{-10}$
6	$3.388\ 10^{-10}$	$3.019\ 10^{-10}$
9	$2.622\ 10^{-10}$	$2.266\ 10^{-10}$

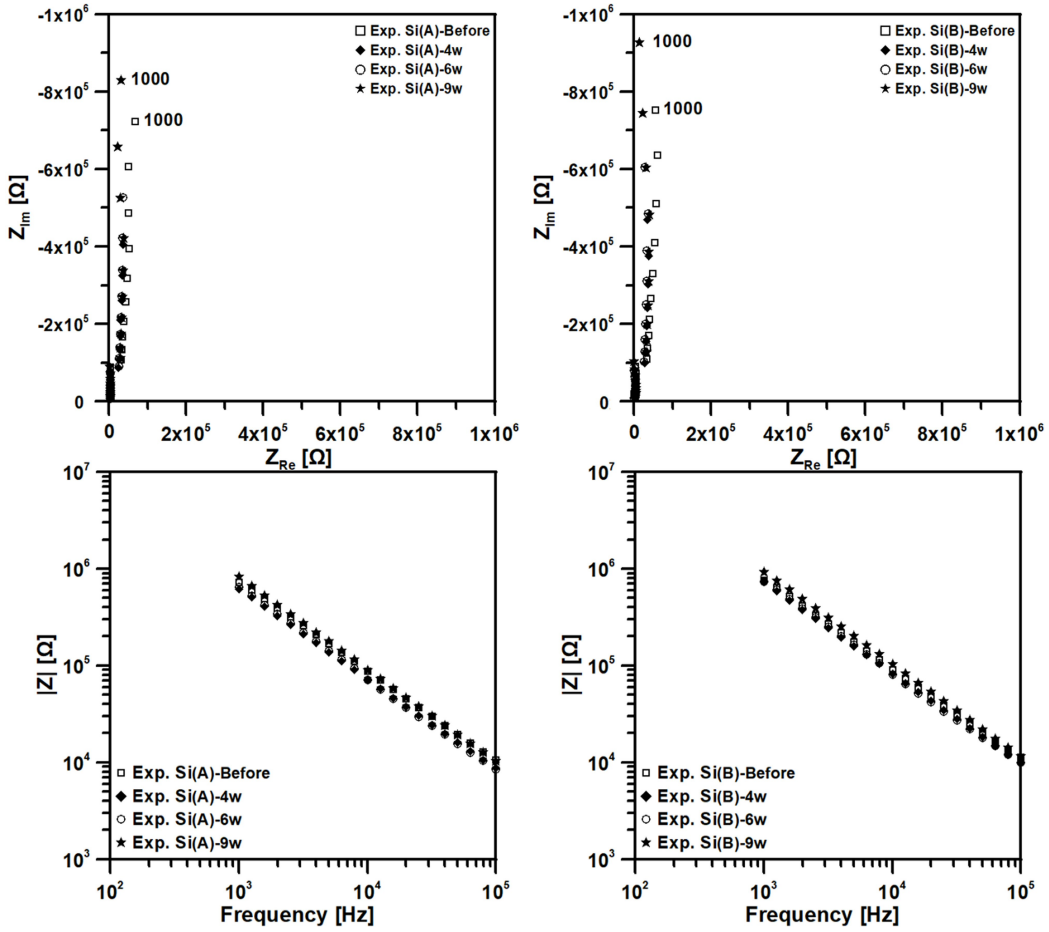

Figure 7.16: Nyquist and impedance magnitude plots for the specimens painted with the Exp Si system, during their 9-week examination in the climatic chamber. Left: specimen (A), Right: specimen (B)

Experimental silicone system exhibited small variations after UV aging, similarly to the behavior after salt spray. König hardness exhibited slight decrease (which was also observed for specimen (B) of the same system after salt spray) and ranged from 18% to 20.94%. Similar trend with the salt spray behavior was observed for the gloss change, which exhibited small increase. For specimen (A) the increase was 22.69% and for specimen (B) 16.13%. Color change exhibited fluctuations, but eventually after 9 weeks the decrease was 18.42% for specimen (A) and 29.27% for specimen (B). The EIS response was indicative of a coating with intact barrier properties.

7.3.3.4 UV tests on experimental polyurethane (Exp PU1) system

(a) After 4 weeks

(b) After 6 weeks

Figure 7.17: Surface condition of the specimens painted with the Exp PU1 system during their 9-week examination in the climatic chamber. Left: specimen (A), Right: specimen (B)

Table 7.34: König pendulum hardness measurements for specimens painted with the Exp PU1 system during their 9-week examination in the climatic chamber

Duration (Weeks)	Exp PU1 (A)	Exp PU1 (B)
Before	36.00	20.17
4	86.80	83.20
6	96.00	100.20
9	112.80	108.40

Table 7.35: 60° gloss measurements for specimens painted with the Exp PU1 system during their 9-week examination in the climatic chamber

Duration (Weeks)	Exp PU1 (A)	Exp PU1 (B)
Before	66.00	68.60
4	63.33	64.00
6	77.00	67.25
9	71.33	60.50

Table 7.36: Discoloration (DE) measurements for specimens painted with the Exp PU1 system during their 9-week examination in the climatic chamber

Duration (Weeks)	Exp PU1 (A)	Exp PU1 (B)
Standard sample: L=35.92, a=28.75, b=8.26, C=29.91, H=16.03		
Before	0.39	0.32
4	1.18	1.12
6	1.10	0.91
9	1.01	1.19

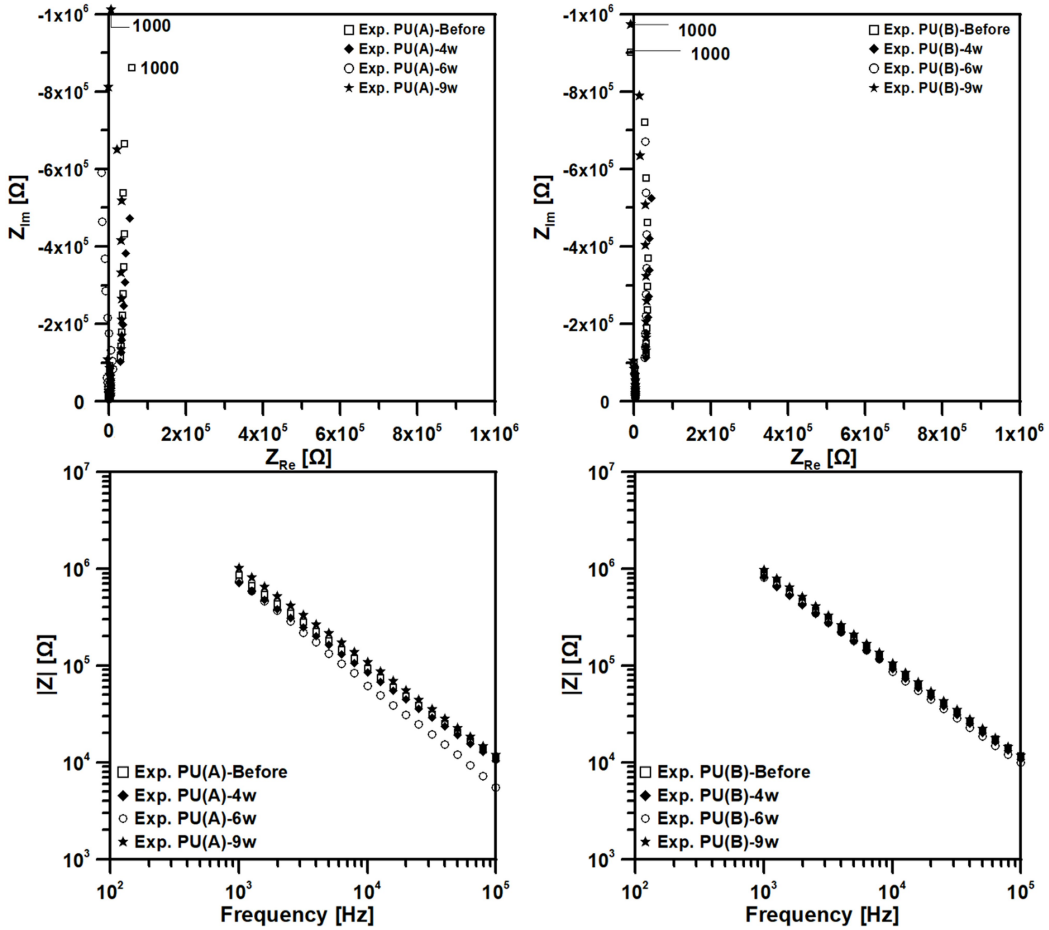

Figure 7.18: Nyquist and impedance magnitude plots for the specimens painted with the Exp PU1 system, during their 9-week examination in the climatic chamber. Left: specimen (A), Right: specimen (B)

Table 7.37: Electric properties of specimens painted with the Exp PU1 system, during their accelerated aging in the climatic chamber

Duration (Weeks)	Coating capacitance (F)-Exp PU1 (A)	Coating capacitance (F)-Exp PU1 (B)
Before	$2.743\ 10^{-10}$	$2.523\ 10^{-10}$
4	$3.655\ 10^{-10}$	$2.912\ 10^{-10}$
6	$1.392\ 10^{-10}$	$2.279\ 10^{-10}$
9	$1.923\ 10^{-10}$	$1.982\ 10^{-10}$

After 9 weeks of UV aging, the experimental polyurethane system exhibited once more an intense increase in König hardness, similarly to the trend observed after salt spray test. The increase was 3 times the initial value for specimen (A) and 5.37 times for specimen (B). In addition, the final hardness value was around 110 for both specimens, around 20 units larger than the hardness of the acrylic system. Gloss did not change in the same manner for both specimens. More specifically, it increased 8% for specimen (A) and decreased 11.8% for specimen (B). However, both changes were small. Color exhibited an increase after UV test for both specimens, in contrary to the specimens after salt spray, which exhibited a decrease. The increase in color was 159% for specimen (A) and 272% for specimen (B). Impedance characteristics remained unaffected.

7.3.3.5 UV tests on anticorrosive polyurethane (PU) system

(a) After 4 weeks

(b) After 6 weeks

Figure 7.19: Surface condition of the specimens painted with the PU system during their 9-week examination in the climatic chamber. Left: specimen (A), Right: specimen (B)

Table 7.38: König pendulum hardness measurements for specimens painted with the PU system during their 9-week examination in the climatic chamber

Duration (Weeks)	PU (A)	PU (B)
Before	50.17	58.17
4	80.75	84.40
6	69.67	98.33
9	56.50	102.80

Table 7.39: 60° gloss measurements for specimens painted with the PU system during their 9-week examination in the climatic chamber

Duration (Weeks)	PU (A)	PU (B)
Before	40.75	11.00
4	36.00	7.25
6	35.25	7.25
9	42.00	7.00

Table 7.40: Discoloration (DE) measurements for specimens painted with the PU system during their 9-week examination in the climatic chamber

Duration (Weeks)	PU (A)	PU (B)
Standard sample: L=36.29, a=28.49, b=8.90, C=29.85, H=17.36		
Before	0.41	0.37
4	0.81	0.66
6	0.71	0.46
9	0.62	0.50

Table 7.41: Electric properties of specimens painted with the PU system, during their accelerated aging in the climatic chamber

Duration (Weeks)	Coating capacitance (F)-PU (A)	Coating capacitance (F)-PU (B)
Before	$2.749\ 10^{-10}$	$2.719\ 10^{-10}$
4	$3.628\ 10^{-10}$	$4.002\ 10^{-10}$
6	$3.391\ 10^{-10}$	$2.759\ 10^{-10}$
9	$2.290\ 10^{-10}$	$2.429\ 10^{-10}$

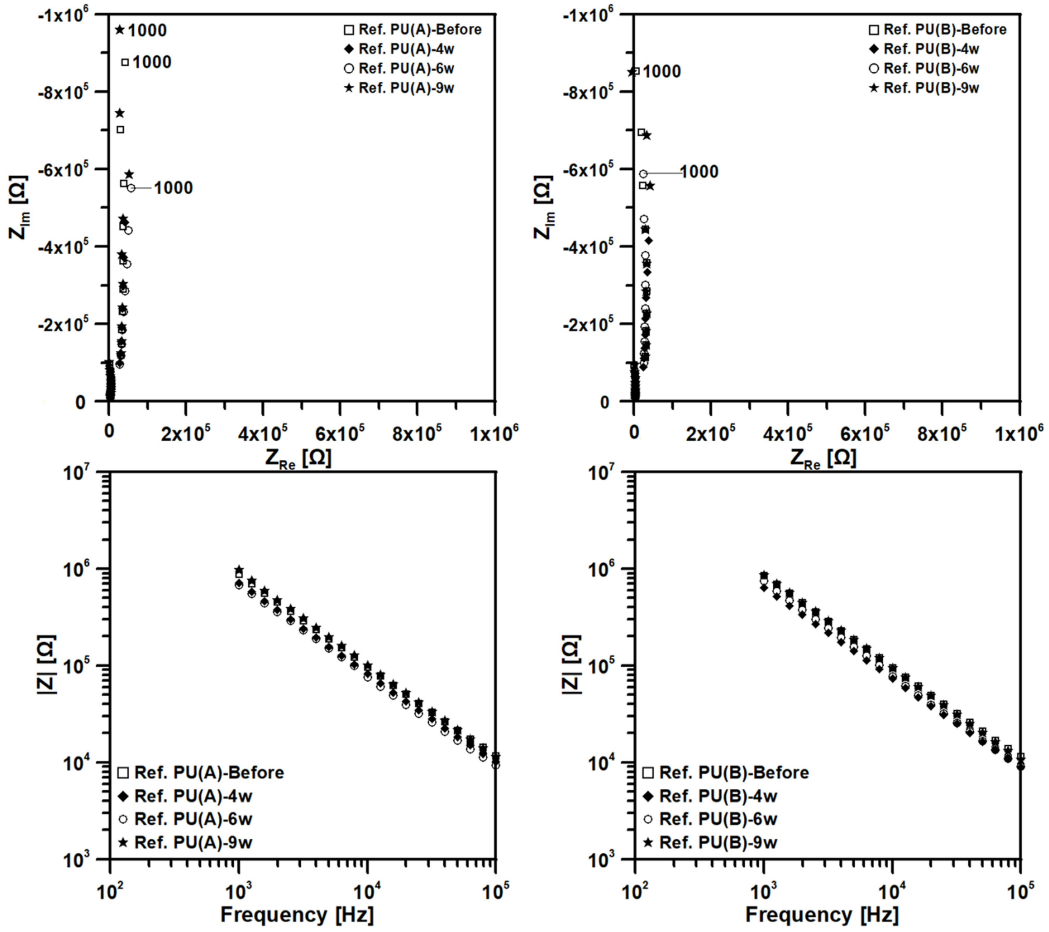

Figure 7.20: Nyquist and impedance magnitude plots for the specimens painted with the PU system, during their 9-week examination in the climatic chamber. Left: specimen (A), Right: specimen (B)

Anticorrosive polyurethane formulation exhibited variations in gloss values between the two specimens, as observed also during the salt spray test. Specimen (A) exhibited a value equal to 40.75, while specimen (B) equal to 11. Gloss increased 3% for the first specimen and decreased 36.4% for the second specimen, exhibiting completely different behavior. With regard to König hardness, both specimens exhibited an initial value ranging from 50 to 58, being similar. However, the rate of increase was totally different. Hardness of specimen (A) increased 12.62%, while hardness of specimen (B) increased 76.72%, reaching a value similar to the ones observed for the experimental polyurethane formulation. A slight discoloration was observed on both specimens. Specimen (A) exhibited a discoloration index increase equal to 51.2%, while specimen (B) equal to 35.1%. Barrier properties remained intact for both specimens.

7.3.4 Conclusions with regard to the results after 9 weeks of UV examination

A ranking between the different systems (taking into consideration the worst values obtained for each coating system) in terms of hardness, gloss and discoloration would be as follows:

- König hardness: Exp. PU (highest increase)<PU<Ref.Si<Acrylic<Exp.Si (most stable behavior)

- 60° gloss: Acrylic<PU<Exp.Si<Exp.PU<Ref. Si
- DE: Acrylic<Exp.PU<Ref.Si<PU<Exp.Si

7.3.5 Electrochemical measurements on intact specimens during a 12-month immersion in artificial seawater in laboratory conditions

7.3.5.1 Reference silicone (Ref Si) system

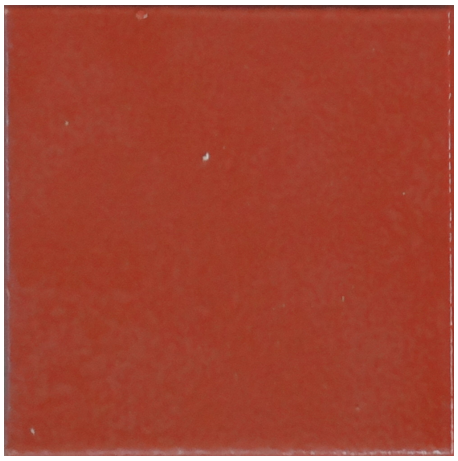

(a) Condition of Ref Si system in intact state

(b) After 3 months

(c) After 6 months

(d) After 9 months

(e) After 12 months

Figure 7.21: Surface condition of the specimens painted with the Ref Si system during their 12-month immersion in artificial seawater. Left: specimen (A), Right: specimen (B)

Table 7.42: König pendulum hardness measurements for specimens painted with the Ref Si system during their 12-month immersion in artificial seawater

Duration (months)	Ref Si (A)	Ref Si (B)
2	34.80	25.00
3	44.20	32.40
4	39.40	33.60
5	45.25	30.00
6	41.50	28.83
7	50.40	30.25
8	50.00	43.80
9	38.60	29.00
10	51.25	31.60
11	61.33	34.83
12	57.17	33.67

Table 7.43: 60° gloss measurements for specimens painted with the Ref Si system during their 12-month immersion in artificial seawater

Duration (months)	Ref Si (A)	Ref Si (B)
Before	41.00	29.00
2	50.00	32.70
3	15.50	25.50
4	14.75	18.25
5	29.00	46.75
6	31.50	28.25
7	34.00	27.25
8	28.50	20.00
9	13.75	18.50
10	25.50	14.75
11	36.25	26.00
12	28.50	25.00

Table 7.44: Discoloration (DE) measurements for specimens painted with the Ref Si system during their 12-month immersion in artificial seawater

Duration (months)	Ref Si (A)	Ref Si (B)
Standard sample: L=36.43, a=32.64, b=11.68, C=34.66, H=19.69		
Before	2.26	2.56
2	1.46	1.53
3	0.95	1.28
4	1.05	1.81
5	1.33	1.23
6	0.59	0.62
7	1.29	1.07
8	1.28	1.20
9	1.00	1.13
10	2.06	1.38
11	0.96	1.17
12	1.01	0.96

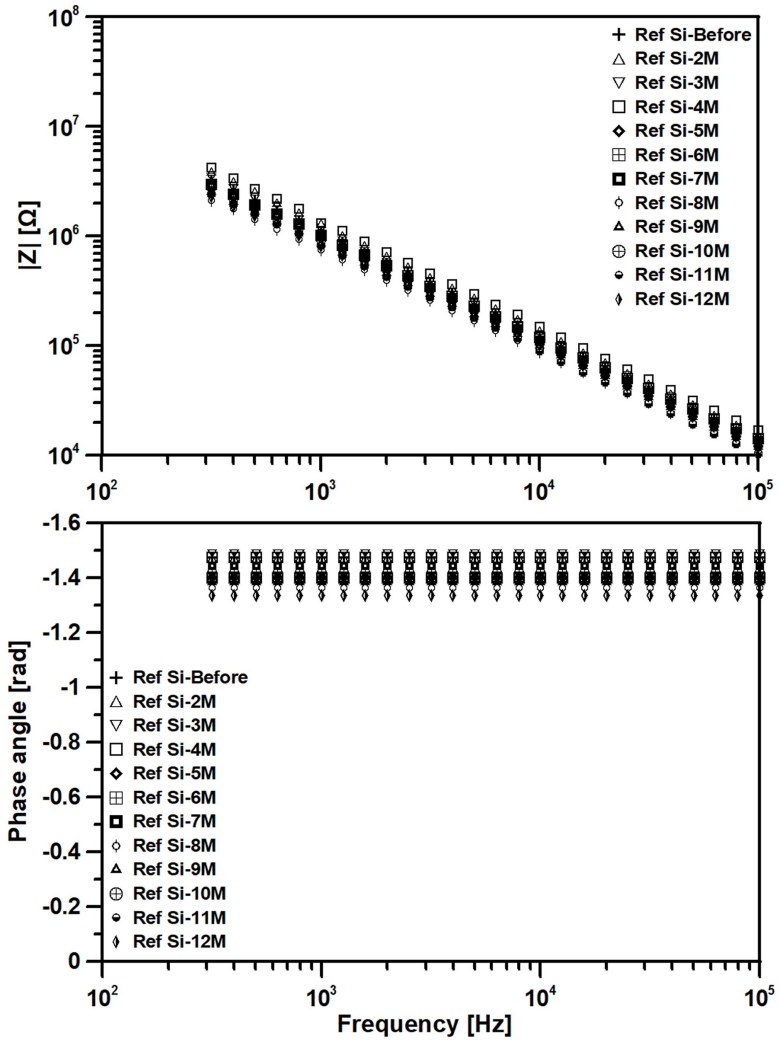

Figure 7.22: Bode plot for specimen (B) painted with the Ref Si system and immersed for 12 months in artificial seawater

Table 7.45: Electric properties of specimen (B) painted with the Ref Si system, during 12 months of immersion in artificial seawater

Duration (Weeks)	Coating capacitance (F)-Ref Si (B)
Before	$1.914\ 10^{-10}$
2	$1.514\ 10^{-10}$
3	$1.904\ 10^{-10}$
4	$1.461\ 10^{-10}$
5	$2.348\ 10^{-10}$
6	$2.468\ 10^{-10}$
7	$2.225\ 10^{-10}$
8	$3.567\ 10^{-10}$
9	$2.792\ 10^{-10}$
10	$2.422\ 10^{-10}$
11	$2.574\ 10^{-10}$
12	$3.409\ 10^{-10}$

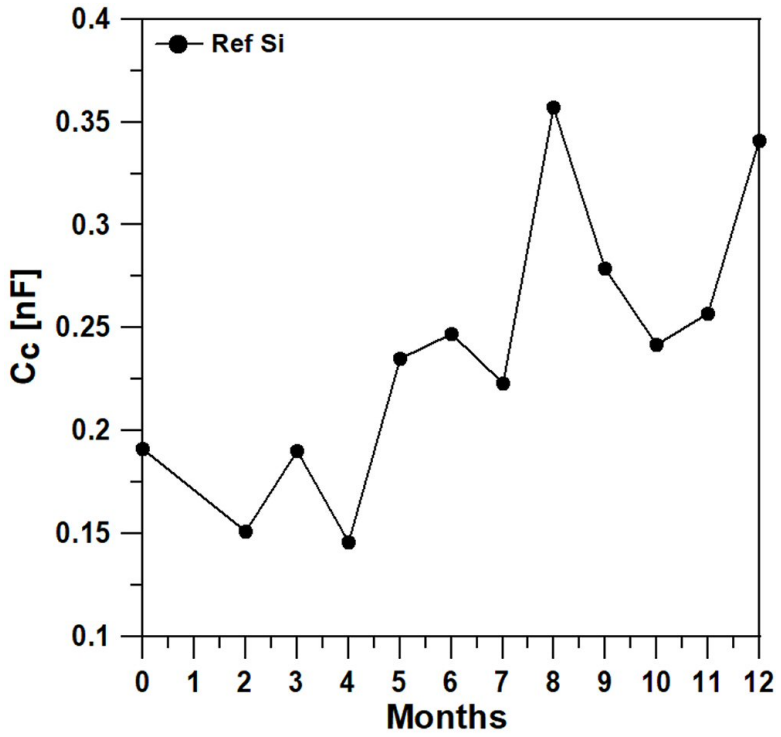

Figure 7.23: Coating capacitance values of specimen (B) painted with the Ref Si system, during 12 months of immersion in artificial seawater

The reference silicone system exhibited stable behavior after 12 months of immersion in 3.5% NaCl solution. Some blistering was observed after 12 months (Fig. 7.21e) on specimen (A). König hardness exhibited gradual increase of 64.8% and 34.7% for specimens (A) and (B), correspondingly. Gloss loss was also small, being 30.5% and 13.8% for the two specimens, respectively. Finally, discoloration index exhibited a decrease after 12 months, equal to 55.3% and 62.5%, respectively. With regard to the presented EIS spectra, only the results of specimen (B) are presented, because the quality of the signals obtained for specimen (A) were not satisfactory, especially for the duration 9 to 12 months, after a Kramers-Kronig (KK) validity test. A pure capacitive response was obtained for specimen (B) for the whole experiment duration (Fig. 7.22). The capacitance values were in the order of 10^{-10} F, implying an intact coat. As can be seen from Fig. 7.23, the coating capacitance exhibited a gradual increase during the experiment, but the change was quite small, ranging from around 0.2 nF to 0.35 nF. As a result no change in electric properties was observed for the Ref. Si painted sample.

7.3.5.2 Acrylic system

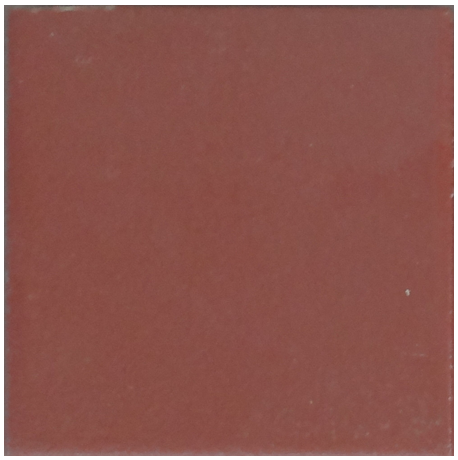

(a) Condition of Acrylic system in intact state

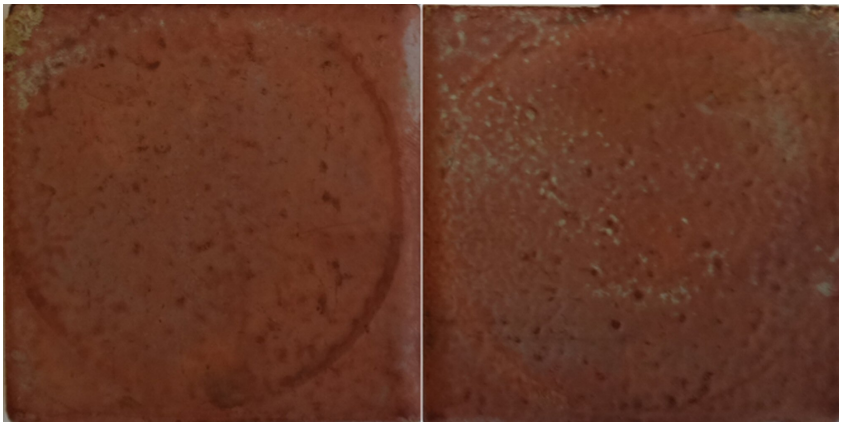

(b) After 3 months

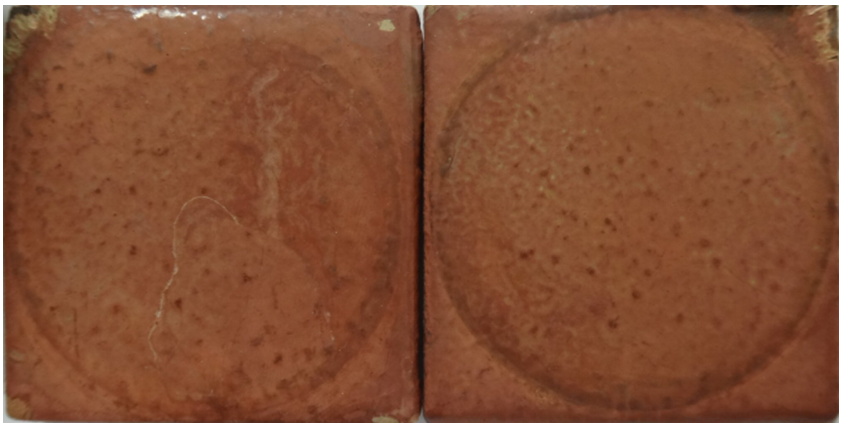

(c) After 6 months

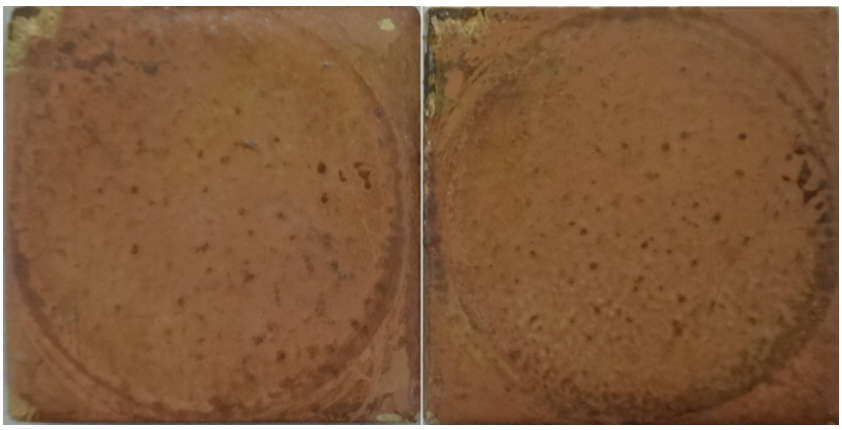

(d) After 9 months

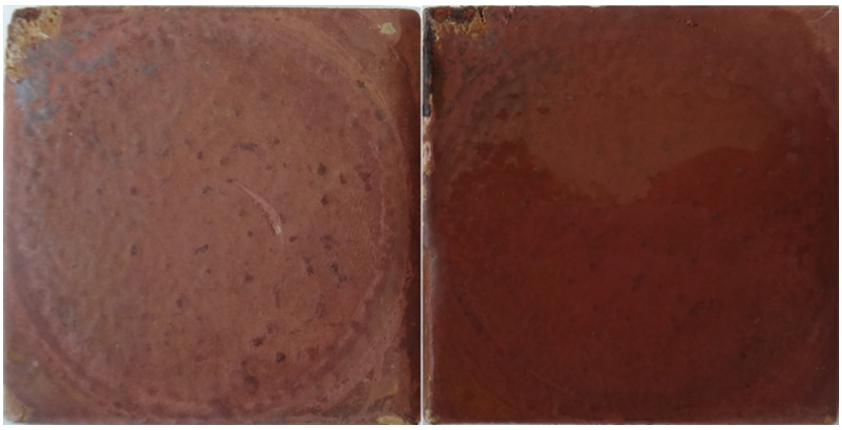

(e) After 12 months

Figure 7.24: Surface condition of the specimens painted with the Acrylic system during their 12-month immersion in artificial seawater. Left: specimen (A), Right: specimen (B)

Table 7.46: König pendulum hardness measurements for specimens painted with the Acrylic system during their 12-month immersion in artificial seawater

Duration (months)	Acrylic (A)	Acrylic (B)
2	35.40	23.60
3	25.60	24.40
4	45.60	34.40
5	32.00	19.00
6	47.83	42.33
7	43.00	28.80
8	65.60	53.20
9	57.50	44.50
10	65.00	66.20
11	63.67	64.17
12	69.00	66.20

Table 7.47: 60° gloss measurements for specimens painted with the Acrylic system during their 12-month immersion in artificial seawater

Duration	Acrylic (A)	Acrylic (B)

(months)		
Before	14.00	14.00
2	3.20	2.50
3	3.00	3.50
4	2.75	3.00
5	2.00	2.00
6	3.00	3.25
7	2.75	3.00
8	3.00	3.25
9	2.50	3.25
10	2.75	2.75
11	3.00	1.50
12	3.50	3.50

Table 7.48: Discoloration (DE) measurements for specimens painted with the Acrylic system during their 12-month immersion in artificial seawater

Duration (months)	Acrylic (A)	Acrylic (B)
Standard sample: L=37.22, a=23.26, b=8.48, C=24.76, H=20.03		
Before	0.46	0.39
2	13.65	12.98
3	15.54	14.33
4	13.52	13.30
5	13.93	13.20
6	10.79	11.50
7	11.22	10.29
8	10.28	10.83
9	10.72	10.72
10	9.20	10.09
11	11.28	15.33
12	10.57	12.71

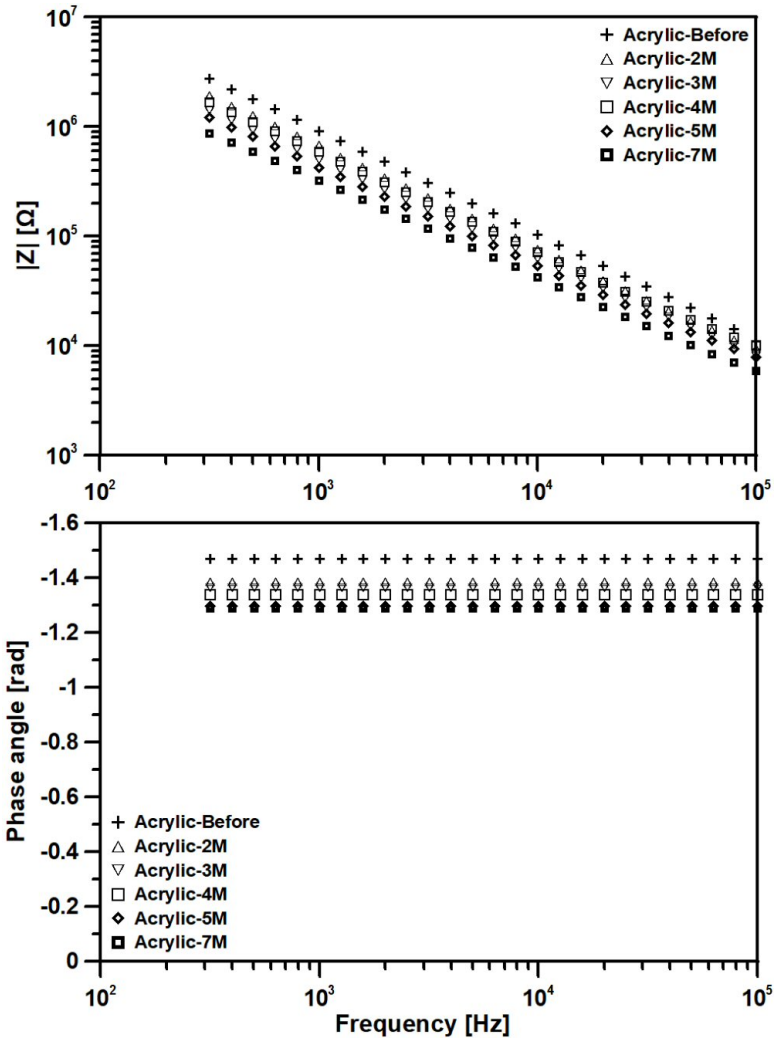

Figure 7.25: Bode graph for specimen (A) painted with the Acrylic system for the first 8 months of immersion in artificial seawater

Table 7.49: Electric properties of specimen (A) painted with the Acrylic system, during during the 12-month immersion in artificial seawater

Duration (Weeks)	Coating capacitance (F)-Acrylic (A)	Coating resistance (Ω)
Before	$2.374\ 10^{-10}$	-
2	$3.819\ 10^{-10}$	-
3	$6.489\ 10^{-10}$	-
4	$5.293\ 10^{-10}$	-
5	$8.132\ 10^{-10}$	-
6	$9.856\ 10^{-10}$	$4.012\ 10^{6}$
7	$1.218\ 10^{-9}$	-
8	$4.204\ 10^{-9}$	$5.566\ 10^{6}$
9	$5.534\ 10^{-10}$	$1.990\ 10^{5}$
10	$6.788\ 10^{-10}$	$4.506\ 10^{5}$
12	$7.270\ 10^{-10}$	$1.246\ 10^{4}$

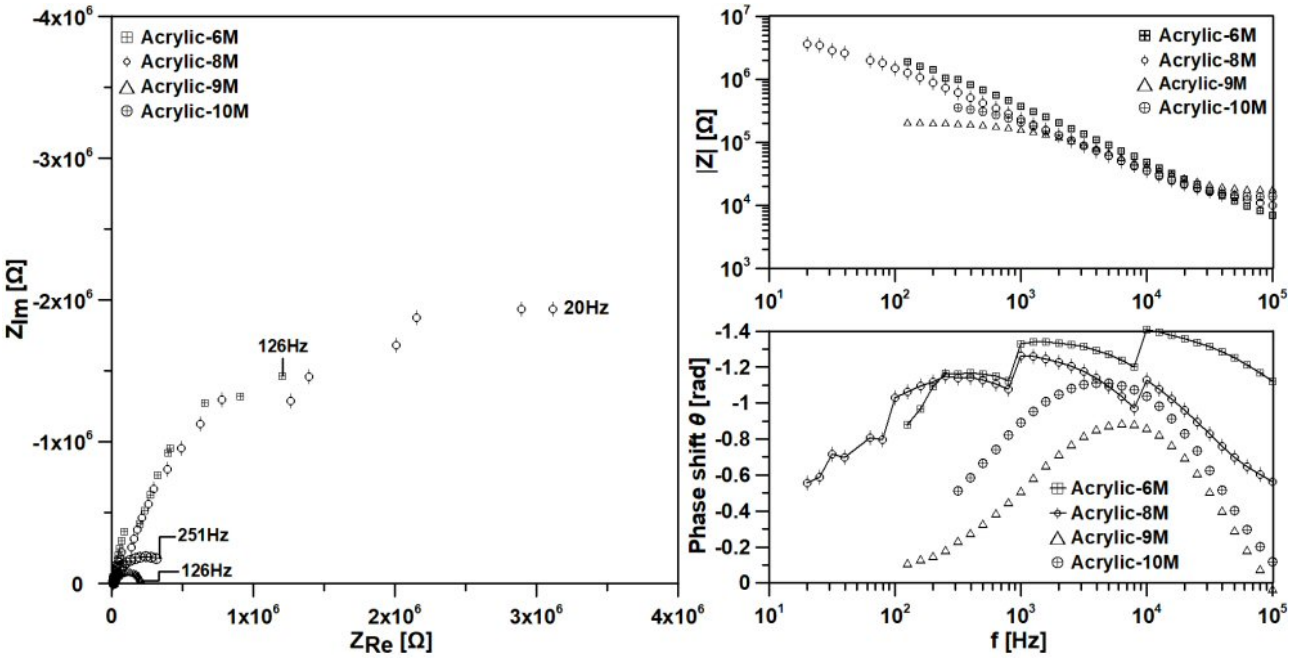

Figure 7.26: Nyquist and Bode graph for specimen (A) painted with the Acrylic system after 6, 8, 9 and 10 months of immersion in artificial seawater

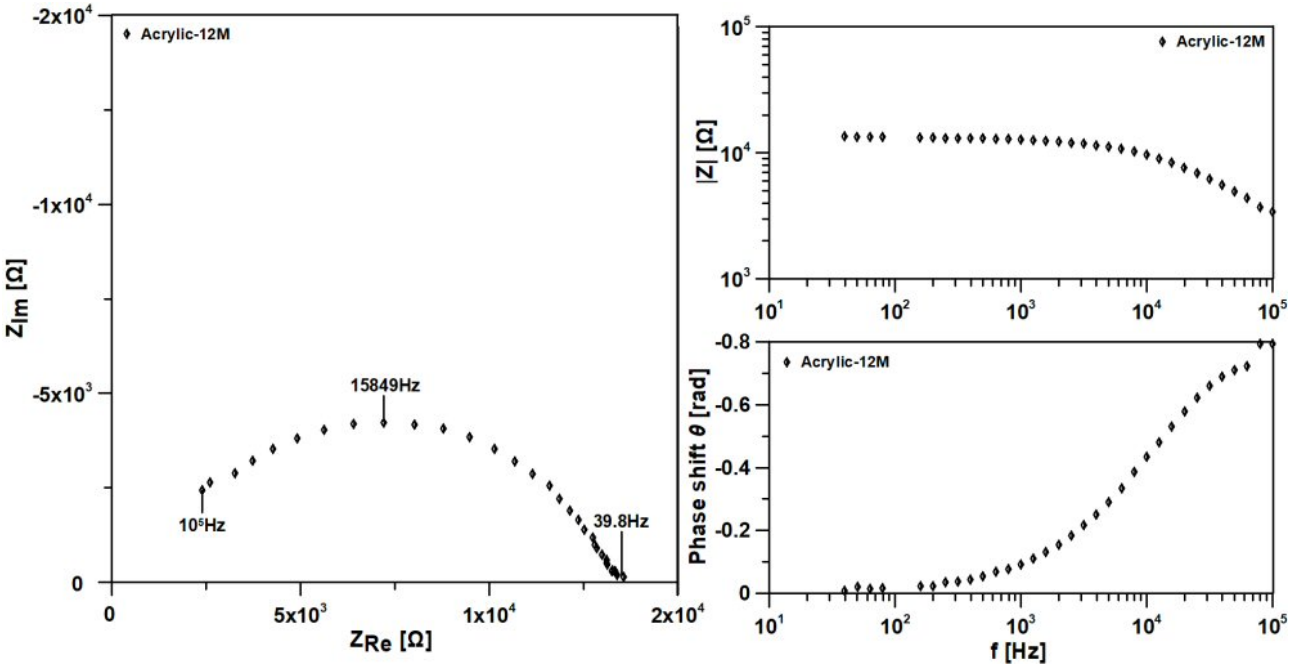

Figure 7.27: Nyquist and Bode graph for specimen (A) painted with the Acrylic system after 12 months of immersion in artificial seawater

The acrylic system exhibited intense discoloration, due to leaching, which was depicted in the discoloration index, becoming 23 and 33 times larger than the initial value. Compared to the previous accelerated aging tests, no checking effect was noticed, probably due to the temperature that the immersion test was performed (room temperature). As mentioned previously, gloss is not a property that could characterize this system. Finally, König hardness increased 94.9% and 180.5% for specimens (A) and (B), respectively. It should be noted that the initial

hardness values of these specimens were smaller than the values obtained for the rest of the acrylic painted specimens examined in accelerated aging.

The EIS results are presented here for specimen (A), since specimen (B) did not exhibit a good response for the last four months of experiment. As mentioned previously, validity of the responses was examined through KK relations. With regard to specimen (A), a pure capacitive response was obtained for the first 5 months of immersion and after 7 months (Fig. 7.25), while for the rest of intervals a one-time cosntant appeared (Figs. 7.26 and 7.27).

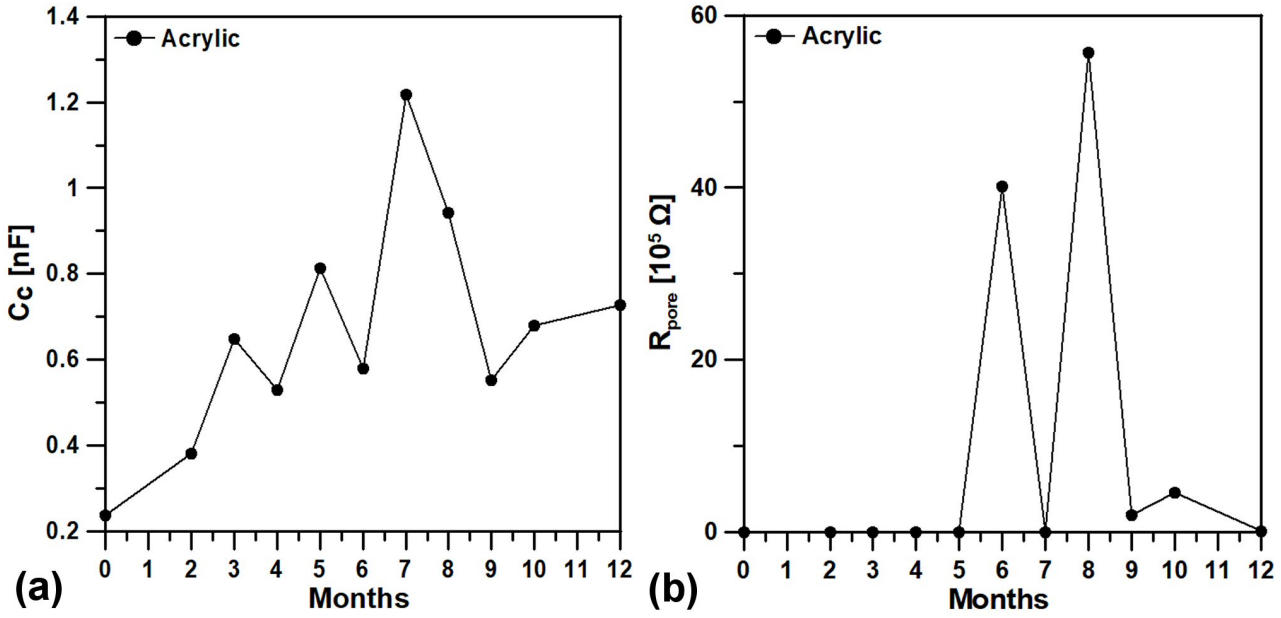

Figure 7.28: Change of a) coating capacitance and b) coating resistance of specimen (A) painted with the Acrylic system, during the 12-month immersion in artificial seawater

As can be seen from Fig. 7.28a, coating capacitance was generally in the order of 10^{-10} F, exhibiting a slight increase throughout the test, reaching however a value of 0.73 nF, implying an intact coat. With regard to coating resistance (Fig. 7.28b), there were intense fluctuations during the experiment, while after 12 months R_{pore} had a value of 1.246 10^4 Ω or 1.339 10^5 Ω cm^2, implying deterioration of barrier properties and increase of permeability [154], in accordance with the (small) increase in capacitance [155].

7.3.5.3 Experimental silicone (Exp Si) system

(a) After 1 month

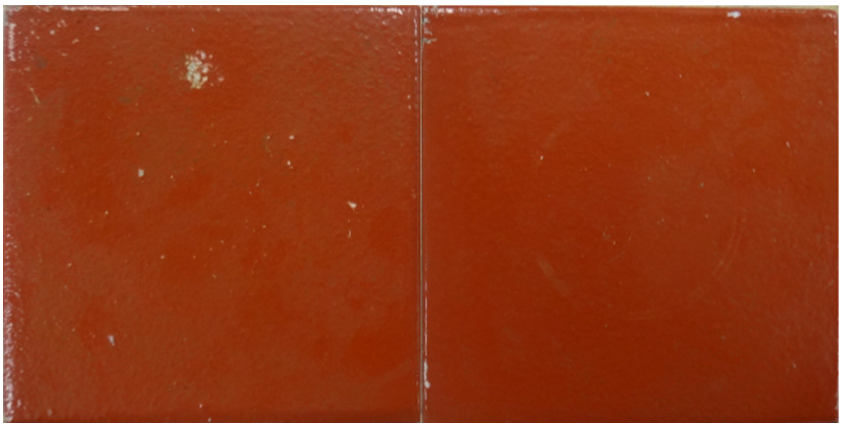

(b) After 3 months

(c) After 6 months

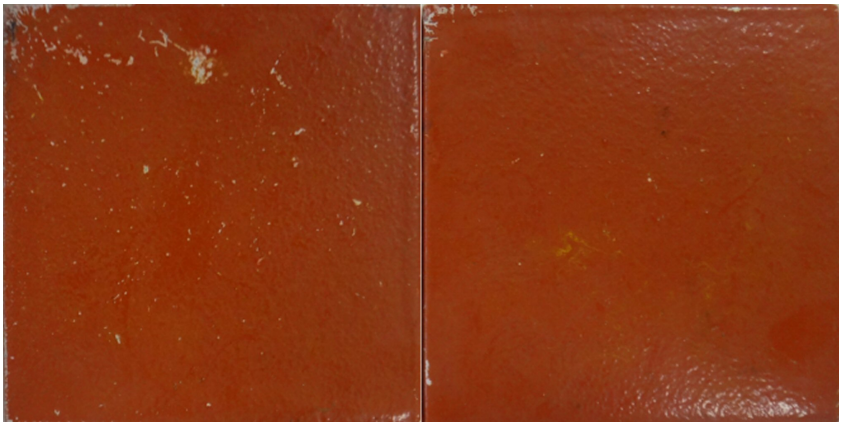

(d) After 9 months

(e) After 12 months

Figure 7.29: Surface condition of the specimens painted with the Exp Si system during their 12-month immersion in artificial seawater. Left: specimen (A), Right: specimen (B)

Table 7.50: König pendulum hardness measurements for specimens painted with the Exp Si system during their 12-month immersion in artificial seawater

Duration (months)	Exp Si (A)	Exp Si (B)
Before	16.50	24.80
1	21.25	24.60
2	24.00	24.20
3	18.80	22.00
4	20.40	20.50
5	19.00	20.83
6	16.67	19.17
7	15.00	21.00
8	20.60	21.50
9	19.80	21.75
10	20.80	23.40
11	18.40	19.40
12	20.75	18.80

Table 7.51: 60° gloss measurements for specimens painted with the Exp Si system during their 12-month immersion in artificial seawater

Duration (months)	Exp Si (A)	Exp Si (B)
Before	17.50	24.00
1	14.00	16.75
2	8.25	16.50
3	13.50	20.25
4	10.50	16.50
5	15.00	20.50
6	15.00	18.25
7	11.50	16.00
8	9.25	9.25
9	10.50	13.00

10	12.75	12.75
11	15.25	21.00
12	15.50	21.75

Table 7.52: Discoloration (DE) measurements for specimens painted with the Exp Si system during their 12-month immersion in artificial seawater

Duration (months)	Exp Si (A)	Exp Si (B)
Standard sample: L=35.71, a=35.04, b=12.52, C=37.21, H=19.66		
Before	0.52	0.70
1	0.96	1.31
2	4.48	3.71
3	4.12	3.09
4	3.12	3.00
5	3.87	3.50
6	3.80	3.51
7	3.33	3.57
8	5.19	4.37
9	4.78	6.00
10	8.44	9.82
11	6.31	8.04
12	7.11	6.32

Table 7.53: Electric properties of the specimens painted with the Exp Si system, during 12 months of immersion in artificial seawater

Duration (Weeks)	Coating capacitance (F)-Exp Si (B)
Before	$2.965\ 10^{-10}$
1	$5.097\ 10^{-10}$
2	$1.099\ 10^{-9}$
3	$4.543\ 10^{-10}$
4	$1.376\ 10^{-9}$
5	$5.230\ 10^{-10}$
6	$4.539\ 10^{-10}$
7	$8.303\ 10^{-10}$
8	$4.597\ 10^{-9}$
9	$6.616\ 10^{-10}$
10	$1.999\ 10^{-9}$
11	$5.906\ 10^{-10}$
12	$8.839\ 10^{-10}$

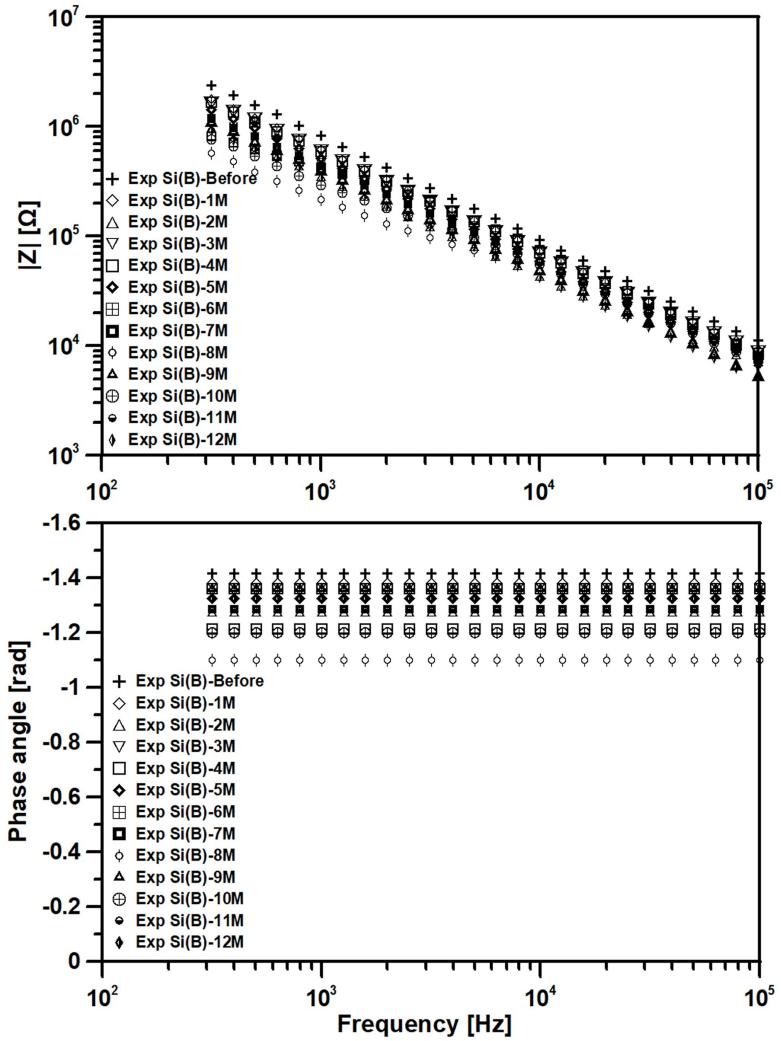

Figure 7.30: Bode graph for specimen (B) painted with the Exp Si system during 12 months of immersion in artificial seawater

The experimental silicone formulation exhibited large discoloration, compared to the reference silicone, since the discoloration index after 12 months of immersion was 13.7 and 9 times larger than the initial color values for specimens (A) and (B), respectively. Also, as can be seen in Fig. 7.29e, a blister was observed on the upper left side of the specimen. However, it was limited to the topcoat layer only. König hardness exhibited an increase for specimen (A) equal to 25.8% and a decrease for specimen (B) equal to 24.2%. Also, the initial hardness values of the two specimens exhibited variations, being 16.5 and 24.8, respectively. Gloss loss was observed in both specimens, being equal to 11.4% and 9.4%, respectively. These differences were limited only on the top coat, hence, both specimens retained their barrier properties (Table 7.53). The fluctuations in phase shift, ranging from -1 to -1.57 rad is attributed to the quality of the obtained signals. Even though some variations in the obtained capacitance were observed during the course of the experiment (Fig. 7.31), no actual degradation has commenced on either of the examined painting systems.

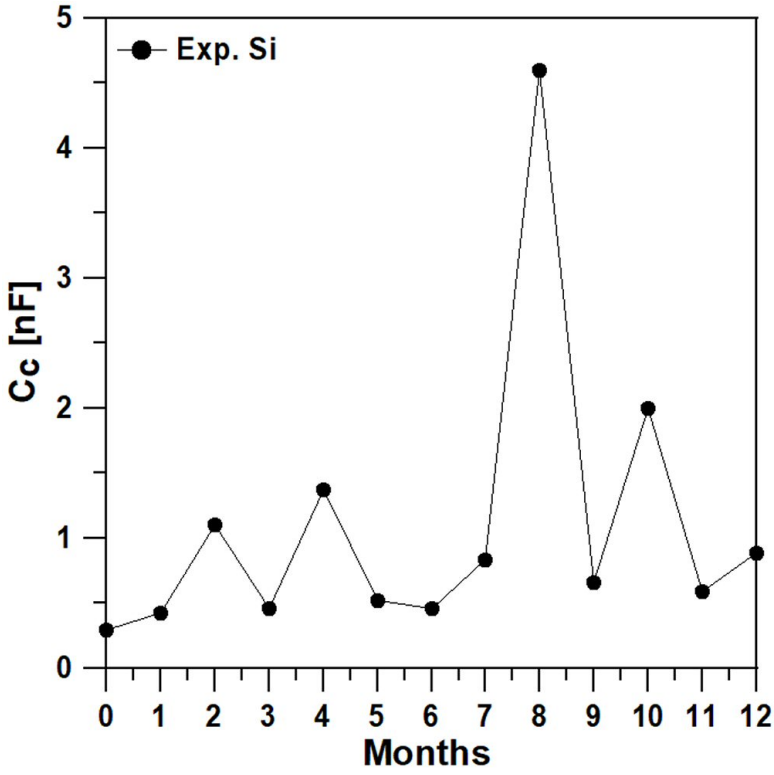

Figure 7.31: Change of coating capacitance of specimen (B) painted with the Exp. Si system, during the 12-month immersion in artificial seawater

7.3.5.4 Experimental polyurethane (Exp PU1) system

(a) After 1 month

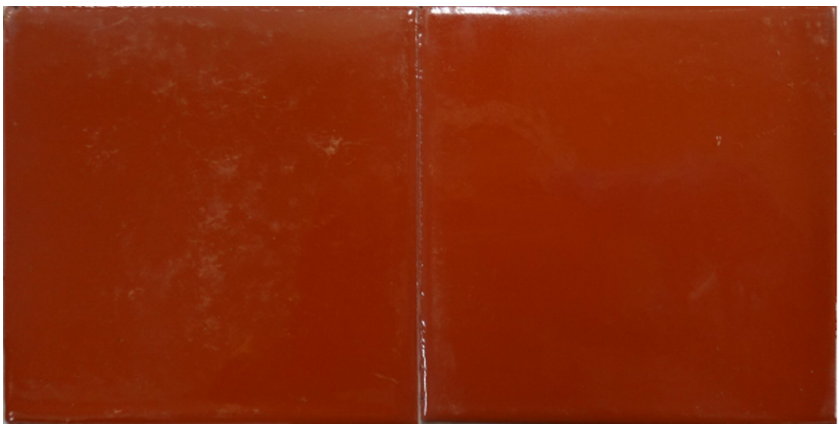

(b) After 3 months

(c) After 6 months

(d) After 9 months

(e) After 12 months

Figure 7.32: Surface condition of the specimens painted with the Exp PU1 system during their 12-month immersion in artificial seawater. Left: specimen (A), Right: specimen (B)

Table 7.54: König pendulum hardness measurements for specimens painted with the Exp PU1 system during their 12-month immersion in artificial seawater

Duration (months)	Exp PU1 (A)	Exp PU1 (B)
Before	21.83	21.83
1	16.67	16.33
2	34.00	33.20
3	38.60	35.60
4	52.40	51.00
5	50.33	45.33
6	59.17	57.50
7	42.60	42.75
8	36.60	34.80
9	26.80	26.20
10	36.60	33.60
11	40.80	39.00
12	55.20	55.00

Table 7.55: 60° gloss measurements for specimens painted with the Exp PU1 system during their 12-month immersion in artificial seawater

Duration (months)	Exp PU1 (A)	Exp PU1 (B)
Before	62.75	84.00
1	68.00	77.75
2	59.25	82.75
3	64.50	79.75
4	68.50	80.25
5	73.00	74.75
6	55.75	58.25
7	58.25	60.25
8	49.50	63.25
9	45.67	69.75
10	24.00	27.00
11	77.33	89.67
12	76.33	81.00

Table 7.56: Discoloration (DE) measurements for specimens painted with the Exp PU1 system during their 12-month immersion in artificial seawater

Duration (months)	Exp PU1 (A)	Exp PU1 (B)
Standard sample: L=35.92, a=28.75, b=8.26, C=29.91, H=16.03		
Before	0.51	0.46
1	0.59	0.57
2	0.77	0.57
3	0.92	0.76
4	0.46	0.59

5	1.01	0.76
6	1.29	1.42
7	0.67	1.04
8	1.19	1.24
9	1.44	1.42
10	1.50	1.30
11	1.04	1.37
12	0.74	0.75

Table 7.57: Electric properties of specimen (B) painted with the Exp PU1 system, during 12 months of immersion in artificial seawater

Duration (Weeks)	Coating capacitance (F)	Coating resistance (Ω)
Before	$2.363\ 10^{-10}$	-
1	$5.272\ 10^{-10}$	-
2	$5.496\ 10^{-10}$	$5.738\ 10^{5}$
3	$3.208\ 10^{-10}$	-
4	$3.213\ 10^{-10}$	-
5	$2.742\ 10^{-10}$	$1.375\ 10^{4}$
6	$3.012\ 10^{-10}$	$3.811\ 10^{5}$
7	$3.446\ 10^{-10}$	$5.339\ 10^{4}$
8	$3.117\ 10^{-10}$	$1.283\ 10^{5}$
9	$5.642\ 10^{-10}$	-
10	$1.389\ 10^{-9}$	$5.578\ 10^{5}$
11	$4.333\ 10^{-10}$	-
12	$4.761\ 10^{-10}$	$3.274\ 10^{4}$

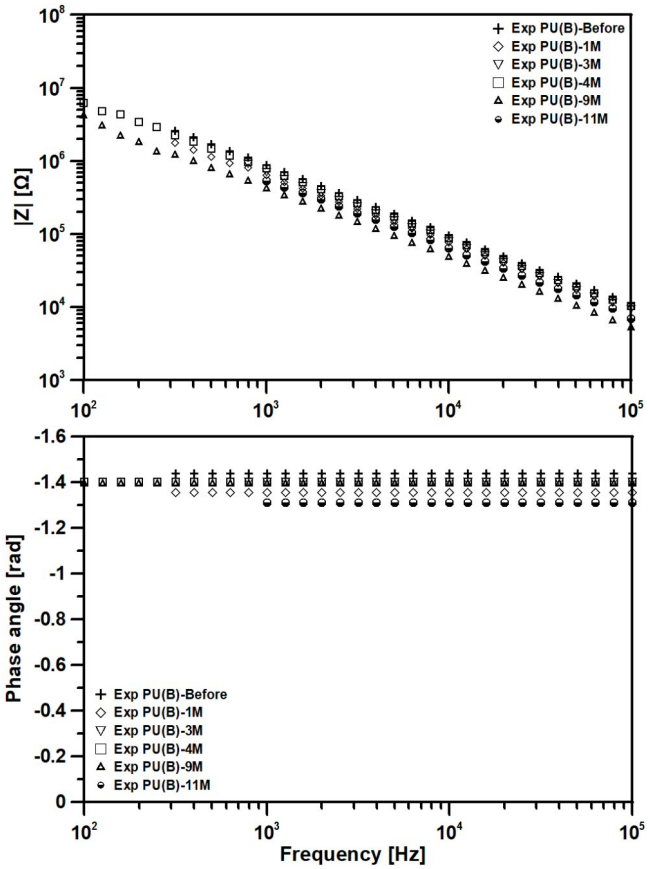

Figure 7.33: Bode graph for specimen (B) painted with the Exp PU1 system for intervals with pure capacitive behavior

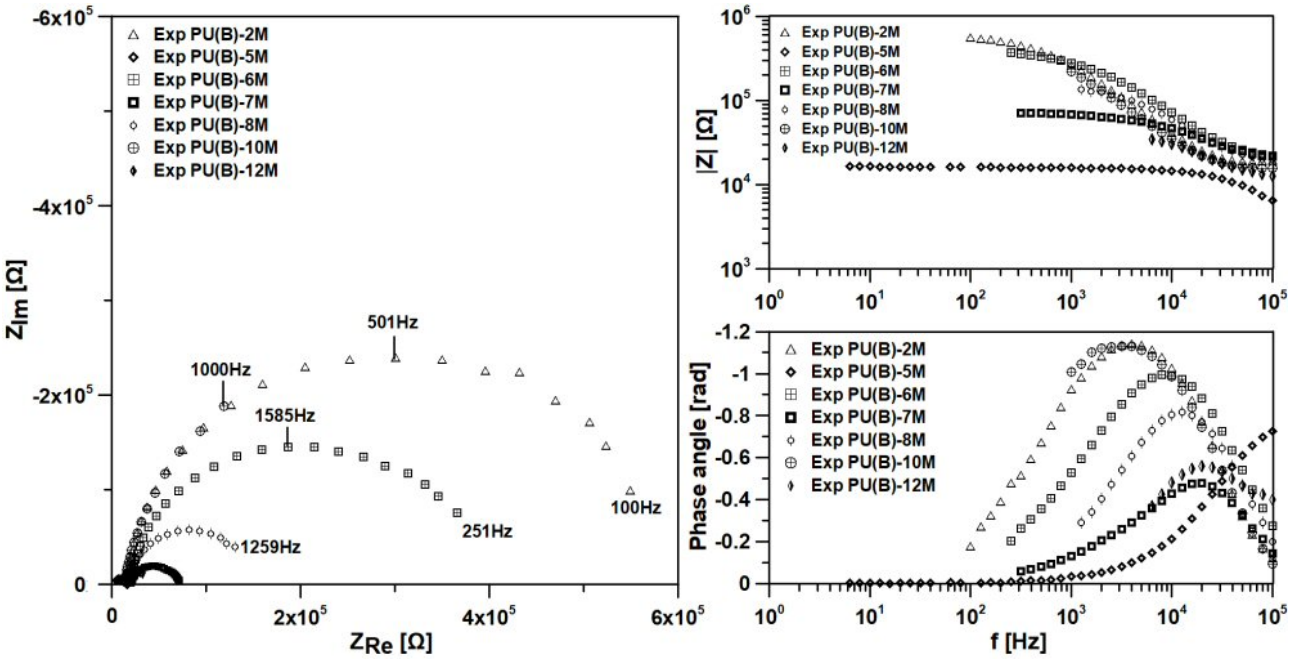

Figure 7.34: EIS graph for specimen (B) painted with the Exp PU1 system for intervals with one time-cosntant

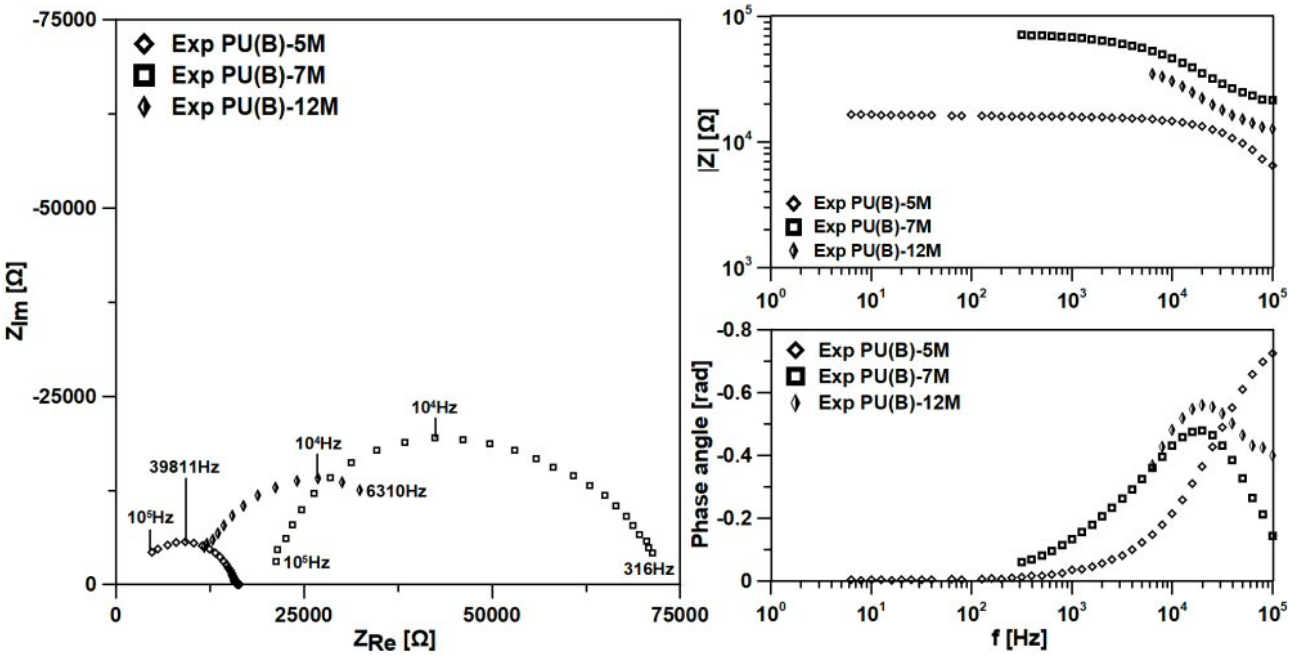

Figure 7.35: EIS graph for specimen (B) painted with the Exp PU1 system, where intervals 5, 7 and 12 months are presented in magnification.

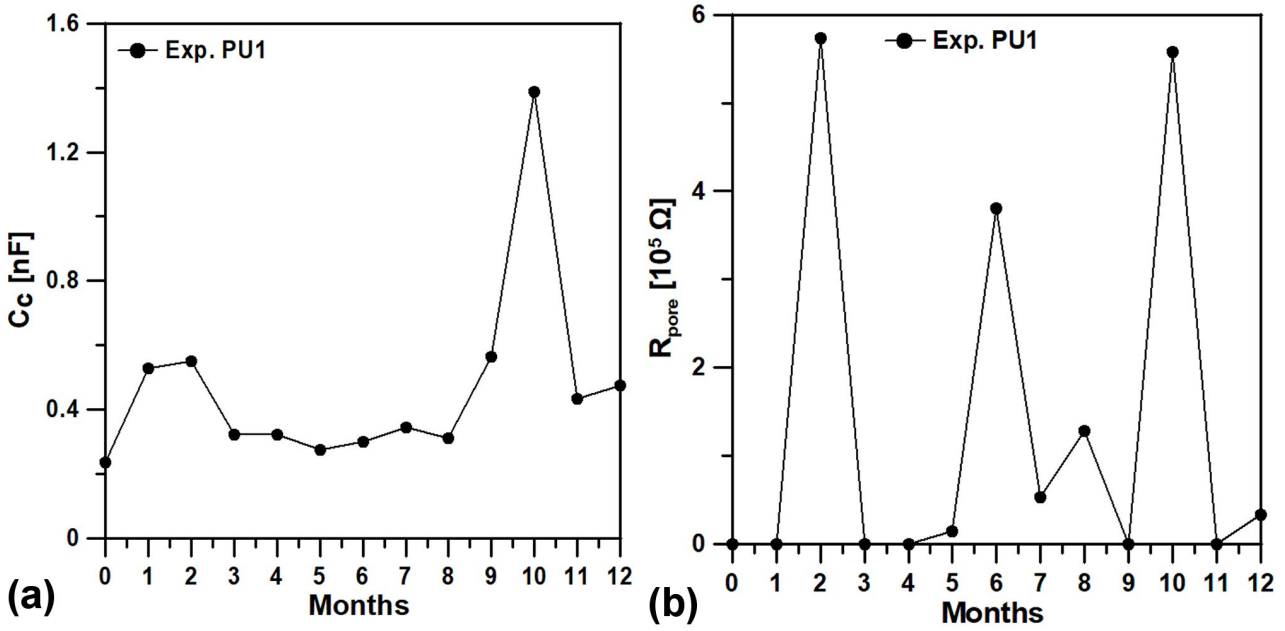

Figure 7.36: Change of a) coating capacitance and b) coating resistance of specimen (B) painted with the Exp. PU1 system, during the 12-month immersion in artificial seawater

During the 12-month immersion of experimental polyurethane system, the specimens retained their gloss properties, since for specimen (A) a gloss increase equal to 21.6% was measured, while for specimen (B) a gloss loss equal to 3.57% was measured. A very interesting finding is related to the König hardness values for both specimens, which exhibited samilar initial and final values. Indeed, as observed in Table 7.54, an initial value of 21.83 was measured for both specimens, while after the end of the experiment the increase in hardness was 152.9% for specimen (A) and 151.9% for specimen (B), being similar. The increase in pendulum hardness

after the end of the immersion test was not as sharp and profound as after the rest accelerated aging tests. Discoloration index exhibited also small variations during the test, increasing amount equal to 45% for specimen (A) and 63% for specimen (B), slightly larger than the gloss variation values observed during the rest accelerated aging tests.

With regard to EIS results, only specimen (B) is presented, since the quality of the responses for specimen (A) could not lead to trustworthy conclusions, especially regarding signals after 2, 5, 6, 7, 10 and 12 months. With regard to specimen (B), the intervals where a pure capacitive response was obtained, are presented in Fig. 7.33. The intervals where only the capacitor was measured were after 1, 3, 4, 9 and 11 months. The rest of intervals exhibited one time-constant Nyquist plots with diameter (R_{pore}) variations among the intervals (Fig. 7.34). The EIS responses after 5, 7 and 12 months are also presented in mangification in Fig. 7.35. In order to be able to better assess the electrochemical response of the system, the variations of coating capacitance and coating resistance with time are presented in Figs. 7.36a,b, while the corresponding values are also presented in Table 7.57. From Fig. 7.36a it could be concluded that the coating capacitance retained its small value throughout the experiment, despite the intense peak after 10 months. With regard to coating resistance, as appears in Fig. 7.36b, intense variations were observed not always consistent with the corresponding capacitance fluctuations, as can be observed after 2, 6 and 10 months of immersion. The largest value of R_{pore} was 5.738 10^5 Ω or 6.168 10^6 Ω cm^2, being close to the threshold of 10^6 Ω cm^2 [152] for sufficient corrosion protection in the long run.

The EIS responses from the specimens during the 12-month immersion in 3.5% NaCl aqueous solution indicated that the coating capacitance of all specimens was generally smaller than 10^{-9} F, indicating an intact coat. Fluctuations of the measured values of coating capacitance and coating resistance were observed, which could arise from changes of the physical properties of the polymeric matrices, leading to differences in pore size, density and/or conductivity throughout the testing period. This could justify the alternations between purely capacitive and one time-constant behavior for the acrylic and experimental polyurethane systems.

7.3.6 Conclusions with regard to the results after 12 months of laboratory immersion test

A ranking between the different systems (taking into consideration the worst values obtained for each coating system) in terms of hardness, gloss and discoloration would be as follows:

- König hardness: Acrylic (largest increase)<Exp.PU1<Ref.Si<Exp.Si (most stable behavior)
- 60° gloss: Acrylic<Ref.Si<Exp. PU1<Exp.Si
- DE: Acrylic<Exp.Si<Exp.PU1≤Ref.Si

7.3.7 EIS testing of parameters for intact coatings

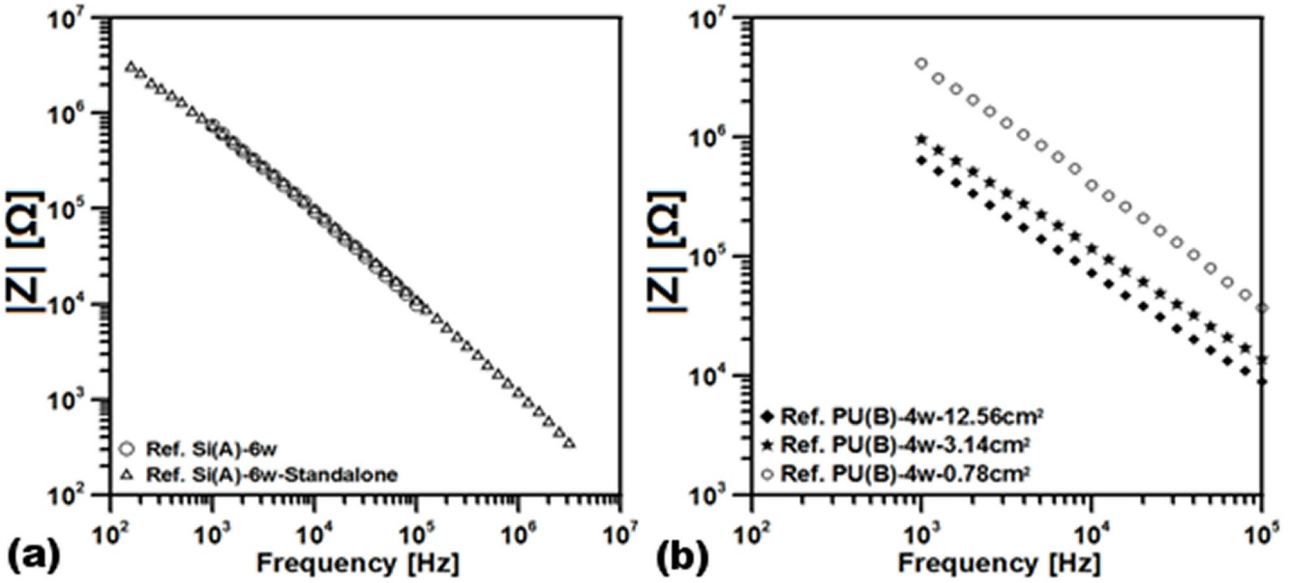

Figure 7.37: Impedance magnitude plots showing a) extension of high frequency measurements using standalone configuration and b) effect of examined surface on the obtained impedance

EIS investigation included also an effort to determine the upper and lower frequency limit for a purely capacitive signal. As can be seen from Fig. 7.37a, when the potentiostat was connected to the impedance/phase gain analyzer, the signal was limited to the frequency range 10^5-10^3 Hz. The value of 1000 Hz was a threshold, since at lower frequencies only noise was measured. This problem was solved using a standalone configuration or, in other words, disconnecting the potentiostat from the impedance and performing the measurements using only the impedance analyzer. As can be seen from the same figure, the frequency range using this technique increased, starting above 10^6 Hz to almost 10^2 Hz. Apparently, this configuration could be applied only for cases when no open circuit potential is measured and the response is purely capacitive.

Investigation was also performed with regard to the effect of exposed surface to measured impedance. As can be seen from Fig. 7.37b, the larger the exposed surface is the smaller the low frequency impedance would be for a high impedance intact coat. Larger exposed surfaces make the line in the magnitude plot to move in parallel towards lower |Z| values. This finding is in accordance to the equation for ideal capacitor, $C = \epsilon\epsilon_o A/d$, where a larger surface (A) would lead to higher capacitance (C), hence in smaller |Z| value for ω=1, since C and |Z| are inversely proportional, connected with the relationship $|Z|=1/\omega C$.

7.3.8 Water quality measurements from laboratory immersion test

Table 7.58: Water pH and conductivity measurements of immersion solution, during the 12-month immersion of reference paints

Duration	Ref Si		Acrylic		Temp.
(months)	pH	Conductivity (mS/cm)	pH	Conductivity (mS/cm)	°C
1	6.14	51.2	7.38	52.7	17.7
2	6.29	51.8	7.59	54.1	22.2
3	5.99	52.4	7.60	53.8	22.6
4	5.58	54.1	7.75	55.8	25.3
5	5.07	62.4	7.86	63.6	28.0
6	5.03	64.7	7.89	66.7	24.0
7	4.15	69.1	7.80	70.4	21.6
8	4.37	74.1	7.99	71.9	20.5
9	5.29	77.4	8.20	80.8	19.8
10	5.10	78.8	8.41	80.2	18.1
11	6.14	51.2	7.38	52.7	17.7
12	6.29	51.8	7.59	54.1	22.2

Table 7.59: Water pH and conductivity measurements of immersion solution, during the 12-month immersion of experimental paints

Duration	Exp PU1		Exp Si		Temp.
(months)	pH	Conductivity (mS/cm)	pH	Conductivity (mS/cm)	°C
1	6.56	48.4	6.14	51.5	29.2
2	6.94	50.0	6.16	49.1	24.6
3	4.68	51.5	7.20	53.1	21.5
4	7.54	54.1	4.73	53.9	18.8
5	7.25	52.3	5.11	51.6	20.1
6	7.26	53.2	5.05	52.5	18.9
7	7.61	54.9	4.97	53.9	24.4
8	4.94	53.0	4.98	53.2	24.7
9	6.43	54.5	4.19	53.1	28.2
10	6.39	55.6	4.53	54.5	23.9
11	7.03	58.3	5.50	57.2	22.5
12	6.53	58.8	5.84	58.4	19.4

7.3.9 Mechanical testing and determination of physical parameters

7.3.9.1 Water-liquid transmission rate test (permeability)

The aim of this test is to classify the permeability of organic coatings to water liquid. The test complies with the EN 1062-3 standard for "Coating materials and coating systems for exterior masonry and concrete". In order to perform the test, the following steps should be followed.

1. The substrate for the painting system should be clay bricks or mortar slabs. In our case fire bricks with an area of 120 cm^2 were used.

2. Each system was applied on two bricks making a total of 12 bricks.

3. The systems applied on the bricks were each one of the six systems presented in the "Experimental Setup" section. The aforementioned systems were supplied in liquid state and the application of each system onto the bricks was performed in the laboratory with a 5 cm width roller, according to manufacturer's specifications.

4. Only one surface of each brick was painted, one of two largest surfaces, according to the EN 1062-3 standard. The rest of the surfaces were sealed with a sealing epoxy resin, until no pores were visible or until there was a homogenous white layer of resin covering the brick, so that its surface underneath was not visible anymore.

Figure 7.38: Firebricks during the painting procedure; a) painted with primer and b) in the as painted condition

5. The interval between two successive paint applications ranged between 3 to 7 days, in order to achieve complete curing.

6. After completion of the paint application, the test was ready to start and included the following steps:

    a) Weight measurement of bricks in the as painted condition

    b) Conditioning of the bricks at 23±2 °C with 50% RH for 24 h

    c) Weighing after 24 h conditioning

    d) Immersion of bricks in potable water for 24 h, with their surface upside down and immersed 1 cm below the water surface.

    e) Weight after 2 h

    f) Weight after 3 h

    g) Weight after 4 h

    h) Weight after 5 h

    i) Weight after 6 h

j) Weight after 24 h immersion (**weight of 1st period**)

k) Drying at 50 °C for 24h

l) Conditioning at 23±2 °C with 50% RH for 48 h

m) Weight after 48 h conditioning

n) Immersion of bricks in potable water for 24 h, with their surface upside down and immersed 1cm below the water surface.

o) Weight after 24 h immersion (**weight of 2nd period**)

p) *Repeat the procedure for another two periods with 24 h conditioning intervals.*

Figure 7.39: Painted firebricks, during their immersion interval in potable water, as described in step (d)

7. After each period, calculation of the average of the weight gain for the two bricks of each system was performed and the liquid transmission rate w was obtained, using the following formula:

$$w = \frac{dm}{A\sqrt{24}} \tag{7.1}$$

where, w is the transmission rate [kg/(m^2 h$^{0.5}$)], dm is the average weight gain from the two bricks for each system, A is the painted area of each brick (one side painted only) and $\sqrt{24}$, due to the 24-hour immersion of the bricks.

8. Finally, according to the calculated value of w, a classification is made, with regard to the transmission rate.

The procedure presented above is summarized in the following tables, for all the four periods of the experiment.

Table 7.60: Transmission rate calculation after the 1^{st} period (w_1)

	Weight in Step (a) (g)	Weight in Step (c) (g)	Weight of 1^{st} period Step (j) (g)	Water gain (dm) of 1^{st} period (g)	Average (dm) (g)	w_1 kg/(m^2 h$^{0.5}$)
Ref Si(A)	1008.68	1005.89	1017.85	11.96	18.080	0.3075
Ref Si(B)	1001.79	999.54	1023.74	24.20		
Acrylic(A)	999.86	998.04	999.12	1.08	1.065	0.0181
Acrylic(B)	998.89	997.15	998.20	1.05		
Exp PU1(A)	1269.78	1268.24	1269.27	1.03	1.010	0.0172
Exp PU1(B)	1283.25	1281.57	1282.56	0.99		
Exp Si(A)	1280.71	1278.23	1282.80	4.57	3.790	0.0645
Exp Si(B)	1283.39	1281.49	1284.50	3.01		
PU(A)	995.25	992.96	1037.99	45.03	45.935	0.7814
PU(B)	1006.66	1004.82	1051.66	46.84		
Exp PU2(A)	1259.45	1259.45	1260.31	0.86	0.800	0.0136
Exp PU2(B)	1281.24	1281.24	1281.98	0.74		

Table 7.61: Transmission rate calculation after the 2^{nd} period (w_2)

	Weight in Step (a) (g)	Weight in Step (m) (g)	Weight of 2^{nd} period Step (o) (g)	Water gain (dm) of 2^{nd} period (g)	Average (dm) (g)	w_2 kg/(m^2 h$^{0.5}$)
Ref Si(A)	1008.68	1009.38	1010.93	1.55	4.245	0.0722
Ref Si(B)	1001.79	1005.83	1012.77	6.94		
Acrylic(A)	999.86	997.94	998.47	0.53	0.825	0.0140
Acrylic(B)	998.89	997.07	998.19	1.12		
Exp PU1(A)	1269.78	1268.15	1269.35	1.20	0.845	0.0144
Exp PU1(B)	1283.25	1281.46	1281.95	0.49		
Exp Si(A)	1280.71	1278.25	1279.75	1.50	1.785	0.0304
Exp Si(B)	1283.39	1281.37	1283.44	2.07		
PU(A)	995.25	999.53	1003.20	3.67	42.105	0.0358
PU(B)	1006.66	1011.84	1012.38	0.54		
Exp PU2(A)	1259.45	1259.32	1259.92	0.60	0.560	0.0095
Exp PU2(B)	1281.24	1281.10	1281.62	0.52		

Table 7.62: Transmission rate calculation after the 3^{rd} period (w_3)

	Weight in Step (a) (g)	Weight in Step (m) (g)	Weight of 3^{rd} period Step (o) (g)	Water gain (dm) of 3^{rd} period (g)	Average (dm) (g)	w_3 kg/(m^2 h$^{0.5}$)
Ref Si(A)	1008.68	1005.58	1006.25	0.67	3.515	0.0598
Ref Si(B)	1001.79	999.24	1005.60	6.36		
Acrylic(A)	999.86	997.78	998.11	0.33	0.345	0.0059
Acrylic(B)	998.89	996.88	997.24	0.36		
Exp PU1(A)	1269.78	1267.97	1268.41	0.44	0.410	0.0070
Exp PU1(B)	1283.25	1281.23	1281.61	0.38		
Exp Si(A)	1280.71	1277.90	1278.50	0.60	1.060	0.0180
Exp Si(B)	1283.39	1281.19	1282.71	1.52		

PU(A)	995.25	992.75	997.49	4.74	3.630	0.0617
PU(B)	1006.66	1004.58	1007.10	2.52		
Exp PU2(A)	1259.45	1259.10	1259.34	0.24	0.225	0.0038
Exp PU2(B)	1281.24	1280.84	1281.05	0.21		

Table 7.63: Transmission rate calculation after the 4^{th} period (w_4)

	Weight in Step (a) (g)	Weight in Step (m) (g)	Weight of 4^{th} period Step (o) (g)	Water gain (dm) of 4^{th} period (g)	Average (dm) (g)	w_4 kg/(m^2 h$^{0.5}$)
Ref Si(A)	1008.68	1005.61	1006.16	0.55	2.100	0.0357
Ref Si(B)	1001.79	1000.69	1004.34	3.65		
Acrylic(A)	999.86	997.79	998.21	0.42	0.465	0.0079
Acrylic(B)	998.89	996.90	997.41	0.51		
Exp PU1(A)	1269.78	1268.01	1268.39	0.38	0.375	0.0064
Exp PU1(B)	1283.25	1281.27	1281.64	0.37		
Exp Si(A)	1280.71	1277.93	1278.70	0.77	1.330	0.0226
Exp Si(B)	1283.39	1281.18	1283.07	1.89		
PU(A)	995.25	993.42	997.33	3.91	3.605	0.0613
PU(B)	1006.66	1004.75	1008.05	3.30		
Exp PU2(A)	1259.45	1259.10	1259.45	0.35	0.325	0.0055
Exp PU2(B)	1281.24	1280.85	1281.15	0.30		

Table 7.64: Summary of the transmission rates for all paints, during the four periods of the experiment

Period	Ref Si	Acrylic	Exp PU1	Exp Si	PU	Exp PU2
1	0.3075	0.0181	0.0172	0.0645	0.7814	0.0136
2	0.0722	0.0140	0.0144	0.0304	0.0358	0.0095
3	0.0598	0.0059	0.0070	0.0180	0.0617	0.0038
4	0.0357	0.0079	0.0064	0.0226	0.0613	0.0055

Table 7.65: Water-liquid transmission rate classification for all paints after the end of the experiment

System	Classification
Ref Si	III (low)
Acrylic	III (low)
Exp Si	III (low)
Exp PU1	III (low)
PU	III (low)
Exp PU2	III (low)

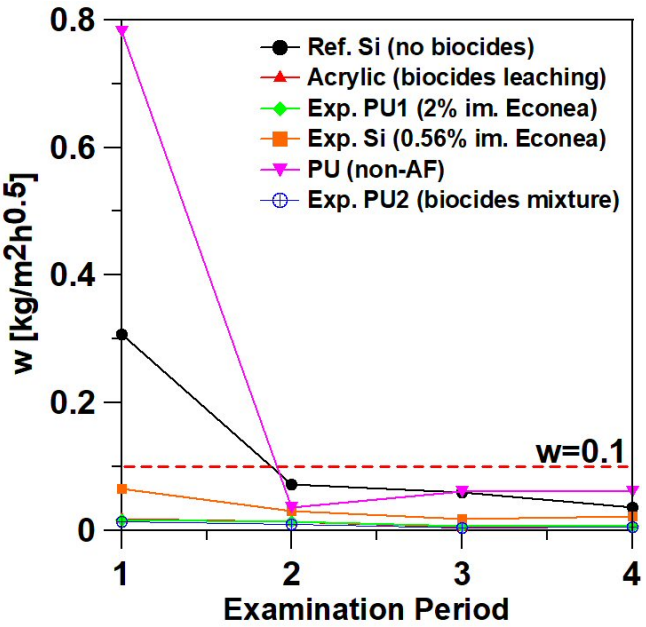

Figure 7.40: Water-liquid transmission rate variation of the examined painting systems, during the course of the experiment

The results presented in Table 7.64 indicate that all systems were characterized by low transmission rate of water liquid, since the value of w_4 was smaller than 0.1 kg/($m^2h^{0.5}$), as proposed by the standard.

7.3.9.2 Cupping test

1. Reference silicone system

Figure 7.41: Indicative gradual cracking of the Ref Si system during cupping test; a) crack initiation, b) front of cracks at the center, c) finish of experiment with obvious substrate exposure

Figure 7.42: Surface view of the cracked specimens painted with the Ref Si system after the end of the cupping test

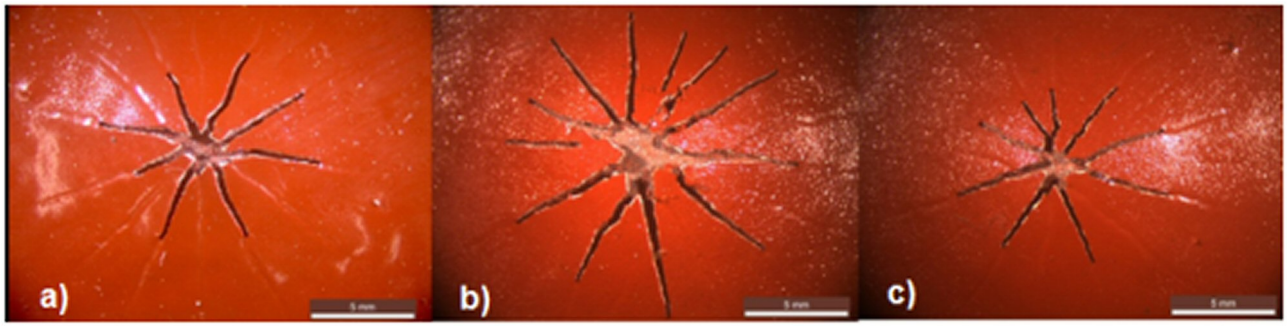

Figure 7.43: Surface view of the cracked specimens painted with the Ref Si system after the end of the cupping test

2. Acrylic system

Figure 7.44: Indicative gradual cracking of the Acrylic system during cupping test; a) crack initiation, b) front of cracks at the center, c) finish of experiment with obvious substrate exposure

Figure 7.45: Surface view of the cracked specimens painted with the Acrylic system after the end of the cupping test

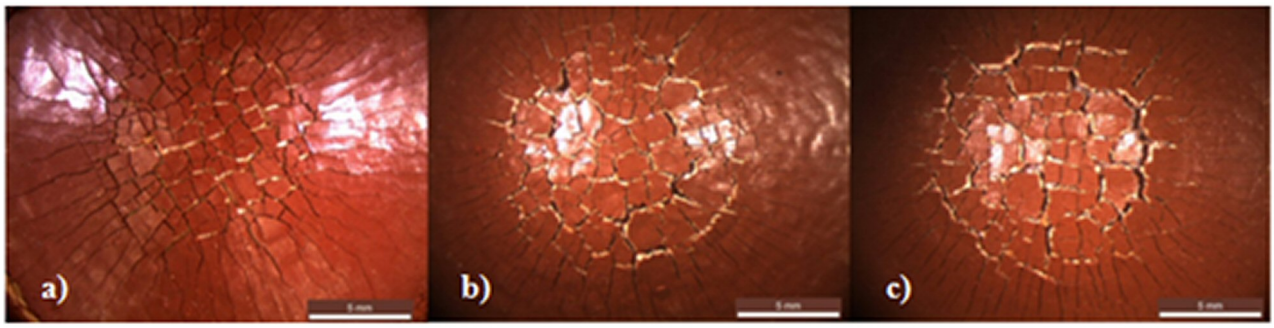

Figure 7.46: Surface view of the cracked specimens painted with the Acrylic system after the end of the cupping test

3. Experimental polyurethane (1) system

Figure 7.47: Indicative gradual cracking of the Exp PU1 system during cupping test; a) crack initiation, b) front of cracks at the center, c) finish of experiment with obvious substrate exposure

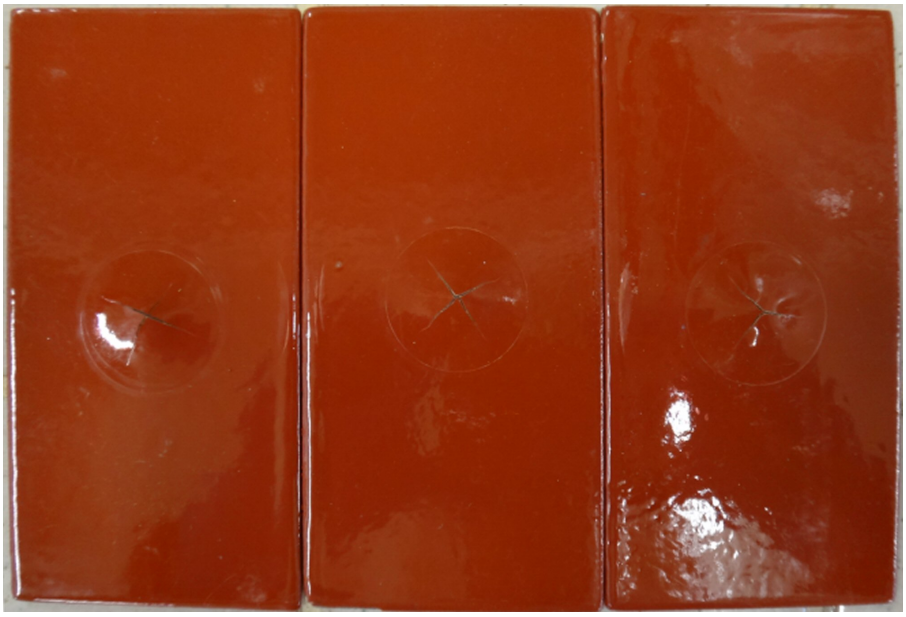

Figure 7.48: Surface view of the cracked specimens painted with the Exp PU1 system after the end of the cupping test

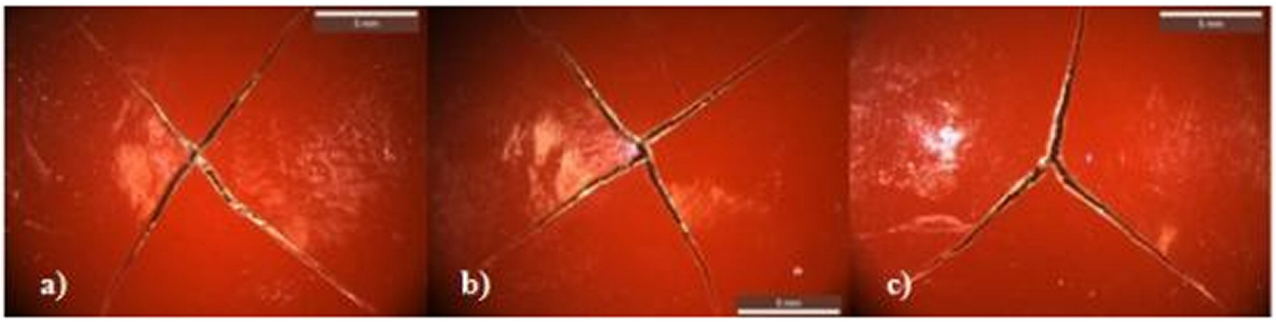

Figure 7.49: Surface view of the cracked specimens painted with the Exp PU1 system after the end of the cupping test

4. Experimental silicone system

Figure 7.50: Indicative gradual cracking of the Exp Si system during cupping test; a) crack initiation, b) front of cracks at the center, c) finish of experiment with obvious substrate exposure

Figure 7.51: Surface view of the cracked specimens painted with the Exp Si system after the end of the cupping test

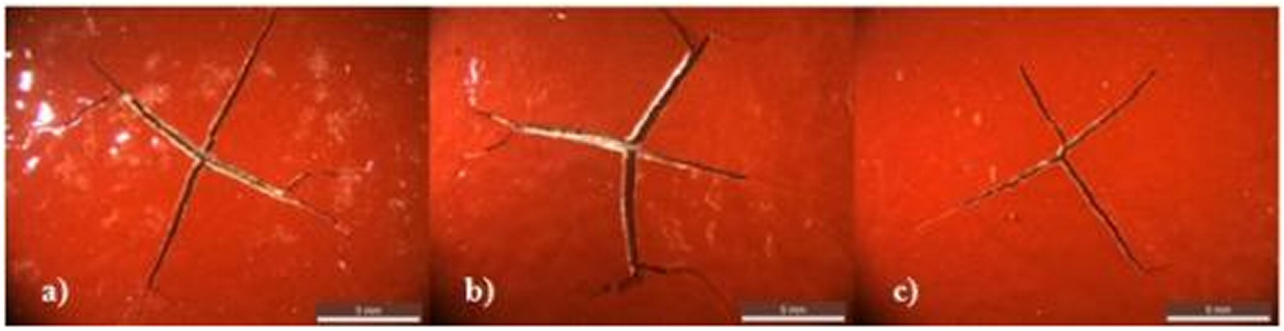

Figure 7.52: Surface view of the cracked specimens painted with the Exp Si system after the end of the cupping test

5. Experimental polyurehane (2) system

Figure 7.53: Indicative gradual cracking of the Exp PU2 system during cupping test; a) crack initiation, b) front of cracks at the center, c) finish of experiment with obvious substrate exposure

Figure 7.54: Surface view of the cracked specimens painted with the Exp PU2 system after the end of the cupping test

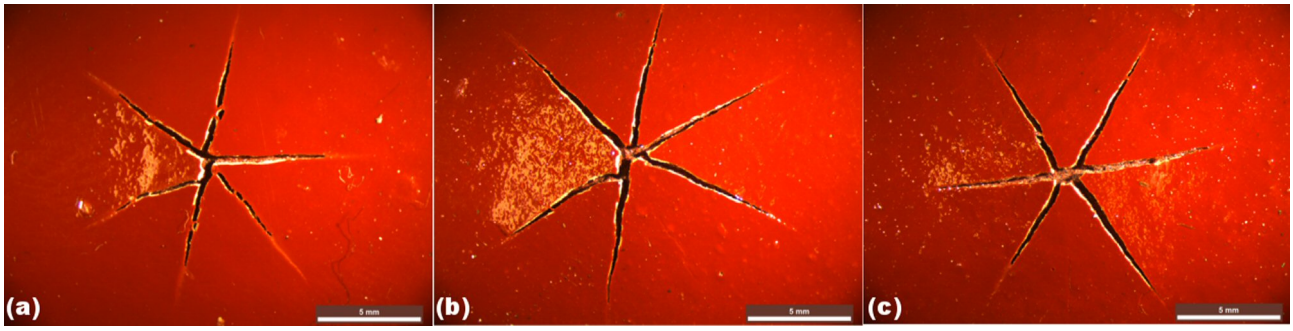

Figure 7.55: Surface view of the cracked specimens painted with the Exp PU2 system after the end of the cupping test

Table 7.66: Indentation Depth (I.D.) during the cupping test

Specimen	ID at first crack (failure) (mm)	Average ID	ID at total detachment (mm)	Average ID
Ref Si (A)	1.23		4.30	
Ref Si (B)	1.95	1.70	3.78	3.93
Ref Si (C)	1.91		3.72	
Acrylic (A)	1.52		6.62	
Acrylic (B)	1.58	1.55	6.27	6.43
Acrylic (C)	1.54		6.39	
Exp PU1 (A)	1.34		3.10	
Exp PU1 (B)	1.70	1.64	3.26	3.23
Exp PU1 (C)	1.87		3.33	
Exp Si (A)	1.16		2.51	
Exp Si (B)	1.26	1.22	2.41	2.27
Exp Si (C)	1.25		1.90	
Exp PU2 (A)	0.81		2.20	
		0.84		2.61

Exp PU2 (B)	0.91	2.88
Exp PU2 (C)	0.81	2.75

A failure ranking in deep drawing would be: Ref.Si>Exp.PU>Acrylic>Exp.Si>Exp. PU2, meaning that the reference silicone system exhibited the first crack at the greatest depth compared to the other systems. However, the final failure, including coating detachment and/or metallic substrate exposure, was noticed in greater depth for the acrylic system followed by the reference silicone, the experimental polyurethane (1), the experimental silicone and finally the experimental polyurethane system (2). The reference silicone, both the experimental polyurethane systems and the experimental silicone system failed following the same mode: few and long cracks extending through the multilayer coat to the substrate. On the contrary, the acrylic system exhibited a unique failure mode: intense microcracking and flaking of the topcoat. The indenter should be further pushed to 6.43 mm, in order for the cracked parts to start being detached from the substrate. According to the ISO 1520 standard, though, failure is considered the depth "until a crack is first observed on the surface of the coating and/or the coating begins to become detached from the substrate". Hence, in our case, the ranking of the coats results from the depth at which the first crack appeared. As a result, the acrylic system, despite the increased depth for total failure, it was ranked in the 3^{rd} place overall.

7.3.9.3 Dirt pick-up test

According to the ASTM D 3719-00 standard, the dirt collection index, Dc, may be calculated as follows:

$$\mathrm{Dc} = \frac{\mathrm{L} * \mathrm{B}}{\mathrm{L} * \mathrm{A}} \times 100 \tag{7.2}$$

where, L*A is the arithmetic mean of the unexposed panel lightness values and L*B after exposure. A wooden base with a tilt of 45° was constructed at NTUA and then placed to a position facing south. The whole setup was placed at the rooftop of School of Chemical Engineering building. The experimental setup is presented in the following figure.

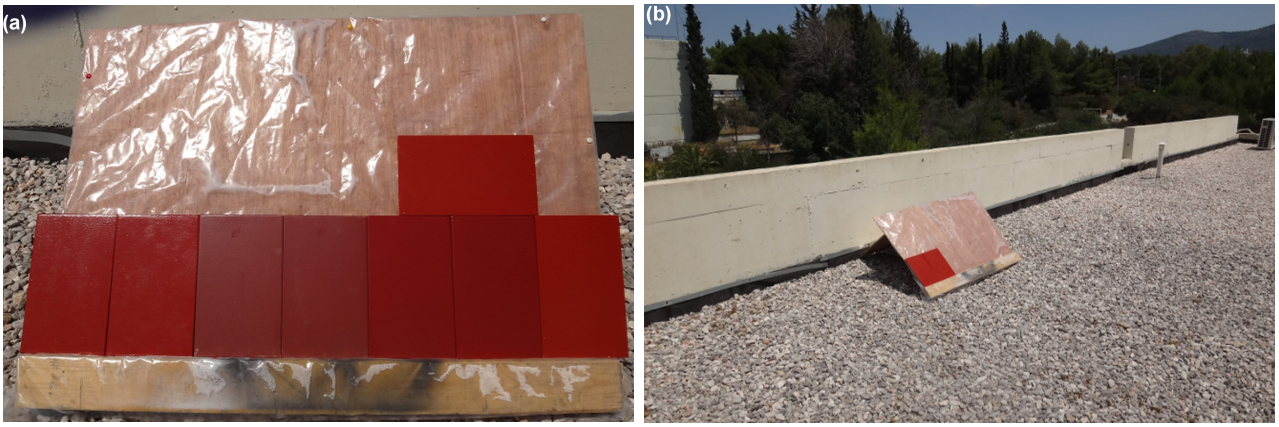

Figure 7.56: Experimental setup for the dirt pick-up test; a) the base with all the specimens positioned and b) a panoramic view of the exposure area

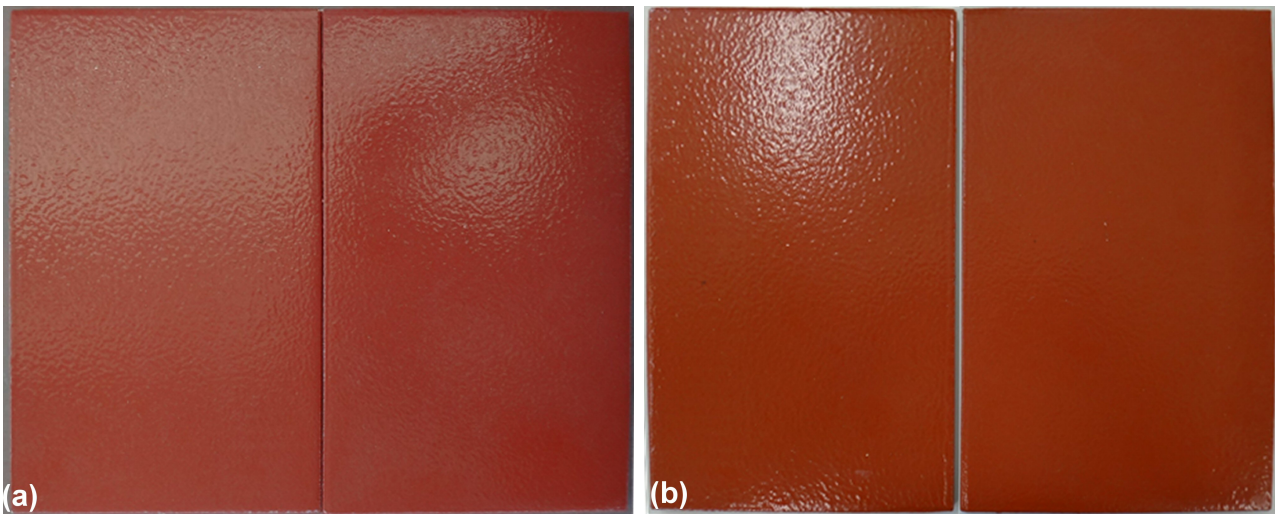

Figure 7.57: Surface condition of plates painted with the Ref Si system, during dirt pick-up test; a) after 30 days and b) after 61 days of outdoor weathering

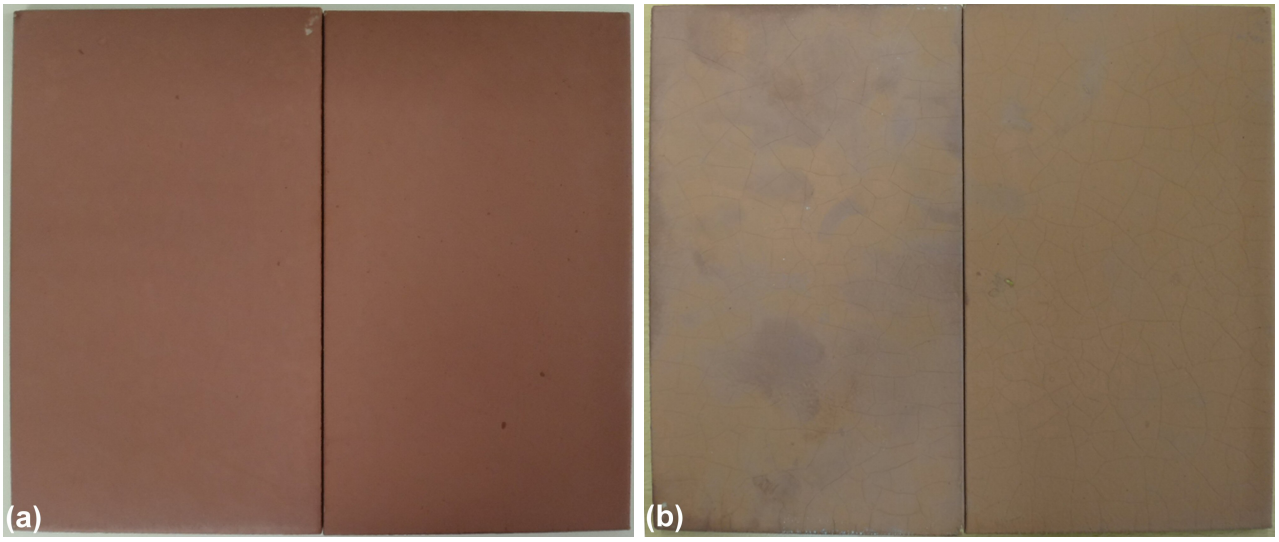

Figure 7.58: Surface condition of plates painted with the Acrylic system, during dirt pick-up test; a) after 30 days and b) after 61 days of outdoor weathering

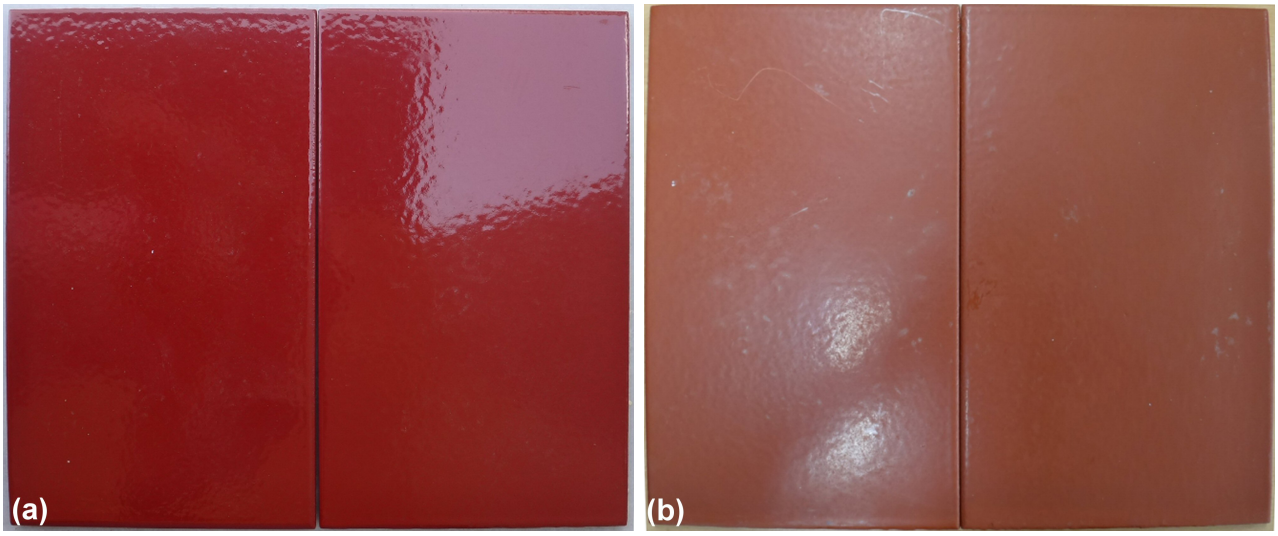

Figure 7.59: Surface condition of plates painted with the Exp PU1 system, during dirt pick-up test; a) after 30 days and b) after 61 days of outdoor weathering

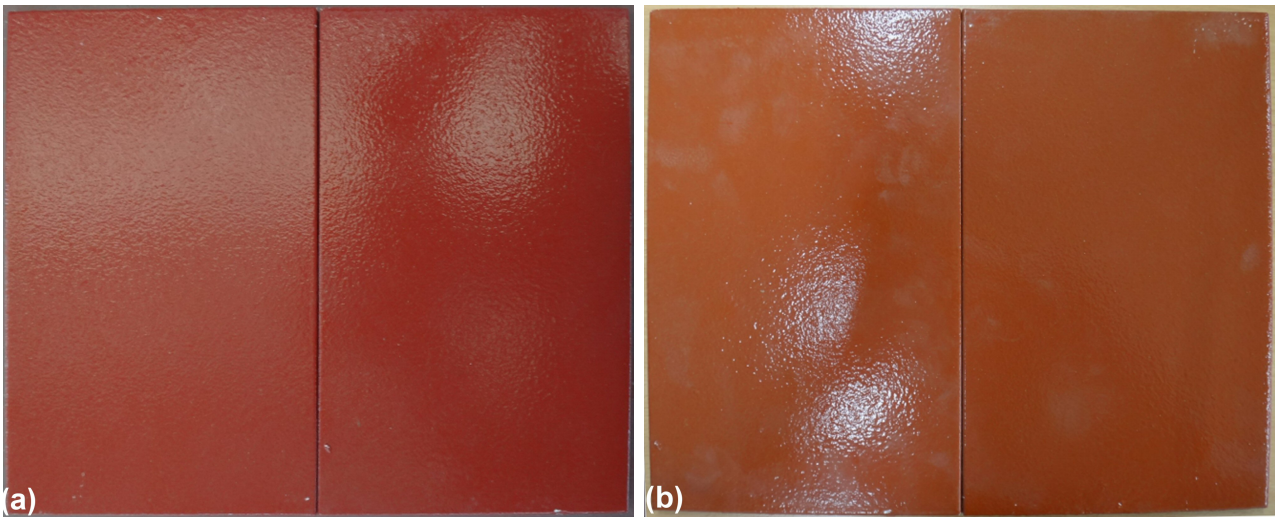

Figure 7.60: Surface condition of plates painted with the Exp Si system, during dirt pick-up test; a) after 30 days and b) after 61 days of outdoor weathering

Table 7.67: Dirt collection index (Dc) calculation after 61 days of outdoor exposure

Specimen	Metric Lightness (L*A)	Average L*A	Metric Lightness (L*B)	Average L*B	Dc
Ref Si (A)	35.54	35.58	35.77	35.81	100.65
Ref Si (B)	35.62		35.84		
Acrylic (A)	36.20	36.16	42.65	42.72	118.14
Acrylic (B)	36.13		42.80		
Exp PU1 (A)	35.77	35.88	35.36	35.11	97.85
Exp PU1 (B)	35.98		34.86		
Exp Si (A)	35.34	35.35	35.98	35.88	101.44
Exp Si (B)	35.37		35.771		
Exp PU2 (A)	36.06	35.86	37.13	36.87	102.82
Exp PU2 (B)	35.65		36.61		

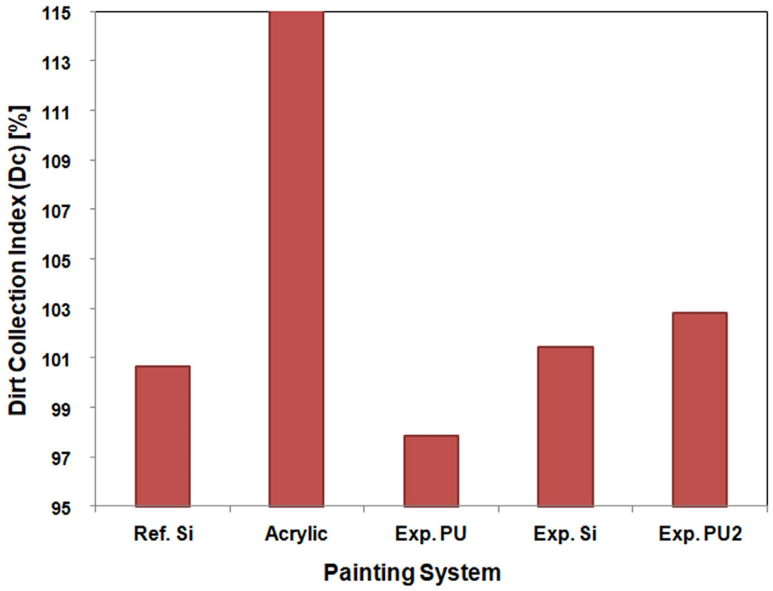

Figure 7.61: Dirt pick up index calculation after 61 days of experiment, according to ASTM D 3719-00

From Fig. 7.61, it is apparent that the acrylic paint, which exhibited an obvious and intense discoloration (Fig. 7.58), exhibited the highest discoloration index. This value reflects mainly the intense discoloration rather than the dirt accumulation of the paint. As stated in paragraph 10.1.2. of the standard: "Any noticeable color change which, for reasons other than dirt accumulation, may have occurred" should be reported. "The dirt collection index is not valid if these color changes or fungal growth are significant". The acrylic paint is a special case, due to the intense chalking effect, arising from its leaching nature. Hence, this large increase in Dc would be hard to distinguish whether it could be attributed to leaching, dirt accumulation or both. Another characteristic of this paint is the checking effect, which was reported during the accelerated aging tests and has been also observed here. Checking effect of the mosaic type and of the ASTM 2 rank was observed (ASTM D 660-93). With regard to the experimental silicone system, indeed the obtained index was attributed to dirt, which was easier to adhere, due to the surface texture of the paint. The same is also true for the reference silicone system. The experimental polyurethane system exhibited the smallest index, even though discoloration had also occurred (Fig. 7.59) and could mask the attached dirt. The same trend was noticed for the experimental polyurethane formulation (2), giving rise to the second highest index. A final ranking would be: Exp.PU (best behavior)>Ref.Si>Exp.Si>Exp.PU2.

7.3.9.4 Chalking test

In the present case, the *method D b• " TNO Type Method* was applied from the ASTM D 4214-98 standard, in order to assess the total chalking susceptibility of the Ref Si, Acrylic, Exp PU1 and Exp Si systems. The specimens used for the test were of dimensions 110 mm×50 mm×6 mm. The procedure includes:

- Application of a piece of cellular tape (13 mm width) onto each specimen's surface, using gentle finger pressure.

- The tape is then removed and applied with the adhesive side onto a black construction paper.
- The tape on the black paper is subsequently compared to the photographic reference standard No. 2, as presented in ASTM D 4214-98 standard.
- The chalking rating is the one that matches more the colored mark left by the paint onto the cellular tape. The reference standard is from white to black, since this standard was first introduced for paints with titanium oxide as a pigment, which is white in color. However, the same procedure may be applied for light colored paints, as well, similarly to the paints examined in the present study.

Figure 7.62: Chalking test on specimens painted with the a) Ref Si and the b) Acrylic systems

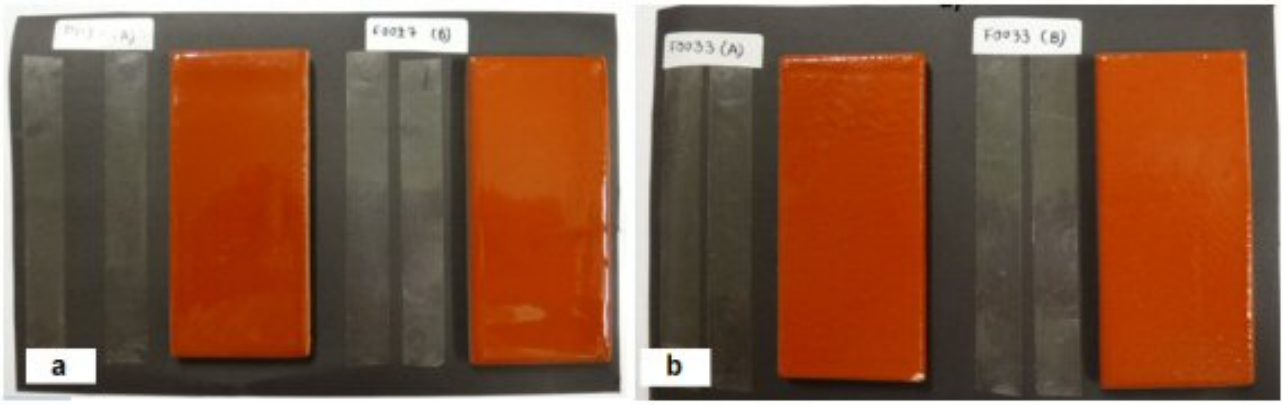

Figure 7.63: Chalking test on specimens painted with the a) Exp PU1 and the b) Exp Si systems

It should be noted that the chalking specimens of the paints presented in Fig. 7.63 were a bit larger than the reference specimens (Fig. 7.62). More specifically, the dimensions of the

new painted specimens were 120 mm×50 mm×4 mm, while the dimensions of the reference specimens were 110 mm×50 mm×6 mm. The dimensions were selected larger for the new specimens, in order to be able to take two measurements from each surface. The chalking rating for all specimens is presented in Table 7.68.

Table 7.68: Chalking rating for all the specimens

System	Chalking rating
Ref Si (A)	2
Ref Si (B)	2
Acrylic (A)	3
Acrylic (B)	3
Exp PU1 (A)	2
Exp PU1 (B)	2
Exp Si (A)	2
Exp Si (B)	2

From the above rating we can conclude that there was no chalking effect on the paints, except for the acrylic paint, which is a self-polishing antifouling paint. Hence, its surface is expected to be chalky, in order to release the biocide. In addition, from all the experiments performed so far (natural and accelerated aging tests), the acrylic system always appeared to release great amount of pigments, which is characteristic of the leaching nature of this paint.

7.4 Conclusions

From the accelerated aging investigation in salt spray and UV chamber of the painting systems, some unique characteristics for each system were determined:

- Reference silicone system remained stable in terms of hardness, after salt spray test, while it retained its gloss after UV test, exhibiting the best behavior.
- Experimental silicone system exhibited the best behavior after both tests in the hardness property and the smallest discoloration after UV aging. For the rest cases, its performance was average.
- Acrylic system retained no gloss, exhibited intense discoloration and checking and increase in hardness. This system exhibited the least satisfactory behavior in terms of gloss and discoloration after both tests, while in terms of hardness was average.
- Experimental polyurethane exhibited the largest increase in hardness in both tests and the smallest gloss change after salt spray test. For the rest cases, its performance was average.
- Anticorrosive polyurethane exhibited variation of properties among the different specimens, but, generally, it exhibited increase in hardness, in slightly less extent than the experimental polyurethane formulation. Also, it presented the best behavior in terms of discoloration after salt spray test.

- In terms of electrical properties, all systems exhibited purely capacitive characteristics, implying that no degradation has commneced during the experiments.

These characteristics were not completely verified during the immersion test, since:

- The experimental silicone formulation exhibited the most stable behavior in terms of hardness and gloss, but it was mediocre in terms of discoloration.
- The reference silicone paint was average in terms of hardness and gloss and exhibited the best behavior in terms of discoloration.
- The experimental polyurethane formulation did not exhibit such a sharp increase in hardness, as was observed after salt spray and UV aging. Generally, it was average for all properties.
- The acrylic system exhibited the worst behavior in all properties. No checking effect was observed.
- In terms of electrical properties, the silicone systems retained a capacitive response throughout the test. The acrylic and experimental polyurethane sytems exhibited both capacitive and capacitive/ pore resistance responses on occasions. The pore resistance values of the acrylic system were larger than the experimental polyurethane, even though both systems exhibited similar values after 12 months of immersion, impyling some loss of barrier properties.

Taking into consideration the system with the best behavior after all measurements in all tests, the experimental silicone formulation exhibited the best behavior 5 times, followed by the reference silicone formulation with 3 times and the experimental polyurethane and anticorrosive polyurethane systems with 1 time each.

Also, the different behavior observed especially for the experimental polyurethane system, in terms of hardness increase and for the acrylic system, in terms of checking presence, could denote that the immersion test imposes smaller stresses on these systems compared to salt spray and UV aging. On the other hand, silicone systems exhibited low intensity blistering, which was not observed during salt spray and UV aging. Despite that, they exhibited the best behavior during their 12-month immersion.

With regard to the results from physical and mechanical properties:

- All systems exhibited low transmission rate in water liquid
- Cupping: reference silicone exhibited the best performance, followed by the experimental polyurethane.
- Dirt pick-up: experimental polyurethane exhibited the best performance, followed by the reference silicone.
- Chalking: only the acrylic system exhibited chalking.

Hence, reference silicone and experimental polyurethane system were even after physical and mechanical properties related tests.

Chapter 8

Conclusions of the PhD thesis

- Assessment of the anticorrosion efficiency of scribed coated specimens during salt spray exposure revealed the better behavior of the experimental polyurethane system with 2% immobilized Econea, followed by the experimental silicone system, the commercial silicone system and finally the commercial SPC acrylic based system. Hence, the newly developed experimental systems surpassed the known anticorrosion efficiency of commercial products, however, between the two experimental formulations, the polyurethane coating exhibited superior performance in flawed condition.The better behavior provided by the Exp. PU1 system was verified through the mixture of the more protective oxides and the least harmful of the oxyhydroxides present as corrosion phases, accompanied by small degree paint deformation, leading to compact corrosion products, which could provide some sealing to the substrate.

- With regard to the corrosion behavior of a representative coated sample with scribes during salt spray exposure, modified restricted diffusion impedance described mass transport of oxygen after 6 and 8 weeks of experiment. After 12 weeks, diffusion impedance could be either modified restricted or modified transmissive, while a decrease in corrosion resistance was observed, indicating that oxygen diffusion was not hindered by the corrosion layer. As a result, corrosion accelerated beyond 8 weeks of exposure in the salt spray chamber.

- The towing tests performed on the flat plate, using 40 and 80-grit sandpapers, revealed that the experimentally calculated equivalent sand roughness height (k_s), according to Schlichting's resistance formula for sand roughened plates, was in close proximity to the nominal roughness of the sandpapers, hence, ensuring their validity. In this way, an initial estimation of k_s value for uniformly rough surfaces could be determined experimentally.

- A more precise estimation of the rough regime and the roughness Reynolds number would require collapse of the experimental roughness functions of the sandpapers onto the Nikuradse (universal) roughness function. This procedure revealed that the appropriate roughness length scale would be 1.7 times the initially estimated k_s, accounting for the polydispersity of the sandpapers. Also, it was observed that the last two data of the 40-grit

roughness function lay in the fully rough regime, which was not readily apparent from the $1000C_F$-Re graph, where a plateau, implying fully rough regime,was obtained for both sandpapers and for the last four data in the highest Reynolds numbers.

- Towing tests of the flat plate painted with the various antifouling systems revealed that, in the laboratory scale the silicone and polyurethane formulations exhibited similar hydrodynamic behavior, fluctuating around the smooth condition, whereas the acrylic system exhibited the highest resistance increase of all. The roughness functions exhibited very good correlation with the Colebrook–type roughness function, which usually describes antifouling paints.

- Extrapolation of smooth model resistance to ship scale revealed the higher total resistance coefficient (C_T) predicted by the Froude method, compared to the ITTC 78 method. Moreover, for the same extrapolation method, the use of Bowden-Davidson formula for correlation allowance lead to higher C_T values, compared to the Townsin's formula for roughness allowance.

- The two versions of the newly proposed methodology for extrapolation of rough model results in ship scale, based on Schlichting diagram for sand roughened plates, provided an upper and lower boundary in the calculated C_T, compared to the extrapolated results for smooth model and for rough plate with 40 and 80-grit sandpapers.

- Antifouling performance assessment in static immersion revealed that the acrylic-based system exhibited the best behavior. However, this paint is based on biocides leaching. From the environmentally friendly paints, the experimental silicone system exhibited the best antifouling behavior. Moreover, in terms of physical damage, the experimental silicone system was the best candidate of all. As a result, in real conditions, where the foulers would be easily removed due to friction, the experimental silicone formulation would provide a long-lasting efficient behavior. Moreover, the barrier properties of the Exp. Si system were retained almost unaffected during the test. Hence, the experimental silicone formulation would be an efficient antifouling and anticorrosive solution for marine applications, if some precautions are followed, concerning its soft elastomeric nature. Finally, the experimental polyurerhane paints (Exp. PU1 and Exp. PU2) would be unsuitable for antifouling purposes.

- Accelerated aging tests in salt spray chamber, UV climatic chamber and through immersion in artificial seawater on intact coated specimens revealed the best behavior of the experimental silicone system (most stable behavior), followed by the reference silicone and, finally, by the Exp. PU1 and the anticorrosive PU system, in terms of 60° gloss, König hardness and discoloration.

- In terms of electrical properties, all systems retained their barrier properties unaffected during salt spray and UV tests. With regard to the laboratory immersion tests, the silicone systems retained a capacitive response throughout the test, while the acrylic and

experimental polyurethane sytems exhibited both capacitive and capacitive/ pore resistance responses on occasions, not necessarily consistent with the duration of immersion, exhibiting, however, after 12 months some loss of barrier properties. Hence, combining the electrochemical results with the previous observations for the rest of the properties, the Exp. Si system exhibited the best behavior overall after accelerated aging on intact specimens.

- With regard to the standardized tests: Water liquid transmission rate was low for all systems, chalking characterized only the acrylic-based paint, resistance to deep drawing was larger for the reference silicone formulation followed by the experimental polyurethane system (Exp. PU1), while the results were opposite for the dirt pick-up test (weathering test for quantification of dirt collection). Hence, reference silicone and experimental polyurethane system were even after physical and mechanical properties related tests.

As a result, the best anticorrosion efficiency in flawed condition (judging by the observed corrosion phases) was provided by the Exp. PU1 system, followed by the Exp. Si formulation. In intact state, the Exp. Si system exhibited the most stable characteristics after accelerated aging. In terms of hydrodynamic efficiency, polyurethane and silicone systems exhibited similar behavior in laboratory scale, being close to the smooth condition. The Colebrook-type roughness function could potentionally describe all systems. In terms of antifouling efficiency, the Acrylic system would be ideal in static immersion, however, the Exp Si system would be the best candidate in real conditions, combining also efficient barrier properties and minimum physical damage, if precautions during ship handling or maneuvering are followed. On the contrary, neither of the examined experimental polyurethane formulations would be suitable as an antifouling paint. Finally, Ref. Si and Exp. PU1 systems exhibited the best behavior after physical and mechanical properties related tests. From these observations it becomes apparent that an ideal paint does not exist. Apparently, if the primary criteria for comparison are the antifouling and hydrodynamic efficiency, which are crucial for an antifouling system, the experimental silicone (Exp. Si) formulation would be the most appropriate, environmentally friendly candidate.

Chapter 9

Innovation of the PhD thesis

The innovative character of the Thesis is summarized in the following points:

- The present study focused on the evaluation of newly developed experimental marine antifouling painting systems, which were formulated according to a newly proposed process, based on biocide immobilization into the polymeric matrix. In this way, the mode of action of these systems would be by contact and not through, the currently widespread, leaching.

- The evaluation of the experimental systems was attained through examination of their antifouling, anticorrosion and hydrodynamic efficiency, as well as, through assessment of their physical and mechanical properties. For reasons of comparison commercial painting systems were also examined. Hence, this Thesis approaches the subject of antifouling paint evaluation thoroughly, delving into all the potential disciplines that could be acquired, in order to make an as rounded an investigation as possible, in terms of paint efficiency.

More specifically, the innovative points per chapter are presented below:

- With regard to the salt spray tests in scribed condition (Chapters 1 and 2): this study links the nature of the corrosion products in the scratched area with the paint efficiency. More specifically, this study combined the degree of paint deformation in the area of the scribes with the nature of the formed corrosion products and their ability to provide protection to the metallic substrate. For identification of rust morphologies, SEM observation, as well as XRD and Raman spectroscopy measurements were conducted, which led to very complex spectra, including mixtures of iron oxides and oxy-hydroxides, making their interpretation quite challenging and innovative. Also, this study could also serve as a general methodology when examining the anticorrosion efficiency of coated scribed samples (irrespectively of the service conditions that the organic coating is intended for).

- With regard to the electrochemical impedance spectroscopy (EIS) examination of scribed coated specimens after salt spray testing (Chapter 3): this study aimed at correlating the EIS spectra with actual physical processes that affect corrosion over time. To this

purpose, the appropriate impedance mechanism for description of dissolved oxygen diffusion was sought. This study includes three innovative characteristics: the first is that it presents and compares characteristic models of diffusion impedance, by applying the PSO optimization procedure, in order to examine the degree that each of the examined theoretical impedance mechanisms could describe the experimental EIS curves. Comparison of the PSO results with the results from the CNLLS procedure is also performed. The second is that it compares the two basic theories that describe steel corrosion (finite-length diffusion and porous electrode theory), while the third is that it compares the two most commonly used equivalent circuits in the literature (Randles and Orazem-Tribollet). Once more, this research could also serve as a general guideline for the interpretation of complex EIS spectra. Finally, taking into consideration the selected diffusion impedance mechanisms, a physical model concerning the structure of the corrosion layer over the steel substrate was proposed, as well as the mode of oxygen diffusion through the pores of this corrosion layer.

- With regard to the hydrodynamic investigation of roughness effect on ship resistance using flat plate and model towing tests (Chapter 4): the new insight provided by this work is that the flat plate was very thin, only 3 mm thick, when in the literature there are reports for 3.2 mm. Moreover, a newly designed experimental setup was constructed for the need of the present experiments. The plate was tested in both smooth and rough condition and the results verified the validity of the newly developed experimental setup, ensuring that Schlichting's formula for sand roughened plates could be applied, in order to make an initial estimation of the equivalent sand roughness height (k_s) for a uniformly rough surface in the fully rough regime. Also, another novelty is that a newly proposed extrapolation method from rough model data in ship scale, based on Schlichting diagrams for rough flat plates, was applied. Finally, a thorough comparison between all the extrapolation methods for both the plate and the ship was attempted.

  Despite these novelties, this work also encompasses an as thorough an investigation as possible, in terms of extrapolating smooth model data in ship scale (comparison of Froude and ITTC 78 methods), the correlation allowances usually encountered and their effects on measured resistance, a wide examination of different trip wires for the flat plate until the optimum is determined and finally the examination of the thin plate with the home made experimental setup in rough condition and the agreement with the Nikuradse results (Nikuradse curve also produced from our laboratory from Nikuradse data). With these experiments, data were provided with regard to the resistance components in rough condition, in order to get an insight of ship C_F, and, finally be able to estimate ship's C_p.

- With regard to the hydrodynamic investigation of paint roughness on ship resistance using flat plate towing tests (Chapter 5): the innovation of this study is that newly developed experimental antifouling painting systems were applied on top of the flat plate of Chapter 3 and a comparison was made, with regard to their hydrodynamic efficiency.

For comparative reasons commercial painting systems were also examined. Generally, the calculated roughness functions were in accordance with the Colebrook-type roughness function.

- With regard to the field tests of commercial and experimental marine antifouling paints in Elefsis Gulf (Chapter 6): similarly to previous chapters, the novelty of the present work lies on the fact that newly designed experimental antifouling paints were examined in the field. In addition, this work could serve as a methodology for performance and presentation of field tests. Finally, this research included also electrochemical, physical properties and mechanical properties examination during immersion, comprising a rounded investigation in the field of static immersion tests.

- With regard to the mechanical testing of experimental and commercial antifouling systems and the electrochemical investigation thereof after accelerated aging tests on intact specimens (Chapter 7): a comprehensive study was performed on newly developed antifouling coatings, in terms of accelerated aging examination for anticorrosion efficiency in intact state (through electrochemical examination), along with mechanical and optical properties determination at frequent intervals. Moreover, standardized mechanical tests were performed for assessment of their mechanical integrity. Commercial products were also examined for comparison. The results of this research provided a ranking among the experimental painting systems and also in comparison to currently used commercial products.

In other words, this thesis could serve as a guide for the selection, performance and presentation of the appropriate experiments, in order to efficiently evaluate and compare organic coatings, generally, or antifouling marine painting systems, specifically.

Chapter 10

Suggestions for further research

Some suggestions for further research are presented below:

- With regard to the salt spray tests in scribed condition: a greater amount of scribed coated specimens could be examined, in order to be able to propose a general mechanism for the corrosion of coated steel in scribed condition, during salt spray tests.
- With regard to the hydrodynamic investigation: the experiments performed on the flat plate with 3D printed fouling could be analyzed, in order to calculate the equivalent sand roughness height of this arbitrarily rough surface and estimate the effect in ship scale. Also, 3D fouling could be applied on propellers (currently scheduled) and ship models, in order to examine the effect in resistance compared to the smooth condition in laboratory scale and, if possible, in ship scale. Surfaces with engineering roughness could also be examined. Finally, the experiments could be conducted at higher Reynolds numbers.
- With regard to the field tests: experiments for longer duration could be performed, possibly for 2 years, in order to gain a more detailed insight, with regard to the antifouling efficiency of antifouling marine paints. Moreover, a site at the open sea could be used, while the examination could be performed every month. Finally, dynamic tests could be performed, in order to compare the results with the findings from static immersion.

Chapter 11

Publications

The work that was published during this PhD is presented right below:

Scientific journals-Published

1. Kiosidou, E.D., Liarokapis, D.E., Tzabiras, G.D., Pantelis., D.I (2017). "Experimental investigation of roughness effect on ship resistance using flat plate and model towing tests". *Journal of Ship Research* 61 (2) 75-90. http://dx.doi.org/10.5957/JOSR.61.2.160044

2. Kiosidou, E.D., Karantonis, A., Pantelis., D.I., Silva, E.R., Bordado, J.C.M (2017). "Rust morphology characterization of polyurethane and acrylic-based marine antifouling paints after salt spray test on scribed specimens". *Journal of Coatings Technology and Research* 14 (6) 1381-1395. https://doi.org/10.1007/s11998-017-9939-0

3. Kiosidou, E.D., Karantonis, A., Pantelis., D.I., Silva, E.R., Bordado, J.C.M (2017)."Rust morphology characterization of silicone-based marine antifouling paints after salt spray test on scribed specimens". *Journal of Coatings Technology and Research* 14 (2) 333-345. https://doi.org/10.1007/s11998-016-9851-z 4

4. Kiosidou, E.D., Karantonis, A., Pantelis., D.I. (2014). "Evaluation of barrier properties of antifouling coatings on naval steel". *Chemical Engineering Transactions* 41 301-306. DOI: 10.3303/CET1441051

International Conferences

1. Kiosidou, E.D., Venetis, A.S., Liarokapis, D.E., Tzabiras, G.D., Pantelis., D.I (2016). "Experimental investigation of roughness effect on the resistance of a flat plate". *Proc. 3rd International Conference on Maritime Technology and Engineering (MARTECH)*, July 4-6, Lisbon, Portugal. ISBN 978-1-138-03000-8 (oral presentation)

2. Kiosidou, E.D., Karantonis, A., Pantelis., D.I. (2014). "A multidisciplinary study for the evaluation of barrier properties of antifouling coatings on naval steel". *Proc. 10th*

European Symposium on Electrochemical Engineering (ESEE), September 28-October 2, Chia Laguna Resort, Domus de Maria (CA), Sardinia, Italy. (poster)

Chapter 12

Curriculum Vitae

Name: Evangelia Kiosidou; e-mail: eva.kiosidou@gmail.com; Tel: 0030-6939638535

Education

2012-2018	BSc, Business Administration, Athens University of Economics and Business (enrolled after entry examination) G.P.A. 8.2/10 ("Very Good")
6/2011-3/2018	PhD, School of Naval Architecture and Marine Engineering, National Technical University of Athens (NTUA) Thesis title: "Study of Environmentally Friendly Antifouling Coatings to Optimize the Energy Efficiency of Ships"
10/2005-2/2011	Diploma (5-year degree), Naval Architecture and Marine Engineering, NTUA Graduation Thesis Title: "Study of austenitic stainless steel AISI 316L butt-welding of thick plates using the FCAW method"–Grade: 10/10 G.P.A. 8.3/10 ("Very Good")

Publications

Journal Papers

1. **Kiosidou, E.D.**, Liarokapis, D.E., Tzabiras, G.D., Pantelis., D.I (2017). "Experimental investigation of roughness effect on ship resistance using flat plate and model towing tests". *Journal of Ship Research* 61 (2) 75-90. http://dx.doi.org/10.5957/JOSR.61.2.160044
2. **Kiosidou, E.D.**, Karantonis, A., Pantelis., D.I., Silva, E.R., Bordado, J.C.M (2017). "Rust morphology characterization of polyurethane and acrylic-based marine antifouling paints after salt spray test on scribed specimens". *Journal of Coatings Technology and Research* 14 (6) 1381-1395. https://doi.org/10.1007/s11998-017-9939-0
3. **Kiosidou, E.D.**, Karantonis, A., Pantelis., D.I., Silva, E.R., Bordado, J.C.M (2017)."Rust morphology characterization of silicone-based marine antifouling paints after salt spray

test on scribed specimens". *Journal of Coatings Technology and Research* 14 (2) 333-345. https://doi.org/10.1007/s11998-016-9851-z 4

4. **Kiosidou, E.D.**, Karantonis, A., Pantelis., D.I. (2014). "Evaluation of barrier properties of antifouling coatings on naval steel". *Chemical Engineering Transactions* 41 301-306. DOI: 10.3303/CET1441051

Conference Papers

1. **Kiosidou, E.D.**, Venetis, A.S., Liarokapis, D.E., Tzabiras, G.D., Pantelis., D.I (2016). "Experimental investigation of roughness effect on the resistance of a flat plate". *Proc. 3rd International Conference on Maritime Technology and Engineering (MARTECH)*, July 4-6, Lisbon, Portugal. ISBN 978-1-138-03000-8
2. **Kiosidou, E.D.**, Karantonis, A., Pantelis., D.I. (2014). "A multidisciplinary study for the evaluation of barrier properties of antifouling coatings on naval steel". *Proc. 10th European Symposium on Electrochemical Engineering (ESEE)*, September 28-October 2, Chia Laguna Resort, Domus de Maria (CA), Sardinia, Italy.
3. Wolgamot, H., Zhang, W., **Kiosidou, E.**, Kim, S.H., Bashir. M.B. (2013). "Considerations for seabed rare earth mining in the Pacific". *Proc. ASME 32nd International Conference on Ocean, Offshore and Arctic Engineering*, OMAE 2013, June 9-14, Nantes, France (OMAE 2013-10844).
4. **Kiosidou, E.D.**, Kyriakongonas, A.P., Papazoglou, V. (2010). "Study of austenitic stainless steel AISI 316L butt welding of thick plates using the FCAW method". *Proc. 4th Pan-Hellenic Conference on Metallic Materials*, November 4-5, Thessaloniki, Greece, ISBN: 978-960-6865-31-2.

Book

Bashir, M., Kim, S.H., **Kiosidou, E.D.**, Wolgamot, H., Zhang, W. (2012). "A Concept for Seabed Rare Earth Mining in the Eastern South Pacific". The LRET Collegium 2012 Series: Volume 1. Series Editors: R.A. Shenoi, P.A. Wilson, S.S. Bennett. ISBN: 978-0-854-32949-6

Presentations

1. **Kiosidou, E.D.** (2016). "Experimental investigation of roughness effect on the resistance of a flat plate". Oral presentation of the performed work, at the 3rd International Conference on Maritime Technology and Engineering (MARTECH), July 4-6, Lisbon, Portugal.
2. **Kiosidou, E.D.** (2012). "A Concept for Seabed Rare Earth Mining in the Eastern South Pacific". Seminar speech with regard to the work performed during "The LRET Research Collegium in Seabed Exploitation", at NTUA, October 18, Athens, Greece.
3. **Kiosidou, E.D.**, Bashir, M., Kim, S.H., Wolgamot, H., Zhang, W. (2012). "A Concept for Seabed Rare Earth Mining in the Eastern South Pacific". Oral presentation of the

work performed during "The LRET Research Collegium in Seabed Exploitation", at Southampton University, September 7, Southampton, UK.

4. **Kiosidou, E.D.** (2010). "Study of austenitic stainless steel AISI 316L butt welding of thick plates using the FCAW method". Oral presentation of the performed work, at the 4th National Convention of Metallic Materials, November 4-5, Thessaloniki, Greece.

Participation in European Research Projects

1. 11/2011–1/2015, **FP7: FOUL-X-SPEL**. "Environmentally Friendly Antifouling Technology to Optimize the Energy Efficiency of Ships", European Collaborative Project.
2. 5/11/2012–16/11/2012, **FP7: SFERA (Solar Facilities for the European Research Area)**. "Accelerated aging of various organic coatings by concentrated solar energy (AgeCoSol)", Plataforma Solar de Almeria (PSA), Spain.
3. 24/9/2012–11/10/2012, **FP7: SFERA (Solar Facilities for the European Research Area)**. "Accelerated aging of various organic coatings by concentrated solar energy (AgeCoSol)", Plataforma Solar de Almeria (PSA), Spain.

Certified Courses

1. 13/7/2015–18/7/2015, **IIMEC 2015 Summer School: "Advanced Material Systems: Experimentation & Modeling"**, Thessaloniki, Greece. Certificate of successful completion, Aristotle University of Thessaloniki.
2. 5/11/2012–16/11/2012, FP7: **SFERA (Solar Facilities for the European Research Area)**. "Accelerated aging of various organic coatings by concentrated solar energy (AgeCoSol)". Certificate of successful completion, SFERA.
3. 24/9/2012–11/10/2012, FP7: **SFERA (Solar Facilities for the European Research Area)**. "Accelerated aging of various organic coatings by concentrated solar energy (AgeCoSol)". Certificate of successful completion, SFERA.
4. 16/7/2012–7/9/2012, **Lloyd'As Register Foundation (LRF): "The LRET Research Collegium in Seabed Exploitation"**, Southampton ,UK. Certificate of successful completion, University of Southampton.
5. 10/2011–6/2012: **Examination on 5 pre-doctoral subjects from the MSc. program "Materials Science and Engineering", NTUA**–Certificate of successful examination, G.P.A. 9.8/10, NTUA

Teaching Duties at NTUA as a PhD Candidate

2012-2015 *Materials Science and Technology I (Metallic Materials)*
Type of class: Undergraduate

Duties:"Thermal Treatment of Steel (Laboratory Class)". Teaching in laboratory, designing and grading of assignments.

2011-2015 *Materials Science and Technology II (Non-Metallic Materials, Corrosion)*
Type of class: Undergraduate
Duties: "Anodic Oxidation of Aluminium (Laboratory Class)". Teaching in laboratory, designing and grading of assignments.

2011-2015 *Welding Science and Technology*
Type of class: Undergraduate/Graduate
Duties: "Introduction to stainless steels and metallurgic phenomena during their welding", "Experimental Measurement of Residual Stresses using the Hole Drilling Method", "Metallurgic phenomena during welding of AH 36 high tensile steel". Designing of presentations, teaching in class.

Working Experience/ Technical Reports/Case Studies

Technical report

2013, "Technical report with the results of accelerated aging experiments with solar radiation on organic coatings", for CHROTEX Company. **E. Kiosidou**, A. Karantonis, D. Pantelis, Report No. STL-348-F13, Athens, May 2013 (in greek).

Case study

2013, "Study of the degradation causes of the bulk-carrier M/V MAX (former ZAIRA), for the American Bureau of Shipping (ABS)". D.I. Pantelis, **E. Kiosidou**, T. Tsiourva, G. Kourouklis, D. G. Karalis, Report No. STL-352-F13, Athens, July 2013 (in greek).

Student internship

2008, Omega Navigation Enterprises Ltd. (July-August), 2-month student internship at Operations Department

2007, Omega Navigation Enterprises Ltd. (July-August), 2-month student internship at Technical Department

Distinctions

Scholarships

1. 2018,"Thomaidio Award" from NTUA, for the publication: Kiosidou *et al.* (2017), "Rust morphology characterization of silicone-based marine antifouling paints after salt spray test on scribed specimens". *Journal of Coatings Technology and Research* 14 (2) 333-345.
2. 2012-2016, Scholarship for PhD Research, Special Account for Research Grants, National Technical University of Athens.

3. 2015, IIMEC 2015 Summer School Scholar: "Advanced Material Systems: Experimentation & Modeling", July 13-18, 2015, Thessaloniki, Greece.
4. 2012, Lloyd's Register Foundation (LRF) Scholar: "The LRET Research Collegium in Seabed Exploitation", July 16-September 7, 2012, University of Southampton.
5. 2011, "Thomaidio Award" from NTUA, for excellent grade performance during the academic year 2009-2010.
6. 2010, Scholarship from National State Scholarship Foundation, for being ranked 1st among the fourth year undergraduate students, for year 2008-2009.
7. 2009, Scholarship from National State Scholarship Foundation, for being ranked 2nd among the third year undergraduate students, for year 2007-2008.
8. 2005-2010, "Michail Stamelos" annual scholarship especially for an honor NTUA undergraduate student that has graduated 1st from High School of Kimi, Evia.
9. 2005, Reward from Eurobank, for being ranked among the 1000 High School Graduates with the highest final grade in Greece.

Awards

1. 2017, Award from Technical Chamber of Greece for honor alumni students with the highest graduation G.P.A. of NTUA.
2. 2012, The Lloyd's Register Educational Trust (LRET) Achievement Award for the LRET Research Collegium in "Seabed Exploitation" participants.
3. 2010, Award from National State Scholarship Foundation for being ranked 1st among the fourth year undergraduate students, for year 2008-2009.

Skills

Foreign Languages

- Holder of Certificate of Proficiency in English (Level: C2)
- Holder of Zertifikat Deutsch (Level: B1)

Computer Skills

- Knowledge of AUTOCAD 2010 Essentials: AUTODESK Certification, April 26, 2010, InfoStudio, Athens, Greece
- ANSA/Meta Certificate: Certificate of attendance of the ANSA & Meta for composites course, July 16, 2015, BETA CAE Systems S.A., Thessaloniki, Greece.

Technical Skills

- Programming Languages: Matlab, Latex
- Naval Design Programs: Tribon, AVEVA
- Electrochemical measurements programs: Zplot, PowerSuite, Versastudio

- Skills with regard to accelerated aging and characterization of coated metals: Operation of QFOG CCT1100 salt spray chamber, Operation of Angelantoni ACS Global Test System 600 climatic chamber, Accelerated aging on organic coatings, Mechanical tests for organic coatings, Antifouling assessment of marine coatings
- Skills with regard to metallographic investigation: Metallographic preperation of metals, optical examination, hardness measurements

Sports/Interests

Gym, Yoga, Zumba, Reading, Travelling

Bibliography

[1] G. Bierwagen, D. Tallman, J. Li, L. He, and C. Jeffcoate, "EIS studies of coated metals in accelerated exposure," *Progress in Organic Coatings*, vol. 46, no. 2, pp. 149–158, 2003.

[2] X. Yang, C. Vang, D. Tallman, G. Bierwagen, S. Croll, and S. Rohlik, "Weathering degradation of a polyurethane coating," *Polymer Degradation and Stability*, vol. 74, no. 2, pp. 341–351, 2001.

[3] X. F. Yang, D. Tallman, G. Bierwagen, S. Croll, and S. Rohlik, "Blistering and degradation of polyurethane coatings under different accelerated weathering tests," *Polymer Degradation and Stability*, vol. 77, no. 1, pp. 103–109, 2002.

[4] G. P. Bierwagen, "Reflections on corrosion control by organic coatings," *Progress in Organic Coatings*, vol. 28, no. 1, pp. 43–48, 1996.

[5] B. Skerry, A. Alavi, and K. Lindgren, "Environmental and electrochemical test methods for the evaluation of protective organic coatings," *JCT, Journal of Coatings Technology*, vol. 60, no. 765, pp. 97–106, 1988.

[6] D. M. Yebra, S. Kiil, and K. Dam-Johansen, "Antifouling technology–past, present and future steps towards efficient and environmentally friendly antifouling coatings," *Progress in Organic Coatings*, vol. 50, no. 2, pp. 75–104, 2004.

[7] S. A. Kumar, T. Balakrishnan, M. Alagar, and Z. Denchev, "Development and characterization of silicone/phosphorus modified epoxy materials and their application as anticorrosion and antifouling coatings," *Progress in Organic Coatings*, vol. 55, no. 3, pp. 207–217, 2006.

[8] S. J. Oh, D. Cook, and H. Townsend, "Atmospheric corrosion of different steels in marine, rural and industrial environments," *Corrosion Science*, vol. 41, no. 9, pp. 1687–1702, 1999.

[9] L. T. H. Lien and H. L. Hong, *Characteristics of corrosion product layer formed on weathering steel exposed to the tropical climate of Vietnam*. Scientific Research Publishing, 2013.

[10] K. García, A. Morales, C. Arroyave, C. Barrero, and D. Cook, "Mössbauer characterization of rust obtained in an accelerated corrosion test," *Hyperfine interactions*, vol. 148, no. 1-4, pp. 177–183, 2003.

[11] Y. Takahashi, E. Matsubara, S. Suzuki, Y. Okamoto, T. Komatsu, H. Konishi, J. Mizuki, and Y. Waseda, "In-situ X-ray diffraction of corrosion products formed on iron surfaces," *Materials transactions*, vol. 46, no. 3, pp. 637–642, 2005.

[12] M. Morcillo, I. Díaz Ocaña, H. Cano, *et al.*, "Atmospheric corrosion of mild steel," *Revista de Metalurgia*, vol. 47, no. 5, pp. 426–444, 2011.

[13] R. A. Antunes, R. U. Ichikawa, L. G. Martinez, and I. Costa, "Characterization of corrosion products on carbon steel exposed to natural weathering and to accelerated corrosion tests," *International Journal of Corrosion*, vol. 2014, 2014.

[14] A. Morales, "An X-ray diffraction study of corrosion products from low carbon steel," *Revista de metalurgia*, pp. 28–31, 2003.

[15] H. Bano, "Morphology and composition of corrosion products formed on painted mild steel in marine atmosphere after 4, 8 and 12 months exposure," *International Journal of Advanced Research*, vol. 3, no. 4, pp. 318–325, 2015.

[16] M. Morcillo, J. Alcántara, I. Díaz, B. Chico, J. Simancas, and D. de la Fuente, "Marine atmospheric corrosion of carbon steels," *Revista de Metalurgia*, vol. 51, no. 2, pp. 10–3989, 2015.

[17] D. De la Fuente, I. Diaz, J. Simancas, B. Chico, and M. Morcillo, "Long-term atmospheric corrosion of mild steel," *Corrosion Science*, vol. 53, no. 2, pp. 604–617, 2011.

[18] S. Li and L. Hihara, "A micro-Raman spectroscopic study of marine atmospheric corrosion of carbon steel: The effect of akaganeite," *Journal of The Electrochemical Society*, vol. 162, no. 9, pp. C495–C502, 2015.

[19] C. Rémazeilles and P. Refait, "On the formation of β-FeOOH (akaganéite) in chloride-containing environments," *Corrosion Science*, vol. 49, no. 2, pp. 844–857, 2007.

[20] Y. Ma, Y. Li, and F. Wang, "The effect of β-FeOOH on the corrosion behavior of low carbon steel exposed in tropic marine environment," *Materials Chemistry and Physics*, vol. 112, no. 3, pp. 844–852, 2008.

[21] F. Dubois, C. Mendibide, T. Pagnier, F. Perrard, and C. Duret, "Raman mapping of corrosion products formed onto spring steels during salt spray experiments. A correlation between the scale composition and the corrosion resistance," *Corrosion Science*, vol. 50, no. 12, pp. 3401–3409, 2008.

[22] S. J. Oh and D. Cook, "Characterization of the corrosion products formed on carbon steel in a marine environment," *Journal of the Korean Physical Society*, vol. 36, no. 2, pp. 106–11O, 2000.

[23] E. Silva, O. Ferreira, A. Tulcidas, R. Bayon, A. Igartua, G. Mendoza, O. Areitioaurtena, and J. Bordado, "Non-releasing biocidal coatings: A new eco-friendly strategy to prevent marine biofouling," in *Proc. Shipping in Changing Climates Conference*, 2015.

[24] E. R. Silva, O. Ferreira, and J. C. Bordado, "Functionalization. process for biocides immobilisation in polymeric matrices," *Patent application, WO2016/093719 A1*, 2016.

[25] W. Kim, C.-Y. Suh, S.-W. Cho, K.-M. Roh, H. Kwon, K. Song, and I.-J. Shon, "A new method for the identification and quantification of magnetite–maghemite mixture using conventional X-ray diffraction technique," *Talanta*, vol. 94, pp. 348–352, 2012.

[26] S. Das and M. J. Hendry, "Application of Raman spectroscopy to identify iron minerals commonly found in mine wastes," *Chemical Geology*, vol. 290, no. 3, pp. 101–108, 2011.

[27] P. Colomban, *Potential and drawbacks of Raman (micro) spectrometry for the understanding of iron and steel corrosion.* INTECH Open Access Publisher, 2011.

[28] J. Dünnwald and A. Otto, "An investigation of phase transitions in rust layers using raman spectroscopy," *Corrosion Science*, vol. 29, no. 9, pp. 1167–1176, 1989.

[29] D. De Faria, S. Venâncio Silva, and M. De Oliveira, "Raman microspectroscopy of some iron oxides and oxyhydroxides," *Journal of Raman spectroscopy*, vol. 28, no. 11, pp. 873–878, 1997.

[30] M. Legodi and D. De Waal, "The preparation of magnetite, goethite, hematite and maghemite of pigment quality from mill scale iron waste," *Dyes and Pigments*, vol. 74, no. 1, pp. 161–168, 2007.

[31] D. Guzonas, P. Rochefort, and C. Turner, "Corrosion product characterisation by fibre optic Raman spectroscopy," *Canadian Nuclear Society Societe Nucleaire Canadienne*, p. 628, 1998.

[32] M. Hanesch, "Raman spectroscopy of iron oxides and (oxy) hydroxides at low laser power and possible applications in environmental magnetic studies," *Geophysical Journal International*, vol. 177, no. 3, pp. 941–948, 2009.

[33] R. A. Antunes, I. Costa, and D. L. A. d. Faria, "Characterization of corrosion products formed on steels in the first months of atmospheric exposure," *Materials Research*, vol. 6, no. 3, pp. 403–408, 2003.

[34] S. Agarwala, Z. Lim, E. Nicholson, and G. Ho, "Probing the morphology-device relation of Fe_2O_3 nanostructures towards photovoltaic and sensing applications," *Nanoscale*, vol. 4, no. 1, pp. 194–205, 2012.

[35] A. Raman, S. Nasrazadani, and L. Sharma, "Morphology of rust phases formed on weathering steels in various laboratory corrosion tests," *Metallography*, vol. 22, no. 1, pp. 79–96, 1989.

[36] D. C. Cook, "Spectroscopic identification of protective and non-protective corrosion coatings on steel structures in marine environments," *Corrosion Science*, vol. 47, no. 10, pp. 2550–2570, 2005.

[37] J. A. Callow and M. E. Callow, "Trends in the development of environmentally friendly fouling-resistant marine coatings," *Nature communications*, vol. 2, p. 244, 2011.

[38] M. P. Schultz and G. W. Swain, "The influence of biofilms on skin friction drag," *Biofouling*, vol. 15, no. 1-3, pp. 129–139, 2000.

[39] A. Abbott, P. Abel, D. Arnold, and A. Milne, "Cost–benefit analysis of the use of tbt: the case for a treatment approach," *Science of the total environment*, vol. 258, no. 1, pp. 5–19, 2000.

[40] M. A. Champ, "A review of organotin regulatory strategies, pending actions, related costs and benefits," *Science of the Total Environment*, vol. 258, no. 1, pp. 21–71, 2000.

[41] S. Dürr and J. C. Thomason, *Biofouling*. John Wiley & Sons, 2009.

[42] I. Omae, "Organotin antifouling paints and their alternatives," *Applied organometallic chemistry*, vol. 17, no. 2, pp. 81–105, 2003.

[43] P. Davies and G. Evrard, "Accelerated ageing of polyurethanes for marine applications," *Polymer Degradation and Stability*, vol. 92, no. 8, pp. 1455–1464, 2007.

[44] S. Quaiser, I. Lynam, M. Wind, A. Celik, and G. Kampf, "Fouling resistant polyurethanes, in particular for maritime use," Mar. 8 2006. US Patent App. 11/908,039.

[45] R. F. Brady and C. L. Aronson, "Elastomeric fluorinated polyurethane coatings for non-toxic fouling control," *Biofouling*, vol. 19, no. sup1, pp. 59–62, 2003.

[46] D. C. Webster, B. J. Chisholm, and S. J. Stafslien, "Mini-review: combinatorial approaches for the design of novel coating systems," *Biofouling*, vol. 23, no. 3, pp. 179–192, 2007.

[47] M. M. Rahman, H.-H. Chun, and H. Park, "Waterborne polysiloxane–urethane–urea for potential marine coatings," *Journal of coatings technology and research*, vol. 8, no. 3, pp. 389–399, 2011.

[48] J. Verborgt and A. A. Webb, "Solvent-free, self-polishing polyurethane matrix for use in solvent-free antifoulings," Nov. 24 2015. US Patent 9,193,875.

[49] E. Kiosidou, A. Karantonis, D. Pantelis, E. Silva, and J. Bordado, "Rust morphology characterization of silicone-based marine antifouling paints after salt spray test on scribed specimens," *Journal of Coatings Technology and Research*, vol. 14, no. 2, pp. 333–345, 2017.

[50] J. K. Saha, *Corrosion of constructional steels in marine and industrial environment: Frontier work in atmospheric corrosion.* Springer Science & Business Media, 2012.

[51] S. J. Oh, D. Cook, and H. Townsend, "Characterization of iron oxides commonly formed as corrosion products on steel," *Hyperfine interactions*, vol. 112, no. 1-4, pp. 59–66, 1998.

[52] N. Boucherit, A. Hugot-Le Goff, S. Joiret, G. Beranger, and H. Chaudanson, "Study of thin oxidation films on iron alloys by Raman spectroscopy," *Thin solid films*, vol. 174, pp. 111–116, 1989.

[53] L. Bellot-Gurlet, D. Neff, S. Reguer, J. Monnier, M. Saheb, and P. Dillmann, "Raman studies of corrosion layers formed on archaeological irons in various media," in *Journal of Nano Research*, vol. 8, pp. 147–156, Trans Tech Publ, 2009.

[54] R. J. Thibeau, C. W. Brown, and R. H. Heidersbach, "Raman spectra of possible corrosion products of iron," *Applied Spectroscopy*, vol. 32, no. 6, pp. 532–535, 1978.

[55] U. Schwertmann and R. M. Cornell, *Iron oxides in the laboratory.* John Wiley & Sons, 2008.

[56] D. De Faria and F. Lopes, "Heated goethite and natural hematite: Can Raman spectroscopy be used to differentiate them?," *Vibrational Spectroscopy*, vol. 45, no. 2, pp. 117–121, 2007.

[57] F. Gilbert, P. Refait, F. Lévêque, C. Remazeilles, and E. Conforto, "Synthesis of goethite from $Fe(OH)_2$ precipitates: Influence of Fe(II) concentration and stirring speed," *Journal of Physics and Chemistry of Solids*, vol. 69, no. 8, pp. 2124–2130, 2008.

[58] P. M. Hallam, M. Gómez-Mingot, D. K. Kampouris, and C. E. Banks, "Facile synthetic fabrication of iron oxide particles and novel hydrogen superoxide supercapacitors," *Rsc Advances*, vol. 2, no. 16, pp. 6672–6679, 2012.

[59] Y. Ma, Y. Li, and F. Wang, "Corrosion of low carbon steel in atmospheric environments of different chloride content," *Corrosion Science*, vol. 51, no. 5, pp. 997–1006, 2009.

[60] D. Koleva, K. van Breugel, J. De Wit, N. Boshkov, and A. Fraaij, "Composition and morphology of product layers in the steel/cement paste interface in conditions of corrosion and cathodic protection in reinforced concrete," *ECS Transactions*, vol. 2, no. 9, pp. 127–139, 2007.

[61] J. T. Keiser, C. W. Brown, and R. H. Heidersbach, "Characterization of the passive film formed on weathering steels," *Corrosion Science*, vol. 23, no. 3, pp. 251–259, 1983.

[62] T. Strivens and C. Taylor, "An assessment of a/c impedance as a basic research and routine testing method for studying corrosion of metals under paint films," *Materials Chemistry*, vol. 7, no. 2, pp. 199–220, 1982.

[63] C.-C. Lin and C.-X. Wang, "Correlation between accelerated corrosion tests and atmospheric corrosion tests on steel," *Journal of Applied electrochemistry*, vol. 35, no. 9, pp. 837–843, 2005.

[64] B. Fastrup and A. Saarnak, "Ac impedance of painted and scribed steel panels under atmospheric exposure," *Progress in organic coatings*, vol. 16, no. 3, pp. 277–290, 1988.

[65] J. Hu, S. Cao, and J. Xie, "Eis study on the corrosion behavior of rusted carbon steel in 3% nacl solution," *Anti-Corrosion Methods and Materials*, vol. 60, no. 2, pp. 100–105, 2013.

[66] E. Kiosidou, A. Karantonis, D. Pantelis, E. Silva, and J. Bordado, "Rust morphology characterization of polyurethane and acrylic-based marine antifouling paints after salt spray test on scribed specimens," *Journal of Coatings Technology and Research*.

[67] J. K. Saha, P. Mitra, S. Paul, and D. Singh, "Performance of different organic coatings on steel substrate by accelerated and in atmospheric exposure tests," no. 17, pp. 102–110, 2010.

[68] B. Skerry and D. Eden, "Electrochemical testing to assess corrosion protective coatings," *Progress in Organic Coatings*, vol. 15, no. 3, pp. 269–285, 1987.

[69] J.-B. Jorcin, E. Aragon, C. Merlatti, and N. Pébère, "Delaminated areas beneath organic coating: A local electrochemical impedance approach," *Corrosion Science*, vol. 48, no. 7, pp. 1779–1790, 2006.

[70] D. van Der Weijde, E. Van Westing, and J. De Wit, "Eis measurements on artificial blisters in organic coatings," *Electrochimica acta*, vol. 41, no. 7-8, pp. 1103–1107, 1996.

[71] G. Tansuğ, T. Tüken, A. Özyılmaz, M. Erbil, and B. Yazıcı, "Mild steel protection with epoxy top coated polypyrrole and polyaniline in 3.5% nacl," *Current Applied Physics*, vol. 7, no. 4, pp. 440–445, 2007.

[72] K. Jüttner, W. Lorenz, M. Kendig, and F. Mansfeld, "Electrochemical impedance spectroscopy on 3-d inhomogeneous surfaces corrosion in neutral aerated solutions," *Journal of the Electrochemical Society*, vol. 135, no. 2, pp. 332–339, 1988.

[73] J. R. Scully, "Polarization resistance method for determination of instantaneous corrosion rates," *Corrosion*, vol. 56, no. 2, pp. 199–218, 2000.

[74] M. Pech-Canul and S. Turgoose, "The electrochemical impedance response of film-covered mild steel in neutral aerated solutions," *Corrosion science*, vol. 35, no. 5-8, pp. 1445–1454, 1993.

[75] A. Bonnel, F. Dabosi, C. Deslouis, M. Duprat, M. Keddam, and B. Tribollet, "Corrosion study of a carbon steel in neutral chloride solutions by impedance techniques," *Journal of the Electrochemical Society*, vol. 130, no. 4, pp. 753–761, 1983.

[76] M. E. Orazem and B. Tribollet, *Electrochemical impedance spectroscopy*, vol. 48. John Wiley & Sons, 2011.

[77] R. De Levie, "On porous electrodes in electrolyte solution–IV," *Electrochimica acta*, vol. 9, no. 9, pp. 1231–1245, 1964.

[78] I. Frateur, C. Deslouis, M. Orazem, and B. Tribollet, "Modeling of the cast iron/drinking water system by electrochemical impedance spectroscopy," *Electrochimica acta*, vol. 44, no. 24, pp. 4345–4356, 1999.

[79] O. E. Barcia, E. D'Elia, I. Frateur, O. R. Mattos, N. Pébère, and B. Tribollet, "Application of the impedance model of de levie for the characterization of porous electrodes," *Electrochimica acta*, vol. 47, no. 13, pp. 2109–2116, 2002.

[80] V. F. Lvovich, *Impedance spectroscopy: applications to electrochemical and dielectric phenomena*. John Wiley & Sons, 2012.

[81] J. Diard, B. Le Gorrec, and C. Montella, "Diffusion impedances," *Hosted by Bio-Logic@ http://biologic. info*, 2012.

[82] A. Lasia, *Electrochemical impedance spectroscopy and its applications*. Springer, 2014.

[83] E. Barsoukov and J. R. Macdonald, *Impedance spectroscopy: theory, experiment, and applications*. John Wiley & Sons, 2005.

[84] J. Dawson and D. John, "Diffusion impedance–an extended general analysis," *Journal of Electroanalytical Chemistry and Interfacial Electrochemistry*, vol. 110, no. 1-3, pp. 37–47, 1980.

[85] C. Ho, I. Raistrick, and R. Huggins, "Application of a-c techniques to the study of lithium diffusion in tungsten trioxide thin films," *Journal of The Electrochemical Society*, vol. 127, no. 2, pp. 343–350, 1980.

[86] R. Cabanel, G. Barral, J. P. Diard, B. Le Gorrec, and C. Montella, "Determination of the diffusion coefficient of an inserted species by impedance spectroscopy: application to the $H/H_xNb_2O_5$ system," *Journal of Applied Electrochemistry*, vol. 23, pp. 93–97, Feb 1993.

[87] D. Bastidas, "Interpretation of impedance data for porous electrodes and diffusion processes," *Corrosion*, vol. 63, no. 6, pp. 515–521, 2007.

[88] J. Bisquert, G. Garcia-Belmonte, P. Bueno, E. Longo, and L. Bulhões, "Impedance of constant phase element (cpe)-blocked diffusion in film electrodes," *Journal of Electroanalytical Chemistry*, vol. 452, no. 2, pp. 229–234, 1998.

[89] J. Bisquert and A. Compte, "Theory of the electrochemical impedance of anomalous diffusion," *Journal of Electroanalytical Chemistry*, vol. 499, no. 1, pp. 112–120, 2001.

[90] C. Ni and L. Lu, "Electrochemical impedance and modelling studies of the corrosion of three commercial stainless steels in molten carbonate," *International Journal of Corrosion*, vol. 2014, 2014.

[91] M. Kendig, F. Mansfeld, and S. Tsai, "Determination of the long term corrosion behavior of coated steel with ac impedance measurements," *Corrosion Science*, vol. 23, no. 4, pp. 317–329, 1983.

[92] K. Korfiatis, "Experimental study of roughness effect on ship resistance," 2014. Diploma Thesis, School of Naval Architecture and Marine Engineering, National Technical University of Athens.

[93] L. D. Chambers, K. R. Stokes, F. C. Walsh, and R. J. Wood, "Modern approaches to marine antifouling coatings," *Surface and Coatings Technology*, vol. 201, no. 6, pp. 3642–3652, 2006.

[94] P. S. Granville, *The frictional resistance and turbulent boundary layer of rough surfaces*. Hydromechanics Laboratory, 1958.

[95] K. A. Flack, M. P. Schultz, and W. B. Rose, "The onset of roughness effects in the transitionally rough regime," *International Journal of Heat and Fluid Flow*, vol. 35, pp. 160–167, 2012.

[96] M. P. Schultz and K. A. Flack, "Turbulent boundary layers on a systematically varied rough wall," *Physics of Fluids*, vol. 21, no. 1, p. 015104, 2009.

[97] K. A. Flack, M. P. Schultz, J. M. Barros, and Y. C. Kim, "Skin-friction behavior in the transitionally-rough regime," *International Journal of Heat and Fluid Flow*, vol. 61, pp. 21–30, 2016.

[98] J. Nikuradse, *Laws of flow in rough pipes*. National Advisory Committee for Aeronautics Washington, 1950.

[99] H. Schlichting, *Boundary-layer theory, 6^{th} ed.* McGraw-Hill, 1968.

[100] K. A. Flack and M. P. Schultz, "Review of hydraulic roughness scales in the fully rough regime," *Journal of Fluids Engineering*, vol. 132, no. 4, pp. 1–10, 2010.

[101] P. S. Granville, "Three indirect methods for the drag characterization of arbitrarily rough surfaces on flat plates," *Journal of Ship Research*, vol. 31, pp. 70–77, 1987.

[102] M. Candries, *Drag, boundary-layer and roughness characteristics of marine surfaces coated with antifoulings*. PhD thesis, University of Newcastle upon Tyne Newcastle upon Tyne,, UK, 2001.

[103] M. Schultz and A. Myers, "Comparison of three roughness function determination methods," *Experiments in fluids*, vol. 35, no. 4, pp. 372–379, 2003.

[104] M. P. Schultz and K. A. Flack, "Turbulent boundary layers over surfaces smoothed by sanding," *Transactions of the ASME–Journal of Fluids Engineering*, vol. 125, no. 5, pp. 863–870, 2003.

[105] C. Grigson, "Drag losses of new ships caused by hull finish," *Journal of ship research*, vol. 36, no. 2, pp. 182–196, 1992.

[106] M. P. Schultz, "The relationship between frictional resistance and roughness for surfaces smoothed by sanding," *Transactions of the ASME–Journal of Fluids Engineering*, vol. 124, no. 2, pp. 492–499, 2002.

[107] M. P. Schultz, "Frictional resistance of antifouling coating systems," *Transactions of the ASME-I-Journal of Fluids Engineering*, vol. 126, no. 6, pp. 1039–1047, 2004.

[108] T. A. Shapiro, "The effect of surface roughness on hydrodynamic drag and turbulence," 2004.

[109] M. P. Schultz, "Effects of coating roughness and biofouling on ship resistance and powering," *Biofouling*, vol. 23, no. 5, pp. 331–341, 2007.

[110] A. Molland, S. R. Turnock, and D. A. Hudson, "Ship resistance and propulsion: Practical estimation of propulsive power," 2011.

[111] I. T. T. C. (ITTC), "1978 ITTC performance prediciton method," in *Proc. 22nd International Towing Tank Conference: Comments on propulsion committee*, 1999.

[112] I. T. T. C. (ITTC), "Final reports and recommendations to the 25th ITTC," in *Proc. 25th International Towing Tank Conference: The specialist committee on powering performance prediction*, 2008.

[113] I. T. T. C. (ITTC), "1978 ITTC performance prediction method," in *Proc. 27th International Towing Tank Conference: Propulsion committee of 27th ITTC*, 2014.

[114] K. M. Forgach, "Comparison of ITTC-78 and DTMB standard ship performance prediction methods," tech. rep., David Taylor Model Basin, Washington DC, 2001.

[115] N. Degiuli, N. Hadžić, M. Pedišić Buča, and G. Semijalac, "Form factor determination of the full, large breadth and shallow draught ship series," *Brodogradnja*, vol. 58, no. 4, pp. 380–388, 2007.

[116] J. C. Murphy, "A novel approach to turbulence stimulation for ship-model testing," tech. rep., Naval Academy, Annapolis MD, 2010.

[117] P. N. Joubert and N. Matheson, "Wind tunnel tests of two lucy ashton reflex geosims," *Journal of Ship Research*, vol. 14, no. 4, 1970.

[118] I. T. T. C. (ITTC), "Ship models," in *Proc. 26th International Towing Tank Conference: Resistance committee of 26th ITTC*, 2011.

[119] I. T. T. C. (ITTC), "Testing and extrapolation methods - resistance. uncertainty analysis, example for resistance test," in *Proc. Specialist committee of 23rd ITTC: Procedures for resistance, propulsion and propeller open water tests*, 2002.

[120] H. W. Coleman and W. G. Steele, *Experimentation, validation, and uncertainty analysis for engineers*. John Wiley & Sons, 2009.

[121] I. T. T. C. (ITTC), "Fresh water and seawater properties," in *Proc. Specialist committee of 26th ITTC on uncertainty analysis*, 2011.

[122] C. Delen and S. Bal, "Uncertainty analysis of resistance tests in ata nutku ship model testing laboratory of istanbul technical university," *Journal of Maritime and Marine Sciences*, vol. 1, no. 2, pp. 8–27, 2015.

[123] I. T. T. C. (ITTC), "General guideline for uncertainty analysis in resistance tests," in *Proc. 27th International Towing Tank Conference: Resistance committee of 27th ITTC*, 2014.

[124] P. S. T. G. Liarokapis DD, Sfakianaki DD, "Experimental investigation of the turbulence stimulator on a sailing yacht mode," in *Proc. 10th International Conference on Marine Sciences and Technologies (Black Sea)*, 2010.

[125] D. Garofallidis, *Experimental and numerical investigation of the flow around a ship model at various Froude numbers*. PhD thesis, School of Naval Architecture and Marine Engineering, National Technical University of Athens, 1996.

[126] E. Almeida, T. C. Diamantino, and O. de Sousa, "Marine paints: the particular case of antifouling paints," *Progress in Organic Coatings*, vol. 59, no. 1, pp. 2–20, 2007.

[127] M. Lejars, A. Margaillan, and C. Bressy, "Fouling release coatings: a nontoxic alternative to biocidal antifouling coatings," *Chemical reviews*, vol. 112, no. 8, pp. 4347–4390, 2012.

[128] R. F. Brady, "Fouling-release coatings for warships," *Defence Science Journal*, vol. 55, no. 1, p. 75, 2005.

[129] M. Candries, M. Atlar, and C. Anderson, "Considering the use of alternative antifoulings: the advantages of foul release systems," in *Proc. ENSUS*, pp. 88–95, 2000.

[130] Y. K. Demirel, M. Khorasanchi, O. Turan, and A. Incecik, "Cfd approach to resistance prediction as a function of roughness," in *Transport Research Arena 2014*, April 2014.

[131] A. Venetis, "Effect of roughness on resistance," Diploma Thesis, School of Naval Architecture and Marine Engineering, National Technical University of Athens,2016.

[132] G. W. Swain and M. P. Schultz, "The testing and evaluation of non-toxic antifouling coatings," *Biofouling*, vol. 10, no. 1-3, pp. 187–197, 1996.

[133] ASTM D 4398-89 (2013), "Standard test method for erosion testing of antifouling paints using high velocity water," *American Society for Testing and Materials*.

[134] ASTM D 4939-89 (2013), "Standard test method for subjecting marine antifouling coating to biofouling and fluid shear forces in natural seawater," *American Society for Testing and Materials*.

[135] G. W. Swain, B. Kovach, A. Touzot, F. Casse, and C. J. Kavanagh, "Measuring the performance of today's antifouling coatings," *Journal of Ship Production*, vol. 23, no. 3, pp. 164–170, 2007.

[136] F. Casse and G. W. Swain, "The development of microfouling on four commercial antifouling coatings under static and dynamic immersion," *International biodeterioration & biodegradation*, vol. 57, no. 3, pp. 179–185, 2006.

[137] J. R. Matias, J. Rabenhorst, A. Mary, and A. A. Lorilla, "Marine biofouling testing of experimental marine paints: Technical considerations on methods, site selection and dynamic tests," in *Proc SSPC 2003 Industrial Protective Coatings Conference and Exhibit (in New Orleans, Louisiana)*, 2003.

[138] C. S. Lim, S. S. C. Lee, W. Leong, Y. N. Xian, and S. L. M. Teo, "A short review of laboratory and field testing of environmentally benign antifouling coatings," *Indian Journal of Geo-Marine Sciences (IJMS)*, vol. 43, no. 11, pp. 2067–2074, 2014.

[139] A. Abdel-Gaber, B. Abd-El Nabey, E. Khamis, O. Abdelattef, H. Aglan, and A. Ludwick, "Influence of natural inhibitor, pigment and extender on corrosion of polymer coated steel," *Progress in Organic Coatings*, vol. 69, no. 4, pp. 402–409, 2010.

[140] ASTM D3623-78a (2012), "Standard test method for testing antifouling panels in shallow submergence," *American Society for Testing and Materials*.

[141] A. Redfield, L. Hutchins, E. Deevy, J. Ayers, H. Turner, F. Laidlaw, J. Ferry, and D. Todd, "Marine fouling and its prevention," *US Naval Inst., Annapolis, Md*, 1952.

[142] ISO1522:2006, "Paints and Varnishes-pendulum damping test," *International Organization for Standardization*.

[143] ASTM D4214-07, "Standard test methods for evaluating the degree of chalking of exterior paint films," *American Society for Testing and Materials*.

[144] A. Nelson-Smith and J. Gee, "Serpulid tubeworms (Polychaeta Serpulidae) around Dale, Pembrokeshire," *Field Studies*, vol. 2, no. 3, pp. 331–357, 1966.

[145] ASTM D772-93, "Standard test method for evaluating degree of flaking (scaling) of exterior paints," *American Society for Testing and Materials*.

[146] ASTM D16-03, "Standard terminology for paint related coatings, materials and applications," *American Society for Testing and Materials*.

[147] F. Jaramillo Isaza, J. G. Castaño, and F. Echeverria Echeverria, "Field study of experimental antifouling paint formulations," *Dyna*, vol. 78, no. 170, pp. 135–143, 2011.

[148] J. H. Bailey, "Spirorbinae (Polychaeta: Serpulidae) from Chios (Aegean Sea)," *Zoological Journal of the Linnean Society*, vol. 48, no. 3, pp. 363–385, 1969.

[149] J. Cancino and R. Hughes, "The zooidal polymorphism and astogeny of Celleporella hyalina (Bryozoa: Cheilostomata)," *Journal of Zoology*, vol. 215, no. 1, pp. 167–181, 1988.

[150] D. Crisp and K. Ekaratne, "Polymorphism in Pomatoceros," *Zoological journal of the Linnean Society*, vol. 80, no. 2-3, pp. 157–175, 1984.

[151] M. E. Çinar, "Polychaetes from the coast of northern Cyprus (eastern Mediterranean Sea), with two new records for the Mediterranean Sea," *CBM-Cahiers de Biologie Marine.*, vol. 46, no. 2, pp. 143–160, 2005.

[152] S. Singh, S. Tambe, G. Gunasekaran, V. Raja, and D. Kumar, "Electrochemical impedance study of thermally sprayable polyethylene coatings," *Corrosion Science*, vol. 51, no. 3, pp. 595–601, 2009.

[153] D. Mitton, S. Toshima, S. Chang, R. Latanision, F. Bellucci, T. Ford, J.-D. Gu, and R. Mitchell, "Biodegradation of polyimide-coated chromium substrates," ACS Publications, 1998.

[154] J. Hu, X. Li, J. Gao, and Q. Zhao, "Ageing behavior of acrylic polyurethane varnish coating in artificial weathering environments," *Progress in organic Coatings*, vol. 65, no. 4, pp. 504–509, 2009.

[155] U. Kharchenko and I. Beleneva, "Evaluation of coatings corrosion resistance with biocomponents as antifouling additives," *Corrosion Science*, vol. 72, pp. 47–53, 2013.

[156] J. C. Kotz, P. M. Treichel, and J. Townsend, *Chemistry and chemical reactivity*. Cengage Learning, 2009.

[157] ASTM D5894-96, "Standard practice for cyclic salt fog/uv exposure of painted metal, (alternating exposures in a fog/dry cabinet and a uv/condensation cabinet)," *American Society for Testing and Materials*.

[158] ASTM G154-06, "Standard practice for operating fluorescent ultraviolet (uv) lamp apparatus for exposure of nonmetallic materials," *American Society for Testing and Materials*.

[159] D. Feldman, "Polymer weathering: photo-oxidation," *Journal of Polymers and the Environment*, vol. 10, no. 4, pp. 163–173, 2002.

[160] J. Hu, X. Li, J. Gao, and Q. Zhao, "Uv aging characterization of epoxy varnish coated steel upon exposure to artificial weathering environment," *Materials & Design*, vol. 30, no. 5, pp. 1542–1547, 2009.

[161] M. Hattori, A. Nishikata, and T. Tsuru, "Eis study on degradation of polymer-coated steel under ultraviolet radiation," *Corrosion Science*, vol. 52, no. 6, pp. 2080–2087, 2010.

[162] G. P. Bierwagen, L. He, J. Li, L. Ellingson, and D. Tallman, "Studies of a new accelerated evaluation method for coating corrosion resistance–thermal cycling testing," *Progress in organic coatings*, vol. 39, no. 1, pp. 67–78, 2000.

[163] L. Jacques, "Accelerated and outdoor/natural exposure testing of coatings," *Progress in polymer science*, vol. 25, no. 9, pp. 1337–1362, 2000.

[164] S. A. Kumar and A. Sasikumar, "Studies on novel silicone/phosphorus/sulphur containing nano-hybrid epoxy anticorrosive and antifouling coatings," *Progress in Organic Coatings*, vol. 68, no. 3, pp. 189–200, 2010.

[165] ASTM B117, "Standard practice for operating salt spray (fog) apparatus," *American Society for Testing and Materials*.

[166] F. Deflorian, S. Rossi, L. Fedrizzi, and P. Bonora, "Testing of protective organic coatings on metals: comparison of salt spray and electrochemical impedance spectroscopy," *Journal of testing and evaluation*, vol. 31, no. 2, pp. 91–97, 2003.

[167] ISO14993:2001, "Corrosion of metals and alloys–accelerated testing involving cyclic exposure to salt mist, "dry" and "wet" conditions," *International Organization for Standardization*.

[168] L. Fedrizzi, A. Bergo, F. Deflorian, and L. Valentinelli, "Assessment of protective properties of organic coatings by thermal cycling," *Progress in Organic Coatings*, vol. 48, no. 2, pp. 271–280, 2003.

[169] K. Bikli, "Study of accelerated aging methods and assessment of organic coatings on naval steel substrate," Diploma Thesis, School of Naval Architecture and Marine Engineering, National Technical University of Athens,2013.

[170] M. Öhman, *Development of ATR-FTIR Kretschmann Spectroscopy for In situ Studies of Metal/Polymer Interfaces: and its Intergration with EIS for Exposure to Corrosive Conditions*. PhD thesis, KTH, 2010.

[171] ISO4624:2002, "Paints and Varnices–pull-off test for adhesion," *International Organization for Standardization*.

[172] F. Deflorian, S. Rossi, L. Fedrizzi, and C. Zanella, "Comparison of organic coating accelerated tests and natural weathering considering meteorological data," *Progress in Organic Coatings*, vol. 59, no. 3, pp. 244–250, 2007.

[173] U. Rammelt and G. Reinhard, "Application of electrochemical impedance spectroscopy (eis) for characterizing the corrosion-protective performance of organic coatings on metals," *Progress in Organic Coatings*, vol. 21, no. 2-3, pp. 205–226, 1992.

[174] J. M. McIntyre and H. Q. Pham, "Electrochemical impedance spectroscopy; a tool for organic coatings optimizations," *Progress in Organic coatings*, vol. 27, no. 1-4, pp. 201–207, 1996.

[175] T. Nguyen, J. Hubbard, and J. Pommersheim, "Unified model for the degradation of organic coatings on steel in a neutral electrolyte," *Journal of Coatings Technology*, vol. 68, pp. 45–56, 1996.

[176] B. Hinderliter, S. Croll, D. Tallman, Q. Su, and G. Bierwagen, "Interpretation of eis data from accelerated exposure of coated metals based on modeling of coating physical properties," *Electrochimica Acta*, vol. 51, no. 21, pp. 4505–4515, 2006.

[177] F. Wong and R. Buchheit, "Utilizing the structural memory effect of layered double hydroxides for sensing water uptake in organic coatings," *Progress in organic coatings*, vol. 51, no. 2, pp. 91–102, 2004.

[178] E. McCafferty, *Introduction to corrosion science*. Springer Science & Business Media, 2010.

[179] ISO1520:2006, "Paints and Varnices–cupping test," *International Organization for Standardization*.

[180] ASTM D3719-00, "Standard test method for quantifying dirt collection on coated exterior panels," *American Society for Testing and Materials*.

[181] BS EN1062-3:1999, "Paints and Varnices– coating materials and coating systems for exterior masonry and concrete. determination and classification of liquid-water transmission rate (permeability)," *International Organization for Standardization*.

[182] ASTM D660-93, "Standard testmethod for evaluating degree of checking of exterior paints," *American Society for Testing and Materials*.

[183] J. Bisquert, "Influence of the boundaries in the impedance of porous film electrodes," *Physical Chemistry Chemical Physics*, vol. 2, no. 18, pp. 4185–4192, 2000.

[184] J. Bisquert, G. Garcia-Belmonte, F. Fabregat-Santiago, N. S. Ferriols, P. Bogdanoff, and E. C. Pereira, "Doubling exponent models for the analysis of porous film electrodes by impedance. relaxation of tio2 nanoporous in aqueous solution," *The Journal of Physical Chemistry B*, vol. 104, no. 10, pp. 2287–2298, 2000.

Appendix A

Appendix of Chapter 3

A.1 Equivalent circuits and total impedance relations for Randles and Orazem Tribollet connections

The corroding system could be described either with a Randles or an Orazem-Tribollet [76] circuit. For the former case, the equivalent circuit is presented in Fig. A.1, while the equation describing the total impedance is given by Eq. A.1.

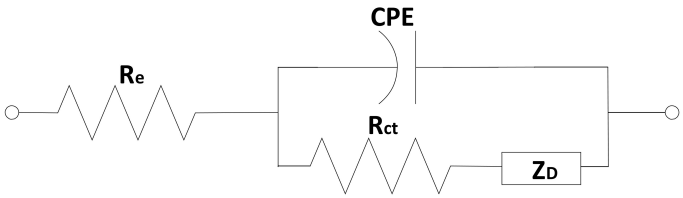

Figure A.1: Randles connection

$$Z_{\mathrm{tot}}(\omega) = R_{\mathrm{e}} + \frac{R_{\mathrm{ct}} + Z_{\mathrm{D}}}{1 + (j\omega)^{n} Q (R_{\mathrm{ct}} + Z_{\mathrm{D}})} \tag{A.1}$$

The connection proposed by Orazem and Tribollet is presented in Fig. A.2, while the equation for total impedance is given by Eq. A.2.

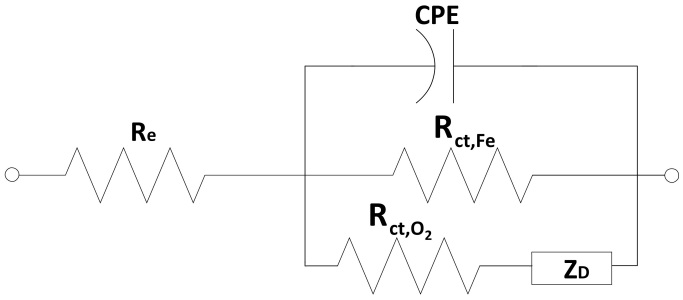

Figure A.2: Orazem-Tribollet connection

$$Z_{\mathrm{tot}}(\omega) = R_{\mathrm{e}} + \frac{R_{\mathrm{ct,Fe}}(R_{\mathrm{ct,O_2}} + Z_{\mathrm{D}})}{(j\omega)^{n} Q R_{\mathrm{ct,Fe}}(R_{\mathrm{ct,O_2}} + Z_{\mathrm{D}}) + R_{\mathrm{ct,O_2}} + Z_{\mathrm{D}} + R_{\mathrm{ct,Fe}}} \tag{A.2}$$

A.2 Rest of diffusion impedance models examined for the experimental data

A.2.1 Results with regard to the restricted diffusion impedance mechanism

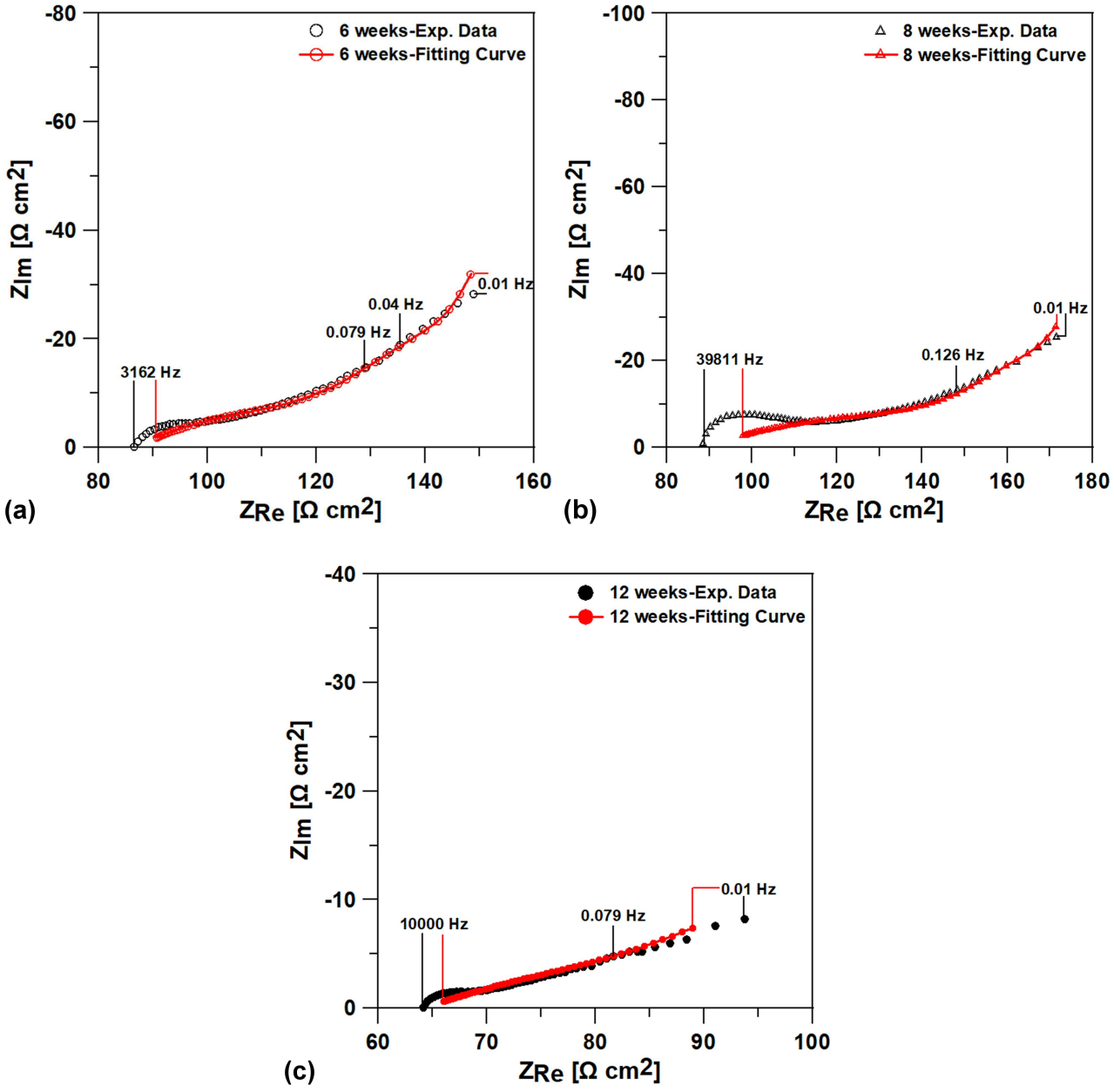

Figure A.3: Fitting curves for the painted scribed specimen after a) 6, b) 8 and c) 12 weeks of experiment in the salt spray chamber, assuming restricted diffusion, Randles connection and CPE for double-layer

Table A.1: PSO fitting results and derived parameters for the painted scribed specimen after 6, 8 and 12 weeks of experiment in the salt spray chamber, assuming restricted diffusion, Randles connection and CPE for double-layer

Parameter	Unit	6 weeks	8 weeks	12 weeks
$\tau_{\mathrm{D,FD}}$	[s]	48.00	62.28	148.96
R_{D}	[Ω cm^2]	121.86	126.99	73.32
R_{ct}	[Ω cm^2]	53.21	86.94	63.51
n		0.297	0.208	0.210
Q	[F s^{n-1} cm^{-2}]	1.07 10^{-2}	6.90 10^{-3}	4.74 10^{-2}
σ'	[Ω cm^2 s$^{-1/2}$]	17.59	16.09	6.01
$\tau_{\mathrm{ct,CPE}}$	[s]	0.15	8.57 10^{-2}	190.17

Table A.2: CNLLS fitting results and derived parameters for the painted scribed specimen after 6, 8 and 12 weeks of experiment in the salt spray chamber, assuming restricted diffusion, Randles connection and CPE for double-layer

Parameter	Unit	6 weeks	8 weeks	12 weeks
$\tau_{\mathrm{D,FD}}$	[s]	62.62±14.5%	72.94±34.8%	147.20±223%
R_{D}	[Ω cm^2]	110.90±6.6%	109.80±15.4%	58.39±107%
R_{ct}	[Ω cm^2]	42.88±4.3%	57.34±3.4%	38.49±18.6%
n		0.360±3.4%	0.325±4.3%	0.249±5.5%
Q	[F s^{n-1} cm^{-2}]	7.27 10^{-3}±8.5%	2.48 10^{-3}±12.7%	3.76 10^{-2}7±10.6%
σ'	[Ω cm^2 s$^{-1/2}$]	14.01	12.86	4.81
$\tau_{\mathrm{ct,CPE}}$	[s]	3.93 10^{-2}	2.47 10^{-3}	4.41

Table A.3: Chi-squared and sum of squares values, as indicators of goodness of fit for the restricted diffusion impedance mechanism

Parameter	6 weeks	8 weeks	12 weeks
χ^2	8.12 10^{-5}	3.33 10^{-4}	6.87 10^{-5}
Sum of Squares	8.36 10^{-3}	4.23 10^{-2}	7.90 10^{-3}

With regard to the results presented in Tables A.1 and A.2 , the fitting values refer to parameters $\tau_{\mathrm{D,FD}}$, R_{D}, R_{ct}, n and Q, while the calculated parameters are σ' and $\tau_{\mathrm{ct,CPE}}$.

A.2.2 Results with regard to the anomalous ADIa diffusion impedance mechanism

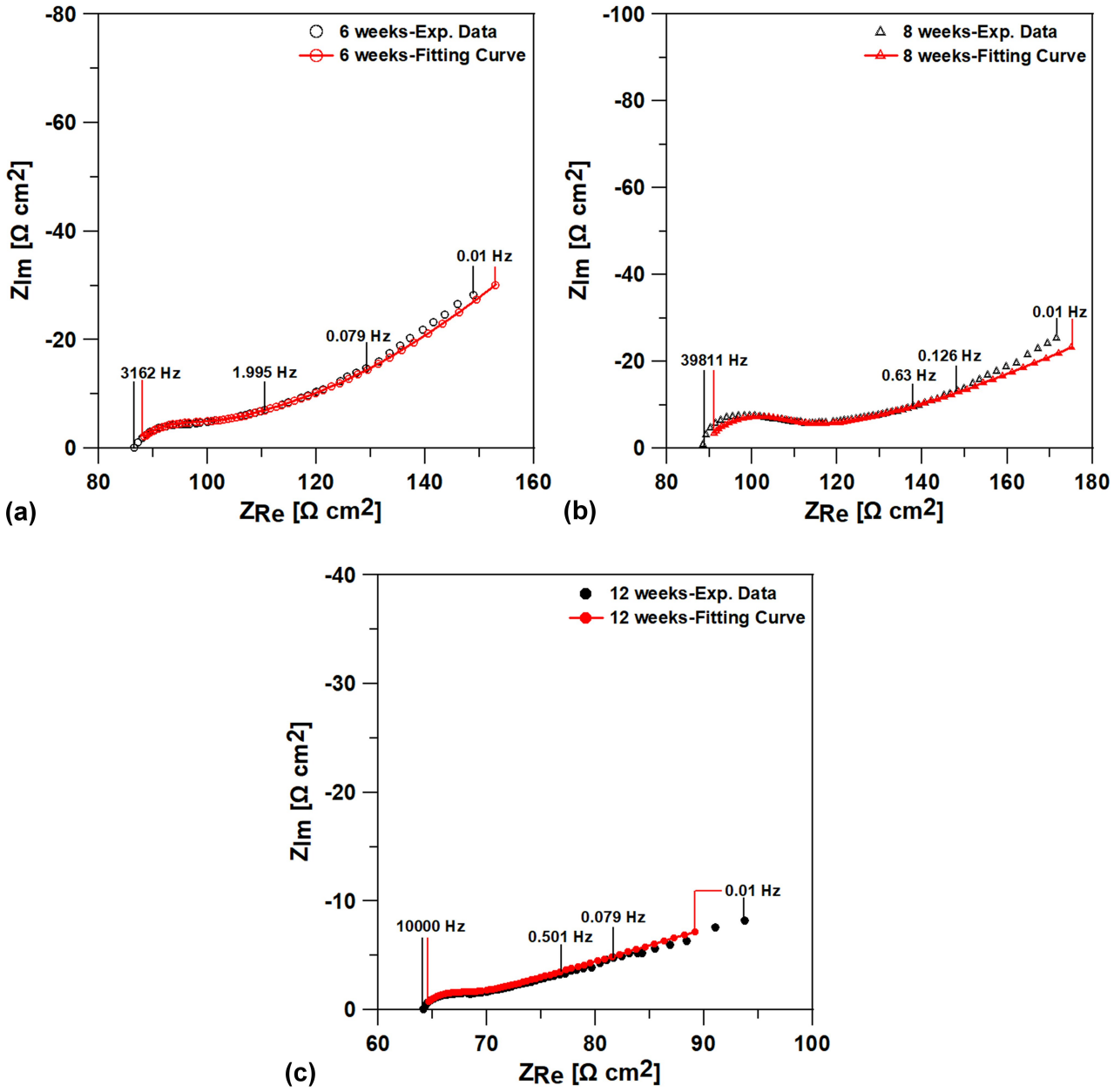

Figure A.4: Fitting curves for the painted scribed specimen after a) 6, b) 8 and c) 12 weeks of experiment in the salt spray chamber, assuming anomalous linear restricted diffusion, Randles connection and CPE for double-layer

Table A.4: Fitting results and derived parameters for the painted scribed specimen after 6, 8 and 12 weeks of experiment in the salt spray chamber, assuming anomalous linear restricted diffusion, Randles connection and CPE for double-layer

Parameter	Unit	6 weeks	8 weeks	12 weeks
$L^2_{\mathrm{D,AD}}/D$	[s]	7.180	5.000	109.096
R_{D}	[Ω cm^2]	88.494	111.919	157.567
γ		0.452	0.287	0.369
R_{ct}	[Ω cm^2]	7.472	9.132	0.980
n		0.696	0.750	0.792
Q	[F s^{n-1} cm^{-2}]	2.926 10^{-4}	1.762 10^{-5}	1.371 10^{-4}
$\tau_{\mathrm{D,AD}}$	[s]	78.525	273.476	3.385 10^{5}
$\tau_{\mathrm{ct,CPE}}$	[s]	1.506 10^{-4}	8.698 10^{-6}	1.300 10^{-5}

With regard to the results presented in Table A.4, the fitting values refer to parameters $L^2_{\mathrm{D,AD}}/D$, R_{D}, R_{ct}, n, Q and γ, while the calculated parameters are $\tau_{\mathrm{D,AD}}$ and $\tau_{\mathrm{ct,CPE}}$.

A.2.3 Results with regard to the transmissive diffusion impedance mechanism

Table A.5: PSO fitting results and derived parameters for the painted scribed specimen after 6, 8 and 12 weeks of experiment in the salt spray chamber, assuming transmissive diffusion, Randles connection and CPE for double-layer

Parameter	Unit	6 weeks	8 weeks	12 weeks
$\tau_{\mathrm{D,FD}}$	[s]	200.36	218.96	12.00
R_{D}	[Ω cm^2]	242.41	238.11	19.48
R_{ct}	[Ω cm^2]	54.51	89.83	26.87
n		0.294	0.204	0.255
Q	[F s^{n-1} cm^{-2}]	1.10 10^{-2}	7.18 10^{-3}	3.21 10^{-2}
σ'	[Ω cm^2 s$^{-1/2}$]	17.13	16.09	5.62
$\tau_{\mathrm{ct,CPE}}$	[s]	0.18	0.12	0.56

Table A.6: CNLLS fitting results and derived parameters for the painted scribed specimen after 6, 8 and 12 weeks of experiment in the salt spray chamber, assuming transmissive diffusion, Randles connection and CPE for double-layer

Parameter	Unit	6 weeks	8 weeks	12 weeks
$\tau_{\mathrm{D,FD}}$	[s]	233.70±120.2%	282.70±360%	19.63±10.9%
R_{D}	[Ω cm^2]	205.40±59.6%	205.80±178.6%	19.83±6.3%
R_{ct}	[Ω cm^2]	45.31±4.9%	58.83±3.6%	22.94±8.3%
n		0.350±3.6%	0.318±4.3%	0.294±4.5%
Q	[F s^{n-1} cm^{-2}]	7.90 10^{-3}±8.8%	2.67 10^{-3}±12.7%	2.54 10^{-2}±10%
σ'	[Ω cm^2 s$^{-1/2}$]	13.44	12.24	4.48
$\tau_{\mathrm{ct,CPE}}$	[s]	5.31 10^{-2}	2.97 10^{-3}	0.16

In Tables A.5 and A.6, the fitted parameters are $\tau_{\mathrm{D,FD}}$, R_{D}, R_{ct}, n, Q, while the calculated parameters are σ' and $\tau_{\mathrm{ct,CPE}}$.

Table A.7: Chi-squared and sum of squares values, as indicators of goodness of fit for the transmissive diffusion impedance mechanism

Parameter	6 weeks	8 weeks	12 weeks
χ^2	$9.40\ 10^{-5}$	$3.49\ 10^{-4}$	$4.79\ 10^{-5}$
Sum of Squares	$9.68\ 10^{-3}$	$4.40\ 10^{-2}$	$5.51\ 10^{-3}$

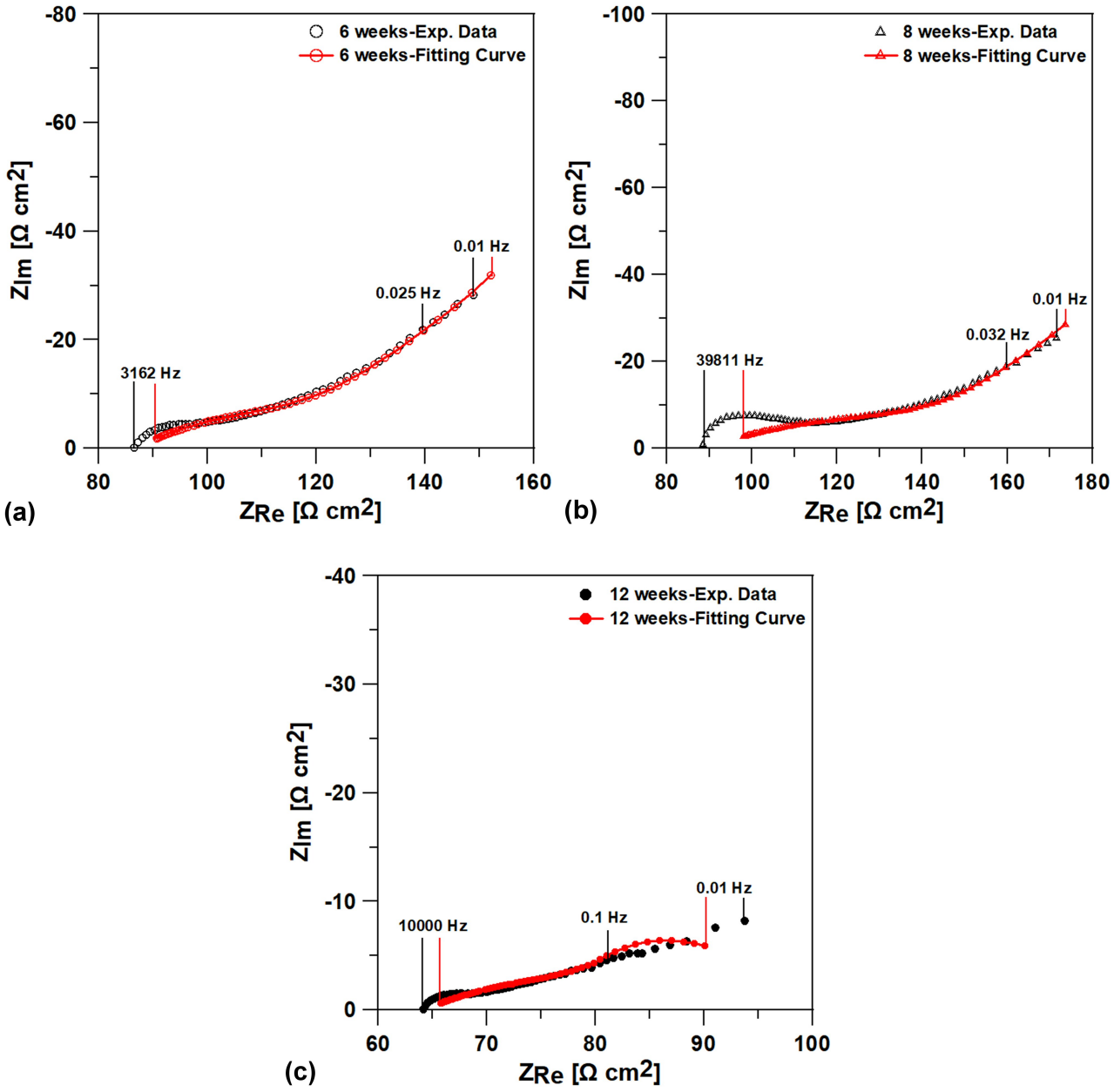

Figure A.5: Fitting curves for the painted scribed specimen after a) 6, b) 8 and c) 12 weeks of experiment in the salt spray chamber, assuming transmissive diffusion, Randles connection and CPE for double-layer

A.2.4 Results with regard to the generalized Warburg impedance mechanism

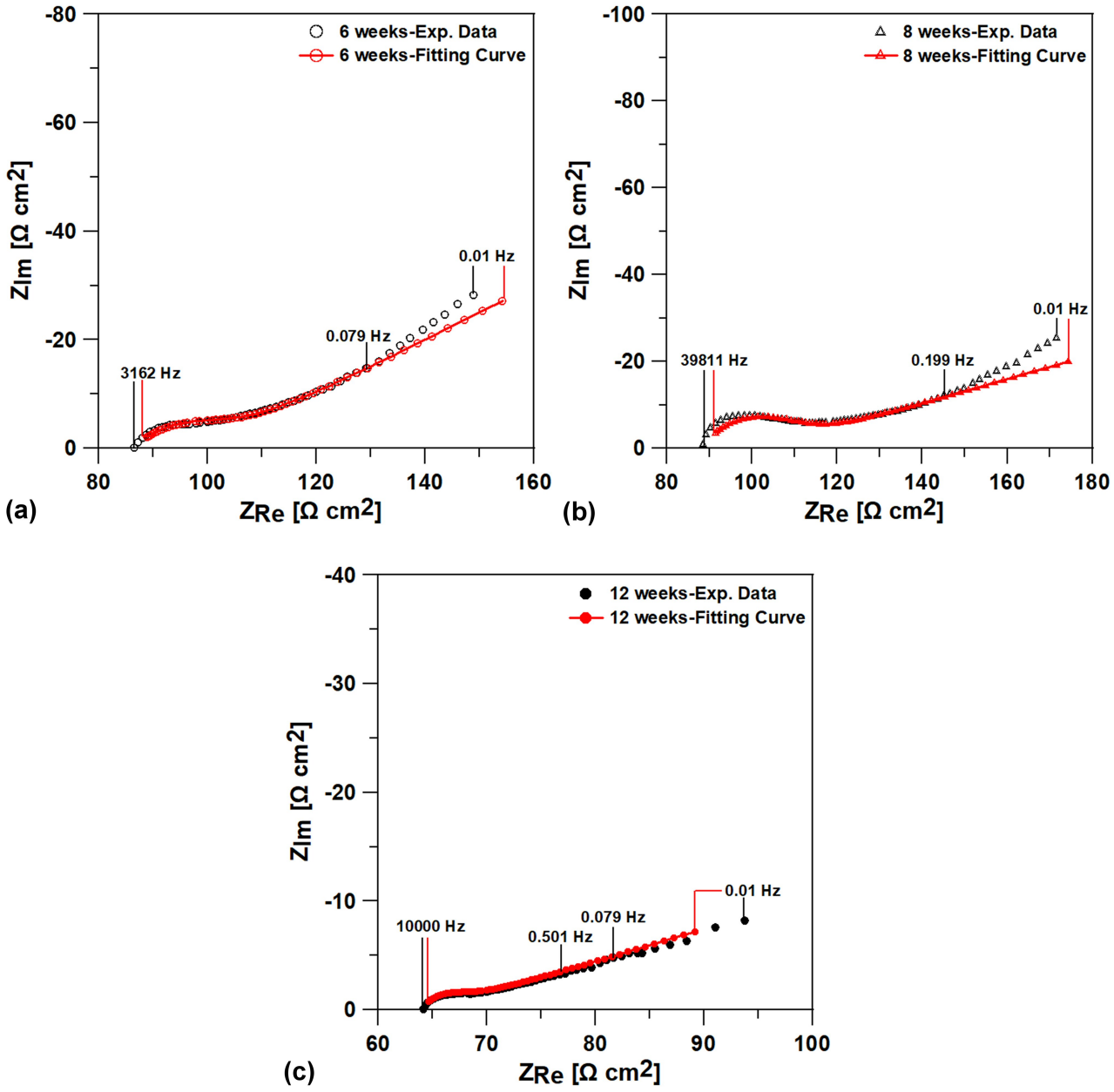

Figure A.6: Fitting curves for the painted scribed specimen after a) 6, b) 8 and c) 12 weeks of experiment in the salt spray chamber, assuming generalized Warburg diffusion, Randles connection and CPE for double-layer

Table A.8: PSO fitting results and derived parameters for the painted scribed specimen after 6, 8 and 12 weeks of experiment in the salt spray chamber, assuming generalized Warburg diffusion, Randles connection and CPE for double-layer

Parameter	Unit	6 weeks	8 weeks	12 weeks
A_{D}	[Ω cm^2 $s^{-n_{\mathrm{D}}}$]	25.57	45.34	15.07
n_{D}		0.302	0.175	0.184
R_{ct}	[Ω cm^2]	16.86	15.04	0.99
n		0.536	0.692	0.791
Q	[F s^{n-1} cm^{-2}]	1.39 10^{-3}	3.49 10^{-5}	1.39 10^{-4}
$\tau_{\mathrm{ct,CPE}}$	[s]	9.04 10^{-4}	1.82 10^{-5}	1.31 10^{-5}

Table A.9: CNLLS fitting results and derived parameters for the painted scribed specimen after 6, 8 and 12 weeks of experiment in the salt spray chamber, assuming generalized Warburg diffusion, Randles connection and CPE for double-layer

Parameter	Unit	6 weeks	8 weeks	12 weeks
A_{D}	[Ω cm^2 $s^{-n_{\mathrm{D}}}$]	23.86±4.0%	44.37±2.8%	14.97±4.1%
n_{D}		0.316±3.1%	0.184±3.1%	0.196±4.1%
R_{ct}	[Ω cm^2]	17.57±7.7%	15.62±7.4%	1.35±44.8%
n		0.567±4.9%	0.762±3.1%	0.832±9.2%
Q	[F s^{n-1} cm^{-2}]	1.17 10^{-3}±23.5%	1.77 10^{-5}±26.3%	1.04 10^{-4}±78.7%
$\tau_{\mathrm{ct,CPE}}$	[s]	1.06 10^{-3}	2.14 10^{-5}	2.34 10^{-5}

Table A.10: Chi-squared and sum of squares values, as indicators of goodness of fit for the generalized Warburg impedance mechanism

Parameter	6 weeks	8 weeks	12 weeks
χ^2	5.54 10^{-5}	6.80 10^{-5}	3.23 10^{-5}
Sum of Squares	5.70 10^{-3}	8.64 10^{-3}	3.71 10^{-3}

In Tables A.8 and A.9 the fitted parameters are A_{D}, n_{D}, R_{ct}, n and Q, while the derived parameter is $\tau_{\mathrm{ct,CPE}}$.

A.2.5 Fitting of the Bode plots for the selected models

In the present paper the results of the regression analysis were presented in a Nyquist representation, because the differences among the examined models could qualitatively be more easily observed. For comprehensiveness reasons, the Bode plots of the selected models, along with their corresponding Nyquist plots are presented herein.

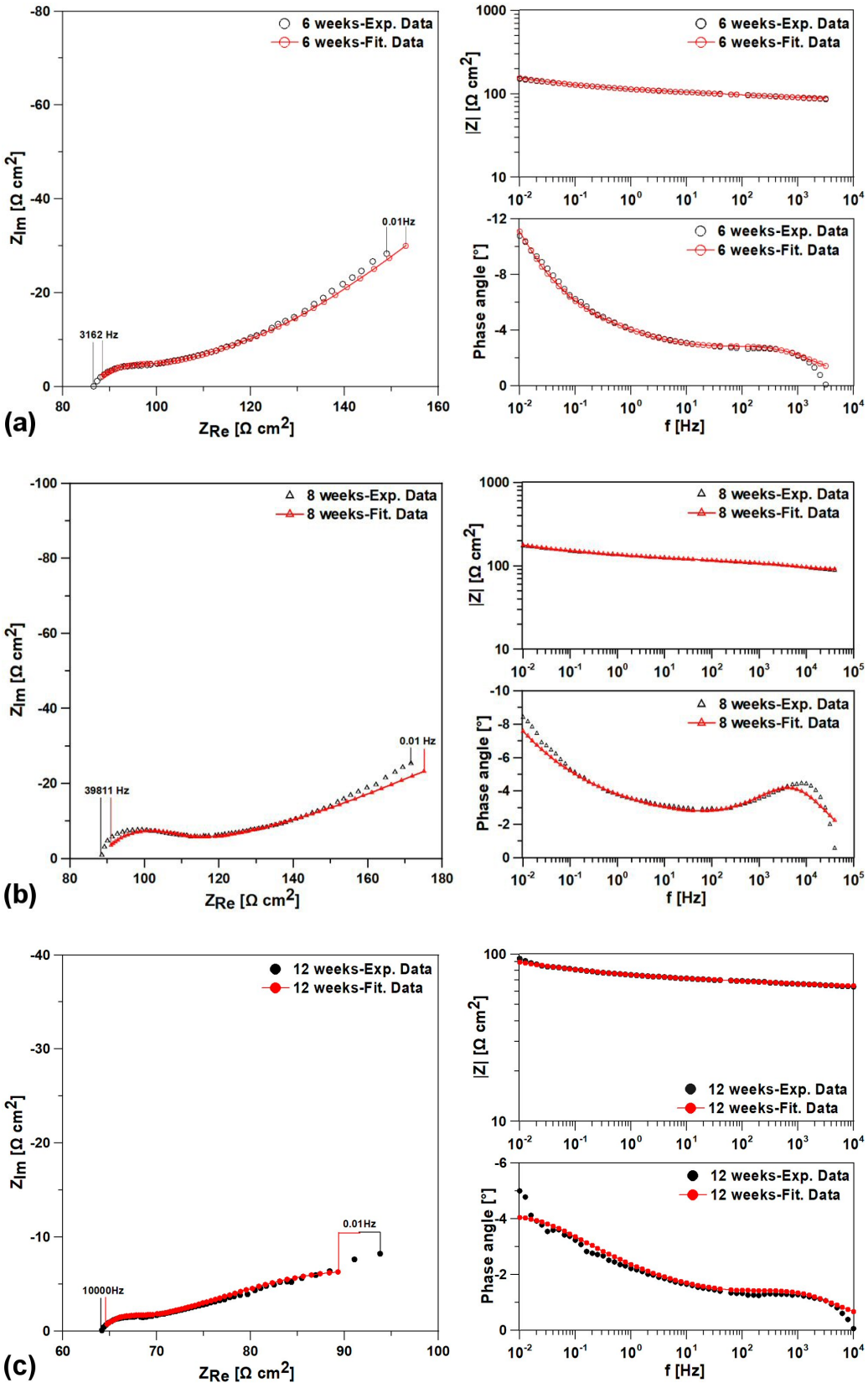

Figure A.7: Fitting curves for Nyquist and Bode plots of the painted scribed specimen after a) 6 and b) 8 weeks of experiment in the salt spray chamber, assuming modified restricted diffusion and c) after 12 weeks of experiment, assuming modified transmissive diffusion, Randles connection and CPE for double-layer

A.2.6 Results based on the cast iron in drinking water problem

The cast iron in drinking water model [76] could not describe the experimental curves. The response was three capacitive loops (as mentioned in the Introduction section), accounting for a microporous layer, possibly green rust, covering the magnetite macropores, the cathodic charge-transfer resistance and the diffusion impedance-anodic charge transfer resistance, respectively. The shape of the obtained curves could not be correlated with the HF semicircle and the LF diffusion tail of the experimental data, as observed in Fig. D.1a. A simpler version of this model, not including a layer circumferentially the magnetite macropores, was also examined. However, the fitting was again not satisfactory (Fig. D.1b). As a result, the equivalent circuit proposed in the cast iron in drinking water problem could not describe the experimental data.

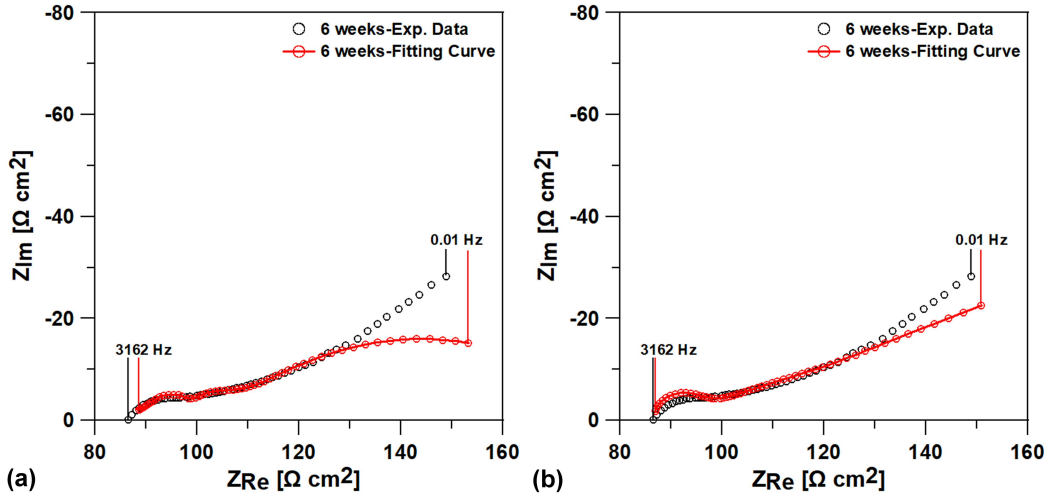

Figure D.1: Indicative fitting curves for the painted scribed specimen after 6 weeks of experiment in the salt spray chamber assuming the cast iron in drinking water model [76]: a) with and b) without presence of a microporous layer circumferentially the magnetite macropores

Appendix B

Appendix of Chapter 3

B.1 Introduction

The repeatability measurements presented herein refer to the impedance results obtained after 6, 8 and 12 weeks of experiment in the salt spray chamber, for the rest 7 specimens examined, in addition to the specimen presented in Chapter 3. Also, it should be noted that the same procedure as the one presented in Chapter 3 was followed, in order to choose the most appropriate diffusion impedance mechanism for the data; that is to say, the most caharacteristic diffusion impedance mechanisms (restricted, modified restricted, anomalous, transmissive, modified transmissive, generalized Warburg) were examined and their suitability was assessed through the goodness of fit values (chi-squared and sum of squares as ontained from the CNLLS procedure and the value of the objective function as obtained from the PSO algorithm), as well as, their physical interpretation. The comparative results between the different models are not presented here, only the final selected models.

The obtained impedance spectroscopy curves from all the examined specimens (8 in total), for the 6, 8 and 12-week intervals were also regressed using the porous electrode theory. The results are presented in Sec. B.3.

B.2 Results considering finite-length diffusion impedance theory

B.2.1 Results for specimen No. 2

Table B.1: PSO fitting results and derived parameters for the scribed specimen No. 2

Parameter	Unit	6 weeks	8 weeks	12 weeks
$\tau_{\mathrm{D,FD}}$	[s]	232.11	3.11 10^{3}	111.49
R_{D}	[Ω cm^2]	371.60	153.39	25.93
R_{ct}	[Ω cm^2]	-	-	1.719
n		0.894	0.804	0.681
Q	[F s^{n-1} cm^{-2}]	1.32 10^{-5}	4.19 10^{-5}	1.99 10^{-3}
ϕ		0.395	0.352	0.626
σ'	[Ω cm^2 s$^{-1/2}$]	24.39	2.75	2.46
$\tau_{\mathrm{ct,CPE}}$	[s]	-	-	2.39 10^{-4}

Table B.2: CNLLS fitting results and derived parameters for the scribed specimen No. 2

Parameter	Unit	6 weeks	8 weeks	12 weeks
$\tau_{\mathrm{D,FD}}$	[s]	272.40±25.4%	3.02 10^{3}±76.6%	101.70±7.0%
R_{D}	[Ω cm^2]	387.70±5.7%	201.80±13.8%	24.99±2.9%
R_{ct}	[Ω cm^2]	-	-	1.45±7.3%
n		0.942±2.2%	0.831±2.5%	0.777±4.1%
Q	[F s^{n-1} cm^{-2}]	9.65 10^{-6}±18.9%	2.62 10^{-5}±20.8%	8.36 10^{-4}±29.6%
ϕ		0.399±0.7%	0.347±0.7%	0.611±1.8%
σ'	[Ω cm^2 s$^{-1/2}$]	23.49	3.67	2.48
$\tau_{\mathrm{ct,CPE}}$	[s]	-	-	1.76 10^{-4}

Table B.3: Chi-squared and sum of squares values, as indicators of goodness of fit for the selected diffusion impedance models, for specimen No. 2

Parameter	6 weeks	8 weeks	12 weeks
χ^2	2.605 10^{-5}	2.761 10^{-5}	6.386 10^{-6}
Sum of Squares	2.527 10^{-3}	3.175 10^{-3}	7.024 10^{-4}

Table B.4: Objective function values for the selected models for specimen No.2

Examination interval	6 weeks	8 weeks	12 weeks
Objective Function	44.12	22.23	5.72

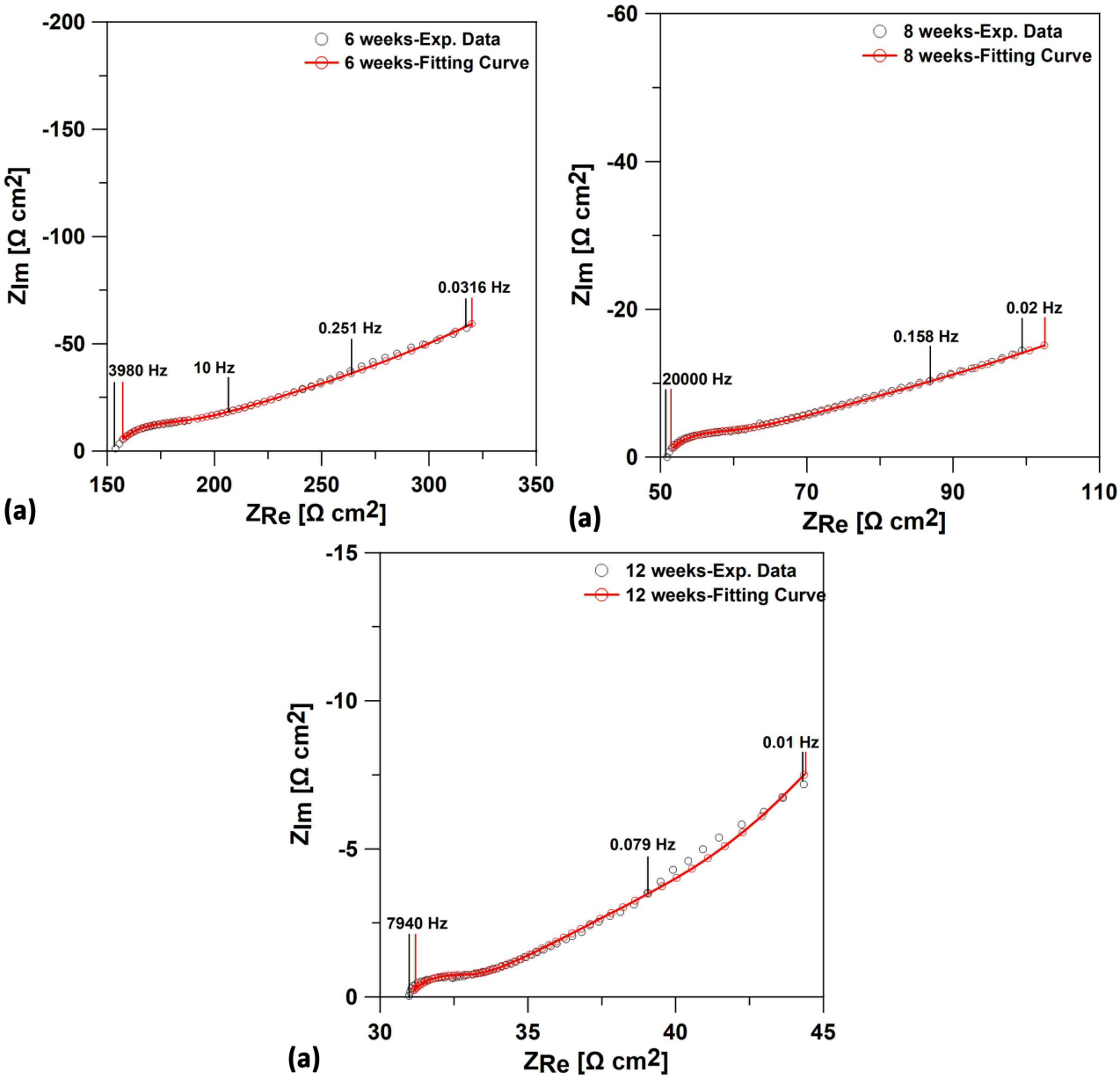

Figure D.1: Fitting curves for the painted scribed specimen No. 2 after a) 6, b) 8 and c) 12 weeks of experiment in the salt spray chamber

B.2.2 Results for specimen No. 3

Table B.5: PSO fitting results and derived parameters for the scribed specimen No. 3

Parameter	Unit	6 weeks	8 weeks	12 weeks
$\tau_{\mathrm{D,FD}}$	[s]	183.72	925.75	27.74
R_{D}	[Ω cm^2]	95.16	71.27	11.82
R_{ct}	[Ω cm^2]	-	0.76	0.492
n		0.821	0.875	0.817
Q	[F s^{n-1} cm^{-2}]	1.02 10^{-4}	7.34 10^{-5}	2.00 10^{-4}
ϕ		0.345	0.435	0.351
σ'	[Ω cm^2 s$^{-1/2}$]	7.02	2.34	2.24
$\tau_{\mathrm{ct,CPE}}$	[s]	-	1.38 10^{-5}	1.25 10^{-5}

Table B.6: CNLLS fitting results and derived parameters for the scribed specimen No. 3

Parameter	Unit	6 weeks	8 weeks	12 weeks
$\tau_{\mathrm{D,FD}}$	[s]	239.00±51.1%	850.20±31.2%	56.16±23.1%
R_{D}	[Ω cm^2]	100.40±10.5%	70.60±7.7%	14.36±6.8%
R_{ct}	[Ω cm^2]	-	0.57±50.5%	0.66±22.8%
n		0.881±2.9%	0.951±5.8%	0.839±3.1%
Q	[F s^{n-1} cm^{-2}]	6.82 10^{-5}±21.8%	3.57 10^{-5}±58.5%	1.64 10^{-4}±27.1%
ϕ		0.350±1.6%	0.433±2.2%	0.380±4.4%
σ'	[Ω cm^2 s$^{-1/2}$]	6.49	2.42	1.92
$\tau_{\mathrm{ct,CPE}}$	[s]	-	1.17 10^{-5}	1.88 10^{-5}

Table B.7: Chi-squared and sum of squares values, as indicators of goodness of fit for the selected diffusion impedance models, for specimen No. 3

Parameter	6 weeks	8 weeks	12 weeks
χ^2	1.512 10^{-5}	1.641 10^{-5}	5.901 10^{-6}
Sum of Squares	1.285 10^{-3}	1.903 10^{-3}	6.963 10^{-4}

Table B.8: Objective function values for the selected models for specimen No.3

Examination interval	6 weeks	8 weeks	12 weeks
Objective Function	13.64	14.01	5.02

B.2.3 Results for specimen No. 4

Table B.9: PSO fitting results and derived parameters for the scribed specimen No. 4

Parameter	Unit	6 weeks	8 weeks	12 weeks
$\tau_{\mathrm{D,FD}}$	[s]	180.61	748.93	80.86
R_{D}	[Ω cm^2]	93.57	64.27	31.06
R_{ct}	[Ω cm^2]	3.51	-	2.86
n		0.817	0.898	0.685
Q	[F s^{n-1} cm^{-2}]	2.08 10^{-5}	3.46 10^{-5}	1.19 10^{-3}
ϕ		0.314	0.347	0.554
σ'	[Ω cm^2 s$^{-1/2}$]	6.96	2.35	3.45
$\tau_{\mathrm{ct,CPE}}$	[s]	8.65 10^{-6}	-	2.49 10^{-4}

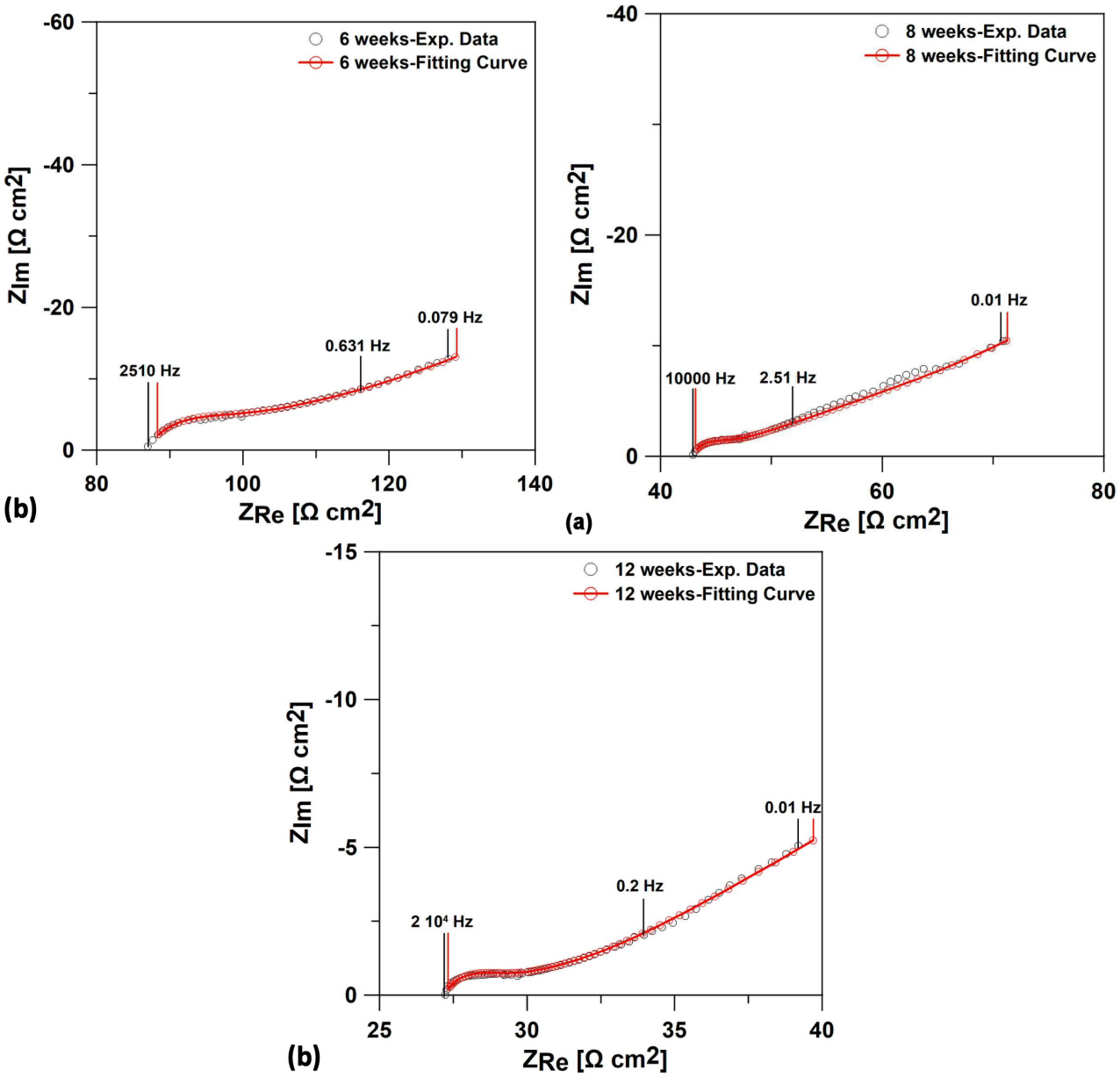

Figure D.2: Fitting curves for the painted scribed specimen No. 3 after a) 6, b) 8 and c) 12 weeks of experiment in the salt spray chamber

Table B.10: CNLLS fitting results and derived parameters for the scribed specimen No. 4

Parameter	Unit	6 weeks	8 weeks	12 weeks
$\tau_{\mathrm{D,FD}}$	[s]	68.94±77.3%	499.20±42.0%	120.30±27.0%
R_{D}	[Ω cm^2]	80.59±20.7%	56.48±9.1%	33.69±6.3%
R_{ct}	[Ω cm^2]	5.12±71.2%	-	2.49±11.8%
n		0.833±5.2%	0.891±5.7%	0.722±4.9%
Q	[F s^{n-1} cm^{-2}]	1.85 10^{-5}±50.8%	4.12 10^{-5}±49.8%	8.46 10^{-4}±33.2%
ϕ		0.334±18.1%	0.336±1.9%	0.528±2.8%
σ'	[Ω cm^2 s$^{-1/2}$]	9.71	2.53	3.07
$\tau_{\mathrm{ct,CPE}}$	[s]	1.48 10^{-5}	-	1.96 10^{-4}

Table B.11: Chi-squared and sum of squares values, as indicators of goodness of fit for the selected diffusion impedance models, for specimen No. 4

Parameter	6 weeks	8 weeks	12 weeks
χ^2	$2.914\ 10^{-5}$	$5.753\ 10^{-5}$	$1.246\ 10^{-5}$
Sum of Squares	$3.205\ 10^{-3}$	$6.847\ 10^{-3}$	$1.296\ 10^{-3}$

Table B.12: Objective function values for the selected models for specimen No.4

Examination interval	6 weeks	8 weeks	12 weeks
Objective Function	72.47	30.24	10.35

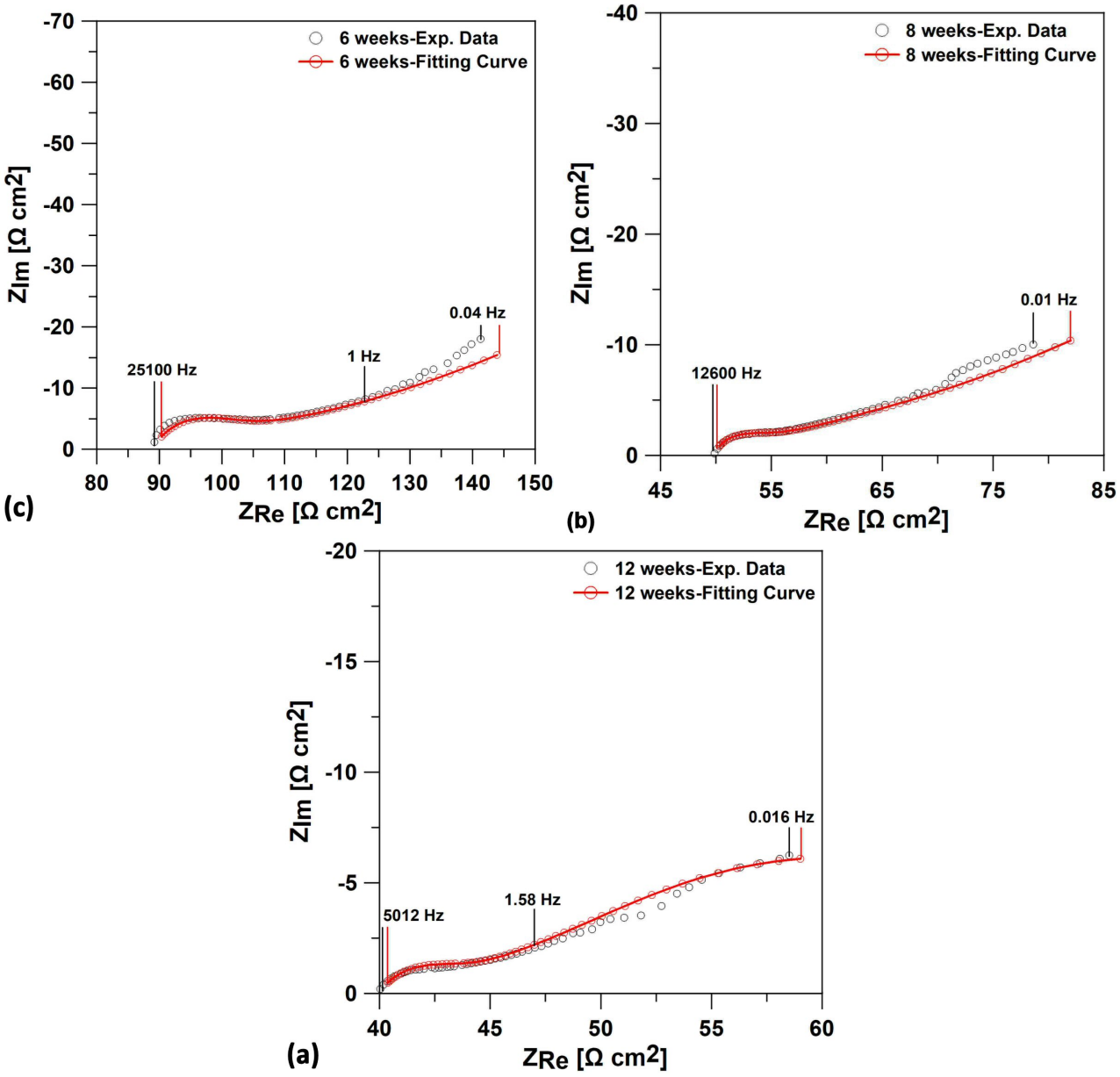

Figure D.3: Fitting curves for the painted scribed specimen No. 4 after a) 6, b) 8 and c) 12 weeks of experiment in the salt spray chamber

B.2.4 Results for specimen No. 5

Table B.13: PSO fitting results and derived parameters for the scribed specimen No. 5

Parameter	Unit	6 weeks	12 weeks
$\tau_{\mathrm{D,FD}}$	[s]	660.69	1.46 10^3
R_{D}	[Ω cm^2]	72.59	47.55
R_{ct}	[Ω cm^2]	-	-
n		0.862	0.757
Q	[F s^{n-1} cm^{-2}]	4.47 10^{-5}	1.64 10^{-4}
ϕ		0.348	0.292
σ'	[Ω cm^2 s$^{-1/2}$]	2.82	1.24
$\tau_{\mathrm{ct,CPE}}$	[s]	-	-

Table B.14: CNLLS fitting results and derived parameters for the scribed specimen No. 5

Parameter	Unit	6 weeks	12 weeks
$\tau_{\mathrm{D,FD}}$	[s]	622.90±40.0%	1.25 10^3±39.2%
R_{D}	[Ω cm^2]	71.07±7.6%	46.49±7.1%
R_{ct}	[Ω cm^2]	-	-
n		0.890±2.2%	0.798±2.7%
Q	[F s^{n-1} cm^{-2}]	3.48 10^{-5}±18.9%	1.17 10^{-4}±20.7%
ϕ		0.347±0.7%	0.292±1.3%
σ'	[Ω cm^2 s$^{-1/2}$]	2.85	1.31
$\tau_{\mathrm{ct,CPE}}$	[s]	-	-

Table B.15: Chi-squared and sum of squares values, as indicators of goodness of fit for the selected diffusion impedance models, for specimen No. 5

Parameter	6 weeks	12 weeks
χ^2	1.863 10^{-5}	1.389 10^{-5}
Sum of Squares	2.031 10^{-3}	1.597 10^{-3}

Table B.16: Objective function values for the selected models for specimen No.5

Examination interval	6 weeks	12 weeks
Objective Function	11.69	10.50

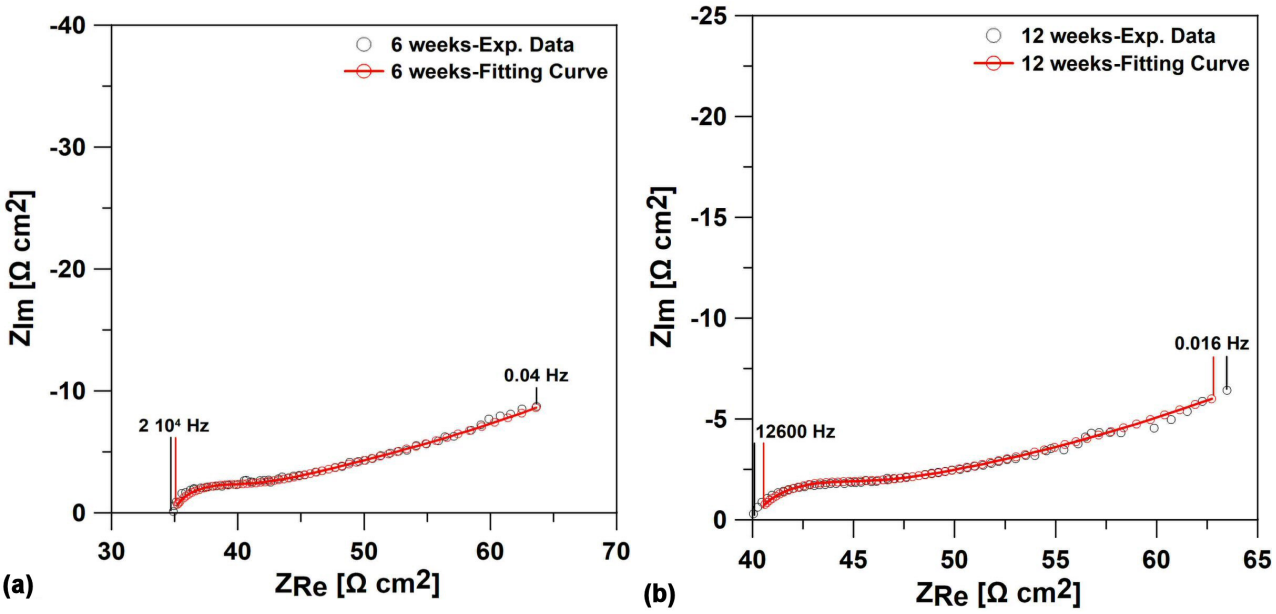

Figure D.4: Fitting curves for the painted scribed specimen No. 5 after a) 6 and b) 12 weeks of experiment in the salt spray chamber

B.2.5 Results for specimen No. 7

Table B.17: PSO fitting results and derived parameters for the scribed specimen No. 7

Parameter	Unit	12 weeks
$\tau_{\mathrm{D,FD}}$	[s]	43.55
R_{D}	[Ω cm^2]	19.95
R_{ct}	[Ω cm^2]	0.80
n		0.631
Q	[F s^{n-1} cm^{-2}]	1.80 10^{-2}
ϕ		0.886
σ'	[Ω cm^2 s$^{-1/2}$]	3.02
$\tau_{\mathrm{ct,CPE}}$	[s]	1.21 10^{-3}

Table B.18: CNLLS fitting results and derived parameters for the scribed specimen No. 7

Parameter	Unit	12 weeks
$\tau_{\mathrm{D,FD}}$	[s]	46.57±4.4%
R_{D}	[Ω cm^2]	20.69±2.4%
R_{ct}	[Ω cm^2]	0.81±11.3%
n		0.658±7.5%
Q	[F s^{n-1} cm^{-2}]	1.71 10^{-2}±39.0%
ϕ		0.910±0.9%
σ'	[Ω cm^2 s$^{-1/2}$]	3.03
$\tau_{\mathrm{ct,CPE}}$	[s]	1.50 10^{-3}

Table B.19: Chi-squared and sum of squares values, as indicators of goodness of fit for the selected diffusion impedance models, for specimen No. 7

Parameter	12 weeks
χ^2	$1.661\ 10^{-5}$
Sum of Squares	$1.594\ 10^{-3}$

Table B.20: Objective function values for the selected models for specimen No.7

Examination interval	12 weeks
Objective Function	3.35

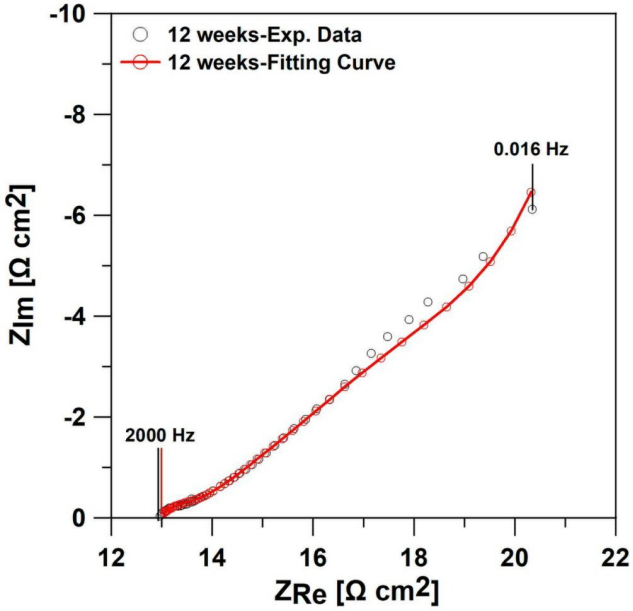

Figure D.5: Fitting curve for the painted scribed specimen No. 7 after 12 weeks of experiment in the salt spray chamber

B.2.6 Results for specimen No. 8

Table B.21: PSO fitting results and derived parameters for the scribed specimen No. 8

Parameter	Unit	12 weeks
$\tau_{\mathrm{D,FD}}$	[s]	70.26
R_{D}	[Ω cm^2]	17.57
R_{ct}	[Ω cm^2]	0.71
n		0.715
Q	[F s^{n-1} cm^{-2}]	$2.65\ 10^{-3}$
ϕ		0.675
σ'	[Ω cm^2 s$^{-1/2}$]	2.10
$\tau_{\mathrm{ct,CPE}}$	[s]	$1.54\ 10^{-4}$

Table B.22: CNLLS fitting results and derived parameters for the scribed specimen No. 8

Parameter	Unit	12 weeks
$\tau_{\mathrm{D,FD}}$	[s]	82.24±12.6%
R_{D}	[Ω cm^2]	18.35±3.9%
R_{ct}	[Ω cm^2]	0.91±6.4%
n		0.738±4.4%
Q	[F s^{n-1} cm^{-2}]	1.97 10^{-3}±30.3%
ϕ		0.663±1.1%
σ'	[Ω cm^2 s$^{-1/2}$]	2.02
$\tau_{\mathrm{ct,CPE}}$	[s]	1.90 10^{-4}

Table B.23: Chi-squared and sum of squares values, as indicators of goodness of fit for the selected diffusion impedance models, for specimen No. 8

Parameter	12 weeks
χ^2	7.049 10^{-6}
Sum of Squares	7.049 10^{-4}

Table B.24: Objective function values for the selected models for specimen No.8

Examination interval	12 weeks
Objective Function	3.11

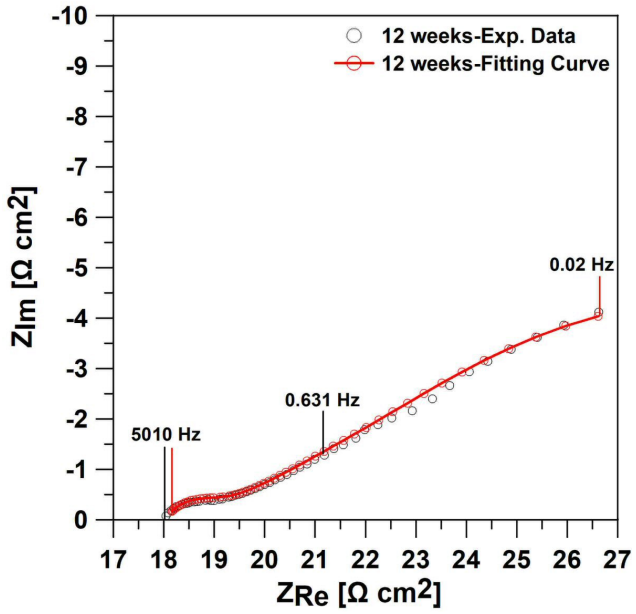

Figure D.6: Fitting curve for the painted scribed specimen No. 8 after 12 weeks of experiment in the salt spray chamber

B.2.7 Summary of results

Table B.25: Summary of selected diffusion impedance mechanisms for all the examined specimens during the 12-week exposure in the salt spray chamber

Specimen No.	6 weeks	8 weeks	12 weeks
1	Mod. Res.	Mod. Res.	Mod. Trans.
2	Mod. Res.	Mod. Res.	Mod. Res.
3	Mod. Res.	Mod. Res.	Mod. Res.
4	Mod. Res.	Mod. Res.	Mod. Trans.
5	Mod. Res.	Porous electrode only	Mod. Res.
6	No reliable signal	No reliable signal	Porous electrode only
7	No reliable signal	Porous electrode only	Mod. Res.
8	No reliable signal	No reliable signal	Mod. Trans.

Table B.26: Summary of the LPR results [Ω cm^2] for all the examined specimens during the 12-week exposure in the salt spray chamber

Specimen No.	6 weeks	8 weeks	12 weeks
1	133.35	207.66	93.22
2	377.60	123.69	45.51
3	146.29	68.34	42.96
4	124.65	56.45	53.44
5	101.09	68.30	49.16
6	62.09	58.18	68.71
7	142.73	65.82	21.25
8	132.53	68.44	26.03

B.3 Results considering the porous electrode theory

The porous electrode theory applied for examinatinon of the experimental curves was based on the work of Bisquert [183] and Bisquert *et al.* [184]. From the former work, models (b), (d) and (f) were applied. Model (b) predicts a doubling exponent at the LF range of the impedance part described using the porous electrode theory, similarly to the modified restricted mechanism. In this case, the boundary is considered purely reflecting ($Z_B \rightarrow \infty$). The transmission line in this case includes a CPE as the interfacial impedance at the pore walls, hence the frequency dispersion comes from the pore walls. In model (d), the HF branch of the part described using the porous electrode theory has a slope smaller than -1, implying non-Warburg behavior at HF, while in the LF range the exponent does not become double. In this case, the transmission line includes a CPE as interfacial impedance and a CPE as boundary impedance. Hence, dispersion arises from both the boundary and the pore walls. In model (f) of the same work, the interfacial impedance is a parallel arrangement of a distributed resistance and a distributed CPE, while the boundary impedance is similar to model (b). Model (f) is also presented in the work of Bisquert *et al.* [184] as Eq. (42). A variation of this model is introduced when the

characteristic frequency of the interfacial process ω_3 is larger than the characteristic frequency ω_L, which usually separates the regimes of different responses.

B.3.1 Results for specimen No. 1

Table B.27: PSO fitting results and derived parameters for the scribed specimen No. 1

Parameter	Unit	6 weeks		8 weeks		12 weeks	
Model		(b)	(d)	(b)	(d)	(f)	(f)-no ω_L
R_1	[Ω cm^2]	88.65	67.17	111.85	72.70	0.45	70.98
Q_B	[F s^{n-1} cm^{-2}]	-	$2.96\ 10^{-2}$	-	$3.24\ 10^{-2}$	-	-
n_B	[Ω cm^2]	-	0.568	-	0.400	-	-
ω_L	[s^{-1}]	-	-	-	-	322.84	-
R_3	[Ω cm^2]	-	-	-	-	18.61	33.26
Q_3	[F s^{n-1} cm^{-2}]	$8.17\ 10^{-2}$	$5.97\ 10^{-2}$	$4.46\ 10^{-2}$	$1.74\ 10^{-2}$	0.61	0.37
n_3	[Ω cm^2]	0.453	0.454	0.287	0.261	0.496	0.446
R_{ct}	[Ω cm^2]	7.57	7.15	9.12	-	4.79	2.73
n		0.694	0.710	0.750	0.944	0.665	0.707
Q	[F s^{n-1} cm^{-2}]	$2.98\ 10^{-4}$	$2.55\ 10^{-4}$	$1.76\ 10^{-5}$	$1.81\ 10^{-6}$	$6.04\ 10^{-4}$	$3.67\ 10^{-4}$
$\tau_{ct,CPE}$	[s]	$1.54\ 10^{-4}$	$1.39\ 10^{-4}$	$8.72\ 10^{-6}$	-	$1.52\ 10^{-4}$	$5.73\ 10^{-5}$

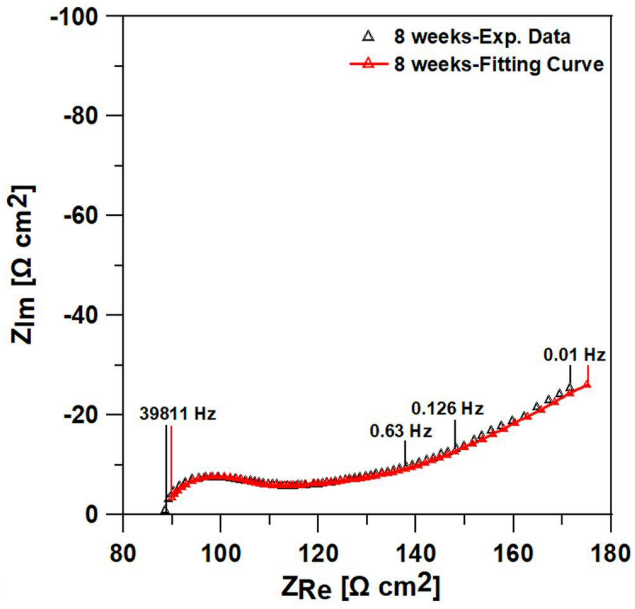

Figure D.7: Fitting curve for the painted scribed specimen No. 1, using the porous electrode theory, after 8 weeks-model (d)

With regard to the curves presented in Fig. D.7a,b, it should be noted that the fitting curves obtained using model (b) were the same as the ones obtained using the modified restricted diffusion impedance mechanism, thus, they were not presented. Finally, with regard to the curve after 12 weeks, model (f) gave the same fitting curve as the modified transmissive diffusion impedance (not presented).

Table B.28: CNLLS fitting results and derived parameters for the scribed specimen No. 1 - 6 weeks

Parameter	Unit	6 weeks	
Model		(b)	(d)
R_1	[Ω cm^2]	95.32±8.7%	59.16±22.2%
Q_B	[F s^{n-1} cm^{-2}]	-	4.18 10^{-2}±18.1%
n_B	[Ω cm^2]	-	0.517±17.1%
Q_3	[F s^{n-1} cm^{-2}]	9.96 10^{-2}±18.7%	3.77 10^{-2}±27.4%
n_3	[Ω cm^2]	0.488±7.6%	0.403±3.5%
R_{ct}	[Ω cm^2]	9.29±21.5%	-
n		0.714±5.6%	1.109±3.8%
Q	[F s^{n-1} cm^{-2}]	2.92 10^{-4}±38.0%	1.05 10^{-5}±37.7%
$\tau_{ct,CPE}$	[s]	2.54 10^{-4}	-

Table B.29: CNLLS fitting results and derived parameters for the scribed specimen No. 1 - 8 weeks

Parameter	Unit	8 weeks	
Model		(b)	(d)
R_1	[Ω cm^2]	110.20±17.3%	64.08±10.2%
Q_B	[F s^{n-1} cm^{-2}]	-	3.82 10^{-2}±5.3%
n_B	[Ω cm^2]	-	0.370±8.2%
Q_3	[F s^{n-1} cm^{-2}]	4.90 10^{-2}±27.3%	1.35 10^{-2}±19.6%
n_3	[Ω cm^2]	0.308±13.7%	0.280±4.5%
R_{ct}	[Ω cm^2]	13.49±26.7%	-
n		0.728±3.5%	1.014±2.2%
Q	[F s^{n-1} cm^{-2}]	1.96 10^{-5}±30.8%	8.54 10^{-7}±26.5%
$\tau_{ct,CPE}$	[s]	1.22 10^{-5}	-

Table B.30: CNLLS fitting results and derived parameters for scribed specimen No. 1 - 12 weeks

Parameter	Unit	12 weeks	
Model		(f)	(f)-no ω_L
R_1	[Ω cm^2]	0.45	186.10±3.3 10^5%
ω_L	[s^{-1}]	322.84	-
R_3	[Ω cm^2]	18.61	14.87 ±3.3 10^5%
Q_3	[F s^{n-1} cm^{-2}]	0.61	1.09 ±3.3 10^5%
n_3	[Ω cm^2]	0.496	0.490±12.3%
R_{ct}	[Ω cm^2]	4.79	3.76±46.3%
n		0.665	0.673±20.1%
Q	[F s^{n-1} cm^{-2}]	6.04 10^{-4}	5.47 10^{-4}±114.6%
$\tau_{ct,CPE}$	[s]	1.52 10^{-4}	-

Table B.31: CNLLS goodness of fit values for scribed specimen No. 1, using the porous electrode theory

Parameter	6 weeks		8 weeks		12 weeks	
Model	(b)	(d)	(b)	(d)	(f)	(f)-no ω_L
χ^2	$3.126\ 10^{-5}$	$2.689\ 10^{-5}$	$3.624\ 10^{-5}$	$1.885\ 10^{-5}$	-	$3.178\ 10^{-5}$
Sum of squares	$3.188\ 10^{-3}$	$2.711\ 10^{-3}$	$4.567\ 10^{-3}$	$2.356\ 10^{-3}$	-	$3.560\ 10^{-3}$

Table B.32: PSO OF values for scribed specimen No. 1, using the porous electrode theory

Parameter	6 weeks		8 weeks		12 weeks	
Model	(b)	(d)	(b)	(d)	(f)	(f)-no ω_L
OF	30.837	29.325	51.555	32.036	20.312	26.469

The results from the CNLLS procedure indicated that model (d) would be unsuitable after 6 weeks, since the CPE-n value was 1.109, with the smallest value being 1.067, as obtained from the estimated uncertainty range. Also, the R_{ct} value would be equal to zero using the CNLLS procedure. Hence, model (b) would be a potential candidate, in terms of porous electrode theory. With regard to the curve after 8 weeks, the CPE-n value was 1.014, with the smallest value being 0.991, hence, there would be a possibility that this model could fit the experimental curve. Compared to model (b), the value of the OF was 32.036 versus 51.555. Finally, with regard to the 12-week curve, model (f) assuming $\omega_3 > \omega_L$ would lead to enormous errors (Table B.30), hence it would not be a possible option. With regard to the general case, as represented using model (f), even though uncertainty ranges were not feasible to estimate, this model could be considered as a potential candidate in terms of porous electrode theory, in accordance to the observation that model (b) gives the same curve and goodness of fit as modified restricted diffusion impedance. Hence, model (f), which predicts the same curve as the modified transmissive case, shall be chosen.

B.3.2 Results for specimen No. 2

Table B.33: PSO fitting results and derived parameters for the scribed specimen No. 2

Parameter	Unit	6 weeks		8 weeks	12 weeks	
Model		(b)	(d)	(b)	(b)	(d)
R_1	[Ω cm^2]	371.72	334.06	153.50	25.63	11.55
Q_B	[F s^{n-1} cm^{-2}]	-	$2.06\ 10^{-3}$	-	-	$6.44\ 10^{-2}$
n_B	[Ω cm^2]	-	0.347	-	-	0.323
Q_3	[F s^{n-1} cm^{-2}]	$2.32\ 10^{-2}$	$2.08\ 10^{-2}$	0.11	0.72	0.27
n_3	[Ω cm^2]	0.395	0.395	0.352	0.623	0.499
R_{ct}	[Ω cm^2]	-	-	-	1.68	0.76
n		0.893	0.893	0.804	0.687	0.871
Q	[F s^{n-1} cm^{-2}]	$1.32\ 10^{-5}$	$1.32\ 10^{-5}$	$4.17\ 10^{-5}$	$1.88\ 10^{-3}$	$2.91\ 10^{-4}$
$\tau_{ct,CPE}$	[s]	-	-	-	$2.29\ 10^{-4}$	$6.36\ 10^{-5}$

Table B.34: CNLLS fitting results and derived parameters for scribed specimen No. 2 - 6 and 8 weeks

Parameter	Unit	6 weeks		8 weeks
Model		(b)	(d)	(b)
R_1	[Ω cm^2]	387.70±5.7%	329.30±77.1%	148.40±14.0%
Q_B	[F s^{n-1} cm^{-2}]	-	9.00 10^{-3}±83.3%	-
n_B	[Ω cm^2]	-	0.615±143.2%	-
Q_3	[F s^{n-1} cm^{-2}]	2.41 10^{-2}±5.5%	2.10 10^{-2}±78.2%	0.11±13.9%
n_3	[Ω cm^2]	0.399±0.7%	0.416±1.16%	0.346±0.7%
R_{ct}	[Ω cm^2]	-	-	-
n		0.942±2.2%	1.023±2.2%	0.828±2.5%
Q	[F s^{n-1} cm^{-2}]	9.65 10^{-6}±18.9%	6.07 10^{-6}±20.0%	3.67 10^{-5}±20.8%
$\tau_{ct,CPE}$	[s]	-	-	

Table B.35: CNLLS fitting results and derived parameters for scribed specimen No. 2 - 12 weeks

Parameter	Unit	12 weeks	
Model		(b)	(d)
R_1	[Ω cm^2]	24.99±2.9%	11.28±494.3%
Q_B	[F s^{n-1} cm^{-2}]	-	3.47 10^{-2}±3158%
n_B	[Ω cm^2]	-	0.371±327%
Q_3	[F s^{n-1} cm^{-2}]	0.67±5.6%	0.23±499%
n_3	[Ω cm^2]	0.611±1.8%	0.421±2.6%
R_{ct}	[Ω cm^2]	1.45±7.3%	-
n		0.777±4.1%	1.119±3.6%
Q	[F s^{n-1} cm^{-2}]	8.36 10^{-4}±29.6%	2.80 10^{-5}±38.5%
$\tau_{ct,CPE}$	[s]	1.76 10^{-4}	-

Table B.36: CNLLS goodness of fit values for scribed specimen No. 2, using the porous electrode theory

Parameter	6 weeks		8 weeks	12 weeks	
Model	(b)	(d)	(b)	(b)	(d)
χ^2	2.605 10^{-5}	2.238 10^{-5}	2.779 10^{-5}	6.385 10^{-6}	4.638 10^{-6}
Sum of squares	2.527 10^{-3}	2.126 10^{-3}	3.252 10^{-3}	7.024 10^{-4}	5.056 10^{-4}

Table B.37: PSO OF values for scribed specimen No. 2, using the porous electrode theory

Parameter	6 weeks		8 weeks	12 weeks	
Model	(b)	(d)	(b)	(b)	(d)
OF	42.607	42.597	22.229	5.719	4.237

The results obtained from model (d) after 6 and 12 weeks of experiment exhibited wide ranges of uncertainties (over 100%), making these models inappropriate to describe the experimental curves. Afrer 8 weeks, only model (b) could describe the experimental curve, hence, this was

the model of choice. For specimen No. 2, model (b) could describe all the experimental curves. As mentioned previously, the fitting curves obtained using model (b) are the same as the curves using the modified restricted diffusion impedance model, hence, they are not presented.

B.3.3 Results for specimen No. 3

Table B.38: PSO fitting results and derived parameters for the scribed specimen No. 3

Parameter	Unit	6 weeks		8 weeks		12 weeks	
Model		(b)	(d)	(b)	(d)	(b)	(d)
R_1	[Ω cm^2]	95.46	71.34	70.70	37.75	11.74	12.22
Q_B	[F s^{n-1} cm^{-2}]	-	2.82 10^{-2}	-	0.27	-	8.45 10^{-2}
n_B	[Ω cm^2]	-	0.618	-	0.619	-	0.333
Q_3	[F s^{n-1} cm^{-2}]	6.37 10^{-2}	4.58 10^{-2}	0.27	0.15	0.27	0.34
n_3	[Ω cm^2]	0.345	0.360	0.434	0.483	0.349	0.454
R_{ct}	[Ω cm^2]	-	-	0.75	1.65	0.48	1.43
n		0.823	0.865	0.878	0.808	0.817	0.725
Q	[F s^{n-1} cm^{-2}]	1.01 10^{-4}	6.87 10^{-5}	7.12 10^{-5}	1.56 10^{-4}	2.01 10^{-4}	5.80 10^{-4}
$\tau_{ct,CPE}$	[s]	-	-	1.36 10^{-5}	3.61 10^{-5}	1.22 10^{-5}	5.62 10^{-5}

Table B.39: CNLLS fitting results and derived parameters for scribed specimen No. 3

Parameter	Unit	6 weeks	
Model		(b)	(d)
R_1	[Ω cm^2]	100.40±10.5%	46.99±27.2%
Q_B	[F s^{n-1} cm^{-2}]	-	4.70 10^{-2}±11.7%
n_B	[Ω cm^2]	-	0.427±28.5%
Q_3	[F s^{n-1} cm^{-2}]	6.77 10^{-2}±9.7%	2.69 10^{-2}±37.9%
n_3	[Ω cm^2]	0.350±1.6%	0.395±6.3%
R_{ct}	[Ω cm^2]	-	-
n		0.881±2.9%	0.972±4.7%
Q	[F s^{n-1} cm^{-2}]	6.82 10^{-5}±21.8%	2.92 10^{-5}±43.2%
$\tau_{ct,CPE}$	[s]	-	-

Table B.40: PSO fitting results and derived parameters for the scribed specimen No. 3

Parameter	Unit	8 weeks	
Model		(b)	(d)
R_1	[Ω cm^2]	70.60±7.7%	41.54±22.6%
Q_B	[F s^{n-1} cm^{-2}]	-	0.26±36.9%
n_B	[Ω cm^2]	-	0.669±29.1%
Q_3	[F s^{n-1} cm^{-2}]	0.26±10.2%	0.17±19.6%
n_3	[Ω cm^2]	0.433±2.2%	0.475±4.6%
R_{ct}	[Ω cm^2]	0.57±50.5%	1.44±31.8%
n		0.952±5.9%	0.863±6.4%
Q	[F s^{n-1} cm^{-2}]	3.57 10^{-5}±58.5%	9.57 10^{-5}±58.0%
$\tau_{ct,CPE}$	[s]	1.18 10^{-5}	3.36 10^{-5}

Table B.41: CNLLS fitting results and derived parameters for scribed specimen No. 3 - 12 weeks

Parameter	Unit	12 weeks	
Model		(b)	(d)
R_1	[Ω cm^2]	14.36±7.7%	13.05±1733%
Q_B	[F s^{n-1} cm^{-2}]	-	4.40 10^{-2}±11435%
n_B	[Ω cm^2]	-	0.342±1431%
Q_3	[F s^{n-1} cm^{-2}]	0.32±8.5%	0.31±1729%
n_3	[Ω cm^2]	0.380±4.4%	0.401±17.3%
R_{ct}	[Ω cm^2]	0.65±22.8%	0.87±61.0%
n		0.839±3.1%	0.814±6.3%
Q	[F s^{n-1} cm^{-2}]	1.64 10^{-4}±27.1%	2.21 10^{-4}±58.7%
$\tau_{ct,CPE}$	[s]	1.84 10^{-5}	2.72 10^{-5}

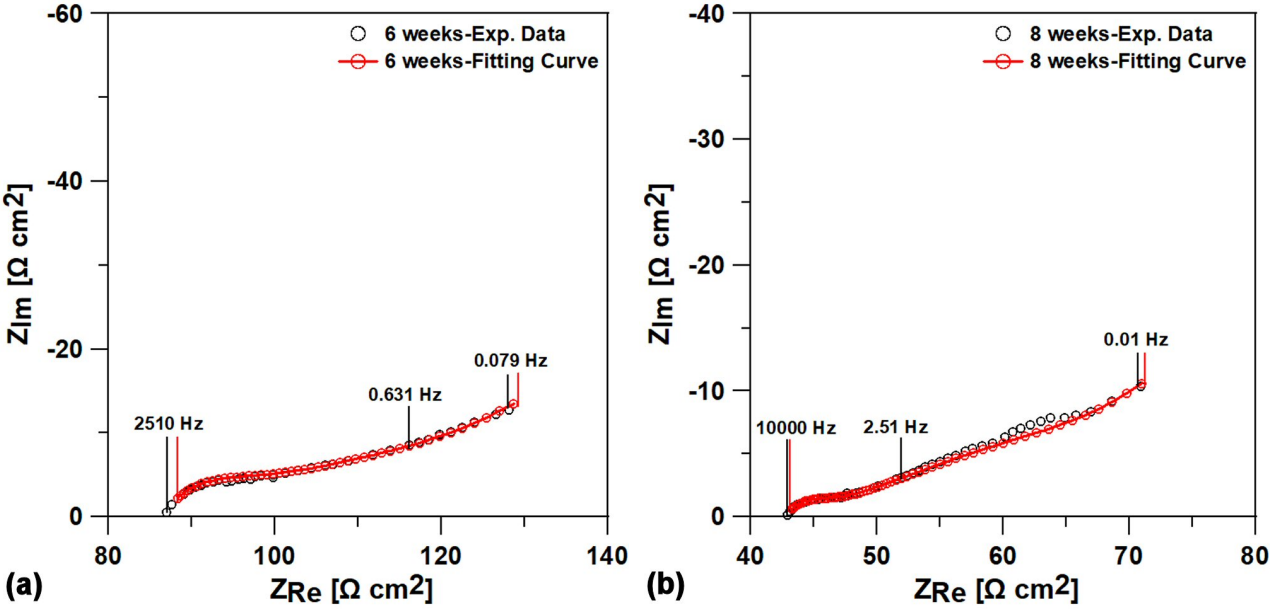

Figure D.8: Fitting curves for the painted scribed specimen No. 3, using the porous electrode theory, after a) 6 weeks-model (d) and b) 8 weeks-model (d)

Table B.42: CNLLS goodness of fit values for scribed specimen No. 3, using the porous electrode theory

Parameter	6 weeks		8 weeks		12 weeks	
Model	(b)	(d)	(b)	(d)	(b)	(d)
χ^2	1.512 10^{-5}	1.376 10^{-5}	1.641 10^{-5}	1.472 10^{-5}	5.901 10^{-6}	5.988 10^{-6}
Sum of squares	1.285 10^{-3}	1.142 10^{-3}	1.903 10^{-3}	1.678 10^{-3}	6.963 10^{-4}	6.946 10^{-4}

Table B.43: PSO OF values for scribed specimen No. 3, using the porous electrode theory

Parameter	6 weeks		8 weeks		12 weeks	
Model	(b)	(d)	(b)	(d)	(b)	(d)
OF	13.646	12.264	14.008	12.513	5.024	5.047

The results obtained from specimen No. 3 after 6 weeks would allow use of both models (b) or (d). Model (d) exhibited a large value for the CPE exponent, which was equal to 0.972 and with the largest value being 1.018. Model (d) had slightly smaller goodness of fit values and OF. After 8 weeks, model (b) exhibited a large CPE exponent, with a value of 0.952 and maximum equal to 1.008. Model (d), on the other hand, exhibited generally no problems and also better goodness of fit values. Finally, after 12 weeks, only model (b) could describe the experimental data, since model (d) exhibited enormous errors.

B.3.4 Results for specimen No. 4

Table B.44: PSO fitting results and derived parameters for the scribed specimen No. 4

Parameter	Unit	6 weeks		8 weeks	12 weeks	
Model		(b)	(d)	(b)	(f)	(f)-no ω_L
R_1	[Ω cm^2]	81.99	50.70	64.14	8.56	53.56
Q_B	[F s^{n-1} cm^{-2}]	-	$3.48\ 10^{-2}$	-	-	-
n_B	[Ω cm^2]	-	0.475	-	-	-
ω_L	[s^{-1}]	-	-	-	0.10	-
R_3	[Ω cm^2]	-	-	-	55.55	18.25
Q_3	[F s^{n-1} cm^{-2}]	$4.86\ 10^{-2}$	$2.02\ 10^{-2}$	0.15	$8.91\ 10^{-2}$	0.67
n_3	[Ω cm^2]	0.323	0.322	0.347	0.516	0.633
R_{ct}	[Ω cm^2]	4.16	-	-	2.34	3.57
n		0.810	0.998	0.898	0.718	0.648
Q	[F s^{n-1} cm^{-2}]	$2.26\ 10^{-5}$	$2.59\ 10^{-6}$	$3.48\ 10^{-5}$	$8.57\ 10^{-4}$	$1.75\ 10^{-3}$
$\tau_{ct,CPE}$	[s]	$1.07\ 10^{-5}$	-	-	$1.75\ 10^{-4}$	$3.97\ 10^{-4}$

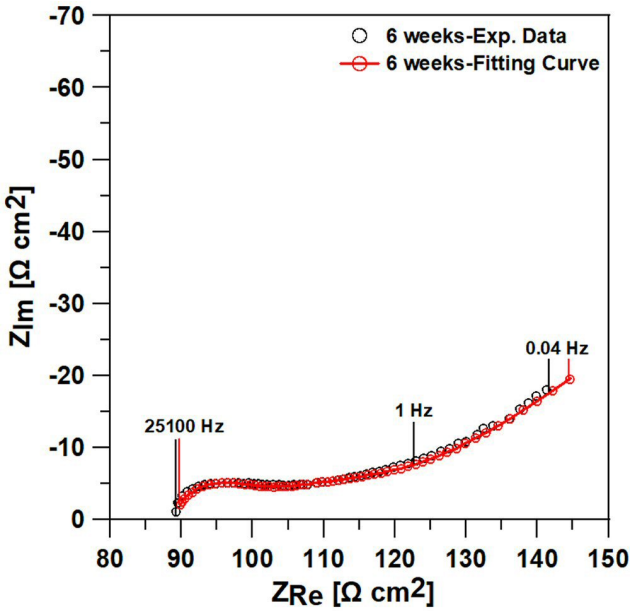

Figure D.9: Fitting curves for the painted scribed specimen No. 4, using the porous electrode theory, after 6 weeks-model (d)

Table B.45: CNLLS fitting results and derived parameters for scribed specimen No. 4 - 6 and 8 weeks

Parameter	Unit	6 weeks		8 weeks
Model		(b)	(d)	(b)
R_1	[Ω cm^2]	80.59±20.7%	54.30±15.5%	56.48±9.1%
Q_B	[F s^{n-1} cm^{-2}]	-	3.61 10^{-2}±13.9%	-
n_B	[Ω cm^2]	-	0.500±15.5%	-
Q_3	[F s^{n-1} cm^{-2}]	5.11 10^{-2}±30.2%	2.18 10^{-2}±24.5%	0.14±8.2%
n_3	[Ω cm^2]	0.334±18.1%	0.312±4.6%	0.336±1.9%
R_{ct}	[Ω cm^2]	5.12±71.2%	-	-
n		0.833±5.2%	0.983±3.3%	0.891±5.7%
Q	[F s^{n-1} cm^{-2}]	1.48 10^{-5}±50.8%	2.82 10^{-6}±36.0%	4.12 10^{-5}±49.8%
$\tau_{ct,CPE}$	[s]	1.48 10^{-5}	-	-

Table B.46: CNLLS fitting results and derived parameters for scribed specimen No. 4 - 12 weeks

Parameter	Unit	12 weeks	
Model		(f)	(f)-no ω_L
R_1	[Ω cm^2]	8.56	97.86±4264%
ω_L	[s^{-1}]	0.10	-
R_3	[Ω cm^2]	55.55	12.67±4282%
Q_3	[F s^{n-1} cm^{-2}]	8.91 10^{-2}	1.15±4265%
n_3	[Ω cm^2]	0.516	0.594±4.1%
R_{ct}	[Ω cm^2]	2.34	3.14±10.9%
n		0.718	0.682±5.0%
Q	[F s^{n-1} cm^{-2}]	8.57 10^{-4}	1.27 10^{-3}±31.7%
$\tau_{ct,CPE}$	[s]	1.75 10^{-4}	3.03 10^{-4}

Table B.47: CNLLS goodness of fit values for scribed specimen No. 4, using the porous electrode theory

Parameter	6 weeks		8 weeks	12 weeks	
Model	(b)	(d)	(b)	(f)	(f)-no ω_L
χ^2	2.914 10^{-5}	1.630 10^{-5}	5.753 10^{-5}	-	1.330 10^{-5}
Sum of squares	3.205 10^{-3}	1.777 10^{-3}	6.847 10^{-3}	-	1.370 10^{-3}

Table B.48: PSO OF values for scribed specimen No. 4, using the porous electrode theory

Parameter	6 weeks		8 weeks	12 weeks	
Model	(b)	(d)	(b)	(f)	(f)-no ω_L
OF	37.747	29.421	30.242	10.148	10.589

With regard to specimen No. 4, after 6 weeks model (b) provided reasonable parameters. Model (d) provided a large CPE-n value, being 0.982, with the maximum being 1.015. However, model (d) exhibited much smaller goodness of fit values. After 8 weeks, only model (b) could fit the

experimental data. The signal was not of very good quality, in general. Finally, after 12 weeks, model (f) assuming $\omega_3 > \omega_L$ exhibited enormous errors, hence, it could not be considered. However, similarly to specimen No. 1 after 12 weeks, model (f) in its general manifestation shall be considered, since it provides a curve similar to the modified transmissive case, as observed also through the similar OF values from the PSO procedure.

B.3.5 Results for specimen No. 5

Table B.49: PSO fitting results and derived parameters for the scribed specimen No. 5

Parameter	Unit	6 weeks		8 weeks	12 weeks	
Model		(b)	(d)	(d)	(b)	(d)
R_1	[Ω cm^2]	72.55	49.99	43.14	47.00	14.67
Q_B	[F s^{n-1} cm^{-2}]	-	$8.26\ 10^{-2}$	0.83	-	$9.81\ 10^{-2}$
n_B	[Ω cm^2]	-	0.773	0.950	-	0.242
Q_3	[F s^{n-1} cm^{-2}]	0.13	$8.84\ 10^{-2}$	$9.47\ 10^{-2}$	0.17	$4.27\ 10^{-2}$
n_3	[Ω cm^2]	0.348	0.356	0.372	0.291	0.343
R_{ct}	[Ω cm^2]	-	-	-	-	-
n		0.862	0.902	0.822	0.753	0.858
Q	[F s^{n-1} cm^{-2}]	$4.47\ 10^{-5}$	$2.99\ 10^{-5}$	$8.25\ 10^{-5}$	$1.72\ 10^{-4}$	$5.52\ 10^{-5}$
$\tau_{ct,CPE}$	[s]	-	-	-	-	-

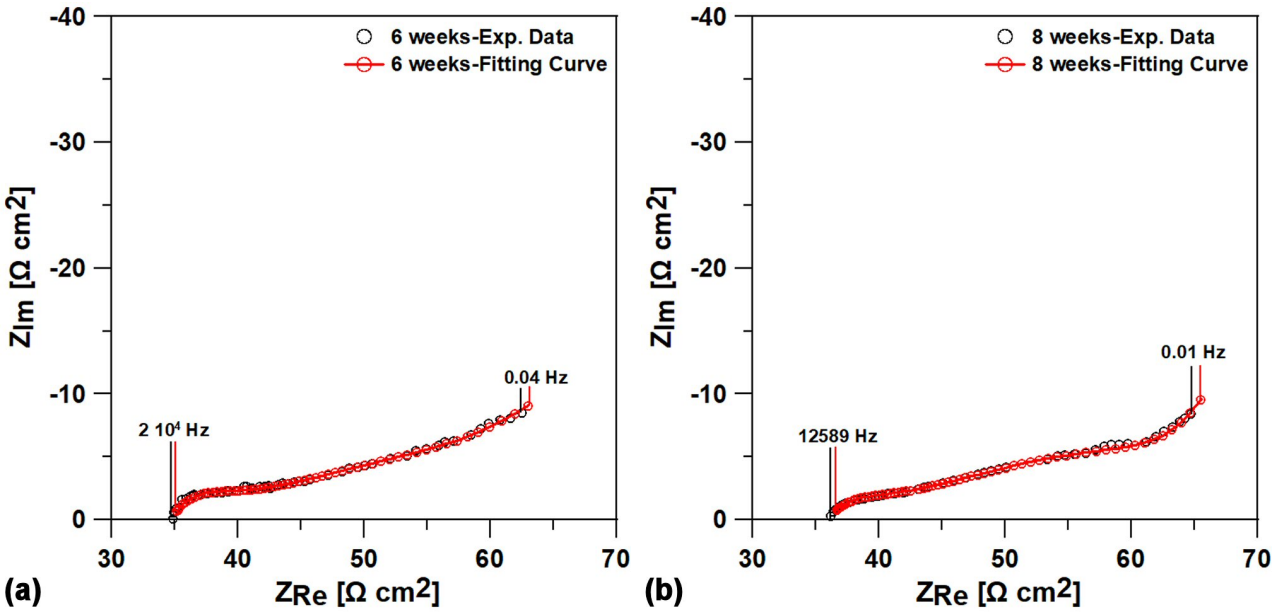

Figure D.10: Fitting curves for the painted scribed specimen No. 5, using the porous electrode theory, after a) 6 weeks-model (d) and b) 8 weeks-model (d)

Table B.50: CNLLS fitting results and derived parameters for scribed specimen No. 5 - 6 weeks

Parameter	Unit	6 weeks	
Model		(b)	(d)
R_1	[Ω cm^2]	67.38±6.3%	44.55±14.7%
Q_B	[F s^{n-1} cm^{-2}]	-	9.19 10^{-2}±13.5%
n_B	[Ω cm^2]	-	0.642±25.0%
Q_3	[F s^{n-1} cm^{-2}]	0.12±5.9%	7.64 10^{-2}±16.6%
n_3	[Ω cm^2]	0.337±0.8%	0.357±1.5%
R_{ct}	[Ω cm^2]	-	-
n		0.841±2.2%	0.917±2.4%
Q	[F s^{n-1} cm^{-2}]	4.59 10^{-5}±18.6%	2.27 10^{-5}±22.6%
$\tau_{ct,CPE}$	[s]	-	-

Table B.51: CNLLS fitting results and derived parameters for scribed specimen No. 5 8 and 12 weeks

Parameter	Unit	8 weeks	12 weeks	
Model		(d)	(b)	(d)
R_1	[Ω cm^2]	43.87±3.1%	46.49±7.1%	9.77±30.5%
Q_B	[F s^{n-1} cm^{-2}]	1.00±13.7%	-	0.10±8.0%
n_B	[Ω cm^2]	0.985±6.1%	-	0.228±7.7%
Q_3	[F s^{n-1} cm^{-2}]	9.80 10^{-2}±4.0%	0.17±6.5%	1.74 10^{-2}±73.1%
n_3	[Ω cm^2]	0.371±1.0%	0.292±1.3%	0.419±14.7%
R_{ct}	[Ω cm^2]	-	-	
n		0.868±2.3%	0.798±2.7%	0.978±7.3%
Q	[F s^{n-1} cm^{-2}]	5.86 10^{-5}±19.5%	1.17 10^{-4}±20.7%	1.54 10^{-5}±81.8%
$\tau_{ct,CPE}$	[s]	-	-	-

Table B.52: CNLLS goodness of fit values for scribed specimen No. 5, using the porous electrode theory

Parameter	6 weeks		8 weeks	12 weeks	
Model	(b)	(d)	(d)	(b)	(d)
χ^2	1.647 10^{-5}	1.349 10^{-5}	1.049 10^{-5}	1.389 10^{-5}	1.273 10^{-5}
Sum of squares	1.796 10^{-3}	1.443 10^{-3}	1.206 10^{-3}	1.597 10^{-3}	1.438 10^{-3}

Table B.53: PSO OF values for scribed specimen No. 5, using the porous electrode theory

Parameter	6 weeks		8 weeks	12 weeks	
Model	(b)	(d)	(d)	(b)	(d)
OF	11.686	10.101	8.610	10.501	9.731

After 6 weeks, models (b) and (d) could describe the experimental curve, with model (d) exhibiting smaller goodness of fit values. After 8 weeks only model (d) was appropriate for the experimental data, even though the n_B value was 0.985 with a maximum value of 1.045.

Finally, after 12 weeks models (b) and (d) could be chosen, with model (b) exhibiting smaller uncertainty ranges, but larger goodness of fit values. With regard to model (d), in particular, Q exhibited 81.8% error, while the CPE-n maximum value would be 1.049.

B.3.6 Results for specimen No. 6

Table B.54: PSO and CNLLS fitting results and derived parameters for scribed specimen No. 6 - 12 weeks

Parameter	Unit	12 weeks	12 weeks-CNLLS
Model		(d)	(d)
R_1	[Ω cm^2]	40.39	40.24±25.8%
Q_B	[F s^{n-1} cm^{-2}]	0.15	0.22±14.8%
n_B	[Ω cm^2]	0.784	0.890±28.4%
Q_3	[F s^{n-1} cm^{-2}]	8.79 10^{-2}	9.30 10^{-2}±20.1%
n_3	[Ω cm^2]	0.335	0.351±10.9%
R_{ct}	[Ω cm^2]	1.45	2.38±50.9%
n		0.850	0.819±4.7%
Q	[F s^{n-1} cm^{-2}]	3.70 10^{-5}	4.46 10^{-5}±44.3%
$\tau_{ct,CPE}$	[s]	9.46 10^{-6}	1.40 10^{-5}

Table B.55: CNLLS goodness of fit values for scribed specimen No. 6, using the porous electrode theory

Paramete	12 weeks
Model	(d)
χ^2	7.528 10^{-6}
Sum of squares	8.130 10^{-4}

Table B.56: PSO OF values for scribed specimen No. 6, using the porous electrode theory

Parameter	12 weeks
Model	(d)
OF	11.872

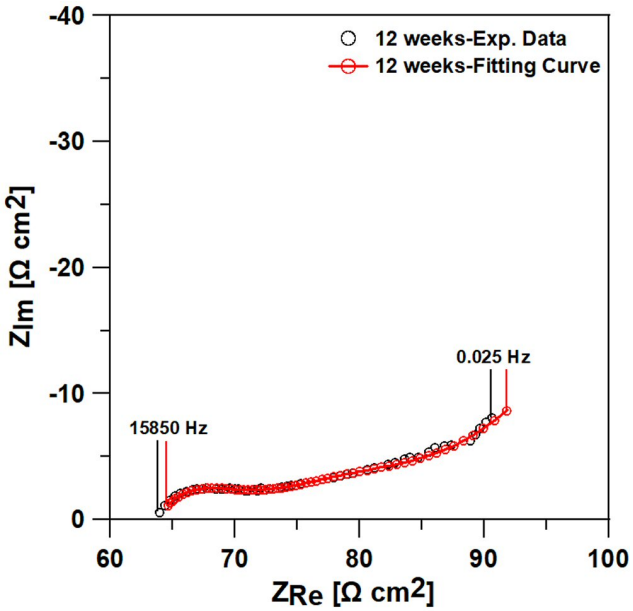

Figure D.11: Fitting curve for the painted scribed specimen No. 6, using the porous electrode theory, after 12 weeks-model (d)

This specimen did not provide a reliable signal after 6 and 8 weeks, hence, the rest experimental curves could not be depicted. After 12 weeks only the porous electrode theory could describe it, using model (d).

B.3.7 Results for specimen No. 7

Table B.57: PSO fitting results and derived parameters for the scribed specimen No. 7

Parameter	Unit	8 weeks	12 weeks	
Model		(d)	(b)	(d)
R_1	[Ω cm^2]	27.36	20.03	18.36
Q_B	[F s^{n-1} cm^{-2}]	0.20	-	8.88 10^{-2}
n_B	[Ω cm^2]	0.437	-	0.796
Q_3	[F s^{n-1} cm^{-2}]	0.10	1.42	1.31
n_3	[Ω cm^2]	0.428	0.886	0.883
R_{ct}	[Ω cm^2]	-	0.82	0.78
n		0.874	0.620	0.638
Q	[F s^{n-1} cm^{-2}]	2.75 10^{-4}	1.96 10^{-2}	1.69 10^{-2}
$\tau_{ct,CPE}$	[s]	-	1.28 10^{-3}	1.13 10^{-3}

Table B.58: CNLLS fitting results and derived parameters for scribed specimen No. 7

Parameter	Unit	8 weeks	12 weeks	
Model		(d)	(b)	(d)
R_1	[Ω cm^2]	23.48±11.2%	23.24±2.9%	20.83±40.8%
Q_B	[F s^{n-1} cm^{-2}]	0.18±14.8%	-	0.77±27.7%
n_B	[Ω cm^2]	0.378±11.3%	-	1.219±57.1%
Q_3	[F s^{n-1} cm^{-2}]	8.57 10^{-2}±14.2%	1.88±4.7%	1.57±42.8%
n_3	[Ω cm^2]	0.444±2.5%	0.884±1.2%	0.910±2.3%
R_{ct}	[Ω cm^2]	-	0.67±16.7%	1.04±22.2%
n		0.957±3.4%	0.731±12.2%	0.558±13.3%
Q	[F s^{n-1} cm^{-2}]	1.49 10^{-4}±28.1%	9.34 10^{-3}±70.6%	3.04 10^{-2}±60.9%
$\tau_{ct,CPE}$	[s]	-	9.67 10^{-4}	2.05 10^{-3}

Table B.59: CNLLS goodness of fit values for scribed specimen No. 7, using the porous electrode theory

Parameter	8 weeks	12 weeks	
Model	(d)	(b)	(d)
χ^2	8.708 10^{-6}	4.495 10^{-5}	4.142 10^{-5}
Sum of squares	8.621 10^{-4}	4.495 10^{-3}	4.059 10^{-3}

Table B.60: PSO OF values for scribed specimen No. 7, using the porous electrode theory

Parameter	8 weeks	12 weeks	
Model	(d)	(b)	(d)
OF	6.804	3.356	3.352

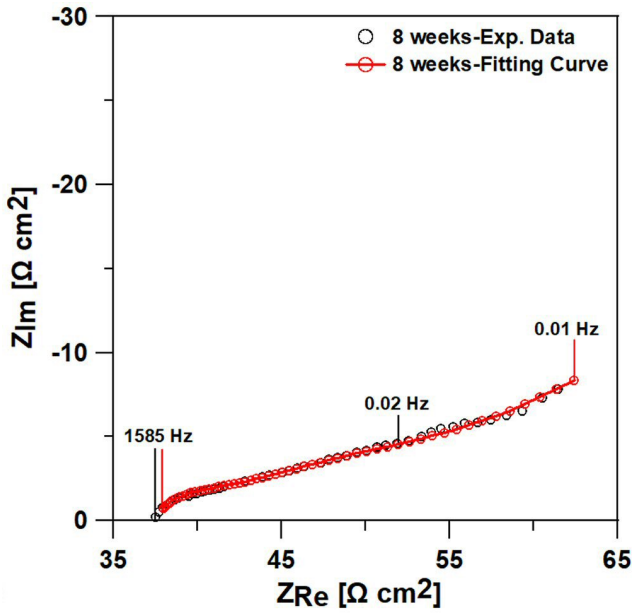

Figure D.12: Fitting curve for the painted scribed specimen No. 7, using the porous electrode theory, after 8 weeks- model (d)

After 12 weeks, the n_B value obtained using model (d) was above 1 (1.219), exhibitng also a wide uncertainty range (57.1%). Most of the parameters had large errors in this model, hence, model (b) was preferred.

B.3.8 Results for specimen No. 8

Table B.61: PSO and CNLLS fitting results and derived parameters for scribed specimen No. 8

Parameter	Unit	12 weeks		
Model		(f)	(f)-no ω_L	(f)-no ω_L-CNLLS
R_1	[Ω cm^2]	7.61	9.25	9.39±5.3%
ω_L	[s^{-1}]	0.062	-	
R_3	[Ω cm^2]	27.22	49.15	13.86±25.7%
Q_3	[F s^{n-1} cm^{-2}]	0.40	0.53	0.46±7.3%
n_3	[Ω cm^2]	0.499	0.725	0.682±3.2%
R_{ct}	[Ω cm^2]	0.32	1.10	0.86±11.2%
n		0.876	0.679	0.771±5.7%
Q	[F s^{n-1} cm^{-2}]	4.81 10^{-4}	3.79 10^{-3}	1.43 10^{-3}±41.7%
$\tau_{ct,CPE}$	[s]	4.44 10^{-5}	3.13 10^{-4}	1.68 10^{-4}

Table B.62: CNLLS goodness of fit values for scribed specimen No. 8, using the porous electrode theory

Parameter	12 weeks	
Model	(f)	(f)-no ω_L
χ^2	-	7.757 10^{-6}
Sum of squares	-	7.679 10^{-4}

Table B.63: PSO OF values for scribed specimen No. 8, using the porous electrode theory

Parameter	12 weeks	
Model	(f)	(f)-no ω_L
OF	3.149	3.229

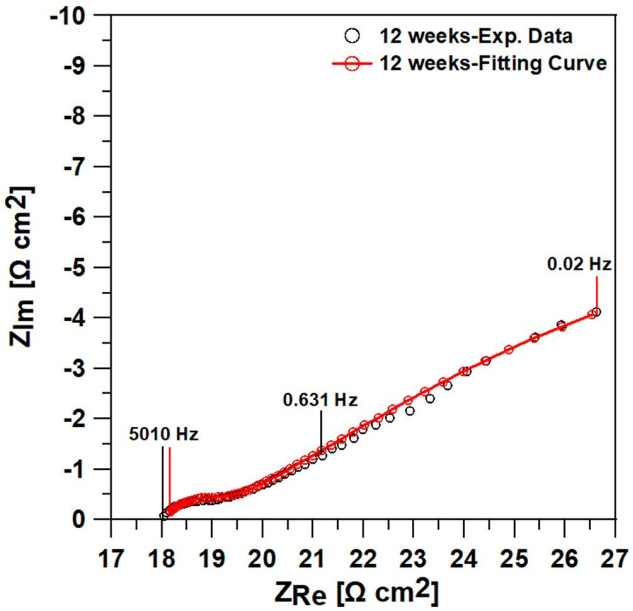

Figure D.13: Fitting curves for the painted scribed specimen No. 8, using the porous electrode theory, after 12 weeks-model (f) with $\omega_3 > \omega_L$

After 12 weeks, the version of model (f) with $\omega_3 > \omega_L$ provided trustworthy results. The obtained curve was similar to the generalized version of model (f) and the modified transmissive case. Since no error estimation can be performed for the general case of model (f), but the obtained curve is similar to the modified transmissive case, it shall be considered as a potential candidate for description of the experimental curve.

B.3.9 Summary of results using the porous electrode theory

Table B.64: Summary of selected porous electrode models for all the examined specimens during the 12-week exposure in the salt spray chamber

Specimen No.	6 weeks	8 weeks	12 weeks
1	(b)	(b)-(d)	(f)
2	(b)	(b)	(b)
3	(b)-(d)	(b)-(d)	(b)
4	(b)-(d)	(b)	(f)
5	(b)-(d)	(d)	(b)-(d)
6	No reliable signal	No reliable signal	(d)
7	No reliable signal	(d)	(b)
8	No reliable signal	No reliable signal	(f)-two versions

B.4 Difference in physical interpretation between finite length diffusion and porous electrode theory

B.4.1 Finite-length diffusion

In the case of finite-length diffusion impedance, the metallic substrate is covered with the porous oxide layer, for which the pore walls are considered inert [76]. In contrast to semi-infinite

diffusion, the diffusion layer thickness in the finite-length diffusion coincides with the corrosion layer thickness and the concentration gradient is considered to be developed within the pores of the oxide structure [74]. This type of impedance, being either transmissive, restricted or even anomalous, is largely the mode of diffusion of injected ions through thin film electrodes. More specifically, in these experiments the transmissive or restricted mode corresponds to the permeability of a boundary, through which the ions may penetrate or not, respectively. Variations of the ideal transmissive or reflective case could aslo be found. For instance, a CPE response is usually observed in the LF branch of restricted impedance, which could arise from some degree of permeability of the back contact (boundary) in injection experiments of ions through film electrodes or due to roughness or porosity of the back contact [88].

With regard to transmissive diffusion, in particular, except for the aforementioned experiments, where it is usually called bounded diffusion and refers to a permeable boundary [81,82], this type of impedance was used as an adjustment of semi-infinite Warburg diffusion, in order to be able to obtain a measurable, real impedance value at lower frequencies. This type of diffusion impedance is usually encountered in corroded flat electrodes. Pech-Canul and Turgoose [74] correlated the transmissive type of dissolved oxygen diffusion impedance through the porous corrosion layer with a restriction of diffusion through this layer. Finally, the limit of this impedance to a real impedance value at low frequencies makes it possible to be directly correlated with the polarization resistance [84].

With regard to the present experiments, modified restricted and modified transmissive diffusion impedance mechanisms efficiently described most of the experimental EIS curves. These specific mechanisms have not been observed in the literature for interpretation of corroding flat electrodes. Hence, the exact physical interpretation would be quite challenging. Borrowing the theory from insertion experiments, the transmissive/restricted response could result from a permeable/impermeable-rough boundary, the role of which could probably serve the porous oxide layer. As a general picture, the oxide layer would consist of the magnetite layer in direct contact with the electrode surface (not separated electrochemically), the rest of the layer would consist of the rest phases observed, such as hematite/maghemite oxides and α, β oxyhydroxides, while the outer rust layer would probably consist mainly of γ oxyhydroxide (lepidocrocite), since it is usually abundant in this region, in contact with the atmosphere.

B.4.2 Porous electrode theory

In this case, the metallic substrate is covered with a porous electroactive layer, which is a mixture of two phases, namely a liquid phase, which corresponds to the electrolytic solution inside the pores and a solid phase, which corresponds to the pore walls [183]. Orazem and Tribollet [76] used the porous electrode theory for interpretation of the cathodic reaction for the cast iron in drinking water problem. In their physical interpretation, magnetite macropores where on top of the cast iron substrate, covered with a microporous layer of green rust and carbonates, while the pores where filled with red rust and electrolytic solution. The observed rust phases in the work of Orazem and Tribollet [76] were similar to the ones observed in

the present study and which are presented in more detail in Kiosidou *et al.* [49, 66], except for the carbonates. Green rust could be apparent in the rust phase, since it transforms also to akaganeite, however, it was not observed during SEM observation. Hence, apart from the microporous layer covering the magnetite layer, the corrosion layer structure as proposed by Orazem and Tribollet [76] could be considered as representative of the corrosion layer structure of the present study.

With regard to the curves described using model (d) [183], the obtained EIS spectra exhibited a CPE response in the LF region, excluding correlation with a transmissive type of distributed diffusion impedance, as is suggested in the work of Barcia *et al.* [79] and Frateur *et al.* [78]. Even though the principle between the two transmission lines remains the same, that is, a distributed electrolyte resistance and a distributed interfacial impedance, there are two major differences: a) the interfacial impedance in the work of Bisquert [183] does not include a diffusion impedance, only the CPE response of the pore walls and b) in the work of Bisquert [183] there is also a boundary impedance Z_B at the electrolyte/electrode interface, which is also a CPE and accounts for the dispersion of the LF branch of the EIS response.

Appendix C

Appendix of Chapter 6

C.1 Foulers dimensions measurements for Exp. Si, Exp. PU1 and PU specimens immersed for 2 months in Elefsis

Table C.1: Mean area of the 32 *serpulidae* with circular cross-section found individually on the painted surface of Exp Si specimen, after 2 months immersion in Elefsis

Mean dimensions (length × width) (mm)	Mean area (mm^2)
15.5 × 0.50	7.75
5.5 × 0.30	1.65
14.0 × 0.45	6.30
14.5 × 0.33	4.78
6.5 × 0.60	3.90
18.0 × 0.60	10.80
12.2 × 1.00	12.20
7.0 × 0.30	2.10
8.5 × 0.50	4.25
3.5 × 0.50	1.75
6.0 × 0.40	2.40
5.1 × 0.70	3.57
3.0 × 0.50	1.50
8.5 × 0.50	4.00
8.5 × 0.60	5.10
4.0 × 0.30	1.20
5.0 × 0.50	2.50
6.0 × 0.45	2.70
15.0× 1.00	15.00
13.5× 0.40	5.40
10.0 × 0.80	8.00
5.0 × 0.50	2.50
6.5 × 0.60	3.90
8.5 × 0.60	5.10
5.0 × 1.00	5.00
3.0 × 0.50	1.50

9.0 × 0.50	4.50
5.5 × 0.80	4.40
11.0 × 1.00	11.00
10.0 × 0.80	8.00
7.0 × 0.50	3.50
7.0 × 0.70	4.90
Total area	161.15

Table C.2: Mean area of the 10 *serpulidae* with circular cross-section found individually on the painted surface of Exp PU1 specimen, after 2 months immersion in Elefsis

Mean dimensions (length × width) (mm)	Mean area (mm^2)
15.0 × 0.45	6.75
10.5 × 1.20	12.60
4.0 × 0.30	1.20
6.0 × 0.30	1.80
5.5 × 0.40	2.20
8.0 × 0.30	2.40
16.7 × 0.50	8.35
5.0 × 0.50	2.50
12.6 × 0.50	6.30
7.58 × 0.30	2.27
Total area	46.37

Table C.3: Mean diameter, number of individuals and total surface area covered by the 38 *spirorbinae* found on the surface of the PU specimen after 2 months immersion in Elefsis

Mean diameter (mm)	Number of individuals
0.6	1
0.8	4
1.0	9
1.1	1
1.2	4
1.3	1
1.4	2
1.5	5
1.6	2
1.7	2
1.9	1
2.0	4
2.1	1
2.5	1
Total area	60.41

C.2 Foulers dimensions measurements for Exp. Si, Exp. PU1 and PU specimens immersed for 4 months in Elefsis

Table C.4: Mean area of the 37 *serpulidae* found on the painted surface of Exp Si specimen, after 4 months immersion in Elefsis

Mean dimensions (length × width) (mm)	Mean area (mm^2)
10.343 × 0.4	4.137
7.686 × 0.4	3.074
4.567 × 0.4	1.827
4.278 × 0.5	2.139
6.000 × 0.5	3.000
18.732 × 0.5	9.366
16.704 × 0.7	11.693
16.838 × 0.5	8.169
6.534 × 0.5	3.267
15.428 × 0.5	7.714
26.379 × 0.6	15.827
7.700 × 0.5	3.850
11.600 × 0.3	3.480
13.000 × 0.3	3.900
8.100 × 0.4	3.240
10.100 × 0.6	6.060
2.000 × 2.4	4.800
21.212 × 0.5	10.606
15.404 × 0.7	10.783
39.899 × 1.01	40.298
12.121 × 0.5	6.061
9.595 × 0.4	3.838
21.717 × 0.5	10.858
10.606 × 0.5	5.303
19.134 × 0.36	6.888
23.354 × 0.7	16.348
11.191 × 0.7	7.834
9.386 × 0.36	3.379
14.801 × 0.54	7.992
9.025 × 1.083	9.774
10.830 × 0.36	3.899
15.162 × 0.7	10.613
8.303 × 0.4	3.321
22.744 × 0.4	9.098
11.552 × 0.4	4.621
18.411 × 0.7	12.888
38.628 × 0.7	27.040
Total area	306.985

Table C.5: Mean diameter and total surface area covered by the 23 *spirorbinae* found on the surface of the Exp Si specimen after 4 months immersion in Elefsis

Mean diameter (mm)	Mean area (mm^2)
0.596	0.279
0.666	0.348
0.404	0.128
1.215	1.159
1.279	1.285
0.754	0.446
1.468	1.692
1.136	1.013
0.833	0.545
1.182	1.097
0.866	0.589
0.596	0.279
1.267	1.261
1.552	1.892
1.055	0.874
1.120	0.985
0.936	0.688
0.408	0.131
1.323	1.375
1.043	0.854
1.229	1.186
1.100	0.950
0.700	0.385
Total area	19.441

Table C.6: Mean area of the 24 *serpulidae* found on the painted surface of Exp PU1 specimen, after 4 months immersion in Elefsis

Mean dimensions (length × width) (mm)	Mean area (mm^2)
3.210 × 0.128	0.411
20.560 × 0.583	11.986
24.707 × 0.571	14.108
19.553 × 0.833	16.288
3.667 × 0.417	1.529
10.394 × 0.290	3.014
6.329 × 0.290	1.835
17.489 × 0.362	6.331
9.958 × 0.435	4.332
4.019 × 0.290	1.165
6.174 × 0.290	1.790
5.082 × 0.667	3.390
4.853 × 0.333	1.616
6.869 × 0.333	2.287

10.441 × 0.5	5.220
4.852 × 0.333	1.616
26.917 × 0.6	16.150
7.136 × 0.4	2.854
41.607 × 2.5	104.017
20.667 × 0.5	10.333
4.673 × 0.2	0.935
16.959 × 0.4	6.784
25.195 × 0.5	12.597
31.172 × 0.8	24.938
Total area	255.526

Table C.7: Mean diameter, number of individuals and total surface area covered by the 452 *spirorbinae* found on the surface of the Exp PU1 specimen after 4 months immersion in Elefsis

Mean diameter (mm)	Number of individuals	Mean area (mm^2)
0.929	28	18.979
0.769	30	13.934
0.740	35	15.053
0.605	108	31.047
1.028	5	4.150
0.795	23	11.417
0.943	62	43.302
1.002	4	3.154
0.851	49	27.870
0.757	34	15.302
0.873	23	13.767
0.591	36	9.786
0.946	15	10.543
Total area		218.304

Table C.8: Mean diameter, number of individuals and total surface area covered by the 239 *spirorbinae* found on the surface of the PU specimen after 4 months immersion in Elefsis

Mean diameter (mm)	Number of individuals	Mean area (mm^2)
0.904	26	16.688
0.523	7	1.504
0.500	27	5.301
1.000	12	9.425
0.546	3	0.702
0.870	28	16.645
0.753	5	2.227
0.765	2	0.919
0.530	12	2.647
0.511	20	4.102
0.600	4	1.131
0.853	9	5.143
0.420	10	1.385

1.044	1	0.856
1.018	7	5.697
0.644	15	4.886
0.627	10	3.088
0.804	5	2.538
0.687	16	5.931
0.869	10	5.931
0.800	10	5.026
Total area		101.772

Table C.9: Mean area of the 67 *serpulidae* on the painted surface of PU specimen, after 4 months immersion in Elefsis

Mean dimensions (length × width) (mm)	Mean area (mm^2)
21.651 × 0.5	10.825
11.300 × 0.6	6.780
19.200 × 0.5	9.600
22.770 × 0.4	9.108
11.594 × 0.4	4.638
12.600 × 0.3	3.780
4.300 × 0.3	1.290
27.765 × 0.7	19.435
3.400 × 0.7	2.380
6.000 × 0.3	1.800
29.072 × 1.5	43.608
9.218 × 0.4	3.687
17.206 × 0.4	6.882
15.223 × 0.4	6.089
5.000 × 0.1	0.500
12.256 × 0.6	7.354
11.862 × 0.4	4.745
10.651 × 0.3	3.195
21.540 × 0.6	12.924
9.206 × 0.4	3.682
14.190 × 0.5	7.095
4.851 × 0.3	1.455
10.105 × 0.5	5.052
12.586 × 0.4	5.034
9.151 × 0.5	4.575
12.522 × 0.5	6.261
15.796 × 0.4	6.318
6.877 × 0.3	2.063
5.269 × 0.4	2.108
6.733 × 0.4	2.693
4.769 × 0.4	1.908
16.069 × 0.3	4.821
20.812 × 0.7	14.568
13.667 × 0.7	9.567

6.434 × 0.5	3.217
2.176 × 0.4	0.870
6.656 × 0.3	1.997
8.200 × 0.2	1.640
19.332 × 0.5	9.666
5.317 × 0.5	2.658
17.330 × 0.6	10.398
14.949 × 0.6	8.969
6.382 × 0.4	2.553
13.054 × 0.4	5.222
4.431 × 0.3	1.329
11.512 × 0.7	8.058
8.400 × 0.4	3.360
18.758 × 0.6	11.255
19.217 × 0.4	7.687
11.752 × 0.4	4.701
13.410 × 0.3	4.023
15.166 × 0.4	6.066
3.900 × 0.2	0.780
11.200 × 0.3	3.360
28.936 × 0.4	11.574
15.842 × 0.3	4.753
11.374 × 0.5	5.687
25.241 × 0.5	12.621
7.206 × 0.3	2.162
8.554 × 0.4	3.422
3.615 × 0.4	1.446
4.373 × 0.5	2.186
32.605 × 1.6	52.168
17.414 × 0.7	12.190
10.107 × 0.3	3.032
7.490 × 0.4	2.996
24.332 × 0.6	14.599
Total area	462.465

Table C.10: White surfaces including *spirobinae* spores found on PU painted specimen after 4 months immersion in Elefsis

Mean dimensions (length × width) (mm)	Mean area (mm^2)
6.107 × 4.888	29.851
5.410 × 1.517	8.207
6.466 × 4.508	29.149
2.930 × 2.308	6.762
8.599 × 3.662	31.489
7.000 × 3.500	24.500
6.556 × 4.852	31.810
Total area	161.768

C.3 Foulers dimensions measurements for Exp. Si, Exp. PU1 and PU specimens immersed for 6 months in Elefsis

Table C.11: Mean area of the 46 *serpulidae* on the painted surface of Exp Si specimen, after 6 months immersion in Elefsis

Mean dimensions (length × width) (mm)	Mean area (mm^2)
17.756 × 0.6	10.654
6.835 × 0.8	5.468
9.549 × 0.7	6.684
9.408 × 0.5	4.704
18.232 × 0.75	13.674
3.793 × 0.6	2.276
13.471 × 0.6	8.083
8.046 × 0.4	3.218
24.910 × 1.083	26.977
45.570 × 1.688	76.922
39.350 × 1.444	56.821
42.599 × 1.083	46.135
8.664 × 1.083	9.383
37.545 × 0.722	27.107
26.715 × 0.722	19.288
11.191 × 0.722	8.080
14.440 × 0.361	5.213
11.913 × 0.361	4.300
20.217 × 0.722	14.597
7.942 × 0.722	5.734
18.050 × 0.722	13.032
24.910 × 1.083	26.977
19.494 × 0.361	7.037
20.939 × 0.722	15.118
7.581 × 0.722	5.473
15.162 × 0.541	8.203
7.942 × 0.541	4.297
18.772 × 0.541	10.156
13.357 × 0.361	4.822
34.296 × 1.083	37.142
10.108 × 0.541	5.468
33.213 × 0.361	11.990
22.383 × 1.083	24.241
37.906 × 0.722	27.368
26.715 × 0.722	19.288
39.711 × 0.361	14.336
32.130 × 0.361	11.599
18.772 × 0.541	10.156
21.661 × 0.500	10.831

34.296 × 0.722	24.762
12.996 × 0.722	9.383
15.884 × 0.722	11.468
14.440 × 0.361	5.213
17.689 × 0.361	6.386
18.772 × 0.361	6.777
10.830 × 0.500	5.415
Total area	692.256

Table C.12: Mean diameter, number of individuals and total surface area covered by the 337 *spirorbinae* found on the surface of the Exp. Si specimen after 6 months immersion in Elefsis

Mean diameter (mm)	Number of individuals	Mean area (mm^2)
1.500	2	3.534
1.750	1	2.405
1.385	1	1.506
2.166	1	3.685
1.805	25	63.971
1.011	307	246.451
Total area		321.552

Table C.13: Mean area of the 4 *amphipods* on the painted surface of Exp Si specimen, after 6 months immersion in Elefsis

Mean dimensions (length × width) (mm)	Mean area (mm^2)
2.831 × 0.4	1.132
3.089 × 0.4	1.236
1.950 × 0.2	0.390
1.712 × 0.2	0.342
Total area	3.100

Table C.14: Mean area of the 4 largest *serpulidae* on the painted surface of Exp PU1 specimen, after 6 months immersion in Elefsis

Mean dimensions (length × width) (mm)	Mean area (mm^2)
46.209 × 2.888	133.451
50.180 × 3.249	163.035
78.700 × 3.249	255.696
77.978 × 4.332	337.801
Total area	889.983

Table C.15: Mean area of the 79 *serpulidae* on the painted surface of Exp PU1 specimen, after 6 months immersion in Elefsis

Mean dimensions (length × width) (mm)	Mean area (mm^2)
14.079 × 0.361	5.082
9.386 × 0.722	6.777
10.830 × 1.083	11.729
8.303 × 1.444	11.989
6.859 × 0.361	2.476
11.191 × 0.722	8.080
14.801 × 0.361	5.343
7.220 × 0.361	2.606
12.121 × 0.500	6.060
6.734 × 0.337	2.269
18.050 × 0.842	15.198
35.353 × 1.347	47.620
21.212 × 0.673	14.276
14.815 × 1.010	14.963
17.508 × 0.337	5.900
12.289 × 0.337	4.141
12.121 × 0.673	8.157
9.764 × 0.505	4.931
15.825 × 0.337	5.333
16.162 × 1.010	16.324
17.508 × 0.337	5.900
17.845× 0.337	6.014
12.795 × 0.337	4.312
10.774 × 0.337	3.631
14.815 × 0.337	4.993
18.518× 0.337	6.241
26.599 × 0.337	8.964
11.111 × 0.337	3.744
13.805 × 0.673	9.291
8.081× 0.673	5.438
10.438 × 0.337	3.518
14.814 × 0.673	9.970
14.814 × 0.673	9.970
7.408× 0.673	4.986
5.724 × 0.337	1.929
7.744 × 0.337	2.610
10.101 × 0.337	3.404
17.845× 0.673	12.010
19.865 × 0.337	6.694
11.111 × 0.337	3.744
15.151 × 0.337	5.106
7.744× 0.673	5.212
8.754 × 0.337	2.950
18.855 × 0.337	6.354
6.397 × 0.337	2.156
10.744× 0.673	7.251

4.040 × 0.337	1.361
3.800 × 0.600	2.280
6.000 × 0.600	3.600
6.300× 0.600	3.780
5.000 × 0.400	2.000
28 individuals of mean dimension 20.202×0.337=6.808	
Total area for the 28	190.624
Total area	549.291

Table C.16: Mean diameter, number of individuals and total surface area covered by the 489 *spirorbinae* found on the surface of the Exp. PU1 specimen after 6 months immersion in Elefsis

Mean diameter (mm)	Number of individuals	Mean area (mm^2)
0.781	2	0.958
0.679	1	0.362
1.150	1	1.039
1.100	3	2.851
0.250	2	0.098
0.350	11	1.056
0.600	1	0.283
0.330	3	0.256
0.550	4	0.948
0.300	1	0.071
0.450	1	0.159
0.400	2	0.251
0.700	4	1.539
1.200	3	3.393
0.611	2	0.586
0.948	3	2.118
0.335	1	0.088
0.289	1	0.065
1.064	2	1.778
1.237	1	1.202
0.750	3	1.326
0.270	1	0.057
1.500	2	3.534
0.800	2	1.006
1.000	4	3.140
0.058	1	0.003
1.171	1	1.077
0.838	2	1.102
0.332	1	0.086
0.723	1	0.410
1.400	2	3.079
2.232	1	3.913
1.300	3	3.982
2.020	2	6.409

0.894	2	1.255
1.556	1	1.901
1.890	1	2.805
1.347	140	199.505
1.683	270	600.650
Total area		854.341

Table C.17: Mean area of the 9 *amphipods* found on the painted surface of Exp. PU1 specimen, after 6 months immersion in Elefsis

Mean dimensions (length × width) (mm)	Mean area (mm^2)
2.45 × 0.45	1.10
2.50 × 0.50	1.25
1.60 × 0.30	0.48
3.20 × 0.56	1.79
2.40 × 0.48	1.15
2.90 × 0.45	1.30
2.50 × 0.40	1.00
1.60 × 0.32	0.51
3.20 × 0.40	1.28
Total area	9.86

Table C.18: Mean area of the 45 *serpulidae* on the painted surface of PU specimen, after 6 months immersion in Elefsis

Mean dimensions (length × width) (mm)	Mean area (mm^2)
72.727 × 3.030	220.363
14.241 × 1.300	18.513
20.805 × 1.300	27.046
21.256 × 0.800	17.005
36.364 × 1.010	36.728
14.646 × 1.515	22.189
29.648× 1.508	44.709
41.206 × 1.508	62.139
28.141 × 1.005	28.282
19.347 × 0.503	9.731
15.076 × 0.503	7.583
14.322× 0.503	7.204
6.030 × 0.503	3.033
13.819 × 0.503	6.951
11.558 × 1.759	20.331
15.578 × 0.503	7.836
11.056× 0.503	5.561
13.066 × 0.400	5.226
9.045 × 0.400	3.618
0.503 × 0.400	0.201

9.548 × 1.005	9.595
13.568× 0.252	3.419
12.061 × 0.252	3.039
9.950 × 0.754	7.502
14.071 × 0.754	10.609
6.533 × 0.400	2.613
5.025× 0.503	2.528
5.528 × 0.400	2.211
15.076 × 0.754	11.367
12.061 × 0.503	6.066
20.101 × 0.252	5.065
7.538× 0.754	5.683
7.538 × 0.754	5.683
5.508 × 0.754	4.153
6.533 × 0.252	1.646
15.076 × 0.252	3.799
16.583× 0.754	12.504
12.061 × 0.252	3.039
7.035 × 1.005	7.070
7.035 × 0.252	1.773
9.045 × 0.252	2.279
9.040× 0.252	2.278
30.654 × 0.252	7.725
25.628 × 0.400	10.251
6.533 × 0.252	1.646
Total area	687.792

Table C.19: Mean diameter, number of individuals and total surface area covered by the 324 *spirorbinae* found on the surface of the PU specimen after 6 months immersion in Elefsis

Mean diameter (mm)	Number of individuals	Mean area (mm^2)
0.395	1	0.122
0.447	2	0.314
0.273	1	0.058
0.286	2	0.128
0.388	1	0.118
0.382	1	0.115
0.512	2	0.411
0.263	2	0.108
0.433	1	0.147
0.328	1	0.084
0.465	20	3.396
0.655	15	5.054
0.483	6	1.097
0.945	17	11.923
0.778	2	0.951
0.740	1	0.430
0.844	1	0.559
1.052	1	0.868

0.410	2	0.263
0.374	1	0.110
0.707	1	0.392
0.300	1	0.071
0.234	1	0.043
0.553	20	4.795
1.350	1	1.431
0.696	1	0.380
0.070	1	0.004
0.590	11	3.007
3.015	2	14.279
1.508	40	71.394
1.005	47	37.284
1.257	20	24.800
2.010	8	25.385
1.759	5	12.150
0.754	10	4.465
2.513	4	19.832
0.503	25	4.958
0.252	38	1.888
0.201	6	0.190
Total area		254.963

C.4 Foulers dimensions measurements for Exp. Si specimen immersed for 8 months in Elefsis

Table C.20: Mean area of the 47 *serpulidae* on the painted surface of Exp Si specimen, after 8 months immersion in Elefsis

Mean dimensions (length × width) (mm)	Mean area (mm^2)
17.895 × 1.158	20.722
24.211 × 1.053	25.494
20.000 × 1.053	21.060
18.421 × 0.789	14.534
32.632 × 1.579	51.526
25.263 × 1.842	46.534
25.263 × 1.579	39.890
44.211 × 3.158	139.618
26.316 × 1.053	27.711
4.842 × 0.947	4.585
24.737 × 0.947	23.426
26.316 × 1.579	41.553
9.474 × 1.053	9.976
8.421 × 0.526	4.429
14.737 × 1.053	15.518
24.211 × 1.579	38.229
26.842 × 1.053	28.265

31.053 × 1.842	57.200
45.263 × 1.842	83.374
40.000 × 1.316	52.640
18.947 × 1.316	24.934
14.737 × 1.053	15.518
19.474 × 1.053	20.506
11.053 × 1.316	14.546
15.789 × 0.526	8.305
16.316 × 1.053	17.181
20.526 × 1.053	21.614
9.474 × 0.526	4.983
28.421 × 1.053	29.927
33.684 × 2.105	70.905
31.053 × 1.579	49.033
18.947 × 1.579	29.917
10.526 × 1.579	16.621
29.474 × 1.053	31.036
57.368 × 1.053	60.409
7.895 × 1.053	8.313
21.579 × 1.053	22.723
43.684 × 2.105	91.955
40.000 × 1.579	63.160
23.684 × 1.579	37.397
30.526 × 1.053	32.144
29.474 × 1.053	31.036
43.684 × 1.053	45.999
7.895 × 1.053	8.313
10.526 × 1.053	11.084
4.211 × 1.053	4.434
37.500 × 2.885	108.188
Total area	1626.465

Table C.21: Mean diameter, number of individuals and total surface area covered by the 141 *spirorbinae* found on the surface of the Exp Si specimen after 8 months immersion in Elefsis

Mean diameter (mm)	Number of individuals	Mean area (mm^2)
1.579	9	17.264
2.105	50	174.006
1.053	29	25.255
0.789	3	1.467
0.526	50	10.865
Total area		229.216

C.5 Foulers dimensions measurements for Exp. Si specimen immersed for 10 months in Elefsis

Table C.22: Mean area of the 30 *serpulidae* on the painted surface of Exp Si specimen, after 10 months immersion in Elefsis

Mean dimensions (length × width) (mm)	Mean area (mm^2)
32.292 × 1.042	33.648
17.188 × 1.042	17.910
62.500 × 1.042	65.125
26.563 × 1.042	27.679
35.938 × 1.042	37.447
46.875 × 1.563	73.266
26.563 × 1.042	27.679
53.125 × 4.167	221.372
79.167 × 1.042	82.492
86.458 × 5.208	450.273
20.313 × 1.563	31.749
11.458 × 1.042	11.939
60.417 × 1.042	62.955
40.625 × 1.042	42.331
32.292 × 0.781	25.220
68.750 × 3.067	210.856
38.542 × 1.823	70.262
20.833 × 1.302	27.125
17.708 × 1.563	27.678
22.917 × 1.563	35.819
6.250 × 1.823	11.394
13.542 × 1.042	14.111
18.229 × 1.042	18.995
33.854 × 1.302	44.078
30.208 × 1.302	39.331
30.729 × 1.042	32.020
27.604 × 1.042	28.763
14.583 × 1.563	22.793
22.917 × 1.563	35.819
28.646 × 1.563	44.774
Total area	1874.903

Table C.23: Mean diameter, number of individuals and total surface area covered by the 156 *spirorbinae* found on the surface of the Exp Si specimen after 10 months immersion in Elefsis

Mean diameter (mm)	Number of individuals	Mean area (mm^2)
0.521	75	15.989
0.781	6	2.874
1.042	14	11.939
1.302	15	19.971
1.563	30	57.561
2.083	11	37.485
2.604	5	26.628

Total area	172.447

C.6 Foulers dimensions measurements for Exp. Si and Exp. PU1 specimens immersed for 10 months in Elefsis

Table C.24: Mean area of the 52 *serpulidae* on the painted surface of Exp Si specimen, after 12 months immersion in Elefsis

Mean dimensions (length × width) (mm)	Mean area (mm^2)
60.118 × 2.224	133.702
34.516 × 0.900	31.064
13.324 × 0.500	6.662
13.028 × 0.444	5.784
4.396 × 0.444	1.952
5.735 × 0.259	1.485
3.391 × 0.259	0.878
3.668 × 0.196	0.719
11.485 × 0.593	6.811
11.280 × 0.593	6.689
7.248 × 0.417	3.022
5.345 × 0.417	2.229
9.375 × 0.521	4.884
16.146 × 0.521	8.412
3.125 × 0.521	1.628
8.333 × 0.521	4.341
3.125 × 0.521	1.628
5.729 × 0.521	2.985
4.688 × 0.521	2.442
13.542 × 0.521	7.055
32.813 × 1.042	34.191
22.396 × 0.521	11.668
12.500 × 0.521	6.513
34.375 × 1.042	35.819
9.375 × 0.521	4.884
7.813 × 0.781	6.102
25.521 × 0.781	19.932
7.292 × 0.781	5.695
14.063× 0.781	10.983
20.833 × 0.521	10.854
20.833 × 1.042	21.708
16.667 × 0.521	8.684
10.417× 1.042	10.855
11.458 × 0.781	8.949
6.250 × 0.521	3.256
7.292 × 0.521	3.799

16.146× 0.521	8.412
9.375 × 0.521	4.884
10.417 × 0.521	5.427
23.958 × 0.521	12.482
29.688× 0.521	15.467
25.000 × 0.521	13.025
10.938 × 1.042	11.397
5.729 × 1.042	5.970
13.542× 0.781	10.576
8.333 × 0.521	4.341
17.708 × 0.781	13.830
5.729 × 0.521	2.985
10.938× 0.521	5.699
4.688 × 0.521	2.442
5.208 × 0.521	2.713
5.215 × 0.521	2.717
Total area	560.631

Table C.25: Mean diameter, number of individuals and total surface area covered by the 175 *spirorbinae* found on the surface of the Exp Si specimen after 12 months immersion in Elefsis

Mean diameter (mm)	Number of individuals	Mean area (mm^2)
0.351	4	0.387
0.642	1	0.324
0.584	2	0.536
1.984	1	3.092
1.832	1	2.636
0.495	3	0.577
1.333	2	2.791
0.810	10	5.153
0.948	1	0.706
1.285	1	1.297
0.275	3	0.178
0.309	1	0.075
1.179	2	2.183
1.915	1	2.880
0.431	2	0.292
0.519	1	0.212
0.222	1	0.039
0.417	7	0.956
1.302	4	5.326
1.563	8	15.350
2.083	1	3.408
1.042	17	14.497
0.521	100	21.319
1.823	1	2.610
Total area		86.822

Table C.26: Mean area of the 8 *serpulidae* on the painted surface of Exp PU1 specimen, after 12 months immersion in Elefsis

Mean dimensions (length × width) (mm)	Mean area (mm^2)
137.158 × 4.372	599.655
31.148 × 2.186	68.090
40.984 × 2.186	89.591
21.858 × 1.639	35.825
21.134 × 1.031	21.789
39.175 × 1.546	60.565
42.268 × 1.546	65.346
18.033 × 1.546	27.879
Total area	968.74

Table C.27: Mean area of encrusting bryozoans observed on the painted surface of Exp PU1 specimen, after 12 months immersion in Elefsis

Mean dimensions (length × width) (mm)	Mean area (mm^2)
8.197 × 6.557	53.748
25.137 × 13.115	329.672
40.984 × 6.011	246.355
18.033 × 21.311	384.301
7.104 × 6.011	42.702
8.197 × 13.661	111.979
11.475 × 17.486	200.652
12.022 × 8.197	98.544
4.918 × 6.011	29.562
7.104 × 7.650	54.346
39.891 × 7.104	283.386
39.344 × 4.372	172.012
19.126 × 12.842	245.606
14.208 × 34.426	489.125
6.557 × 5.464	35.827
4.918 × 5.464	26.872
3.825 × 4.918	18.811
(16.393 × 4.372)/2	35.835
7.104 × 7.650	54.346
7.104 × 5.464	38.816
10.929 × 15.301	167.225
6.557 × 6.011	39.414
(10.929 × 2.732)/2	14.929
8.197 × 14.208	116.463
12.022 × 10.383	124.824
9.290 × 13.661	126.911
7.104 × 6.011	42.702
10.929 × 6.557	71.661

8.197 × 6.011	49.272
10.929 × 5.464	59.716
8.197 × 10.929	89.585
27.322 × 5.464	149.287
(4.918 × 5.464)/2	13.436
10.929 × 3.825	41.803
9.836 × 8.197	80.626
4.372 × 9.836	43.003
5.464 × 5.464	29.855
12.568 × 6.557	82.408
(14.208 × 5.464)/2	38.816
13.115 × 4.918	64.499
(16.393 × 3.825)/2	31.352
Total area	4430.284

C.7 Foulers dimensions measurements for Exp. PU2 specimen immersed for 4 months in Elefsis

Table C.28: Mean diameter, number of individuals and total surface area covered by the 155 *spirorbinae* found on the surface of the Exp PU2 specimen after 4 months immersion in Elefsis

Mean diameter (mm)	Number of individuals	Mean area (mm^2)
0.991	5	3.855
1.330	3	4.167
0.696	4	1.520
0.748	6	2.640
1.617	3	6.159
1.432	5	8.050
0.835	5	2.740
1.129	9	9.009
1.228	7	8.288
0.783	3	1.446
1.254	6	7.416
0.866	5	2.945
1.901	2	5.678
2.147	2	7.240
1.021	7	5.733
0.643	3	0.975
1.850	9	24.201
0.918	8	5.296
0.947	5	3.525
1.530	5	9.190
1.104	9	8.613
1.197	4	4.500
1.356	7	10.108
1.784	7	17.507
1.572	5	9.700
1.501	6	10.620

1.293	4	5.252
2.018	6	19.182
0.563	1	0.249
1.682	4	8.888
Total area		214.692

C.8 Foulers dimensions measurements for Exp. PU2 specimen immersed for 6 months in Elefsis

Table C.29: Mean diameter, number of individuals and total surface area covered by the 403 *spirorbinae* found on the surface of the Exp PU2 specimen after 6 months immersion in Elefsis

Mean diameter (mm)	Number of individuals	Mean area (mm^2)
1.860	5	13.586
0.952	9	6.406
1.559	6	11.453
1.417	7	11.039
1.023	40	32.878
0.912	3	1.960
0.880	11	6.690
0.707	6	2.355
0.411	9	1.194
0.666	13	4.529
1.331	13	18.088
0.470	10	1.735
1.170	71	76.334
0.760	12	5.444
0.558	12	2.935
0.238	7	0.311
0.802	5	2.526
2.959	1	6.877
1.206	8	9.138
1.602	3	6.047
0.590	3	0.820
1.228	58	68.693
0.500	3	0.589
0.304	11	0.798
1.672	63	138.326
0.601	2	0.567
0.355	4	0.396
1.356	5	7.221
0.157	3	0.058
Total area		438.994

Table C.30: Mean area of the 8 *serpulidae* on the painted surface of Exp PU2 specimen, after 6 months immersion in Elefsis

Mean dimensions	Mean area

(length × width) (mm)	(mm^2)
2.980 × 0.180	0.536
3.167 × 0.180	0.570
2.808 × 0.180	0.505
11.822 × 1.161	13.725
2.679 × 0.268	0.718
4.386 × 0.487	2.112
4.572 × 0.357	1.632
5.031 × 0.316	1.590
Total area	21.388

C.9 Foulers dimensions measurements for Exp. PU2 specimen immersed for 8 months in Elefsis

Table C.31: Mean diameter, number of individuals and total surface area covered by the 876 *spirorbinae* found on the surface of the Exp PU2 specimen after 8 months immersion in Elefsis

Mean diameter (mm)	Number of individuals	Mean area (mm^2)
1.397	4	6.131
0.772	89	41.660
0.369	33	3.529
0.829	6	3.239
0.470	21	3.643
0.290	16	1.057
0.230	31	1.288
0.111	2	0.019
0.163	3	0.063
0.268	30	1.692
0.781	3	1.437
0.595	186	51.717
0.301	30	2.135
0.388	23	2.719
0.666	143	49.817
0.515	12	2.500
0.923	12	8.029
0.410	33	4.357
1.000	32	25.133
0.328	33	2.788
0.856	20	11.510
0.710	21	8.314
0.805	5	2.545
0.983	17	12.902
1.626	3	6.229
1.277	11	14.088
0.201	13	0.413
0.908	10	6.475
0.542	10	2.307

1.180	10	10.936
2.813	1	6.215
1.463	2	3.362
1.997	2	6.264
0.454	9	1.457
Total area		305.971

Table C.32: Mean area of the 14 *serpulidae* on the painted surface of Exp PU2 specimen, after 8 months immersion in Elefsis

Mean dimensions (length × width) (mm)	Mean area (mm^2)
4.955 × 0.370	1.833
17.144 × 1.407	24.122
6.360 × 0.148	0.941
3.127 × 0.148	0.463
88.664 × 2.157	191.248
5.579 × 0.147	0.820
6.370 × 0.147	0.936
13.976 × 1.818	25.408
12.936 × 1.222	15.808
3.604 × 0.444	1.600
3.433 × 0.444	1.524
3.846 × 0.147	0.565
5.721 × 4.345	24.858
11.765 × 0.606	7.130
Total area	297.256

Table C.33: Mean area of *bryozoans* found in 16 locations on the painted surface of Exp PU2 specimen, after 8 months immersion in Elefsis

Mean dimensions (length × width) (mm)	Mean area (mm^2)
5.157 × 7.489	38.621
7.494 × 0.114	0.854
1.902 × 0.457	0.869
1.203 × 0.875	1.053
2.193 × 0.938	2.057
1.153 × 0.625	0.721
1.841 × 2.500	4.603
2.058 × 1.778	3.659
1.672 × 1.481	2.476
1.245 × 1.111	1.383
4.316 × 1.828	7.890
12.534 × 14.773	185.165
5.828 × 1.628	9.488
2.355 × 1.298	3.057
(3.885 × 9.175)/2	17.822

$(5.120 \times 9.175)/2$	23.488
Total area	303.206

C.10 Foulers dimensions measurements for Exp. PU2 specimen immersed for 10 months in Elefsis

Table C.34: Mean diameter, number of individuals and total surface area covered by the 467 *spirorbinae* found on the surface of the Exp PU2 specimen after 10 months immersion in Elefsis

Mean diameter (mm)	Number of individuals	Mean area (mm^2)
0.616	40	11.921
0.752	26	11.548
0.594	14	3.880
0.819	31	16.331
0.752	38	16.878
1.764	21	51.322
0.670	75	26.442
0.701	31	11.964
0.576	30	7.817
0.867	35	20.663
0.669	38	13.358
0.472	28	4.899
1.105	13	12.467
0.549	47	11.126
Total area		220.616

Table C.35: Mean area of the 6 *serpulidae* on the painted surface of Exp PU2 specimen, after 10 months immersion in Elefsis

Mean dimensions (length × width) (mm)	Mean area (mm^2)
14.116×0.173	2.442
10.355×1.188	12.302
11.173×0.424	4.737
9.414×0.402	3.784
13.943×0.621	8.659
15.497×0.251	3.890
Total area	35.814

C.11 Foulers dimensions measurements for Exp. PU2 specimen immersed for 12 months in Elefsis

Table C.36: Mean diameter, number of individuals and total surface area covered by the 275 *spirorbinae* found on the surface of the Exp PU2 specimen after 12 months immersion in Elefsis

Mean diameter (mm)	Number of individuals	Mean area (mm^2)
1.106	23	22.097
0.528	22	4.817
0.709	23	9.081
0.975	41	30.611
1.076	64	58.196
0.871	54	32.175
0.576	26	6.775
0.907	22	14.214
Total area		177.966

Table C.37: Mean area of the 7 *serpulidae* on the painted surface of Exp PU2 specimen, after 12 months immersion in Elefsis

Mean dimensions (length × width) (mm)	Mean area (mm^2)
19.165 × 1.006	19.280
16.242 × 0.547	8.884
16.319 × 0.702	11.456
13.798 × 1.045	14.419
17.811 × 1.600	28.498
19.829 × 1.023	20.285
25.549 × 0.908	23.198
Total area	126.02